

# **Geology of the Earthquake Source**

**A Volume in Honour of Rick Sibson**

Edited by

Å. Fagereng, V. G. Toy and J. V. Rowland



**Geological Society  
Special Publication 359**



Geology of the Earthquake Source:  
A Volume in Honour of Rick Sibson

The Geological Society of London  
**Books Editorial Committee**

**Chief Editor**

BOB PANKHURST (UK)

**Society Books Editors**

JOHN GREGORY (UK)

JIM GRIFFITHS (UK)

JOHN HOWE (UK)

RICK LAW (USA)

PHIL LEAT (UK)

NICK ROBINS (UK)

RANDELL STEPHENSON (UK)

**Society Books Advisors**

MIKE BROWN (USA)

ERIC BUFFETAUT (FRANCE)

JONATHAN CRAIG (ITALY)

RETO GIERÉ (GERMANY)

TOM McCANN (GERMANY)

DOUG STEAD (CANADA)

GONZALO VEIGA (ARGENTINA)

MAARTEN DE WIT (SOUTH AFRICA)

**Geological Society books refereeing procedures**

The Society makes every effort to ensure that the scientific and production quality of its books matches that of its journals. Since 1997, all book proposals have been refereed by specialist reviewers as well as by the Society's Books Editorial Committee. If the referees identify weaknesses in the proposal, these must be addressed before the proposal is accepted.

Once the book is accepted, the Society Book Editors ensure that the volume editors follow strict guidelines on refereeing and quality control. We insist that individual papers can only be accepted after satisfactory review by two independent referees. The questions on the review forms are similar to those for *Journal of the Geological Society*. The referees' forms and comments must be available to the Society's Book Editors on request.

Although many of the books result from meetings, the editors are expected to commission papers that were not presented at the meeting to ensure that the book provides a balanced coverage of the subject. Being accepted for presentation at the meeting does not guarantee inclusion in the book.

More information about submitting a proposal and producing a book for the Society can be found on its web site: [www.geolsoc.org.uk](http://www.geolsoc.org.uk).

It is recommended that reference to all or part of this book should be made in one of the following ways:

FAGERENG, Å., TOY, V. G. & ROWLAND, J. V. (eds) 2011. *Geology of the Earthquake Source: A Volume in Honour of Rick Sibson*. Geological Society, London, Special Publications, **359**.

TOY V. G., RITCHIE, S. & SIBSON, R. H. 2011. Diverse habitats of pseudotachylytes in the Alpine Fault Zone and relationships to current seismicity. In: FAGERENG, Å., TOY, V. G. & ROWLAND, J. V. (eds) *Geology of the Earthquake Source: A Volume in Honour of Rick Sibson*. Geological Society, London, Special Publications, **359**, 115–133.

GEOLOGICAL SOCIETY SPECIAL PUBLICATION NO. 359

**Geology of the Earthquake Source:  
A Volume in Honour of Rick Sibson**

EDITED BY

Å. FAGERENG

University of Cape Town, South Africa

V. G. TOY

University of Otago, New Zealand

and

J. V. ROWLAND

University of Auckland, New Zealand

2011

Published by

The Geological Society

London

## THE GEOLOGICAL SOCIETY

The Geological Society of London (GSL) was founded in 1807. It is the oldest national geological society in the world and the largest in Europe. It was incorporated under Royal Charter in 1825 and is Registered Charity 210161.

The Society is the UK national learned and professional society for geology with a worldwide Fellowship (FGS) of over 10 000. The Society has the power to confer Chartered status on suitably qualified Fellows, and about 2000 of the Fellowship carry the title (CGeoL). Chartered Geologists may also obtain the equivalent European title, European Geologist (EurGeoL). One fifth of the Society's fellowship resides outside the UK. To find out more about the Society, log on to [www.geolsoc.org.uk](http://www.geolsoc.org.uk).

**The Geological Society Publishing House** (Bath, UK) produces the Society's international journals and books, and acts as European distributor for selected publications of the American Association of Petroleum Geologists (AAPG), the Indonesian Petroleum Association (IPA), the Geological Society of America (GSA), the Society for Sedimentary Geology (SEPM) and the Geologists' Association (GA). Joint marketing agreements ensure that GSL Fellows may purchase these societies' publications at a discount. The Society's online bookshop (accessible from [www.geolsoc.org.uk](http://www.geolsoc.org.uk)) offers secure book purchasing with your credit or debit card.

To find out about joining the Society and benefiting from substantial discounts on publications of GSL and other societies worldwide, consult [www.geolsoc.org.uk](http://www.geolsoc.org.uk), or contact the Fellowship Department at: The Geological Society, Burlington House, Piccadilly, London W1J 0BG: Tel. +44 (0)20 7434 9944; Fax +44 (0)20 7439 8975; E-mail: [enquiries@geolsoc.org.uk](mailto:enquiries@geolsoc.org.uk).

For information about the Society's meetings, consult *Events* on [www.geolsoc.org.uk](http://www.geolsoc.org.uk). To find out more about the Society's Corporate Affiliates Scheme, write to [enquiries@geolsoc.org.uk](mailto:enquiries@geolsoc.org.uk).

Published by The Geological Society from:

The Geological Society Publishing House, Unit 7, Brassmill Enterprise Centre, Brassmill Lane, Bath BA1 3JN, UK

(*Orders*: Tel. +44 (0)1225 445046, Fax +44 (0)1225 442836)

Online bookshop: [www.geolsoc.org.uk/bookshop](http://www.geolsoc.org.uk/bookshop)

The publishers make no representation, express or implied, with regard to the accuracy of the information contained in this book and cannot accept any legal responsibility for any errors or omissions that may be made.

© The Geological Society of London 2011. All rights reserved. No reproduction, copy or transmission of this publication may be made without written permission. No paragraph of this publication may be reproduced, copied or transmitted save with the provisions of The Copyright Licensing Agency Ltd, Saffron House, 6–10 Kirby Street, London EC1N 8TS, UK. Users registered with the Copyright Clearance Center, 222 Rosewood Drive, Danvers, MA 01923, USA: the item-fee code for this publication is 0305-8719/11/\$15.00.

### **British Library Cataloguing in Publication Data**

A catalogue record for this book is available from the British Library.

ISBN 978-1-86239-337-0

Typeset by Techset Composition Ltd, Salisbury, UK

Printed by MPG Books Ltd, Bodmin, Cornwall, UK

### **Distributors**

#### **North America**

For trade and institutional orders:

The Geological Society, c/o AIDC, 82 Winter Sport Lane, Williston, VT 05495, USA

*Orders*: Tel. +1 800-972-9892

Fax +1 802-864-7626

E-mail: [gsl.orders@aidcvt.com](mailto:gsl.orders@aidcvt.com)

For individual and corporate orders:

AAPG Bookstore, PO Box 979, Tulsa, OK 74101-0979, USA

*Orders*: Tel. +1 918-584-2555

Fax +1 918-560-2652

E-mail: [bookstore@aapg.org](mailto:bookstore@aapg.org)

Website: <http://bookstore.aapg.org>

#### **India**

Affiliated East-West Press Private Ltd, Marketing Division, G-1/16 Ansari Road, Darya Ganj, New Delhi 110 002, India

*Orders*: Tel. +91 11 2327-9113/2326-4180

Fax +91 11 2326-0538

E-mail: [affiliat@vsnl.com](mailto:affiliat@vsnl.com)

# Contents

Preface	vii
---------	-----

## Introduction

FAGERENG, Å. & TOY, V. G. Geology of the earthquake source: an introduction	1
---	---

## Observations in active fault zones

BOULLIER, A.-M. Fault-zone geology: lessons from drilling through the Nojima and Chelungpu faults	17
---	----

ELLSWORTH, W. L. & MALIN, P. E. Deep rock damage in the San Andreas Fault revealed by P- and S-type fault-zone-guided waves	39
---	----

## Fault rocks and fault-slip styles

FAGERENG, Å. Geology of the seismogenic subduction thrust interface	55
---	----

ROWE, C. D., MENEGHINI, F. & MOORE, J. C. Textural record of the seismic cycle: strain-rate variation in an ancient subduction thrust	77
---	----

SMITH, S. A. F., HOLDsworth, R. E., COLLETTINI, C. & PEARCE, M. A. The microstructural character and mechanical significance of fault rocks associated with a continental low-angle normal fault: the Zuccale Fault, Elba Island, Italy	97
---	----

## The base of the seismogenic zone

TOY, V. G., RITCHIE, S. & SIBSON, R. H. Diverse habitats of pseudotachylytes in the Alpine Fault Zone and relationships to current seismicity	115
---	-----

ALLEN, J. L. & SHAW, C. A. Seismogenic structure of a crystalline thrust fault: fabric anisotropy and coeval pseudotachylyte–mylonitic pseudotachylyte in the Grizzly Creek Shear Zone, Colorado	135
--	-----

ALTENBERGER, U., PROSSER, G., RUGGIERO, M. & GÜNTER, C. Microstructure and petrology of a Calabrian garnet-bearing pseudotachylyte – a link to lower-crustal seismicity	153
---	-----

MOECHER, D. P. & STELTENPOHL, M. G. Petrological evidence for co-seismic slip in extending middle–lower continental crust: Heier’s zone of pseudotachylyte, north Norway	169
--	-----

NÜCHTER, J.-A. & ELLIS, S. Mid-crustal controls on episodic stress-field rotation around major reverse, normal and strike-slip faults	187
---	-----

## Effects of fluids on faulting

BARKER, S. L. L. & COX, S. F. Evolution of fluid chemistry and fluid-flow pathways during folding and faulting: an example from Taemas, NSW, Australia	203
--	-----

NURIEL, P., ROSENBAUM, G., UYSAL, T. I., ZHAO, J., GOLDING, S. D., WEINBERGER, R., KARABACAK, V. & AVNI, Y. Formation of fault-related calcite precipitates and their implications for dating fault activity in the East Anatolian and Dead Sea fault zones	229
---	-----

UPTON, P., CRAW, D., YU, B. & CHEN, Y.-G. Controls on fluid flow in transpressive orogens, Taiwan and New Zealand 249

UJIIE, K., TSUTSUMI, A. & KAMEDA, J. Reproduction of thermal pressurization and fluidization of clay-rich fault gouges by high-velocity friction experiments and implications for seismic slip in natural faults 267

#### Fault reactivation v. initiation

NORTJE, G. S., OLIVER, N. H. S., BLENKINSOP, T. G., KEYS, D. L., McLELLAN, J. G. & OXENBURGH, S. New faults v. fault reactivation: implications for fault cohesion, fluid flow and copper mineralization, Mount Gordon Fault Zone, Mount Isa District, Australia 287

SCHOLZ, C. H. First-order splay faults: dip-slip examples 313

#### Future directions

SIBSON, R. H. The scope of earthquake geology 319

Index 333

## Preface

'Never came reformation in a flood, with such heady  
currance, scouring faults'

*W. Shakespeare – King Henry Vth*

In early 2009, Emeritus Professor Richard (Rick) H. Sibson retired from most active teaching in the Department of Geology at the University of Otago, New Zealand (Fig. 1). Rick is an extraordinary teacher, who enjoys putting on a 'show', where impeccably presented science is peppered with judicious use of quotes from the classical literature (and well-directed chalk). His series of introductory lectures to first-year students at the University of Otago, which focus on earth resources and their depletion, has, over the years, inspired many to pursue a Geology major. At higher levels, he has ensured students have a solid grounding in problem solving from a quantitative standpoint, and rigorous training in the principles of structural geology. He has also supervised a number of graduate students, all of whom have benefited from his suggestions to think about the implications of their research in a wider context and most of whom have gone on to hold high-profile positions in academia or industry.

Furthermore, during his teaching and research career, Rick revolutionized the understanding of faulting processes, earthquakes and fluid flow in the Earth's crust, and pioneered the integrated interpretation of fault dynamics, earthquake mechanics and fluid–rock interaction. Through a series of landmark publications over the past 35 years, he has significantly influenced global research directions in the fields of structural geology and seismotectonics.

Rick was born and raised in Auckland, New Zealand. His early education at Kings College was supplemented by interaction with his uncle, renowned naturalist Charles Alexander Flemming, and by his father, a Classics teacher and amateur ornithologist; we suspect numerous bird-watching trips in place of summer holidays prompted his interest in Geology, which is difficult to pursue in swamps. After graduating with a BSc(Hons) in Geology from the University of Auckland in 1968, Rick moved to Imperial College London, where he obtained MSc and PhD degrees. His PhD research on exhumed fault rocks from the Outer Hebrides Fault Zone precipitated his efforts to integrate structural geology and seismology – in what has now

become the interdisciplinary field of earthquake science. It was here that he recognized pseudotachylite as the friction melt formed in ancient earthquakes, and that the idea of thermal pressurization as a fault-weakening mechanism was born.

Rick's geological field observations in the Outer Hebrides led to the idea that the base of the crustal seismogenic zone may be controlled by the depth of the brittle–viscous transition in the dominant mineral phase. He tested this idea against geophysical data by collating earthquake locations during a year-long visit at the US Geological Survey in 1981. His papers that deal with the relative importance of brittle and ductile deformation, and the seismic style of crustal faults – written under the influence of his colleagues at Menlo Park during this time – are still frequently cited today.

After his time at USGS, Rick moved to University of California at Santa Barbara, where he stayed until he moved back to New Zealand in 1990, to become Head of Department of Geology at the University of Otago. Students at both of these universities have benefited from Rick's dedication to teaching, and from the geological insights he has shared with undergraduate and graduate students through the years. His teaching drew heavily from his research interests; one could say he was a pioneer of the concept of 'research-informed teaching'. His insights into active fault-zone processes and his ability to link active deformation to observations in exhumed fault zones has become a framework not only for understanding earthquake mechanics, the extent of the seismogenic zone and the fault reactivation during tectonic inversion, but has also been successfully applied to economic geology and the understanding of fault-hosted hydrothermal mineralization. The 'fault valve' theory has been particularly useful for understanding the interplay between fluid flow and local stress regimes, in light of the transient permeability changes intimately linked to the earthquake cycle.

To recognize Rick's considerable scientific contributions during the course of his teaching career, a special symposium, 'Geological and Geophysical Signatures of Earth Deformation and Fluid Flow', was held as part of the Geosciences '09 conference in Oamaru, New Zealand, 23–27 November 2009. This Special Publication is partly based on papers presented in this workshop, but also contains



**Fig. 1.** Rick after a hang-glider flight at Coronet Peak, Central Otago, New Zealand (photograph courtesy of Simon Cox).

contributions from authors who were not able to participate in the symposium and now join in celebrating Rick's career through their participation in this dedicated volume.

We are grateful to the University of Otago for funding in support of the symposium at Geosciences '09, to the convenors (Phaedra Upton and Virginia Toy) and organizing committee of Geosciences '09, without whom the symposium, and consequently this volume, would not have been possible, and particularly to Rick's numerous colleagues for participating in the symposium. We also wish to

thank all the reviewers who volunteered their time to improve the papers in this volume; their effort is greatly appreciated.

Finally, although Rick has retired from his teaching post at the University of Otago, he is still an active participant in our scientific community. We eagerly anticipate the research he will publish in coming years.

ÅKE FAGERENG  
VIRGINIA G. TOY  
JULIE ROWLAND

# Geology of the earthquake source: an introduction

ÅKE FAGERENG<sup>1\*</sup> & VIRGINIA G. TOY<sup>2</sup>

<sup>1</sup>*Department of Geological Sciences, University of Cape Town, Private Bag X3,  
Rondebosch 7701, South Africa*

<sup>2</sup>*Department of Geology, University of Otago, PO Box 56, Dunedin 9054, New Zealand*

\*Corresponding author (e-mail: [ake.fagereng@uct.ac.za](mailto:ake.fagereng@uct.ac.za))

**Abstract:** Earthquakes arise from frictional ‘stick–slip’ instabilities as elastic strain is released by shear failure, almost always on a pre-existing fault. How the faulted rock responds to applied shear stress depends on its composition, environmental conditions (such as temperature and pressure), fluid presence and strain rate. These geological and physical variables determine the shear strength and frictional stability of a fault, and the dominant mineral deformation mechanism. To differing degrees, these effects ultimately control the partitioning between seismic and aseismic deformation, and are recorded by fault-rock textures. The scale-invariance of earthquake slip allows for extrapolation of geological and geophysical observations of earthquake-related deformation. Here we emphasize that the seismological character of a fault is highly dependent on fault geology, and that the high frequency of earthquakes observed by geophysical monitoring demands consideration of seismic slip as a major mechanism of finite fault displacement in the geological record.

Rick Sibson has, throughout his career, pointed out that earthquakes occur in rocks (e.g. Sibson 1975, 1977, 1984, 1986, 1989, 2002, 2003). This simple fact implies that fault rocks exert a critical control on earthquake nucleation and propagation, and should contain an integrated record of earthquakes. Reading this record, Sibson has added significantly to our understanding of how faults work. His intuitive ability to relate structures in exhumed rocks to seismological observations of active deformation has contributed significantly to bridging the gap between how geologists and geophysicists think about fault mechanics, and has led to the development of earthquake science as a truly interdisciplinary field. This volume celebrates Rick Sibson’s career by bringing together a collection of papers that present innovative studies spanning a range of topics within the field of earthquake geology. Included are descriptions of fault-zone rocks from active and ancient faults, rock deformation experiments at seismic slip rates, and theoretical treatments of fault initiation and slip.

In this introduction the mechanism of earthquake faulting – generally accepted to be the release of tectonic elastic strain energy stored in a rock volume – by fast slip on a pre-existing or new fault (Brace & Byerlee 1966) is discussed. Also included is a short discussion on how rate- and state-variable frictional stability may affect the rate at which fault slip occurs (Dieterich 1972, 1979). The deformation mechanisms likely to be active at different conditions within a fault zone, which may lead to seismic or aseismic deformation, are outlined, and

the geological and physical parameters likely to control their prevalence discussed. The mechanisms by which rocks were deformed can be inferred from their textures (Knipe 1989); these relationships for the typical fault rocks encountered in exhumed fault zones are reviewed in this introduction. A conceptual fault-zone model building on previous review works (e.g. Sibson 1983; Scholz 2002) that is based on observations of the depth-distribution of fault rocks, inferred variability in deformation mechanism, fault strength and frictional stability with depth is also described. It is explained how this model provides basic controls on the depth limits of the crustal seismogenic zone. Earthquake size and scaling parameters, in relation to interpreting data from different scales and methods, are also briefly reviewed; and, finally, the chapters in this Special Publication are outlined.

## Earthquake mechanism and frictional stability

Faults slip at a range of speeds, including slow creep at plate tectonic rates (order of  $1\text{--}10\text{ cm year}^{-1}$ ), fast frictional sliding ( $c. 1\text{ m s}^{-1}$ ) during earthquake slip and displacement at a range of recently discovered, intermediate slip rates (such as slow slip and low-frequency earthquakes: see the review by Peng & Gomberg 2010 and references therein). The mechanisms of fault creep and slip at intermediate velocities are not yet obvious, but earthquake slip is generally thought to arise from ‘stick–slip’

frictional instability on a pre-existing fault (Brace & Byerlee 1966) or, less commonly, by failure on a new fault surface. In this model, based on the elastic rebound theory first suggested by Reid (1911), elastic strain accumulates in rock surrounding the existing or potential fault surface (Fig. 1a), until the resultant shear stress on the plane exceeds its frictional strength and failure occurs. Thus, earthquake faulting is a frictional process, where rupture initiation depends on frictional resistance on the existing or potential fault plane. The shear stress at failure,  $\tau_f$ , is commonly approximated by the empirical Amontons' law:

$$\tau_f = C_0 + \mu_s(\sigma_n - P_f) \quad (1)$$

where  $C_0$  is cohesive strength,  $\mu_s$  is the static coefficient of friction,  $\sigma_n$  is normal stress and  $P_f$  is fluid pressure. Equation (1) indicates the shear stress conditions at which a fault will slip; however, it does not define at what rate this slip occurs.

Experimental studies of fault friction, generally in homogeneous rock samples, have indicated that a rate- and state-variable friction law can describe observed sliding behaviour on laboratory faults

(Dieterich 1972, 1979; Scholz *et al.* 1972; Ruina 1983; Marone 1998; Scholz 1998). Rate- and state-variable effects on fault friction include an increase in  $\mu_s$  with loading time,  $t$ , related to an increase in real contact area with time under an applied normal stress (Dieterich 1972). In addition, the dynamic friction ( $\mu_d$ ), the sliding resistance experienced on a fault after slip has initiated, appears to vary with slip velocity,  $v$  (Fig. 1b) (Scholz *et al.* 1972). Although there are several forms of a constitutive equation fitting laboratory observations of rock friction, a commonly used description of the time and velocity dependence of friction is the Dieterich–Ruina law (Beeler *et al.* 1994):

$$\begin{aligned} \mu &= \mu_0 + a \ln(v/v_0) + b \ln(v_0 \theta/D); \\ d\theta/dt &= 1 - \theta v/D \end{aligned} \quad (2)$$

where  $\mu_0$  is the coefficient of friction at a reference slip velocity ( $v_0$ ),  $D$  is the critical slip distance, interpreted as the slip increment needed for renewal of surface contacts (Dieterich 1979),  $a$  and  $b$  are empirical material constants, and  $\theta$  is a state variable that evolves over time. Geological effects, such as

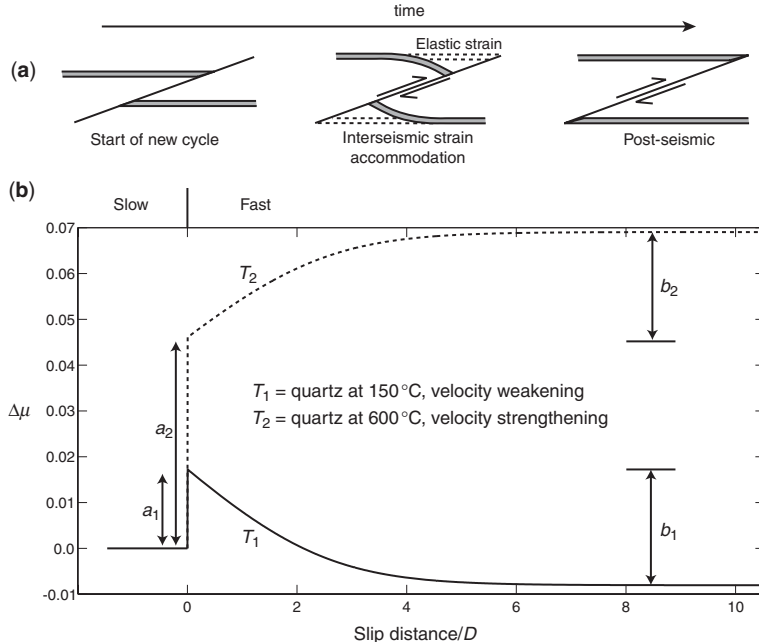


**Fig. 1.** (a) Fault movement by elastic rebound. Starting from a relaxed state at the beginning of a seismic cycle, the rock surrounding the fault accumulates elastic strain. When this strain reaches a value where the resultant shear stress on the fault exceeds its frictional strength, displacement occurs on the fault, releasing stored elastic strain in the wall rock. (b) Example of the velocity dependence of friction, using material properties ( $a$  and  $b$ ) for quartz from Blanpied *et al.* (1995) and Equation (2), at temperatures of 150 °C (solid line) and 600 °C (dashed line). Note the different evolution of the frictional coefficient ( $\mu$ ) predicted for velocity-weakening and velocity-strengthening conditions.

mineralogy, fluid pressure, dominant deformation mechanism and rock structure, as well as environmental variables including temperature and pressure, are here included in the empirical material constants  $a$ ,  $b$  and  $D$ , and in the time-dependent state variable,  $\theta$ .

Stick-slip instabilities, proposed by Brace & Byerlee (1966) to result in earthquake slip, may only occur where the fault material exhibits unstable or conditional frictional stability (Scholz 2002). Frictional stability depends on the empirical constants  $a$ ,  $b$  and  $D$ ; where, if the difference ( $a - b$ ) is positive, the material is said to be ‘velocity strengthening’ and  $\mu$  increases with slip (Fig. 1b). Such material is inherently stable and cannot slip at seismic velocities (Dieterich 1979). However, if ( $a - b$ ) is negative, friction decreases with slip (Fig. 1b) and the material is ‘velocity weakening’. In this case, the material is either unstable or conditionally stable; earthquakes may only nucleate in the unstable regime but can propagate into conditionally unstable regions (Scholz 1998).

The rate- and state-friction formulations imply that the seismogenic behaviour of a fault depends purely on its frictional stability, not on mechanical strength. Although Equation (2) is a good empirical fit to experimental data, geological controls on the empirical constants  $a$ ,  $b$  and  $D$ , and the physical meaning of the state variable,  $\theta$ , are largely unknown. Also, because rock friction experiments have commonly been performed using homogeneous samples in dry conditions at room temperature, it is uncertain how well these friction laws (e.g. Equation 2) approximate the frictional behaviour of natural heterogeneous fault rocks at seismogenic depths in the presence of a fluid phase and ongoing chemical reactions. The value of shear stress at failure (Equation 1) is also likely to be affected by fluid-pressure-driven fluctuations in effective normal stress and time-dependent changes in cohesion by mineral precipitation and cementation. The slip behaviour of natural faults is therefore likely to be a complex function of several geological parameters. Mineral deformation mechanisms other than frictional sliding may be of particular importance during crustal deformation.

## Fault-zone deformation mechanisms

### *Granular flow*

At shallow depths, ductile shear, a macroscopically continuous deformation, can occur by granular flow. Frictional grain-boundary sliding occurs, with little or no breaking or modification of single particles (Borradaile 1981). Rigid grains must be able to rotate and flow past each other, that is, the aggregate must be able to dilate. This mechanism is therefore suppressed by high confining pressure and assisted

by fluid presence between grains (Carter 1975). Because of high porosity and, commonly, high fluid content, diagenetic chemical processes such as cementation in pore spaces, recrystallization and fluid-assisted diffusional mass transfer into sites of low stress are also likely to contribute to this sort of deformation (Maltman 1994). These chemical processes are unlikely to accommodate much displacement but, rather, lead to an increase in cohesion and rigidity, suppressing granular flow and increasing the ability of the rock to store elastic strain. A shallow transition from continuous granular flow to frictional, discontinuous deformation of cohesive rock capable of elastic rebound may therefore occur in response to increasing confining pressure, and to mechanical and chemical cementation (Moore & Saffer 2001).

### *Grain-size-sensitive creep*

In a general sense, deformation mechanisms comprising a mixture of grain-boundary sliding and material transfer by solid-state or solution-accommodated diffusion are termed grain-size-sensitive creep because they have an inverse dependence on grain size (Ashby & Verrall 1973; Zeuch 1983). Diffusive mass transfer occurs when a chemical potential gradient is created by a gradient in normal stress along a grain boundary subject to a local stress field (Gibbs 1877; Paterson 1973). Diffusion of material occurs from relatively high normal stress regions to zones of low or negative compressive stress. At high temperatures solid-state diffusion may occur along grain boundaries or through the crystal lattice, but diffusivity is generally too low for this mechanism to operate at crustal conditions (particularly  $<350$  °C: McClay 1977). Despite this, rock textures in low-grade metamorphic rocks commonly indicate strain accommodation by diffusive mass transfer. Such fabrics, which generally involve truncated objects and ubiquitous fibrous growths, are interpreted as evidence for fluid-assisted diffusive mass transfer (e.g. Sorby 1853; Durney 1972). This is commonly known as ‘pressure solution’ but as that technically only refers to dissolution under non-hydrostatic stress (Durney 1972), this phenomenon is here termed dissolution–precipitation creep.

In the presence of a reactive fluid phase in fine-grained rocks, dissolution–precipitation creep can occur at low temperatures (down to  $<150$  °C in sili-cilastic rocks: e.g. McClay 1977; Duebendorfer *et al.* 1998). Commonly described in low-grade metamorphic rocks, it is recognized as a major flow mechanism competing with frictional sliding and cataclasis in the mid- to upper crust (Gratier & Gueydan 2007 and references therein). However, these mechanisms operate at different rates,

timescales and stress conditions. Whereas frictional sliding can occur at rates of up to  $\text{m s}^{-1}$ , dissolution–precipitation creep generally occurs at slow shear strain rates in the range of  $10^{-15}\text{--}10^{-11} \text{ s}^{-1}$  (Pfiffner & Ramsay 1982). Frictional sliding also occurs episodically at relatively high differential stress, and between episodes of failure a relatively long period of quiescence is required to build up the necessary shear stress for reactivation (Equation 1). Dissolution–precipitation creep, on the other hand, can be active continuously for tens to thousands of years under low differential stress (Gratier & Gueydan 2007). Experimentally, it has also been shown that frictional sliding and dissolution–precipitation creep can operate simultaneously, in a ‘frictional–viscous flow’ (Bos & Spiers 2001). In this case, frictional sliding on weak planes results in cavitation that is accommodated by dissolution–precipitation of intervening and surrounding material. This appears to be a particularly efficient mechanism in gouge containing interconnected planes of phyllosilicates (Niemeijer & Spiers 2006).

The dissolution–precipitation creep process can be divided into dissolution, transport and precipitation phases, of which the slowest determines the rate of the process as a whole (Rutter 1976). All these processes have a strong dependence on grain size, where strain rate is inversely proportional to grain size, or to grain size cubed in the case of diffusion-limited creep (Rutter 1976). In highly fractured rocks fracture spacing may be at least as important as grain size (Gratier *et al.* 2009). Consequently, microfracturing, leading to both decreased grain size and decreased fracture spacing, significantly increases the rate of dissolution–precipitation creep (Gratier & Gueydan 2007; Gratier *et al.* 2009). Thus, dissolution–precipitation creep is likely to be an important deformation mechanism in fine-grained, fractured, fluid-saturated rocks, which are commonly present within fault gouge of the crustal earthquake source.

### *Dislocation creep*

The third macroscopically ductile deformation mechanism rocks may experience is the movement of atomic-scale line defects by dislocation glide and climb, which, with recovery, is known as dislocation creep. While brittle failure of intact rock, frictional sliding and dissolution–precipitation creep are generally considered the dominant rock deformation mechanisms at low temperature (subgreenschist-facies conditions), viscous flow by dislocation creep is inferred to be the most important mineral deformation mechanism at higher temperatures (greenschist-, amphibolite- and lower-granulite-facies conditions: Passchier & Trouw 2005). As

this review focuses on rock deformation within the seismogenic zone, the depth at which dislocation creep becomes more efficient than frictional failure is important as it may control the depth to the base of the seismogenic crust (Sibson 1984; Scholz 1988). The flow law for dislocation creep may be expressed as (Hirth *et al.* 2001):

$$\dot{\epsilon} = Af_{\text{H}_2\text{O}}^m(\sigma_1 - \sigma_3)^n e^{(-Q/RT)} \quad (3)$$

where  $\dot{\epsilon}$  is pure shear strain rate,  $A$  is a material constant,  $f_{\text{H}_2\text{O}}$  is water fugacity,  $m$  is a water fugacity exponent,  $n$  is the stress exponent,  $(\sigma_1 - \sigma_3)$  is differential stress,  $R$  is the universal gas constant,  $T$  is temperature and  $Q$  is activation energy.

The variables  $A$ ,  $n$  and  $Q$  are solely functions of the deforming material, so the primary factors that affect the rate of dislocation creep in the absence of lithological variation are differential stress, temperature and composition. It is commonly inferred that temperature exerts the primary control, leading to a temperature-dependent transition from frictional to viscous deformation in the crust, which occurs at  $T \sim 350^\circ\text{C}$  for quartz (Kohlstedt *et al.* 1995; Scholz 1998; Stöckhert *et al.* 1999) and  $T \sim 450^\circ\text{C}$  for feldspar (Tullis & Yund 1991). Mafic rocks are brittle to greater temperatures, with a brittle–viscous transition in olivine at temperatures in excess of  $650\text{--}700^\circ\text{C}$  (Karato & Wu 1993; Passchier & Trouw 2005). Boettcher *et al.* (2007) observed a change from velocity-weakening to velocity-strengthening behaviour of olivine in laboratory friction experiments, and extrapolated the temperature dependence of this transition to approximately  $600^\circ\text{C}$  at geological strain rates. They interpret the physical reasoning for this transition in frictional stability to be the onset of dislocation glide, allowing for asperity deformation and slip-hardening (Boettcher *et al.* 2007). Thus, if dislocation creep is the major viscous deformation mechanism in the mid- to lower crust, thermal structure and mineralogy determine the maximum depth of frictional failure and unstable frictional behaviour, possibly also constraining the depth of the seismogenic zone (Scholz 1988). However, if other mechanisms (e.g. grain-size-sensitive creep) are more important, temperature may not provide the primary control.

### **Fault-rock assemblages and fault-zone structure**

The deformation mechanisms outlined in the previous section produce distinctive textures, so the fault-rock assemblages may be used to assess the dominant mechanisms active during deformation (e.g. Sibson 1977; Knipe 1989). However, fault-rock

microstructures result from a complex combination of protolith, the pressure–temperature–fluid pressure conditions during initial deformation and the exhumation path (Snoke *et al.* 1998; Smith *et al.* 2011), thus requiring careful assessment of cross-cutting relationships and post-deformation overprinting.

### *Rock textures produced in the frictional regime*

In a monolithological fault zone, predominant fault-rock type can be expected to change with depth (Sibson 1977; Woodcock & Mort 2008). At shallow levels, incohesive (unless post-kinematically cemented) rocks with random fabrics are observed (Fig. 2a, b), classified as fault breccia (clast/matrix ratio  $>0.3$ ; Fig. 2a) and gouge (clast/matrix ratio  $<0.3$ ; Fig. 2b). These rocks probably form by granular flow at low confining pressures, such as in the top few kilometres of active fault zones where low levels of microseismic activity are commonly observed. They experience dilatancy hardening at relatively low shear strains (Marone *et al.* 1990), so should be velocity strengthening, and contain clays, such as montmorillonite, which have a low frictional coefficient (Morrow *et al.* 1992). They are therefore probably records of aseismic slip, or were produced around the shallow termination of upward-propagating ruptures.

Cohesive rocks formed by cataclastic processes, defined as fracturing and rotation of mineral grains and grain fragments accompanied by dilatancy and frictional sliding along grain boundaries, are referred to as cataclasites (Sibson 1977; Woodcock & Mort 2008). Although Sibson (1977) classified cataclasites as containing only random fabrics, it has been demonstrated that cataclasites may also develop a foliation defined by alignment of elongate grains (Chester *et al.* 1985). Cataclasites comprise angular grains in a fine matrix (Fig. 2b, c), with greater matrix fraction and decreasing total grain size accompanying increased finite fault displacement. Within a fault zone, one or more principal slip zones (psz) are commonly defined by thin layers of ultracataclasite (with  $>90\%$  matrix) (Sibson 2003). Some fault zones may have one distinct principal slip zone surrounded by a commonly asymmetric, substantially thicker, highly fractured, damage zone (Chester & Chester 1998), while other faults comprise numerous anastomosing, thin slip zones surrounding lenses of fractured protolith (Faulkner *et al.* 2003).

Within cataclastic fault rocks, it is notoriously difficult to assess whether deformation textures formed during displacement at seismic, aseismic or intermediate slip rates. Cowan (1999) proposed that only pseudotachylite (lithified friction melt;

Fig. 2d) provides a definite record of seismic slip. However, pseudotachylite is rare in fault zones exhumed from seismogenic depths, indicating that friction melt is either rarely produced or rarely preserved relative to the frequency of earthquake slip events observed on active faults (Sibson & Toy 2006). Transfer of seismic slip across a dilational step-over may lead to a significant fluid pressure drop in the dilatant region (Sibson 1985), causing formation of an implosion breccia comprising wall-rock fragments cemented by hydrothermal precipitates (Fig. 2a) (Sibson 1986; Pavlis *et al.* 1993), but it cannot be said with certainty that the slip leading to dilatancy happened at seismic rates (Cowan 1999). Other structures that may be associated with seismic slip include rounded spherical aggregates in clayey gouge, observed in laboratory shear experiments at fast slip rates (Boutareaud *et al.* 2008; Ujiie *et al.* 2011) and in samples from natural, seismogenic faults (Boullier *et al.* 2009; Boullier 2011), and incrementally developed hydrothermal veins (Boullier & Robert 1992; Fagereng 2011). Unfortunately, these structures are either difficult to recognize in exhumed rocks, which have experienced overprinting by further deformation at depths shallower or deeper than the seismogenic regime, or may also be interpreted as resulting from slower slip rates.

Cataclastic fault rocks may also form in the presence of dissolution–precipitation creep (Gratier & Gamond 1990), as testified by ubiquitous pressure-solution selvage seams in many fault-rock assemblages (e.g. Fig. 2c). Distinct microstructures resulting from dissolution–precipitation creep or cataclasis have been observed in simulated fault rocks experimentally deformed either at much less than, or close to, seismic slip rates, which display, respectively, velocity-strengthening and velocity-weakening behaviour (e.g. Niemeijer & Spiers 2007). By correlation to these experiments, it is reasonable to infer that natural microstructures result from aseismic creep or seismic slip (e.g. van Diggelen *et al.* 2010; Rowe *et al.* 2011). However, as it is likely that frictional sliding and dissolution–precipitation creep coexist as the main deformation mechanisms in the seismogenic crust, and, as discussed above, operate at different timescales within the earthquake cycle, discontinuous deformation textures produced by frictional slip and continuous flow by dissolution–precipitation creep may cross-cut and destroy each other forming complex resultant textures (Fig. 2c) (e.g. Knipe 1989, 1990; Gratier & Gueydan 2007). A better understanding of the interplay between frictional sliding and dissolution–precipitation creep is therefore likely to be important for understanding the mechanics of earthquake nucleation and propagation, as it may be possible that the diffusive

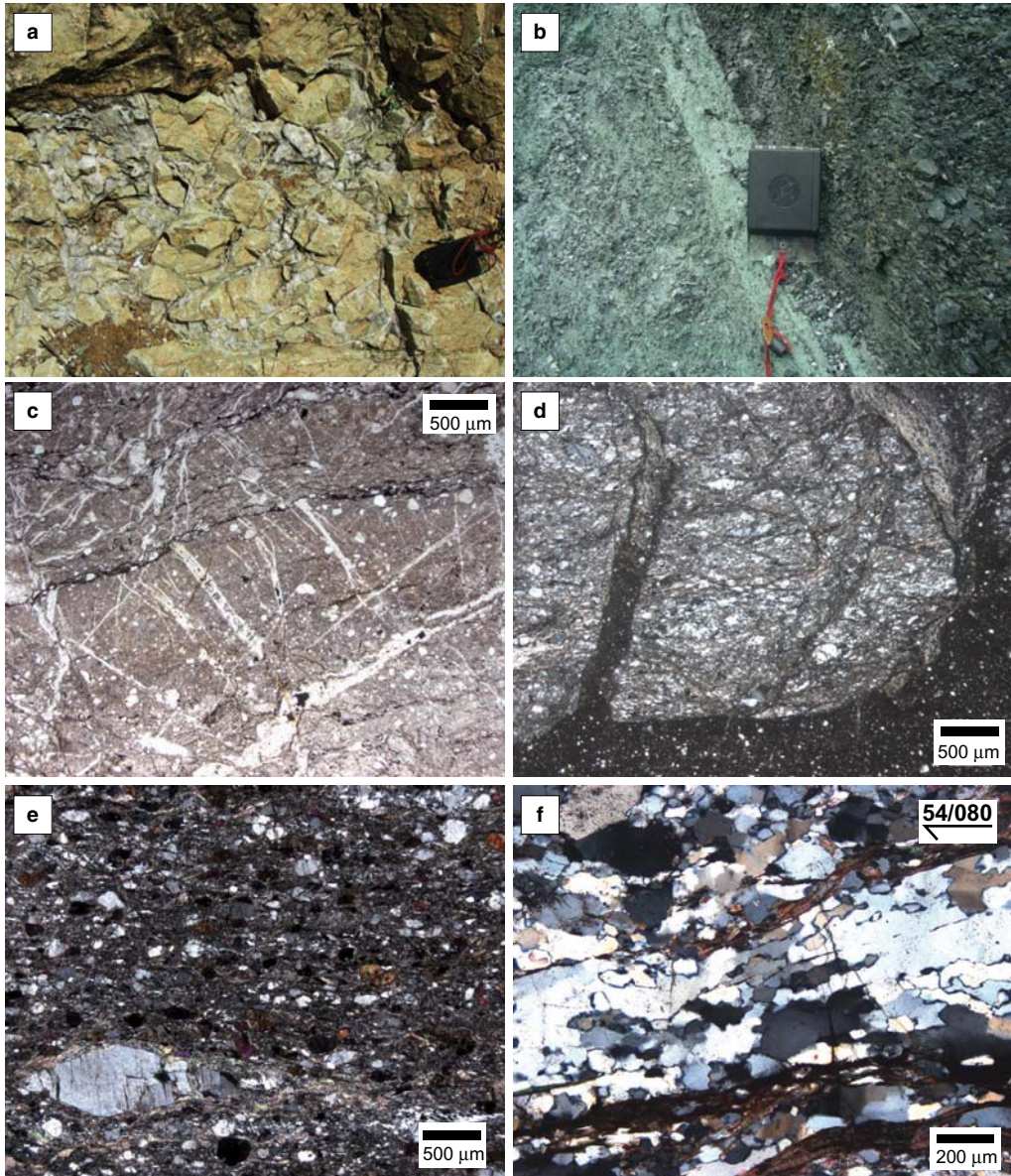


**Fig. 2.** Examples of natural fault-rock textures. (a) Calcite-cemented dolomite fault breccia from the Naukluft Thrust, Namibia. (b) Two distinct packages of cataclasite (mint and dark green) separated by a zone of uncemented, very fine-grained fault gouge running diagonally from top left to bottom right. The compass in (a) and (b) is 8 cm long. (c) Photomicrograph of ultracataclasite, with cross-cutting pressure-solution selvages (subhorizontal) truncating hydrothermal quartz veins (subvertical). (d) Photomicrograph with crossed polars of a pseudotachylite fault vein (horizontal) with two injection veins (subvertical) into protocataclasite derived from quartzofeldspathic mylonite. The pseudotachylite injection veins have been altered to chlorite towards their ends. (e) Mylonite, with fabric indicating that quartz and mica behaved viscously, deforming into elongate polygranular masses, while individual feldspars formed porphyroclasts that underwent microfracturing. (b)–(e) are all from the hanging wall of New Zealand's Alpine Fault Zone. (f) Quartzofeldspathic mylonite with fabric diagnostic of continuous deformation in all phases – quartz, feldspar and mica – from the Grebe Shear Zone, Fiordland, New Zealand (courtesy of J. Scott).

mechanism is at least as important as frictional faulting at seismogenic depths (Rutter & Mainprice 1979, Gratier & Gueydan 2007).

Seismic coupling,  $\chi$ , refers to the ratio of fault displacement accommodated by seismic slip (cumulate over multiple earthquake cycles) over total plate tectonic slip rate. For most crustal faults,  $\chi$  appears to be indistinguishable from 1, that is, the vast majority of slip occurs seismically (e.g. Scholz 2002). Exceptions to this, shown by faults accommodating significant displacement at aseismic or intermediate slip rates, are found in the San Andreas Fault System (Hill *et al.* 1990), and along several subduction thrust interfaces (Ruff & Kanamori 1980). The implication of  $\chi = 1$  is that fault rocks deformed by slip at seismogenic depths are more likely to have experienced seismic slip than not. It may therefore be appropriate to reconsider the proposal of Cowan (1999), who suggested that fault slip is most likely to have been aseismic and that faults should be considered to have slipped slowly until proven fast. Instead, we propose that the fact that earthquakes appear to be the main mode of discontinuous deformation in the frictional regime (e.g. Sibson 1989) should lead us to assume that most shallow crustal fault rocks were deformed seismically. Hence, we should also look for ways of defining rocks deformed by slower slip styles.

### *Rock textures produced in the viscous regime*

The frictional process required for earthquake faulting is pressure-dependent because high confining pressure prevents frictional sliding and promotes ductile flow (Byerlee 1968). Viscous creep, on the other hand, is primarily temperature-dependent, and becomes more efficient as temperature increases with depth (Equation 3). From these relationships arise commonly presented crustal strength curves, which predict a frictional–viscous transition at the cross-over point between the frictional and viscous strength curves as calculated based on Equations 1 and 3 (Fig. 3) (Sibson 1977; Brace & Kohlstedt 1980). The conditions at which this transition occurs depend on the behaviour of the mineral constituents of the fault rocks, primarily quartz, feldspar and mica in quartzofeldspathic continental crust, their relative proportions, and phase arrangement.

At depths where temperatures are high enough for efficient recovery, and where high confining pressures prevent easy frictional sliding, rocks develop mylonitic textures by dislocation creep, with or without dissolution–precipitation creep (White 1973; Sibson 1977; Hippert & Egydio-Silva 1996). In quartz and mica, these textures are commonly developed at pressures and temperatures above the onset of greenschist-facies conditions

( $T > 300$  °C) (Voll 1976; Sibson 1984; Stöckhert *et al.* 1999; Mariani *et al.* 2006). Fluid–rock reaction and hydrolytic weakening mechanisms may also allow creep to occur at shallower levels where a reactive fluid phase is present (Wintsch *et al.* 1995; Hippert & Egydio-Silva 1996).

Conversely, in feldspars dislocation creep only becomes the dominant mode of deformation above approximately 450 °C, when deformation is commonly accompanied by mineralogical change (Pryer 1993; Passchier & Trouw 2005). Consequently, quartzofeldspathic mylonites developed at  $300 < T < 450$  °C tend to have semi-discontinuous tectonite fabrics developed by viscous creep of quartz and mica combined with cataclastic deformation of feldspar (Fig. 2e). In this mixed brittle–viscous regime, bulk rheology depends on the ratio of high- to low-viscosity minerals, and the geometry of the phase distribution in the rock (Handy 1990). Consequent variations in bulk rheology may also be reflected in the seismic style of actively deforming, heterogeneous shear zones (Fagereng & Sibson 2010).

At temperatures exceeding 500 °C, quartzofeldspathic rocks tend to deform by continuous viscous shearing flow (Fig. 2f), commonly distributed over shear zones several hundreds of metres thick. Within such viscous shear zones, pseudotachylites are sometimes observed (Sibson 1980; Clarke & Norman 1993), indicating that frictional sliding at seismic velocity can occur within a regime where viscous mechanisms accommodate deformation most of the time. In some cases, pseudotachylites have formed in the deep crust in relation to dehydration reactions in a cold, subducting slab at eclogite-facies conditions (e.g. Austrheim & Boundy 1994), while in other instances, ruptures nucleated within the frictional regime have propagated downwards into normally aseismic, viscously deforming crust (Lin *et al.* 2005; Moecher & Steltenpohl 2011). Despite different mechanisms, these deep occurrences of pseudotachylite signify that dynamic changes in physical parameters, such as fluid pressure or shear strain rate, can lead to transient shear instabilities (or velocity weakening) and earthquake slip at depths normally considered deeper than the earthquake source.

### **Conceptual fault model**

So far, we have reviewed the concepts of elasticity and frictional stability that govern brittle faulting, and have discussed the main deformation mechanisms inferred for the mid- to upper crust, and typical fault-rock assemblages. Likely variations in geological features, dominant deformation mechanisms, frictional stability, seismic behaviour and

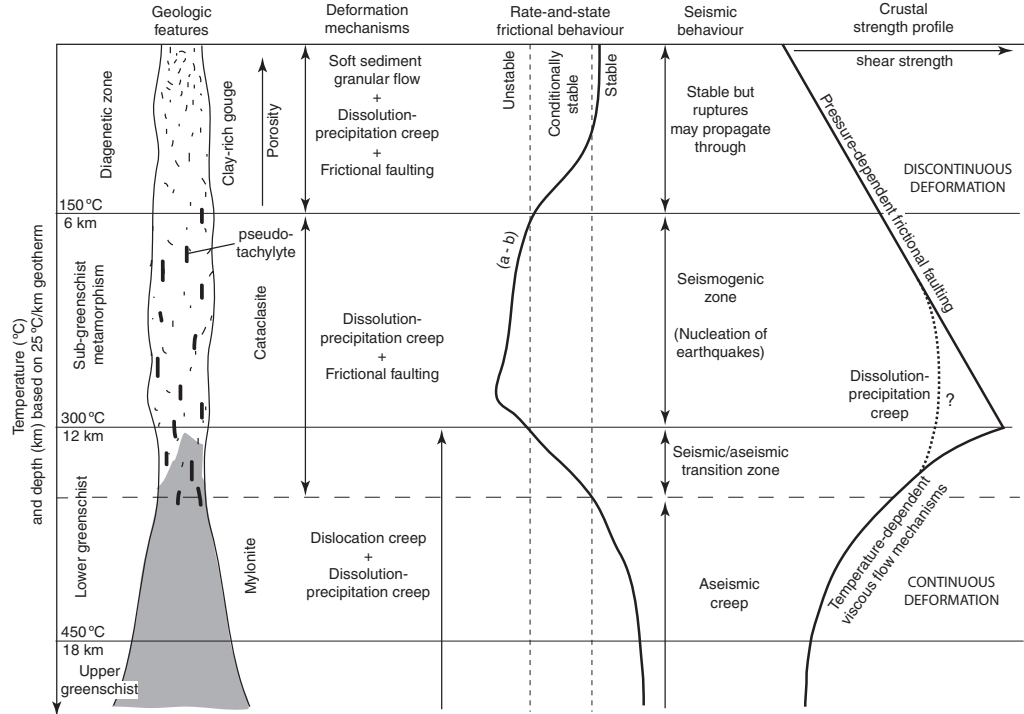


**Fig. 3.** Conceptual fault-zone model, modified from Sibson (1983) and Scholz (1988, 2002).

crustal strength with depth are summarized in Figure 3. Major transition zones appear to occur at temperatures of approximately 150 and 300 °C, corresponding to depths of approximately 6 and 12 km, respectively, assuming a typical continental geothermal gradient of 25 °C km<sup>-1</sup>.

The upper (colder) transition represents a transition from shallow, predominantly aseismic, deformation into the top of the seismogenic zone. Above this transition, rocks are poorly lithified and a fault zone predominantly consists of clay-rich gouge. Diagenetic chemical reactions occur, causing progressive cementation and decreasing porosity with depth, accompanied by increasing frictional shear strength as  $\sigma_n$  increases with increasing overburden pressure. The dominant flow mechanisms are granular flow and dissolution–precipitation creep, accompanied by brittle failure in more cemented rocks. Frictional properties at shallow depths are also presumed to be stable to conditionally stable; thus, generally aseismic frictional sliding is predicted on pre-existing planes (Scholz 1998), although it is likely that large ruptures that nucleate at greater depths will propagate to the surface through this regime.

The temperature range from approximately 150 to about 300 °C represents the predicted crustal

seismogenic zone, within which earthquake ruptures nucleate and can easily propagate. Very low-grade (subgreenschist) metamorphic reactions occur throughout this temperature range. The dominant deformation mechanisms are frictional sliding and dissolution–precipitation creep, leading to mixed frictional–viscous behaviour (Gratier & Gamond 1990; Niemeijer & Spiers 2007). Assuming a quartz-dominant lithology, frictional properties are predicted to lie in the unstable field (Blanpied *et al.* 1995), and temperatures are too low for deformation by viscous creep to accommodate tectonic strain rates (Hirth *et al.* 2001). Shear strength is highly dependent on the fluid pressure state, and on the dominant deformation mechanism.

At greenschist-facies conditions (>300–350 °C) dislocation creep and diffusive mass transfer are inferred to dominate in continental crustal material. However, in mafic rocks, these mechanisms only become dominant over frictional failure at significantly higher temperatures (Karato & Wu 1993). At depths where viscous flow mechanisms dominate, brittle or frictional failure occurs locally, in the event of local elevation of strain rate, fluid pressure, or in the presence of different material properties such as composition or grain size. As

earthquakes occur by frictional instability, seismic events are not expected to nucleate in these creeping materials, although ruptures may propagate into them because of elevated strain rates at the rupture tip. At high temperatures ( $>350^{\circ}\text{C}$ ), frictional properties of a quartz-dominant lithology are expected to lie in the field of frictional stability (Blanpied *et al.* 1995), suggesting aseismic frictional sliding will occur and that propagating ruptures will be rapidly arrested.

The transition from frictional sliding to viscous dislocation creep depends on material properties, temperature, effective normal stress and strain rate (Equation 3), and therefore probably occurs at different depths in different parts of a natural fault zone. Similarly, the frictional stability depends on material properties. Thus, because most natural faults contain a range of geological materials and experience a range of conditions, the transition from stable to unstable sliding is likely to be irregular in space (and time?).

### The crustal seismogenic zone

The fault model in Figure 3 may be translated to different heat flow regimes by changing the thermal gradient, and hence the depths on the vertical axis. The temperature and depth variability of various factors affecting slip style emphasizes the complex interplay of physical parameters determining the up- and down-dip limits of the crustal seismogenic zone.

In theory, the seismogenic zone is defined by where earthquakes can nucleate, and in practice it is defined by the depth-distribution of microseismic activity and mainshock–aftershock sequences. The latter is problematic because there are many major crustal fault zones that have not experienced significant earthquakes since seismometers have been available to record earthquake arrivals (e.g. New Zealand's central Alpine Fault: Evison 1971), so there is little control on the depth to which ruptures may propagate. Furthermore, although commonly defined as a range of crustal depths, the extent of the seismogenic zone may vary along strike of a single structure, and comprise regions of strong and weak coupling on a fault plane (Bilek & Lay 2002). However, it is unclear how interseismic coupling relates to the seismogenic zone (e.g. Kaneko *et al.* 2010).

The depth of the seismogenic zone varies significantly between tectonic settings, but the temperature at its base is generally around  $350^{\circ}\text{C}$  in continental crust (Scholz 2002). This is approximately coincident with the expected frictional–viscous transition, so may be defined by a transition from the shallow elastic–frictional regime to creep

by viscous mechanisms at greater depths (e.g. Sibson 1983, 1984; Scholz 1988). If this interpretation is correct, then the intercept between Equations (1) and (3) defines the greatest depth at which earthquakes can nucleate. The corollary is that the peak strength that the crust can sustain then defines the depth to the base of the seismogenic zone, and this then depends strongly on strain rate, the composition and the viscosity of the dominant mineral phase, and the frictional resistance on pre-existing faults, as defined by their frictional coefficient and the effective normal stress ( $\sigma_n - P_f$ ).

In addition to variations in dominant deformation mechanism, the frictional stability along faults may also determine seismogenic behaviour. As earthquake nucleation requires frictional instability, seismic slip is confined to velocity-weakening materials at conditions favouring frictional sliding and elastic strain in surrounding rock. As quartz is velocity-strengthening above  $300\text{--}350^{\circ}\text{C}$  and below approximately  $150^{\circ}\text{C}$  (Blanpied *et al.* 1995), seismogenesis in quartz-dominated continental crust is constrained to  $T < 350^{\circ}\text{C}$ . The base of the seismogenic zone is thus likely to be controlled by a range of parameters including composition, strain rate, temperature and effective stress, and is therefore complicated by the probable heterogeneity in both composition and fluid pressure distribution within the continental crust.

### Earthquake size and scaling relationships

Within the heterogeneous rocks of the earthquake source, earthquakes occur over a large range of length scales (Gutenberg & Richter 1944) but follow a consistent self-similar pattern (Kanamori & Anderson 1975; Hanks & Kanamori 1979): that is,  $10^{-4} < u/L < 10^{-5}$ , where  $u$  is average slip and  $L$  is fault length (Wells & Coppersmith 1994). This implies that irrespective of earthquake size, slip distance scales with the size of the fault on which sliding occurs.

Earthquake size is traditionally measured by the earthquake magnitude. A variety of magnitude scales, based on measuring the amplitude of a specific seismic wave at a specific frequency, have been used through history. This approach is problematic because of the difficulties encountered in correcting for distance and instrument response, and the different source spectra for different magnitude events.

While earthquake magnitude is a logarithmic scale based on instrument response to seismic radiation, the seismic moment (Aki 1967) provides a physically meaningful measure of earthquake size.

Seismic moment (in N m) is defined as a scalar by the relationship:

$$M_0 = GuA \quad (4)$$

where  $G$  is shear modulus and  $A$  is rupture area. Hanks & Kanamori (1979) designed a magnitude scale based on the seismic moment, the moment magnitude scale, where magnitude,  $M_w$ , is proportional to  $\log_{10} M_0$ . A consequence of this relationship is that  $M_w$  is proportional to rupture area (Aki 1981).

Dynamic rupture characteristics, that is, slip acceleration, distance and velocity, vary linearly with stress drop,  $\Delta\tau$  (Scholz 2002). A number of studies have found that  $\Delta\tau$  is relatively constant over a large range of magnitudes and tectonic settings (Kanamori & Anderson 1975; McGarr 1999; Allmann & Shearer 2009). The mean stress drop is approximately 3 MPa, although variation over the range  $0.03 < \Delta\tau < 30$  MPa is evident in published data sets (Scholz 2002; Choy *et al.* 2007; Allmann & Shearer 2009).

A consequence of constant  $\Delta\tau$  is that it is possible to estimate the relationships between  $u$ ,  $L$  and  $M_w$  (Hanks & Kanamori 1979; Wells & Coppersmith 1994; Sibson 2011). The effect of these scaling relationships on earthquake rupture area is shown graphically in Figure 4. As well as illustrating the variation in rupture size with earthquake magnitude, Figure 4 emphasizes the difficulty of studying earthquake parameters at outcrop scale, which is important when using geological observations to make inferences about earthquake mechanics – as discussed in many contributions within this volume. For example, 25 km, a typical map-scale study area, is equivalent to the rupture length of an elliptical  $M_w$  6 rupture. A typical single outcrop of about 20 m, on the other hand, is only visible on an  $M_w$  4 sized rupture plane in Figure 4, and anything larger than an  $M_w$  2 is inferred to rupture more than the entire outcrop. It is important to be mindful of these scaling relationships when comparing geological and geophysical earthquake observations, as different processes are visible (and invisible) at different scales.

The empirical Gutenberg–Richter relationship (Ishimoto & Iida 1939; Gutenberg & Richter 1944) is another fundamental earthquake scaling relationship. This frequency–magnitude relationship is a consequence of the self-similar scaling of earthquakes over many magnitudes, and implies that, in any region, for each unit decrease in magnitude, the earthquake frequency increases by a factor of  $10^\beta$ . The relationship appears to hold to magnitudes down to  $M_w - 1$  in scientific borehole experiments (Abercrombie 1995). The value of  $\beta$  is approximately 1.0 in most regions (Frohlich &

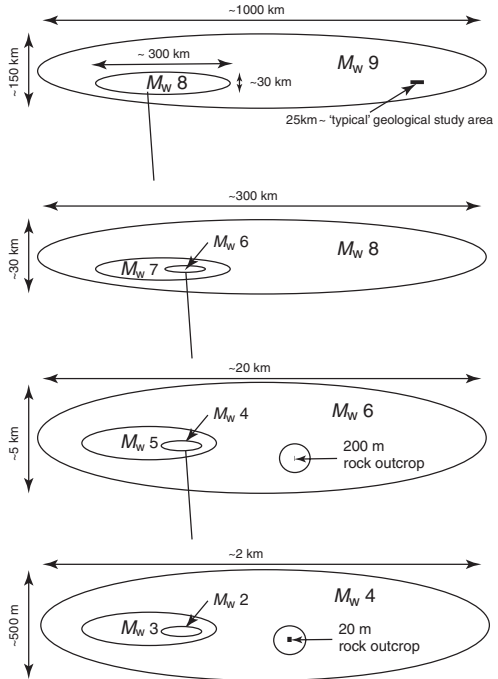


**Fig. 4.** Relative size of the rupture areas from earthquakes of  $M_w$  9 down to  $M_w$  2, based on relationships determined by Kanamori & Anderson (1975) and Hanks & Kanamori (1979). Dimensions have been adapted to elliptical rupture areas for ease of presentation and for more realistic shapes of the larger earthquakes, where the down-dip dimension is limited by the thickness of the seismogenic zone.

Davis 1993), implying a 10-fold increase in frequency for each unit decrease in magnitude. As the world experiences one  $M_w$  8 earthquake a year, on average, this implies that 10  $M_w$  7 events, 100  $M_w$  6, 1000  $M_w$  5, and so on, occur every year.

If applied to a single fault, the frequency–magnitude relationship tends to significantly underestimate the size of the largest earthquake possible on the fault (Wesnousky *et al.* 1983; Schwartz & Coppersmith 1984). This may be a consequence of the different scaling of small and large earthquakes (Scholz 1997), but is also an effect of the basis for the frequency–magnitude relationship. It is commonly inferred that the Gutenberg–Richter relationship derives from a power-law distribution of faults; each fault failing in a characteristic earthquake during which an entire fault segment fails – in other words, the characteristic earthquake is dependent on the fault size (King 1983; Schwartz & Coppersmith 1984; Wells & Coppersmith 1994; Wesnousky 1999). The geological implication is that there is likely to be some parameter limiting

the earthquake size on any given fault, which may be recognized as a geological or geometrical feature determining the end points of a rupture (Sibson 1989).

These scaling relationships imply a scale-invariance in the dynamics of earthquakes, suggesting that information about the geological effects of earthquakes at a range of scales, derived from microscopic to outcrop scale studies, can be extrapolated to the mechanics of larger events. However, we must always be mindful that most geological studies are performed at scales very different from those considered by geophysicists observing active faults (Fig. 4). The chapters in this volume, outlined in the next and final section of this introductory chapter, therefore span a range of scales from microscopic observations of natural and laboratory faults, through to field studies of fault rocks from a range of inferred depths and settings, to larger-scale geophysical and theoretical contributions.

## Chapters in this volume

The first two original research papers describe observations from drilling projects in active fault zones. These contributions – based on direct observations of rocks actively deforming within the seismogenic zone – set the scene for studies involving interpretations of exhumed fault rocks, laboratory experiments and theoretical models, which all rely on understanding what an active fault zone looks like. In the first of these chapters, **Boullier** reviews geological observations from drilling projects in the Nojima and Chelungpu faults, both responsible for recent large earthquakes. Her review highlights how both fault-zone geology and fluid pressure state vary considerably between these two faults, so that no unique solution can be applied to the geology of all crustal fault zones. **Ellsworth & Malin** present seismological observations from the San Andreas Fault Observatory at Depth, where they identify a new type of fault-guided seismic wave ( $F_\phi$ ). They argue that fault-guided seismic waves in this location propagate within an approximately 30 m-wide damage zone, which extends to a depth of 7 km, that is, into the seismogenic zone. They suggest that this damage zone arises either from fracturing around the principal slip zone of large earthquakes or is generated by aseismic creep.

While deep drilling projects have the advantage of direct sampling from known depths in well-characterized active faults, deformation structures developed within the seismogenic zone may also be studied in exhumed fault-rock assemblages. Outcrops provide natural laboratories at much larger observational scale than a drill core, but depth,

temperature and geological setting during deformation must be interpreted. In the second group of papers, **Fagereng** discusses observations in an exhumed mélange shear zone, interpreted as under-thrust sedimentary rocks and scattered basalts deformed below a subduction décollement. He highlights how a subduction megathrust comprises a wide zone of heterogeneous rock, within which slip occurs by both localized and distributed deformation, and speculates on how observations in the exhumed shear zone can be interpreted in terms of the fault-slip behaviour within modern analogues. **Rowe et al.** also present geological observations from a fossil subduction thrust interface. They find three mutually cross-cutting fault-rock textures, and interpret that these were produced during slip at seismic, aseismic and intermediate slip rates during different parts of the earthquake cycle. Field and microstructural observations from a different tectonic setting, a low-angle normal fault, are presented by **Smith et al.**, who also review the extensive literature available on the Zuccale Fault. They identify a range of deformation mechanisms that were active broadly contemporaneously within the fault core. The relative importance of these mechanisms appears to have varied over time as a function of temperature, fluid presence, fault-zone structure and mineralogy, resulting in fundamental changes in fault-slip behaviour. Overall, these three chapters present new ideas on how to interpret fault-rock assemblages in relation to the range of seismic styles observed in active faults, and address questions of the deformation mechanisms responsible for different slip modes within the seismogenic zone.

**Toy et al.** then describe pseudotachylite occurrences in the transpressional Alpine Fault Zone, New Zealand, which, although ubiquitous, are insufficiently abundant to account for all increments of earthquake slip on this fault. They propose that many of the pseudotachylite veins were formed during moderate magnitude events near the base of the seismogenic zone and that some represent events that propagated downwards into normally aseismic regimes. Voluminous pseudotachylites are mostly restricted to exhumed slivers of the footwall of the fault. A distinct group of pseudotachylites are interpreted to have formed at shallower depths, in the middle seismogenic zone, probably in the presence of fluid patches on heterogeneous fault planes; this observation challenges the view that thermal pressurization can significantly lower fault strength at asperity contacts.

This paper provides a transition to a third group of papers that discuss rupture processes at the base of the seismogenic zone and into the mid- to lower crust. **Allen & Shaw** present a study of a several hundreds of metres wide, high-strain shear zone,

which they interpret as an anisotropically weakened zone generated in the mid-crust. The shear zone hosts pseudotachylite veins, which they interpret as evidence of first-generation ruptures in intact rock. Some of the pseudotachylites were generated in a regime where creep could still occur, possibly by down-dip propagation of shallower-level ruptures. They suggest that the anisotropy of the sheared rocks constrained rupture geometry as they were exhumed into the seismogenic zone. A petrographical study by **Altenberger *et al.*** also illustrates that earthquakes may nucleate below expected seismogenic zone depths. These authors determine the pressure–temperature conditions of formation for a pseudotachylite vein, from which they calculate a formation depth of 21–23 km with an ambient temperature of 800 °C. The textures observed in the vein suggest that it formed by initial viscous deformation followed by brittle failure, perhaps as increasing strain rate resulted in grain-size reduction and an increased surface area promoted frictional melting. **Moecher & Steltenpohl** also describe pseudotachylites formed at warmer conditions than normally expected for earthquake nucleation. They report host rock temperatures exceeding 600 °C for multiple generations of friction melt in extensional shear zones developed during late- to post-Caledonian crustal extension. They suggest that frictional melting of rocks normally deforming by slow creep in the aseismic regime occurred as earthquake ruptures, nucleated at shallower depths, propagated at high strain rates, into the viscous regime below the base of the seismogenic zone. To complement the descriptions of rocks representing seismic slip at and below the seismogenic zone, **Nüchter & Ellis** present numerical models of coseismic loading around major faults in a range of tectonic settings. Their models predict a coseismic stress drop in the upper crust, accompanied by loading to high stress at depths below the base of the seismogenic zone. In all of these papers it is clear that, although it is rare for earthquakes to nucleate below the seismogenic zone, earthquakes significantly change the surrounding stress field. This, combined with high strain rates and strength anisotropy, may lead to slip propagation into the normally viscous regime, and significant loading of the mid- to lower crust.

Many active and ancient fault zones contain clear evidence of the effects of fluids on faulting. The fourth set of papers focuses on fluid flow in crustal fault zones. **Barker & Cox** studied a swarm of hydrothermal quartz–calcite veins developed incrementally during progressive fold growth and associated reverse faulting. They conclude that, in this setting, fluid pathways changed dynamically as permeability varied from high to low during cycles of episodic slip, fracture development and

fracture healing. Fault-related calcite veins are also described by **Nuriel *et al.***, who investigate the structure, petrography, geochemistry and geochronology of calcite precipitates along the East Anatolian and Dead Sea fault zones. The nature of the calcite precipitates and their relationships to faulting vary significantly, and Nuriel *et al.* conclude that geochemical and structural analysis, combined with U–Th geochronology, can be used to provide age constraints on the timing of brittle deformation. **Upton *et al.*** also present a study of fluid flow in active settings as they compare and contrast the distribution of heat flow, hot springs and hydrothermal veins in Taiwan and New Zealand – two young, transpressive orogens. Both orogens have two fluid-flow systems centred at the drainage divide: a shallow topographically driven system involving dominantly meteoric water where steep veins develop in an extensional regime; and a deeper flow of mineralizing, rock-exchanged fluids in which subhorizontal veins form during vertical stretching. In Taiwan, veins were formed locally during embrittlement of initially weak slates; in New Zealand, a more uniform rheology leads to distributed vein formation. In the last chapter in this section, **Ujije *et al.*** present high-velocity friction experiments in which clay-rich fault gouge is subjected to thermal pressurization and fluidization. In both wet and dry tests, fault weakening occurs as fluid pressure increases (and therefore effective normal stress decreases) within the fault plane. In the dry tests, this is caused by thermal pressurization as water is released from clay dehydration driven by frictional heating. In wet tests, fluid pressure is increased by both frictional heating and shear-enhanced compaction of the gouge. In addition to concluding that earthquake ruptures may be enhanced by fluid pressurization in both wet and dry experiments, these authors show the microstructures that developed during this process, which can be compared to observed fault rocks that may have accommodated similar effects.

Earthquakes regularly occur on pre-existing faults, particularly if weakened by fluid presence. However, it is important to consider when a fault may be reactivated as opposed to when it is preferable for new faults to initiate. **Nortje *et al.*** analyse relative timing and orientation data for mineralized faults in the Mount Gordon Fault Zone, Mt Isa, Australia. Here, deformation was accommodated by the initiation of multiple new orientations of strike-slip faults, rather than by reactivation of pre-existing structures. This implies that the existing faults had high cohesion and/or insufficient fluid pressure for reactivation. They also conclude that pre-existing faults with high cohesion may have acted as barriers to fluid flow, so that intersections between new and

old faults host mineralization as a result of the interaction between newly formed, high-permeability faults, and cohesive, relatively impermeable, pre-existing structures. For more general cases, Scholz presents a theoretical treatment of how splay faults form at acute angles to the primary fault when the main fault becomes misaligned for reactivation. He gives compelling examples from literature on active faults of how, in the dip-slip case, splay faults commonly develop when the main fault orientation is guided by a pre-existing weak plane, which becomes frictionally misaligned with the greatest principal compressive stress.

As outlined above, the 16 original papers in this volume cover a range of topics on the slip behaviour of faults in various tectonic settings. The variety in approach and methodology in the chapters, and the range of geological features they describe, is testament to the wide scope of earthquake geology, as Sibson describes in the final chapter of this book. In his chapter, Rick outlines his thoughts on the future directions of the field of earthquake geology. He points out that earthquakes influence a wide range of geological processes at a variety of distances from the rupture source. While palaeoseismology has traditionally focused on fault-zone surface processes, Sibson highlights the need to expand the concept to near-field and far-field effects, both on the surface and in the subsurface. His conclusion, that many processes commonly considered smooth and progressive are rather intermittent and tied to the seismic cycle, should be kept in mind by all geologists studying deformation of the Earth's lithosphere.

## Summary

The uniformitarian approach of considering Earth deformation as slow and constant on geological timescales has become engrained in geological thought. In this volume, rocks deformed by earthquake slip are identified in settings of crustal shortening, extension and transpression. Experiment and theory suggest that seismic slip is common. It is time to reconsider the common approach of assuming exhumed faults were aseismic until proven guilty of seismic slip, especially given the high frequency of earthquakes recorded by seismic networks around the globe. Future studies need to identify the mechanisms behind aseismic slip, the factors governing the partitioning between seismic and aseismic deformation, and identify what characterizes an earthquake nucleation site.

Å. Fagereng acknowledges funding from the UCT Research Development Fund. The authors thank R. Law for review comments that improved the final manuscript.

## References

- ABERCROMBIE, R. E. 1995. Earthquake source scaling relationships from –1 to 5 ML using seismograms recorded at 2.5-km depth. *Journal of Geophysical Research*, **100**, 24 015–24 036.
- AKI, K. 1967. Scaling law of seismic spectrum. *Bulletin of the Seismological Society of America*, **72**, 1217–1231.
- AKI, K. 1981. A probabilistic synthesis of precursory phenomena. In: SIMPSON, D. & RICHARDS, P. (eds) *Earthquake Prediction*. American Geophysical Union, Washington, DC, 566–574.
- ALLMANN, B. P. & SHEARER, P. M. 2009. Global variations of stress drop for moderate to large earthquakes. *Journal of Geophysical Research*, **114**, B01310, doi:10.1029/2008JB005821.
- ASHBY, M. F. & VERRALL, R. A. 1973. Diffusion accommodated flow and superplasticity. *Acta Metallurgica*, **21**, 149–163.
- AUSTRHEIM, H. & BOUNDY, T. M. 1994. Pseudotachylite generated during seismic faulting and eclogitization of the deep crust. *Science*, **265**, 82–83.
- BEELER, N. M., TULLIS, T. E. & WEEKS, J. D. 1994. The roles of time and displacement in the evolution effect in rock friction. *Geophysical Research Letters*, **21**, 1987–1990.
- BILEK, S. L. & LAY, T. 2002. Tsunami earthquakes possibly widespread manifestations of frictional conditional stability. *Geophysical Research Letters*, **29**, 1673, doi:10.1029/2002GL015215.
- BLANPIED, M. L., LOCKNER, D. A. & BYERLEE, J. D. 1995. Frictional slip of granite at hydrothermal conditions. *Journal of Geophysical Research*, **100**, 13 045–13 064.
- BOETTCHER, M. S., HIRTH, G. & EVANS, B. 2007. Olivine friction at the base of oceanic seismogenic zones. *Journal of Geophysical Research*, **112**, B01205, doi:10.1029/2006JB004301.
- BORRADAILE, G. J. 1981. Particulate flow of rock and the formation of cleavage. *Tectonophysics*, **72**, 305–321.
- BOS, B. & SPIERS, C. 2001. Experimental investigation into the microstructural and mechanical evolution of phyllosilicate-bearing fault rock under conditions favouring pressure solution. *Journal of Structural Geology*, **23**, 1187–1202.
- BOULLIER, A.-M. 2011. Fault-zone geology: lessons from drilling through the Nojima and Chelungpu faults. In: FAGERENG, Å., TOY, V. G. & ROWLAND, J. V. (eds) *Geology of the Earthquake Source: A Volume in Honour of Rick Sibson*. Geological Society, London, Special Publications, **359**, 17–38.
- BOULLIER, A.-M. & ROBERT, F. 1992. Palaeoseismic events recorded in Archaean gold-quartz vein networks, Val d'Or, Abitibi, Quebec, Canada. *Journal of Structural Geology*, **14**, 161–179.
- BOULLIER, A.-M., YEH, E.-C., BOUTAREAUD, S., SONG, S.-R. & TSAI, C.-H. 2009. Microscale anatomy of the 1999 Chi-Chi earthquake fault zone. *Geochemistry Geophysics Geosystems*, **10**, Q03016, doi:10.1029/2008GC002252.
- BOUTAREAUD, S., CALUGARU, D.-G., HAN, R., FABBRI, O., MIZOGUCHI, K., TSUTSUMI, A. & SHIMAMOTO, T. 2008. Clay-clast aggregates: a new structural evidence

- for seismic sliding? *Geophysical Research Letters*, **35**, L05302, doi:10.1029/2007GL032554.
- BRACE, W. & BYERLEE, J. D. 1966. Stick-slip as a mechanism for earthquakes. *Science*, **153**, 990–992.
- BRACE, W. F. & KOHLSTEDT, D. L. 1980. Limits on lithospheric stress imposed by laboratory experiments. *Journal of Geophysical Research*, **85**, 6248–6252.
- BYERLEE, J. D. 1968. Brittle–ductile transition in rocks. *Journal of Geophysical Research*, **73**, 4741–4750.
- CARTER, R. M. 1975. A discussion and classification of subaqueous mass-transport with particular reference to grain-flow, slurry-flow and fluxoturbidites. *Earth-Science Reviews*, **11**, 145–177.
- CHESTER, F. M. & CHESTER, J. S. 1998. Ultracataclasite structure and friction processes on the Punchbowl fault, San Andreas system, California. *Tectonophysics*, **295**, 199–221.
- CHESTER, F. M., FRIEDMAN, M. & LOGAN, J. M. 1985. Foliated cataclasites. *Tectonophysics*, **111**, 139–146.
- CHOY, G. L., McGARR, A., KIRBY, S. H. & BOATWRIGHT, J. 2007. An overview of the global variability in radiated energy and apparent stress. In: McGARR, A., ABERCROMBIE, R. & DI TORO, G. (eds) *Earthquakes: Radiated Energy and the Physics of Faulting*. American Geophysical Union, Geophysical Monographs, **170**, 15–24.
- CLARKE, G. L. & NORMAN, R. 1993. Generation of pseudotachylite under granulite facies conditions, and its preservation during cooling. *Journal of Metamorphic Geology*, **11**, 319–335.
- COWAN, D. S. 1999. Do faults preserve a record of seismic slip? A field geologist's opinion. *Journal of Structural Geology*, **21**, 995–1001.
- DIETERICH, J. H. 1972. Time-dependence of rock friction. *Journal of Geophysical Research*, **77**, 3690–3679.
- DIETERICH, J. H. 1979. Modeling of rock friction 1. Experimental results and constitutive equations. *Journal of Geophysical Research*, **84**, 2161–2168.
- DUEBENDORFER, E. M., VERMILYE, J., BEISER, P. A. & DAVIS, T. L. 1998. Evidence for aseismic deformation in the western Transverse Ranges, southern California: implications for seismic risk assessment. *Geology*, **26**, 271–274.
- DURNEY, D. W. 1972. Solution-transfer, an important geological deformation mechanism. *Nature*, **235**, 315–317.
- EVISON, F. F. 1971. Seismicity of the Alpine Fault, New Zealand. *Royal Society of New Zealand Bulletin*, **9**, 161–165.
- FAGERENG, Å. 2011. Geology of the seismogenic subduction thrust interface. In: FAGERENG, Å., TOY, V. G. & ROWLAND, J. V. (eds) *Geology of the Earthquake Source: A Volume in Honour of Rick Sibson*. Geological Society, London, Special Publications, **359**, 55–76.
- FAGERENG, Å. & SIBSON, R. H. 2010. Melange rheology and seismic style. *Geology*, **38**, 751–754, doi: 10.1130/G30868.1.
- FAULKNER, D. R., LEWIS, A. C. & RUTTER, E. H. 2003. On the internal structure and mechanics of large strike-slip fault zones: field observations of the Carboneras fault in southeastern Spain. *Tectonophysics*, **367**, 235–251.
- FROHLICH, C. & DAVIS, S. D. 1993. Teleseismic *b* values; or, much ado about 1.0. *Journal of Geophysical Research*, **98**, 631–644.
- GIBBS, J. W. 1877. On the equilibrium of heterogeneous substances. *Transactions of the Connecticut Academy*, **3**, 108–248, 343–524.
- GRATIER, J. P. & GAMOND, J. F. 1990. Transition between seismic and aseismic deformation in the upper crust. In: KNIFE, R. J. & RUTTER, E. H. (eds) *Deformation Mechanisms, Rheology and Tectonics*. Geological Society, London, Special Publications, **54**, 461–473.
- GRATIER, J. P. & GUEYDAN, F. 2007. Deformation in the presence of fluids and mineral reactions. In: HANDY, M. R., HIRTH, G. & HOVIUS, N. (eds) *Tectonic Faults: Agents of Change on a Dynamic Earth*. MIT Press, Cambridge, MA, 319–356.
- GRATIER, J. P., GUIGUET, R., RENARD, F., JENATTON, L. & BERNARD, D. 2009. A pressure solution creep law for quartz from indentation experiments. *Journal of Geophysical Research*, **114**, B03403, doi:10.1029/2008JB005652.
- GUTENBERG, B. & RICHTER, C. F. 1944. Frequency of earthquakes in California. *Bulletin of the Seismological Society of America*, **34**, 185–188.
- HANDY, M. R. 1990. The solid-state flow of polymimetic rocks. *Journal of Geophysical Research*, **95**, 8647–8661.
- HANKS, T. C. & KANAMORI, H. 1979. A moment magnitude scale. *Journal of Geophysical Research*, **84**, 2348–2350.
- HILL, D. P., EATON, J. P. & JONES, L. M. 1990. Seismicity, 1980–86. In: WALLACE, R. E. (ed.) *The San Andreas Fault System, California*. US Geological Survey, Professional Paper, **1515**, 115–151.
- HIPPERT, J. & EGYDIO-SILVA, M. 1996. New polygonal grains formed by dissolution–redeposition in quartz mylonite. *Journal of Structural Geology*, **18**, 1345–1352.
- HIRTH, G., TEYSIER, C. & DUNLAP, W. 2001. An evaluation of quartzite flow laws based on comparisons between experimentally and naturally deformed rocks. *International Journal of Earth Sciences*, **90**, 77–87.
- ISHIMOTO, M. & IIDA, K. 1939. Observations sur les séismes enregistrés par le microseismograph construit dernièrement (I). *Bulletin of the Earthquake Research Institute, Tokyo University*, **17**, 443–478.
- KANAMORI, H. & ANDERSON, D. L. 1975. Theoretical basis of some empirical relations in seismology. *Bulletin of the Seismological Society of America*, **65**, 1073–1095.
- KANEKO, Y., AVOUAC, J.-P. & LAPUSTA, N. 2010. Towards inferring earthquake patterns from geodetic observations of interseismic coupling. *Nature Geoscience*, **3**, 363–369.
- KARATO, S. & WU, P. 1993. Rheology of the upper mantle – A synthesis. *Science*, **260**, 771–778.
- KING, G. C. P. 1983. The accommodation of large strains in the upper lithosphere of the Earth and other solids by self-similar fault systems: the geometrical origin of *b*-value. *Pure and Applied Geophysics*, **121**, 761–815.
- KNIFE, R. J. 1989. Deformation mechanisms – recognition from natural tectonites. *Journal of Structural Geology*, **11**, 127–146.
- KNIFE, R. J. 1990. Microstructural analysis and tectonic evolution in thrust systems: examples from the Assynt region of the Moine Thrust Zone, Scotland.

- In: BARBER, D. J. & MEREDITH, P. G. (eds) *Deformation Processes in Minerals, Ceramics and Rocks*. Mineralogical Society of Great Britain and Ireland. Unwin Hyman, London, 228–261.
- KOHLSTEDT, D. L., EVANS, B. & MACKWELL, S. J. 1995. Strength of the lithosphere: constraints imposed by laboratory experiments. *Journal of Geophysical Research*, **100**, 17 587–17 602.
- LIN, A., MARUYAMA, T., STALLARD, A., MICHIBAYASHI, K., CAMACHO, A. & KANO, K. 2005. Propagation of seismic slip from brittle to ductile crust: evidence from pseudotachylite Woodroffe thrust, central Australia. *Tectonophysics*, **402**, 221–235.
- MALTMAN, A. (ed.) 1994. *The Geological Deformation of Sediments*. Chapman & Hall, London.
- MARIANI, E., BRODIE, K. H. & RUTTER, E. H. 2006. Experimental deformation of muscovite shear zones at high temperatures under hydrothermal conditions and the strength of phyllosilicate-bearing faults in nature. *Journal of Structural Geology*, **28**, 1569–1587.
- MARONE, C. 1998. Laboratory-derived friction laws and their application to seismic faulting. *Annual Review of Earth and Planetary Sciences*, **26**, 643–696.
- MARONE, C., RALEIGH, C. B. & SCHOLZ, C. H. 1990. Frictional behavior and constitutive modeling of simulated fault gouge. *Journal of Geophysical Research*, **95**, 7007–7025.
- McCLAY, K. R. 1977. Pressure solution and Coble creep in rocks and minerals. *Journal of the Geological Society, London*, **134**, 57–70.
- McGARR, A. 1999. On relating apparent stress to the stress causing earthquake fault slip. *Journal of Geophysical Research*, **104**, 3003–3011.
- MOECHER, D. P. & STELTENPOHL, M. G. 2011. Petrological evidence for co-seismic slip in extending middle-lower continental crust: Heier's zone of pseudotachylite, north Norway. In: FAGERENG, Å., TOY, V. G. & ROWLAND, J. V. (eds) *Geology of the Earthquake Source: A Volume in Honour of Rick Sibson*. Geological Society, London, Special Publications, **359**, 169–186.
- MOORE, J. C. & SAFFER, D. 2001. Updip limit of the seismic zone beneath the accretionary prism of southwest Japan: an effect of diagenetic to low-grade metamorphic processes and increasing effective stress. *Geology*, **29**, 183–186.
- MORROW, C., RADNEY, B. & BYERLEE, J. 1992. Frictional strength and the effective pressure law of montmorillonite and illite clays. In: EVANS, B. & WONG, T. (eds) *Fault Mechanics and Transport Properties of Rocks*. Academic Press, New York, 69–88.
- NIEMEIJER, A. R. & SPIERS, C. J. 2006. Velocity dependence of strength and healing behaviour in phyllosilicate-bearing fault gouge. *Tectonophysics*, **427**, 231–253.
- NIEMEIJER, A. R. & SPIERS, C. J. 2007. A microphysical model for strong velocity weakening in phyllosilicate-bearing fault gouges. *Journal of Geophysical Research*, **112**, B10405, doi:10.1029/2007JB005008.
- PASSCHIER, C. W. & TROUW, R. A. J. 2005. *Microtectonics*. Springer, Berlin.
- PATERSON, M. S. 1973. Nonhydrostatic thermodynamics and its geological applications. *Reviews of Geophysics and Space Physics*, **11**, 355–389.
- PAVLIS, T. L., SERPA, L. F. & KEENER, C. 1993. Role of seismogenic processes in fault-rock development – an example from Death Valley, California. *Geology*, **21**, 267–270.
- PENG, Z. & GOMBERG, J. 2010. An integrated perspective of the continuum between earthquakes and slow-slip phenomena. *Nature Geoscience*, **3**, 599–607.
- PIFFNER, O. A. & RAMSAY, J. G. 1982. Constraints on geological strain rates: arguments from finite strain states of naturally deformed rocks. *Journal of Geophysical Research*, **87**, 311–321.
- PRYER, L. L. 1993. Microstructures of feldspars from a major crustal thrust zone: the Grenville Front, Ontario, Canada. *Journal of Structural Geology*, **15**, 21–36.
- REID, H. F. 1911. *The Elastic-Rebound Theory of Earthquakes*. University of California Publications, Bulletin of the Department of Geology, **6**, 413–444.
- ROWE, C. D., MENEGHINI, F. & MOORE, J. C. 2011. Textural record of the seismic cycle: strain-rate variation in an ancient subduction thrust. In: FAGERENG, Å., TOY, V. G. & ROWLAND, J. V. (eds) *Geology of the Earthquake Source: A Volume in Honour of Rick Sibson*. Geological Society, London, Special Publications, **359**, 77–96.
- RUFF, L. & KANAMORI, H. 1980. Seismicity and the subduction process. *Physics of the Earth and Planetary Interiors*, **23**, 240–252.
- RUINA, A. 1983. Slip instability and state variable friction laws. *Journal of Geophysical Research*, **88**, 10 359–10 370.
- RUTTER, E. H. 1976. The kinetics of rock deformation by pressure solution. *Philosophical Transactions of the Royal Society of London*, **283**, 203–219.
- RUTTER, E. H. & MAINPRICE, D. H. 1979. On the possibility of slow fault slip controlled by a diffusive mass transfer process. *Gerlands Beiträge zur Geophysik*, **88**, 154–162.
- SCHOLZ, C. H. 1988. The brittle–plastic transition and the depth of seismic faulting. *Geologische Rundschau*, **77**, 319–328.
- SCHOLZ, C. H. 1997. Size distributions for large and small earthquakes. *Bulletin of the Seismological Society of America*, **87**, 1074–1077.
- SCHOLZ, C. H. 1998. Earthquakes and friction laws. *Nature*, **391**, 37–42.
- SCHOLZ, C. H. 2002. *The Mechanics of Earthquakes and Faulting*, 2nd edn. Cambridge University Press, Cambridge.
- SCHOLZ, C. H., MOLNAR, P. & JOHNSON, T. 1972. Detailed studies of frictional sliding of granite and implications for the earthquake mechanism. *Journal of Geophysical Research*, **77**, 6392–6406.
- SCHWARTZ, D. P. & COPPERSMITH, K. J. 1984. Fault behavior and characteristic earthquakes: examples from the Wasatch and San Andreas Fault Zones. *Journal of Geophysical Research*, **89**, 5681–5698.
- SIBSON, R. H. 1975. Generation of pseudotachylite by ancient seismic faulting. *Geophysical Journal of the Royal Astronomical Society (now Geophysical Journal International)*, **43**, 775–794.
- SIBSON, R. H. 1977. Fault rocks and fault mechanisms. *Journal of the Geological Society*, **133**, 191–213.

- SIBSON, R. H. 1980. Transient discontinuities in ductile shear zones. *Journal of Structural Geology*, **2**, 165–171.
- SIBSON, R. H. 1983. Continental fault structure and the shallow earthquake source. *Journal of the Geological Society*, **140**, 741–767.
- SIBSON, R. H. 1984. Roughness at the base of the seismogenic zone: Contributing factors. *Journal of Geophysical Research*, **89**, 5791–5799.
- SIBSON, R. H. 1985. Stopping of earthquake ruptures at dilational fault jogs. *Nature*, **316**, 248–251.
- SIBSON, R. H. 1986. Earthquakes and rock deformation in crustal fault zones. *Annual Review of Earth and Planetary Sciences*, **14**, 149–175.
- SIBSON, R. H. 1989. Earthquake faulting as a structural process. *Journal of Structural Geology*, **11**, 1–14.
- SIBSON, R. H. 2002. Geology of the crustal earthquake source. In: LEE, W. H. K., KANAMORI, H., JENNINGS, P. C. & KISSLINGER, C. (eds) *International Handbook of Earthquake and Engineering Seismology – Part A*. Academic Press, New York, 455–473.
- SIBSON, R. H. 2003. Thickness of the seismic slip zone. *Bulletin of the Seismological Society of America*, **93**, 1169–1178.
- SIBSON, R. H. 2011. The scope of earthquake geology. In: FAGERENG, Å., TOY, V. G. & ROWLAND, J. V. (eds) *Geology of the Earthquake Source: A Volume in Honour of Rick Sibson*. Geological Society, London, Special Publications, **359**, 319–332.
- SIBSON, R. H. & TOY, V. G. 2006. The habitat of fault-generated pseudotachylite: presence v. absence of friction melt. In: MCGARR, A., ABERCROMBIE, R. & DI TORO, G. (eds) *Earthquakes: Radiated Energy and the Physics of Faulting*. American Geophysical Union, Geophysical Monographs, **170**, 153–166.
- SMITH, S. A. F., HOLDSWORTH, R. E., COLLETTINI, C. & PEARCE, M. A. 2011. The microstructural character and mechanical significance of fault rocks associated with a continental low-angle normal fault: the Zuccale Fault, Elba Island, Italy. In: FAGERENG, Å., TOY, V. G. & ROWLAND, J. V. (eds) *Geology of the Earthquake Source: A Volume in Honour of Rick Sibson*. Geological Society, London, Special Publications, **359**, 97–114.
- SNOKE, A. W., TULLIS, J. & TODD, V. R. (eds). 1998. *Fault-related Rocks: A Photographic Atlas*. Princeton University Press, Princeton, NJ.
- SORBY, H. C. 1853. On the origin of slaty cleavage. *Edinburgh New Philosophical Journal*, **55**, 137–148.
- STÖCKHERT, B., BRIX, M. F., KLEINSCHRODT, R., HURFORD, A. J. & WIRTH, R. 1999. Thermochronometry and microstructures of quartz – a comparison with experimental flow laws and predictions on the temperature of the brittle–plastic transition. *Journal of Structural Geology*, **21**, 351–369.
- TULLIS, J. & YUND, R. A. 1991. Diffusion creep in feldspar aggregates: experimental evidence. *Journal of Structural Geology*, **13**, 987–1000.
- UJIIE, K., TSUTSUMI, A. & KAMEDA, J. 2011. Reproduction of thermal pressurization and fluidization of clay-rich fault gouges by high-velocity friction experiments and implications for seismic slip in natural faults. In: FAGERENG, Å., TOY, V. G. & ROWLAND, J. V. (eds) *Geology of the Earthquake Source: A Volume in Honour of Rick Sibson*. Geological Society, London, Special Publications, **359**, 267–286.
- VAN DIGGELEN, E., HOLDSWORTH, R. E., DE BRESSER, J. H. P., SPIERS, C., SMITH, S. A., WALKER, R. J. & BOWEN, L. 2010. The microstructural character and evolution of fault rocks from SAFOD and potential weakening mechanisms along the San Andreas Fault. In: *2010 American Geophysical Union Fall Meeting*. American Geophysical Union, San Francisco, CA, Abstract T52B-06.
- VOLL, G. 1976. Recrystallization of quartz, biotite and feldspars from Erstfeld to the Leventina Nappe, Swiss Alps, and its geological significance. *Schweizerische Mineralogische und Petrographische Mitteilungen*, **56**, 641–647.
- WELLS, D. L. & COPPERSMITH, K. J. 1994. New empirical relationships among magnitude, rupture length, rupture width, rupture area, and surface displacement. *Bulletin of the Seismological Society of America*, **84**, 974–1002.
- WESNOUSKY, S. G. 1999. Crustal deformation and the stability of the Gutenberg–Richter relationship. *Bulletin of the Seismological Society of America*, **89**, 1131–1137.
- WESNOUSKY, S. G., SCHOLZ, C. H., SHIMAZAKI, K. & MATSUDA, T. 1983. Earthquake frequency distribution and the mechanics of faulting. *Journal of Geophysical Research*, **88**, 9331–9340.
- WHITE, S. 1973. Syntectonic recrystallisation and texture development in quartz. *Nature*, **244**, 276–278.
- WINTSCH, R. P., CHRISTOFFERSEN, R. & KRONENBERG, A. K. 1995. Fluid–rock reaction weakening of fault zones. *Journal of Geophysical Research*, **100**, 13 021–13 032.
- WOODCOCK, N. H. & MORT, K. 2008. Classification of fault breccias and related fault rocks. *Geological Magazine*, **145**, 435–440.
- ZEUCH, D. H. 1983. On the inter-relationship between grain-size-sensitive creep and dynamic recrystallization of olivine. *Tectonophysics*, **93**, 151–168.

# Fault-zone geology: lessons from drilling through the Nojima and Chelungpu faults

ANNE-MARIE BOULLIER

*ISTerre – CNRS, Université Joseph Fourier, Maison des Géosciences, BP 53, 38041 Grenoble Cedex 09, France (e-mail: Anne-Marie.Boullier@obs.ujf-grenoble.fr)*

**Abstract:** Several drilling projects have been conducted through active faults with the aim of learning about the geology of the fault zones and tentatively correlating the structure and mineralogy of the fault zones with their seismological behaviour during recent earthquakes. Here we present the major results obtained from structural and mineralogical studies of core samples retrieved from the dextral reverse strike-slip Nojima Fault (Japan) within granitic rocks following the Kobe earthquake (1995), and from the Chelungpu Thrust Fault (Taiwan) within alternating silts and shales following the Chi-chi earthquake (1999). We show how these projects, despite not fulfilling all their objectives, have still contributed to a better geological knowledge of the fault zones, to a better characterization of the slip zones related to the recent earthquakes particularly of their thickness, microstructures and deformation mechanisms, and to a better understanding of the nature and role of fluids within the fault zone. They have also led to new questions, and to new approaches, for studying fault-rock samples. For all of these reasons, they have stimulated international scientific research into fault-zone geology.

In 1993, a conference was held in California by the US Geological Survey on ‘Mechanical Effects of Fluids in Faulting’. This led to a special issue of the *Journal of Geophysical Research*, in the introduction of which Hickman *et al.* (1995) reported recommendations for three significant topics for future research, one of which was ‘fault zone drilling combined with surface-based geophysical and geological investigations’ (p. 13 838). Since that time, several fault-zone drilling projects have been conducted around the world, such as the Nojima Fault project following the 1995 Kobe earthquake, the Corinth Rift (Greece) Laboratory, the San Andreas Fault Observatory at Depth (SAFOD) in Parkfield (California), the Taiwan Chelungpu fault Drilling Project (TCDP) following the 1999 Chi-chi earthquake and the Wenchuan earthquake Fault Scientific Drilling (WFSD) through the Longmen Shan active fault zone (following the 2008 Wenchuan earthquake, China). Other projects have drilled plate boundaries along subduction zones, such as the shallow Barbados accretionary prism (Leg ODP 156) or the NanTroSeize experiment, which is still in progress through the Nankai Trough.

In a recent review, Zoback *et al.* (2007) summarized the principal objectives and scientific goals of fault-zone drilling: ‘The objective of fault-zone drilling projects is to directly study the physical and chemical processes that control deformation and earthquake generation within active fault zones’ (p. 649). More recently, the ICDP–SCEC international workshop on ‘Rapid Response Drilling: Past, Present, and Future’, held in Tokyo, Japan in

November 2008 (see Brodsky *et al.* 2009), pointed out the importance of knowing how fault strength recovers slowly in the long interval between earthquakes, and what combinations of physical and chemical properties of fault rocks lead faults to slip or to creep. In order to fulfill these objectives, the active fault zone and the active slip zone related to the last earthquake had first to be recognized so that their thickness, mineralogy, chemical composition and microstructures could be studied. The major geological questions addressed by fault-zone drilling projects are the following. Can we interpret microstructures in terms of deformation mechanisms, strain-rate, slip-weakening or slip-hardening processes? Can we estimate the fracture and heat contribution in the energy budget of an earthquake? What is the importance of fluids before, during and after an earthquake? What are the mechanisms and kinetics of fault healing? What are the physical properties (seismic velocities, electrical resistivity, density, porosity, permeability) of fault-zone materials compared to country rocks, and how do they vary in time and space? As predicted by Hickman *et al.* (1995), these drilling programmes have partly answered these questions and have contributed to a better understanding of the active faults, as illustrated by the huge number of scientific papers that have arisen from the studies of core samples. In fact, these are too numerous to cite herein. These studies have also enabled important new questions to be defined, and have also stimulated a large number of laboratory measurements and experiments.

Of course, boreholes are needlepoints through faults, and surface surveys and detailed studies should not be neglected. However, they provide continuous and unaltered sampling through the faults. In this paper I will focus on and tentatively summarize the main results that have specifically arisen from the Nojima (Japan) and Chelungpu (Taiwan) drilling projects.

## The Nojima Fault (Japan)

### *General context*

The 1995 Hyogo-ken Nanbu earthquake (Kobe earthquake,  $M 7.2$ ) caused 6432 fatalities and disastrous damage in the Kobe city and Awaji Island area. One year after the earthquake, five boreholes were successfully drilled through the Nojima Fault in Awaji Island by the Geological Survey of Japan (GSJ) and the National Research Institute for Earth Science and Disaster Prevention (NIED) at Hirabayashi, and by the Disaster Prevention Research Institute (DPRI, Kyoto University) at Ogura, with the aim of better understanding seismic processes. These boreholes, which were completed within 14 months of the Kobe earthquake, were the first to penetrate through active faults following a recent earthquake. The Nojima Fault is a NE-striking and SE-dipping dextral reverse fault running along the west coast of the Awaji Island, which cuts across the Cretaceous Ryoke granodiorite and its porphyry dykes (Fig. 1a). Its Quaternary offset and average slip rate have been established by Murata *et al.* (2001) to be 490–540 m and 0.4–0.45 m per  $10^3$  years, respectively, for the last 1.2 Ma based on the displacement of an unconformity below the sedimentary Kobe Group (Fig. 1b). The basal part of this group has been dated to Middle–Late Eocene (Yamamoto *et al.* 2000), that is, 40 Ma. These geological data and dates represent important constraints for interpreting the structure and mineralogy of the fault rocks observed in core samples.

### *The active fault zone*

Drill holes were nearly vertical and at low angle to the orientation that is inferred for the Nojima Fault from its steeply dipping surface rupture ( $75\text{--}85^\circ\text{SE}$ ; Awata & Mizuno 1998). Conventional borehole logging during drilling illustrated the evolution of physical properties of rocks with depth. Measured parameters, were sonic wave velocity ( $V_p$ ), borehole diameter, resistivity, porosity, density, gamma-ray and temperature (Ito *et al.* 1996; Ikeda 2001). By combining these data with continuous observation of core samples on-site, the main fault zone was located at 389.5, 624.5 and

1140 m depth in the DPRI 500, Hirabayashi GSJ and NIED drill holes, respectively (Fig. 1b, c). Another borehole approached the fault at approximately 1700 m depth (DPRI 1800, Fig. 1b) but did not go entirely through it (Lin *et al.* 2007).

The logging tools give a first image of the structure of the fault. In the GSJ borehole, for example, the resistivity decreases regularly above and increases abruptly below all faults regardless of their importance (Pezard *et al.* 2000). Conversely, the natural gamma radioactivity displays a wide maximum above the fault, decreases sharply on the fault and then increases regularly below it, until the baseline (Pezard *et al.* 2000). Both trends indicate an asymmetry of the fault zone, and a tendency towards more extensive fracturing and alteration of the hanging wall as the fault is approached. This result illustrates that logging tools are powerful methods to locate damage and fault zones in boreholes. The Stoneley wave analysis was used to determine the location of the permeable zone around the Principal Slip Zone (PSZ; Sibson 2003) in the Hirabayashi GSJ drill hole within the 623–625 m depth interval predicted by observations of the surface rupture (Kiguchi *et al.* 2001). It is important to note that no temperature anomaly was measured in any borehole.

### *Characterization of the fault zone*

An identical procedure was followed for core handling for all drill holes (Matsuda *et al.* 2001; Tanaka *et al.* 2001a; Lin *et al.* 2007). Core pieces were fixed using epoxy resin and cut into two halves. One of these halves was for archiving, but was polished for naked-eye observations. The other half was made into thin sections, and used for experiments and analyses. This method has advantages for microstructural studies because it allowed multiscale observations of samples from cores to thin sections. However, it caused complications in the measurement of physical properties of the fault rocks.

Formation Micro-Imaging (FMI<sup>TM</sup>: Schlumberger, Houston, TX), a downhole logging technique that was performed after the GSJ drilling, provides an image of the electric resistivity of the borehole, and thus indicates the number and orientation of the fractures. The fractures tend to strike east–west far from the fault, as expected due to the orientation of the present-day stress field, but they become normal to the fault close to it and parallel to it within the fault core (Ito & Kiguchi 2005). FMI and images of the core were compared to reorientate the core samples in a geographical coordinate system (Ohtani *et al.* 2000b). However, this was not possible for the whole length of the borehole, particularly in sections with few fractures.

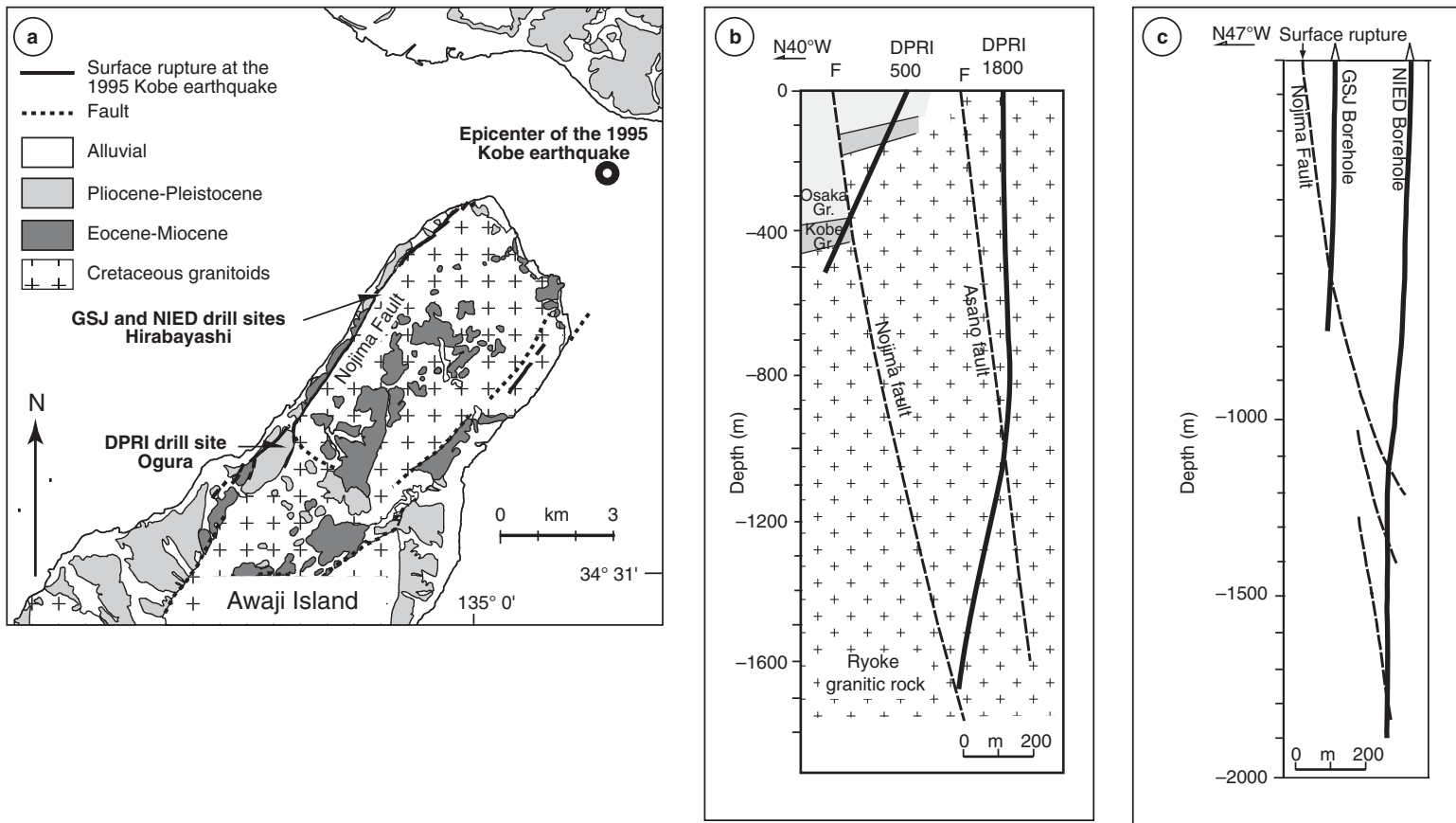


**Fig. 1.** (a) Geological map of the northern part of the Awaji Island and location of the DPRI, Hirabayashi GSJ and NIED drill sites (after Ohtani *et al.* 2000b). (b) Cross-section showing the vertical offset of the Nojima Fault, and the orientation of the DRPI 500 and DPRI 1800 boreholes at Ogura (after Lin *et al.* 2007). (c) Cross-section showing the orientation of the GSJ and NIED boreholes at Hirabayashi (after Tanaka *et al.* 2007b).

Nevertheless, observations of thin sections normal to the core indicate evidence of two nearly orthogonal directions of compression in the form of kinked biotites (Boullier *et al.* 2004a), and healed (fluid inclusion planes) or sealed (calcite) micro-fractures (Takeshita & Yagi 2001). These two stress tensors are consistent with the geodynamics of Japan, which displays left-lateral transcurrent faults striking 045° during the Late Cretaceous–Paleocene (Kanaori 1990) that were reactivated as right-lateral faults during Late Pliocene–Quaternary times (Fabbri *et al.* 2004).

Systematic studies of polished slabs (see, for e.g. Fig. 2) and thin sections have provided important data on the distribution of deformation microstructures, geochemical composition and mineralogy of the core samples in all boreholes (Ohtani *et al.* 2000a, 2001; Fujimoto *et al.* 2001 2007a; Kobayashi *et al.* 2001; Lin *et al.* 2001, 2007; Matsuda *et al.* 2001, 2004; Tanaka *et al.* 2001a, b). Most of these studies have used Sibson's (1977) classification of fault rocks. First, these authors used the distribution of deformation and alteration textures in order to define the fault core where most of the displacement is accommodated. The damage zone was defined as the zone made up of a network of subsidiary structures between the fault core and the undeformed protolith (Caine *et al.* 1996). The fault core and damage zone are 0.3 and more than 46.5 m wide, respectively, in the Hirabayashi GSJ borehole (Ohtani *et al.* 2000a, 2001; Fujimoto *et al.* 2001; Tanaka *et al.* 2001a). The fault damage zone is 70 m wide in the Hirabayashi NIED drill hole (Tanaka *et al.* 2007b), and even larger (130 m) if the 1140 and 1312 m fault zones are considered the bounding faults of a fault zone (Lockner *et al.* 2009). The Nojima Fault Zone becomes wider and more complex with depth, branching into two faults between the Hirabayashi GSJ and the NIED drill holes.

Secondly, correlations between deformation intensity and geochemical composition were possible thanks to the homogeneity of the starting material, the Ryoke granodiorite (Fig. 2a). Mass balance calculations considering TiO<sub>2</sub> and P<sub>2</sub>O<sub>5</sub> as immobile elements indicate important volume loss (compaction) in the fault core but volume gain (dilation) in the damage zone in the Hirabayashi GSJ and the NIED boreholes (Tanaka *et al.* 2001a, 2007b). Volume gain in the damage zone corresponds also to an LOI (loss on ignition) increase and to a decrease in the P-wave velocity (Fujimoto *et al.* 2001). These results are consistent with the permeability and strength evolution around the fault as measured by Mizoguchi *et al.* (2008a) on surface samples and by Lockner *et al.* (2009) on drill core samples. The fault zone is ‘a thin, low-strength, low-permeability fault zone core flanked

by zones of high permeability rock that have undergone relatively limited total shear’ (Lockner *et al.* 2009, p. 1662).

### *The Principal Slip Zone*

Although it was a challenging prospect, the Principal Slip Zone (PSZ: Sibson 2003), where displacement took place during the Kobe earthquake, was located by means of careful observations of core samples and polished slabs from three drill holes. In the DPRI 500 drill hole (Fig. 1b) the PSZ is localized to the contact between foliated gouges from the Ryoke granodiorite and from the Osaka group, and is described as a fault surface (Lin *et al.* 2001; Tanaka *et al.* 2001b). This would suggest that the PSZ related to the Kobe earthquake has no apparent thickness at this depth. However, thanks to electron spin resonance (ESR) intensity measured across the dark-grey fault plane by Fukuchi & Imai (2001), and to comparisons made of ESR analyses of natural and experimental fault gouge samples produced from high-speed slip tests (Fukuchi *et al.* 2005), it has been demonstrated that a thermal effect related to the earthquake was recorded in a 6 mm-wide zone. This could be explained by the frictional heating of the pore water in the fault gouge above boiling, and its diffusion into the fault gouge (Fukuchi & Imai 2001). Darkening of the gouge and the presence of an increased ferrimagnetic resonance (FMR) signal in the PSZ are related to the formation of ferrimagnetic iron oxides, an indication that frictional heating may have induced temperatures of at least 350–400 °C during seismic slip at a depth of 390 m (Fukuchi *et al.* 2005).

In the Hirabayashi GSJ drill hole (Fig. 1c), after much debate, it was concluded that the PSZ was found at a depth of 625.27 m in a millimetre-thick slip zone (Tanaka *et al.* 2001a). In the Hirabayashi NIED drill hole (Fig. 1c), Tanaka *et al.* (2007b) located the PSZ at a depth of 1140.57–1140.66 m in a 10 mm-thick Ca-rich ultracataclasite layer in which intense grain-size reduction has occurred. However, Lockner *et al.* (2009) suggested that two activated fault strands were crossed by this drill hole at depths of 1140 and 1312 m. All of these observations on drill holes through the Nojima Fault demonstrate that thickness of the PSZ increases with depth and that fault-healing processes may be very efficient, making it difficult to determine the presence of the PSZ in all drill holes only 1 year after the Kobe earthquake.

### *Pseudotachylites and seismic processes*

The most striking rocks observed either in the GSJ or NIED drill holes are pseudotachylites (Figs 2c & 3a), which are associated with ultracataclasites



**Fig. 2.** Photographs of polished drill core slabs from the Hirabayashi GSJ borehole. The depths of the upper and lower limits of the samples are specified at the top of each image (top of the core is always to the left). The sample number (bottom) indicates the number of the drill core box and the number of the sample within that box. The scale marker is 2.5 cm long. (a) Undeformed and almost unaltered Ryoke granodiorite. (b) Very fine-grained compacted ultracataclasite in the core of the fault. Note the reddish colour related to siderite veinlets and the pale honey-coloured veins filled by siderite + ankerite. (c) Very fine-grained compacted ultracataclasite (bottom left) associated with layered pseudotachylytes in the core of the fault.

(Ohtani *et al.* 2000a; Boullier *et al.* 2001; Tanaka *et al.* 2001a; Otsuki *et al.* 2003). These rocks are rarely observed in faults, as predicted by Sibson & Toy (2006), but clearly result from seismic slip

(Sibson 1975) and therefore provide information on seismic processes and the energy budget of earthquakes (Kanamori & Heaton 2000). Otsuki *et al.* (2003) suggested that the ultracataclasites observed

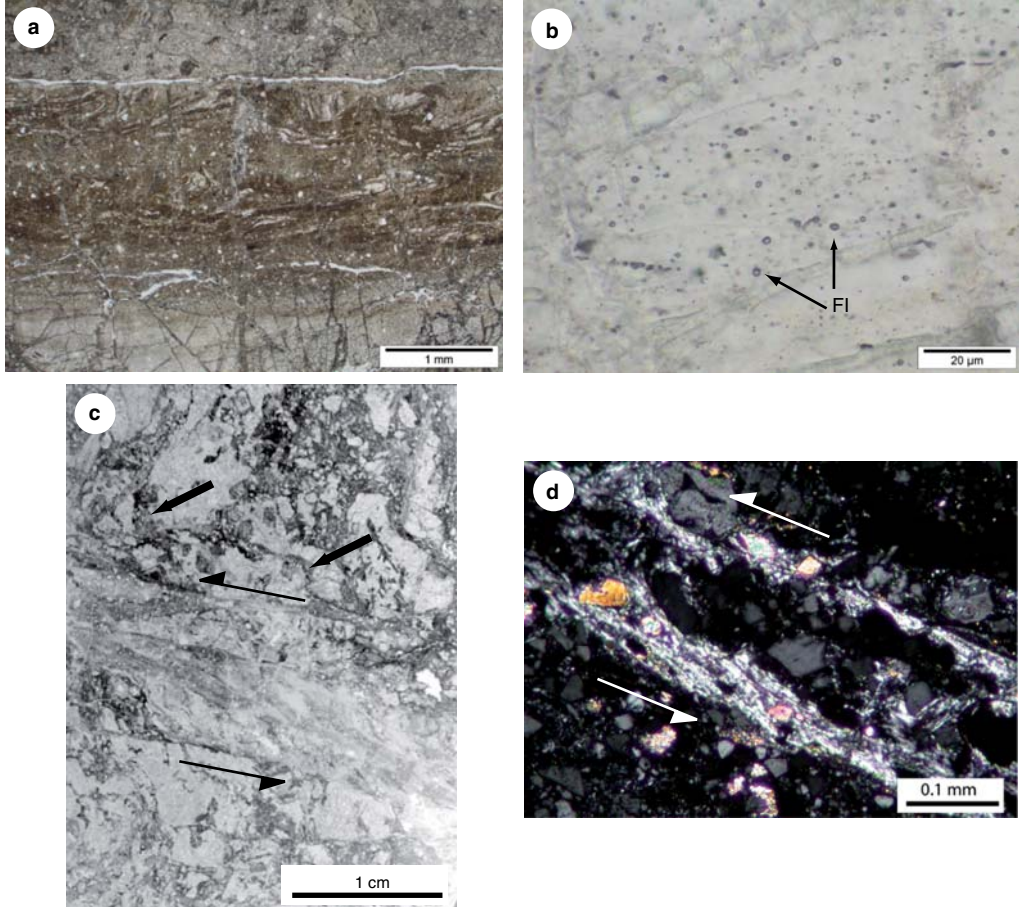


**Fig. 3.** Microphotographs of thin sections from the Hirabayashi GSJ borehole. (a) Pseudotachylite from the sample 99–05 (Fig. 2c, upper-right corner). Note the flow structures in the dark brown layer. Plane polarized light. (b) Transparent pseudotachylite fragment in the ultracataclasite from sample 99–05 (Fig. 2c, lower-left corner), which contains numerous  $\text{CO}_2$ -rich fluid inclusions (FI). Plane polarized light. (c) Scan of a thin section in sample 100–35 at 633.07 m depth showing a clay-rich, low-angle reverse shear zone deforming the fine-grained carbonate veins (short thick arrows). (d) Detail of the shear zone in Figure 3c showing the C/S arrangement of clays (presumably illite). Crossed polars.

in these drill holes behaved as fluidized granular material, in which frictional resistance decreased abruptly to nearly zero during seismic slip. They also proposed that the viscosity of the pseudotachylitic melt evolved during seismic slip, based on the temperature reached and the percentage of unmelted grains. As observed in the Hirabayashi GSJ drill hole and surface outcrops, the pseudotachylites are laminated with some contorted and folded layers (Fig. 3a) (Boullier *et al.* 2001; Tanaka *et al.* 2001a; Otsuki *et al.* 2003) that could be indicators of high-velocity seismic slip (Mizoguchi *et al.* 2009). The glass is not recrystallized and does not display spherulites or crystallites as often described

in pseudotachylites (see, for e.g. Di Toro & Pennachioni 2004). However, there are abundant rounded vesicles that appear to be fluid inclusions (Fig. 3b). Microthermometry on some of these fluid inclusions indicates that they are filled by a very dense  $\text{CO}_2\text{-H}_2\text{O}$  fluid. The intersection of isochoric lines with the present-day  $24 \text{ }^{\circ}\text{C km}^{-1}$  geothermal gradient indicates that the fluid inclusions were trapped at  $380 \text{ }^{\circ}\text{C}$  and  $410 \text{ MPa}$  (Boullier *et al.* 2001) or at  $270 \text{ }^{\circ}\text{C}$  and  $250 \text{ MPa}$  if a  $30 \text{ }^{\circ}\text{C km}^{-1}$  geothermal gradient is considered (Boullier *et al.* 2004a). The lower estimate is probably more realistic as no mylonites were found in the Nojima Fault. Such trapping conditions imply that

these pseudotachylites were formed at a depth of more than 9 km in the seismogenic zone before exhumation of the Ryoke granodiorite and deposition of the Kobe group at 40 Ma. They therefore formed during an early stage of seismic activity on the Nojima Fault (Boullier *et al.* 2001). This deduction has been confirmed by fission-track data of zircon, which provided a 56 Ma age for the pseudotachylites (Murakami & Tagami 2004). The presence of fluid inclusions also indicates that the pseudotachytic melt was saturated in fluids when cooling, which suggests that this frictional melt formed in an already altered initial material containing fluid as a free phase and/or structurally bound in minerals. Famin *et al.* (2008) measured the CO<sub>2</sub> and H<sub>2</sub>O content of the pseudotachytic melts using Fourier transform infrared (FTIR) microanalysis. This demonstrated that the younger layers have a decreasing CO<sub>2</sub> content due to the decreasing pressure of formation, and that a significant mass of CO<sub>2</sub> may have been exsolved during each pseudotachyte-generating seismic event. Consequently, because CO<sub>2</sub> saturation in silicate melts is pressure-dependent, the CO<sub>2</sub> content in pseudotachytic glass may be used as a proxy for the depth of pseudotachyte formation.

### *Energy budget of the earthquake*

Boullier *et al.* (2001) used the calculations proposed by Kanamori & Heaton (2000) to evaluate the thermal budget of earthquakes that resulted in pseudotachyte formation. Based on the thickness of the pseudotachyte layers (1 mm) and on the temperature increase due to frictional melting (1000 °C), they deduced that each pseudotachyte layer corresponds to  $M$  6– $M$  7 earthquakes, assuming the 3–4 MPa initial frictional stress calculated by Bouchon *et al.* (1998) from the slip model of Irikura *et al.* (1996). Therefore, the pseudotachylites now observed at a depth of 625 m in the Hirabayashi GSJ borehole were formed during approximately 56 Ma-old earthquakes similar in magnitude ( $M$  6– $M$  7 v.  $M_w$  6.9) to the recent Kobe earthquake.

Grain-size distribution (GSD) has been recently used by many authors to characterize fault rocks and gouges related to seismic events, with the aim of estimating the fracture energy of earthquakes (see a review in Keulen *et al.* 2007). This technique has also been used to characterize aseismic faulting and cataclasis accompanying hydrothermal alteration in the Cajon Pass drill hole (Blenkinsop & Sibson 1992). Keulen *et al.* (2007) measured GSD in cataclasites from the Hirabayashi GSJ drill hole and in experimentally deformed granitoids. In both cases, GSD was not fractal and two slopes ( $D$ ) were observed in all log–log GSDs. In experimental

or natural examples,  $D$  values of 0.9–1.1 were measured for grains smaller than about 1 µm. Two different  $D$  were measured for cracked grains (1.5–1.6) and gouges (2.0–2.6) for grains larger than 1 µm, which is the grinding limit of quartz. These results show that grain-size reduction in fault zones develops by a two-stage process: rupturing creates cracked grains; further displacement of fragments causes further comminution by wear and attrition. Healing processes may also modify GSD as demonstrated by experiments of hydrostatic or non-hydrostatic healing of fault gouges (Keulen *et al.* 2008). Thus, we should be cautious when using GSD for calculating the fracture energy of an earthquake because GSD is the sum of several cumulated seismic events and is the product of different mechanisms occurring during the whole evolution of the gouge zone.

### *Fluids: before, during and after earthquakes*

Multistage alteration of fault rocks has been recognized by Ohtani *et al.* (2000a), Fujimoto *et al.* (2001), Tanaka *et al.* (2001a, 2007b) and Boullier *et al.* (2004a), as summarized in Table 1. Using the relationships between hydrothermal minerals and structures, it is possible to correlate hydrothermal alteration with deformation episodes.

The older hydrothermal stage is weak, static and characterized by chlorite. It is attributed to the cooling of the granodiorite between 90 and 74 Ma (Takahashi 1992; Murakami *et al.* 2002).

The second stage is widespread and, at least in the Hirabayashi GSJ drill hole, is represented by zeolites. Laumontite, the most common mineral formed in this stage, is observed throughout the damage zone as an alteration product of plagioclase, filling veins and sealing fractures. The hydrothermal alteration in the low-strain damage zone in the Hirabayashi GSJ drill hole is very similar to that observed in the Cajon Pass drill hole (Blenkinsop & Sibson 1992) in terms of starting material (granitic rock), alteration product (laumontite formed at the expense of plagioclase) and deformation textures (almost no crack–seal textures, extensional fractures with flow structures and dilatant cataclasis). Some dilatant microstructures could thus result from aseismic deformation related to volume change induced by replacement of plagioclase by laumontite (Blenkinsop & Sibson 1992). Laumontite is present as clasts in ultracataclasites (pale green in Fig. 2b); in particular in those associated with pseudotachylites. This indicates that the first stage of seismic activity and alteration occurred before 40 Ma under decreasing pressure and temperature conditions between the formation of pseudotachylites at >270 °C and >250 MPa (see earlier), and the stability field of laumontite, which

**Table 1.** Hydrothermal episodes in the Nojima Fault. Principal occurrences and features of the hydrothermal minerals in the GSJ drill hole (modified from Boullier et al. 2004a)

Mineral	Chlorite	Zeolite: laumontite Minor calcite	Siderite	Ankerite and siderite	Clays
Temperature	c. 300 °C	c. 150–280 °C		<100 °C	
Texture	As rosettes in small cavities (ripidolite)	In blocky coarse-grained veins	In thin veinlets parallel to the flattening plane within the core of the fault zone	In hydraulic fractures including fragments of cataclasite and minerals, located above the slip zone	Alteration and replacement of minerals, in fractures
	In cracks together with albite	In hydraulic fractures, with small fragments of cataclasites or minerals			Very fine-grained crystals
Replaced mineral	Biotite and amphibole	Plagioclase		Plagioclase, biotite and amphibole	Plagioclase, micas, laumontite
Mechanisms of formation	Hydrothermal processes during cooling of the granodiorite	<i>In situ</i> replacement Vein filling Hydraulic fracture-fill	Taber growth	Hydraulic fracture-fill	<i>In situ</i> replacement
Subsequent deformation		Cataclasis Dissolution–precipitation processes: stylolites and veins	Cataclasis	Dissolution–precipitation processes: stylolites and schistosity Cataclasis in thin fine-grained gouge zones	Cataclasis in thin fine-grained gouge and shear zones Orientated parallel to schistosity
Age	Prior to the Kobe Group deposition	Contemporaneous with pseudotachylites	Quiescence stage: between 56 and 1.2 Ma	Younger than c.1.2 Ma <sup>c</sup>	Contemporaneous with or younger than carbonates <sup>d</sup>
	Between 90 and 74 Ma <sup>a</sup>	Prior to the Kobe Group deposition c. 56 Ma <sup>b</sup>			

<sup>a</sup>After Takahashi (1992) and Murakami *et al.* (2002).

<sup>b</sup>After Murakami & Tagami (2004).

<sup>c</sup>After Murata *et al.* (2001).

<sup>d</sup>After Lin *et al.* (2007).

is between 280 and 150 °C depending on the pressure (Zen & Thompson 1974). These observations are also consistent with the decreasing CO<sub>2</sub> content of the pseudotachylitic glass measured by Famin *et al.* (2008).

The third stage of alteration is characterized by thin veinlets of siderite emplaced within the flattening plane in cataclasites and ultracataclasites (reddish brown zones in Fig. 2b) within the core of the main fault zone around 625 m in the Hirabayashi GSJ drill hole (Boullier *et al.* 2004a), and within the 1140, 1300 and 1800 m fault cores of the Hirabayashi NIED drill hole (Boullier unpublished observations). These veins are not associated with any significant phase of deformation, nor with structures resulting from dilatancy, and are deformed in later gouge zones or cross-cut by later carbonate veins (see Table 1 and Boullier *et al.* 2004a). For these reasons, they have been correlated with a quiescence stage by Boullier *et al.* (2004a).

The fourth hydrothermal stage is characterized by hydraulic fractures filled by small-grain-size euhedral ankerite and siderite crystals (pale honey-coloured fractures in Fig. 2b) (Fujimoto *et al.* 2001; Boullier *et al.* 2004b; Moore *et al.* 2009). Undeformed hydrofractures of this type are mainly localized in the hanging wall of the main fault zone in the Hirabayashi GSJ drill hole but they are also observed below the fault where they are deformed by late gouge zones (Fig. 3c). Their internal structure strongly suggests that they were induced by coseismic hydraulic fracturing and fast nucleation of carbonates due to a sudden fluid or CO<sub>2</sub> partial pressure drop due to fracturing (Boullier *et al.* 2004b).

The latest stage of alteration is characterized by clays. Smectite has been found in the GSJ 625 m (Fujimoto *et al.* 2001) and NIED 1140 m (Matsuda *et al.* 2004) fault zones. Illite is also observed in small conjugate low-angle reverse shear zones located below the principal 625 m fault core (Fig. 3c) in which it displays a C/S microstructure (Fig. 3d). These small shear zones lie below the principal 625 m fault core and may be observed on the FMI images (Ito & Kiguchi 2005). They also correspond to the 625–635 m depth interval where deformation of the borehole has been seen on the BHTV (Bore Hole TeleViewer) acoustic scans (Célérier *et al.* 2000).

The present-day fluids that are circulating in the GSJ 625 m fault zone have been analysed. Their chemical composition is in equilibrium with the carbonates precipitated in the hydraulic fractures described earlier, and with illite and Camontmorillonite. This also indicates that the fluids are flowing upwards and originate from a reservoir situated at a depth of 4 km (Fujimoto *et al.* 2007)

based on the 24 °C geothermal gradient measured in the Hirabayashi GSJ borehole (Kitajima *et al.* 1998). Lin *et al.* (2003) have proposed that, because these fluids are meteoric in origin, they have infiltrated the active Nojima Fault by a fluid suction-pumping process inspired by the so-called seismic pumping model (Sibson *et al.* 1975).

### *Processes of healing by dissolution–precipitation*

Fluids are also involved in the chemical compaction of gouges, ultracataclasites or fine-grained vein-filling material by dissolution–precipitation processes, although fluid advection is not necessary. Evidence of these processes has been found in the 625 m fault zone of the Hirabayashi GSJ borehole in the form of stylolitic surfaces in fine-grained laumontite dilatant veins of the second hydrothermal stage (Boullier *et al.* 2004a), and in the indentation of grains in gouges or in fine-grained carbonate veins of the third hydrothermal stage (Boullier *et al.* 2004b). The dissolution–precipitation processes are diffusion controlled, and therefore dependent on the diffusion distance between the source and sink of solute, and on the mineral which is dissolved (Gratier *et al.* 2003). Consequently, although these are very slow processes, they may be very efficient under low stresses in fine-grained material, such as those mentioned earlier, and therefore contribute to the post-seismic or interseismic sealing of the fault, to the decrease in permeability of very fine-grained ultracataclasites as measured by Lockner *et al.* (2009) and to the stress build-up in the lead-up to the next seismic rupture. Minerals involved in these processes are mostly laumontite during the first stage and carbonates during the second stage of seismic activity of the Nojima Fault. A decrease in permeability should result in an increase in fluid pressure. However, there are no observational data, such as horizontal extensional veins, that would suggest that an abnormal fluid pressure regime existed in the case of the Nojima Fault, as it does for the fault-valve model (Sibson *et al.* 1988; Sibson 1990).

### *Lessons from the Nojima Fault drilling projects*

The first lesson from the Nojima Fault drilling projects is that the geology of this fault is considerably more complex than initially thought. The fault-zone thickness, structure and mineralogy are the result of two distinct periods of seismic activity accompanied by intense hydrothermal alteration separated by a period of quiescence. All of these stages are recorded in the fault-rock

microstructures. The recognition of very peculiar pseudotachylytes in the core of the fault that are attributed to the first period of activity has induced significant interest in this type of rocks. As a result, a number of high-velocity rotary shear friction experiments have been performed on 'hard' rocks (e.g. Di Toro *et al.* 2004; Hirose & Shimamoto 2005). Natural gouges from the Nojima Fault have also been used as initial material for similar high-velocity experiments to investigate their behaviour during seismic slip (Mizoguchi *et al.* 2009).

Observations of the internal structure of the Nojima Fault have also illustrated that we need more information on the permeability and thermal properties of faults in order to understand and predict their seismological behaviour (e.g. Wibberley & Shimamoto 2003, 2005; Uehara & Shimamoto 2004; Mizoguchi *et al.* 2008a; Lockner *et al.* 2009). Permeability is highly dependent on fracturing and healing processes, and rates and kinetics of these processes are of considerable importance. Recently, highly permeable pulverized rocks have been discovered along the San Andreas Fault by Dor *et al.* (2006) and along the Arima–Takatsuki tectonic line (Mitchell *et al.* 2009). Some textures of dilatant fractures at depth in the Hirabayashi GSJ drill hole are similar to naturally (Rockwell *et al.* 2009) and experimentally (Doan & Gary 2009) pulverized samples. Could they be the expression of pulverization at depth or high strain-rate brittle deformation in the fault zone? This question illustrates that the determination of strain rate on the basis of microstructures in fault rocks remains a major question, and more comparisons need to be made between experimentally and naturally deformed samples.

The Hirabayashi NIED borehole intercepted three fault zones (Tanaka *et al.* 2007b), while the DPRI 1800 borehole intercepted two (Lin *et al.* 2007). Some of these fault zones were activated by the Kobe earthquake, but others were not. As illustrated by the fact that it was difficult to identify the principal slip zone of the Kobe earthquake only 1 year after this event, fault-healing processes may be extremely efficient and so rapidly obliterate the evidence of localized slip. Therefore, can we still ask whether the non-activated faults are locked or inactive? Detailed comparative, collaborative studies by the principal investigators of each of these drill holes are needed to provide more information on the deformation and healing microstructures and mechanisms to address this question.

Nevertheless, the Japanese drill holes through the Nojima Fault have confirmed the international interest in fault-zone geology, and advanced the general understanding on faulting and seismic processes in basement rocks.

## The Chelungpu Fault (Taiwan)

### General context

The Chi-chi earthquake (21 September 1999,  $M_w = 7.6$ , c. 2400 fatalities) produced a surface rupture of 80 km, with up to 10 m of offset on the northern part of the Chelungpu thrust fault (Fig. 4a, b) (Kao & Chen 2000). From reconstruction of balanced cross-sections, Yue *et al.* (2005) determined that the Sanyi–Chelungpu thrust system has accommodated 14 km of total displacement, and that 0.3 km of total slip has been accommodated on a newly propagated North Chelungpu Chinshui detachment within the Chinshui Shale, where the Chi-chi earthquake occurred (Fig. 4b). Thus, in contrast with the Nojima Fault, the Chelungpu Fault has a relatively simple tectonic history.

The Chi-chi earthquake was recorded by the very dense Taiwan Strong Motion and GPS Networks, allowing models of spatial slip distribution (Ma *et al.* 2001), as well as determination of rupture velocity (Chen *et al.* 2001), and of coseismic and post-seismic deformation (Pathier *et al.* 2003; Yu *et al.* 2003). During the Chi-chi earthquake, the northern segment of the Chelungpu Fault was characterized by large displacement (8–10 m), high slip velocity ( $2\text{--}4 \text{ m s}^{-1}$ ) and low level of high-frequency radiation. In contrast, smaller displacement (3–4 m), lower slip velocities ( $0.5 \text{ m s}^{-1}$ ) and higher rates of acceleration of the ground motion were measured in the southern part (Ma *et al.* 2003).

Initially, two shallow boreholes penetrated the Chelungpu Fault in March 2001 at depths of 455 m (northern site, Fengyuan) and 211 m (southern site, Nantou). These provided initial important observations, such as a temperature rise in the northern site on the suspected fault zone activated by the Chi-chi earthquake (Tanaka *et al.* 2002) and differences in fault-zone architecture: clay-rich injections (Otsuki *et al.* 2005; Ujiie 2005) and pseudotachylite fragments (Otsuki *et al.* 2005) are described in the northern and southern boreholes, respectively. As the lithofacies and geological structure are similar at both the northern and southern sites, the difference in fault-rock microstructures are interpreted as indicating different frictional properties of the fault in these two segments (Otsuki *et al.* 2005; Ujiie 2005).

### The active fault zone

The Taiwan Chelungpu Fault Drilling Project (TCDP, Fig. 4) was started in 2002. The TCDP site was chosen near the town of DaKeng, about 2 km east of the surface rupture (Fig. 4b) in order to allow investigation of the slip-weakening

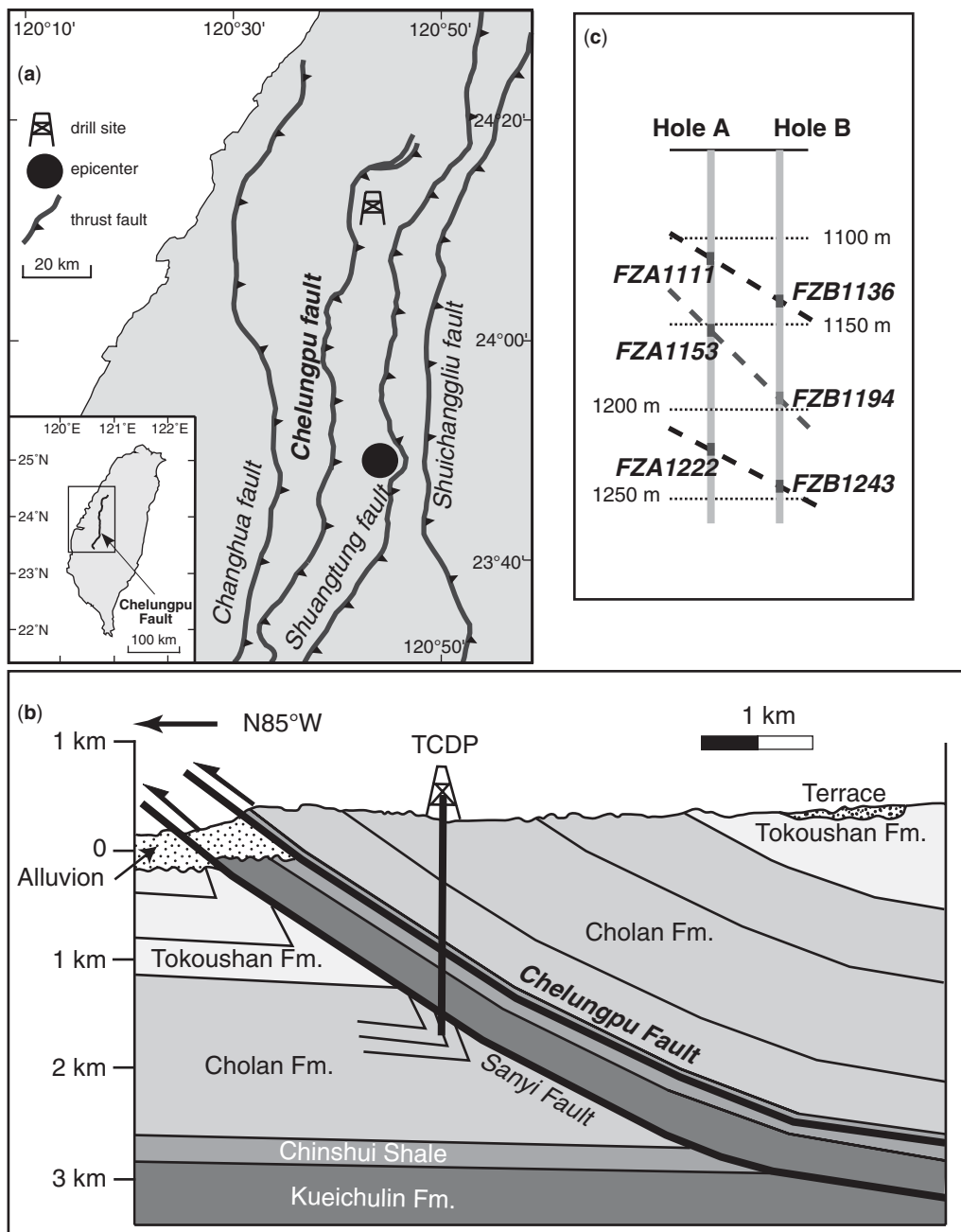


**Fig. 4.** (a) Sketch of the western Taiwanese foothills showing the principal thrust faults, the Chi-chi earthquake epicentre and the location of TCDP drill site. (b) Schematic cross-section passing through the TCDP drill site indicating the principal sedimentary formations and the principal faults (after Hung *et al.* 2007). (c) Correlation between the principal fault zones of the Chelungpu Fault system in Hole A and Hole B (after Hirono *et al.* 2007).

mechanisms responsible for the seismological characteristics of the Chi-chi earthquake in the northern part of the Chelungpu Fault. Two vertical

boreholes were drilled 40 m apart (Hole A, 2000.3 m deep, in 2004; and Hole B, 1352.6 m deep, in 2005), and a side-track was drilled from

a depth of 950 to 1280 m from Hole B (Hole C in 2005). TCDP holes penetrated through Pliocene and Upper Miocene alternating sandstones, siltstones and shales (Fig. 4b) (Song *et al.* 2007).

One major feature in the TCDP cores is the colour change of the rocks (from light grey to dark grey, and black) that accompanied deformation. This has been used as a macroscopic on-site criteria for locating fault zones (Yeh *et al.* 2007). Three major fault zones were recognized in the Chelungpu Fault system in Hole A at 1111, 1153 and 1221 m depth (Hung *et al.* 2007; Sone *et al.* 2007; Song *et al.* 2007; Yeh *et al.* 2007) that may correlate to fault zones at 1136, 1194 and 1243 m depth, respectively, in Hole B (Fig. 4c) (Hirono *et al.* 2007). In Hole B the recognition of fault zones was facilitated by the use of systematic non-destructive and continuous measurements performed on the retrieved cores at the Kochi Institute for Core Sample Research (JAMSTEC) such as density, porosity, magnetic susceptibility, natural gamma-ray radiation and gamma-ray attenuation, magnetic susceptibility and X-ray computed tomography (X-ray CT) (Hirono *et al.* 2007). Some, but not all, fault zones also include cm-thick fault-parallel disks of hard black ultracataclasites: at 1153 and 1221 m depth in Hole A (Yeh *et al.* 2007); and at 1194, 1243 and 1341 m depth in Hole B (Hirono *et al.* 2007).

Among these fault zones, the one located at 1111 m depth in Hole A (FZA1111, Fig. 4c) was determined on-site as the fault zone activated by the Chi-chi earthquake on the basis of several arguments: high-resolution shallow seismic reflection profiles predicting a depth at 1200 m with 10% error; high strain fault kinematics were determined as thrust by fault plane and slickenside orientations consistent with the measured focal mechanism of the Chi-chi earthquake; high fluid content (Ma *et al.* 2006; Song *et al.* 2007; Yeh *et al.* 2007), fracture density and physical properties measured by logging tools, in particular low resistivity, low density, and distinct  $V_p$  and  $V_s$  (Hung *et al.* 2007). The total thickness of the FZA1111 fault zone is 5.5 m (Yeh *et al.* 2007). It corresponds to the fault zone at a depth of 1136 m in Hole B (FZB1136, Fig. 4c), which has a 3.5 m total thickness and is characterized by a lower contrast related to higher permeability on X-ray CT images (Hirono *et al.* 2008).

### *Energy budget of the earthquake*

One major question arising from the TCDP concerns the thermal budget of the earthquake, and many papers have been devoted to that point. First, temperature measurements were performed in 2005 in Hole A. A 0.06 °C temperature anomaly was found around the FZA1111 (Kano *et al.* 2006),

consistent with the 0.1 °C anomaly measured earlier in the shallow boreholes (Mori & Tanaka 2002; Tanaka *et al.* 2006). As discussed by Kano *et al.* (2006) and Tanaka *et al.* (2006, 2007a), the temperature anomaly may occur: (i) as residual heat generated during the Chi-chi earthquake; or (ii) as a possible result of fluctuations of geothermal gradient related to changes of physical and thermal properties of fault rocks; or (iii) as the result of warm fluid upflow in the fault zone due to its high permeability, deduced from hydraulic tests (Doan *et al.* 2006) and measurements on core samples (Tanikawa *et al.* 2009). Unfortunately, it is not yet possible to resolve these possibilities in the TCDP boreholes.

Ma *et al.* (2006) calculated the grain-size distribution in the very fine-grained gouge recognized as the Chi-Chi PSZ by Kuo *et al.* (2005) in order to better constrain the energy budget of earthquakes. By comparison with the seismic surface fracture energy determined from near-field seismic data, they concluded that the contribution of gouge surface energy represents 6% of the earthquake breakdown work, which is slightly higher than the less than 1% value obtained on mature Californian faults by Chester *et al.* (2005) and Rockwell *et al.* (2009).

### *The Chi-Chi PSZ*

The Chi-Chi PSZ was recognized by Kuo *et al.* (2005, 2009) in the lower part of FZA1111 (Fig. 5), just above a hard, but fragile, black disk that broke into pieces during on-site core handling. This interpretation was based on the absence of reworking microstructures such as later fractures in the very fine-grained gouge, veins or schistosity, and on the presence of smectite as the dominant clay mineral. The authors also observed the presence of glassy material in small quantities (<25%) and suggested that melting of clay minerals due to strong shear heating occurred in the PSZ and that most of the resulting pseudotachylite was promptly converted into smectite (Kuo *et al.* 2009).

Boullier *et al.* (2009) presented a detailed study of the FZA1111 fault zone, focusing on the Chi-Chi PSZ. The latter is a 2 cm-thick, very fine-grained isotropic gouge (Fig. 6a), and contains matrix-supported clasts and clay clast aggregates (CCAs, Fig. 6b), which are microstructures that have been reproduced by Boutareaud *et al.* (2008, 2010) during high-velocity rotary shear experiments where a liquid to vapour transition occurred in the pore water. As such, CCAs are new symptomatic markers of seismic slip in clay-rich gouges, like pseudotachylites are in 'hard' rocks (Sibson 1975). Clasts of the lower black ultracataclasites are also present in the PSZ and display an inverse grain-size

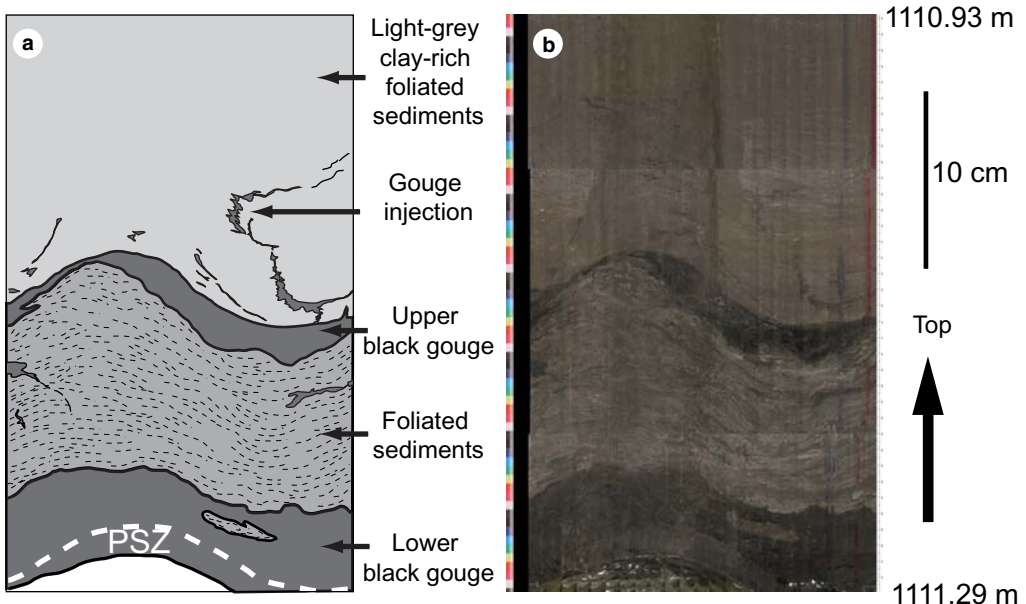


**Fig. 5.** Sketch (a) and unrolled scanning image (b) of the fault zone of FZA1111 showing the principal structural characteristics of the fault zone activated during the Chi-chi earthquake. PSZ, Principal Sip Zone (Sibson 2003) where slip occurred during the Chi-chi earthquake (after Boullier *et al.* 2009).

segregation according to the Brazil Nut Effect (Boullier *et al.* 2009). All of these microstructural criteria lead Boullier *et al.* (2009) to propose that the gouge was fluidized as the result of a 300–400 °C coseismic temperature rise inducing thermal pressurization (Sibson 1973). This phenomenon may explain the gouge injections observed above the FZA1111 (Fig. 5) and in the northern

shallow borehole (Otsuki *et al.* 2005; Ujiie 2005). The Chi-Chi PSZ in FZB1136 is very different from the PSZ in FZA1111; it is a thin (<0.3 v. 2 cm) ultracataclasite, locally exhibiting a layering defined by variations in concentrations of clay minerals and clasts (Boullier *et al.* 2009) similar to foliated gouges experimentally reproduced by Boutareaud *et al.* (2008) and Mizoguchi *et al.* (2009).

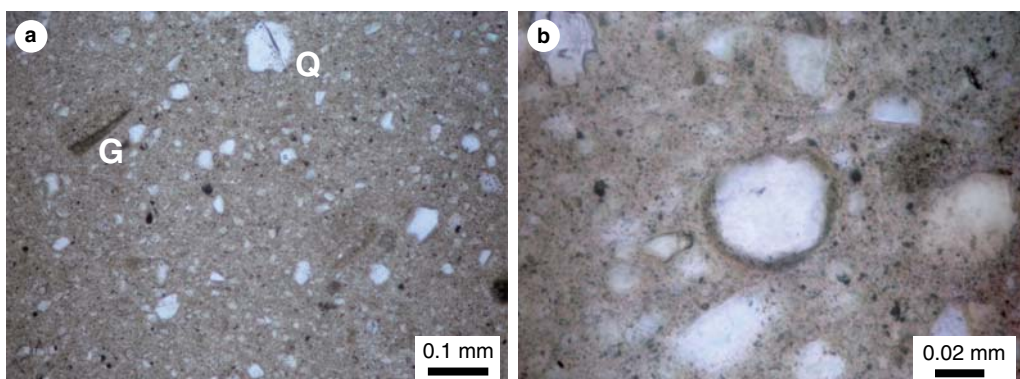


**Fig. 6.** Microstructures in the isotropic gouge within the PSZ shown in Figure 5 (after Boullier *et al.* 2009). All microphotographs are oriented as in Figure 5. (a) General view of the isotropic gouge showing the matrix-supported clasts which are either monomineralic, such as fractured quartz fragment (Q), or fine-grained polymimetic gouge fragments (G). Plane polarized light. (b) Clay-clast aggregate (CCA) with a round quartz core and a brownish cortex made of clays. Plane polarized light.

Continuous *in situ* and non-destructive measurement of the magnetic susceptibility in Hole B has shown that fault zones, and FZB1136 in particular, are characterized by an important increase in the magnetic susceptibility that has been interpreted by Hirono *et al.* (2006) as being due to the production of ferrimagnetic iron oxydes induced by frictional heat as experimentally reproduced during high-speed frictional testings (Fukuchi *et al.* 2005). Recently, Chou *et al.* (2009, 2010) and Aubourg *et al.* (2010) performed a very detailed and complete analysis of magnetic properties on FZB1136 using a U-channel sample. They measured the magnetic susceptibility, the isothermal remanent magnetization and S-ratio, and the anhysteretic remanent magnetization every cm, together with low-temperature magnetic properties to identify the magnetic minerals. Their measurements have been precisely compared with microstructures described by Boullier *et al.* (2009). The principal results are as follows: (i) a palaeomagnetic component close to the modern dipole is recovered all along the FZB1136; (ii) very small amounts of fine-grained magnetite and pyrrhotite constitute the magnetic assemblage in the PSZ; and (iii) authigenic goethite has been clearly identified by transmission electron microscopy (TEM) in and above the PSZ, and attributed to circulation and post-seismic cooling of hot fluids in the FZB1136 (Chou *et al.* 2009, 2010; Aubourg *et al.* 2010). Therefore, they confirmed that frictional heating occurred in the Chi-Chi PSZ.

Through measurement of major and trace element chemistry, as well as isotope ratios of core samples, Ishikawa *et al.* (2008) illustrated that the three fault zones exhibit sharp compositional peaks of fluid-mobile elements and strontium isotopes. They suggested that coseismic hot ( $>350^{\circ}\text{C}$ ) fluids circulated and interacted with the fault rocks where they mobilized these elements. Hashimoto *et al.* (2008) attributed the low iron content of chlorite in the fault zone as resulting from a temperature rise and rock–fluid interactions in the three fault zones (FZB1136, FZB1194 and FZB1243). All of these results are consistent with the magnetic characteristics of FZB1136 quoted earlier.

Coseismic rise of temperature in the fault zones has been documented in a number of other publications about the TCDP. Because the hard disks of black ultracataclasites are noticeable features of the TCDP core samples, they have been investigated using different methods. Hirono *et al.* (2006) have shown that the anomalies in magnetic susceptibility measured on the black ultracataclasites in FZB1194 and FZB1243 coincide with the evidence for frictional melt and a decrease in inorganic carbon that they attribute to thermal decomposition of carbonate minerals at about  $850^{\circ}\text{C}$ . However, the effect of

thermal decomposition of carbonates may be very complex if the mass and energy balance, and the kinetics of the endothermic reaction of calcite decomposition, are taken into account (Sulem & Famin 2009). Otsuki *et al.* (2009) confirmed that the hard black disks correspond to pseudotachylytic layers indicative of a single (FZB1314) or multiple (FZB1194, FZB1243) seismic events, and that coseismic temperature rise has been heterogeneous in the pseudotachylytic layer and may be estimated in the  $750\text{--}1750^{\circ}\text{C}$  range.

In conclusion, although different authors agree that frictional heating occurred on fault zones in the Chelungpu Fault, they propose different values for the temperature rise. It appears that the coseismic thermal rise was around  $300\text{--}400^{\circ}\text{C}$  in the Chi-Chi PSZ in FZA1111 and FZB1136 (Ishikawa *et al.* 2008; Boullier *et al.* 2009), and may have reached  $750^{\circ}\text{C}$  or more in the hard disks of black ultracataclasites observed in Hole B on the FZB1194 and FZB1243 fault zones that correspond to ancient seismic events (Hirono *et al.* 2006; Otsuki *et al.* 2009).

Several gouge layers corresponding to ancient seismic events are visible in FZA1111 and FZB1136 fault zones. They differ from the PSZ because they display a sequence of small conjugate shear zones, a fault-parallel schistosity associated with deformed calcite veins, both being folded together in some places, and dissolution seams around hard objects (Boullier *et al.* 2009). These microstructures are consistent with a fault-normal shortening and are symptomatic of a low-rate deformation by dissolution–precipitation processes that occur during the post-seismic or the interseismic stage (Gratier & Gueydan 2007).

#### *Fluids: before, during and after earthquakes*

Boullier *et al.* (2009) described thin calcite veins above the Chi-Chi PSZ in FZA1111 within compacted gouges, which form three-dimensional (3D) dilatational patches and display evidence of increasing strain with increasing distance from the PSZ. They were formed by hydraulic fracturing, and are undeformed just above the PSZ where they are interpreted by Boullier *et al.* (2009) as being induced by fluid escape, and fracturing and sealing related to the Chi-chi earthquake. Farther from the PSZ, veins are planar or shortened and folded, and orientated at a high angle to the fault. In the damage zone, the silty and sandy layers are dilated, fractured and sealed by calcite, while shaly layers are not. This suggests that clay-rich layers may have acted as impermeable caps allowing compartmentalization of fluids in the sandy sediments and the formation of small-sized so-called ‘Hill fault/fracture-meshes’ (Sibson 1994, p. 72).

It has been shown earlier that fluids played an important role during the Chi-chi earthquake because they have been coseismically thermally pressurized. However, the relative scarcity of calcite veins in the active damage zone compared to the large volume of laumontite and carbonate veins in the Nojima Fault demonstrates that the volumes of fluids involved in deformation on the Chelungpu Fault are much smaller than those involved in the Nojima Fault. Regardless, their role in the Chelungpu faulting process illustrates that fluids may greatly influence the seismological behaviour of faults even if they are present in small quantities.

### *Lessons from the Taiwan Chelungpu Fault Drilling project*

One major lesson from the TCDP concerns the thermal budget of an earthquake. In order to measure frictional heat arising from the fault slip, the temperature must be measured in the vicinity of the PSZ as quickly and as deeply as possible after an earthquake (Brodsky *et al.* 2009). However, observations from the TCDP illustrate that part of the frictional heat produced by the earthquake may be transformed into mechanical (thermal pressurization) and chemical (mineral transformations, fluid–rock interactions) work. One major contribution of TCDP to earthquake understanding has been the demonstration that the energy budget of an earthquake cannot be separated into simple fracturing, radiation and thermal terms but should also take into account chemical and mineralogical transformations.

As the Chelungpu Fault occurs in sedimentary rocks made of alternating silts and shales, clays are important minerals within the fault zone. The TCDP results show that the behaviour of clays during coseismic slip is fundamental in order to understand slip-weakening mechanisms. Therefore, for the same reasons that the Japanese drilling projects have stimulated experiments on ‘hard’ rocks, the TCDP has stimulated high-velocity rotary shear friction experiments on ‘soft’ rocks from the Chelungpu Fault (Mizoguchi *et al.* 2008b; Sone & Shimamoto 2009; Tanikawa & Shimamoto 2009) and numerical modelling of the thermal pressurization related to dehydration of clays (Sulem *et al.* 2007). The high-velocity experiments on clayey gouges have produced microstructures that have been recognized in the Chi-Chi PSZ and are key in interpreting natural fault gouges. For example, CCAs, new indicators of seismic slip, thermal pressurization and slip weakening, have been described (Boutareaud *et al.* 2008, 2010).

The studies undertaken on the TCDP samples have demonstrated that the mineralogy of the PSZ

is of considerable importance, and that chemical and mineralogical transformations may occur in the PSZ due to the frictional heat produced there. However, the proposed values for the frictional heat differ significantly between different publications. The effect of thermal decomposition of minerals may be very complex, and to model its mechanical effects, such as slip weakening due to thermal pressurization, it is necessary to take into account the mass and energy balance and the kinetics of the chemical decomposition (Sulem & Famin 2009).

Again, the distribution of physical properties, and transport properties in particular, within the core and the damage zones of the fault is of primary importance in understanding the coseismic slip behaviour of the PSZ, and thermal pressurization in particular. The permeability structure of the Chelungpu Fault has been investigated in several studies using the TCDP samples (Louis *et al.* 2008; Chen *et al.* 2009; Tanikawa *et al.* 2009; Wang *et al.* 2009), which have demonstrated that drilling projects through active faults should include such measurements. To do so, core handling is of primary importance. The core-handling workflows were different for Hole A and Hole B samples. The results of continuous non-destructive analyses performed on Hole B samples only, were made available a short time after drilling. However, it has been shown that these rock analyses are not sufficient and that detailed studies are necessary to provide precise information on microstructures and mineralogy. For example, whole-rock analyses pointed to the fact that there is an important magnetic susceptibility record in the black ultracataclasites that may be significant in terms of mineral transformations and thermal pressurization (Hirono *et al.* 2006). However, only detailed subsequent investigations have deciphered the exact nature of this magnetic signal and shown that the Chi-Chi PSZ records the present-day Earth’s magnetic field (Chou *et al.* 2010). TCDP has led to numerous analyses of magnetic properties of fault rocks, which contributed to the development of new techniques and approaches of the fault-zone geology.

The work carried out on the TCDP so far represents significant progress in understanding fault-zone processes. However, we still need more information on clay mineralogy, composition and volume of pore fluids before and after the earthquake in order to understand fully the mechanical and slip-weakening effects of mineral transformations in the PSZ. Regardless, the numerous studies on TCDP samples have contributed to a better knowledge of thrust faults in clay-rich rocks and, consequently, have provided good preparation for the international community for other

drilling projects such as NanTroSeize in the Nankai Trough.

## Conclusions

This paper has focused on the contributions of the Japanese and Taiwanese drilling projects to a better understanding of the geology of fault zones. Some results have probably been missed, as it is impossible to cite all of the papers published on the subject. Each project has provided its own unique set of results because the faults cross-cut different parent rocks, and occur in different geodynamic and tectonic contexts. Consequently, different processes and deformation mechanisms have been activated during earthquakes on the Nojima and Chelungpu faults. In addition, large volumes of fluids were involved in the alteration of the Nojima wall rocks, while only small volumes of fluids were present in the Chelungpu fault system. This illustrates that there is no unique process applicable to all faults around the world. Fortunately, other projects are in progress that will investigate other fault types: the San Andreas Fault Observatory at Depth (SAFOD) in Parkfield (California); the Wenchuan earthquake Fault Scientific Drilling (WFSD) through the Longmen Shan active fault zone (China); the NanTroSeize project through the Nankai accretionary prism and subduction zone; and the Deep Fault Drilling Project (DFDP) through the Alpine Fault (New Zealand). With the help of these projects, combined with surface studies, we can expect to obtain some answers to the remaining questions.

Drilling projects, although not the only way to do so, have been undertaken in order to understand earthquakes as large-scale phenomena recorded by seismologists, and have triggered many micro-scale studies that have led to a better knowledge of the PSZ that controls the seismological behaviour of faults during earthquakes (Sibson 2003). Thus, questions at a macro-scale have stimulated research at a micro-scale. Reciprocally, answers provided from micro-scale studies have explained some macroscopic behaviours of active faults. We may cite as an example, the recognition of thermal pressurization in the Chi-Chi PSZ that explains the peculiar seismic behaviour of the northern segment of the Chelungpu Fault during the Chi-chi earthquake.

Let us reconsider the objectives of drilling projects through active faults (Zoback *et al.* 2007) designed ‘to directly study the physical and chemical processes that control deformation and earthquake generation within active fault zones’ (p. 649). It is apparent that we still need information on the thermal signature and heat production of

earthquakes, the pressure and composition of pore fluid, the healing processes and their kinetics, and the mechanisms of aseismic creep on faults. On-going and future drilling projects through active faults will certainly improve our knowledge and understanding, and provide supplementary information to help address these questions by stimulating intense and fruitful collaboration between geologists and seismologists.

The author thanks her Japanese (K. Fujimoto, H. Ito and T. Ohtani) and Taiwanese (Y.-M. Chou, L.-W. Kuo, T.-K. Lee, S.-R. Song and E.-C. Yeh) colleagues for allowing her to collaborate with them on the fantastic and precious samples from the Hirabayashi and TCDF boreholes. These studies of the geology of fault zones are part of more comprehensive projects with French colleagues, and have been financially supported by the CNRS and/or Ministère des Affaires Etrangères (PICS 1050 France–Japan, PAI ORCHID 2006, International Laboratory CNRS–NSC France–Taiwan ADEPT) and by ANR (ACTS Taiwan, ANR-06-CATT-001-01). A.-M. Boullier also thanks M. Bouchon for critically reading a first draft of this manuscript, T. Shimamoto for his constructive review and V. G. Toy for her help in making the message clearer. Last, but not least, she is grateful to R. Sibson for advising and encouraging her every time she met him in Europe, North America or New Zealand for discussions on mylonites, pseudotachylites, gold mines, earthquakes, birds, history, poetry and many other subjects.

## References

- AUBOURG, C., CHOU, Y.-M., SONG, S. R., BOULLIER, A. M. & LEE, C. T. 2010. A new portrait of mm-thick principal slip zone of the ChiChi earthquake (Mw 7.6; 1999). In: *Western Pacific Geophysical Meeting*, Taipei, Taiwan, Supplement, **91**. American Geophysical Union, Washington, DC, Abstract T33B-03.
- AWATA, Y. & MIZUNO, K. 1998. *Strip Map of the Surface Fault Ruptures Associated with the 1995 Hyogo-ken Nanbu Earthquake, Central Japan – The Nojima, Ogura and Nadagawa Earthquake Faults*. Geological Survey of Japan, Tsukuba.
- BLENKINSOP, T. G. & SIBSON, R. H. 1992. Aseismic fracturing and cataclasis involving reaction softening within core material from the Cajon Pass drill hole. *Journal of Geophysical Research*, **97**, 5135–5144.
- BOUCHON, M., SEKIGUCHI, H., IRIKURA, K. & IWATA, T. 1998. Some characteristics of the stress field of the 1995 Hyogo-ken Nanbu (Kobe) earthquake. *Journal of Geophysical Research*, **103**, 24 271–24 282.
- BOULLIER, A. M., FUJIMOTO, K. ET AL. 2004a. Structural evolution of the Nojima Fault (Awaji Island, Japan) revisited from the GSJ drill hole at Hirabayashi. *Earth Planets Space*, **56**, 1233–1240.
- BOULLIER, A. M., FUJIMOTO, K. ET AL. 2004b. Textural evidence for recent co-seismic circulation of fluids in the Nojima Fault zone, Awaji Island, Japan. *Tectonophysics*, **378**, 165–181.

- BOULLIER, A. M., OHTANI, T., FUJIMOTO, K., ITO, H. & DUBOIS, M. 2001. Fluid inclusions in pseudotachylites from the Nojima Fault, Japan. *Journal of Geophysical Research—Solid Earth*, **106**, 21 965–21 977.
- BOULLIER, A. M., YEH, E. C., BOUTAREAUD, S., SONG, S. R. & TSAI, C. H. 2009. Microscale anatomy of the 1999 Chi-chi earthquake fault zone. *Geochemistry, Geophysics, Geosystems*, **10**, Q03016, doi: 10.1029/2008GC002252.
- BOUTAREAUD, S., BOULLIER, A. M., ANDREANI, M., CALUGARU, D. G., BECK, P., SONG, S. R. & SHIMAMOTO, T. 2010. Clay clast aggregates in gouges: new textural evidence for seismic faulting. *Journal of Geophysical Research—Solid Earth*, **115**, B02408, doi: 10.1029/2008JB006254.
- BOUTAREAUD, S., CALUGARU, D. G., HAN, R., FABBRI, O., MIZOGUCHI, K., TSUTSUMI, A. & SHIMAMOTO, T. 2008. Clay-clast aggregates: a new structural evidence for seismic fault sliding? *Geophysical Research Letters*, **35**, L05302, doi: 10.1029/2007GL032554.
- BRODSKY, E. E., MA, K.-F., MORI, J., SAFFER, D. & THE PARTICIPANTS OF THE ICDP/SCEC INTERNATIONAL WORKSHOP 2009. Rapid response fault drilling: past, present and future. *Scientific Drilling*, **8**, 66–74.
- CAINE, J., EVANS, J. & FORSTER, C. 1996. Fault zone architecture and permeability structure. *Geology*, **26**, 1025–1028.
- CÉLÉRIER, B. P., PEZARD, P. A., ITO, H. & KIGUCHI, T. 2000. Borehole wall geometry across the Nojima Fault: BHTV acoustic scans analysis from the GSJ Hirabayashi Hole, Japan. In: ITO, H., FUJIMOTO, K., TANAKA, H. & LOCKNER, D. (eds) *International Workshop of the Nojima Fault Core and Borehole Data Analysis*. GSJ Interim Report, EQ/00/1. USGS Open-File Report, **000-129**. Geological Survey of Japan, Tsukuba, Japan, 233–238.
- CHEN, K. C., HUANG, B. S. ET AL. 2001. An observation of rupture pulses of the 20 September 1999 Chi-Chi, Taiwan, earthquake from near-field seismograms. *Bulletin of the Seismological Society of America*, **91**, 1247–1254.
- CHEN, T. M. N., ZHU, W. L., WONG, T. F. & SONG, S. R. 2009. Laboratory characterization of permeability and its anisotropy of Chelungpu Fault rocks. *Pure and Applied Geophysics*, **166**, 1011–1036.
- CHESTER, J. S., CHESTER, F. M. & KRONENBERG, A. K. 2005. Fracture surface energy of the Punchbowl Fault, San Andreas system. *Nature*, **437**, 133–136.
- CHOU, Y.-M., LEE, T.-Q., AUBOURG, C., BOULLIER, A. M. & SONG, S.-R. 2009. Magnetic mineralogy and its correspondence with SEM observations on FZB1136 fault gouge of the Chi-chi earthquake, Chelungpu Fault, Taiwan. In: *EGU General Assembly*, Vienna, **11**. European Geosciences Union, Vienna, Abstract EGU2009-5950.
- CHOU, Y.-M., SONG, S. R., AUBOURG, C., LEE, C. T. & YEH, E. C. 2010. The paleomagnetic record of Chi-chi earthquake (Mw 7.6, 1999). In: *Western Pacific Geophysical Meeting*, Taipei, Taiwan, Supplement, **91**. American Geophysical Union, Washington, DC, Abstract T31A-061.
- DI TORO, G. & PENNACCHIONI, G. 2004. Superheated friction-induced melts in zoned pseudotachylites within the Adamello tonalites (Italian Southern Alps). *Journal of Structural Geology*, **26**, 1783–1801.
- DI TORO, G., GOLDSBY, D. L. & TULLIS, T. E. 2004. Friction falls toward zero in quartz rock as slip velocity approaches seismic rates. *Nature*, **427**, 436–439.
- DOAN, M. L. & GARY, G. 2009. Rock pulverization at high strain rate near the San Andreas Fault. *Nature Geoscience*, **2**, 709–712.
- DOAN, M. L., BRODSKY, E. E., KANO, Y. & MA, K. F. 2006. In situ measurement of the hydraulic diffusivity of the active Chelungpu Fault, Taiwan. *Geophysical Research Letters*, **33**, L16317, doi: 10.1029/2006GL026889.
- DOR, O., BEN-ZION, Y., ROCKWELL, T. K. & BRUNE, J. 2006. Pulverized rocks in the Mojave section of the San Andreas Fault Zone. *Earth and Planetary Science Letters*, **245**, 642–654.
- FABBRI, O., IWAMURA, K., MATSUNAGA, S., COROMINA, G. & KANAORI, Y. 2004. Distributed strike-slip faulting, block rotation, and possible intracrustal vertical decoupling in the convergent zone of southwest Japan. In: GROCOTT, J., TIKOFF, B., McCAFFREY, K. J. W. & TAYLOR, G. (eds) *Vertical Coupling and Decoupling of the Lithosphere*. Geological Society, London, Special Publications, **227**, 141–166.
- FAMIN, V., NAKASHIMA, S., BOULLIER, A. M., FUJIMOTO, K. & HIRONO, T. 2008. Earthquakes produce carbon dioxide in crustal faults. *Earth and Planetary Science Letters*, **265**, 487–497.
- FUJIMOTO, K., TANAKA, H., HIGUCHI, T., TOMIDA, N., OHTANI, T. & ITO, H. 2001. Alteration and mass transfer inferred from the Hirabayashi GSJ drill penetrating the Nojima Fault, Japan. *The Island Arc*, **10**, 401–410.
- FUJIMOTO, K., UEDA, A., OHTANI, T., TAKAHASHI, M., ITO, H., TANAKA, H. & BOULLIER, A.-M. 2007. Borehole water and hydrologic model around the Nojima Fault, SW Japan. *Tectonophysics*, **443**, 174–182.
- FUKUCHI, T. & IMAI, N. 2001. ESR and ICP analyses of the DPRI 500 m drill core samples penetrating through the Nojima Fault, Japan. *The Island Arc*, **10**, 465–478.
- FUKUCHI, T., MIZOGUCHI, K. & SHIMAMOTO, T. 2005. Ferrimagnetic resonance signal produced by frictional heating: a new indicator of paleoseismicity. *Journal of Geophysical Research—Solid Earth*, **110**, B12404, doi: 10.1029/2004JB003485.
- GRATIER, J. P. & GUEYDAN, F. 2007. Deformation in the presence of fluids and mineral reactions: effect of fracturing and fluid–rocks interaction on seismic cycle. In: HANDY, M. R., HIRTH, G. & HOVIUS, N. (eds) *Tectonic Faults, Agents of Change on a Dynamic Earth*. Dahlem Workshop Reports. MIT Press, Cambridge, MA, 319–356.
- GRATIER, J. P., FAVREAU, P. & RENARD, F. 2003. Modeling fluid transfer along California faults when integrating pressure solution crack sealing and compaction processes. *Journal of Geophysical Research*, **108**, 28–52.
- HASHIMOTO, Y., TADAI, O. ET AL. 2008. Characteristics of chlorites in seismogenic fault zones: the Taiwan Chelungpu Fault Drilling Project (TCDP) core sample. *e-Earth*, **3** (<http://www.electronic-earth.net/3/issue1.html>), 1–6.
- HICKMAN, S., SIBSON, R. H. & BRUHN, R. 1995. Introduction to special section: mechanical involvement of

- fluids in faulting. *Journal of Geophysical Research*, **100**, 12 831–12 840.
- HIROSE, T. & SHIMAMOTO, T. 2005. Growth of molten zone as a mechanism of slip weakening of simulated faults in gabbro during frictional melting. *Journal of Geophysical Research—Solid Earth*, **110**, B05202, doi: 10.1029/2004JB003207.
- HIRONO, T., SAKAGUCHI, M. ET AL. 2008. Characterization of slip zone associated with the 1999 Taiwan Chi-chi earthquake: X-ray CT image analyses and microstructural observations of the Taiwan Chelungpu Fault. *Tectonophysics*, **449**, 63–84, doi: 10.1016/j.tecto.2007.12.002.
- HIRONO, T., LIN, W. R. ET AL. 2006. High magnetic susceptibility of fault gouge within Taiwan Chelungpu Fault: nondestructive continuous measurements of physical and chemical properties in fault rocks recovered from Hole B, TCDP. *Geophysical Research Letters*, **33**, L15303, doi: 10.1029/2006GL026133.
- HIRONO, T., YEH, E. C. ET AL. 2007. Non-destructive continuous physical property measurements of core samples recovered from hole B, Taiwan Chelungpu-Fault Drilling Project. *Journal of Geophysical Research*, **112**, B07404, doi: 10.1029/2006JB004738.
- HUNG, J. H., WU, Y. H., YEH, E. C., WU, J. C. & PARTY, A. T. S. 2007. Subsurface structure, physical properties, and fault zone characteristics in the scientific drill holes of Taiwan Chelungpu-Fault Drilling Project. *Terrestrial, Atmospheric and Oceanic Sciences*, **18**, 271–293.
- IKEDA, R. 2001. Outline of the fault zone drilling project by NIED in the vicinity of the 1995 Hyogo-ken Nanbu earthquake, Japan. *The Island Arc*, **10**, 199–205.
- IRIKURA, K., IWATA, T., SEKIGUCHI, H., PITARKA, A. & KAMAE, K. 1996. Lesson from the 1995 Hyogo-Ken Nanbu earthquake: why were such destructive motions generated to buildings? *Journal of Natural Disaster Science*, **17**, 99–127.
- ISHIKAWA, T., TANIMIZU, M. ET AL. 2008. Coseismic fluid–rock interactions at high temperatures in the Chelungpu Fault. *Nature Geoscience*, **1**, 679–683.
- ITO, H. & KIGUCHI, T. 2005. Distribution and properties of fractures in and around the Nojima Fault in the Hirabayashi GSJ borehole. In: HARVEY, P. K., BREWER, T. S., PEZARD, P. A. & PETROV, V. A. (eds) *Petrophysical Properties of Crystalline Rocks*. Geological Society, London, Special Publications, **240**, 61–74.
- ITO, H., KUWAHARA, T. ET AL. 1996. Structure and physical properties of the Nojima Fault (in Japanese with English abstract). *BUTSURU-TANSA (Geophysical Exploration)*, **49**, 522–535.
- KANAMORI, H. & HEATON, T. H. 2000. Microscopic and macroscopic physics of earthquakes. In: RUNDLE, J., TURCOTTE, D. L. & KLEIN, W. (eds) *GeoComplexity and the Physics of Earthquakes*. American Geophysical Union, Geophysical Monograph, **120**, 147–163.
- KANAORI, Y. 1990. Late Mesozoic–Cenozoic strike-slip and block rotation in the inner belt of Southwest Japan. *Tectonophysics*, **177**, 381–399.
- KANO, Y., MORI, J., FUJIO, R., ITO, H., YANAGIDANI, T., NAKAO, S. & MA, K.-F. 2006. Heat signature on the Chelungpu Fault associated with the 1999 Chi-Chi, Taiwan earthquake. *Geophysical Research Letters*, **33**, L14306, doi: 10.1029/2006GL026733.
- KAO, H. & CHEN, W. P. 2000. The Chi-chi earthquake sequence: active out-of-sequence thrust faulting in Taiwan. *Science*, **288**, 2346–2349.
- KEULEN, N., HEILBRONNER, R., STUENITZ, H., BOULLIER, A. M. & ITO, H. 2007. Grain size distributions of fault rocks: a comparison between experimentally and naturally deformed granitoids. *Journal of Structural Geology*, **29**, 1282–1300.
- KEULEN, N., STUENITZ, H. & HEILBRONNER, R. 2008. Healing microstructures of experimental and natural fault gouge. *Journal of Geophysical Research—Solid Earth*, **113**, B06205, doi: 10.1029/2007JB005039.
- KIGUCHI, T., ITO, H., KUWAHARA, Y. & MIYAZAKI, T. 2001. Estimating the permeability of the Nojima Fault Zone by a hydrophone vertical seismic profiling experiment. *The Island Arc*, **10**, 348–356.
- KITAJIMA, T., KOBAYASHI, Y., IKEDA, R., IIO, Y. & OMURA, K. 1998. Terrestrial heat flow in Nojima-Hirabayashi, Awaji Island. *Chikyu Monthly*, **21**, 108–113 (in Japanese).
- KOBAYASHI, K., HIRANO, S. ET AL. 2001. Distribution of fault rocks in the fracture zone of the Nojima Fault at a depth of 1140 m: observations from the Hirabayashi NIED drill core. *The Island Arc*, **10**, 411–421.
- KUO, L. W., SONG, S. R. & CHEN, H. Y. 2005. Characteristics of clay mineralogy in the fault zone of the TCDP and its implication. In: *Eos, Transactions of the AGU, Fall Meeting Supplement*, **86**. American Geophysical Union, Washington, DC, Abstract T43D-05.
- KUO, L.-W., SONG, S.-R., YEH, E.-C. & CHEN, H.-F. 2009. Clay mineral anomalies in the fault zone of the Chelungpu Fault, Taiwan, and their implications. *Geophysical Research Letters*, **36**, L18306, doi: 10.1029/2009GL039269.
- LIN, A., MARUYAMA, T. & KOBAYASHI, K. 2007. Tectonic implications of damage zone-related fault-fracture networks revealed in drill core through the Nojima Fault, Japan. *Tectonophysics*, **443**, 161–173.
- LIN, A., TANAKA, N., UDA, S. & SATISH-KUMAR, M. 2003. Repeated coseismic infiltration of meteoric and seawater into deep fault zones: a case study of the Nojima Fault zone, Japan. *Chemical Geology*, **202**, 139–153.
- LIN, A. M., SHIMAMOTO, T. ET AL. 2001. Comparative study of cataclastic rocks from a drill core and outcrops of the Nojima Fault zone on Awaji Island, Japan. *The Island Arc*, **10**, 368–380.
- LOCKNER, D. A., TANAKA, H., ITO, H., IKEDA, R., OMURA, K. & NAKA, H. 2009. Geometry of the Nojima Fault at Nojima-Hirabayashi, Japan – I. A simple damage structure inferred from Borehole Core Permeability. *Pure and Applied Geophysics*, **166**, 1649–1667.
- LOUIS, L., CHEN, T. M. N., DAVID, C., ROBION, P., WONG, T. F. & SONG, S. R. 2008. Anisotropy of magnetic susceptibility and P-wave velocity in core samples from the Taiwan Chelungpu-Fault Drilling Project (TCDP). *Journal of Structural Geology*, **30**, 948–962.
- MA, K. F., BRODSKY, E. E., MORI, J., JI, C., SONG, T. R. A. & KANAMORI, H. 2003. Evidence for fault lubrication during the 1999 Chi-Chi, Taiwan, earthquake (Mw7.6). *Geophysical Research Letters*, **30**, 1244, doi: 10.1029/2002GL015380.

- MA, K. F., MORI, J., LEE, S. J. & YU, S. B. 2001. Spatial and temporal distribution of slip for the 1999 Chi-Chi, Taiwan earthquake. *Bulletin of the Seismological Society of America*, **91**, 1069–1087.
- MA, K. F., TANAKA, H. ET AL. 2006. Slip zone and energetics of a large earthquake, from the Taiwan Chelungpu-Fault Drilling Project. *Nature*, **444**, 473–476, doi: 10.1038/nature05253.
- MATSUDA, T., ARAI, T. ET AL. 2001. Examination of mineral assemblage and chemical composition in the fracture zone of the Nojima Fault at a depth of 1140 m: analyses of the Hirabayashi NIED drill cores. *The Island Arc*, **10**, 422–429.
- MATSUDA, T., OMURA, K. ET AL. 2004. Fracture-zone conditions on a recently active fault: insights from mineralogical and geochemical analyses of the Hirabayashi NIED drill core on the Nojima Fault, southwest Japan, which ruptured in the 1995 Kobe earthquake. *Tectonophysics*, **378**, 143–163.
- MITCHELL, T. M., SHIMAMOTO, T. & BEN-ZION, Y. 2009. Pulverized fault rocks and damage asymmetry along the Arima-Takatsuki tectonic line, Japan: fault structure, damage distribution and textural characteristics. In: *Transactions of the AGU, Fall Meeting, Supplement*, **86**. American Geophysical Union, Washington, DC, Abstract T54A-02.
- MIZOGUCHI, K., HIROSE, T., SHIMAMOTO, T. & FUKUYAMA, E. 2008a. Internal structure and permeability of the Nojima Fault, southwest Japan. *Journal of Structural Geology*, **30**, 513–524.
- MIZOGUCHI, K., HIROSE, T., SHIMAMOTO, T. & FUKUYAMA, E. 2009. High-velocity frictional behavior and microstructure evolution of fault gouge obtained from Nojima Fault, southwest Japan. *Tectonophysics*, **471**, 285–296.
- MIZOGUCHI, K., TAKAHASHI, M., TANIKAWA, W., MASUDA, K., SONG, S. R. & SOH, W. 2008b. Frictional strength of fault gouge in Taiwan Chelungpu Fault obtained from TCDP Hole B. *Tectonophysics*, **460**, 198–205.
- MOORE, D. E., LOCKNER, D. A., ITO, H., IKEDA, R., TANAKA, H. & OMURA, K. 2009. Geometry of the Nojima Fault at Nojima-Hirabayashi, Japan – II. Microstructures and their implications for permeability and strength. *Pure and Applied Geophysics*, **166**, 1669–1691.
- MORI, J. & TANAKA, H. 2002. Energy budget of the 1999 Chi-Chi, Taiwan earthquake. In: *Eos, Transactions of the AGU, Fall Meeting, Supplement*, **83**. American Geophysical Union, Washington, DC, Abstract S71E-09.
- MURAKAMI, M. & TAGAMI, T. 2004. Dating pseudotachylite of the Nojima Fault using the zircon fission-track method. *Geophysical Research Letters*, **31**, L12604, doi: 10.1029/2004GL020211.
- MURAKAMI, M., TAGAMI, T. & HASEBE, N. 2002. Ancient thermal anomaly of an active fault system: zircon fission-track evidence from Nojima GSJ 750 m borehole samples. *Geophysical Research Letters*, **29**, B05202, doi: 10.1029/2004JB003207.
- MURATA, A., TAKELMURA, K., MIYATA, T. & LIN, A. 2001. Quaternary vertical offset and average slip rate of the Nojima Fault on Awaji Island, Japan. *The Island Arc*, **10**, 360–367.
- OHTANI, T., FUJIMOTO, K., ITO, H., TANAKA, H., TOMIDA, N. & HIGUCHI, T. 2000a. Fault rocks and past to recent fluid characteristics from the borehole survey of the Nojima Fault ruptured in the 1995 Kobe earthquake, southwest Japan. *Journal of Geophysical Research–Solid Earth*, **105**, 16 161–16 171.
- OHTANI, T., MIYAZAKI, T., TANAKA, H., KIGUCHI, T., FUJIMOTO, K. & ITO, H. 2000b. Reorientation of cores and distribution of macroscopic fractures along the GSJ borehole penetrating the Nojima Fault zone. In: ITO, H., FUJIMOTO, K., TANAKA, H. & LOCKNER, D. (eds) *International Workshop of the Nojima Fault Core and Borehole Data Analysis*. GSJ Interim Report, **EQ/00/1**. USGS Open-File Report, **000-129**. Geological Survey of Japan, Tsukuba, Japan, 271–276.
- OHTANI, T., TANAKA, H., FUJIMOTO, K., HIGUCHI, T., TOMIDA, N. & ITO, H. 2001. Internal structure of the Nojima Fault zone from the Hirabayashi GSJ drill core. *The Island Arc*, **10**, 392–400.
- OTSUKI, K., HIRONO, T. ET AL. 2009. Analyses of pseudotachylite from Hole-B of Taiwan Chelungpu Fault Drilling Project (TCDP); their implications for seismic slip behaviors during the 1999 Chi-chi earthquake. *Tectonophysics*, **469**, 13–24.
- OTSUKI, K., MONZAWA, N. & NAGASE, T. 2003. Fluidization and melting of fault gouge during seismic slip: identification in the Nojima Fault zone and implications for focal earthquake mechanisms. *Journal of Geophysical Research–Solid Earth*, **108**, 2192, doi: 10.1029/2001JB001711.
- OTSUKI, K., UDKI, T., MONZAWA, N. & TANAKA, H. 2005. Clayey injection veins and pseudotachylite from two boreholes penetrating the Chelungpu Fault, Taiwan: their implications for the contrastive seismic slip behaviors during the 1999 Chi-chi earthquake. *The Island Arc*, **14**, 22–36.
- PATHIER, E., FRUNEAU, B., DEFFONTAINES, B., ANGELIER, J., CHANG, C. P., YU, S. B. & LEE, C. T. 2003. Coseismic displacements of the footwall of the Chelungpu Fault by the 1999 Taiwan, Chi-chi earthquake from InSAR and GPS data. *Earth and Planetary Science Letters*, **212**, 73–88.
- PEZARD, P., ITO, H., HERMITTE, D. & REVIL, A. 2000. Electrical properties and alteration of granodiorites from the GSJ Hirabayashi hole, Japan. In: ITO, H., FUJIMOTO, K., TANAKA, H. & LOCKNER, D. (eds) *International Workshop of the Nojima Fault Core and Borehole Data Analysis*. GSJ Interim Report, **EQ/00/1**. USGS Open-File Report, **000-129**. Geological Survey of Japan, Tsukuba, Japan, 255–262.
- ROCKWELL, T., SISK, M., GIRTY, G., DOR, O., WECHSLER, N. & BEN-ZION, Y. 2009. Chemical and physical characteristics of pulverized tejon lookout granite adjacent to the San Andreas and Garlock Faults: implications for earthquake physics. *Pure and Applied Geophysics*, **166**, 1725–1746.
- SIBSON, R. H. 1973. Interactions between temperature and pore-fluid pressure during earthquake faulting and a mechanism for partial or total stress relief. *Nature–Physical Science*, **243**, 66–68.
- SIBSON, R. H. 1975. Generation of pseudotachylite by ancient seismic faulting. *Geophysical Journal of the Royal Astronomical Society*, **43**, 775–794.

- SIBSON, R. H. 1977. Fault rocks and fault mechanisms. *Journal of the Geological Society, London*, **133**, 191–213.
- SIBSON, R. H. 1990. Rupture nucleation on unfavorably oriented faults. *Bulletin of the Seismological Society of America*, **80**, 1580–1604.
- SIBSON, R. H. 1994. Crustal stress, faulting and fluid flow. In: PARNELL, J. (ed.) *Geofluids: Origin, Migration and Evolution of Fluids in Sedimentary Basins*. Geological Society, London, Special Publications, **78**, 69–84, doi: 10.1144/GSL.SP.1994.078.01.07.
- SIBSON, R. H. 2003. Thickness of the seismic slip zone. *Bulletin of the Seismological Society of America*, **93**, 1169–1178.
- SIBSON, R. H. & TOY, V. G. 2006. The habitat of fault-generated pseudotachylite: presence v. absence of friction-melt. In: MCGARR, A., ABERCROMBIE, R. & KANAMORI, H. (eds) *Earthquakes: Radiated Energy and the Physics of Faulting*. American Geophysical Union, Geophysical Monograph, **170**, 153–166.
- SIBSON, R. H., MOORE, J. M. & RANKIN, A. H. 1975. Seismic pumping – a hydrothermal fluid transport mechanism. *Journal of the Geological Society, London*, **131**, 653–659.
- SIBSON, R. H., ROBERT, F. & POULSEN, K. H. 1988. High-angle reverse faults, fluid-pressure cycling, and Mesothermal gold-quartz deposits. *Geology*, **16**, 551–555.
- SONE, H. & SHIMAMOTO, T. 2009. Frictional resistance of faults during accelerating and decelerating earthquake slip. *Nature Geoscience*, **2**, 705–708, doi: 10.1038/Ngeo637.
- SONE, H., YEH, E. C. ET AL. 2007. Mesoscopic structural observations of cores from the Chelungpu Fault system, Taiwan Chelungpu-Fault Drilling Project hole-A, Taiwan. *Terrrestrial, Atmospheric and Oceanic Sciences*, **18**, 359–377.
- SONG, S. R., KUO, L. W., YEH, E. C., WANG, C. Y., HUNG, J. H. & MA, K. F. 2007. Characteristics of the lithology, fault-related rocks and fault zone structures in TCDP Hole-A. *Terrrestrial, Atmospheric and Oceanic Sciences*, **18**, 243–269.
- SULEM, J. & FAMIN, V. 2009. Thermal decomposition of carbonates in fault zones: slip-weakening and temperature-limiting effects. *Journal of Geophysical Research–Solid Earth*, **114**, B03309, doi: 10.1029/2006GL027285.
- SULEM, J., LAZAR, P. & VARDOLAKIS, I. 2007. Thermo-poro-mechanical properties of clayey gouge and application to rapid fault shearing. *International Journal for Numerical and Analytical Methods in Geomechanics*, **31**, 523–540.
- TAKAHASHI, Y. 1992. K-Ar ages of the granitic rocks in Awaji Island with an emphasis on timing of mylonitization. *Journal of Mineralogy, Petrology and Economic Geology*, **87**, 291–299.
- TAKESHITA, T. & YAGI, K. 2001. Paleostress orientation from 3-D orientation distribution of microcracks in quartz from the Cretaceous granodiorite core samples drilled through the Nojima Fault, south-west Japan. *The Island Arc*, **10**, 495–505.
- TANAKA, H., CHEN, W. C., WANG, C. Y., MA, K. F., URATA, N., MORI, J. & ANDO, M. 2006. Frictional heat from faulting of the 1999 Chi-Chi, Taiwan earthquake. *Geophysical Research Letters*, **33**, L16316, doi: 10.1029/2006GL026673.
- TANAKA, H., FUJIMOTO, K., OHTANI, T. & ITO, H. 2001a. Structural and chemical characterization of shear zones in the freshly activated Nojima Fault, Awaji Island, southwest Japan. *Journal of Geophysical Research*, **106**, 8789–8810.
- TANAKA, H., HINOKI, S. I., KOSAKA, K., LIN, A. M., TAKEMURA, K., MURATA, A. & MIYATA, T. 2001b. Deformation mechanisms and fluid behavior in a shallow, brittle fault zone during coseismic and interseismic periods: results from drill core penetrating the Nojima Fault, Japan. *The Island Arc*, **10**, 381–391.
- TANAKA, H., CHEN, W. M., KAWABATA, K. & URATA, N. 2007a. Thermal properties across the Chelungpu Fault zone and evaluations of positive thermal anomaly on the slip zones: are these residuals of heat from faulting? *Geophysical Research Letters*, **34**, L01309, doi: 10.1029/2006GL028153.
- TANAKA, H., OMURA, K., MATSUDA, T., IKEDA, R., KOBAYASHI, K., MURAKAMI, M. & SHIMADA, K. 2007b. Architectural evolution of the Nojima Fault and identification of the activated slip layer by Kobe earthquake. *Journal of Geophysical Research–Solid Earth*, **112**, B07304, doi: 10.1029/2005JB003977.
- TANAKA, H., WANG, C. Y., CHEN, W. M., SAKAGUCHI, A., UJIIE, K., ITO, H. & ANDO, M. 2002. Initial science report of shallow drilling penetrating into the Chelungpu Fault zone, Taiwan. *Terrestrial Atmospheric and Oceanic Sciences*, **13**, 227–251.
- TANIKAWA, W. & SHIMAMOTO, T. 2009. Frictional and transport properties of the Chelungpu fault from shallow borehole data and their correlation with seismic behavior during the 1999 Chi-chi earthquake. *Journal of Geophysical Research–Solid Earth*, **114**, B01402, doi: 10.1029/2008JB005750.
- TANIKAWA, W., SAKAGUCHI, M., HIRONO, T., LIN, W., SOH, W. & SONG, S. R. 2009. Transport properties and dynamic processes in a fault zone from samples recovered from TCDP Hole B of the Taiwan Chelungpu Fault Drilling Project. *Geochemistry, Geophysics, Geosystems*, **10**, Q04013, doi: 10.1029/2008GC002269.
- UEHARA, S. & SHIMAMOTO, T. 2004. Gas permeability evolution of cataclasite and fault gouge in triaxial compression and implications for changes in fault-zone permeability structure through the earthquake cycle. *Tectonophysics*, **378**, 183–195.
- UJIIE, K. 2005. Fault rock analysis of the northern part of the Chelungpu Fault and its relation to earthquake faulting of the 1999 Chi-chi earthquake, Taiwan. *The Island Arc*, **14**, 2–11.
- WANG, J. H., HUNG, J. H. & DONG, J. J. 2009. Seismic velocities, density, porosity, and permeability measured at a deep hole penetrating the Chelungpu Fault in central Taiwan. *Journal of Asian Earth Sciences*, **36**, 135–145.
- WIBBERLEY, C. A. J. & SHIMAMOTO, T. 2003. Internal structure and permeability of major strike-slip fault-zones: the Median Tectonic Line in Mie prefecture, Southwest Japan. *Journal of Structural Geology*, **25**, 59–78.
- WIBBERLEY, C. A. J. & SHIMAMOTO, T. 2005. Earthquake slip weakening and asperities explained by thermal

- pressurization. *Nature*, **436**, 689–692, doi: 10.1038/nature03901.
- YAMAMOTO, Y., KURITA, H. & MATSUBARA, T. 2000. Eocene calcareous nannofossils and dinoflagellate cysts from the Iwaya Formation in Awajishima Island, Hyogo Prefecture, southwest Japan, and their geologic implications. *Journal of the Geological Society of Japan*, **106**, 379–382.
- YEH, E. C., SONE, H. ET AL. 2007. Core description and characteristics of fault zones from Hola-A of the Taiwan Chelungpu-Fault Drilling Project. *Terrestrial, Atmospheric and Oceanic Sciences*, **18**, 327–357.
- YU, S. B., HSU, Y. J., KUO, L. C., CHEN, H. Y. & LIU, C. C. 2003. GPS measurement of postseismic deformation following the 1999 Chi-Chi, Taiwan, earthquake. *Journal of Geophysical Research*, **108**, 2520, doi: 10.1029/2003JB002396.
- YUE, L. F., SUPPE, J. & HUNG, J. H. 2005. Structural geology of a classic thrust belt earthquake: the 1999 Chi-chi earthquake Taiwan (Mw7.6). *Journal of Structural Geology*, **27**, 2058–2083, doi: 10.1016/j.jsg.2005.05.020.
- ZEN, E. & THOMPSON, A. B. 1974. Low grade regional metamorphism: mineral equilibrium relations. *Annual Review of Earth and Planetary Sciences*, **2**, 197–212.
- ZOBACK, M. D., HICKMAN, S. & ELLSWORTH, W. E. 2007. The role of fault zone drilling. In: KANAMORI, H. & SCHUBERT, G. (eds) *Earthquake Seismology. Treatise on Geophysics*, Volume 4. Elsevier, Amsterdam, 649–674.



# Deep rock damage in the San Andreas Fault revealed by P- and S-type fault-zone-guided waves

WILLIAM L. ELLSWORTH<sup>1</sup>\* & PETER E. MALIN<sup>2</sup>

<sup>1</sup>*US Geological Survey, 345 Middlefield Road, MS-977, Menlo Park, CA 94025, USA*

<sup>2</sup>*Institute of Earth Science and Engineering, University of Auckland, Auckland 1142, New Zealand*

\*Corresponding author (e-mail: [ellsworth@usgs.gov](mailto:ellsworth@usgs.gov))

**Abstract:** Damage to fault-zone rocks during fault slip results in the formation of a channel of low seismic-wave velocities. Within such channels guided seismic waves, denoted by  $F_g$ , can propagate. Here we show with core samples, well logs and  $F_g$ -waves that such a channel is crossed by the SAFOD (San Andreas Fault Observatory at Depth) borehole at a depth of 2.7 km near Parkfield, California, USA. This laterally extensive channel extends downwards to at least half way through the seismogenic crust, more than about 7 km. The channel supports not only the previously recognized Love-type- ( $F_L$ ) and Rayleigh-type- ( $F_R$ ) guided waves, but also a new fault-guided wave, which we name  $F_\Phi$ . As recorded 2.7 km underground,  $F_\Phi$  is normally dispersed, ends in an Airy phase, and arrives between the P- and S-waves. Modelling shows that  $F_\Phi$  travels as a leaky mode within the core of the fault zone. Combined with the drill core samples, well logs and the two other types of guided waves,  $F_\Phi$  at SAFOD reveals a zone of profound, deep, rock damage. Originating from damage accumulated over the recent history of fault movement, we suggest it is maintained either by fracturing near the slip surface of earthquakes, such as the 1857 Fort Tejon  $M$  7.9, or is an unexplained part of the fault-creep process known to be active at this site.

When a fault moves in the ‘elastico-frictional’ regime in the Earth’s crust, it both releases elastic energy stored in the surrounding rocks and reduces the strength of the fault through non-elastic processes (Sibson 1977). The resulting brittle shearing and fracturing are not limited to a sliding surface, and this results in a damage zone containing a mixed suite of gouges, cataclasites and breccias (Sibson 1977).

Surface and mine exposures of exhumed fault zones has led to the development of a canonical model of crustal faults (Chester & Chester 1998; Faulkner *et al.* 2003; Sibson 2003; Chester *et al.* 2004). This model is characterized by one or more very narrow slip zones (millimetres to decimetres) where most of the fault displacement occurs. This plane is embedded in a broader damage zone that is tens to hundreds of metres wide. The damage zone is thought to form as a consequence of several causes. These include: the changing geometry of the principal slip zone at jogs and stepovers (Sibson 1986); preferential shearing in less-competent lithologies within the fault zone (Fagereng & Sibson 2010); and earthquake-concentrated stresses exceeding the rock strength adjacent to the fault surface (Andrews 2005). This latter mechanism operates along straight fault segments as well as at geometrical complexities.

As a result of these mechanisms, macroscopic and microscopic fracturing in the fault zone increases. Consequently, seismic-wave velocities are reduced and attenuation ( $1/Q$ , where  $Q$  is the quality factor) is increased within the damage zone. The resulting low-velocity, low- $Q$  zone forms a waveguide that follows the fault. Within this waveguide special seismic waves, denoted by  $F_g$ , can propagate (Ben-Zion & Aki 1990; Li & Leary 1990; Li *et al.* 1990; Malin *et al.* 1996). These include low-frequency SH/Love-type ( $F_L$ ) and PSV/Rayleigh-type ( $F_R$ ) fault-zone-guided waves. These waves are routinely observed along surface ruptures of major earthquakes; as, for example, after the 1992 Landers, California earthquake (Li & Vidale 2001).

The depth extent of the low-velocity channel, however, has been controversial. Some researchers argue that it is a near-surface feature, reaching only down to the top of the seismogenic zone: less than about 3–5 km (e.g. Ben-Zion *et al.* 2003; Peng *et al.* 2003; Lewis *et al.* 2005; Lewis & Ben-Zion 2010). Others argue that it extends well into the elastico-frictional regime: approximately 5–10 km (e.g. Korneev *et al.* 2003; Li & Malin 2008; Wu *et al.* 2010). In some cases, different wave types from the same recordings have been used to argue for shallow (Yang & Zhu 2010) or deep (Li & Vernon 2001) damage.

These conflicting conclusions illustrate the non-uniqueness of  $F_g$  interpretations based on surface measurements (see Ben-Zion & Aki 1990; see also Ben-Zion 1998 for a discussion of fault-property v. depth trade-offs). Consequently, new approaches and new data are needed to plumb the depths of fault-zone damage.

In this paper we report on such advances at the San Andreas Fault Observatory at Depth site. Our data include core samples and well logs,  $F_L$  and  $F_R$  observations, and a new type of fault-guided wave,  $F_\Phi$ , all gathered at a depth of 2.7 km. Our observations show that the low-velocity channel within the damage zone extends deep into the seismogenic zone. Further, owing to its width and degree of velocity reduction, we suggest that it is a zone of accumulated damage created by multiple large earthquakes rupturing the San Andreas Fault at the SAFOD site.

## San Andreas Fault Observatory at Depth

Extending 4 km diagonally into the Earth and crossing the Pacific–North American plate boundary, the San Andreas Fault Observatory at Depth (SAFOD) is a portal into the workings of a plate-boundary fault (Hickman *et al.* 2007; Zoback *et al.* 2010, 2011). Drilled in phases in 2004, 2005 and 2007 near Parkfield, California, USA, it is a component of the US National Science Foundation's EarthScope Program.

SAFOD is situated within the transition zone between the central creeping San Andreas Fault and the locked segment last ruptured in the magnitude 7.8 1857 Fort Tejon earthquake (Fig. 1a). It lies NW of the rupture zone of the  $M 6.0$  1966 and 2004 Parkfield earthquakes. Further, at the present time, the local fault motion occurs almost entirely

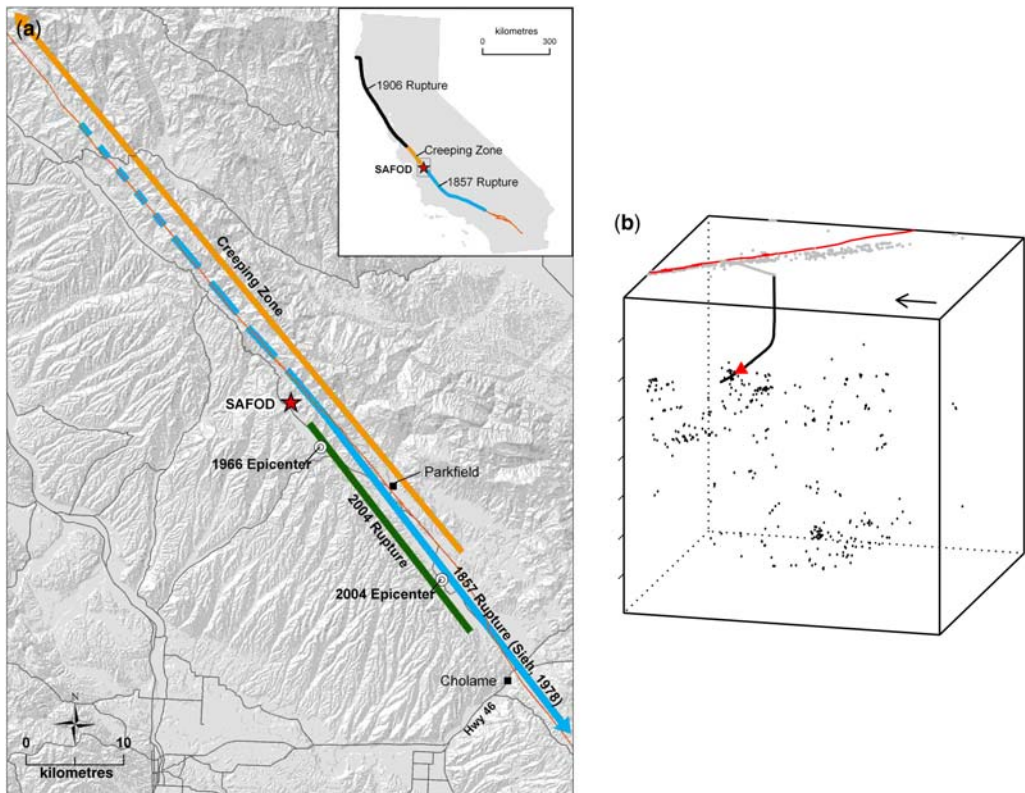


**Fig. 1.** Map (a) showing the location of SAFOD on the San Andreas Fault in central California. This site is near the southern terminus of the central creeping segment of the SAF and immediately north of the rupture of the 2004 Parkfield earthquake. The rupture extent of the 1857 Ft Tejon earthquake as described by Sieh (1978) is also shown. Block diagram (b) shows the relationship of the SAFOD borehole to hypocentres of the microearthquakes. The crustal cube shown is 8 km on each side. The earthquake locations are shown relative to the surface trace of the SAF and the subsurface and projected surface trajectories of SAFOD main hole to this fault. The borehole seismograph (red triangle) recording the  $F_g$ -waves was located approximately 40 m SW of the SAF, at 3281 m as measured along the borehole and at a true vertical depth of 2670 m below the local ground level.

by aseismic creep (Murray & Langbein 2006). High-precision double-difference locations of repeating microearthquakes by Waldhauser &

Schaff (2008) define the active fault as a varying set of narrow, nearly vertical planar zones (Fig. 2). In places, the fault appears as either as a single zone of seismicity with widths of approximately 10 m or less. In others it contains several equally narrow planes within a zone about 0.5 km wide (Thurber *et al.* 2004, 2006; Waldhauser *et al.* 2004) (Fig. 2c).

Within these zones microearthquakes are characteristically clustered in horizontal, rake-parallel streaks that extend along strike for several kilometres. Individual planes of earthquakes can be traced from the upper limit of seismicity (*c.* 2 km) to its base (*c.* 15 km). This suggests that at the SAFOD site there are vertically continuous, deeply penetrating faults of the type described by Chester & Chester (1998) on an abandoned and exhumed main trace of the San Andreas Fault in southern California.

The SAFOD borehole crosses the plate boundary from the SW to the NE (Fig. 1b). The borehole begins on the Pacific plate as a vertical hole in Cenozoic sediments above Cretaceous-age Salinian-terrain granites. It then deviates towards the NE through Salinian arkosic sandstones (Draper Springer *et al.* 2009) and crosses into Cretaceous North American sedimentary rocks (Solum *et al.* 2006). We term this transition as the Geological Boundary Fault (GBF). The currently active traces of the fault at the SAFOD site, however, are contained within the Cretaceous sedimentary rocks located to the NE of the GBF.

Two actively creeping traces of the SAF cross the SAFOD borehole. They were identified by progressive deformation of the steel casing between drilling phases in 2005 and 2007 (Zoback *et al.* 2010, 2011). Minor casing deformation was observed at a depth of 3192 m as measured along the borehole and major deformation was observed at 3302 m. These correspond to depths below the ground surface of 2620 and 2675 m, respectively (Zoback *et al.* 2010). At these locations, creep deforms the steel casing of the borehole in approximately 2 m-wide zones. These are referred to as the Southwest Deforming Zone (SDZ) and the Central Deforming Zone (CDZ) (Fig. 3) (Zoback *et al.* 2011). Drill core recovered from the SDZ and CDZ revealed them to consist of cohesionless,

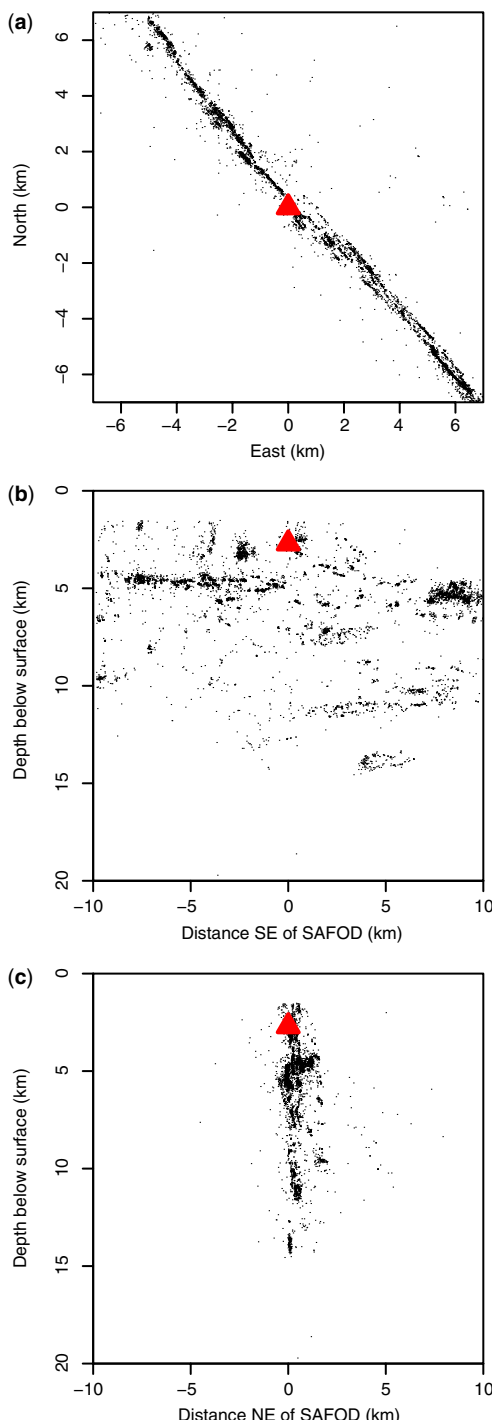


**Fig. 2.** Locations of earthquakes surrounding the SAFOD site as determined by Waldhauser & Schaff (2008) using waveform cross-correlation timing and the double-difference method. The position of the SAFOD seismometer is marked by a red triangle on the map in (a), and on the longitudinal cross-section (b) and transverse cross-section (c). Earthquake source dimensions for  $M \geq 3$  events are shown in (b).

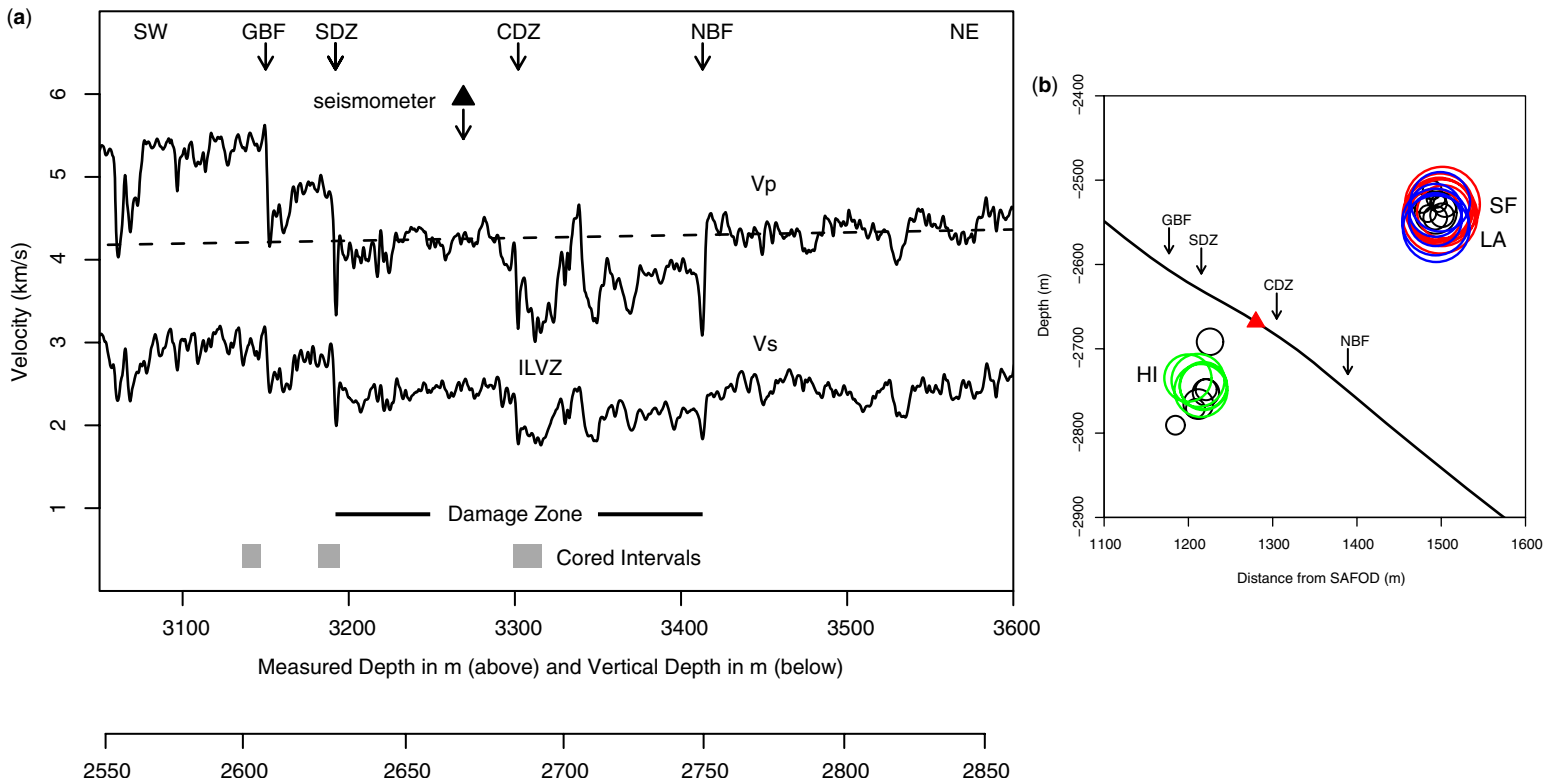


**Fig. 3.** (a) SAFOD open hole seismic P- and S-wave velocity logs. Both measured depth along the  $56^\circ$  inclined borehole and true depth below ground are indicated on the horizontal scales. The geological transition from Pacific plate (SW) to North American (NE) rocks occurs at the Geological Boundary Fault (GBF). The dashed line through the P-velocities beyond the Northeastern Boundary Fault (NBF) is the velocity commonly observed for NA sedimentary rocks in central California (Brocher 2008). Local, metre-scale reductions of as much as 40% can be seen at the main creeping SAF (CDZ), at these secondary creeping fault SDZ, and at the GBF and NBF faults. Note the presence of an approximately 30–60 m-wide zone of about 20% velocity reduction – the ILVZ – immediately beyond the CDZ. We suggest that this channel gives rise to the  $F_\Phi$ -wave we have identified and modelled here, and show that it extends at least 7 km into the crust at SAFOD. (b) Transverse cross-section showing the trajectory of the SAFOD borehole as it crosses GBF, SDZ, CDZ and NBF. The SAFOD seismometer location is indicated by the red triangle. Also shown are the locations and source dimensions of the SAFOD drilling target earthquakes. The source dimensions are shown as circles projected onto the auxiliary fault planes. Earthquakes in the ‘Hawaii’ (HI) cluster are located 50–100 m NW of the borehole. Earthquakes in the ‘Los Angeles’ (LA) and ‘San Francisco’ (SF) clusters are located 100–200 and 200–300 m NW of the borehole, respectively.

foliated gouge, limited to an approximately 2 m interval at the depth where the casing deformations were observed (Fig. 4). It should be noted that these very narrow zones are themselves embedded within a much broader damage zone, as described in more detail later. The fault gouge forming the SDZ and CDZ has anomalous physical properties, with extreme reductions in velocity of P- and S-waves (Zoback *et al.* 2010). Most significantly, this phyllosilicate gouge is extremely weak. Its coefficient of static friction,  $\mu$ , is approximately 0.15, in marked contrast to the stronger  $\mu$  rocks with values of around 0.4–0.6 in the remainder of the damage zone (Lockner *et al.* 2011). With such extreme variations in frictional strength, it is not surprising that fault slip could be highly localized (Fagereng & Sibson 2010).

A complex, approximately 200 m-wide zone of anomalously low P- and S-velocities bounded by the SDZ and the Northeastern Boundary Fault (NBF) has been identified as the damage zone by Zoback *et al.* (2010, 2011) (Fig. 3). The SDZ is also associated with the seismically active fault trace containing the repeating earthquakes on the

'Hawaii' side of the fault zone (Fig. 3b). The CDZ resides near the centre of the damage zone. It is interpreted to be the main trace of the SAF by virtue of its higher slip rate. It forms the southwestern border of an inner, 30–60 m-wide zone of greatly reduced seismic velocities – the inner low-velocity zone or ILVZ in Figure 3. These latter velocities are intermediate to the extreme lows of the 2 m-wide CDZ and higher ones of the damage zone. This suggests a hierarchical structure with damage and velocity reduction increasing on shorter and shorter length scales.

Core samples of the CDZ and approximately 15 m of the associated ILVZ were obtained in SAFOD Phase 3 drilling in 2007 (Zoback *et al.* 2010) (Fig. 4). Numerous small faults and calcite-filled fractures are found in the Cretaceous-age sedimentary rocks of the damage zone (Holdsworth *et al.* 2011). Some of these features are geologically young, but others are probably older given that the SAF at Parkfield has moved over 320 km since the Miocene (Irwin 1990) and currently creeps at  $3.5 \text{ cm year}^{-1}$ . The active traces of the SAF intersected by SAFOD thus appear as narrow active



**Fig. 4.** Photographs of drill core through the main trace of the SAF in core runs G-4 (A–F), G-5 (G–L) and G-6 (M–Q) from SAFOD Core Atlas ([http://www.icdp-online.org/contenido/icdp/upload/projects/safod/phase3/Core\\_Photo\\_Atlas\\_v3.pdf](http://www.icdp-online.org/contenido/icdp/upload/projects/safod/phase3/Core_Photo_Atlas_v3.pdf)). Core sections A–Q are arranged from 3295 m, measured depth on the SW side (left) to 3312 m on the NE side (right). The individual sections are approximately 90 cm in length. Short sections at the bottom of each core run in the core catcher are not shown. The cores are unoriented, but have a consistent roll angle within each run. Arrows bracket the ultra-low-strength foliated fault gouge of the CDZ in sections B–E (Lockner *et al.* 2011). Rounded porphyroclasts of serpentine, sandstone and siltstone are entrained in the pervasively sheared, scaly, cohesionless gouge. The gouge is bounded by more intact siltstones and sandstones (sections A–B and H–I). Macroscopic fracturing increases markedly in sections J–Q, corresponding to a 30 m-wide zone of decreased velocities (Fig. 3).

fault ‘cores’ with an associated wider zone of highly fractured rock (e.g. as in Sibson 2003; Chester *et al.* 2004).

### Fault-zone-guided waves observed inside the San Andreas Fault

During 53 days of recording by a borehole seismometer in the SAFOD hole in February, May, July, August and September 2006, the Northern California Seismic Network detected 62 earthquakes within 10 km of SAFOD. These events were relocated by Waldhauser & Schaff (2008) using the double-difference and waveform cross-correlation timing methods. Their locations are plotted in Figure 5. Half (31) of these events have prominent secondary phases following the P-wave and 95% (58) have them following the S-wave (e.g. see Figs 6–8).

The SAFOD seismograph was a three-component Oyo Geospace DS-250 seismometer placed 2670 m below ground level. At this point

the seismometer was approximately 40 m short of the CDZ (i.e. to its SW). The DS-250’s 15 Hz geophones were digitized down-hole at 4000 samples s<sup>-1</sup>, a much higher sampling rate than either the Parkfield area surface-based or borehole seismic networks.

All of the secondary phases show the ‘normal dispersion’ characteristic of guided seismic waves and many have very clear guided-wave Airy phases. They also have group velocities and frequency content lower than the P- and S-body waves. Based on these characteristics, we have identified the signals following the S-wave as the well-known fault-zone-guided SH- and PSV-waves,  $F_L$  and  $F_R$  (Li *et al.* 1990; Malin *et al.* 1996).

### A new type of seismic wave

The normally dispersed waves arriving in between the P- and S-waves are, however, new to seismology. For the earthquake shown in Figure 6a, this phase arrives after the impulsive P-wave body and

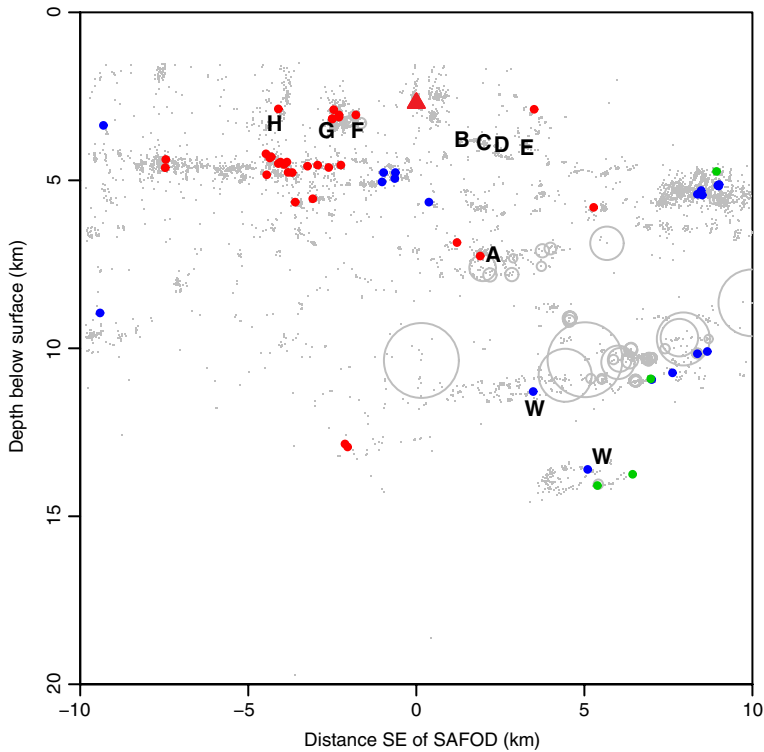


**Fig. 5.** A longitudinal cross-section along the San Andreas Fault showing the double-difference hypocentre locations of Waldhauser & Schaff (2008) in grey. Earthquakes recorded by the SAFOD borehole seismometer (the red triangle) in 2006 that display clear  $F_L$ - and  $F_R$ -waves indicated by blue dots. Earthquakes that display clear  $F_\phi$ -waves in addition to  $F_L$  and  $F_R$  are shown by red dots. Events without clear  $F_g$ -waves are shown by green dots. Letters A–H identify the events discussed in the text. The two events studied by Wu *et al.* (2010) marked by ‘W’s.

well before the S-wave. Figure 6 show that it is normally dispersed, is higher frequency than the post-S-guided waves and ends abruptly in an Airy phase. It is prominent on the radial (P) and SV (fault-perpendicular) components, and absent on the SH (fault-parallel) component. It also appeared only when the seismograph was placed very close to the CDZ. These characteristics suggest that this phase originates in constructively interfering PSV-waves in a low-velocity channel – in other words, a fault-guided wave. Since it travels faster than the S-wave, it must involve P-waves propagating in the waveguide. However, its mode of propagation must be different from the fully trapped P- and S-waves associated with  $F_L$  and  $F_R$ . Otherwise it would share their arrival times and frequency content.

In this case, as the P-waves reflect from the boundaries of the waveguide they must convert some of their energy into SV-waves (Aki & Richards 2002). These SV-waves cannot be fully trapped inside the guide as then the new phase's reflection conditions would be those of  $F_L$  and  $F_R$ , and it would arrive after the S-wave. Consequently, the new phase must be 'leaking' S-waves as it propagates along the waveguide. For this reason we designated it as ' $F_\Phi$ ', the ' $\Phi$ ', referring to its origin as a leaky mode P-wave travelling within the fault (e.g. Phinney 1961).

Like the other types of fault-guided waves, the generation, propagation and detection of  $F_\Phi$ -waves depends in part on the geometric relationships of the source, receiver, waveguide and waveguide–wall property contrasts. It also depends on the continuity of the waveguide: no major discontinuities can exist between the source and receiver, although moderate complexity in the waveguide geometry can occur (Igel *et al.* 2002).

An earthquake source and seismic receiver located within a geometrically simple, constant low-velocity channel will invariably generate seismograms with  $F_g$ -type waves.  $F_g$ -waves can also be generated by a source located outside of the waveguide from the interaction between the body waves and structural complexities in the waveguide. This includes irregularities such as small offsets and constrictions of the waveguide's walls (Fohrmann *et al.* 2004). In particular, the base of a shallow waveguide can produce  $F_g$ -waves from sources located below it (Igel *et al.* 2002; Fohrmann *et al.* 2004). We have paid particular attention to this possibility in our modelling study of  $F_\Phi$ . As we will show, the degree of  $F_\Phi$  generation and propagation is sensitive to all of these characteristics.

Further, a result of its energy loss due to its leaky characteristics,  $F_\Phi$  attenuates more rapidly with distance than the fully trapped fault-zone-guided waves. This partially explains why this phase has

not been identified in ground-level recordings that contain the other  $F_g$ -waves. A further reason is that the new phase is composed of higher-frequency waves: 20–80 v. 1–30 Hz for  $F_L$  and  $F_R$ . It is therefore subject to much higher intrinsic and scattering losses during propagation to the surface. An even greater damping effect would take place if its low-velocity channel were to broaden or branch near the surface, as in the case of a strike-slip 'flower' structure.

## Deep rock damage in the San Andreas Fault at SAFOD

In this section we examine the  $F_g$ -waves from several events located below and recorded by the SAFOD borehole seismograph at a depth of 2.7 km (Fig. 5). These include one approximately 7 km deep and slightly to the SE of SAFOD (event A, Fig. 6), four shallower ones also to the SE (events B–E, Fig. 7) and three events to the NE (events F–H, Fig. 8). For each, we compare the observed seismograms with synthetic seismograms computed for an earthquake source inside a low-velocity zone bounded by two half spaces. The aim of the modelling was to match the arrival times, frequency contents and relative amplitudes of the body and  $F_g$ -waves. The calculations were performed using the fk program of Zhu & Rivera (2002). The relevant model parameters for this code are the values of  $V_P$ ,  $V_S$ , and  $Q_P$  and  $Q_S$ , in the low-velocity channel and bounding half spaces. Models that incorporate more elements of the three-dimensional (3D) structure as known from seismic tomography (Zhang *et al.* 2009) would be needed to better match the waveforms.

Event A in Figure 6 occurred at 03:58:12.97 on 6 February 2006 at a depth of 7.25 km (Waldauser & Schaff 2008). The epicentre is 1.9 km SE of SAFOD, so the radial distance to the subsurface seismometer is 5.0 km. Our models of the observed travel-time separations between P and  $F_\Phi$ , and between S and  $F_L$  and  $F_R$ , require that the half-space velocities on the two sides of the fault be unequal. This is in good agreement with the SAFOD site travel-time tomography results of Zhang *et al.* (2009).

Zhang *et al.* also show that the P and S travel times are controlled by the faster half space, while  $F_L$  and  $F_R$  are controlled by the slower half space. The observed travel times for event A thus sets the half space velocities in the model to  $V_P = 5.48$  and  $4.64 \text{ km s}^{-1}$  and  $V_S = 3.44$  and  $2.66 \text{ km s}^{-1}$  to the SW and NE of the fault, respectively. The body-wave attenuation in the half spaces was set to  $Q_P = 200$  and  $Q_S = 200$ , based on the measurements of Imanishi *et al.* (2004).

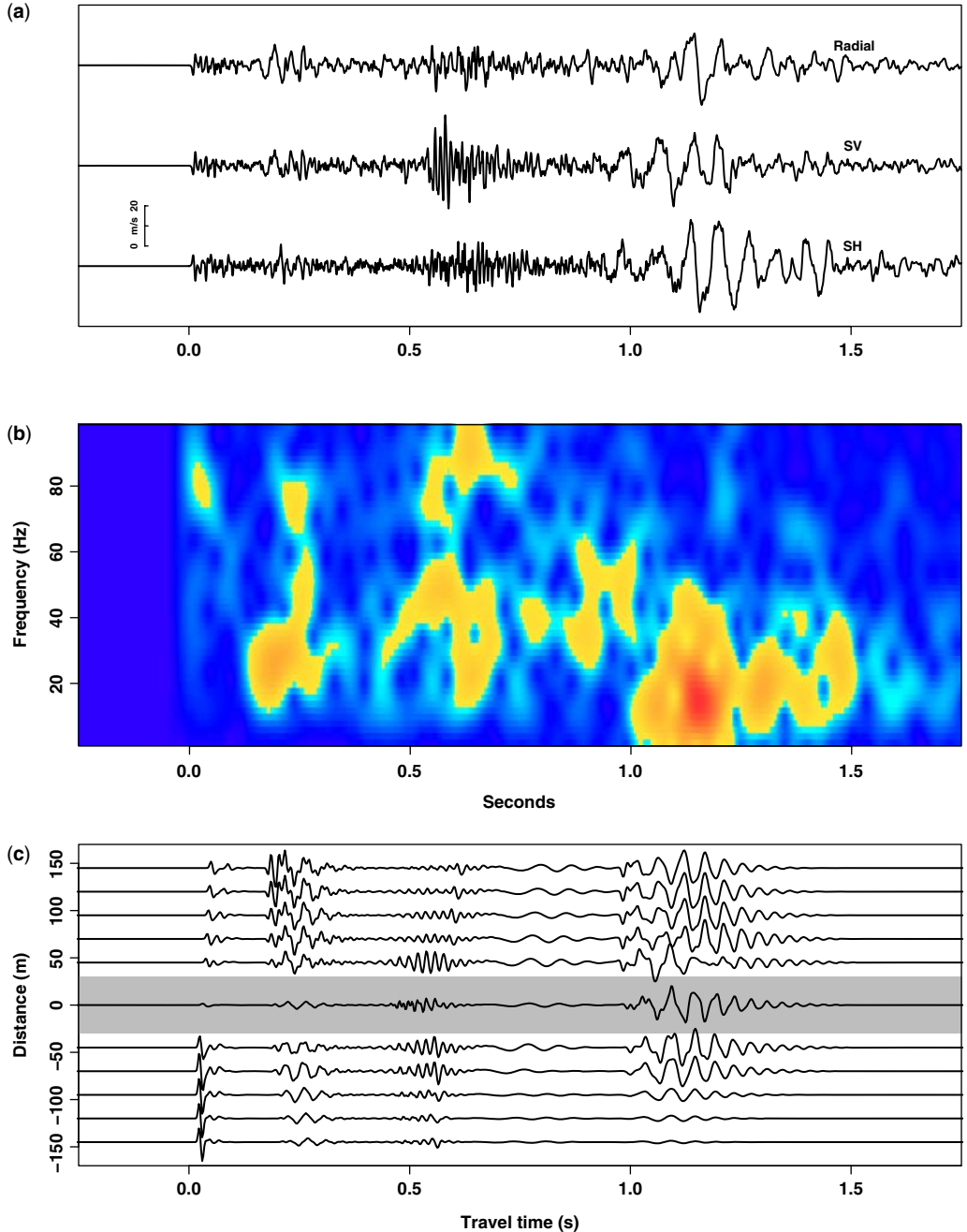


**Fig. 6.** (a) Velocity seismograms for the three-component motions of event A (Fig. 5). The phases  $P$ ,  $F_g$ ,  $S$ , and  $F_L$  and  $F_R$  are indicated. The seismograms have been rotated into the radial (toward the source), SV (motion perpendicular to the waveguide) and SH (motion parallel to the waveguide). Note the large amplitudes and normal dispersions of the  $F_g$ -waves. (b) Spectrogram of the time-varying frequency content of the radial component of the motion shown in Figure 6a. Warm colours denote higher amplitudes. The high-frequency P-wave is followed by the lower-frequency  $F_g$ -wave that is normally dispersed with frequency increasing with time from 20 Hz to its abrupt termination in an Airy phase at 80 Hz. The broad band S-wave is followed by the lower-frequency  $F_L$ - and  $F_R$ -waves that also display normal dispersion, with frequency increasing from 10 to 30 Hz. (c) Synthetic seismograms for a  $P$ ,  $F_g$ ,  $S$ , and  $F_L$  phases for

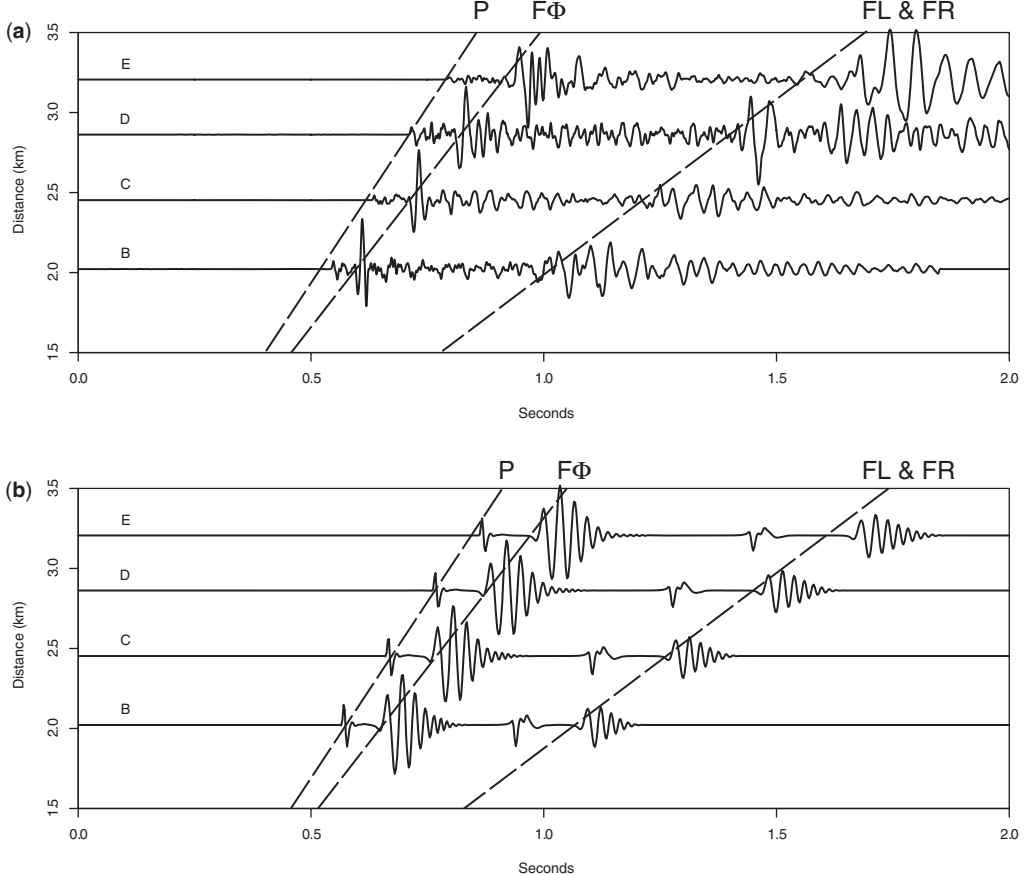


**Fig. 7.** (a) A record section of borehole-parallel components of motion for events B–E shown as a function of radial distance from the SAFOD seismograph. Dashed lines indicate arrival times of P-,  $F_\phi$ - and  $F_R$ -waves. While the  $F_\phi$ -wave shows clear normal dispersion with lower propagation velocity of the higher frequencies, the P-wave shows no dispersion. (b) Synthetic seismogram record section corresponding to data in (a) for a 30 m-wide waveguide with 20% lower velocities than in the slower-velocity half space. The receiver is located 20 m inside the higher-velocity half space.

The time-varying, radial-component, frequency content of event A is displayed in the spectrogram in Figure 6b. The high-frequency P-wave is followed by a lower-frequency  $F_\phi$  that is normally dispersed, with frequency increasing from 20 Hz to its abrupt termination in an Airy phase at 80 Hz. The broadband S-wave is followed by the lower-frequency  $F_L$ - and  $F_R$ -waves, which are also

normally dispersed, with frequency increasing from 10 to 30 Hz.

Our model of the ILVZ is of a 30–60 m-wide low-velocity channel with a velocity reduction of 20%. Within it  $Q_P$  is reduced to 100 and  $Q_S$  to 40 (e.g. see Blakeslee *et al.* 1989). The models in Figure 6c are consistent with the seismometer being in the higher-velocity half space and within

**Fig. 6. (Continued)** receivers located 5 km from an impulsive source in the centre of a 60 m-wide low-velocity channel. In this figure the shaded strip indicates the low-velocity channel. The seismograms are plotted by perpendicular distance from the waveguide. The slower half space is at the top and the faster half space in the bottom. The initial arrivals on the fast side of the ILVZ are body waves in the faster half space and head waves in the slower half space. The modelled  $F_\phi$ - and  $F_L$ -wave groups propagate at the velocity of the slower half space. The observed waveforms best match a receiver located 40 m into the high-velocity half space – the actual position of the SAFOD borehole seismometer.

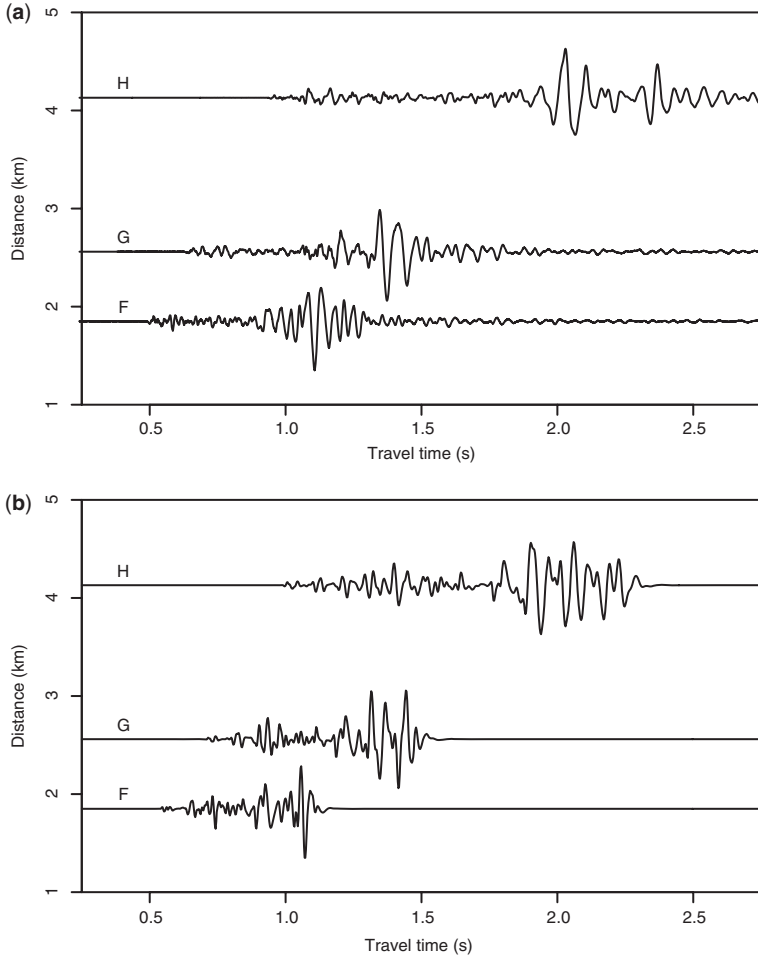


**Fig. 8.** (a) A record section of borehole-parallel components of motion for events F–H shown as a function of radial distance from the SAFOD seismograph. Note the absence of clear body-wave phases compared to those in Figures 6 and 7. (b) Synthetic seismogram model record section corresponding to the data in Figure 7a for a 200 m-wide waveguide with 20% lower velocities than in the slower-velocity half space. Both the model source and the receiver are located inside the low-velocity zone.

40 m of the ILVZ. Otherwise, the relative amplitudes and frequencies of  $P$ ,  $F_\Phi$ ,  $S$  and  $F_L$  and  $F_R$  are poorly matched by the synthetics. Further, the results show that the ILVZ must be less than 100 m wide. The  $Q_P$  seems to be approximately 40, and  $Q_S$  is somewhere between 20 and 100.

The 60 m-wide ILVZ in Figure 6c matches the lower-frequency content of  $F_L$  and  $F_R$ , but degrades the match to  $F_\Phi$ . Most significantly, using the velocities that give the best travel-time fits for the combination of phase, the models require that the waveguide exist along the entire path between event A and the seismometer. From this we conclude that rock damage in the form

of a low-velocity channel extends at least half way through the 15 km-deep seismogenic zone at SAFOD.

Events B–E form a profile at a depth of 4 km, and between 2.0 and 3.2 km radial distance from the SAFOD seismometer (Fig. 7). The initially compact  $F_\Phi$ -wave train of nearby event B becomes noticeably dispersed by the longer travel path from event E (Fig. 7a). Using the same modelling procedure followed for event A, we find that the waveguide for event E has similar properties to those inferred for event A, with a 20% waveguide-velocity reduction relative to the slower half space NE of the fault.

While this simple model captures many of the features of the different wave types, it is unable to match them in detail. This could mean that the waveguide geometry and velocities vary along the propagation path between the events. Hence, rather than being a problem, the waves might contain detailed information about the structure of the ILVZ that could be retrieved with more sophisticated modelling approaches.

The combined characteristics of the body waves and  $F_g$ -waves are very sensitive to both the location of the source and the receiver relative to the waveguide. Events F–H have very weak body waves relative to the  $F_g$ -waves (Fig. 8). These earthquakes are located 1.8–4.1 km NW of the SAFOD seismometer and 0.5 km below it. The weak P-wave could be a consequence of the receiver being near the P-wave node of this event's right-lateral focal mechanism. However, this should be the position of maximum amplitude for the S-wave on the SV component, which is not observed. Instead, our models show that the observed suppression of the body waves is due to both the source and receiver being located within or very close to the waveguide.

Using the same modelling procedure followed for event A, we find that the waveguide is broader at these shallower depths: roughly 100–200 m wide. Its properties are similar to those of the damage zone encountered by the SAFOD borehole (Fig. 3a). Models that include a 30 m-wide ILVZ within the wider waveguide generate a high-frequency  $F_\phi$  phase, which we do not observe. This suggests either that the ILVZ is absent or discontinuous between SAFOD and the active strand of the fault to the NE.

Events F–H are representative of the seismograms for shallow earthquakes located to the NW of SAFOD when the seismometer is located near the CDZ (Fig. 5). Their low-frequency, emergent and long-duration  $F_g$ -waves contrast with the seismograms of earthquakes located to the SE (Figs 6 & 7). Evidently, lateral changes in the geology of the fault zone and wall rocks can lead to differences in the propagation of  $F_g$ -waves. Such changes appear to occur on scales that are well below the resolution of local earthquake tomography, even when performed with very dense surface- and borehole-recorded body-wave data (Zhang *et al.* 2009).

The absence of  $F_\phi$ -waves from earthquakes located further SE of SAFOD (Fig. 5) confirms the multistranded nature of the SAF at this location. We infer that these events take place on a strand not directly connected to the ILVZ at SAFOD (Fig. 5) (see also Malin *et al.* 2006). This is in good agreement with the geometry of fault segments inferred from the double-difference earthquake locations of Waldhauser *et al.* (2004), Thurber *et al.* (2006) and Waldhauser & Schaff (2008) (Fig. 2).

## Discussion

Although a shallow low-velocity zone along the SAF at SAFOD was well known from surface observations of  $F_L$ - and  $F_R$ -waves, its extension into the seismogenic zone has been controversial (Ben-Zion *et al.* 2003; Lewis *et al.* 2005; Li & Malin 2008; Lewis & Ben Zion 2010; Wu *et al.* 2010). From the analysis of  $F_L$ - and  $F_R$ -waves recorded by surface and shallow borehole stations in the Parkfield area, Lewis & Ben Zion (2010) concluded that these signals originate by the trapping of body waves in a waveguide that extends to a depth of about 3 km. Hence, a shallow waveguide could explain some of the  $F_g$ -waves observed in SAFOD from sources at depths of 3–5 km.

Such a model, however, has difficulty explaining the distribution of the deeper events that do and do not generate  $F_g$ -waves (Fig. 5). According to the shallow waveguide hypothesis,  $F_g$ -waves from earthquakes located below it are excited when their body waves strike the base of the waveguide (Fohrmann *et al.* 2004). As Figure 5 shows, however, only some earthquakes with near-fault locations generate  $F_g$ -waves. This is inconsistent with their model.

Alternatively, if the waveguide is continuous between source and receiver, only the events located within or very close to the waveguide will generate  $F_g$ -waves (Fohrmann *et al.* 2004). The earthquakes in Figure 5 that fail to generate them could be on different fault strands than the one containing the SAFOD seismometer. As the multi-stranded nature of the fault is well known from earthquake locations (Thurber *et al.* 2004, 2006; Waldhauser *et al.* 2004) (Fig. 2c), this possibility seems at least equally likely.

The shallow waveguide hypothesis is also inconsistent with the results of Wu *et al.* (2010). They used low-pass filtering to analyse  $F_L$ - and  $F_R$ -waves recorded by the SAFOD seismometer. Their study focused on a pair of earthquakes located at depths of 10.6 and 12.6 km, and epicentral distances of 2.7 and 5.4 km to the SE (Fig. 5). These events have a nearly collinear propagation path to the seismometer. Consequently, as the shallower path is common to both events, these signals directly sample the properties between the two earthquakes. If the observed  $F_g$ -waves were generated at the base of a shallow low-velocity zone, they would have nearly identical dispersion characteristics because the waves would share the same waveguide path lengths to the receiver. Alternatively, if the waveguide extends between the sources, the deeper event would show increased dispersion of the  $F_g$ -waves due to its longer propagation path in the waveguide. Wu *et al.* (2010) measured the differential dispersion and found that these particular

$F_g$ -waves were propagating in a continuous source-to-receiver channel approximately 150 m wide and with a 24% velocity reduction that extended from the deeper source to the seismometer.

The channel width and the velocities derived from our  $F_L$  and  $F_R$  models, and the dispersion analysis of Wu *et al.* (2010), can be checked against the *in situ* well-log P- and S-wave velocities measured in the SAFOD borehole (Fig. 3). As noted earlier, an approximately 200 m-wide zone of about 10% lower seismic velocities identified by Zoback *et al.* (2010) lies between the SDZ and the NBF. A narrower region of significantly lower average velocities lies in the approximately 100 m interval between the CDZ and the NBF. Here the average velocities drop by about an additional 15%. We suggest that the low-pass filtered signals analysed by Wu *et al.*, as well as the  $F_g$ -waves seen to the NW, are likely to have been propagating in this channel.

Concerning the new  $F_\Phi$ -waves that we have also modelled here, they require a narrower waveguide – the ILVZ. The well-log velocities in the roughly 30–60 m interval to the NE of the CDZ are also anomalously low, especially when compared to other Cretaceous sedimentary rocks at similar depths of burial in California (Brocher 2008). This channel has an average velocity reduction of roughly 20%. These values are in general agreement with the models in Figures 6 and 7, especially for the slightly further events.

The velocity logs show that within a 2 m-wide interval at the CDZ, the P- and S-velocities are depressed by as much as 40% relative to the surrounding rocks (Hickman *et al.* 2007; Zoback *et al.* 2010). Waves trapped within such a narrow fault zone would have an Airy phase cut-off frequency and dispersion characteristics at much higher frequencies than those we could have observed.

The SAFOD drill cores sample the southwestern half of the zone that we have modelled here as the channel of the new  $F_\Phi$ -wave. These cores show that the sedimentary rocks are highly sheared and fractured, suggesting pervasive brittle deformation throughout this channel (Fig. 4). Many of the fractures are not healed, and their presence is entirely consistent with the reduced wave velocities. We thus infer that the velocity reduction we have modelled here arises from damage to the rock matrix on both the microcrack and macroscopic scales during recent fault movement.

What process can account for the deep, extensive and, apparently, geologically persistent 30–60 m-wide channel that we have observed both directly and in models of the various seismic waves? It is unlikely that such a disturbance could have been created by the 2004  $M \sim 6$  Parkfield earthquake. Geodetic and strong motion data show this rupture

terminated several kilometres to the SW of the SAFOD site (Johanson *et al.* 2006; Liu *et al.* 2006; Murray & Langbein 2006).

Instrumental and historical accounts indicate that no event capable of producing the observed low-velocity channel has ruptured the SAFOD segment since the 1857 Fort Tejon  $M 7.9$  earthquake (Toppozada & Branum 2006). That event ruptured over 300 km of the San Andreas Fault, principally to the SE of SAFOD, and had maximum ground offsets of over 5 m (Zielke *et al.* 2010). Historical accounts of this event suggest that its rupture extended NW from Cholame to as much as 80 km into the central creeping segment of the San Andreas Fault (Sieh 1978) (Fig. 1a). This is 50 km to the NW beyond the SAFOD site.

It has long been observed that the transition from creep to locking occurs along the southern 50–60 km of the central creeping segment of the fault (Lisowski & Prescott 1981; Titus *et al.* 2006). Along this transition, the creep rate steadily decreases from 35 mm year<sup>-1</sup> to zero at Cholame.

Parkfield earthquake ruptures cover, at most, the southernmost 30 km or so of this transition. The sum of the co- and post-seismic slip of these  $M \sim 6$  events and interseismic creep, however, does not keep pace with the long-term slip rate of the fault even there (Murray & Langbein 2006). This leads to a slip deficit that must be released occasionally in great earthquakes such as that in 1857.

The pervasive shearing and fracture seen within the remarkably wide  $F_\Phi$ -supporting damage zone would be consistent with brittle deformation resulting from the 1857 event. The low velocities occur within the dilatational quadrant for right-lateral slip on the fault plane of this event – the quadrant where fracturing caused by the rupture front occurs (Andrews 2005). Recurrent minor slip on this surface in the Parkfield  $M \sim 6$  events and its afterslip could help maintain the damage.

Such maintenance, however, may not be necessary as Cochran *et al.* (2009) reported the presence of a long-lived damage zone along the southern California Calico Fault, which has not ruptured in historic time. Perhaps the waveguide owes its existence to a combination of mechanical damage (cracks and microcracks) and chemical alteration processes. Alternatively, fault creep alone might be capable of creating and maintaining the zone of active fractures (Chester & Chester 2000). At SAFOD the Parkfield earthquake initiated a post-seismic transient increase in the creep rate as seen in surface geodetic measurements (Murray & Langbein 2006). This resulted in shortened recurrence times for the SAFOD target earthquakes (Fig. 5b). Perhaps this type of deformation combined with continued lower-level creep can locally maintain some degree of fault damage.

Given the limited spatial extend of these two alternative, non-earthquake mechanisms, why a continuous, 30 m-wide damage zone would form preferentially to the NE side of the main trace is not clear. Future laboratory studies of the frictional behaviour, microstructures and mineralogy of both the fault core and damage zone materials should shed light on mechanisms of velocity reduction in these rocks. The results from seismological observations of fault-zone-guided waves made at depth, however, clearly demonstrate that whatever its origin, the damage zone is an intrinsic fault structure and extends deep into the seismogenic crust, just as Rick Sibson said it would in 1977.

Over the course of the past 18 years, the conception, development, planning and execution of the first scientific drill hole into the seismogenic zone of a major plate boundary fault has been a community effort, involving hundreds of scientists, drilling engineers and other specialists. The authors wish to thank in particular M. D. Zoback and S. H. Hickman for their leadership and innumerable contributions in the field that led to the success of the SAFOD project. The paper benefitted from helpful reviews by Y. Ben-Zion and C. Thurber. The  $F_\Phi$  terminology used here for the new fault-zone-guided wave recognizes the contributions of R. A. Phinney to the study of leaky mode-guided waves.

## References

- AKI, K. & RICHARDS, P. G. 2002. *Quantitative Seismology*. University Science Books, Sausalito, CA.
- ANDREWS, D. J. 2005. Rupture dynamics and energy loss outside the slip zone. *Journal of Geophysical Research*, **110**, B01307, doi: 10.1029/2004JB003191.
- BEN-ZION, Y. 1998. Properties of seismic fault zone waves and their utility for imaging low-velocity structures. *Journal of Geophysical Research*, **103**, 12 567–12 585.
- BEN-ZION, Y. & AKI, K. 1990. Seismic radiation from an SH line source in a laterally heterogeneous planar fault zone. *Bulletin of the Seismological Society of America*, **80**, 971–994.
- BEN-ZION, Y., PENG, Z. ET AL. 2003. A shallow fault zone structure illuminated by trapped waves in the Karadere-Dusce branch of the North Anatolian Fault, Western Turkey. *Geophysical Journal International*, **152**, 699–717.
- BLAKESLEE, S. N., MALIN, P. E. & ALVAREZ, M. G. 1989. Fault-zone attenuation of high-frequency seismic waves. *Geophysical Research Letters*, **16**, 1321–1324.
- BROCHER, T. 2008. Compressional and shear-wave velocity versus depth relations for common rock types in Northern California. *Bulletin of the Seismological Society of America*, **98**, 950–968.
- CHESTER, F. M. & CHESTER, J. S. 1998. Ultracataclasite structure and frictional processes of the Punchbowl Fault, San Andreas system, California. *Tectonophysics*, **295**, 199–221.
- CHESTER, F. M. & CHESTER, J. S. 2000. Stress and deformation along wavy frictional faults. *Journal of Geophysical Research*, **105**, 23, 421–23, 430.
- CHESTER, F. M., CHESTER, J. S., KIRSCHNER, D. L., SCHULZ, S. E. & EVANS, J. P. 2004. Structure of large-displacement, strike-slip faults in the brittle continental crust. In: KARNER, G. D., TAYLOR, B., DRISCOLL, N. W. & KOHLSTEDT, D. L. (eds) *Rheology and Deformation in the Lithosphere at Continental Margins*. Columbia University Press, New York, 223–260.
- COCHRAN, E. S., LI, Y.-G., SHEARER, P. M., BARBOT, S., FIALKO, Y. & VIDALE, J. E. 2009. Seismic and geodetic evidence for extensive, long-lived fault damage zones. *Geology*, **37**, 315–318, doi: 10.1130/G25306A.1.
- DRAPER SPRINGER, S., EVANS, J. P., GARVER, J. I., KIRSCHNER, D. & JANECKE, S. U. 2009. Arkosic rocks from the San Andreas Fault Observatory at Depth (SAFOD) borehole, central California: implications for the structure and tectonics of the San Andreas fault zone. *Lithosphere*, **1**, 206–226, doi: 10.1130/L13.1.
- FAGERENG, Å. & SIBSON, R. H. 2010. Mélange rheology and seismic style. *Geology*, **38**, 751–754, doi: 10.1130/G30868.1.
- FAULKNER, D. R., LEWIS, A. C. & RUTTER, E. H. 2003. On the internal structure and mechanics of large strike-slip fault zones: field observations of the Carboneras fault in southern Spain. *Tectonophysics*, **367**, 235–251.
- FOHRMANN, M., IGEL, H., JAHNKE, G. & BEN-ZION, Y. 2004. Guided waves from sources outside faults: an indication for shallow fault zone structure? *Pure and Applied Geophysics*, **161**, 2125–2137.
- HICKMAN, S., ZOBACK, M., ELLSWORTH, W., BONESS, N., MALIN, P., ROECKER, S. & THURBER, C. 2007. Structure and properties of the San Andreas Fault in Central California: recent results from the SAFOD experiment. *Scientific Drilling*, Special Issue No. 1, 29–32.
- HOLDSWORTH, R. E., VAN DIGGELEN, E., SPIRES, C., DE BRESSER, H., WALKER, R. & BOWEN, L. 2011. Fault rocks from the SAFOD core samples: implications for weakening at shallow depths along the San Andreas Fault, California. *Journal of Structural Geology*, **33**, 132–144.
- IGEL, H., JAHNKE, G. & BEN-ZION, Y. 2002. Numerical simulation of fault zone guided waves: accuracy and 3-D effects. *Pure and Applied Geophysics*, **159**, 2067–2083.
- IMANISHI, K., ELLSWORTH, W. L. & PREJEAN, S. G. 2004. Earthquake source parameters determined by the SAFOD Pilot Hole seismic array. *Geophysical Research Letters*, **31**, L12S09, doi: 10.1029/2004GL019420.
- IRWIN, W. P. 1990. 3. Geology and plate tectonic development. In: WALLACE, R. E. (ed.) *The San Andreas Fault System*. US. Geological Survey, Professional Paper, **1515**, 61–81.
- JOHANSON, I. A., FIELDING, E. J., ROLANDONE, F. & BURGMANN, R. 2006. Coseismic and postseismic slip of the 2004 Parkfield earthquake from space-geodetic data. *Bulletin of the Seismological Society of America*, **96**, S269–S282.

- KORNEEV, V. A., NADEAU, R. M. & McEVILLY, T. V. 2003. Seismological Studies at Parkfield IX: fault-zone imaging using guided wave attenuation. *Bulletin of the Seismological Society of America*, **93**, 1415–1426.
- LEWIS, M. A. & BEN-ZION, Y. 2010. Diversity of fault zone damage and trapping structures in the Parkfield section of the San Andreas Fault from comprehensive analysis of near fault seismograms. *Geophysical Journal International*, **183**, 1579–1595, doi: 10.1111/j.1365-246X.2010.04816.x.
- LEWIS, M. A., PENG, Z., BEN-ZION, Y. & VERNON, F. L. 2005. Shallow seismic trapping structure in the San Jacinto fault zone near Anza, California. *Geophysical Journal International*, **162**, 867–881.
- LI, Y.-G. & LEARY, P. C. 1990. Fault zone trapped seismic waves. *Bulletin of the Seismological Society of America*, **80**, 1245–1271.
- LI, Y.-G. & MALIN, P. 2008. San Andreas Fault damage at SAFOD viewed with fault-guided waves. *Geophysical Research Letters*, **35**, L08304, doi: 10.1029/2007GL032924.
- LI, Y.-G. & VERNON, F. L. 2001. Characterization of the San Jacinto fault zone near Anza, California, by fault zone trapped waves. *Journal of Geophysical Research*, **106**, 30, 671–30, 688.
- LI, Y.-G. & VIDALE, J. E. 2001. Healing of the shallow fault zone from 1994–1998 after the 1992 M 7.5 Landers, California, earthquake. *Geophysical Research Letters*, **28**, 2999–3002.
- LI, Y.-G., LEARY, P. C., AKI, K. & MALIN, P. E. 1990. Seismic trapped modes in the Oroville and San Andreas fault zones. *Science*, **249**, 763–766.
- LISOWSKI, M. & PRESCOTT, W. H. 1981. Short-range distance measurements along the San Andreas fault system in central California, 1975 to 1979. *Bulletin of the Seismological Society of America*, **71**, 1607–1624.
- LIU, P., CUSTÓDIO, S. & ARCHULETA, R. J. 2006. Kinematic inversion of the 2004 M 6.0 Parkfield earthquake including an approximation to site effects. *Bulletin of the Seismological Society of America*, **96**, S143–S158.
- LOCKNER, D. A., MORROW, C. A., MOORE, D. E. & HICKMAN, S. H. 2011. Low strength of Deep San Andreas Fault Gouge from SAFOD Core. *Nature*, **472**, 82–85, doi: 10.1038/nature09927.
- MALIN, P. E., LOU, M. & RIAL, J. A. 1996. FR waves: a second fault-guided mode with implications for fault property studies. *Geophysical Research Letters*, **23**, 3547–3550.
- MALIN, P., SHALEV, E., BALVEN, H. & LEWIS-KENEDI, C. 2006. Structure of the San Andreas Fault at SAFOD from P-wave tomography and fault-guided wave mapping. *Geophys. Research Letters*, **33**, L13314, doi: 10.1029/2006GL025973.
- MURRAY, J. & LANGBEIN, J. 2006. Slip on the San Andreas Fault at Parkfield, California, over two earthquake cycles and implications for seismic hazard. *Bulletin of the Seismological Society of America*, **96**, S283–S303.
- PENG, Z., BEN-ZION, Y., ZHU, L. & MICHAEL, A. J. 2003. Inference of a shallow fault zone layer in the rupture zone of the 1992 Landers, California earthquake from locations of events generating trapped waves and travel time analysis. *Geophysical Journal International*, **155**, 1021–1041.
- PHINNEY, R. A. 1961. Propagation of leaking interface waves. *Bulletin of the Seismological Society of America*, **51**, 527–555.
- SIBSON, R. H. 1977. Fault rocks and fault mechanisms. *Journal of the Geological Society of London*, **133**, 191–213.
- SIBSON, R. H. 1986. Brecciation processes in fault zones. *Pure and Applied Geophysics*, **124**, 159–175.
- SIBSON, R. H. 2003. Thickness of the seismic slip zone. *Bulletin of the Seismological Society of America*, **93**, 1169–1178.
- SIEH, K. E. 1978. Slip along the San Andreas Fault associated with the great 1857 earthquake. *Bulletin of the Seismological Society of America*, **68**, 1421–1448.
- SOLUM, J. G., HICKMAN, S. H., LOCKNER, D. A., MOORE, D. E., VAN DER PLUIJM, B. A., SCHLEICHER, A. M. & EVANS, J. P. 2006. Mineralogical characterization of protolith and fault rocks from the SAFOD Main Hole. *Geophysical Research Letters*, **33**, L21314, doi: 10.1029/2006GL027285.
- THRUBER, C., ROECKER, S., ZHANG, H., BAHER, S. & ELLSWORTH, W. 2004. Fine-scale structure of the San Andreas fault zone and location of the SAFOD target earthquakes. *Geophysical Research Letters*, **31**, L12S02, doi: 10.1029/2003GL019398.
- THRUBER, C. H., ZHANG, H., WALDHAUSER, F., HARDEBECK, J., MICHAEL, A. & EBERHART-PHILLIPS, D. 2006. Three-dimensional compressional wavespeed model, earthquake relocations, and focal mechanisms for the Parkfield, California, region. *Bulletin of the Seismological Society of America*, **96**, S38–S49, doi: 10.1785/0120050825.
- TITUS, S. J., DEMETS, C. & TIKOFF, B. 2006. Thirty-five year creep rates for the creeping segment of the San Andreas Fault and effects of the 2004 Parkfield earthquake: constraints from alignment arrays, continuous Global Positioning Systems, and creepmeters. *Bulletin of the Seismological Society of America*, **96**, S250–S268.
- TOPPOZADA, T. & BRANUM, D. 2006. San Andreas M~6 earthquakes within 40 km of the Priest Valley end zone of the 1857 faulting. *Bulletin of the Seismological Society of America*, **96**, S385–S396.
- WALDHAUSER, F. & SCHAFF, D. P. 2008. Large-scale relocation of two decades of Northern California seismicity using cross-correlation and double-difference methods. *Journal of Geophysical Research*, **113**, B08311, doi: 10.1029/2007JB005479.
- WALDHAUSER, F., ELLSWORTH, W. L., SCHAFF, D. P. & COLE, A. 2004. Streaks, multiplets, and holes: high-resolution spatio-temporal behavior of Parkfield seismicity. *Geophysical Research Letters*, **31**, L18608, doi: 10.1029/2004GL020649.
- WU, J., HOLE, J. A. & SNOKE, J. A. 2010. Fault zone structure at depth from differential dispersion of seismic guided waves: evidence for a deep waveguide on the San Andreas Fault. *Geophysical Journal International*, **182**, 343–354, doi: 10.1111/j.1365-246X.2010.04612.x.

- YANG, H. & ZHU, L. 2010. Shallow low-velocity zone of the San Jacinto fault from local earthquake waveform modeling. *Geophysical Journal International*, **183**, 421–432, doi: 10.1111/j.1365-246X.2010.04744.x.
- ZHANG, H., THURBER, C. & BEDROSIAN, P. 2009. Joint inversion for V<sub>p</sub>, V<sub>s</sub>, and V<sub>p</sub>/V<sub>s</sub> at SAFOD, Parkfield, California. *Geochemistry, Geophysics, Geosystems*, **10**, Q11002, doi: 10.1029/2009GC002709.
- ZHU, L. & RIVERA, L. A. 2002. A note on the dynamic and static displacements from a point source in multi-layered media. *Geophysical Journal International*, **148**, 619–627.
- ZIELKE, O., ARROWSMITH, J. R., GRANT LUDWIG, L. & AKÇI, S. O. 2010. Slip in the 1857 and earlier large earthquakes along the Carrizo Plain, San Andreas Fault. *Science*, **327**, 1119–1122.
- ZOBACK, M., HICKMAN, S. & ELLSWORTH, W. 2010. Scientific drilling into the San Andreas Fault zone. *EOS, Transactions of the American Geophysical Union*, **91**, 197–204.
- ZOBACK, M., HICKMAN, S. & ELLSWORTH, W. 2011. Scientific drilling into the San Andreas Fault Zone – an overview of SAFOD's first five years. *Scientific Drilling*, **11**, 14–28, doi: 10.2204/iodp.sd.11.02.2011.



# Geology of the seismogenic subduction thrust interface

ÅKE FAGERENG

*Department of Geology, University of Otago, PO Box 56, Dunedin 9054, New Zealand  
(e-mail: [ake.fagereng@uct.ac.za](mailto:ake.fagereng@uct.ac.za))*

*Department of Geological Sciences, University of Cape Town, Private Bag X3,  
Rondebosch 7701, South Africa*

**Abstract:** A microseismically active layer of underthrust sediments is commonly inferred along subduction thrust interfaces. The exhumed Chrystals Beach Complex, in the Otago Schist, New Zealand, may be analogous to an actively deforming underthrust rock assemblage. The complex contains asymmetric competent lenses of sandstone, chert and basalt enclosed in a cleaved mudstone matrix. Continuous fabrics such as folds, boudins and asymmetric phacoids formed by distributed cataclasis and dissolution–precipitation creep. Discontinuous deformation is evident in an extensive fault-fracture mesh involving mutually cross-cutting subvertical extension veins and subhorizontal slickenfibre shear surfaces.

The Hikurangi margin provides an example of along-strike variations in seismic style, possibly related to heterogeneous fluid-pressure state and interface geology. In both the ancient and active subduction-related shear zone, fluid-pressure state appears to be a critical control on frictional failure, which primarily occurs on weak, fluid-overpressured discontinuities. Continuous, aseismic deformation occurs where other mineral deformation mechanisms, such as dissolution–precipitation creep, are preferred. The geometry and composition of the underthrust rock assemblage appear to be first-order controls on megathrust fluid-pressure distribution, bulk rheology and dominant deformation mechanism, and thus may be significant controls on megathrust seismic style.

This contribution compares geological observations from an exhumed accretionary mélange, the Chrystals Beach Complex, Otago Schist, New Zealand, with geophysical observations along an active subduction thrust interface, the Hikurangi margin, New Zealand, and other modern analogues. The study aims to address the relative importance of factors affecting varying seismic style along subduction megathrusts.

Although most subduction-related moment release occurs during large earthquakes, subduction-zone megathrusts accommodate slip in a variety of styles, ranging from regular earthquakes ( $M_w \leq 9.5$ ) through slow slip and non-volcanic tremor to transient and continuous aseismic creep (Schwartz & Rokosky 2007; Peng & Gomberg 2010 and references therein). Heterogeneity in seismic style is commonly observed both down-dip and along-strike on active subduction thrust interfaces, but the physical reasons for these variations in slip mode are poorly understood (Hyndman 2007 and references therein). Thermal effects on subduction-zone seismicity have been studied by numerous authors (e.g. Tichelaar & Ruff 1993; Peacock 1996; Hyndman *et al.* 1997; Oleskevich *et al.* 1999) but, although the depth-limits of the seismogenic zone appear to be, in part, thermally controlled, temperature alone cannot explain the full range of observed megathrust

behaviour (e.g. Harris & Wang 2002; McCaffrey *et al.* 2008; Fagereng & Ellis 2009).

A layer of sheared, fluid-saturated, trench-fill sediment and fragments of oceanic crust and seamounts, either from sediment underplating or from erosion from the overlying accretionary prism, has been inferred to occur along subduction thrust interfaces (Shreve & Cloos 1986; von Huene & Scholl 1991). Variations in seismic velocities have been interpreted to represent a fluid-rich sediment layer, commonly 1–2 km thick, along a number of active subduction megathrusts (e.g. Eberhart-Phillips & Reyners 1999; Tsuru *et al.* 2002; Abers 2005; Sage *et al.* 2006; Tobin & Saffer 2009; Park *et al.* 2010). These sediments are probably weaker than the surrounding crust and may therefore act as a lubricating layer, preferentially accommodating shear displacement between the two converging plates (Shreve & Cloos 1986). This layer is unlikely to be a homogeneous, viscous shear zone, but rather comprises a variety of rock units with a range of mechanical behaviours (Fagereng & Sibson 2010).

If most subduction thrust interface seismicity occurs within, or at the boundaries of, the sheared weak sediment layer, the bulk rheology of these shear zones provides a first-order control on the seismic style of subduction megathrusts (Fagereng & Sibson 2010). In this chapter I address the

deformation processes occurring within underthrust sediments, based on observations in ancient and active fault zones along the New Zealand plate boundary. Much literature is available on the active Hikurangi subduction margin, and the properties of the subduction interface were recently reviewed by Wallace *et al.* (2009). This contribution focuses on observations from the Chrystals Beach Complex, and on interpreting the geological structures in this assemblage in relation to factors that may determine the behaviour of a subduction megathrust.

### Geological setting of the Chrystals Beach Complex

The Chrystals Beach Complex has a structural thickness of less than 4 km and is exposed along approximately 25 km of the SE Otago coastline, about 60 km south of the city of Dunedin (Figs 1 & 2). The complex has been interpreted as an accretionary mélange (Nelson 1982), possibly formed by Late Triassic subduction of oceanic crust towards the south under the Gondwana continental margin (Hada *et al.* 2001). Radiolarian fossils (Campbell & Campbell 1970; Aita & Bragin 1999) indicate Triassic deposition, and detrital zircon ages (Adams *et al.* 2007) indicate a sediment source of Early–Late Triassic age. Graphitization and K–Ar

ages indicate peak metamorphic ages in the Middle–Late Jurassic (Nishimura *et al.* 2000). Pumpellyite–actinolite-facies metamorphic assemblages and mineral chemistry indicate peak pressure–temperature ( $P$ – $T$ ) conditions of  $\leq 550$  MPa ( $c.$  25 km) and approximately 300 °C within the southern Chrystals Beach Complex (Fagereng & Cooper 2010a). The metamorphic grade increases progressively to the north (Nishimura *et al.* 2000), but only rocks within the pumpellyite–actinolite-facies Chrystals Beach–Quoin Point section are considered in this study (Figs 1 & 2), as these exposures exhibit the best preserved structural fabrics. The complex lies on the southwestern edge of the Otago Schist, which has been interpreted as a metamorphosed accretionary wedge where the regional metamorphic gradients (highest grade along the central axis, decreasing toward the flanks) were produced by burial and later uplift of the rocks in the prism (e.g. Mortimer 2000). In this setting, the Chrystals Beach Complex could have been deformed either within the accretionary wedge, or represent underthrust sediments from below a décollement (Fagereng & Cooper 2010b).

Nelson (1982) divided the lithology of the complex into two main units, a sandstone–shale and a volcanogenic association. The former is predominant (>90% by area), and consists of a

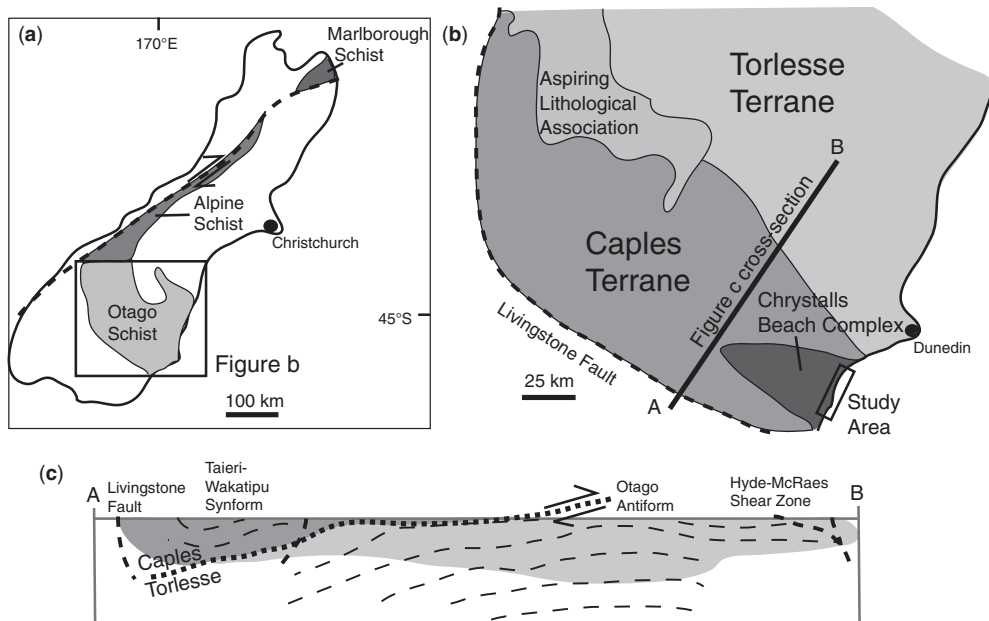


**Fig. 1.** Simple geological map of the Haast Schist: (a) with a close-up of the Otago Schist; (b) (after Mortimer 1993) showing the location of the study area. Sketch cross-section in (c) shows the inferred relationship between the Caples and Torlesse terranes (after Mortimer 2003).

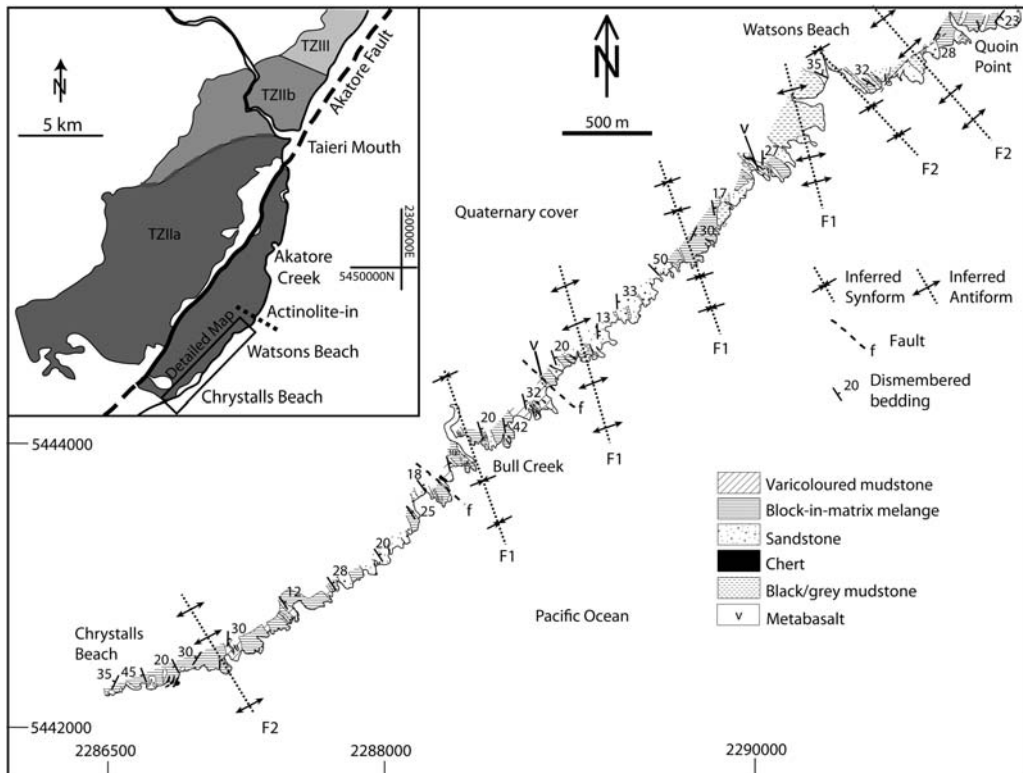


**Fig. 2.** Geological map of the Chrystals Beach Complex from Chrystals Beach in the south to Quoin Point in the north (after Robinson 1958; Nelson 1982; Hada *et al.* 1988, 2006; Bishop 1994). Inferred fold-axial surface traces are based on maps by Hada *et al.* (1988), where  $F_1$  folds are tight, steeply inclined to recumbent, and  $F_2$  are later open, upright folds. Insert: general geological map of SE Otago (after Bishop 1994). Grid references to New Zealand map grid: TZ, textural zone.

dismembered sequence of interbedded sandstone and grey/black mudstone, while the latter comprises varicoloured chert and mudstone, basalts and black radiolarian chert (Nelson 1982). Rocks that would belong to the volcanogenic association may be found within sandstone–shale association rock assemblages, and vice versa. The mélange matrix is phyllitic, with a weak scaly cleavage subparallel to elongate fragments of dismembered bedding. The composition of these fragments is typically metamorphosed sandstone, chert and minor basalt. The matrix mineral assemblage is quartz + albite + chlorite + white mica  $\pm$  calcite  $\pm$  pumpellyite  $\pm$  epidote. Sandstones are primarily composed of quartz and feldspar (albite  $\pm$  orthoclase) with accessory chlorite, white mica, epidote, calcite and pumpellyite. A weak cleavage is sometimes developed in these sandstones and is subparallel to the scaly cleavage in the phyllitic matrix. Cherts are usually found in thin layers, separated by thicker beds of mudstone, and some cherts have developed a surface layer of manganese oxide.

Both chert and varicoloured mudstones are predominantly composed of microcrystalline quartz, with a very fine-grained matrix of secondary minerals and amorphous material. Metabasalt is present in rare small lenses in the south, but larger (up to 200 m) outcrops are present further north (towards the structural base of the mélange). These rocks contain chlorite + albite + white mica + pumpellyite + epidote  $\pm$  calcite  $\pm$  clinopyroxene  $\pm$  titanite  $\pm$  actinolite, and are of inferred mid-ocean ridge and ocean island basalt affinity (Fagereng & Cooper 2010b). The mixed basalt affinities and the smaller ‘out-of-place’ lenses highlight the complex mixing of material that has occurred in the mélange.

### Geological structures in the Chrystals Beach Complex

The Chrystals Beach Complex rock assemblage has been intensely sheared in a mixed

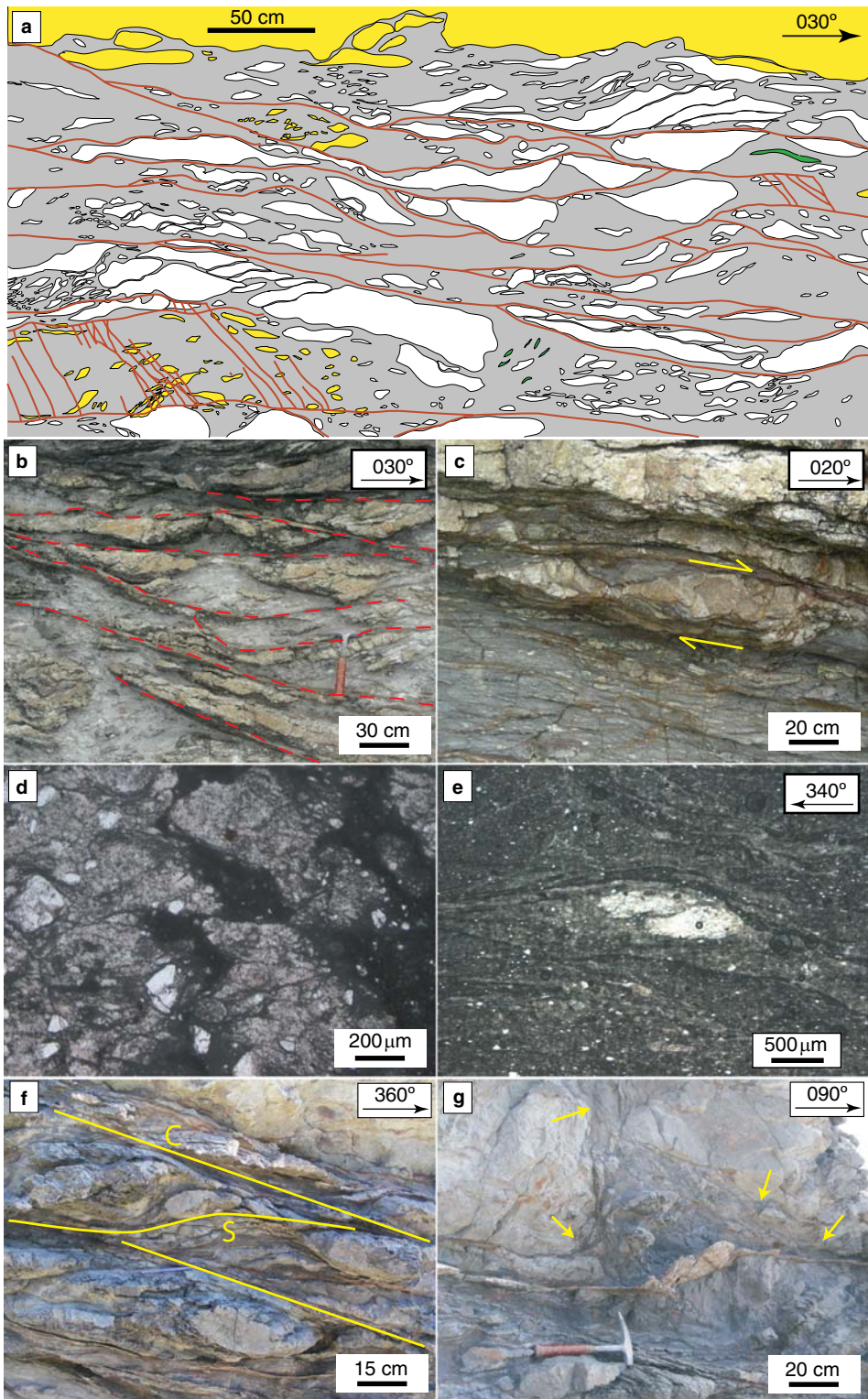


Fig. 3.

continuous-discontinuous style (Fig. 3a, b) (Nelson 1982; Fagereng & Sibson 2010). Outcrops of interbedded mudstone and sandstone are similar in appearance to ‘broken formation’ as described by Hsü (1968), and some may also choose to call these rocks ‘olistostromes’. However, because of their highly sheared appearance, beyond the soft sediment nature expected in an olistostrome, the mixture is here referred to as mélange, using the term as defined by Silver & Beutner (1980): a mappeable, fragmented, composite rock body, consisting of blocks dispersed in a matrix. This appearance is evident from thin-section scale, with mm-size competent lenses (phacoids) in a very fine-grained matrix, to map scale with phacoids of length up to 100 m enclosed by less competent material.

### Continuous deformation fabrics

The earliest penetrative fabric recorded in the assemblage is a subhorizontal foliation (Fig. 4) formed by layer-parallel stratal disruption. This fabric is termed  $S_{0+1}$  reflecting inheritance of primary bedding. Stratal disruption was accommodated by boudinage, pinch-and-swell structures and local folding (Fig. 3a–c). Dismembered competent beds are commonly split into sigmoidal lenses, showing a top-to-the-north sense of shear in the current attitude (Fig. 3a–c). Dismembered beds pinch out at the ends, suggesting they were pulled apart within the bedding plane. Contacts between mudstone and sandstone are generally irregular, and in places blurred by apparent mixing of the lithologies (Fig. 3d). These features suggest that the sediments were relatively mobile, and predominantly deformed by independent particulate flow, during initial layer-parallel extension and mixing of shear-zone materials (e.g. Kleist 1974).

Sandstone layers are disrupted without the breaking of grains, and irregular boundaries attest to some deformation while sand was still poorly lithified (Fig. 3d). Scaly cleavage within mudstone matrix, defined by fine-grained opaque minerals and preferentially oriented phyllosilicates, bends around chert and sandstone phacoids (Fig. 3e). This cleavage is interpreted as  $S_1$  and is generally subparallel to  $S_{0+1}$ . Grains have been dissolved where in contact

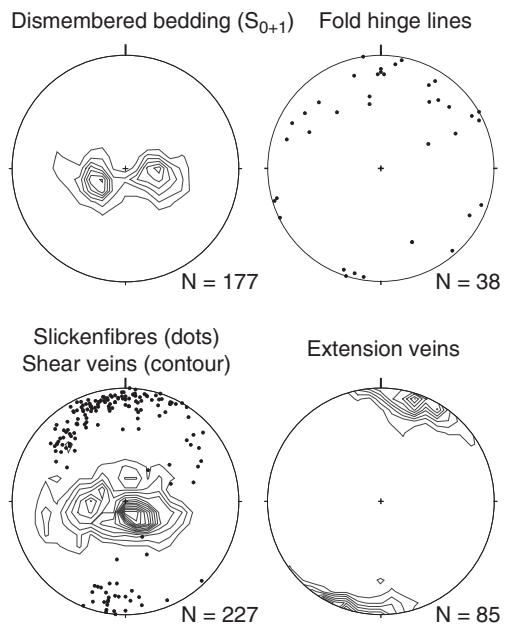


**Fig. 4.** Regional structural data collected throughout the southern roughly 5 km of shoreline exposure of the Chrystals Beach Complex (between Chrystals Beach and Quoin Point, Fig. 2) plotted on lower-hemisphere, equal-area stereoplots. Dismembered bedding is generally subhorizontal. Hinge-line trends are variable but similar to fibre trends, indicating variable rotation of hinge lines after (or during) folding. Shear veins are generally flat-lying and subparallel to  $S_{0+1}$ , with slickenfibres trending roughly north–south. Extension veins are generally subvertical, with poles oriented within the range of slickenfibre trends.

with  $S_1$ , indicating the importance of dissolution–precipitation creep in the formation of this cleavage.

In some <10 m-thick zones of localized shearing,  $S_1$  defines a fabric geometrically analogous to  $S-C$  fabric as commonly described in mylonites (Fig. 3f) (Lister & Snoke 1984).  $C$ -surfaces are subparallel to  $S_1$  outside the  $S-C$  fabric zones, while  $S$ -surfaces are rotated by up to 45° relative to  $C$ -surfaces. Evidence of brittle shear is rare along  $C$ - and  $S$ -surfaces, indicating a ductile origin.

**Fig. 3.** Illustrations of mélange fabrics in the Chrystals Beach Complex. (a) Outcrop map (vertical cliff) of competent chert (white), sandstone (yellow) and basaltic (green) lenses in a mudstone (dark grey) matrix cut by a vein-filled fault-fracture mesh (red lines). (b) Photograph of chert lenses in a mudstone matrix cut by shallow-dipping anastomosing slickenfibre shear veins (dashed red lines). (c) Asymmetric boudin showing a top-to-the-north shear sense. (d) Photomicrograph (plane polarized light) of contact between mudstone and sandstone, where dykelets of mudstone and blurred contacts suggest deformation of poorly lithified sediments. (e) Photomicrograph (plane polarized light) of a small chert lens in mudstone matrix, where pressure-solution cleavage planes (seams of insoluble material and preferentially oriented micaceous minerals) bend around the phacoid. (f) Localized shear zone comprising sandstone phacoids in a mudstone matrix, where an  $S-C$ -like fabric has developed. (g) Folded  $S_{0+1}$  with injections of mudstone (arrows) into cracks in sandstone layering, also note folded subhorizontal shear vein.

Sandstone and chert phacoids within the mudstone matrix have generally developed asymmetric shapes within the  $S-C$  fabric zones (Fig. 3f). Both  $S$ -surfaces and phacoids have commonly developed a sigmoidal shape, where they are deflected towards  $C$ -surfaces (Fig. 3f). The deformation of the phacoids involved some disaggregation near  $C$ -surfaces, and therefore the  $S-C$  fabric probably developed while the sandstone lenses were partially lithified.  $S-C$  fabric geometry generally indicates a top-to-the-north sense of shear (e.g. Fig. 3f). That  $S_1$  is part of an  $S-C$  structure suggests a simple shear and volume loss origin for this foliation, at least in some locations.

Hada *et al.* (1988, 2006) inferred large-scale folding of the complex, with at least two deformation phases: (1) tight, recumbent to steeply inclined, west-verging folds with north-south-trending hinge lines; and (2) later, open, upright folds with NW-SE-trending hinge lines (Fig. 2). The first phase is assumed from inferred overturned strata in the region surrounding Bull Creek (Fig. 2), while the second phase is evident from changes in bedding attitude (Fig. 2) (Hada *et al.* 1988). Late, open, upright folds, folding foliation, are also seen in other parts of the Otago Schist – for example, the Otago Antiform (e.g. Mortimer 1993) – and in the Shimanto Belt of Japan, where such folds are interpreted to have formed during post-accretionary folding within the accretionary prism (Ujiie 2002).

Outcrop-scale folds, folding relatively competent beds within a relatively incompetent matrix, have a large range of hinge line trends from NW to NE (Fig. 4), generally oblique or subparallel to the inferred north-south shear direction. Fold attitudes are dominantly non-cylindrical, and generally steeply inclined to recumbent, with  $S_1$  as an axial-planar cleavage. Fold vergence generally indicates a top-to-the-north sense of shear. Some later stage folds have an upright, open attitude, and fold both dismembered bedding and  $S_1$ . In some outcrop-scale folds, mud injections into folded competent beds are observed (Fig. 3g), indicating that some folding occurred while mudstone was still mobile and only partly lithified. Some folding therefore occurred in an early stage of mélange development. Folded veins (e.g. in Fig. 3g) demonstrate that folding must still have been occurring after initiation of brittle fracture and vein precipitation.

#### *Discontinuous deformation fabrics*

An extensive network of anastomosing quartz-calcite veins is ubiquitous throughout the complex (Fig. 3a, b). Some veins are folded, and some folds are cut by veins, suggesting mixed continuous-discontinuous behaviour at some point in the time-evolution of the mélange. The vein network

includes subhorizontal slickenfibre-coated shear surfaces and subvertical extension veins (Figs 3a, 4 & 5a, b), forming a fault-fracture mesh (cf. Hill 1977; Sibson 1996). Both kinematic vein types have a ‘crack–seal’ microstructure (Ramsay 1980a), suggesting incremental mesh development. Displacement increments determined from ‘crack–seal’ spacing is typically in the range of 10–100  $\mu\text{m}$  (Fagereng *et al.* 2010).

Slickenfibres, shear fracture arrays and dilational stepovers generally show a top-to-the-north sense of shear. Variation in this shear sense occurs in places, and a single fibre may show multiple directions of growth (Fig. 5a), caused by rotation around a subvertical axis. This rotation is commonly localized, and is probably caused by competent blocks rotating within the matrix, rather than a change in the general shear direction within the mélange. Slickenfibre shear veins appear to have multiple internal slip surfaces, a macroscopic ‘crack–seal’ texture and a pressure-solution selvage that is commonly present along the vein margin (Fig. 5c, d) (Fagereng *et al.* 2010). Internal slip surfaces within fibrous shear veins appear as thin layers of black material interpreted as pressure-solution selvage (Fig. 5c, d). Fagereng *et al.* (2010) interpreted these planes as ‘micro-transforms’, which accommodated localized slip on planes connecting dilational sites in which the slickenfibre veins precipitated. The ‘micro-transforms’ are inclined at an oblique angle, commonly less than 15°, to the fibre-coated shear surface (Fig. 5c, d).

Extension veins are typically subvertical and their average pole lies within the range of slickenfibre trends (Fig. 4). The subvertical extension veins intersect the subhorizontal slickenfibre shear veins at a high angle of  $80^\circ \pm 5^\circ$  (Figs 4 & 5b). In contrast to the shear veins, a dissolution selvage is rarely observed in extension vein wall rock. Extension fractures have mostly developed within more competent layers, while shear veins usually occur within the mudstone matrix or along phacoid boundaries. In particular, extension veins are commonly concentrated in dilational stepovers, where they link adjacent shear veins (Fig. 5b). Shear and extension veins are here mutually cross-cutting, and are interpreted to have formed concurrently in the same stress field (Fagereng *et al.* 2010). Extension fractures have also formed at boudin necks, where boudins were not completely separated in the ductile phase and layer-parallel extension continued in a brittle failure mode (Fig. 6a, b). Dense networks of closely spaced extension veins with relatively regular orientations have formed preferentially within some competent sandstone layers (Fig. 5e), commonly in the immediate hanging wall of slickenfibre shear veins. The observations of the fault-fracture mesh are summarized in Figure 5f.

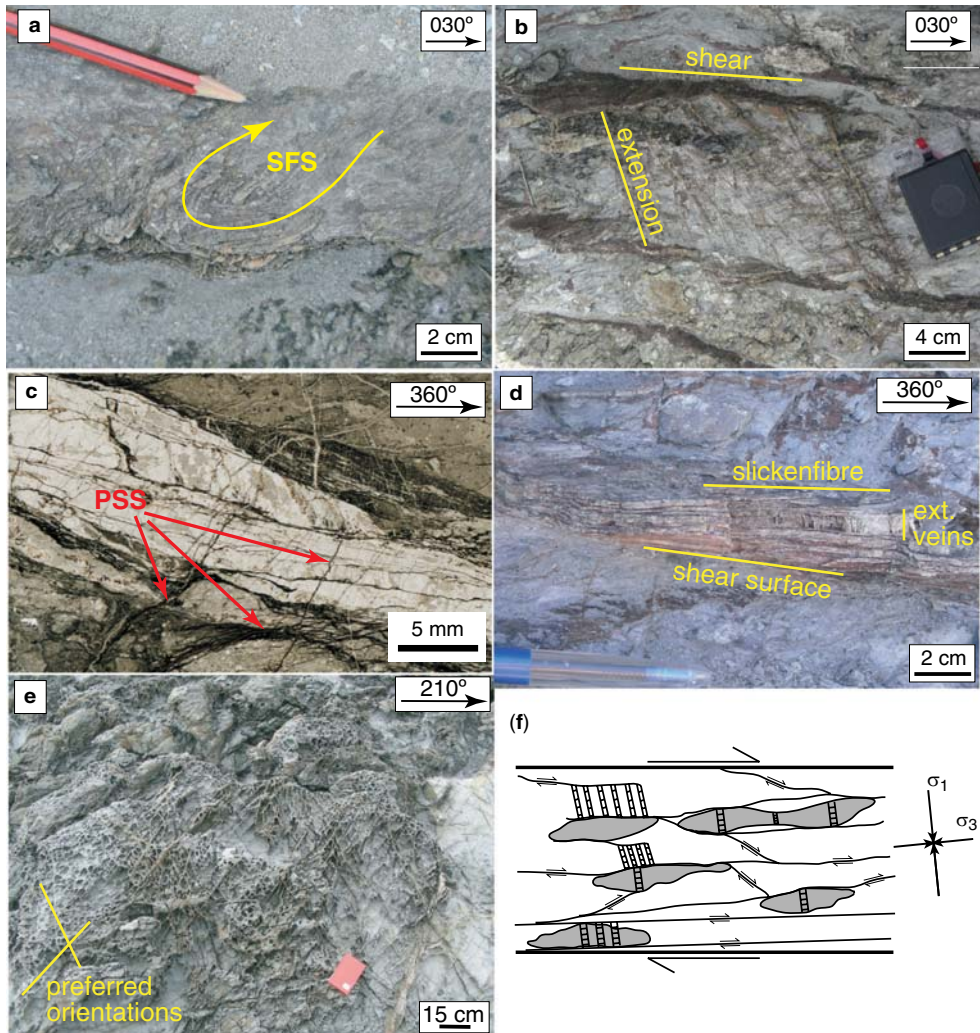


**Fig. 5.** Illustrations of the fault-fracture mesh developed in the Chrystalls Beach Complex. (a) Slickenfibre shear surface (SFS) with a fibre turning  $180^\circ$  indicating rotation of the hanging wall-block during fibre growth. (b) Dilational stepover comprising shear veins connected by extension veins. Note the high-angle intersection between shear and extension veins. (c) Scanned thin section cut parallel to slickenfibres and perpendicular to shear vein. Note the abundant pressure-solution seams (PSS). (d) Macroscopic appearance of a slickenfibre shear vein in a vertical section parallel to fibres and perpendicular to the vein. (e) Dense network of extension veins, taken looking vertically down on the fractures. (f) Cartoon showing the general appearance of the fault-fracture mesh. Lines are shear surfaces linked by hatched extension veins in a mudstone matrix (white) containing relatively competent phacoids (grey). These mesh structures are observed at length-scales from centimetres to tens of metres, and are ubiquitous throughout the coastal exposures of the complex. The stress field is inferred based on extension veins forming perpendicular to  $\sigma_3$  and shear veins developing in the same stress field (after Fagereng *et al.* 2010).

## Deformation mechanisms in the Chrystalls Beach Complex

### Deformation sequence

Figure 6c–e shows an outcrop where asymmetric phacoids, slickenfibres, dilational stepovers and

a thrust duplex within a chert layer all indicate top-to-the-north movement.  $S_{0+1}$  and slickenfibre-coated shear veins are subparallel and subhorizontal. Subvertical extension veins strike approximately  $080^\circ$  and the poles to these veins are subparallel to slickenfibres.

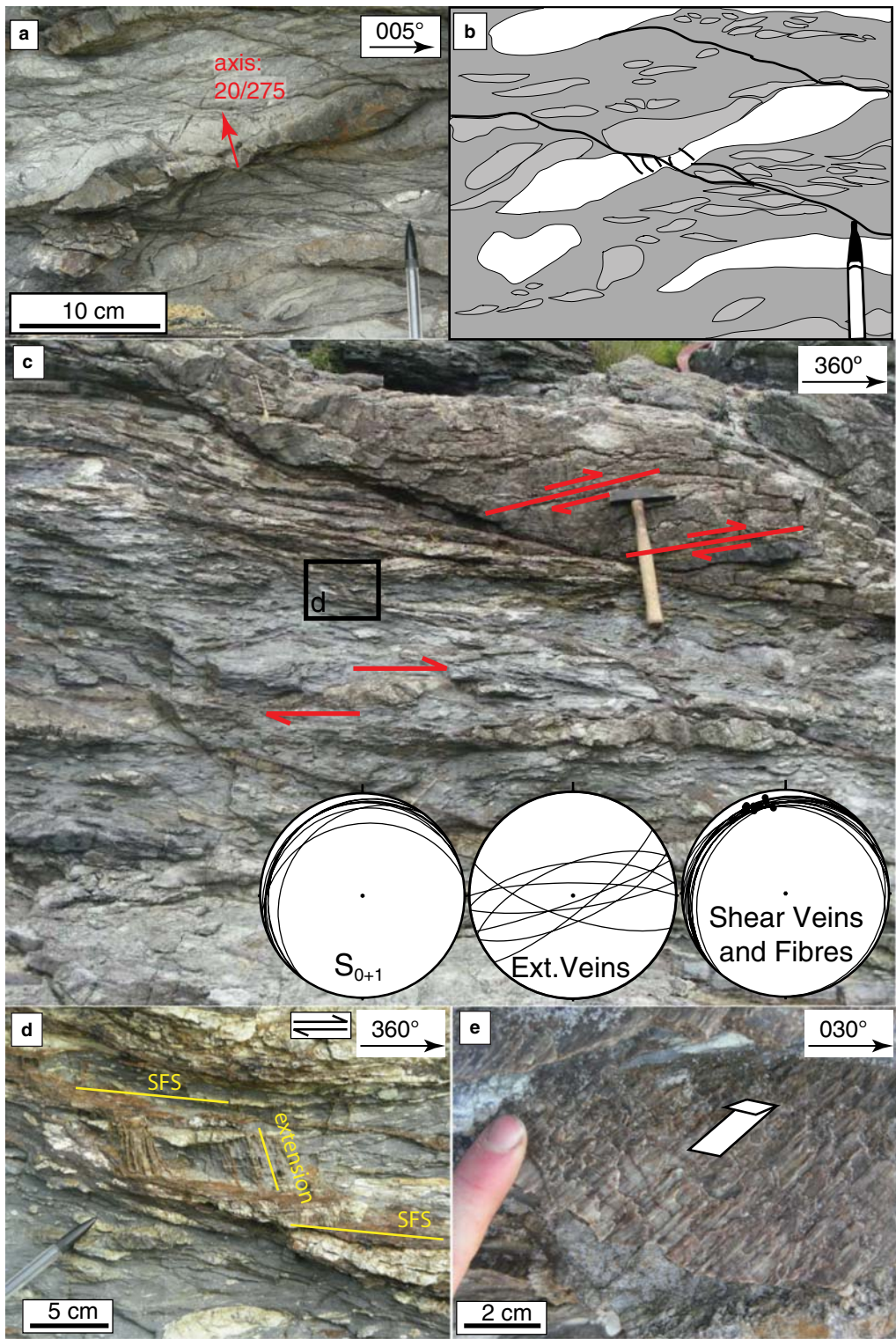


Fig. 6.

Axes of subhorizontal pinch-and-swell structures and boudin necks generally trend east–west, indicating north–south extension (Fig. 6a, b). Where extension veins have formed in boudin necks, or cut through extended phacoids, the opening directions of these fractures are subparallel to the extension direction indicated by the ductile fabric. It therefore appears that extension of competent, dismembered beds began by pinch-and-swell and boudinage in the ductile regime, and continued by brittle extension fracture concentrated at boudin necks (Fig. 6a, b). A similar sequence has been reported from the Shimanto Belt, where Hashimoto *et al.* (2006) interpreted the rocks as having deformed in a sequence of cataclasis, dissolution–precipitation creep and brittle extension fracture, coupled to decreasing porosity. Note that this represents a progressive transition from shallow ductile deformation to deeper brittle failure governed by increasing cementation and compaction.

Shear sense remained approximately constant, top-to-the-north, for the duration of the deformation sequence (Fig. 6a–e). Similarity in shear direction between early continuous structures and later discontinuous deformation has previously been attributed to a change in mélange physical properties, inferred to be related to the aseismic–seismic transition at the shallow seismic front (Shibata & Hashimoto 2005). The polyphase deformation within the complex is treated as a progressive evolution from initially shallow ductile, to deeper brittle behaviour as the rocks lithified (as also suggested by Nelson 1982). This differs from the traditional view of multiple separate deformation phases. The inferred, progressive deformation sequence is summarized as follows (Fig. 7).

- (1) *Pre-lithification:* The assemblage deformed by distributed soft sediment particulate flow. Initial layering was flattened and pulled apart as shearing accompanied volume loss.
- (2) *Syn-lithification:* Dismembered sand and chert beds lithified before the surrounding mudstone, and acted as competent lenses in a relatively incompetent matrix. The matrix deformed ductilely by dissolution–precipitation creep, while competent lenses ‘floated’ in the matrix as rigid particles in a viscous

flow. In this regime, brittle inclusions deformed by extension fracture governed by imposed fibre stresses (Cox 1952; Ji & Zhao 1993).

- (3) *Post-lithification:* The dominant deformation mechanism in the mélange depended on the distribution of sandstone and mudstone. Where both phases coexisted, the main mode of deformation was shear failure – accompanied by slickenfibre growth – at the contact between competent lenses and surrounding matrix, caused by the localization of strain-rate discontinuities at these boundaries (Goodwin & Tikoff 2002; Fagereng & Sibson 2010). Changes in stress distribution occurred following shear failure, and induced extension fracture at rupture tips and in dilatational stepovers. Within the matrix, small grain size and low tensile strength promoted deformation by dissolution–precipitation creep, while in competent lenses higher tensile strength and larger grain size favoured brittle failure.
- (4) *Exhumation:* Open, upright, long-wavelength folds and minor faulting have affected parts of the mélange, cross-cutting other fabrics (Fig. 2) (Fagereng 2010). Static metamorphic recrystallization overprints primary quartz microstructure in many veins, and is inferred to represent static recrystallization during a thermal relaxation phase post-dating deepest burial (Fagereng & Cooper 2010a).

Because lithologies evolve differently in the proposed time-progression of the shear zone, various parts of the mélange were deforming by different mechanisms at similar stages of mélange development (Fig. 8) (Fagereng & Sibson 2010). If deformation occurs by ductile matrix flow, geometrically approximating simple shear, then the strain rate depends on the thickness of the ductile shear zone, that is the volume of flowing matrix material (Ramsay 1980b; White 2004; Fagereng & Sibson 2010). Thus, if the matrix volume fraction is high, strain is distributed and strain rate is low; at low matrix volume fractions strain is likely to be localized and strain rate is high (Fig. 8) (White 2004; Fagereng & Sibson 2010). It is therefore likely that, above some critical mudstone volume

**Fig. 6.** Structural fabrics from which shear sense and deformation sequence may be deduced. Photograph (a) and interpretative sketch (b) of an asymmetric boudinaged sandstone phacoid that has been extended by east–west-striking extension fractures in the boudin neck, indicating a deformation sequence begun by north–south ductile extension and top-to-the-north shear, and continued by brittle extension fracture. (c) Photograph of an outcrop where top-to-the-north shear is reflected by duplex faulting, asymmetric phacoids, dilatational stepovers involving slickenfibre surfaces (SFS) connected by extension veins (d), and the slip vector recorded by slickenfibres (e). In (e), the white arrow shows the hanging wall displacement direction. Outcrop features (not all on the photograph) are illustrated in lower-hemisphere, equal-area stereoplots.

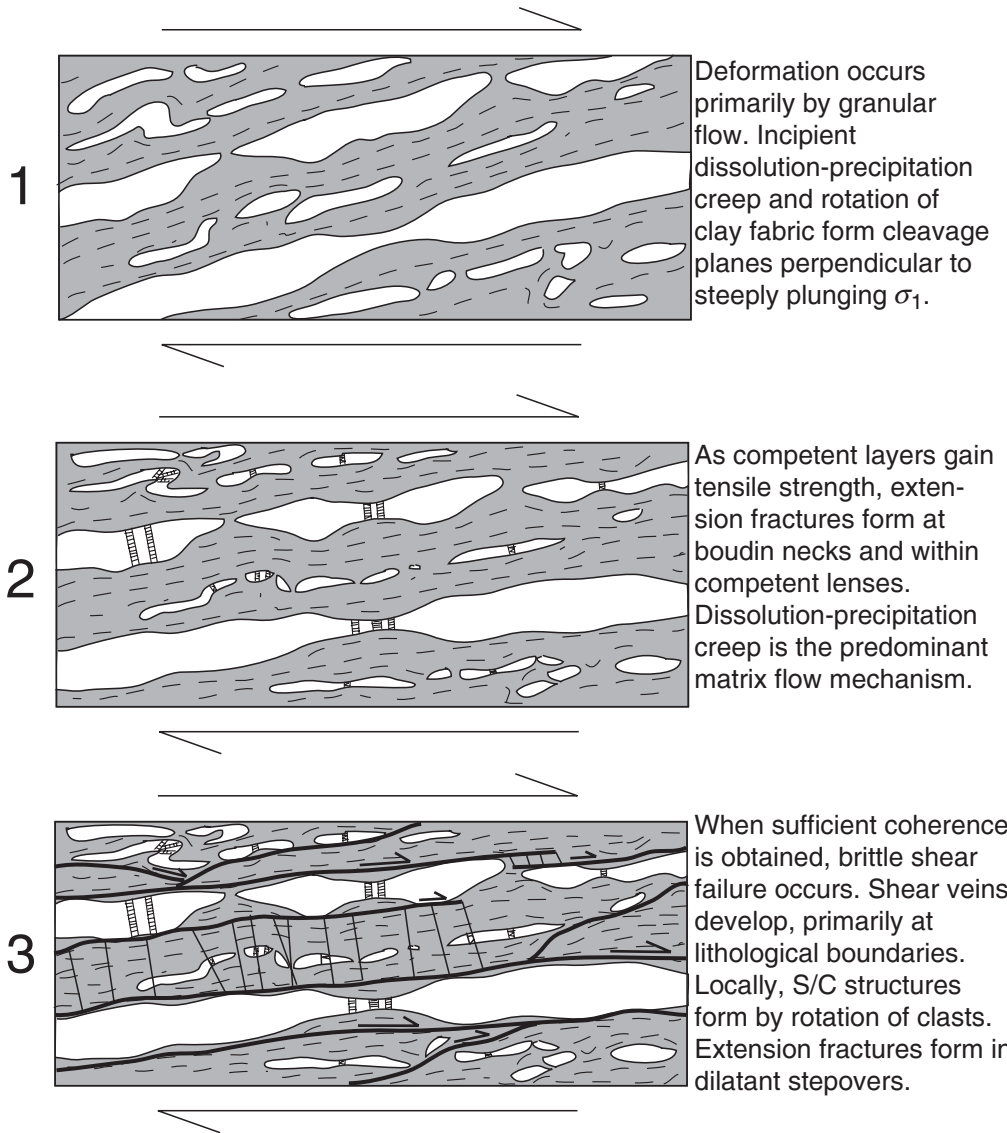


**Fig. 7.** Inferred deformation sequence forming the macroscopic mélange fabric components observed in the Chrystalls Beach Complex.

fraction, the macroscopic deformation of the mélange was dominated by matrix flow. At mudstone volume fractions below this value, the macroscopic failure mode was dominated by deformation of competent rock (Fagereng & Sibson 2010). The critical proportion of incompetent material may depend on the magnitude of competency contrast, tensile strength and the geometry of the mélange, in particular whether the competent material forms a connected framework supporting the complex as a whole (Handy 1990; Goodwin &

Tikoff 2002). Variations in frictional properties, with velocity-strengthening behaviour in matrix minerals and velocity-weakening behaviour of quartz-dominated, competent lenses and slicken-fibre-coated shear surfaces, may also have had an effect on the dominant seismic style (Marone 1998 and references therein). Differences in permeability and initial volatile content between different lithological phases provide additional rheological heterogeneity by imposing a heterogeneous fluid-pressure distribution.

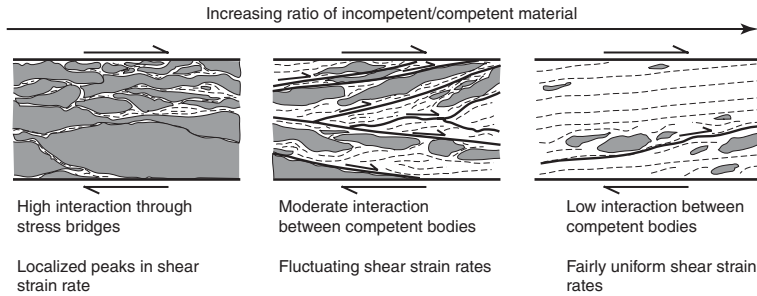


**Fig. 8.** Cartoons illustrating end-member bulk mechanical behaviours of a mélange shear zone as a function of the volume ratio of incompetent (white) to competent (grey) material (after Fagereng & Sibson 2010).

### Flow mechanisms of continuous deformation

Early continuous structures, such as folds cut by later brittle fractures, show evidence of mobile, poorly lithified mudstone flowing into space created by deformation of more competent layers, and mixing of different mudstone layers. At least some of this early flow occurred without the breaking of grains. Similarly, early boudinage and pinch-and-swell structures are inferred to have formed by distributed cataclastic flow of sandy layers before increased cohesion allowed further extension to take place by extension fracturing.

Anastomosing seams of fine-grained dark material cut through the assemblage, and are particularly concentrated within the fine-grained matrix material. Electron probe micro-analyser results have shown that these seams are greatly depleted in silica compared with the surrounding rock (Fagereng 2010). Material has been dissolved at grain boundaries in contact with these seams, and they may therefore be interpreted as dissolution selvages from a process of dissolution–precipitation creep.  $S_1$  in general therefore represents a pressure-solution cleavage.

Although independent particulate flow within soft sediments occurred in the early stages of mélange formation, leading to mixing of mobile lithologies and flow of mobile mudstone into cracks, dissolution–precipitation creep is inferred to have been the predominant ductile deformation mechanism throughout the lifetime of the shear zone. The case for dissolution–precipitation creep in the mélange is based on: (1) the presence of ubiquitous stylolites; (2) dissolved grain boundaries; (3) mutually cross-cutting stylolites (depleted in silica) and quartz veins that indicate dissolution of wall rock and precipitation in veins; and (4) the low-grade metamorphic environment and exceedingly fine-grained ( $<5\text{ }\mu\text{m}$ ) mudstone, which provide conditions for very efficient dissolution–precipitation creep (e.g. McClay 1977). This flow mechanism also contributes to porosity loss by

precipitation in low-stress pore spaces, enhancing cementation and eventually promoting brittle failure in high-tensile strength, velocity-weakening (Blanpied *et al.* 1995) quartz cement. This is probably a spatial and temporal control on the initial onset of brittle failure, and therefore a possible factor determining the depth to the shallow ductile–brittle transition in active fault zones (e.g. Moore *et al.* 2007).

### Conditions for discontinuous deformation

In a fluid-saturated rock assemblage, normal stresses are reduced by a fluid pressure,  $P_f$ , to effective stresses:  $\sigma'_n = \sigma_n - P_f$  (Hubbert & Rubey 1959). The principal effective compressive stresses are then defined as:

$$\begin{aligned}\sigma'_1 &= (\sigma_1 - P_f) > \sigma'_2 = (\sigma_2 - P_f) > \sigma'_3 \\ &= (\sigma_3 - P_f).\end{aligned}$$

Failure conditions, and the orientations of fractures formed in homogeneous, isotropic intact rock, can be described by classical, macroscopic failure theory involving an empirical composite Griffith–Coulomb failure envelope in a Mohr diagram of shear stress ( $\tau$ ) v.  $\sigma'_n$  (Fig. 9). A prediction of this theory is that fractures form containing  $\sigma_2$ , and at an angle  $\theta_i$  to  $\sigma_1$  (Fig. 9).

Three styles of macroscopic brittle failure occur in intact rock: (1) extension fractures; (2) shear fractures or faults; and (3) hybrid extensional-shear fractures (Fig. 9) (Ramsay & Chester 2004). Extension fractures occur on planes perpendicular to  $\sigma_3$ , when  $\sigma'_3 = -T_0$ , where  $T_0$  is the tensile strength of intact rock (Hubbert & Willis 1957). To reduce  $\sigma'_3$  sufficiently for extension fracturing to occur, differential stress must be low:  $(\sigma_1 - \sigma_3) < 4T_0$  (e.g. Secor 1965).

In the Chrystalls Beach Complex, the presence of hydraulic extension fractures within competent lenses and in boudin necks therefore indicate that the hydrofracture condition,  $P_f > \sigma_3$ , was locally

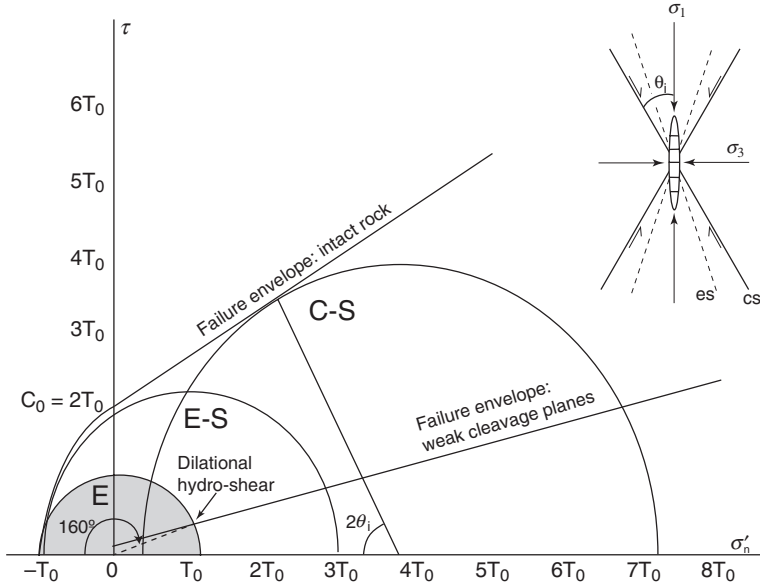


**Fig. 9.** Mohr diagram of shear stress,  $\tau$ , against effective normal stress,  $\sigma'_n$ , showing the Griffith–Coulomb failure envelopes for intact rock and a pre-existing weak cleavage plane with low intrinsic cohesion, normalized to tensile strength,  $T_0$ . Only the top half ( $\tau > 0$ ) of the diagram is shown. Circle E-S (white) represents a stress state where extensional shears (E-S) initiate, whereas Mohr circle C-S illustrates the stress field necessary for shear failure of intact rock, where new faults form at angle  $\theta_i$  to  $\sigma_1$ . Mohr circle E (shaded) represents the condition where dilatational hydro-shear occurs by simultaneous extension fracture of intact rock, and reshear of a cleavage plane oriented at  $80^\circ$  to  $\sigma_1$  (the dashed line represents the radius of this Mohr circle). Insert shows orientations of newly formed fractures relative to the principal stresses, assuming  $\sigma_2$  going into the page. Adapted from Sibson (1998).

attained (Secor 1965). Tensile fracturing also puts an upper bound on differential stress (Etheridge 1983), and with a typical  $T_0 = 10$  MPa in intact sandstone (Lockner 1995),  $(\sigma_1 - \sigma_3)$  was no greater than 40 MPa during formation of the extension fractures in the mélange. This is a high estimate for maximum differential stress given the likelihood of pre-existing microfractures in this assemblage.

If faults form according to the empirical Coulomb criterion, they initiate as planes containing  $\sigma_2$  and at an angle  $\theta_i = 45^\circ - \varphi_i$  to  $\sigma_1$  (Fig. 9), where  $\varphi_i$  is the angle of internal friction (the slope of the Coulomb failure envelope, typically  $25^\circ$ – $45^\circ$ ) (Jaeger *et al.* 2007). If differential stress is too large for extension fractures to form, but small enough for  $\sigma'_3$  to enter the tensional field without initiation of shear fractures, hybrid extensional-shear fractures are expected to occur. Because of the curvature of the composite failure envelope in the tensile field, extensional-shear fractures are expected to form in an orientation bisecting extension and shear fractures at an acute angle (Fig. 9). Thus, no shear fractures should initiate at an angle  $\theta_i > 45^\circ$  to  $\sigma_1$  (Ramsay & Chester 2004).

In the Chrystalls Beach Complex, however, mutually cross-cutting shear veins and extension

veins intersect at an angle of  $80^\circ \pm 5^\circ$ . As extension veins form perpendicular to  $\sigma_3$ , and both shear and extension veins contain  $\sigma_2$ , this suggests that the shear veins were active at an angle  $80^\circ \pm 5^\circ$  to  $\sigma_1$ . These veins were termed ‘dilatational hydro-shears’ by Fagereng *et al.* (2010), and interpreted to require the extensional hydrofracture condition to be locally attained along frictionally weak planes. The necessary frictionally weak planes were provided by the cleavage ( $S_1$ ) formed during early ductile flow. Thus, shear failure along pre-existing weak cleavage planes accommodated slip at high angles to  $\sigma_1$ , coincident with extensional shear failure in competent units and dilatational stepovers, in this anisotropic fluid-overpressured assemblage. Shear may have occurred by frictional failure on weak cleavage planes (Fig. 9), or by a non-frictional process, such as dissolution–precipitation creep of surrounding and intervening material (as described by Bos & Spiers 2001; Niemeijer & Spiers 2006). Over time, this development of subhorizontal shear surfaces linked by subvertical extension fractures, in a deformation regime approximating bulk simple shear accommodated by mixed continuous–discontinuous deformation, led to the formation of a vein-filled fault-fracture mesh

(Sibson 1996). In this mesh structure, creation of structural permeability by fracturing competes with permeability destruction by fracture sealing by hydrothermal precipitation, thus causing time-dependent, heterogeneous distribution of fluid overpressure (Sibson 1996; Fagereng *et al.* 2010). A similar combination of high fluid pressures and the presence of low-frictional strength surfaces has been proposed to account for ‘weak’ faulting, slip at high angles to  $\sigma_1$ , on the San Andreas Fault (Zoback *et al.* 1987).

### **Is the Chrystalls Beach Complex analogous to actively deforming underthrust sediments?**

The systematic structures and consistent foliation and displacement direction in the Chrystalls Beach Complex suggest that it is not a diapiric mélange, but formed by tectonic or gravitational shear (e.g. Cowan 1985; Orange 1990). Gravitational flow predominantly occurs by particulate flow, with minor breaking of grains. Such deformation is present locally in the Chrystalls Beach Complex, but dissolution–precipitation creep is proposed as the predominant ductile deformation mechanism. An inferred progressive deformation sequence from ductile to brittle, with consistent shear direction (Fig. 6c), also indicates that a tectonic origin is more likely for the Chrystalls Beach mélange. The mélange fabric has a consistent asymmetry comprising  $S-C$  foliations resembling those described in some mylonites (Berthé *et al.* 1979; Lister & Snoke 1984), and shear vein arrays as commonly developed in tectonic mélanges (e.g. Hashimoto & Kimura 1999; Kusky & Bradley 1999; Meneghini & Moore 2007). In previous studies it has been inferred that such systematic asymmetric fabrics are indicative of mélange formation by tectonic shear (e.g. Cowan 1985; Hashimoto & Kimura 1999; Kusky & Bradley 1999). By comparison with other continuous–discontinuous tectonic shear zones in a variety of settings, it is therefore concluded that mélange formation in the Chrystalls Beach Complex occurred by mixed continuous–discontinuous tectonic shear, where the mineral deformation mechanisms accommodating ductile flow (dissolution–precipitation creep and distributed cataclasis) differ from those experienced by most mylonites (dislocation creep). Mélange shear-zone deformation is therefore a style of continuous–discontinuous shearing at seismogenic depths, shallower than the commonly considered brittle–viscous transition from pressure-dependent frictional sliding to temperature-dependent dislocation creep (<300–400 °C: Sibson 1984).

The inferred deformation sequence suggests that the structural elements in the Chrystalls Beach mélange formed in a time-progressive sequence of increasing cohesive strength (Fig. 7). This is typical of deformation within a thickening accretionary prism or of underthrust sediments below the décollement, where tectonic shear is accompanied by progressive consolidation by porosity reduction and cementation (Moore & Byrne 1987; Hashimoto *et al.* 2006; Morgan *et al.* 2007), and clay mineral transformation (Vrolijk 1990). The subduction interface décollement zone separates two distinct structural regimes (Byrne & Fisher 1990; Housen *et al.* 1996). Deformation within the accretionary prism (Fig. 10) is commonly inferred to occur with a subhorizontal to gently plunging  $\sigma_1$  (Davis *et al.* 1983; Byrne & Fisher 1990) while, below the décollement, shearing is accompanied by layer-parallel extension, and  $\sigma_1$  is inferred to be subvertical (e.g. Byrne & Fisher 1990; Magee & Zoback 1993).

The vertical extension veins common in the Chrystalls Beach Complex indicate a locally subhorizontal  $\sigma_3$  at the time of fracturing. Local subhorizontal extension within subducting sediments has been suggested in a number of previous studies (e.g. Moore & Byrne 1987; Byrne & Fisher 1990; Hashimoto & Kimura 1999). Similar features could also occur in normal or reverse faults within the accretionary prism, but these faults are generally out-of-sequence and neither subhorizontal nor subparallel to cleavage. The Chrystalls Beach Complex is thus inferred to have formed by subduction of sediments beneath a décollement, where  $\sigma_1$  was subvertical. Petrological studies indicate that the mélange is composed of a mixture of ocean floor and arc-derived materials, with ocean-floor rocks predominant at deeper structural levels (Coombs *et al.* 2000; Fagereng & Cooper 2010b). It therefore seems likely that the formation process involved subduction of oceanic crust underneath an arc terrane, in line with previous suggestions by Hada *et al.* (2001) that the complex formed during subduction of oceanic crust underneath the Gondwana margin.

Considering that accretionary prisms are generally thought to grow by underplating (e.g. Cloos & Shreve 1996), the deformation history of the Chrystalls Beach Complex may not be unusual within the Otago Schist. On the contrary, large parts of the schist are likely to have formed by a process involving the mixing of materials in a trench setting, followed by underthrusting to some depth and, finally, incorporation into the accretionary prism by underplating. Previous treatment of the Chrystalls Beach Complex as an anomalous assemblage may therefore need reconsideration, and the question can be asked whether most (or all?) of the Otago Schist

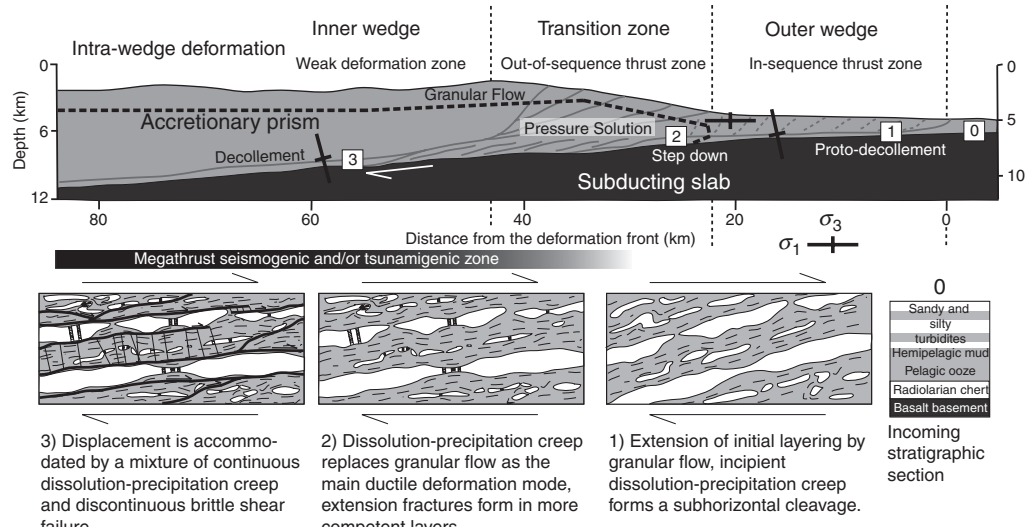


**Fig. 10.** Figure showing accretionary prism geometry and deformation modes (after Moore & Byrne 1987; Byrne & Fisher 1990; Kimura *et al.* 2007). Numbers refer to the inferred location of each phase in the progressive deformation sequence in the Chrystals Beach Complex. Stratigraphy of the incoming plate after Underwood (2007).

once resembled the current exposures of the Chrystals Beach Complex.

If the Chrystals Beach Complex formed by sediment subduction and underplating, then similar rock assemblages should be actively deforming in currently active subduction margins. We next consider active deformation along the Hikurangi subduction margin, before concluding this chapter with a comparison of active and ancient subduction-related deformation.

## Active deformation along the Hikurangi margin

### Geophysical observations

Along the east coast of the North Island of New Zealand, the oceanic Pacific plate is subducted obliquely westwards beneath continental lithosphere of the Australian plate at a rate of around 40 mm year<sup>-1</sup> in the southern North Island, increasing to about 50 mm year<sup>-1</sup> on the northern east coast North Island (Fig. 11) (Anderson & Webb 1994; Wallace *et al.* 2004). The subduction thrust interface exhibits a mixture of interseismically locked and weakly coupled behaviour (Reyners 1998; Wallace *et al.* 2004). At depths of 20–30 km, usually expected to lie within the seismogenic zone of subduction megathrusts (e.g. Hyndman *et al.* 1997), interseismic behaviour varies from fully creeping (north) to fully locked

(south) along strike (Fig. 11) (Wallace *et al.* 2004). Along-strike variations in various physical properties were reviewed by Wallace *et al.* (2009) and are summarized in Figure 11.

In the north, there is significant topography on the downgoing slab, while the interface appears relatively smooth in the south (Davy *et al.* 2008; Barnes *et al.* 2010). From along-strike variations in the plate-boundary interface  $V_P/V_S$  and  $Q_P$  (where  $V_P$  and  $V_S$  and P and S wave velocities, respectively,  $Q_P$  is the inverse of P-wave attenuation) (Eberhart-Phillips *et al.* 2005, 2008), and offshore seismic reflection studies (Barker *et al.* 2009; Barnes *et al.* 2010), it has been inferred that the margin changes character from significant subduction and/or underplating of sediments in the central and northern margin, to accretion and little sediment subduction in the south. The northern margin therefore has a sediment layer of varying thickness along the subduction thrust interface. From anomalously high  $V_P/V_S$  ratios, Eberhart-Phillips & Reyners (1999) inferred the presence of an, on average,  $\leq 2$  km-thick layer of underthrust sediments below Raukumara Peninsula. Locally, because of changes in slab topography, this layer reaches a thickness in excess of 5 km (Eberhart-Phillips & Reyners 1999). Recent seismic reflection studies also indicate a  $\geq 1$  km-thick layer of sediments along the interface offshore from Gisborne, in an area of repeating slow slip events (Bell *et al.* 2010). Although several factors are likely to affect along-strike variations in

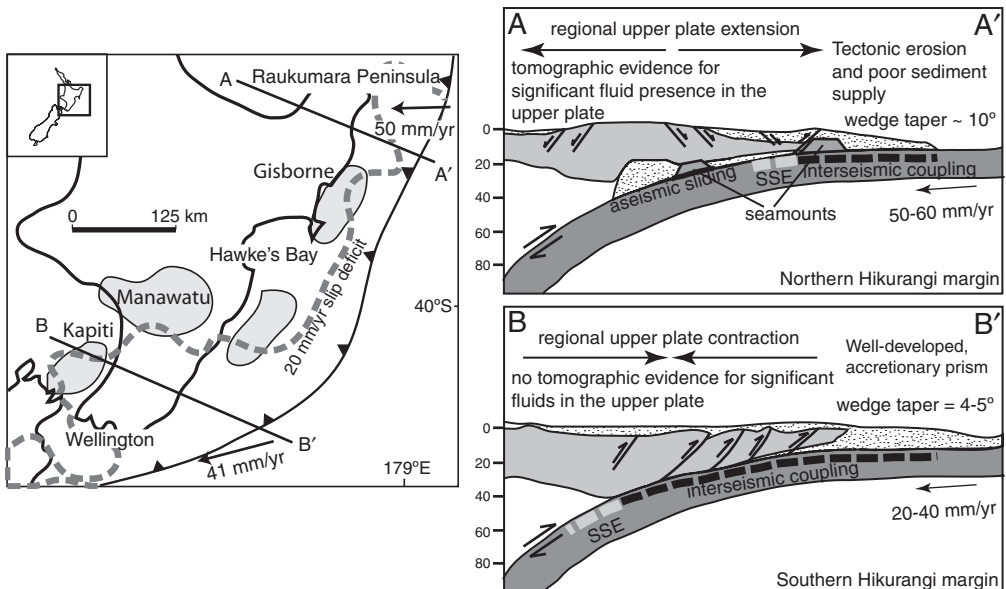


**Fig. 11.** Map of the North Island of New Zealand with tectonic and seismic features. Cartoon cross-sections of the southern and northern parts of the margin after Wallace *et al.* (2009). Arrows represent plate convergence vectors and convergence velocities from Anderson & Webb (1994). The dashed contour of  $20 \text{ mm year}^{-1}$  slip deficit is taken from Wallace *et al.* (2004), and the area of strong interseismic coupling is between this contour and the deformation front. Shaded areas represent areas of slip in slow slip events (SSE), after McCaffrey *et al.* (2008).

seismic style along the Hikurangi margin (Wallace *et al.* 2009), the variations in thickness of under-thrust sediment probably leads to local variations in the interface geology, which – as in the Chryssalls Beach Complex – may affect the dominant deformation style.

In addition to microseismicity, episodic slow slip events (SSEs) – as recognized in well-studied subduction zones worldwide (e.g. Hirose *et al.* 1999; Dragert *et al.* 2001) – have been recorded in four locations near the base of the interseismically locked zone along the Hikurangi margin (Fig. 11) (Douglas *et al.* 2005; Wallace & Beavan 2006, 2010). In other locations – for example, Japan and North America – SSEs are commonly associated, spatially and temporally, with non-volcanic tremor (e.g. Obara 2002; Rogers & Dragert 2003; Peterson & Christensen 2009). Delahaye *et al.* (2009) examined seismic records from the duration of two slow slip events in the northern, creeping, fault segment, and found no tremor signals. However, Delahaye *et al.* (2009) discovered an increase in microseismic activity during the slow slip events. Reyners & Bannister (2007) suggested that the 2003–2004 Kapiti slow slip event triggered an earthquake swarm in the subducting plate, and a slow slip event offshore of Gisborne initiated immediately (within a day) after a  $M_w$  6.6 earthquake in December 2007 (Francois-Holden *et al.* 2008). Stress changes

from slow slip events on the Hikurangi megathrust may therefore cause increased earthquake activity rather than non-volcanic tremor (Delahaye *et al.* 2009), and seismic stress change also appears able to initiate slow slip events.

#### Factors determining seismic style along the Hikurangi margin

If interseismic coupling depth reflects the extent of the seismogenic zone, and slow slip events occur near the transition from unstable to stable frictional sliding at the base of the seismogenic interface, the southern Hikurangi margin is capable of generating large earthquakes, while in the central and northern margin displacement may primarily be accommodated by aseismic creep (Fig. 11). It is commonly inferred that the down-dip limit of the seismogenic subduction thrust interface occurs where it intersects the  $350^\circ\text{C}$  isotherm or the hanging wall Moho, whichever is shallower (e.g. Hyndman *et al.* 1997). However, thermal models (McCaffrey *et al.* 2008; Fagereng & Ellis 2009) suggest that slow slip events and the down-dip limit of the interseismically locked zone in the Hawke's Bay region occur at significantly colder temperatures of  $100$ – $200^\circ\text{C}$ . Crustal strength curves constructed by Fagereng & Ellis (2009) indicate that localized

frictional sliding may be inhibited by high effective stress in segments where the interseismic coupling depth is shallow, as a result of high hanging-wall permeability (Eberhart-Phillips *et al.* 2008; Reyners & Eberhart-Phillips 2009). In the locked segment, hanging wall permeability appears lower, causing higher fluid pressure and lower inferred effective normal stress on the interface (Reyners & Eberhart-Phillips 2009). Fluid-pressure distribution may therefore be a significant control on interseismic coupling, but as many physical parameters vary along strike in the Hikurangi margin, several factors are likely to influence seismic style (Wallace *et al.* 2009). For example, the smoother interface in the south may allow for larger potential rupture size (Ruff 1989). To assess the likely geological factors affecting deformation along the Hikurangi megathrust and other modern analogues, observations in the Chrystalls Beach Complex are compared with parameters inferred from geophysical observations.

### Comparison of the Chrystalls Beach Complex to modern analogues

Whether or not the Chrystalls Beach mélange represents underthrust sediments along a fossil subduction thrust interface, it is interpreted as an approximately 4 km-thick mixed continuous-discontinuous shear zone comprising highly sheared, fluid-saturated, trench-fill sediments and minor pillow basalts. It is analogous in composition and deformation history to a tabular, heterogeneous, shear zone inferred present in underthrust sediments of variable thickness along the Hikurangi margin and other active subduction megathrusts. The mélange may, however, have developed by progressive underplating and therefore not be representative of the thickness of the active zone of deformation at any one time. The observations made in the Chrystalls Beach Complex and presented here are not unusual. Similar structural features have been observed in numerous exhumed subduction-related mélanges (e.g. Moore & Wheeler 1978; Ujiiie 2002; Fukui & Kano 2007; Meneghini & Moore 2007; Vannucchi *et al.* 2008; Bachmann *et al.* 2009), indicating that continuous-discontinuous deformation of a tabular zone of trench-fill sediments is common along subduction margins. The thickness of this deforming zone at any one time has, however, still not been determined.

#### Aseismic deformation

In a mixed continuous-discontinuous shear zone, displacement is accommodated by matrix flow, hydrofracture within rigid lenses and shear failure

concentrated at shear-strain rate gradients at the edge of rigid blocks and along pre-existing weak cleavage planes (Goodwin & Tikoff 2002; Fagereng & Sibson 2010). In the matrix, deformation is predominantly accommodated by dissolution–precipitation creep and/or particulate flow. Within actively deforming underthrust sediments, at similar pressure, temperature, fluid pressure and stress conditions as in the Chrystalls Beach Complex, this deformation mechanism is also likely to accommodate deformation at relatively low strain rates. In the weakly coupled northern Hikurangi margin there is a more than 1 km-thick subducting sediment layer along the megathrust interface (Fig. 11) (Reyners *et al.* 1999), and aseismic slip may therefore be accommodated by distributed, continuous deformation of the subducting sedimentary rock assemblage, analogous to matrix deformation in the Chrystalls Beach Complex. Microseismicity in this fault segment may then correspond to small-displacement slip on numerous shear discontinuities in a fault-fracture mesh, as developed in the Chrystalls Beach Complex.

#### Seismic style

In a mélange, length scales of discontinuous deformation are likely to be imposed by the volume fraction and distribution of competent lenses, mechanical layering and shear-zone thickness (Fagereng & Sibson 2010). The bulk rheology of a heterogeneous shear zone is critically dependent on the volume fraction of incompetent/competent material (Fig. 8). Analogous to bulk strength of a mineral aggregate (Handy 1990; Ji 2004), a small amount (perhaps  $\leq 20\%$ ) of matrix rock may be sufficient to lead to a weak bulk rheology, depending on the geometry of the shear zone (Fig. 8) (Fagereng & Sibson 2010). Thus, subduction megathrust earthquakes are inferred to nucleate in regions where the subduction thrust predominantly comprises interacting rigid blocks, moderate seismicity is likely to be observed where moderate interaction between phacoids occur, and aseismically creeping shear-zone segments may be characterized by a subduction interface fault zone dominated by a flowing matrix and little interaction between few rigid inclusions (Fagereng & Sibson 2010). Fluid-pressure conditions may, however, affect this hypothesis, as the existence of a frictionally weak, overpressured planar discontinuity may allow for a large rupture area. Ruff (1989) correlated large megathrust ruptures with fault segments characterized by a smooth sediment layer along the interface, also implying that a large fault plane of easy rupture propagation is required in addition to a nucleation site.

Frequency–magnitude relationships suggest that small earthquakes are very common in the mid- to upper-crust (e.g. Gutenberg & Richter 1944). Yet, pseudotachylite, the only unequivocal geological evidence for palaeoseismicity (Cowan 1999), is relatively rare in the rock record (Sibson & Toy 2007). The generation of friction melt, however, requires more heat than commonly released in small earthquakes ( $< M_w 3$ ; e.g. Sibson & Toy 2007). Hydraulic implosion breccia in dilational stepovers, showing signs of episodic hydrothermal mineralization, has previously been interpreted as a product of episodic seismic slip (Sibson 1986). Boullier & Robert (1992) explained an incrementally developed vein network in Val d'Or, Canada, as a record of Archean seismic activity involving fluid-pressure cycling. The vein-forming processes in the Chrystals Beach Complex involved episodic fracture, solution transfer and fluid-pressure cycling in a fault-fracture mesh (cf. Hill 1977; Sibson 1996). The development of 'dilational hydro-shears', near perpendicular to  $\sigma_1$ , within this fracture network is inferred to require strength anisotropy, low effective stress ( $P_f > \sigma_3$ ) and low differential stress (Fig. 9) (Fagereng *et al.* 2010). This discontinuous deformation may occur seismically, by incremental frictional failure on shear surfaces or by an aseismic process, such as sliding on weak planes assisted by dissolution–precipitation creep of intervening and surrounding phyllosilicates (Bos & Spiers 2001; Niemeijer & Spiers 2006). Here incremental slip by frictional sliding may be analogous to regular earthquakes (over a range of magnitudes), while incremental localized aseismic sliding may be analogous to slow slip events. As the quartz commonly coating the slickenfibre surfaces in the Chrystals Beach Complex is generally velocity weakening and prone to stick–slip behaviour (Blanpied *et al.* 1995), one could consider whether the 10–100  $\mu\text{m}$  displacement increments recorded by the slickenfibres represent very small episodic earthquakes, as recorded in the tremor source (e.g. Shelly *et al.* 2007).

Seismic tremor is commonly correlated with slow slip in hot hydrated subduction zones (Rogers & Dragert 2003; Obara *et al.* 2004). It has also been suggested that non-volcanic tremor is created by hydrofracturing and fluid movement through a rock mass (Katsumata & Kamaya 2003), as previously also suggested for volcanic tremor (Hill 1977). Extension veins in the Chrystals Beach Complex may have accommodated extension and fluid redistribution following displacement on slickenfibre shear surfaces. If these swarms of extension veins reflect fluid movement in a fault-fracture mesh, they may be analogous to tremor sequences associated with active megathrusts. The recent interpretation that slow slip, non-volcanic

tremor and very low-frequency earthquakes are different manifestations of the same process (Shelly *et al.* 2006, 2007) is compatible with shear-zone displacement occurring by different brittle failure modes within a fault-fracture mesh (Sibson 1996, 1998).

The critical trigger for slickenfibre growth and the creation of swarms of subvertical extension veins has been noted to be a combination of very low differential stress and high fluid pressure. Similarly, slow slip and tremor appear to occur in zones of very low effective stress (e.g. Ito & Obara 2006; Shelly *et al.* 2006; Schwartz & Rokosky 2007; Matsubara *et al.* 2009). The timing and position of such events is therefore critically dependent on when and where such stress conditions can be achieved. In the Chrystals Beach Complex, the spatial distribution of slickenfibres and extension veins depends on the distribution of lithological heterogeneities, allowing for containment of fluid overpressure between permeable and impermeable units, and the presence of weak, subhorizontal planes. The timing of failure in the mélange then depends on two main factors: (1) the kinetics of dehydration reactions providing the fluids and creating the near-lithostatic overpressure conditions; and (2) the kinetics of vein precipitation (destruction of structural permeability). These same factors may also provide the spatial and temporal controls on active slow slip and tremor. As long as heterogeneous subducting sediments are present along the plate-boundary interface, slow slip and tremor are therefore expected to occur where sufficient fluids have been produced and contained below the subduction thrust interface. This was also concluded by Peacock (2009) based on thermal structure and metamorphic petrology in a number of well-studied subduction margins. Slow slip and tremor have not been correlated with a particular metamorphic reaction, but appear to occur where fluids are released along the prograde  $P - T$  – time path, which varies between subduction zones of different thermal structure (Peacock 2009).

In the southern Hikurangi, the megathrust interface is inferred to be locked, impermeable and fluid overpressured. Slow slip events have occurred at the down-dip end of this megathrust segment (Wallace & Beavan 2010). No tremor has been observed in relation to slow slip in southern Hikurangi, but detailed seismic studies necessary for the detection of tremor signals have not been carried out in this region. The suggestion that the southern Hikurangi megathrust is overpressured, and that this fluid overpressure can lead to mesh-generation and tremor associated with slow slip, may therefore be tested by future seismic study revealing whether or not non-volcanic tremor occurs below the southern North Island.

No tremor has been observed during shallow slow slip events in the Hawke's Bay region, despite careful study of the seismic catalogue (Delahaye *et al.* 2009). This agrees with the inference that this megathrust segment is relatively permeable, and does not allow for sufficient fluid pressure to generate a fault-fracture mesh. Although future studies and improved detection capabilities may show tremor also in this region. Slow slip events may here be a result of localized slip on over-pressured planar surfaces or accelerated distributed shearing of the underthrust rock assemblage. Increased microseismic activity during slow slip events (Delahaye *et al.* 2009) may be a different manifestation of the stress and/or fluid-pressure redistribution inferred to cause non-volcanic tremor in a location where conditions are not favourable for mesh generation.

## Conclusions

The composition and geometry of the underthrust sediment layer may be of critical importance to the deformation style of a subduction thrust interface for two reasons. (1) The bulk rheology of the subduction thrust interface depends on the volume fraction and the distribution of competent/incompetent rock within the underthrust sediment layer along the megathrust. (2) The fluid content and permeability of different lithological units within the underthrust rock assemblage are likely to determine the distribution of interface fluid pressure. It should therefore be considered that the subduction thrust interface may be a tabular zone, within which geological variability could be correlated with geophysically observed variations in megathrust seismic style.

The importance of the containment of fluid overpressure along the megathrust impinges on several phenomena already described in this chapter. Along the Hikurangi margin, it is suggested that strong interseismic coupling occurs where fluid overpressure is contained to great depths, while aseismic creep predominates where fluids can escape to the hanging wall. In the mélange, shear discontinuities have formed along pre-existing weak planes of high fluid pressure, concentrated at material heterogeneities. Brittle failure has occurred in competent, fluid-overpressured phacoids, while incompetent matrix rock exhibits continuous fabrics. In both settings, frictional failure requires weak planes and fluid overpressure, while ductile behaviour occurs in response to high brittle shear strength or material properties where other deformation mechanisms are preferred, in particular dissolution–precipitation creep in fine-grained rock under subgreenschist conditions. It also seems that frictional sliding occurs preferentially in material with

velocity-weakening laboratory-derived frictional properties (e.g. quartz-coated shear surfaces and sandstone phacoids), and distributed shear occurs in velocity-strengthening, phyllosilicate-rich matrix. In both active and ancient subduction-related shear zones, the distribution and containment of fluid overpressure, and the ratio of competent to incompetent material, are critical factors determining deformation style, and this probably also applies to other faults that are tabular features at a range of levels in the crust.

Treating the Chrystals Beach mélange as analogous to an underthrust rock assemblage, geological observations demonstrate that deformation along a subduction thrust interface may be distributed over a wide tabular zone. Within this shear zone,  $\sigma_1$  trajectories appear to be subvertical and at a high angle to shear surfaces (Fig. 5f), analogous to inferred stress trajectories adjacent to the San Andreas Fault (Zoback *et al.* 1987). The shear-zone boundaries were not observed, however, and the bulk of the displacement may have been accommodated along a discrete plane, such as a décollement commonly inferred to be present at the top of the underthrust sediments. It is of critical importance to determine whether plate-boundary displacements, in subduction zones and otherwise, are accommodated on a single planar feature or – as suggested in this study – distributed within a continuous-discontinuous tabular shear zone. In the tabular shear-zone model, homogeneous ductile flow must be discriminated from slip on an unknown number of shear discontinuities.

This chapter arises from a PhD thesis supervised by R. Sibson, whose constructive criticism was invaluable for the study. Comments from S. Cox, D. Craw, S. Ellis, T. Little, R. Norris, and V. G. Toy on early versions are greatly appreciated, and reviews by J. C. Moore and an anonymous reviewer significantly improved the final manuscript. Funding was provided through a GNS Science Hazards Scholarship.

## References

- ABERS, G. A. 2005. Seismic low-velocity layer at the top of subducting slabs: observations, predictions, and systematics. *Physics of the Earth and Planetary Interiors*, **149**, 7–29.
- ADAMS, C. J., CAMPBELL, H. J. & GRIFFIN, W. L. 2007. Provenance comparisons of Permian to Jurassic tectonostratigraphic terranes in New Zealand: perspectives from detrital zircon age patterns. *Geological Magazine*, **144**, 701–729.
- AITA, Y. & BRAGIN, N. 1999. Non-Tethyan Triassic Radiolaria from New Zealand and northeastern Siberia. *Geodiversitas*, **21**, 503–526.
- ANDERSON, H. & WEBB, T. 1994. New Zealand seismicity: patterns revealed by the upgraded National Seismograph Network. *New Zealand Journal of Geology and Geophysics*, **24**, 477–493.

- BACHMANN, R., ONCKEN, O., GLODNY, J., SEIFERT, W., GEORGIEVA, V. & SUDO, M. 2009. Exposed plate interface in the European Alps reveals fabric styles and gradients related to an ancient seismogenic coupling zone. *Journal of Geophysical Research*, **114**, B05402, doi: 10.1029/2008JB005927.
- BARKER, D. H. N., SUTHERLAND, R., HENRYS, S. & BANNERISTER, S. 2009. Geometry of the Hikurangi subduction thrust and upper plate, North Island, New Zealand. *Geochemistry, Geophysics, Geosystems*, **10**, Q02007, doi: 10.1029/2008GC002153.
- BARNES, P. M., LAMARCHE, G. ET AL. 2010. Tectonic and geological framework for gas hydrates and cold seeps on the Hikurangi subduction margin, New Zealand. *Marine Geology*, **272**, 26–48, doi: 10.1016/j.margeo.2009.03.012.
- BELL, R., SUTHERLAND, R., BARKER, D. H. N., HENRYS, S., BANNERISTER, S., WALLACE, L. & BEAVAN, J. 2010. Seismic reflection character of the Hikurangi subduction interface, New Zealand, in the region of repeated Gisborne slow slip events. *Geophysical Journal International*, **180**, 34–48.
- BERTHÉ, D., CHOUKROUNE, P. & JEGOUZO, P. 1979. Orthogneiss, mylonite and non-coaxial deformation of granites: the example of the South Armorican shear zone. *Journal of Structural Geology*, **1**, 31–42.
- BISHOP, D. G. 1994. *Geology of the Milton Area. Scale 1:50 000*. Institute of Geological and Nuclear Sciences Geological Map. GNS Science, Lower Hutt, New Zealand.
- BLANPIED, M. L., LOCKNER, D. A. & BYERLEE, J. D. 1995. Frictional slip of granite at hydrothermal conditions. *Journal of Geophysical Research*, **100**, 13,045–13,064.
- BOS, B. & SPIERS, C. 2001. Experimental investigation into the microstructural and mechanical evolution of phyllosilicate-bearing fault rock under conditions favouring pressure solution. *Journal of Structural Geology*, **23**, 1187–1202.
- BOULLIER, A.-M. & ROBERT, F. 1992. Palaeoseismic events recorded in Archaean gold-quartz vein networks, Val d'Or, Abitibi, Quebec, Canada. *Journal of Structural Geology*, **14**, 161–179.
- BYRNE, T. & FISHER, D. 1990. Evidence for a weak and overpressured décollement beneath sediment-dominated accretionary prisms. *Journal of Geophysical Research*, **95**, 9081–9097.
- CAMPBELL, J. K. & CAMPBELL, J. D. 1970. Triassic tube fossils from Tuapeka rocks, Akatore, South Otago. *New Zealand Journal of Geology and Geophysics*, **13**, 392–399.
- CLOOS, M. & SHREVE, R. L. 1996. Shear-zone thickness and the seismicity of Chilean- and Marianas-type subduction zones. *Geology*, **24**, 107–110.
- COOMBS, D. S., LANDIS, C. A., HADA, S., ITO, M., ROSER, B. P., SUZUKI, T. & YOSHIKURA, S. 2000. Geochemistry and terrane correlation of the Chrystalls Beach-Brighton coastal block, southeast Otago, New Zealand. *New Zealand Journal of Geology and Geophysics*, **43**, 355–372.
- COWAN, D. S. 1985. Structural styles in Mesozoic and Cenozoic melanges in the western Cordillera of North America. *Geological Society of America Bulletin*, **96**, 451–462.
- COWAN, D. S. 1999. Do faults preserve a record of seismic slip? A field geologist's opinion. *Journal of Structural Geology*, **21**, 995–1001.
- COX, H. L. 1952. The elasticity and strength of paper and other fibrous materials. *British Journal of Applied Physics*, **3**, 72–79.
- DAVIS, D., SUPPE, J. & DAHLEN, F. A. 1983. Mechanics of fold-and-thrust belts and accretionary wedges. *Journal of Geophysical Research*, **88**, 1153–1172.
- DAVY, B., HOERNLE, K. & WERNER, R. 2008. Hikurangi Plateau: crustal structure, rifted formation, and Gondwana subduction history. *Geochemistry, Geophysics, Geosystems*, **9**, Q07004, doi: 10.1029/2007GC001855.
- DELAHAYE, E. J., TOWNSEND, J., REYNERS, M. & ROGERS, G. 2009. Microseismicity but no tremor accompanying slow slip in the Hikurangi subduction zone, New Zealand. *Earth and Planetary Science Letters*, **277**, 21–28.
- DOUGLAS, A., BEAVAN, J., WALLACE, L. & TOWNSEND, J. 2005. Slow slip on the northern Hikurangi subduction interface, New Zealand. *Geophysical Research Letters*, **32**, L16305, doi: 10.1029/2005GL023607.
- DRAGERT, H., WANG, K. & JAMES, T. S. 2001. A silent slip event on the deeper Cascadia subduction interface. *Science*, **292**, 1525–1528.
- EBERHART-PHILLIPS, D. & REYNERS, M. 1999. Plate interface properties in the northeast Hikurangi subduction zone, New Zealand, from converted seismic waves. *Geophysical Research Letters*, **26**, 2565–2568.
- EBERHART-PHILLIPS, D., REYNERS, M., CHADWICK, M. & CHIU, J. M. 2005. Crustal heterogeneity and subduction processes: 3-D  $V_p$ ,  $V_p/V_s$  and  $Q$  in the southern North Island, New Zealand. *Geophysical Journal International*, **162**, 270–288.
- EBERHART-PHILLIPS, D., REYNERS, M., CHADWICK, M. & STUART, G. 2008. Three-dimensional attenuation structure of the Hikurangi subduction zone in the central North Island, New Zealand. *Geophysical Journal International*, **174**, 418–434.
- ETHERIDGE, M. A. 1983. Differential stress magnitudes during regional deformation and metamorphism – upper bound imposed by tensile fracturing. *Geology*, **11**, 231–234.
- FAGERENG, Å. 2010. *Subduction-related Fault Processes – Ancient and Active*. PhD thesis, University of Otago, New Zealand.
- FAGERENG, Å. & COOPER, A. F. 2010a. The metamorphic history of rocks buried, accreted and exhumed in an accretionary prism: an example from the Otago Schist, New Zealand. *Journal of Metamorphic Geology*, **28**, 935–954.
- FAGERENG, Å. & COOPER, A. F. 2010b. Petrology of metabasalts from the Chrystalls Beach accretionary mélange – implications for tectonic setting and terrane origin. *New Zealand Journal of Geology and Geophysics*, **53**, 57–70.
- FAGERENG, Å. & ELLIS, S. 2009. On factors controlling the depth of interseismic coupling on the Hikurangi subduction interface, New Zealand. *Earth and Planetary Science Letters*, **278**, 120–130, doi: 10.1016/j.epsl.2008.11.033.
- FAGERENG, Å. & SIBSON, R. H. 2010. Melange rheology and seismic style. *Geology*, **38**, 751–754, doi: 10.1130/G30868.1.

- FAGERENG, Å., REMITTI, F. & SIBSON, R. H. 2010. Shear veins observed along planar anisotropy at high angles to greatest compressive stress. *Nature Geoscience*, **3**, 482–485, doi: 10.1038/NGEO898.
- FRANCOIS-HOLDEN, C., BANNISTER, S. ET AL. 2008. The M 6.6 Gisborne Earthquake of 2007: preliminary records and general source characterisation. *Bulletin of the New Zealand National Society for Earthquake Engineering*, **41**, 266–277.
- FUKUI, A. & KANO, K. 2007. Deformation process and kinematics of mélange in the Early Cretaceous accretionary complex of the Mino-Tamba Belt, eastern southwest Japan. *Tectonics*, **26**, TC2006, doi: 10.1029/2006TC001945.
- GOODWIN, L. B. & TIKOFF, B. 2002. Competency contrast, kinematics and the development of foliations and lineations in the crust. *Journal of Structural Geology*, **24**, 1065–1085.
- GUTENBERG, B. & RICHTER, C. F. 1944. Frequency of earthquakes in California. *Bulletin of the Seismological Society of America*, **34**, 185–188.
- HADA, S., ITO, M., LANDIS, C. A. & CAWOOD, P. 2001. Large-scale translation of accreted terranes along continental margins. *Gondwana Research*, **4**, 628–629.
- HADA, S., YOSHIKURA, S., AITAM, Y. & SATO, K. 1988. Notes on the geology and paleontology of the Chrystals Beach Complex, South Island, New Zealand. In: *Preliminary Report on the Accretion Complex Geology of Otago Coast Section in the South Island, New Zealand*. Department of Geology, Faculty of Science, Kochi University, Japan, 21–28.
- HADA, S., YOSHIKURA, S., LANDIS, C. A. & COOMBS, D. S. 2006. Mélange fabric of the Chrystals Beach Complex, southeast Otago, New Zealand. *Chishitsugaku Zasshi (Journal of the Geological Society of Japan)*, **112**, XI–XII.
- HANDY, M. R. 1990. The solid-state flow of polymineralic rocks. *Journal of Geophysical Research*, **95**, 8647–8661.
- HARRIS, R. N. & WANG, K. 2002. Thermal models of the Middle America Trench at the Nicoya Peninsula, Costa Rica. *Geophysical Research Letters*, **29**, 2010–2013.
- HASHIMOTO, Y. & KIMURA, G. 1999. Underplating process from mélange formation to duplexing: example from the Cretaceous Shimanto Belt, Kii Peninsula, southwest Japan. *Tectonics*, **18**, 92–107.
- HASHIMOTO, Y., NAKAYA, T., ITO, M. & KIMURA, G. 2006. Tectonolithification of sandstone prior to the onset of seismogenic subduction zone: evidence from tectonic melange of the Shimanto Belt, Japan. *Geochemistry, Geophysics, Geosystems*, **7**, Q06013, doi: 10.1029/2005GC001062.
- HILL, D. P. 1977. A model for earthquake swarms. *Journal of Geophysical Research*, **82**, 1347–1352.
- HIROSE, H., HIRAHARA, K., KIMATA, F., FUJII, N. & MIYAZAKI, S. 1999. A slow thrust slip event following the two 1996 Hyuganada earthquakes beneath the Bungo Channel, southwest Japan. *Geophysical Research Letters*, **26**, 3237–3240.
- HOUSEN, B. A., TOBIN, H. J., LABAUME, P., LEITCH, E. C., MALTAN, A. J. OCEAN DRILLING PROGRAM LEG 156 SHIPBOARD SCIENCE PARTY. 1996. Strain decoupling across the decollement of the Barbados accretionary prism. *Geology*, **24**, 127–130.
- HSU, K. J. 1968. Principles of melanges and their bearing on the Franciscan-Knoxville paradox. *Geological Society of America Bulletin*, **79**, 1063–1074.
- HUBBERT, M. K. & RUBEY, W. W. 1959. Role of fluid pressure in mechanics of overthrust faulting. *Geological Society of America Bulletin*, **70**, 115–206.
- HUBBERT, M. K. & WILLIS, D. G. 1957. Mechanics of hydraulic fracturing. *American Institute of Mining Engineers Petroleum and Gas Transactions*, **210**, 153–168.
- HYNDMAN, R. D. 2007. The seismogenic zone of subduction thrust faults: What we know and don't know. In: DIXON, T. & MOORE, J. (eds) *The Seismogenic Zone of Subduction Thrust Faults*. Colombia University Press, New York, 15–41.
- HYNDMAN, R. D., YAMANO, M. & OLESKEVICH, D. A. 1997. The seismogenic zone of subduction thrust faults. *The Island Arc*, **6**, 244–260.
- ITO, Y. & OBARA, K. 2006. Very low frequency earthquakes within accretionary prism are very low stress-drop earthquakes. *Geophysical Research Letters*, **33**, L09302, doi: 10.1029/2006GL025883.
- JAEGER, J. C., COOK, N. G. W. & ZIMMERMAN, R. W. 2007. *Fundamentals of Rock Mechanics*, 4th edn. John Wiley, Chichester.
- JI, S. C. 2004. A generalized mixture rule for estimating the viscosity of solid–liquid suspensions and mechanical properties of polyphase rocks and composite materials. *Journal of Geophysical Research*, **109**, B10207, doi: 10.1029/2004JB003124.
- JI, S. C. & ZHAO, P. L. 1993. Location of tensile fracture within rigid–brittle inclusions in a ductile flowing matrix. *Tectonophysics*, **220**, 23–31.
- KATSUMATA, A. & KAMAYA, N. 2003. Low frequency continuous tremor around the Moho discontinuity away from volcanoes in the southwest Japan. *Geophysical Research Letters*, **30**, 1020, doi: 10.1029/2002GL015981.
- KIMURA, G., KITAMURA, Y., HASHIMOTO, Y., YAMAGUCHI, A., SHIBATA, T., UJIIE, K. & OKAMOTO, S. 2007. Transition of accretionary wedge structures around the up-dip limit of the seismogenic subduction zone. *Earth and Planetary Science Letters*, **255**, 471–484.
- KLEIST, J. R. 1974. Deformation by soft sediment extension in the Coastal Belt, Franciscan Complex. *Geology*, **2**, 501–504.
- KUSKY, T. M. & BRADLEY, D. C. 1999. Kinematic analysis of melange fabrics: examples and applications from the McHugh Complex, Kenai Peninsula, Alaska. *Journal of Structural Geology*, **21**, 1773–1796.
- LISTER, G. S. & SNOKE, A. 1984. S–C mylonites. *Journal of Structural Geology*, **6**, 617–638.
- LOCKNER, D. A. 1995. Rock failure. In: AHRENS, T. J. (ed.) *Rock Physics and Phase Relations, A Handbook of Physical Constants*. American Geophysical Union, Washington, DC, 127–147.
- MAGEE, M. E. & ZOBACK, M. D. 1993. Evidence for a weak interplate thrust fault along the northern Japan subduction zone and implications for the mechanics of thrust faulting and fluid expulsion. *Geology*, **21**, 809–812.

- MARONE, C. 1998. Laboratory-derived friction laws and their application to seismic faulting. *Annual Reviews of Earth and Planetary Sciences*, **26**, 643–696.
- MATSUBARA, M., OBARA, K. & KASAHARA, K. 2009. High-Vp/Vs zone accompanying non-volcanic tremors and slow-slip events beneath southwestern Japan. *Tectonophysics*, **472**, 6–17, doi: 10.1016/j.tecto.2008.06.013.
- MCCAFFREY, R., WALLACE, L. & BEAVAN, J. 2008. Slow slip and frictional transition at low temperature at the Hikurangi subduction zone. *Nature Geoscience*, **1**, 316–320.
- MCCLAY, K. R. 1977. Pressure solution and Coble creep in rocks and minerals. *Journal of the Geological Society, London*, **134**, 57–70.
- MENEGRINI, F. & MOORE, J. C. 2007. Deformation and hydrofracture in a subduction thrust at seismogenic depths: the Rodeo Cove thrust zone, Marin Headlands, California. *Geological Society of America Bulletin*, **119**, 174–183, doi: 10.1130/B25807.1.
- MOORE, J. C. & BYRNE, T. 1987. Thickening of fault zones: a mechanism of melange formation in accreting sediments. *Geology*, **15**, 1040–1043.
- MOORE, J. C. & WHEELER, R. L. 1978. Structural fabric of a Mélange: Kodiak Islands, Alaska. *American Journal of Science*, **278**, 739–765.
- MOORE, J. C., ROWE, C. D. & MENEGRINI, F. 2007. How accretionary prisms elucidate seismogenesis in subduction zones. In: DIXON, T. H. & MOORE, J. C. (eds) *The Seismogenic Zone of Subduction Thrust Faults*. Colombia University Press, New York, 288–315.
- MORGAN, J. K., RAMSEY, E. B. & ASK, M. V. S. 2007. Deformation and mechanical strength of sediments at the Nankai subduction zone: implications for prism evolution and décollement initiation and propagation. In: DIXON, T. H. & MOORE, J. C. (eds) *The Seismogenic Zone of Subduction Thrust Faults*. Colombia University Press, New York, 210–256.
- MORTIMER, N. 1993. *Geology of the Otago Schist and adjacent rocks. Scale 1:500 000*. Institute of Geological and Nuclear Sciences Geological Map, 7. GNS Science, Lower Hutt, New Zealand.
- MORTIMER, N. 2000. Metamorphic discontinuities in orogenic belts: example of the garnet-biotite-albite zone in the Otago Schist, New Zealand. *International Journal of Earth Sciences*, **89**, 295–306.
- MORTIMER, N. 2003. A provisional structural thickness map of the Otago Schist, New Zealand. *American Journal of Science*, **303**, 603–621.
- NELSON, K. D. 1982. A suggestion for the origin of mesoscopic fabric in accretionary melange, based on features observed in the Chrystalls Beach Complex, South Island, New Zealand. *Geological Society of America Bulletin*, **93**, 625–634.
- NIEMEIJER, A. R. & SPIERS, C. J. 2006. Velocity dependence of strength and healing behaviour in phyllosilicate-bearing fault gouge. *Tectonophysics*, **427**, 231–253.
- NISHIMURA, Y., COOMBS, D. S., LANDIS, C. A. & ITAYA, T. 2000. Continuous metamorphic gradient documented by graphitization and K–Ar age, southeast Otago, New Zealand. *American Mineralogist*, **85**, 1625–1636.
- OBARA, K. 2002. Non-volcanic deep tremor associated with subduction in southwest Japan. *Science*, **96**, 1679–1681.
- OBARA, K., HIROSE, H., YAMAMIZU, F. & KASAHARA, K. 2004. Episodic slow slip events accompanied by non-volcanic tremors in southwest Japan subduction zone. *Geophysical Research Letters*, **31**, L23602, doi: 10.1029/2004GL020848.
- OLESKIEWICH, D. A., HYNDMAN, R. D. & WANG, K. 1999. The updip and downdip limits to subduction earthquakes: thermal and structural models of Cascadia, south Alaska, SW Japan and Chile. *Journal of Geophysical Research*, **104**, 14 965–14 991.
- ORANGE, D. L. 1990. Criteria helpful in recognizing shear-zone and diapiric mélanges: examples from the Hoh accretionary complex, Olympic Peninsula, Washington. *Geological Society of America Bulletin*, **102**, 935–951.
- PARK, J. O., FUJIE, G. ET AL. 2010. A low-velocity zone with weak reflectivity along the Nankai subduction zone. *Geology*, **38**, 283–286.
- PEACOCK, S. M. 1996. Thermal and petrologic structure of subduction zones. In: BEBOUT, A., SCHOLL, D., KIRBY, S. & PLATT, J. (eds) *Subduction: Top to Bottom*. American Geophysical Union, Washington DC, 119–134.
- PEACOCK, S. M. 2009. Thermal and metamorphic environment of subduction zone episodic tremor and slip. *Journal of Geophysical Research*, **114**, B00A07, doi: 10.1029/2008JB005978.
- PENG, Z. & GOMBERG, J. 2010. An integrated perspective of the continuum between earthquakes and slow-slip phenomena. *Nature Geoscience*, **3**, 599–607.
- PETERSON, C. L. & CHRISTENSEN, D. H. 2009. Possible relationship between nonvolcanic tremor and the 1998–2001 slow slip event, south central Alaska. *Journal of Geophysical Research*, **114**, B06302, doi: 10.1029/2008JB006096.
- RAMSAY, J. G. 1980a. The crack-seal mechanism of rock deformation. *Nature*, **284**, 135–139.
- RAMSAY, J. G. 1980b. Shear zone geometry: a review. *Journal of Structural Geology*, **2**, 83–99.
- RAMSAY, J. G. & CHESTER, F. M. 2004. Hybrid fracture and the transition from extension fracture to shear fracture. *Nature*, **428**, 63–66.
- REYNERS, M. 1998. Plate coupling and the hazard of large subduction thrust earthquakes at the Hikurangi subduction zone, New Zealand. *New Zealand Journal of Geology and Geophysics*, **41**, 343–354.
- REYNERS, M. & BANNISTER, S. 2007. Earthquakes triggered by slow slip at the plate interface in the Hikurangi subduction zone, New Zealand. *Geophysical Research Letters*, **34**, L14305, doi: 10.1029/2007GL030511.
- REYNERS, M. & EBERHART-PHILLIPS, D. 2009. Small earthquakes provide insight into plate coupling and fluid distribution in the Hikurangi subduction zone, New Zealand. *Earth and Planetary Science Letters*, **282**, 299–305.
- REYNERS, M., EBERHART-PHILLIPS, D. & STUART, G. 1999. A three-dimensional image of shallow subduction: crustal structure of the Raukumara Peninsula, New Zealand. *Geophysical Journal International*, **137**, 873–890.

- ROBINSON, P. 1958. *Structural and Metamorphic Geology of the Brighton-Taieri Mouth Area, East Otago, New Zealand*. MSc thesis, University of Otago, New Zealand.
- ROGERS, G. C. & DRAGERT, H. 2003. Episodic tremor and slip on the Cascadia subduction zone: the chatter of silent slip. *Science*, **300**, 1942–1943.
- RUFF, L. 1989. Do trench sediments affect great earthquake occurrence in subduction zones? *Pure and Applied Geophysics*, **129**, 263–282.
- SAGE, F., COLLOT, J.-Y. & RANERO, C. R. 2006. Interplate patchiness and subduction-erosion mechanisms: evidence from depth-migrated seismic images at the central Ecuador convergent margin. *Geology*, **34**, 997–1000.
- SCHWARTZ, S. Y. & ROKOSKY, J. M. 2007. Slow slip events and seismic tremor at Circum-Pacific subduction zones. *Reviews of Geophysics*, **45**, RG3004, doi: 10.1029/2006RG000208.
- SECOR, D. T. 1965. Role of fluid pressure in jointing. *American Journal of Science*, **263**, 633–646.
- SHELLY, D. R., BEROZA, G. C. & IDE, S. 2007. Non-volcanic tremor and low-frequency earthquake swarms. *Nature*, **446**, 305–307.
- SHELLY, D. R., BEROZA, G. C., IDE, S. & NAKAMURA, S. 2006. Low-frequency earthquakes in Shikoku, Japan, and their relationship to episodic tremor and slip. *Nature*, **442**, 188–191.
- SHIBATA, T. & HASHIMOTO, Y. 2005. Deformation style of slickenlines on melange foliations and change in deformation mechanisms along subduction interface: example from the Cretaceous Shimanto Belt, Shikoku, Japan. *Gondwana Research*, **8**, 433–442.
- SHREVE, R. L. & CLOOS, M. 1986. Dynamics of sediment subduction, melange formation, and prism accretion. *Journal of Geophysical Research*, **91**, 10 229–10 245.
- SIBSON, R. H. 1984. Roughness at the base of the seismogenic zone: contributing factors. *Journal of Geophysical Research*, **89**, 5791–5799.
- SIBSON, R. H. 1986. Earthquakes and rock deformation in crustal fault zones. *Annual Review of Earth and Planetary Sciences*, **14**, 149–175.
- SIBSON, R. H. 1996. Structural permeability of fluid-driven fault-fracture meshes. *Journal of Structural Geology*, **18**, 1031–1043.
- SIBSON, R. H. 1998. Brittle failure mode plots for compressional and extensional tectonic regimes. *Journal of Structural Geology*, **20**, 655–660.
- SIBSON, R. H. & TOY, V. G. 2007. The habitat of fault-generated pseudotachylite: presence v. absence of friction melt. In: McGARR, A., ABERCROMBIE, R. & DI TORO, G. (eds) *Earthquakes: Radiated Energy and the Physics of Faulting*. American Geophysical Union, Washington, DC, 153–166.
- SILVER, E. & BEUTNER, E. 1980. Melanges—Penrose conference report. *Geology*, **8**, 32–34.
- TICHELAAR, B. W. & RUFF, L. 1993. Depth of seismic coupling along subduction zones. *Journal of Geophysical Research*, **98**, 2017–2037.
- TOBIN, H. J. & SAFFER, D. M. 2009. Elevated fluid pressure and extreme mechanical weakness of a plate boundary thrust, Nankai Trough subduction zone. *Geology*, **37**, 679–682.
- TSURU, T., PARK, J. O., MIURA, S., KODAIRA, S., KIDO, Y. & HAYASHI, T. 2002. Along-arc structural variation of the plate boundary at the Japan Trench margin: implication of interplate coupling. *Journal of Geophysical Research*, **107**, 2357, doi: 10.1029/2001JB001664.
- UJIIE, K. 2002. Evolution and kinematics of an ancient décollement zone, mélange in the Shimanto accretionary complex of Okinawa Island, Ryukyu Arc. *Journal of Structural Geology*, **24**, 937–952.
- UNDERWOOD, M. B. 2007. Sediment inputs to subduction zones: Why lithostratigraphy and clay mineralogy matters. In: DIXON, T. H. & MOORE, J. C. (eds) *The Seismogenic Zone of Subduction Thrust Faults*. Colombia University Press, New York, 42–86.
- VANNUCCHI, P., REMITTI, F. & BETTELLI, G. 2008. Geological record of fluid flow and seismogenesis along an erosive subducting plate boundary. *Nature*, **451**, 699–703, doi: 10.1038/nature06486.
- VON HUENE, R. & SCHOLL, D. W. 1991. Observations at convergent margins concerning sediment subduction, subduction erosion, and the growth of continental crust. *Reviews of Geophysics*, **29**, 279–316.
- VROLIJK, P. 1990. On the mechanical role of smectite in subduction zones. *Geology*, **18**, 703–707.
- WALLACE, L. M. & BEAVAN, J. 2006. A large slow slip event on the central Hikurangi subduction interface beneath the Manawatu region, North Island, New Zealand. *Geophysical Research Letters*, **33**, L11301, doi: 10.1029/2006GL026009.
- WALLACE, L. M. & BEAVAN, J. 2010. Diverse slow slip behavior at the Hikurangi subduction margin, New Zealand. *Journal of Geophysical Research*, **115**, B12402, doi: 10.1029/2010JB007717.
- WALLACE, L. M., BEAVAN, J., McCAFFREY, R. & DARBY, D. 2004. Subduction zone coupling and tectonic block rotations in the North Island, New Zealand. *Journal of Geophysical Research*, **109**, B12406, doi: 10.1029/2004JB003241.
- WALLACE, L. M., REYNERS, M. ET AL. 2009. Characterising the seismogenic zone of a major plate boundary subduction thrust: the Hikurangi Margin, New Zealand. *Geochemistry Geophysics Geosystems*, **10**, Q10006, doi: 10.1029/2009GC002610.
- WHITE, J. C. 2004. Instability and localization of deformation in lower crustal granulites, Minas fault zone, Nova Scotia, Canada. In: ALSOP, G. I., HOLDSWORTH, R. E., McCAFFREY, K. J. & HAND, M. (eds) *Flow Processes in Faults and Shear Zones*. Geological Society, London, Special Publications, **224**, 25–37.
- ZOBACK, M. D., ZOBACK, M. L. ET AL. 1987. New evidence on the state of stress of the San Andreas fault system. *Science*, **238**, 1105–1111.

# Textural record of the seismic cycle: strain-rate variation in an ancient subduction thrust

CHRISTIE D. ROWE<sup>1,2\*</sup>, FRANCESCA MENEGHINI<sup>3</sup> & J. CASEY MOORE<sup>1</sup>

<sup>1</sup>*Earth and Planetary Sciences, University of California Santa Cruz,  
1156 High Street, Santa Cruz, CA 95064, USA*

<sup>2</sup>*Department of Geological Sciences, University of Cape Town, Private Bag X3,  
Rondebosch 7701, South Africa*

<sup>3</sup>*Dipartimento di Scienze della Terra, Università di Pisa, via S. Maria, 53, 56126 Pisa, Italy*

\*Corresponding author (e-mail: cdrowe@ucsc.edu)

**Abstract:** Active faults slip at different rates over the course of the seismic cycle: earthquake slip ( $c. 1 \text{ m s}^{-1}$ ), interseismic creep ( $c. 10\text{--}100 \text{ mm year}^{-1}$ ) and intermediate rate transients (e.g. afterslip and slow slip events). Studies of exhumed faults are sometimes able to identify seismic slip surfaces by the presence of frictional melts, and slow creep by textures diagnostic of rate-limited plastic processes. The Pasagshak Point Thrust preserves three distinct fault rock textures, which are mutually cross-cutting, and can be correlated to different strain rates. Ultrafine-grained black fault rocks, including pseudotachylite, were formed during seismic slip on layers up to 30 cm thick. Well-organized  $S-C$  cataclasites 7–31 m thick were formed by slow creep, with pressure solution as a dominant, rate-limiting mechanism. These must have formed at strain rates consistent with long-term plate-boundary motion, but solution-creep healing acted to reduce porosity of the cataclasites and eventually restricted fluid connectivity such that creep by this mechanism could not continue. Disorganized, non-foliated, rounded clast cataclasites were formed at shear rates faster than solution creep and are interpreted as representing shear at intermediate strain rates. These could have formed during afterslip or delocalization of slip associated with an earthquake rupture.

**Supplementary material:** Detailed map of Pasagshak Peninsula is available at <http://www.geolsoc.org.uk/SUP18493>.

Subduction plate boundaries display a variety of slip rates on the plate-boundary fault at seismogenic depths, ranging from fast slip during earthquakes (of the order of  $1 \text{ m s}^{-1}$ ) to plate-boundary slip rates (of the order of millimetres or centimetres per year or less: Schwartz & Rokosky 2007). Intermediate slip rates are observed during afterslip following an earthquake, or during independent slow slip events (Schwartz & Rokosky 2007). The recognition of the geological signature of these different strain rates in exhumed faults has presented a challenge (Sibson 1989). This is partly due to the fact that, in contrast to the implication of boundaries drawn on traditional ‘deformation mechanism maps’ (e.g. Rutter 1986), strain at most pressure–temperature–rate ( $P-T$ -rate) conditions is accommodated by multiple mechanisms simultaneously (Hirth & Tullis 1992). Therefore, the resultant deformation fabrics are determined by the interaction of multiple processes, and not characteristic of a single deformation mechanism. By comparison with experiment, it is possible to relate some observed fault rock

fabrics with the transitions in dominance between various deformation mechanisms, whose activities depend differently on temperature and strain rate (Hirth & Tullis 1992; Niemeijer *et al.* 2010).

The apparent correlation between the limits of the seismogenic zone and approximate thermal limits ( $c. 150\text{--}350^\circ\text{C}$ : Oleskevich *et al.* 1999; Peacock & Wang 1999) enables us to constrain the deformation mechanisms that may be active in rocks at the appropriate mineralogy, depth and temperature where variable slip rates are accommodated.

Seismic slip ( $c. 1 \text{ m s}^{-1}$ ) causes frictional heating, and is therefore most easily recognized by the presence of frictional melt (preserved as pseudotachylite: Sibson 1975; Cowan 1999). Slow strain in the same depth interval (seismogenic zone) is accommodated by a combination of solution creep and granular flow (Rutter & Elliott 1976; Tullis & Yund 1987; Ring & Brandon 1999). While accommodating slip, these processes also contribute to interseismic fault healing (Bos *et al.* 2000; Keulen *et al.* 2008; Niemeijer *et al.* 2010). A third category of deformation at

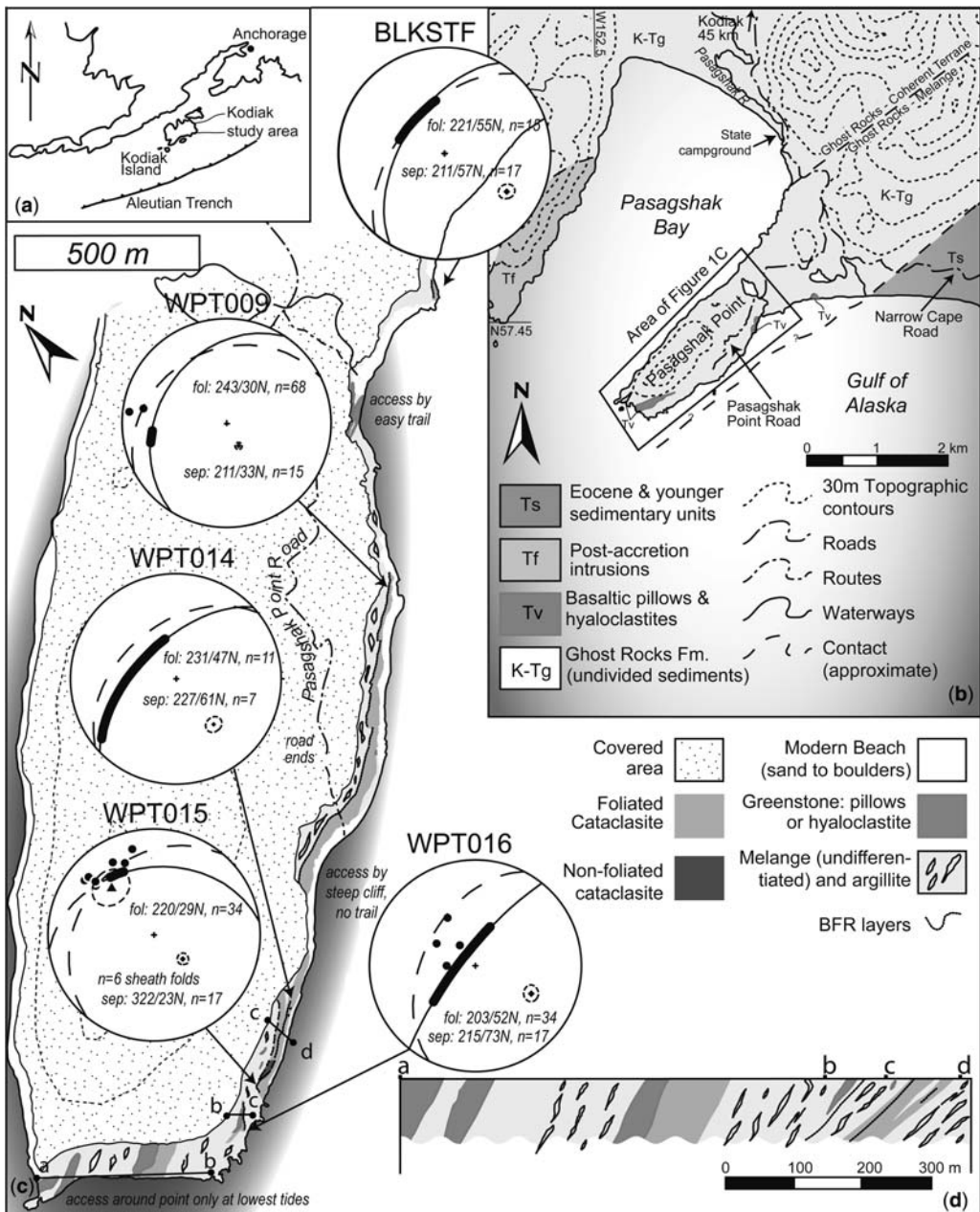


**Fig. 1.** Study location. (a) Inset map shows the location of Kodiak Island relative to the coast of North America. (b) Pasagshak Bay, Kodiak Island. Coastline modified from Google Earth. Topographical contours from USGS 30 m quads (Alaska). Felsic intrusive contacts from Farris *et al.* (2006). Pasagshak Point is 45 km from the city of Kodiak on the Narrow Cape Road. (c) Geological map of Pasagshak Point. Coastline from Digitalglobe (Longmont, CO), topographical contours from USGS 30 m quads (Alaska), showing locations of detailed outcrop studies (Waypoints BLKSTF, 009, 014, 015 and 016). Line segments (a)–(d) show the location of the cross-section. Potential means of access are shown; only the trail in the NE is safe in all conditions; the whole field area is unsafe at high tides or in inclement weather or high swell. For all stereonets, the black dashed plane is the mean cataclastic foliation (fol) with the mean pole shown as a solid diamond with the 95% confidence range shown by dashed black ellipses. Solid dots are slickenlines on cataclastic shear surfaces. The solid black plane is the separation arc (sep) established by folds of

intermediate strain rates includes intermediate slip rates on thin surfaces, as well as fast slip, distributed over greater thicknesses of fault rock. Some examples include slow slip events, post-seismic slip and intervals of low propagation velocity or low moment release during large earthquakes.

Numerous field studies have reported textural evidence of stress cycling in exhumed faults, and have related these to the seismic cycle (e.g. Power & Tullis 1989; Meneghini & Moore 2007; Nüchter & Stöckhert 2007; Birtel & Stöckhert 2008; Smith *et al.* 2008 among others). These studies equate hydrofracture, brecciation and rapid fracture propagation with seismic events and pressure solution, or crack healing, to the interseismic interval (e.g. Gratier *et al.* 2002). However, in the absence of conclusive evidence of fast slip (frictional melt: Cowan 1999), these stress cycles can only be inferred to record the seismic cycle.

An early Tertiary plate-boundary subduction thrust exposed at Pasagshak Point, Kodiak Island, Alaska, displays a sequence of contrasting styles of cataclasite that are mutually cross-cutting with a frictional melt-bearing ultrafine-grained black fault rock (BFR) (pseudotachylite: Rowe *et al.* 2005; Meneghini *et al.* 2010). Comparison with recent experiments allows us to examine the changes in strain rate represented by the different cataclasite textures. Meneghini *et al.* (2010) presented detailed microstructural and geochemical data describing the BFRs and our interpretation of their seismic origins. This contribution places the seismic and aseismic fault rock textures in the context of the seismic cycle on the palaeo-plate boundary of the Pasagshak Point Thrust.

## Geological setting

The Kodiak complex is composed of discrete units of deep-marine sedimentary and igneous rock, which were deposited and accreted to North America during Mesozoic–Cenozoic subduction, and contiguous with the modern active forearc wedge (Moore 1969; Connelly 1978; Plafker *et al.* 1994). The Ghost Rocks Formation was deposited on a subducting ridge flank in the latest Cretaceous–earliest Paleocene (Byrne 1982, 1984; Haeussler *et al.* 2003; Farris *et al.* 2006). The structural base is a mélange zone along which Eocene marine sediments were thrust under the Ghost Rocks Formation (Moore 1969) (Fig. 1b). Shear localization toward the base of

a décollement zone is similar to that observed in the mélange in the Shimanto Belt, Japan (Ujiie 2002).

The structurally lower part of the formation is composed of blocks of coherent bedded turbidites and sandstones separated by bands of highly disrupted strata (Byrne 1982, 1984). The section varies from massive sandstone beds associated with sand-dominant turbidite sections, to massive argillite units and argillite-dominant turbidite sections. Greenstones occur as pillow basalts with hyaloclastite and local interstitial limestone or as hyaloclastite lenses lying along bedding. Shear bands and local small-offset faults are prevalent in massive sandstones, suggesting early-stage distributed deformation (Byrne 1982; Fisher & Byrne 1987; DiTullio & Byrne 1990). Prehnite and pumpellyite in the greenstones are the only metamorphic indicator minerals found in the formation (Moore 1969; Byrne 1982).

Pasagshak Point is a strike-parallel peninsula at the structural base of the formation (Fig. 1; see also Supplementary publication fig. SUP18493). The mélange consists of up to 100 m blocks of sandstone and argillite in an argillaceous matrix and is cross-cut by narrow (7–31 m) cataclastic shear zones that contain pseudotachylite-bearing ultrafine-grained black fault rocks (Rowe *et al.* 2005; Meneghini *et al.* 2010). The SE coast of the peninsula offers an approximately 3.5 km strike-parallel cross-section, including nearly 1 km of dip-parallel section (Fig. 1c, d). These fault strands were identified as a palaeo-subduction thrust by previous workers (Byrne 1984; Rowe *et al.* 2005; Rowe 2007; Meneghini *et al.* 2009), and are collectively referred to as the Pasagshak Point Thrust.

## Temperature during fault activity

Fluid-inclusion thermobarometry suggests fluid temperatures during subduction-related quartz vein precipitation of  $240\text{--}260 \pm 20^\circ\text{C}$  at depths of 12–14 km (Vrolijk *et al.* 1988; Rowe 2007). However, the thermal history of the wall rocks has not previously been determined. Vitrinite reflection of six samples of argillite taken from the formational mélange adjacent to the cataclasite zones was measured by J. Hower at the University of Kentucky Center for Applied Energy Research (CAER). Samples from the cataclasites also contained vitrinite particles but they were too small to analyse. The vitrinite reflectance data (Fig. 2) yield a mean

**Fig. 1.** (Continued) opposite asymmetries (Hansen 1971) and  $S\text{--}C$  fabrics in cataclasites, with the bold segment representing the range of possible slip. The black triangle shows the mean flow axis of sheath folds within the BFR with 95% confidence ellipses. (d) Structural section of the Pasagshak Point Thrust. The thickness of the units varies along strike.

value of  $\%R_o = 4.9 \pm 0.9$ . Using the relationship of Ohmori *et al.* (1997), as determined for similar rocks in SW Japan, and applying the model of Sweeney & Burnham (1990), the approximate temperature indicated by the vitrinite reflectance values is calculated as  $250 \pm 10^\circ\text{C}$  (Fig. 2). This is equivalent to the fluid-inclusion trapping temperatures and is consistent with metamorphic minerals observed in metavolcanic rocks of the Ghost Rocks mélange (pumpellyite reported by Vrolijk 1987), and represents the maximum temperatures experienced by the formation. This temperature places the depth of fault activity well within the seismogenic zone of analogous modern faults (Moore *et al.* 2007).

### Cataclasites in the Pasagshak Point Thrust

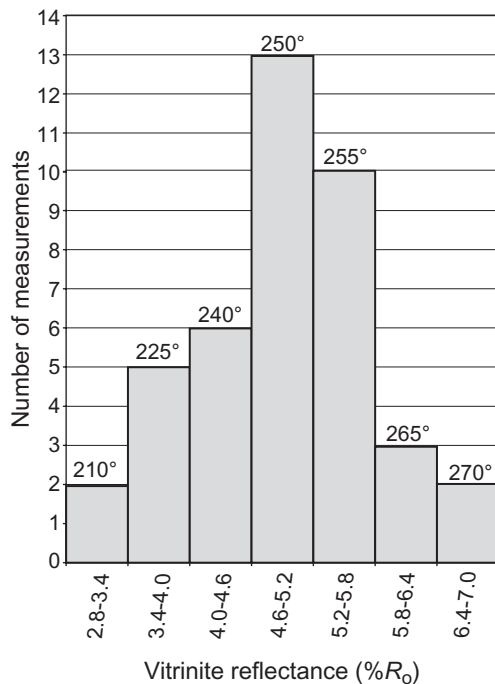
We identified four anastomosing brittle shear zones cross-cutting the mélange (shown as cataclasite in Fig. 1) within a structural thickness of less than 1 km. At several outcrops it is possible to measure

the cataclasites zones, which are 7–31 m thick (Table 1; see also Supplementary publication fig. SUP18493), similar to the 31 m-thick décollement at the toe of the Barbados accretionary prism (Maltman *et al.* 1997). The cataclasites units are interpreted as fault strands that accommodated higher strain than the surrounding mélange due to the total destruction of the original bedding and transposition or destruction of previous mélange fabrics. Ultrafine-grained black fault rocks (BFRs) lie in well-defined faults cross-cutting the cataclasite, and are found as recycled clasts within the cataclasite (Rowe *et al.* 2005). The shear surfaces and shear-sense indicators are parallel in the mélange, cataclasites and BFR faults (Fig. 3), but the cataclasites and BFRs consistently cross-cut the mélange and mutually cross-cut each other. Therefore, the BFR–cataclasite fault strands are interpreted as localized surfaces of late-stage slip along the palaeo-subduction thrust.

The cataclasites contain clasts of sandstone, argillite and ultrafine-grained black fault rock in a matrix of comminuted sandstone and argillite. Clast abundance and strength of matrix foliation vary in the cataclasites. Two field classes of cataclasites were identified: foliated (Fig. 4a, b, d–f), which are either clast or matrix-rich; and non-foliated, matrix-supported (Fig. 5a, b, d–f). The coarsest clasts are up to about 15 cm (Figs 4a & 5b) and typical clasts are 1–3 cm (Figs 4b & 5a). These are three orders of magnitude smaller than the sandstone fragments in the host mélange. Clast size and abundance in the cataclasite is related to the original sandstone:argillite ratio of the parent lithology, the degree of disruption and the specific deformation mechanisms dominantly responsible for the fabric. These descriptions represent end members of a continuum of textures.

*Clast-rich foliated cataclasites* contain the most continuous bedding fragments, although bedding is dismembered and the original orientation is indistinguishable (Figs 4a & 6a). The overall proportion of sandstone–siltstone clasts is 0–70% of outcrop surface area. The foliation is defined by wavy-planar surfaces of aligned clasts and argillitic matrix cleavage, with local tight folds whose axial plane is at a low angle to foliation. Small asymmetric folds, clast asymmetry and imbricated fabrics indicate shear sense (top to SE; Figs 1 & 3). Folds are only local, with axial traces from tens of centimetres up to 1 m at most.

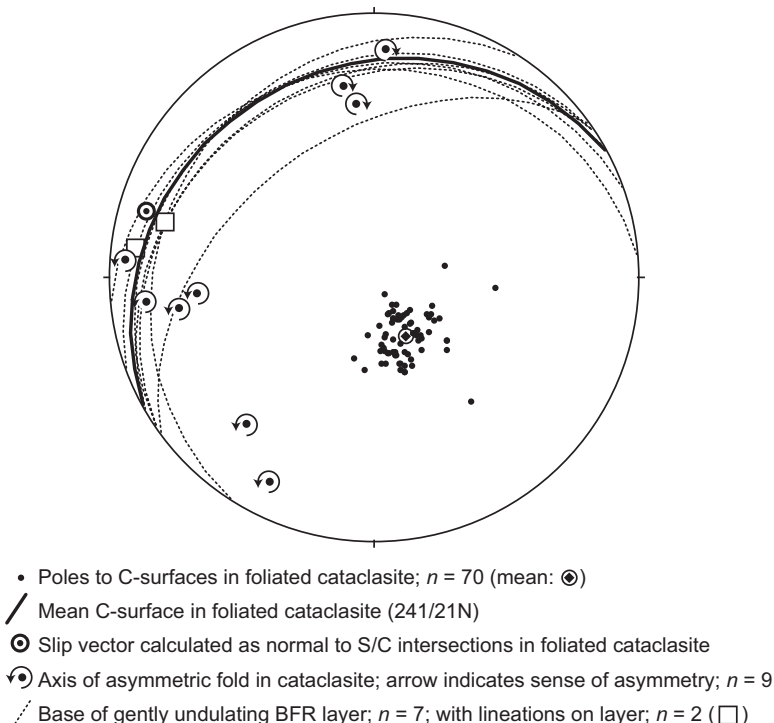
*Matrix-rich foliated cataclasites* have a narrow range of clast size and frequency. The fabric in these units is dominated by planar to gently anastomosing phyllosilicate cleavage and the alignment of the sandstone clasts, which are elongate and locally similar in size (Fig. 4b, d–f). A few exposures have argillitic cataclasites that are nearly devoid of



**Fig. 2.** Vitrinite reflectance data for six samples of argillitic mélange (host rock to the cataclasites). The number of measurements is shown on the vertical axis. Results are binned in intervals of  $\Delta \%R_o = 0.8$ . The mean  $\%R_o$  value in each bin is used to calculate estimated maximum temperature based on the relationship from Ohmori *et al.* (1997). Estimated temperatures are shown at the top of each bar.

**Table 1.** Cataclasite zones in Pasagshak Point Thrust

Thickness (m)	Location	BFR present?	Notes
10	BLKSTF	Yes	Two through-going layers of aphanitic BFR with foliated, greenstone-bearing cataclasite between them and foliated argillaceous cataclasite below
$\geq 7$	WPT009	Yes	Strongly planar foliated cataclasite with increasing fabric intensity towards the top where the aphanitic BFR layer injects into cracks in the sandstone hanging wall
14	WPT014	Yes	Strongly foliated cataclasite with abundant small sandstone clasts and some bands of dominantly argillaceous cataclasites. Through-going BFR layer and injections up-section into the cataclasite, and isolated whisps and swirls of BFR in the cataclasite
$\geq 25$	WPT015 (non-foliated)	Yes (clasts) – Figure 5a & c	Thick homogeneous layer of massive, non-foliated cataclasite. The upper contact is sharp against the sandstone mélange; the lower contact is a BFR-bearing fault against foliated cataclasite
16	WPT015 (foliated)	Yes – Figure 7	Foliated coarse cataclasite with a high proportion of sandstone clasts and local zones of asymmetric folds. A thick BFR layer separates the top of the cataclasite from the sandstone hanging wall
14	WPT016	Yes	Foliated cataclasite with gradational bands of finer and coarser clasts, abundant clasts of BFR
31	06P2	No	Thick foliated argillaceous cataclasite

**Fig. 3.** Consistency of orientation of cataclastic and BFR fabrics, an example from WPT009. Note the fit of the slip vectors indicated by cataclasite and by BFR.

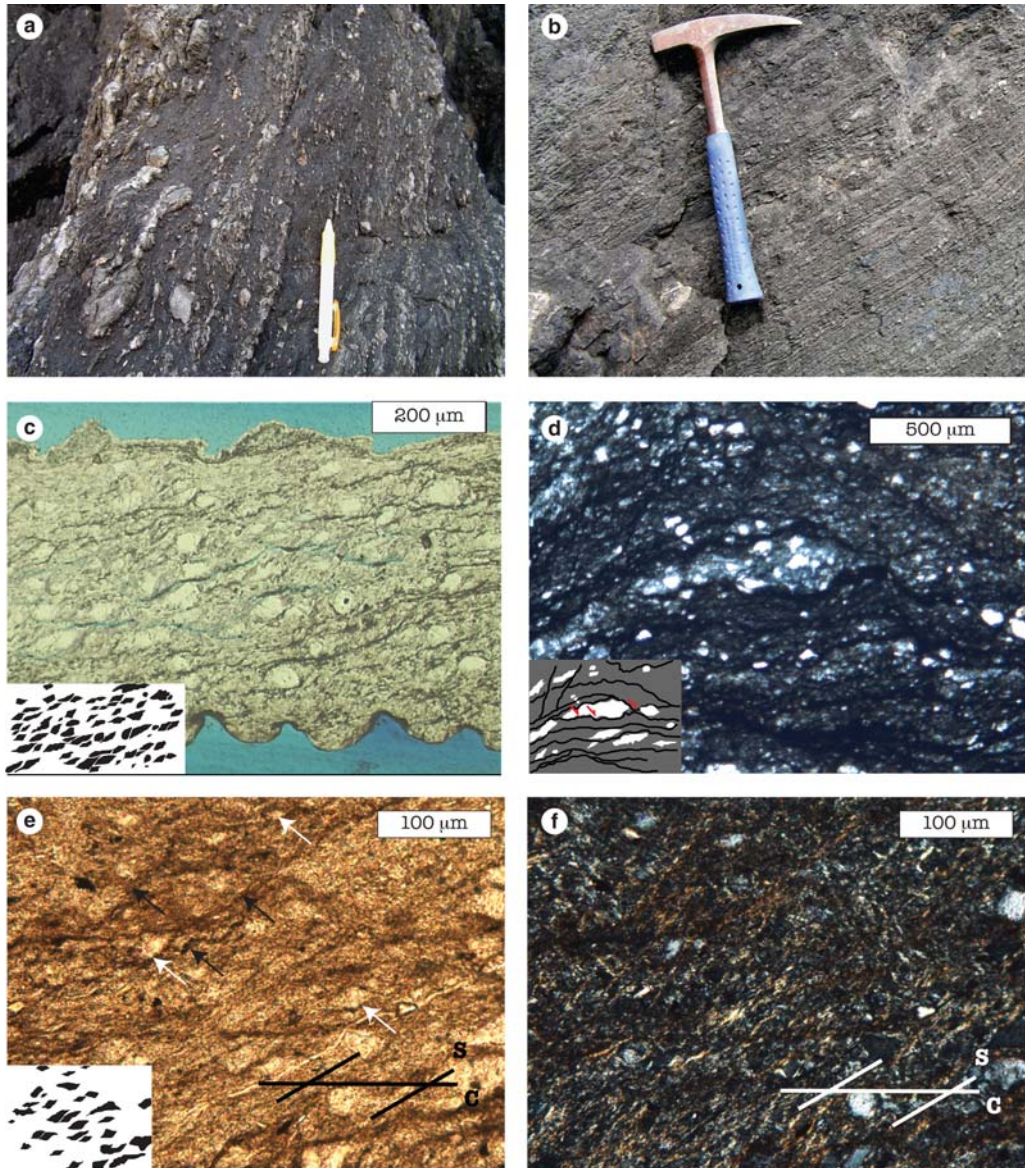


**Fig. 4.** Textures of foliated cataclasites. Field photographs are contrast enhanced. (a) Clast-rich foliated cataclasite with intense local folding. The pencil given for scale is 15 cm. WPT015. (b) Clast-poor foliated cataclasite. Clast size is homogenous; shear fabric is planar. Clasts are angular sandstone fragments with their long axes aligned parallel to shear fabric. The rock hammer given for scale is 45 cm. WPT009. (c) Example of experimentally deformed artificial halite–muscovite gouge (total displacement 30 mm; displacement rate  $0.3 \mu\text{m s}^{-1}$ ). Photomicrograph provided by André Niemeijer. Inset shows a grain map of the whole image used for aspect ratio and orientation data (Fig. 6). (d) Photomicrograph (cross-polarized light) of matrix-rich foliated catacasite. Sandstone fragments are boudinaged by intergranular slip on the grain scale. Inset interpretive sketch shows wavy foliation surfaces and microfaults cutting sandstone fragments. (e) Plane-polarized light (PPL) and (f) cross-polarized light (XPL): fabric of foliated matrix-rich cataclasites. Slip surfaces (*C*-surfaces) are parallel to the long axis of the photographs. Solution surfaces (*S*) are inclined at  $30^\circ$  (black arrows point to solution surfaces). In PPL (e), note the long axes of the quartz grains established by quartz overgrowth parallel to *S*-surfaces (white arrows indicate grains with well-developed overgrowths). Inset shows a grain map of the whole image used for aspect ratio and orientation data (Fig. 6). In XPL (f), the long axes of the birefringent illite grains follow the *S*-surfaces and the shear surfaces (*C*) are extinct.

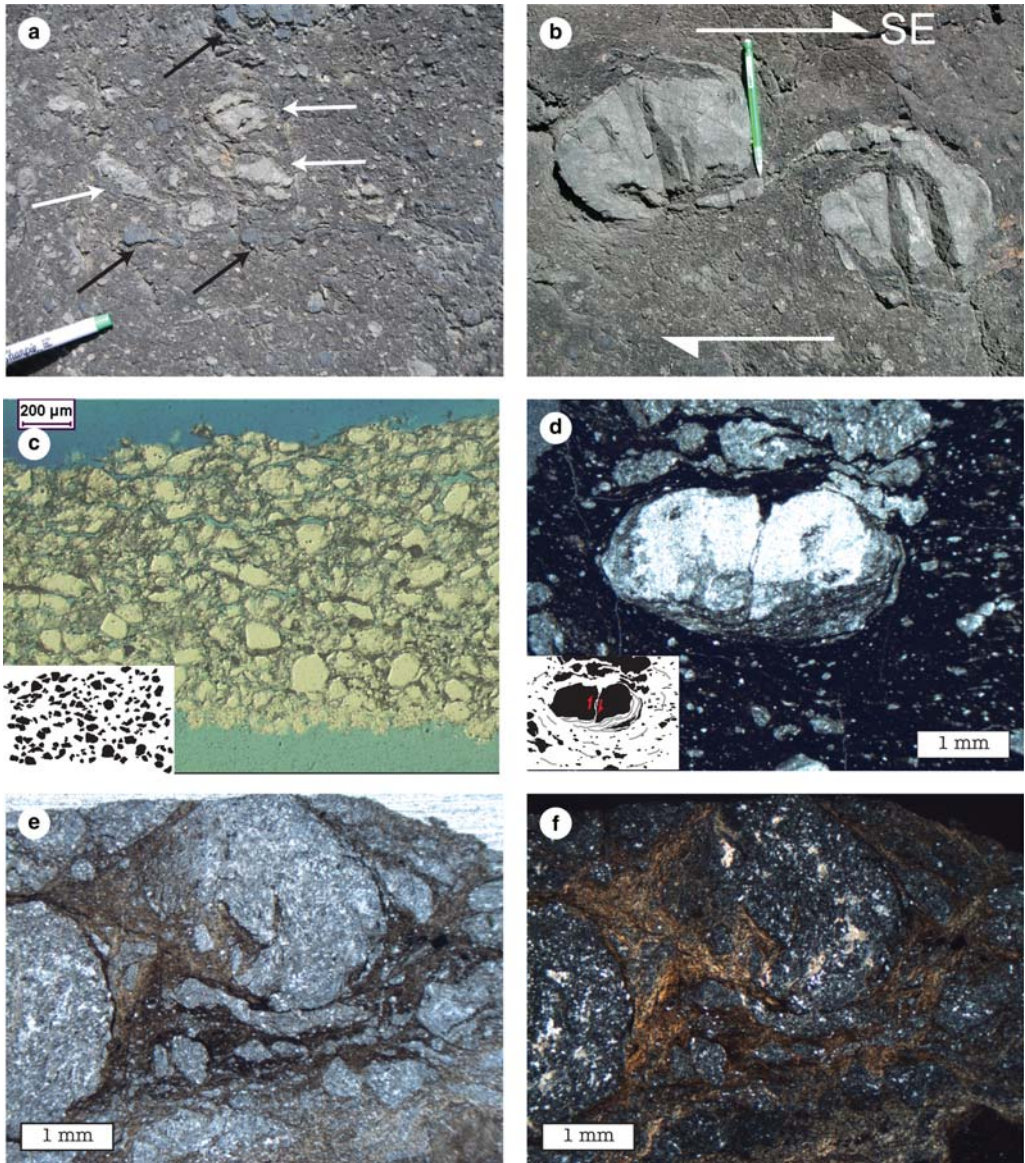


**Fig. 5.** Textures of non-foliated cataclasites. Field photographs are contrast enhanced. **(a)** Non-foliated cataclasite at WPT015. Clasts are composed of sandstone (white arrows) or BFR (black arrows). No matrix foliation is present. The diameter of the pen is approximately 1 cm. **(b)** Delicate sandstone paired delta-clasts indicate top-to-the-SE rotation within non-foliated cataclasite at WPT015. The pencil is 15 cm. **(c)** Example of experimentally deformed artificial halite–muscovite gouge (total displacement 30 mm; displacement rate  $13 \mu\text{m s}^{-1}$ ). Photomicrograph provided by André Niemeijer. Inset shows grain tracing of the whole image used for determination of axial ratio and orientation of grains. **(d)** Sandstone fragments in argillitic matrix, cross-polarized light. Concentric wrapping of fabric around clasts indicates clast rotation relative to the matrix. Mechanisms of clast evolution include microfaults (centre) and relative slip of individual sand grains to form clast tails along wrapped foliation (above centre clast). Inset shows a grain map of the whole image used for aspect ratio and orientation data (Fig. 6), with grey lines showing matrix fabric orientation. **(e)** Plane-polarized light (PPL) and **(f)** cross-polarized light (XPL): rounded sandstone fragment with spirals of argillitic matrix encapsulated within it (similar morphology to a snowball garnet). Boudinaged sandstone fragments just below the round clast suggest stretching parallel to the clast boundary. Bright orange-brown interference colours of chlorite (**f**) show the alignment of matrix phyllosilicates parallel to the clast boundary, showing matrix wrapping around the rounded clast.

sandstone clasts, but may contain thin stringers of greenstone. The planar cleavage tends to be very close to parallel with the cross-cutting surfaces of the BFR (Meneghini *et al.* 2010).

Figure 4d–f shows the microstructure of the foliated cataclasite on the grain scale. In Figure 4d, small sandstone clasts have been extended by grain-scale shears. Matrix fabric is formed by anastomosing wavy dark solution seams. At the micro-scale, the fabrics are qualitatively similar to those seen at outcrop scale. Figure 4e, f shows well-organized S–C fabrics on the grain scale. Individual sand grains are flattened along dark solution surfaces parallel to S (black arrows in Fig. 4e) and elongated by quartz overgrowths forming points on the ends (white arrows in Fig. 4e). C-surfaces appear as sharp, dark surfaces that cut off the edges of some grains.

*Non-foliated cataclasite* is matrix-supported with weak or no matrix cleavage and well-mixed textures (Figs 5a, b & 6b). The presence of very delicate structural features and the inclusion of clasts of pseudotachylite-bearing fault rock require that the structures and fabric are tectonic in origin. These structures include complex clast tails (Fig. 5b) and very long and thin, delicately folded sandstone bedding fragments. Clasts of BFR that have been brittlely deformed are ubiquitous (Figs 5d & 6b). Massive cataclasite is only observed in one of the four cataclastic fault strands (WPT015; red in Fig. 1), where it forms a unique section at least 25 m thick.

On the micro-scale, the textures are very similar to those observed at outcrop scale. Self-similarity is a well-established characteristic of fault rocks (Sammis *et al.* 1986; Hippert 1999; Heilbronner & Keulen 2006). Figure 5d shows an approximately 2 mm siltstone clast that is cut by a microfault. The smaller clasts and matrix fabric are aligned concentric to the 2 mm grain. The smaller clasts of sandstone show elongation by oblique microfaults, similar to the elongate grains in the foliated cataclasites. In Figure 5e, small extensional faults cut a thin stringer of sandstone that is wrapped around another very rounded clast. In cross-polarized light (Fig. 5f) it is possible to see the chlorite and illite grains that are also concentric to the larger rounded clast.

In all of the cataclasites, the quartz and feldspar grains and the sandstone fragments (collectively: framework grains) are cut by microfractures (e.g. Fig. 5d). The visible phyllosilicate grains in the matrix are chlorite and illite (collectively: phyllosilicate grains), which are locally well-aligned.

In the foliated cataclasites, the framework grains are similarly shaped and oriented at all scales of observation. Individual grains are flattened or cut off along zone-parallel shear surfaces and elongated along inclined surfaces, parallel to the orientation

of matrix phyllosilicates. The mechanisms of grain elongation include microfaulting on the scale of sandstone clasts (e.g. Fig. 4d), and quartz overgrowth on the scale of individual monomineralic sand grains (e.g. Fig. 4e). The strong alignment of framework and phyllosilicate grains observed at the micro-scale is consistent with the orientation and mechanism of evolution of macroscopic clasts. The argillitic matrix evolved by solution creep and frictional sliding. Within it, the sandstone fragments were modified by pressure solution and cataclastic flow. These well-aligned clasts and matrix foliation bestow the strong parting to the rock encountered on the outcrop scale.

The non-foliated catclasites do not express a planar alignment of grains. The phyllosilicates and sandstone or siltstone clasts are locally aligned parallel to the boundaries of larger clasts, making a concentric wrapping fabric. This variation in alignment results in a massive texture on the outcrop scale, where a weak alignment of large clasts points towards particle rotation with flow. There is no parting foliation developed in the matrix.

Notably absent from the cataclasites are any microtextures characteristic of crystal-plastic deformation mechanisms, such as subgrains, undulose extinction, bulging or interfingering grain boundaries (Tullis & Yund 1987; Hirth & Tullis 1992; Kruehl 1996). Only rare examples of these features were observed within detrital grains, implying that these microstructures were inherited.

## Characterizing the textures of the cataclasites

Grain aspect ratio and orientation were compared between natural and experimental fault rocks across multiple scales. In order to capture the dominant grain populations, photographs were orientated parallel to local shear direction and perpendicular to local foliation, with outcrop-scale examples spanning several tens of cubic centimetres in areas (Fig. 6a, b) and micro-scale examples on the scale of several square millimetres. Photographs on these scales contain enough clasts to generate statistically relevant data, but are also locally compromised by shadows and variable surface weathering. These areas were manually isolated (light grey areas in Fig. 6c, d). Commonly used methods of digitally identifying clast boundaries produced unsatisfactory results with these images owing to the interference of shadows and overlapping colour or grey-scale values between matrix and clasts. Therefore, individual clast boundaries were traced by hand and classified as sandstone/siltstone (dark grey) or BFR (black) to produce Figure 6c, d. The foliated cataclasite image contains 688 clasts

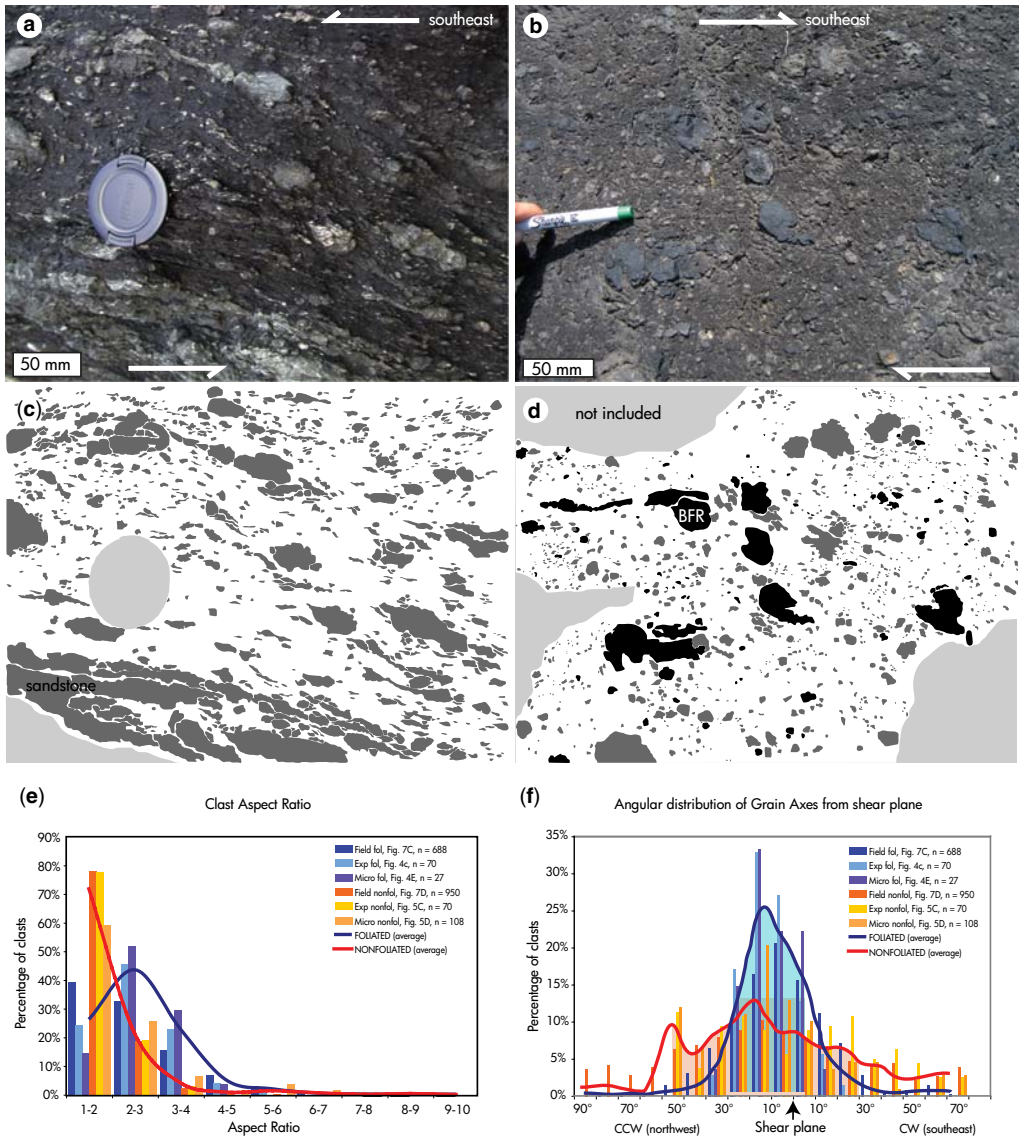


**Fig. 6.** Clast aspect ratio and orientation for foliated v. non-foliated cataclasites. **(a)** Foliated cataclasite. **(b)** Non-foliated cataclasite. **(c) & (d)** Clast maps of foliated cataclasite from image (a) and (b). The areas illustrated are the same as the entire photographs (a) and (b). The light grey areas were not included in the clast count due to photograph quality or irregular outcrop surface. The medium grey represents sandstone clasts. Black represents clasts of BFR. White areas are the matrix. Maps were created manually using Adobe Illustrator to trace clasts in the photographs. **(e) & (f)** Aspect ratio (e) and long axis orientation (f) of outcrop- and micro-scale images of foliated and non-foliated cataclasites, and experimental textures produced by André Niemeijer and colleagues. Images used for clast counting are insets in Figures 4c, e, 5c, d & 6c, d.

large enough to be counted (*c.* 2 mm) and the non-foliated cataclasite image contains 950 countable grains. The grains were manually outlined in petrographical images of experimentally produced (Fig. 4c) and natural (Fig. 4e) foliated cataclasites,

and experimental (Fig. 5c) and natural (Fig. 5d) non-foliated cataclasites. The size threshold for counting grains in the experimental images is about 40  $\mu\text{m}$ . In the photomicrographs of the Pasagshak Point Thrust rocks, the threshold is about 25  $\mu\text{m}$  in the foliated

rock and about 60  $\mu\text{m}$  for the non-foliated rock. The scales were individually determined for each image to capture the characteristic grain size of the sample. These images were then analysed using Grey Scale Image Analysis for MATLAB (Bjørk 2006).

The significant textural characteristics that contribute to the outcrop classification of foliated v. non-foliated cataclasites are clearly distinguished by examining the aspect ratio (Fig. 6e) and orientation of clasts (Fig. 6f) in the two types. The aspect ratios of clasts in the foliated samples indicate 26% roughly equant grains, while 72% of the grains in the non-foliated samples are roughly equant (where roughly equant is defined as  $1 \leq \text{aspect ratio} < 2$ ). The foliated cataclasite has a much broader range in aspect ratio, with 30% of clasts having aspect ratios greater than 3, while only 7% of the clasts in non-foliated samples are so elongate.

The alignment of the long axes of clasts also shows a significantly different pattern for the foliated v. non-foliated case. Seventy-five per cent of the clasts in the foliated cataclasite are aligned within the primary shear foliation or inclined at less than  $30^\circ$  in an S-surface orientation (blue curve in Fig. 6f). In contrast, only 41% of clasts in the non-foliated cataclasite fall into this same range around the shear foliation, while the long axis orientation is spread broadly (orange curve in Fig. 6f).

## Formation and slip behaviour of the cataclasites

The temperature and depth during deformation, and the mineralogy are identical in the two types of cataclasites. However, distinctively different textures are observed. Therefore, based on previously established deformation mechanism maps, the rheology and deformation mechanisms active during strain may be controlled by differences in strain rate (Rutter & Elliott 1976; Rutter 1983). The action of different deformation mechanisms, or the same set of deformation mechanisms acting at different relative rates to accommodate the strain, may result in different rock fabrics.

At  $250 \pm 10^\circ\text{C}$ , solution creep (sometimes called pressure solution) and cataclastic flow are the dominant deformation mechanisms in quartz-rich rocks (Rutter & Elliott 1976; Rutter 1983). Dislocation glide is so slow as to be effectively inactive at temperatures of about  $250^\circ\text{C}$  (Stöckhert *et al.* 1999). ‘Cataclastic flow’ can be further subdivided into grain rolling, grain sliding and grain breakage (Sibson 1977), all of which can occur at any temperature if the strain rate or differential stress is sufficiently high. Each of these mechanisms can be expected to evolve the cataclasite texture in a

particular way, as demonstrated by a review of relevant experiments, see later.

The fabric of both types of cataclasites is self-similar over several orders of magnitude, as demonstrated by comparison of the outcrop- and micro-scale photographs in Figures 4 and 5. This is consistent with previous observations of subduction mélanges (Kusky & Bradley 1999) and shear fabrics generally (Hippert 1999). In our observations, the strong foliation in the matrix of the foliated cataclasites at outcrop scale (Fig. 4a, b) is caused by the strong alignment of individual phyllosilicate grains at the micro-scale (Fig. 4d–f). The non-foliated cataclasites show weak planar or clast-wrapping partings at outcrop scale (Fig. 5a, b), which are again caused by the concentric alignment of phyllosilicate grains around the clasts (Fig. 5d–f).

Pressure solution, driven by solubility gradients within the rock and differential stress, causes phyllosilicate grains to grow or reorientate perpendicular to the maximum principal stress – in this case, causing strong alignment along surfaces (S), which are normal to the principal stress (Fig. 4f). The solution and precipitation of quartz flattens grains in the S-plane, and precipitates grain tails in the pressure shadows, elongating in the S-plane (Fig. 4e). Any independent rotation of grains, relative to each other or the matrix, destroys this aligned fabric.

In contrast, where cataclastic flow includes a significant component of rotation, this alignment will be destroyed and local grain interactions will determine the orientation of phyllosilicates. This is observed on the outcrop scale in Figure 5b, where the partings in the matrix are concentric to the boundaries of the large sandstone clast, and on the microscopic scale in Figure 5f, where the birefringent grains of chlorite and illite wrap the grain boundaries in a similar fashion. It is important to note that solution creep may have been acting on the grains, but the fabric disruption by cataclastic flow dominated over the fabric development by solution creep.

## Analogue experiments

Shearing experiments, using two-mineral mixtures (one soluble phase and one phyllosilicate phase), offer an excellent analogue for sandstone/shale rocks in fault zones. Microtextures characteristic of solution–cataclasis interaction have been produced experimentally by fluctuating strain rates in a wet muscovite–halite gouge (Bos *et al.* 2000; Bos & Spiers 2001, 2002a, b; Niemeijer & Spiers 2005, 2006). These experiments have been successful in producing textures that replicate observations of natural fault rocks (Bos & Spiers 2002a;

Niemeijer & Spiers 2006) and exhibit frictional-viscous rheology (Bos *et al.* 2000).

At low rates of shearing, the muscovite–halite gouges exhibited low-strength, velocity-strengthening behaviour (Bos & Spiers 2002a; Niemeijer & Spiers 2006). At higher rates of shearing, the gouges displayed low-strength and velocity-weakening behaviour, and dilation of the samples was observed (Kanagawa 2002; Niemeijer & Spiers 2006; Niemeijer *et al.* 2010). Most tellingly, the transition between the two behavioural regimes (which was accompanied by high strength) was controlled by slip rate. Niemeijer & Spiers (2006) interpreted their observations as a balance between compaction by solution creep and dilation by cataclastic flow.

These experimentally produced fabrics replicate the textures observed in the cataclasites of the Pasagshak Point Thrust, where the fault rocks are composed of phyllosilicates (illite + chlorite) and framework grains (quartz + albite) that play similar roles to the muscovite and halite, respectively, used in the experiments. By scaling the strain rates to appropriate values for the mineralogy and temperature of fault activity, one can examine the transition between foliated and non-foliated fabrics. The rate of solution creep in quartzose rocks can be constrained by experiment. Gratier *et al.* (1999) showed that strain rates of the order of  $10^{-12} \text{ s}^{-1}$  were accommodated by solution transfer in quartz indenter experiments at  $350^\circ\text{C}$  (at the equivalent of about 12 km depth). However, Anzalone *et al.* (2006) showed that mica–quartz interactions could increase the rate at which this process is effective by several orders of magnitude. This is discussed further later.

### Foliated cataclasites

The wet low-speed ( $<1 \mu\text{m s}^{-1}$ ; approximate strain rate of  $10^{-5} \text{ s}^{-1}$ ) experiments of Niemeijer & Spiers (2005, 2006, e.g. samples ‘msc5’ and ‘shs2’) produced a well-organized  $S$ – $C$  fabric with elongated halite clasts parallel to  $S$ -surfaces in a matrix of finely banded muscovite and thin stringers of halite (Fig. 4c, provided by André Niemeijer). The fabric is defined by a strong grain-preferred orientation, parallel or at low angles to the shear plane (accomplished by grain rotation during shearing) and increasing aspect ratio of deformable clasts (in this case, halite) owing to pressure solution. The increased aspect ratio of the halite grains was accomplished by solution and precipitation of the halite in consistent orientations. This reshaping of the halite grains, as well as rotation during shear, contributed to the alignment of the fine-grained muscovite–halite matrix. The experimental samples show a foliation inclined at approximately  $15^\circ$

( $S$ -surface) to the shear surface ( $C$ -surface) (Bos & Spiers 2001). Similar to mylonitic  $S$ – $C$  fabrics, the  $S$ -surfaces are parallel to the plane of flattening (Moore 1978; Lister & Snoke 1984).

The foliated cataclasites in the Pasagshak Point Thrust (Figs 4a, b & 6a) contain boudins and elongated stringers of greywacke sandstones that conform to  $S$ -orientations in a strongly foliated matrix of sheared argillite. On the micro-scale, the planar or gently anastomosing  $C$ -surfaces show evidence of pressure solution and shear (Fig. 4d–f). Based on the similarity between the experimental and natural fabrics and mechanisms, the foliated cataclasites are interpreted to have formed by a combination of processes at a strain rate that can be accommodated by collaboration of grain breakage and sliding, and pressure solution along grain contacts. Solution creep contributes to grain-scale alignment in the matrix, as well as the strong preferred orientation of large clasts (Fig. 6e). Cataclasite also contributes to the elongation of large (predominantly sandstone) clasts when tails on clasts are extended by microfaulting during shear. This can be observed in the angular pinch–swell shapes of the sandstone clasts in the long axis direction. The low variability in the long-axis orientations (Fig. 6f) limits the possibility of clast rotation.

These results suggest that the combination of granular flow with pressure solution is important for creating the foliated fabrics in the brittle realm (e.g. Shimamoto 1989; Gratier *et al.* 1999). Thus, the strain rate during formation of the foliated cataclasites can be constrained by the relation of fabric style to the rate of slip and rate of pressure solution (at known temperature–pressure conditions). The pressure-solution analogy offers the only rate-limiting process we understand to have influenced the evolution of these cataclasites.

### Non-foliated cataclasites

An unsorted, unfoliated cataclastic texture was formed by Niemeijer & Spiers (2005, 2006) in two types of experiments: first, the dry run-in experiments at low speeds ( $<1 \mu\text{m s}^{-1}$ ; their sample ‘msc5’); and, second, the wet high-speed experiments ( $5$  and  $13 \mu\text{m s}^{-1}$ , their samples ‘msc7’ and ‘msc8’; approximate strain rates of  $4 \times 10^{-3}$  and  $10^{-2} \text{ s}^{-1}$ , respectively). These samples had no clear foliation in large grains or matrix and equant grains. The only significant difference between the two high-speed samples was the amount of dilation that occurred, which was pronounced in both cases and increased at higher speeds. Most tellingly, slow, wet experiments that produced foliated fabrics, such as those described above, could be made to suddenly change to non-foliated equant

fabrics by a sudden increase in strain rate (Bos & Spiers 2001; Niemeijer & Spiers 2006).

The massive, non-foliated cataclasite (seen only at WPT 015; Fig. 5) exhibits no sorting weak-clast alignment (Fig. 6f), and a mixture of angular and rounded, roughly equant clasts (Fig. 6e). The matrix grains show no preferred orientation, and tend to wrap clasts locally but form no planar fabrics. These attributes are commonly found in gouges from brittle faults, particularly those interpreted to have experienced fluidization (Lin 1996; Monzawa & Otsuki 2003; Otsuki *et al.* 2003). The experimental sample (Fig. 5c) does not look as much like the natural samples (Fig. 5d–f) as in the foliated case. This is probably a function of framework grain-size ranges and clast:matrix proportions, both of which were set in the experiment by the initial materials used. However, the key characteristics of the non-foliated fabric, that is, the grain aspect ratios and wrapping alignment, are similar between the natural and experimental examples (Fig. 6e, f). We suggest that this non-foliated cataclasite formed by a similar mechanism to the experiments described above; that is, by cataclastic flow. The experimental example offers two scenarios for creating such textures; the common feature is that the rate of solution creep does not meet the shear strain rate. Niemeijer & Spiers (2006) achieved this by running dry experiments, or by running wet experiments at a higher strain rate than solution creep could accommodate at local conditions. The dominance of cataclastic flow as the deformation mechanism results in grain rounding (by rolling and fracturing) and dilation. This interpretation is in accordance with Sibson (1977), who observed that occasional seismic slip in a predominantly plastic zone could be expected to form random-fabric fault rocks.

#### *Solution creep and cataclasite fabric*

In the Pasagshak Point Thrust, the foliated cataclasites clearly formed by a collaboration between solution creep, which elongated and aligned both large and matrix grains, and granular sliding, without a significant rotation of grains. The non-foliated cataclasite fabric formed by dilation, grain rotation and breakage. We suggest that the non-foliated cataclasites were produced at the expense of the foliated cataclasite. As solution-creep rate is limited by the diffusion rate of dissolved species through pore fluid, which is influenced by the connectedness of fluid networks in the rock, two explanations are suggested by comparison to the experiments: (1) the rocks were dry, and the lack of connected pore fluid inhibited solution creep; or (2) the non-foliated cataclasite was deformed at a rate faster than the maximum

allowable rate of solution creep under local conditions.

We find it unlikely that the deformation occurred in a dry fault for several reasons. First, water was probably present in the system, as is estimated from modern subduction thrusts at the pressure–temperature conditions of the Pasagshak Point Thrust (Jarrard 2003). Second, the non-foliated cataclasite represents only one strand of a fault in which the other strands are all foliated (solution-creep-facilitated) cataclasites. The non-foliated strand was not spatially or temporally isolated from the other strands. Third, the dilation associated with the cataclastic flow would draw formation water into the slipping zone, facilitating solution creep if the slip rate was sufficiently low. Therefore, the best explanation is that the non-foliated cataclasite was created by a transient, localized (within a 25 m-thick fault zone) strain-rate increase, which disrupted the foliated fabric, similar to the effects observed by Niemeijer & Spiers (2006) when increasing strain rate in their analogue experiments.

#### **Ultrafine-grained black fault rocks (BFRs)**

The pseudotachylite-bearing ultrafine-grained black fault rocks (BFRs) in the Pasagshak Point Thrust are as diverse as the cataclasites (Rowe *et al.* 2005; Rowe 2007; Meneghini *et al.* 2010). BFRs were not observed anywhere in the mélange; they are only found in cataclasite zones. They occur in thick, vitreous planar layers within or along the edge of cataclasite fault strands, complexly flow-banded compound layers (Fig. 7), and as matrix within the cataclasite, and all are distinctively blue-black with a sparkly–vitreous luster. Meneghini *et al.* (2010) gave a thorough description of the chemistry and microstructures found in BFRs and a discussion of their origins, briefly summarized here.

*Aphanitic black fault rock* is vitreous and chert-like in outcrop, usually occurring in tabular layers with parallel partings (Rowe *et al.* 2005; Meneghini *et al.* 2010). *Grain-supported black fault rock* has a cataclastic texture dominated by clasts of aphanitic BFR as well as individual mineral grains derived from the sedimentary parent rock. The granular texture is expressed on the weathered outcrop surface as darker colour and matte luster (Fig. 7). *Clast-bearing black fault rock* is a general term for mixed clastic rocks with a significant matrix component of black micron-scale grains, which impart the characteristic black sooty luster. These three types occur singly or in compound layers (e.g. Fig. 7). The complex interbanding of different types occurs in very thick layers, such as shown in Figure 7, an outcrop photograph from WPT015 (see Fig. 1 for location.)

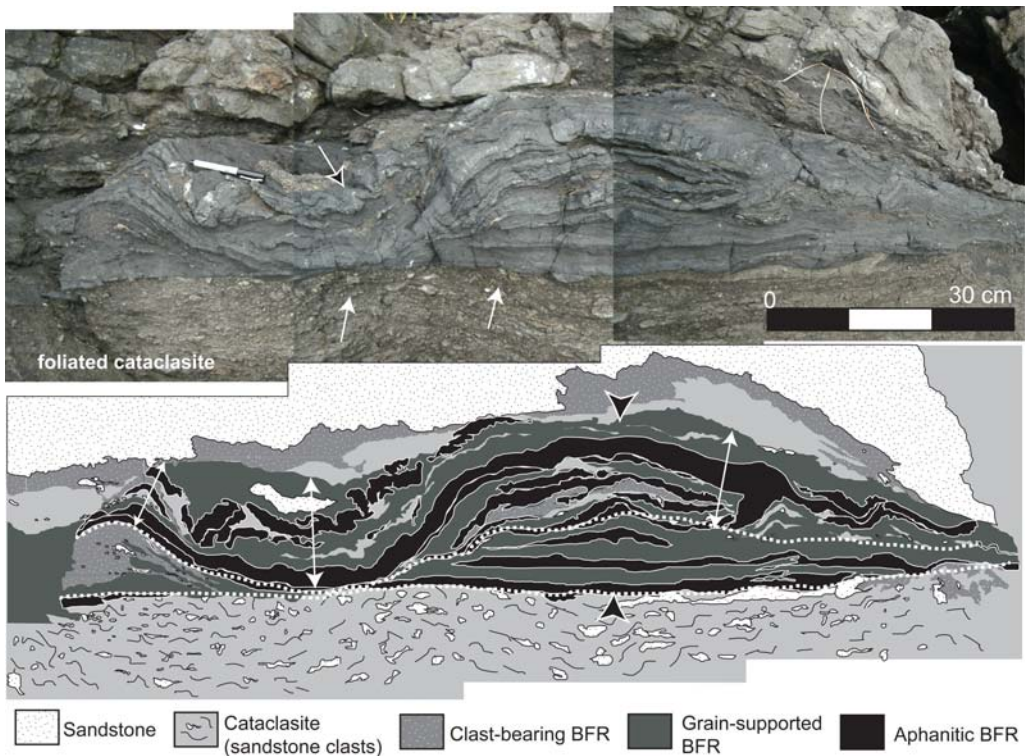


**Fig. 7.** Thick composite layer of BFR at WPT015, and interpretive sketch of the photograph. The hanging wall is deformed sandstone and the footwall is foliated cataclasite. Rounded sandstone clasts in cataclasite footwall are sharply cross-cut by the base of the BFR layer (white arrows on the photograph). Black-headed arrow indicates the location of cuspate–lobate folds. Dotted white line on the interpretive sketch divides event assemblages (two or fewer BFR-forming events, both cross-cut by a sharp fault against the foot-wall cataclasite). The thickest part of the layer (indicated by black arrowheads on the sketch) is approximately 30 cm. Upper composite layer thickness (interpreted as a single event horizon) varies from 12.5 cm (south) to 20.4 cm (middle) to 19.5 cm (north) (shown by white double arrows on the interpretive sketch).

Meneghini *et al.* (2010) showed that the aphanitic BFR contains two distinct textures on the micron-scale: crystalline textures, interpreted as pseudotachylite; and microgranular, interpreted to have formed by brittle grain fracturing. The intimate flow banding of pseudotachylite and microgranular layers, often forming macroscopic folds (e.g. Fig. 7), demonstrates that the cataclastic flow in the microgranular layers occurred on the same timescale (the timescale of pseudotachylite solidification; Rowe *et al.* (2005)). The boundaries between pseudotachylite and microgranular fault rock, as well as the boundaries between BFR and cataclasite, were also deformed by granular flow on these same timescales (e.g. seismic to immediately post-seismic timescales) at rates of the order of  $\text{cm s}^{-1}$  (Rowe *et al.* 2005; Brodsky *et al.* 2009; Meneghini *et al.* 2010).

As shown in the interpreted sketch (Fig. 7), the approximately 30 cm layer contains only one

internal cross-cutting surface that is through-going (white dotted line). The volumes between the cross-cutting surface and the edges of the layer are internally coherently deformed, with the multiple layers of different BFR types folding or pinching and swelling together. This outcrop therefore contains a maximum of two active layers (or event layers). For the purposes of the analysis below, we will therefore use 30 cm as the maximum thickness of the slip surface during earthquake slip. The presence of the pseudotachylite-bearing fault rocks demonstrate that multiple earthquakes occurred on the Pasagshak Point Thrust, and the recycled, comminuted clasts of BFR found in cataclasites demonstrate that interseismic deformation was also localized on the thrust surface. Below, we compare the strain-rate constraints given by the field observations to variable slip rates observed on modern plate-boundary faults.

## Seismic cycle and strain rates

The relationship between the cataclasites and the BFRs is a good indication of relative deformation rate, as it demonstrates that the long-term evolution of the cataclasites is punctuated by seismic events that form cross-cutting structures. This repetition of deformation rates and mechanisms interpreted from the rock textures invokes an obvious parallel to the seismic cycle. Of the documented deformation mechanisms in the Pasagshak Point Thrust, two are clearly rate-limiting: solution creep and frictional melting. We have argued above that dilational granular flow, at least in this case, can be considered rate-distinct in that it represents strain rates exceeding the rate of solution creep at local conditions.

### *Comparison to slip rates on modern faults*

Strain rate along the subduction thrust ( $\dot{\gamma}$ ) is given by:

$$\dot{\gamma} = \dot{u}/h$$

where  $\dot{u}$  is the slip rate on the subduction thrust and  $h$  is the thickness of the deforming zone. Although it is likely that some component of plate convergence rates are accommodated by distributed plastic deformation off the plate-boundary fault, we will explore the case where seismic slip, intermediate rate slip (such as slow slip events or post-seismic slip) and the majority of interseismic creep occur on the plate-boundary thrust. Our measurements of the cataclasite zones in the Pasagshak Point Thrust give observations for the thickness of the deforming zone ( $h$ ) at seismogenic depths of 7–31 m. Estimates of  $\dot{u}$  can be derived from observations of modern convergence rates on similar subduction zones (e.g. Nankai Trough 40 mm year<sup>-1</sup>; Cascadia 40–45 mm year<sup>-1</sup>; South Alaska 65 mm year<sup>-1</sup>; Chile 84 mm year<sup>-1</sup>; Oleskevich *et al.* 1999). These slip rates correspond to a strain rate of the order of around 10<sup>-12</sup> s<sup>-1</sup> for a subduction thrust surface about 20 m thick (Fig. 8). As these modern examples of long-term slip rate include the contribution of seismic slip, we consider this an upper bound on the interseismic strain rate.

The rate of solution creep in sedimentary rocks is limited by a number of factors, most importantly by the diffusion rate of dissolved ions through an interconnected fluid phase (e.g. Farver & Yund 1999; Renard *et al.* 2000). Geological studies have suggested that the maximum strain rate accommodated by solution creep in quartz rocks is about 10<sup>-12</sup> s<sup>-1</sup> (Gueydan *et al.* 2005; Mamani 2010). However, the interaction of quartz or feldspar with phyllosilicates has been shown to accelerate pressure solution of the tectosilicate (e.g. Renard *et al.* 1997)

by up to 5 times (Hickman & Evans 1995) or more (Anzalone *et al.* 2006). Shimizu (1995) calculated rates of solution creep of the order of approximately 10<sup>-8</sup>–10<sup>-11</sup> s<sup>-1</sup> for subducting sediments at 250 °C, and van Noort *et al.* (2008) observed 10<sup>-7.8</sup> s<sup>-1</sup> in compaction experiments at 300 °C. It is important to note that geological strain rates may certainly fall below the maximum rate allowed by the deformation mechanism, as in the geochronologically constrained 10<sup>-13</sup>–10<sup>-14</sup> s<sup>-1</sup> measured by Stöckhert *et al.* (1999) in quartz–muscovite rocks at 300 °C.

Therefore, in theory, common tectonic plate rates of the order of 40–80 mm year<sup>-1</sup> could probably be fully accommodated by solution creep in argillitic cataclasites within a zone 7–31 m thick at strain rates of around 10<sup>-10</sup> s<sup>-1</sup> ('Foliated cataclasites', Fig. 8), even in the conservative case that neglects deformation of the encompassing mélange or partitioning of slip into seismic events. In practice, the slip rate accommodated by solution creep must be lower than the long-term plate rate at most subduction margins where some or all of the slip takes place during earthquakes. Therefore, it is likely that solution creep is most efficient when permeability of the fault rocks is high (e.g. post-seismically), but as it acts to compact the rocks, it effectively restricts the movement of dissolved cations and reduces the rate of creep. In fact, this healing and shut-off of solution creep is a prerequisite for storing elastic strain in the plate boundary. The porosity of our cataclasite samples is 4.5 ± 0.6% (four repeat measurements for each of eight diverse samples representing all the mapped cataclasites: Brodsky *et al.* 2009). The narrow range of measured porosities suggests that this value may represent a threshold porosity where solution creep becomes inactive.

Intermediate strain rates on plate-boundary faults occur during afterslip, slow slip events and, possibly, during seismic slip when the slip surface expands in thickness (locally and temporarily). Slow slip events, where well located, appear to occur in conditionally stable regions of the décollement, deeper than the locked zone (25–45 km depth: Rogers & Dragert 2003; Shelly *et al.* 2006), shallower, towards the toe, (Obana & Kodaira 2009), or in patches within the seismogenic zone (Perfettini *et al.* 2010). We therefore consider afterslip and slow slip events, whether or not they are associated with a normal earthquake, as possible intermediate strain-rate episodes.

*Afterslip* refers to a period of slip exceeding the plate rate, lasting months or years after a large earthquake, and often reaching near equal total slip to the coseismic slip. In some cases, afterslip has been shown to occur on segments near the main rupture, thereby 'catching up' on total slip for adjacent,

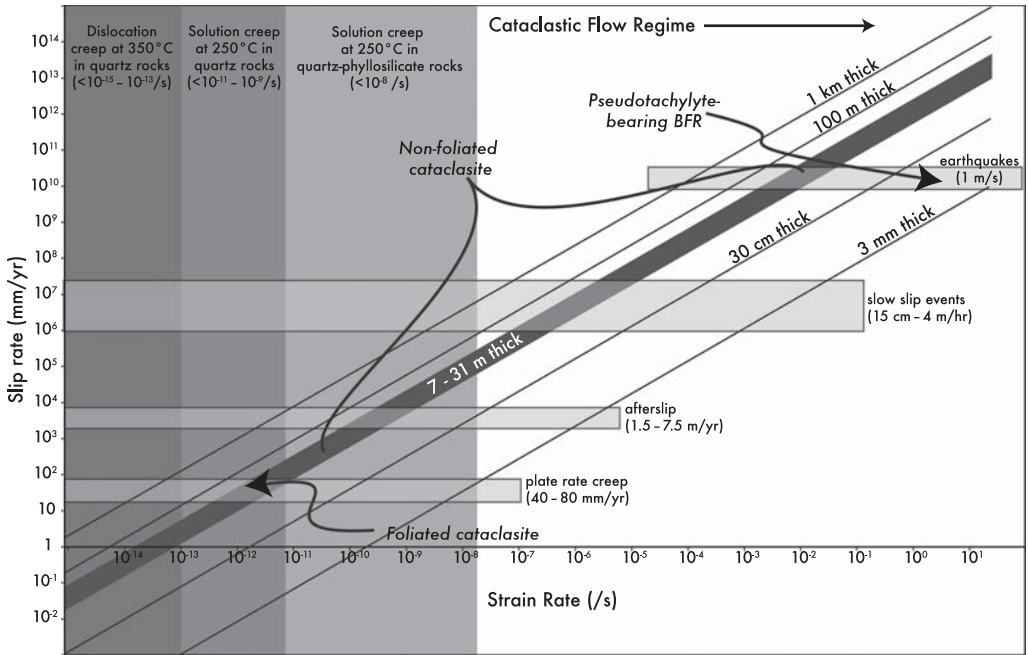


**Fig. 8.** Slip rate v. strain rate for different fault thicknesses. Slip rates corresponding to plate rate creep, afterslip, slow earthquake and seismic slip are shown in green boxes. Tinted boxes show theoretical, experimental or geochronological limits on strain rates accommodated by different mechanisms at relevant temperatures. The red box shows the upper limit in strain rate for dissolution creep in quartz rocks at 350 °C as measured geochronologically (Stöckhert *et al.* 1999). At 250 °C, we found no reports of diagnostic textures indicating dislocation creep in quartz-rich rocks. The orange box shows the strain-rate limit for solution creep calculated from natural strain in quartz-rich rocks (Gueydan *et al.* 2005; Mamtnani 2010). The yellow box shows the calculated limit of solution creep for subducting sediments at 250 °C (Shimizu 1995). Curves represent the slip rate–strain rate curve for various fault thicknesses. The range of cataclasite zone thicknesses at the Pasagshak Point Thrust is shown as a thick blue line. The interpreted position of foliated cataclasites (solution-creep-dominant), non-foliated cataclasites (faster than solution creep) and BFR (seismic) are indicated.

up- or down-dip segments (e.g. Chen *et al.* 2007; Iinuma *et al.* 2008). However, in many cases, geodetic observations are best matched by slip on the coseismic rupture surface. Hutton *et al.* (2001) showed approximately 3.5 m of slip in a 4 year period following the 1995  $M_w$  8.8 Colima–Jalisco earthquake (equivalent to 875 mm year $^{-1}$ ), Cheloni *et al.* (2010) showed 25 cm of slip in 60 days following the 2008  $M_w$  6.3 L’Aquila earthquake (equivalent to 1520 mm year $^{-1}$ ) and Harsh (1982) measured 5–20 mm day $^{-1}$  (equivalent to 1826–7305 mm year $^{-1}$ ) after the 1979  $M_w$  6.5 Imperial Valley earthquake. In all cases, the afterslip rates declined from peaks immediately after the event, so these rates are a minimum estimate of peak afterslip rates. These slip rates, imposed on the 7–31 m-thick fault surfaces that we have measured, correspond to strain rates of the order of  $10^{-8}$ – $10^{-7}$  s $^{-1}$  ('Non-foliated cataclasite', Fig. 8). These

slip rates could be accommodated by solution creep if the deforming thickness was much greater, and therefore the strain rate lower ( $>1$  km, Fig. 8), but geodetic observations in modern plate boundaries are better matched by slip along a narrow fault zone (Harsh 1982; Hutton *et al.* 2001; Cheloni *et al.* 2010).

There are examples of *slow slip events* as precursors to, or adjacent to, rupture areas of great subduction thrust earthquakes. These slip events are observed geodetically as they do not produce a seismic signal. Linde & Sacks (2002) reported fore-slip at 15 cm h $^{-1}$  culminating in the Tonankai earthquake of 1944 (c.  $1 \times 10^6$  mm year $^{-1}$ ; Fig. 8). In the northern part of the rupture zone of the great Sumatra–Andaman earthquake of 2004, Singh *et al.* (2006) used tidal gauges to determine that approximately 3 m of slip occurred coseismically (during the timescale of the rupture front passing),

followed by roughly a further 2 m of slip over about 30 min. This translates to a slip rate of  $4 \text{ m h}^{-1}$  for the 30 min interval ( $3.5 \times 10^7 \text{ mm year}^{-1}$ , Fig. 8).

## Ranges of intermediate strain rates

An important question is whether the textures in the non-foliated cataclasites can be considered diagnostic of intermediate shear strain rates. It is clear that the textures represent granular flow as the dominant deformation mechanism, and experiments have shown that the transition from viscous deformation to granular flow is associated with weakening. Therefore, it is likely that this transition is associated with, or resulted from, acceleration of slip. However, if the rate of solution creep is depressed by low temperature or lack of available fluid media for solute transport, or if the permeability in the rock is too low to allow fluids to migrate into the deforming zone, granular flow could dominate the rock textures at slower strain rates.

The absence of evidence for solution creep places a lower bound on the strain rate of formation of the non-foliated cataclasites, but what is the upper bound? Brodsky *et al.* (2009) examined an injection feature in the Pasagshak Point Thrust wherein seismic fault rock (BFR) injected into the host cataclasite, disrupting the fabric, which accommodated the injection by granular flow. They determined the rate of injection to have been of the order of  $10 \text{ cm s}^{-1}$ . Furthermore, they showed that the BFR produced during seismic slip injected the wall rock in the 10–100 s following peak slip. During a seismic rupture, the strain rate might be effectively decreased by delocalization of the slip surface, either in localized ‘soft’ patches or during deceleration following the passage of the rupture front. Textures formed during slip at these strain rates ( $10 \text{ cm s}^{-1}$  as suggested by Singh *et al.* (2006) over  $7\text{--}31 \text{ m-thick}$  slip zone results in  $c. 10^{-3} \text{ s}^{-1}$ ) might also show evidence of granular flow and dilation, similar to the texture of the non-foliated cataclasite.

The great Sumatra earthquake of 2004 offers an interesting example of variations in rupture propagation and slip speed during a large earthquake. The earthquake propagated from Sumatra northwards towards the Andaman Islands, apparently then hit some geological barrier and slowed towards the north such that most of the slip there was essentially aseismic (Singh *et al.* 2006). Although Gahalaut *et al.* (2010) argued convincingly that the area of slow slip was well correlated to the region where the  $90^\circ\text{E}$  ridge is subducting, they do not offer a mechanism by which this change in the subducting plate character should cause rupture and result in slip rates decreasing in

the affected area. Rupture and slip speeds also decrease in areas with partially consolidated sediments in the plate interface owing to the lower rigidity in the sediments (Polet & Kanamori 2000). This lower rigidity is a result of the granular materials’ capacity to loose strength during perturbation (Moukarzel 1998), an attribute probably shared with some granular fault rocks (including the Pasagshak Point Thrust non-foliated cataclasite).

Fault rocks like the Pasagshak Point Thrust non-foliated cataclasite are not as well known as the more abundant *S-C* cataclasites and mélange previously described in subduction thrusts. The slip conditions in which they form represent a small portion of the total strain occurring over the seismic cycle (in time and/or volume), so they are probably volumetrically rare relative to the total scale of deformation. Like pseudotachylytes, they are easily destroyed by small amounts of solution creep (Sibson & Toy 2007; Bjørnerud 2010) and are unlikely to be preserved.

## Conclusion

The Pasagshak Point Thrust contains fault rocks that distinctly record three general rates of slip on the palaeo-plate-boundary fault: seismic slip, recorded by pseudotachyte-bearing, ultrafine-grained BFRs; solution creep on discrete foliated cataclasites, representing interseismic creep; and an intermediate strain-rate texture in non-foliated cataclasites. This intermediate strain rate could represent anything from afterslip at 10 times the plate rate, and faster than solution creep at these *P-T* conditions, to slow slip events, to a delocalization of the shear surface during or immediately after seismic slip.

Research supported by grants NSF OCE-0203664, OCE-0549017-01 and OCE-0848977 from the US MARGINS Program. F. Meneghini’s travel to the USA has been partially supported by MIUR COFIN 2005 grants to M. Marroni. We thank the USCG Kodiak Base, particularly Lt B. Maul, J. Maumarc, R. Knox, K. Kranenburg and G. Thorn, for the opportunity to map from the sky in a Dolphin-HH65 helicopter. Helicopter support was arranged by J. Berkson, Marine Science Advisor, US Coast Guard. Thanks to A. Wells McKiernan for help in the field, and to D. Saffer for supporting him. We are grateful to the Kodiak State Parks system for accommodation at the Pasagshak River campsite and particularly to the campground host there for her hospitality. Thank you to A. Yamaguchi and A. Tsutsumi for very helpful conversations in the field. We are sincerely grateful to J. Hower for his generous assistance with vitrinite reflection measurements and with interpretation of the same. Reviewers A. Niemeijer and H. Stünitz are appreciated for their very helpful reviews, and Dr Niemeijer in particular for extended discussions of his experimental work and providing the photographs included in Figures 4 and 5. We thank J. Kirkpatrick for help with image processing. Suggestions

from numerous people improved the manuscript; in particular we thank G. di Toro, E. Brodsky, V. G. Toy and Å. Fagereng. C. Curtis and K. Whitney are thanked for manuscript assistance.

## References

- ANZALONE, A., BOLES, J., GREENE, G., YOUNG, K., ISRAELACHVILI, J. & ALCANTAR, N. 2006. Confined fluids and their role in pressure solution. *Chemical Geology*, **230**, 220–231.
- BIRTEL, S. & STÖCKHERT, B. 2008. Quartz veins record earthquake-related brittle failure and short term ductile flow in the deep crust. *Tectonophysics*, **457**, 53–63.
- BJØRK, T. E. 2006. *Quantification and Modeling of Deformation Processes; Motivated by Observations from the Hornelen Basin, Bremangerlandet*. PhD thesis, University of Oslo.
- BJØRNERUD, M. 2010. Rethinking conditions necessary for pseudotachylite formation: observations from the Otago schists, South Island, New Zealand. *Tectonophysics*, **490**, 69–80.
- BOS, B. & SPIERS, C. J. 2001. Experimental investigation into the microstructural and mechanical evolution of phyllosilicate-bearing fault rock under conditions favouring pressure solution. *Journal of Structural Geology*, **23**, 1187–1202.
- BOS, B. & SPIERS, C. J. 2002a. Fluid-assisted healing processes in gouge-bearing faults: insights from experiments on a rock analogue system. *Pure and Applied Geophysics*, **159**, 2537–2566.
- BOS, B. & SPIERS, C. J. 2002b. Frictional–viscous flow of phyllosilicate-bearing fault rock: microphysical model and implications for crustal strength profiles. *Journal of Geophysical Research*, **107**, 2028, doi: 10.1029/2001JB000301.
- BOS, B., PEACH, C. J. & SPIERS, C. J. 2000. Frictional–viscous flow of simulated fault gouge caused by the combined effects of phyllosilicates and pressure solution. *Tectonophysics*, **327**, 173–194.
- BRODSKY, E. E., ROWE, C. D., MENEGHINI, F. & MOORE, J. C. 2009. A geological fingerprint of extremely low viscosity fault fluids mobilized during an earthquake. *Journal of Geophysical Research*, **114**, B01303, doi: 10.1029/2008JB005633.
- BYRNE, T. 1982. Structural evolution of coherent terranes in the Ghost Rocks Formation, Kodiak Island, Alaska. In: LEGGETT, J. K. (ed.) *Trench–Forearc Geology: Sedimentation and Tectonics on Modern and Ancient Active Plate Margins*. Geological Society, London, Special Publications, **10**, 229–242.
- BYRNE, T. 1984. Early deformation in mélangé terranes of the Ghost Rocks Formation, Kodiak Islands, Alaska. In: RAYMOND, L. A. (ed.) *Mélanges: Their Nature, Origin and Significance*. Geological Society of America, Special Paper, **198**, 21–51.
- CHELONI, D., D'AGOSTINO, N. ET AL. 2010. Coseismic and initial post-seismic slip of the 2009 Mw 6.3 L'Aquila earthquake, Italy, from GPS measurements. *Geophysical Journal International*, **181**, 1539–1546.
- CHEN, J. L., WILSON, C. R., TAPLEY, B. D. & GRAND, S. 2007. GRACE detects coseismic and postseismic deformation from the Sumatra–Andaman earthquake. *Geophysical Research Letters*, **34**, L13302, doi: 10.1029//2007BL03056.
- CONNELLY, W. 1978. Uyak Complex, Kodiak Islands, Alaska: a Cretaceous subduction complex. *Geological Society of America Bulletin*, **89**, 755–769.
- COWAN, D. S. 1999. Do faults preserve a record of seismic slip? A field geologist's opinion. *Journal of Structural Geology*, **21**, 995–1001.
- DiTULLIO, L. & BYRNE, T. 1990. Deformation paths in the shallow levels of an accretionary prism: the Eocene Shimanto belt of southwest Japan. *Geological Society of America Bulletin*, **102**, 1420–1438.
- FARRIS, D. W., HAEUSSLER, P. J., FRIEDMAN, R., PATERSON, S., SALTUS, R. & AYUSO, R. 2006. Emplacement of the Kodiak batholith and slab-window migration. *Geological Society of America Bulletin*, **118**, 1360–1376.
- FARVER, J. R. & YUND, R. A. 1999. Oxygen bulk diffusion measurements and TEM characterization of a natural ultramylonite: implications for fluid transport in mica-bearing rocks. *Journal of Metamorphic Geology*, **17**, 669–683.
- FISHER, D. & BYRNE, T. 1987. Structural evolution of underthrusted sediments, Kodiak Islands, Alaska. *Tectonics*, **6**, 775–793.
- GAHALAUT, V. K., SUBRAHMANYAM, C., KUNDU, B., CATHERINE, J. K. & AMBIKAPATHY, A. 2010. Slow rupture in Andaman during 2004 Sumatra–Andaman earthquake: a probable consequence of subduction of 90°E ridge. *Geophysical Journal International*, **180**, 1181–1186, doi: 10.1111/j.1365682246X.2009.04449.x.
- GRATIER, J.-P., FAVREAU, P., RENARD, F. & PILI, E. 2002. Fluid pressure evolution during the earthquake cycle controlled by fluid flow and pressure solution crack sealing. *Earth Planets Space*, **54**, 1139–1146.
- GRATIER, J.-P., RENARD, F. & LABAUME, P. 1999. How pressure solution creep and fracturing processes interact in the upper crust to make it behave in both a brittle and viscous manner. *Journal of Structural Geology*, **21**, 1189–1197.
- GUEYDAN, F., MEHL, C. & PARRA, T. 2005. Stress–strain rate history of a midcrustal shear zone and the onset of brittle deformation inferred from quartz recrystallized grain size. In: GAPAIS, D., BRUN, J. P. & COBBOLD, P. R. (eds) *Deformation Mechanisms, Rheology and Tectonics: from Minerals to the Lithosphere*. Geological Society, London, Special Publications, **243**, 127–142.
- HAEUSSLER, P. J., BRADLEY, D. C., WELLS, R. & MILLER, M. L. 2003. Life and death of the Resurrection plate: evidence for its existence and subduction in the north-eastern Pacific in Paleocene–Eocene time. *Geological Society of America Bulletin*, **115**, 867–880.
- HANSEN, E. 1971. *Strain Facies*. Springer, New York.
- HARSH, P. W. 1982. Distribution of afterslip on the Imperial Fault. In: *The Imperial Valley, California Earthquake of October 15, 1979*. US Geological Survey, Professional Paper, **1254**, 193–203.
- HEILBRONNER, R. & KEULEN, N. 2006. Grain size and shape analysis of fault rocks. *Tectonophysics*, **427**, 199–216.
- HICKMAN, S. H. & EVANS, B. 1995. Kinetics of pressure solution at halite–silica interfaces and intergranular

- clay films. *Journal of Geophysical Research*, **100**, 13 113–13 132.
- HIPPERTT, J. 1999. Are S–C structures, duplexes and conjugate shear zones different manifestations of the same scale-invariant phenomenon? *Journal of Structural Geology*, **21**, 975–984.
- HIRTH, G. & TULLIS, J. 1992. Dislocation creep regimes in quartz aggregates. *Journal of Structural Geology*, **14**, 145–159.
- HUTTON, W., DEMETS, C., SÀNCHEZ, O., SUÀREZ, G. & STOCK, J. 2001. Slip kinematics and dynamics during and after the 1995 October 9 Mw = 8.0 Colima–Jalisco earthquake, Mexico, from GPS geodetic constraints. *Geophysical Journal International*, **146**, 637–658.
- IINUMA, T., OHTA, Y. ET AL. 2008. Postseismic slip associated with the 2007 Chuetsu-oki, Niigata, Japan Earthquake (M 6.8 on 16 July 2007) as inferred from GPS data. *Earth Planets Space*, **60**, 1087–1091.
- JARRARD, R. D. 2003. Subduction fluxes of water, carbon dioxide, chlorine, and potassium. *Geochemistry Geophysics Geosystems*, **4**, 8905, doi: 10.1029/2002GC000392.
- KANAGAWA, K. 2002. Frictional behavior of synthetic gouge-bearing faults under the operation of pressure solution. *Earth Planets Space*, **54**, 1147–1152.
- KEULEN, N., STÙNITZ, H. & HEILBRONNER, R. 2008. Healing microstructures of experimental and natural fault gouge. *Journal of Geophysical Research*, **113**, B06205, doi: 10.1029/2007JB005039.
- KRUHL, J. H. 1996. Prism- and basal-plane parallel sub-grain boundaries in quartz: a microstructural geothermobarometer. *Journal of Metamorphic Geology*, **14**, 581–589.
- KUSKY, T. M. & BRADLEY, D. C. 1999. Kinematic analysis of mélange fabrics: examples and applications from the McHugh Complex, Kenai Peninsula, Alaska. *Journal of Structural Geology*, **21**, 1773–1796.
- LIN, A. 1996. Injection veins of crushing-originated pseudotachylite and fault gouge formed during seismic faulting. *Engineering Geology*, **43**, 213–224.
- LINDE, A. T. & SACKS, I. S. 2002. Slow earthquakes and great earthquakes along the Nankai trough. *Earth and Planetary Science Letters*, **203**, 265–275.
- LISTER, G. S. & SNOKE, A. W. 1984. S–C mylonites. *Journal of Structural Geology*, **6**, 617–638.
- MALTMAN, A., LABAUME, P. & HOUSEN, B. 1997. Chapter 22: Structural geology of the décollement at the toe of the Barbadoes accretionary prism. In: SHIPLEY, T. H., OGAWA, Y., BLUM, P. & BAHR, J. M. (eds) *Proceedings of the Ocean Drilling Program, Scientific Results*, **156**. Ocean Drilling Program, College Station, TX, 279–292.
- MAMTANI, M. A. 2010. Strain-rate estimation using fractal analysis of quartz grains in naturally deformed rocks. *Journal of the Geological Society of India*, **75**, 202–209.
- MENEGRINI, F. & MOORE, J. C. 2007. Deformation and hydrofracture in a subduction thrust at seismogenic depths: the Rodeo Cove thrust zone, Marin Headlands, California. *Geological Society of America Bulletin*, **119**, 174–183.
- MENEGRINI, F., DI TORO, G., ROWE, C. D., MOORE, J. C., TSUTSUMI, A. & YAMAGUCHI, A. 2010. Record of mega-earthquakes in subduction thrusts: the black fault rocks of Pasagshak Point (Kodiak Island, Alaska). *Geological Society of America Bulletin*, **122**, 1280–1297, doi: 10.1030/B30049.1.
- MENEGRINI, F., MARRONI, M., MOORE, J. C., PANDOLFI, L. & ROWE, C. D. 2009. The process of underplating in the geologic record: structural diversity between the Franciscan Complex (California), the Kodiak Complex (Alaska) and the Internal Ligurian Units (Italy). *Geological Journal*, **44**, 126–152, doi: 10.1002/gj.1144.
- MONZAWA, N. & OTSUKI, K. 2003. Comminution and fluidization of granular fault materials: implications for fault slip behavior. *Tectonophysics*, **367**, 127–143.
- MOORE, G. W. 1969. New formations on Kodiak and adjacent islands, Alaska. *US Geological Survey Bulletin*, **1274-A**, A27–A35.
- MOORE, J. C. 1978. Orientation of underthrusting during latest Cretaceous and earliest Tertiary time, Kodiak Islands, Alaska. *Geology*, **6**, 209–213.
- MOORE, J. C., ROWE, C. & MENEGRINI, F. 2007. How can accretionary prisms elucidate seismogenesis in subduction zones? In: DIXON, T. & MOORE, J. C. (eds) *Seismogenic Zone of Subduction Thrust Faults. Margins: Theoretical and Experimental Earth Science Series*, **2**. Columbia University Press, New York, 288–314.
- MOUKARZEL, C. F. 1998. Isostatic phase transition and instability in stiff granular materials. *Physical Review Letters*, **81**, 1634–1637.
- NIEMEIJER, A., MARONE, C. & ELSWORTH, D. 2010. Frictional strength and strain weakening in simulated fault gouge: competition between geometrical weakening and chemical strengthening. *Journal of Geophysical Research*, **115**, B10207, doi: 10.1029/2009JB000838.
- NIEMEIJER, A. R. & SPIERS, C. J. 2005. Influence of phyllosilicates on fault strength in the brittle–ductile transition: insights from rock analog experiments. In: BRUHN, D. & BURLINI, L. (eds) *High-Strain Zones: Structure and Physical Properties*. Geological Society, London, Special Publications, **245**, 303–327.
- NIEMEIJER, A. R. & SPIERS, C. J. 2006. Velocity dependence of strength and healing behaviour in simulated phyllosilicate-bearing fault gouge. *Tectonophysics*, **427**, 231–253.
- NÜCHTER, J.-A. & STÖCKHERT, B. 2007. Vein quartz microfabrics indicating progressive evolution of fractures into cavities during postseismic creep in the middle crust. *Journal of Structural Geology*, **29**, 1445–1462.
- OBANA, K. & KODAIRA, S. 2009. Low-frequency tremors associated with reverse faults in a shallow accretionary prism. *Earth and Planetary Science Letters*, **287**, 168–174.
- OHMORI, K., TAIRA, A., TOKUYAMA, H., SAKAGUCHI, A., OKAMURA, M. & AIHARA, A. 1997. Paleothermal structure of the Shimanto accretionary prism, Shikoku, Japan: role of an out-of-sequence thrust. *Geology*, **25**, 327–330.
- OLESKIEWICH, D. A., HYNDMAN, R. D. & WANG, K. 1999. The updip and downdip limits to great subduction earthquakes: thermal and structural models of Cascadia, south Alaska, SW Japan, and Chile. *Journal of Geophysical Research*, **104**, 14,965–14,991.
- OTSUKI, K., MONZAWA, N. & NAGASE, T. 2003. Fluidization and melting of fault gouge during

- seismic slip: identification in the Nohima fault zone and implications for focal earthquake mechanisms. *Journal of Geophysical Research*, **108**, B42192, doi: 10/1029/2001JB001711, 2003.
- PEACOCK, S. M. & WANG, K. 1999. Seismic consequences of warm versus cool subduction metamorphism: examples from southwest and northeast Japan. *Science*, **286**, 937–939.
- PERFETTINI, H., AVOUAC, J.-P. ET AL. 2010. Seismic and aseismic slip on the Central Peru megathrust. *Nature*, **465**, 78–81, doi: 10.1038/nature09062.
- PLAFKER, G., MOORE, J. C. & WINKLER, G. R. 1994. Chapter 12: Geology of the southern Alaska margin. In: PLAFKER, G. & BERG, H. C. (eds) *The Geology of North America, G-1*. Geological Society of America, Boulder, CO, 389–449.
- POLET, J. & KANAMORI, H. 2000. Shallow subduction zone earthquakes and their tsunamigenic potential. *Geophysics Journal International*, **142**, 684–702.
- POWER, W. L. & TULLIS, T. E. 1989. The relationship between slickenside surfaces in fine-grained quartz and the seismic cycle. *Journal of Structural Geology*, **11**, 879–893.
- RENARD, F., BROSSE, E. & GRATIER, J. P. 2000. The different processes involved in the mechanism of pressure solution in quartz-rich rocks and their interactions. In: WORDEN, R. H. & MORAD, S. (eds) *Quartz Cementation in Sandstones*, Volume 29. Blackwell Science, Oxford, 67–78.
- RENARD, F., ORTOLEVA, P. & GRATIER, J. P. 1997. Pressure solution in sandstones: influence of clays and dependence on temperature and stress. *Tectonophysics*, **280**, 257–266.
- RING, U. & BRANDON, M. T. 1999. Ductile deformation and mass loss in the Franciscan Subduction Complex: implications for exhumation processes in accretionary wedges. In: RING, U., BRANDON, M. T., LISTER, G. S. & WILLETT, S. D. (eds) *Exhumation Processes: Normal Faulting, Ductile Flow and Erosion*. Geological Society, London, Special Publications, **154**, 55–86.
- ROGERS, G. & DRAGERT, H. 2003. Episodic tremor and slip on the Cascadia Subduction Zone: the chatter of silent slip. *Science*, **300**, 1942–1943.
- ROWE, C. D. 2007. *Snapshots of the earthquake cycle: an approach to subduction zone Paleo-Seismicity*. PhD, University of California. 185pp.
- ROWE, C. D., MOORE, J. C., MENEGHINI, F. & MCKERNAN, A. W. 2005. Large-scale pseudotachylites and fluidized cataclasites from an ancient subduction thrust fault. *Geology*, **33**, 937–940.
- RUTTER, E. H. 1983. Pressure solution in nature, theory and experiment. *Journal of the Geological Society*, **140**, 725–740.
- RUTTER, E. H. 1986. On the nomenclature of mode of failure transitions in rocks. *Tectonophysics*, **122**, 381–387.
- RUTTER, E. H. & ELLIOTT, D. 1976. The kinetics of rock deformation by pressure solution [and discussion]. *Philosophical Transactions of the Royal Society London A*, **283**, 203–219, doi: 10.108/rsta1976.0079.
- SAMMIS, C. G., OSBORNE, R. H., ANDERSON, J. L., BANERDT, M. & WHITE, P. 1986. Self-similar cataclasis in the formation of fault gouge. *Pure & Applied Geophysics*, **124**, 53–78.
- SCHWARTZ, S. Y. & ROKOSKY, J. M. 2007. Slow slip events and seismic tremor at circum-Pacific subduction zones. *Reviews of Geophysics*, **45**, RG3004, doi: 10.1029/2006RG000208.
- SHELLY, D. R., BEROZA, G. C., IDE, S. & NAKAMURA, S. 2006. Low-frequency earthquakes in Shikoku, Japan, and their relationship to episodic tremor and slip. *Nature*, **442**, 188–191, doi: 10.1038/nature04931.
- SHIMAMOTO, T. 1989. The origin of S-C mylonites and a new fault zone model. *Journal of Structural Geology*, **11**, 51–64.
- SHIMIZU, I. 1995. Kinetics of pressure solution creep in quartz: theoretical considerations. *Tectonophysics*, **245**, 121–134.
- SIBSON, R. H. 1975. Generation of pseudotachylite by ancient seismic faulting. *Geophysical Journal of the Royal Astronomical Society*, **43**, 775–794.
- SIBSON, R. H. 1977. Fault rocks and fault mechanisms. *Journal of the Geological Society, London*, **133**, 191–213.
- SIBSON, R. H. 1989. Earthquake faulting as a structural process. *Journal of Structural Geology*, **11**, 1–14.
- SIBSON, R. H. & TOY, V. G. 2007. The habitat of fault-generated pseudotachylite: Presence v. absence of friction-melt. In: ABERCROMBIE, R., MCGARR, A., KANAMORI, H. & DI TORO, G. (eds) *Earthquakes: Radiated Energy and the Physics of Faulting*. American Geophysical Union, Geophysical Monograph, **170**, 153–166.
- SINGH, S. K., ORTIZ, M., GUPTA, H. K. & RAMADASS, D. G. A. 2006. Slow slip below Port Blair, Andaman, during the great Sumatra-Andaman earthquake of 26 December 2004. *Geophysical Research Letters*, **33**, L03313, doi: 10.1029/2005GL025025.
- SMITH, S. A. F., COLLETTINI, C. & HOLDsworth, R. E. 2008. Recognizing the seismic cycle in ancient faults: CO<sub>2</sub>-induced fluidization of breccias in the footwall of a sealing low-angle normal fault. *Journal of Structural Geology*, **30**, 1034–1046.
- STÖCKHERT, B., BRIX, M. R., KLEINSCHRODT, R., HURFORD, A. J. & WIRTH, R. 1999. Thermochronometry and microstructures of quartz—a comparison with experimental flow laws and predictions on temperature of the brittle–plastic transition. *Journal of Structural Geology*, **21**, 351–369.
- SWEENEY, J. J. & BURNHAM, A. K. 1990. Evaluation of a simple model of vitrinite reflectance based on chemical kinetics. *AAPG Bulletin*, **74**, 1559–1570.
- TULLIS, J. & YUND, R. A. 1987. Transition from cataclastic flow to dislocation creep of feldspar: mechanisms and microstructures. *Geology*, **15**, 606–609, doi: 10.1130/00917613.
- UJIIE, K. 2002. Evolution and kinematics of an ancient décollement zone, mélange in the Shimanto accretionary complex of Okinawa Island, Ryukyu Arc. *Journal of Structural Geology*, **24**, 937–952.
- VAN NOORT, R., SPIERS, C. J. & PENNOCK, G. M. 2008. Compaction of granular quartz under hydrothermal conditions: controlling mechanisms and grain boundary processes. *Journal of Geophysical Research*, **113**, B12206, doi: 10.1029/2008JB005815.
- VROLIJK, P. 1987. *Paleohydrogeology and Fluid Evolution of the Kodiak Accretionary Complex, Alaska*. PhD thesis, University of California.
- VROLIJK, P., MYERS, G. & MOORE, J. C. 1988. Warm fluid migration along tectonic mélanges in the Kodiak Accretionary Complex, Alaska. *Journal of Geophysical Research*, **93**, 10 313–10 324.



# The microstructural character and mechanical significance of fault rocks associated with a continental low-angle normal fault: the Zuccale Fault, Elba Island, Italy

S. A. F. SMITH<sup>1,4\*</sup>, R. E. HOLDSWORTH<sup>1</sup>, C. COLLETTINI<sup>2,4</sup> & M. A. PEARCE<sup>3</sup>

<sup>1</sup>*Reactivation Research Group, Department of Earth Sciences, University of Durham, Durham DH1 3LE, UK*

<sup>2</sup>*Geologia Strutturale e Geofisica, Dipartimento Di Scienze della Terra, Università degli Studi di Perugia, Perugia 06120, Italy*

<sup>3</sup>*Geospatial Research Ltd, Department of Earth Sciences, University of Durham, Durham DH1 3LE, UK*

<sup>4</sup>*Present address: Istituto Nazionale di Geofisica e Vulcanologia (INGV), 605 Via di Vigna Murata, 00143 Rome, Italy*

\*Corresponding author (e-mail: steven.smith@ingv.it)

**Abstract:** The core of the Zuccale low-angle normal fault contains a distinctive fault-rock zonation that developed during exhumation, composed of a diversity of fault rocks derived from lithologically heterogeneous wall rocks. Field and microstructural analyses indicate that deformation mechanisms active within the fault core, including brittle fracture, dissolution–precipitation creep and crystal-plasticity, were active broadly contemporaneously. Initially, deformation was accommodated within frictionally weak and inherently stable talc-phyllonites. Although the talc-phyllonites can account for slip at low angles, grain-scale weakening effects were limited by changes over time to the structure of the fault core, resulting from interactions with subsidiary footwall faults. Ultimately, the talc-phyllonites were dismembered into a series of isolated lenses incapable of transmitting grain-scale weakening up to the fault scale. Following this, deformation was accommodated within well-connected units of dolomite-, quartz- and calcite-bearing cataclastite, fault breccia, and foliated fault gouge. Deformation progressively migrated through this latter sequence as a result of precipitation-hardening due to the widespread growth of dolomite. The complexity of fault-zone structure, combined with changes to fault-rock distribution over time, may have resulted in fundamental changes in fault-slip behaviour, an important point to consider given the recent spectrum of slip mechanisms identified along many tectonic faults.

Many outcrops of natural fault zones preserve a significant diversity of fault-rock types (e.g. Sibson 1977; Imber *et al.* 2001; Watts *et al.* 2007) that reflects the interaction between a large number of structural and metamorphic processes occurring at different times and crustal depths (Knipe 1989). Fault-rock type can significantly influence the permeability structure (Caine *et al.* 1996), strength (e.g. Holdsworth 2004; Jefferies *et al.* 2006; Moore & Rymer 2007; Collettini *et al.* 2009a) and frictional stability (e.g. Marone 1998; Faulkner *et al.* 2003) of fault zones, with important implications for seismicity and fluid-flow-related mineralization (Scholz 2002; Tullis *et al.* 2007). A key problem faced in many fault-zone studies concerns the spatial and temporal relationships between the constituent fault rocks (Knipe 1989). Have the fault rocks formed under different environmental conditions and been juxtaposed against one another

during progressive displacement? Or are they broadly contemporaneous having formed due to variations in lithology, fluid composition and strain rate? Or are they the result of a mixture of these two end-member possibilities? In all cases, this spatial and temporal heterogeneity is likely to result in a complex and continuously evolving mechanical structure (e.g. Childs *et al.* 1996; Chester & Chester 1998; Wibberley *et al.* 2008), whilst also providing valuable information on aspects of the exhumation history (Davis 1987; Watts *et al.* 2007).

This problem is particularly significant in low-angle normal faults, many of which preserve a significant diversity of fault rocks (e.g. Davis 1987; Lister & Davis 1989; Manatschal 1999; Cowan *et al.* 2003; Collettini & Holdsworth 2004; Hayman 2006). Normal faults that initiate and slip at low angles (<30°) are particularly important places to study fault rocks and fault mechanics

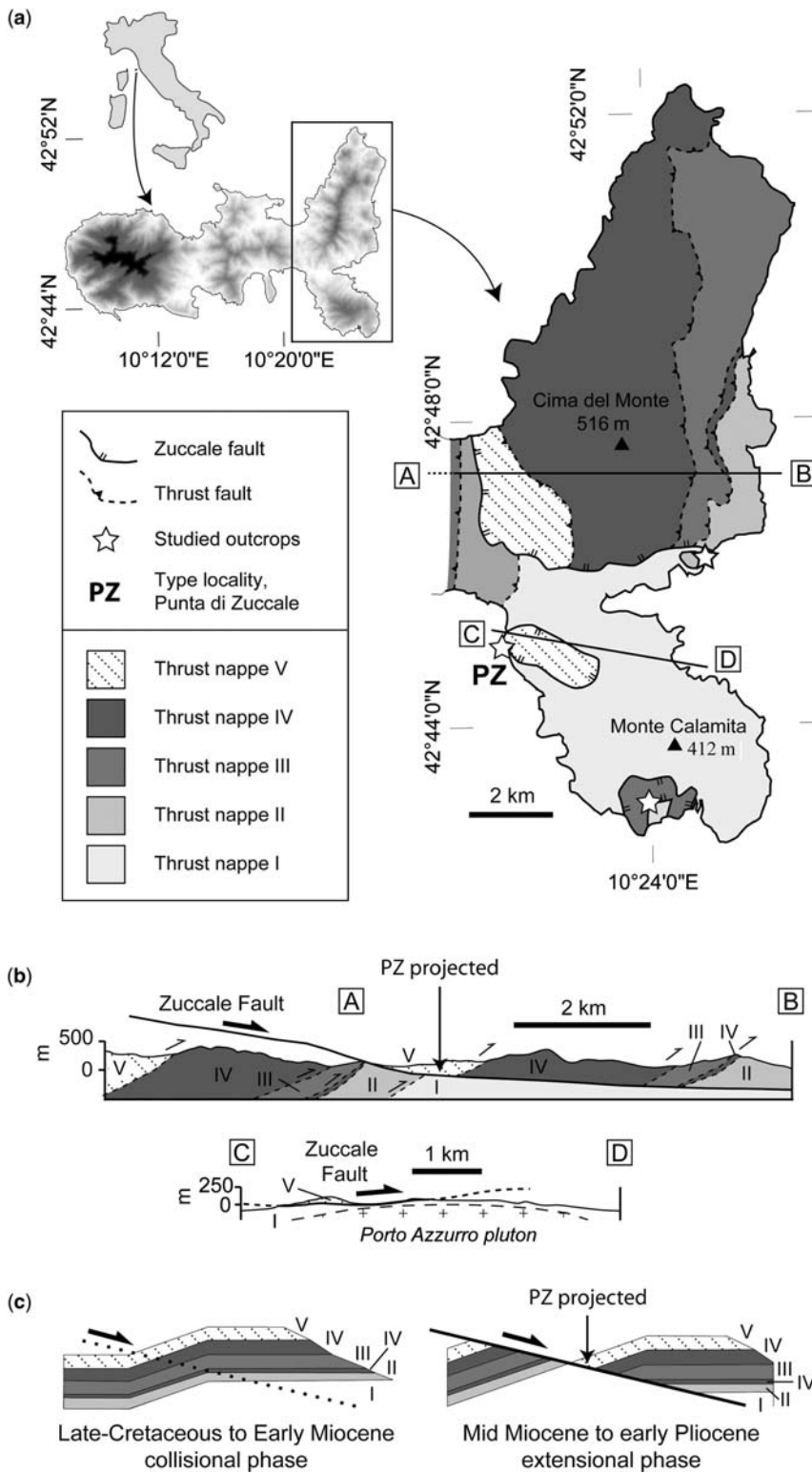


**Fig. 1.**

because they probably represent weak faults compared to the surrounding crust and to laboratory-determined values of rock friction (Byerlee 1978; Collettini & Sibson 2001). This requires a mechanical weakening of the constituent fault rocks, and, in the case of a large, crustal-scale structure, that weakening needs to be effective across a broad range of crustal depths and geological conditions (Axen 2004; Holdsworth *et al.* 2011).

Continental low-angle normal faults with displacements of more than about 10–15 km typically expose footwalls containing a continuum of ductile, semi-brittle and brittle fault rocks that record deformation under decreasing pressure and temperature conditions (e.g. Davis 1987; Miller 1992). These relationships were originally recognized along low-angle normal faults associated with ‘Cordilleran’ metamorphic core complexes in western North America (e.g. Coney 1980; Davis 1980, 1987), but they have subsequently been documented in other metamorphic core complexes in areas such as the Aegean Sea (Lister 1984; Kumerics *et al.* 2005; Mehl *et al.* 2005). Recent studies in the Black Mountains region of Death Valley, California (Cladouhos 1999; Cowan *et al.* 2003; Hayman *et al.* 2004; Hayman 2006), and in the eastern Swiss Alps (Manatschal 1999), have shown that upper-crustal brittle deformation was focused initially into broader zones of breccia and cataclasite, and later within relatively thin layers (<2–3 m) of fine-grained, foliated fault gouge (Manatschal *et al.* 2000; Hayman 2006).

In this paper, we present mineralogical and textual descriptions of upper-crustal fault rocks found along the Zuccale Fault, a kilometre-scale low-angle normal fault exposed on the Island of Elba, Italy. We summarize and build on previous work (e.g. Collettini & Holdsworth 2004; Smith *et al.* 2007, 2008; Collettini *et al.* 2009b), providing the most complete description of the fault rocks so far published. The Zuccale Fault possesses a distinctive fault-rock ‘zonation’, and a rich diversity of microstructures that record the operation of multiple deformation mechanisms. Some of the diversity reflects progressive changes in deformation process with time and provides important qualitative constraints on the exhumation history of the fault zone. Other associations point to the near simultaneous operation of different fault-zone processes, and shed new light

on how variable, yet broadly contemporaneous, deformation mechanisms may influence the slip behaviour along such faults.

## Geological setting and previous work

The northern Tyrrhenian–Apennine region of Italy has experienced two main phases of post-Cretaceous deformation, both of which migrated progressively from west to east (Elter *et al.* 1975; Pauselli *et al.* 2006). (1) Cretaceous–Quaternary collision between the Adria microplate and the Corsica–Sardinia microplate was followed by (2) Miocene–recent post-collisional extension, resulting in the opening of the Tyrrhenian basins (e.g. Alvarez 1972; Keller *et al.* 1994; Keller & Coward 1996; Jolivet *et al.* 1998). Eastwards migration of post-collisional extension (Malinverno & Ryan 1986; Doglioni *et al.* 1999; Rosenbaum & Lister 2004) was in part accommodated along a crustal-scale system of shallowly east-dipping low-angle normal faults (Barchi *et al.* 1998; Collettini & Barchi 2002; Collettini *et al.* 2006b; Pauselli *et al.* 2006; Chiaraluce *et al.* 2007). Prolonged regional uplift exhumed inactive low-angle normal faults in western Tuscany (Carmignani & Kligfield 1990) and in the Tyrrhenian islands, including the late Miocene–early Pliocene Zuccale Fault on the island of Elba (Daniel & Jolivet 1995; Keller & Coward 1996; Rossetti *et al.* 1999; Collettini & Holdsworth 2004).

Elba is composed of a series of thrust nappes that formed during late Cretaceous–early Miocene compression (Fig. 1). Trevisan *et al.* (1967) recognized five nappes, which he termed ‘complexes’, composed of diverse oceanic and continental units, all of which dip to the west (Fig. 1). These five nappes were cross-cut and displaced approximately 6 km eastwards by the later formed, shallowly east-dipping Zuccale Fault (Fig. 1) (Keller & Pialli 1990; Keller *et al.* 1994; Collettini & Holdsworth 2004). Movement along the Zuccale Fault was accompanied by syntectonic intrusion of upper-crustal igneous bodies, including the major Porto Azzurro pluton (Dini *et al.* 2002; Rocchi *et al.* 2002; Perugini & Poli 2007; Smith *et al.* 2011).

Collettini & Holdsworth (2004) recognized a series of distinctive types of fault rock within the

**Fig. 1.** (a) Geological map of Elba highlighting the five thrust nappes that are cross-cut and displaced by the Zuccale Fault. Thrust nappe I, Palaeozoic basement schists; thrust nappe II, Tuscan metamorphic sequence; thrust nappe III, Tuscan limestone sequence; thrust nappe IV, Ligurian ophiolite sequence; thrust nappe V, Cretaceous and Eocene flysch sequence (Trevisan *et al.* 1967). (b) Simplified cross-sections highlighting the geometry of the Zuccale Fault, determined by structural mapping, structure contour analysis and borehole data taken from Bortolotti *et al.* (2001). (c) Schematic diagram reconstructing the nappe sequence at the end of the collisional phase (early Miocene), which was subsequently cross-cut by the Zuccale Fault (mid-Miocene–early Pliocene).

Zuccale Fault that developed during prolonged fluid-assisted deformation and were exhumed from a depth of less than 8 km (their L1–L5 in Fig. 2). They showed that one of the principal characteristics of the Zuccale Fault is the presence of early brecciated fault rocks that were overprinted by foliated, phyllosilicate-rich fault rocks following the onset of stress-induced dissolution–precipitation creep. Collettini *et al.* (2009b) studied one of the fault-rock units in detail (L3), documenting the development of interconnected networks of talc due to influx of silica-rich fluids and reaction with dolomite protolith.

Allied rock deformation experiments by Collettini *et al.* (2009a) and Smith & Faulkner (2010) were used to assess the frictional properties of the various fault rocks. Both studies concluded that slip accommodated by interconnected networks of talc, a mineral that possesses a friction coefficient of  $<0.2$  over a wide range of pressures and temperatures (Moore & Lockner 2008), could explain movement along the Zuccale Fault at low angles. In addition, Smith & Faulkner (2010) suggested that late-stage movements could have been accommodated by fault gouges with a moderately low friction coefficient of around 0.4 or less.

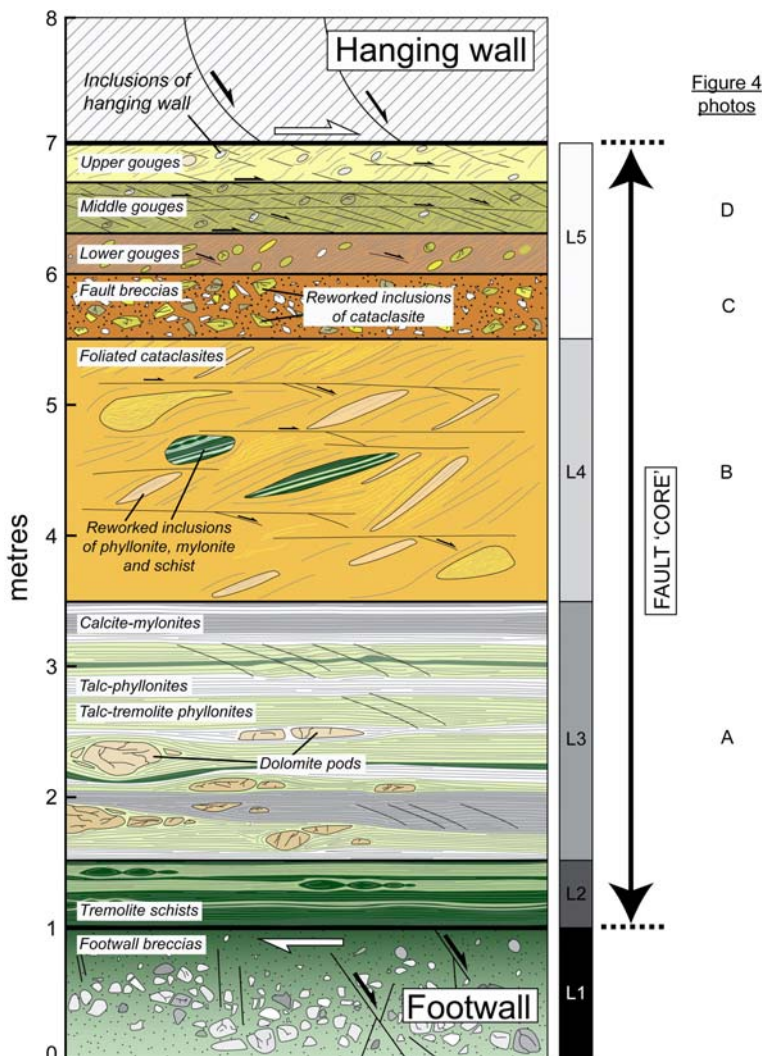


**Fig. 2.** Schematic structural log illustrating the fault-rock ‘zonation’ within the core of the Zuccale Fault. The structural log highlights the relative thickness and typical fabrics of each fault-rock type. L1–L5 refers to the fault-rock subdivisions used by Collettini & Holdsworth (2004) and Smith & Faulkner (2010).

## Analytical techniques

Analysis of fault rocks was carried out on 70 thin sections and 15 polished blocks prepared from samples collected at the type locality, Punta di Zuccale. Thin sections were studied using an optical microscope. Polished blocks were carbon coated and analysed using a Phillips XL30 W-filament scanning electron microscope (SEM) with an accelerating voltage of 20 keV and beam current of 1–3 nA. Electron backscatter diffraction analysis (EBSD; Prior 1999) was performed on one sample of calcite mylonite (described below). Maps of crystallographic orientation were collected using the same SEM with an accelerating voltage of 20 keV, a beam current of approximately 5 nA and a 1.25 µm step size. EBSD patterns were indexed automatically against a calcite match unit using Oxford-HKL Channel 5 software. Post-processing was carried out to remove isolated errors and replace these with the mean orientation of the surrounding pixels using an algorithm constrained by pattern quality. Maps are used to identify lattice misorientation between adjacent pixels, and sub-grain boundaries (with interpixel misorientations of <10°) are superimposed. Pole figures reveal the bulk preferred orientation of the sample and are constructed by taking one measurement from each grain and contouring the resulting data using a cone with an opening half-width of 15°. This prevents large grains (which have many more pixels than small grains) dominating the preferred orientation.

Fault-rock mineralogy was determined using a combination of optical microscopy, qualitative energy dispersive spectrometry (EDS) in the SEM and semi-quantitative X-ray diffraction analysis (XRD) carried out on 18 samples. XRD analysis was performed using a Phillips PW1050 instrument on <10 µm powders prepared by crushing samples using an agate ball mill or micronising mill. SiroQuant 3.0 software was used to quantify mineralogy.

## Fault-rock distribution and cross-cutting relationships

All of the field and microstructural observations presented below were derived from the type locality, Punta Di Zuccale (Fig. 1). At Punta di Zuccale, the fault zone is particularly well exposed for distances of hundreds of metres both parallel and perpendicular to the top-to-the-east transport direction, allowing an assessment of fault-zone geometry, fault-rock distribution, and the influence of minor faults in both the footwall and hanging wall. At other localities on Elba where the Zuccale

Fault is well exposed (Fig. 1a), field investigations by the authors indicate that the fault rocks are often overprinted by late iron-mineralization and skarn deposits related to regional magmatic activity (Tanelli *et al.* 2001), rendering interpretation of the fault-rock sequence more difficult.

At Punta di Zuccale, the Zuccale Fault places interbedded sandstones, marls and mudstones in the hanging wall against quartz–mica schists in the footwall (Figs 1–3). The hanging wall belongs to a Cretaceous deep-water turbidite sequence, while the footwall is part of the Palaeozoic metamorphic basement found extensively throughout the Tyrrhenian Islands and central Italy (Bortolotti *et al.* 2001). At Punta di Zuccale, the footwall is capped by a thin sequence (<20 m) of quartzites, thought to represent the metamorphosed Triassic cover (Bortolotti *et al.* 2001).

The Zuccale Fault at Punta di Zuccale consists of a well-defined fault core between 3 and 8 m thick (Figs 2 & 3). We consider the fault core that part of the fault zone containing well-developed fault rocks such as cataclasites and gouges that accommodated most of the strain and displacement. This differs slightly from some authors who use the term ‘core’ as a genetic term for the area of strain localization that develops within a broader fault zone after a long history of brittle damage (following Chester *et al.* 1993). The lower margin of the Zuccale Fault core lies at the boundary between the footwall and a unit of amphibole schists (Figs 2 & 3). The upper margin of the fault core lies at the boundary between the hanging wall and a unit of foliated fault gouges (Figs 2 & 3). In the upper part of the footwall, at Punta di Zuccale, there are a series of fault breccias up to about 5 m thick (recognized by Collettini & Holdsworth 2004 as forming prior to the foliated rocks within the fault core), some of which contain evidence of fluidization (Smith *et al.* 2008). Although the footwall breccias contain important evidence of local fluctuations of fluid pressure, they are not a regionally significant fault-rock unit. Instead, the breccias developed only in areas of the footwall containing the thin cap of Triassic quartzites (such as at Punta di Zuccale).

Fault rocks in the fault core are arranged into a series of shallowly dipping zones, each up to several metres thick and containing abundant top-to-the-east shear-sense criteria, such as asymmetric folds, shear bands and reworked clasts with asymmetric tails (Figs 2 & 3). It should be noted that not all of the fault rocks are present everywhere within the fault core, partly reflecting the influence of subsidiary footwall faults that locally disrupt the shallowly dipping fault-rock zonation (Smith *et al.* 2007). At Punta di Zuccale, the fault-rock sequence consists of the following units, from bottom to top (Figs 2 & 3):

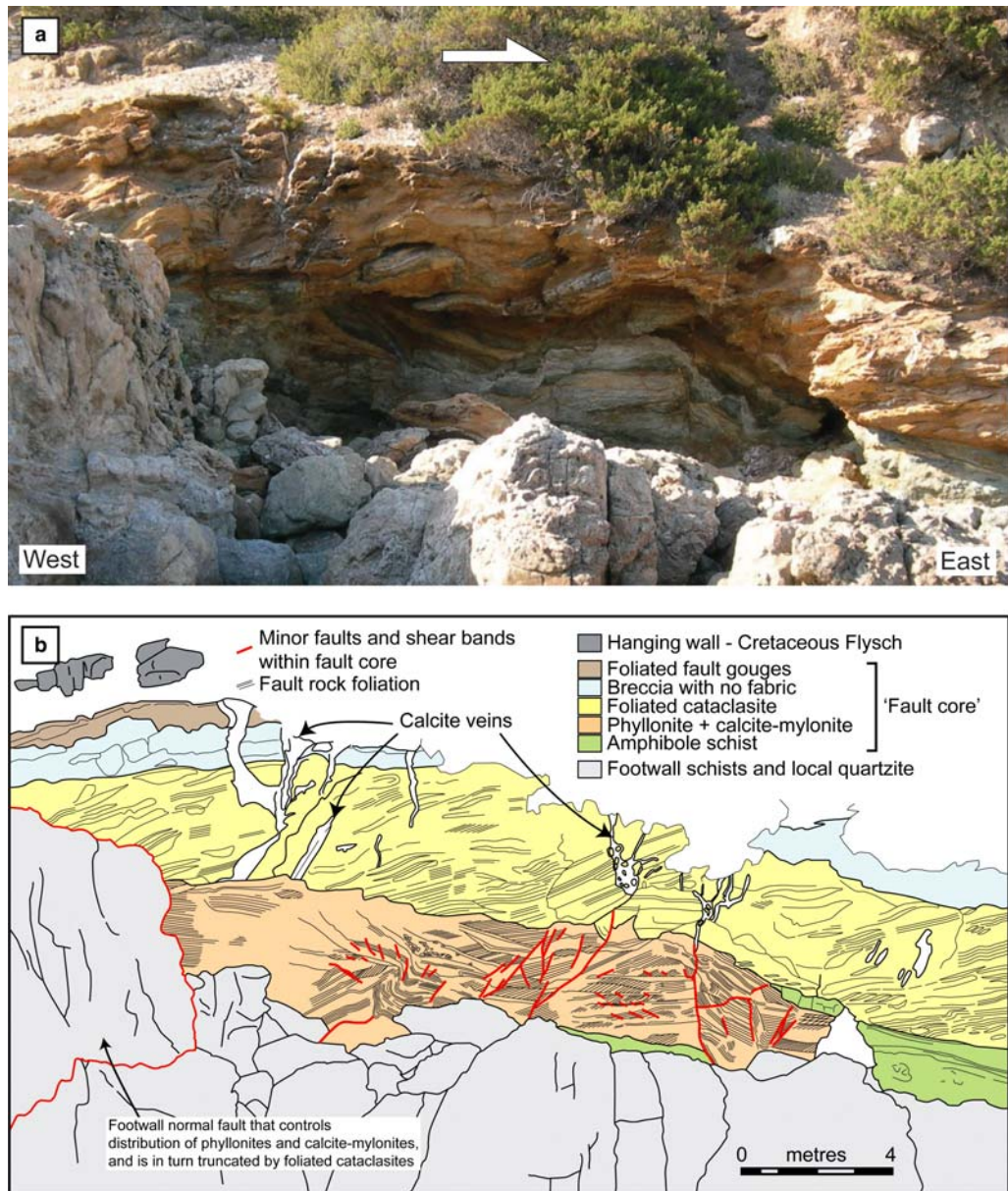


**Fig. 3.** Photograph (a) and detailed sketch (b) of the fault core at Punta di Zuccale. The fault core is between 3 and 8 m thick, and contains a series of shallowly dipping fault-rock units. Most of the fault rocks are pervasively foliated. The fault core is cross-cut by calcite hydrofracture veins, while the footwall contains a network of subsidiary normal faults that strongly influenced the distribution of fault rocks in the fault core (Smith *et al.* 2007). Note that in (b) the irregular contacts between the various fault rocks are mainly due to outcrop topography and not intrusions or 'injections' of one fault rock into another.

- *Amphibole schists:* these occur as a dark green–black, 5 cm–1.5 m-thick unit at the base of the fault core (Fig. 2).
- *Phyllonites and calcite-ultramylonites:* these two fault-rock components occur as an intensely foliated orange, white and green unit towards the

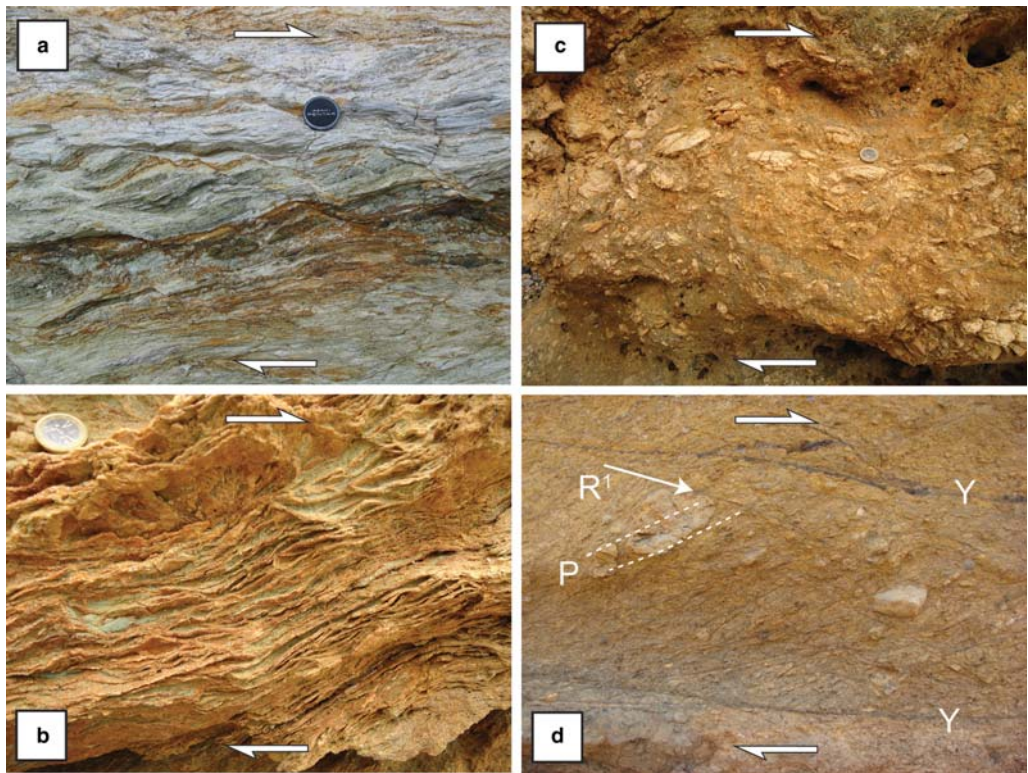


**Fig. 4.** Outcrop photographs of some of the fault-rock units within the fault core. All of the photographs are oriented with east to the right of the photograph and west to the left. (a) Strongly foliated phyllonites and calcite-ultramylonites. (b) Foliated cataclasites containing networks of thin dolomite veins. (c) Coarse fault breccias that lack internal structure and fabric. (d) Foliated fault gouges containing rounded survivor grains and clay-lined Reidel shears.

base of the fault core (Figs 2 & 4a). The principal foliation is defined by a compositional banding of calcite-, tremolite- and phyllosilicate-rich layers centimetres to tens of centimetres in thickness (Fig. 4a).

- *Foliated cataclasites:* these occur as a 3–4 metre-thick, yellow–light brown unit in the centre of the fault core (Figs 2 & 4b). The principal foliation is defined by: (a) preferred orientation of included clasts of amphibole schist, calcite-ultramylonite and phyllonite; (b) compositional banding of quartz- and dolomite-rich horizons centimetres thick; and (c) dolomite vein networks lying parallel to the compositional banding (e.g. Fig. 4b).
- *Breccias without internal fabric:* the breccias are up to 1.5 m thick, yellow–light brown in colour and contain no internal fabric (Figs 2 & 4c). They are dominated by angular clasts up to 20 cm in size, mainly derived from the underlying foliated cataclasites (>80% of clasts).

Note that these are distinct from the breccias found in the upper part of the footwall at Punta di Zuccale.

- *Foliated fault gouges:* these can be subdivided into three distinct variants (lower, middle and upper fault gouges). The gouges occupy the upper 50 cm–2 m of the fault core (Fig. 2) and are separated by laterally continuous shear surfaces enriched in dark-grey clays (Fig. 4d). All of the gouges contain a pervasive foliation, inclined roughly 25°–30° anticlockwise to the margins of the fault core (i.e. in a P-orientation, Fig. 4d) (Chester *et al.* 1985) and defined by: (a) preferred orientation of well-rounded survivor grains – isolated grains that appear to have largely escaped grain-fracturing processes (e.g. Engelder 1974; Cladouhos 1999); (b) compositional variations between quartz and carbonate layers up to several centimetres thick; and (c) clay-rich seams that anastomose around survivor grains.

At least locally at Punta di Zuccale, this fault-rock sequence represents a temporal sequence, in that fault rocks towards the top of the fault core are ‘younger’, and appear to have been stacked on top of fault rocks towards the base of the fault core. This temporal sequence is based on several cross-cutting criteria. First, reworked clasts of the underlying fault-rock units are often present within the overlying fault-rock units, but never vice versa. For example, clasts of amphibole schist can be found in the overlying phyllonites, calcite ultramylonites and foliated cataclasites (Fig. 2). Clasts of the phyllonites can be found in the overlying foliated cataclasites, and clasts of the foliated cataclasites are found throughout the breccias and fault gouges (Fig. 2). Secondly, as summarized in Smith *et al.* (2007), the phyllonites and calcite-ultramylonites are found as a series of isolated fault-rock lenses that were progressively dismembered owing to extensional movements across subsidiary footwall normal faults (Fig. 3). The footwall normal faults, which have displacements up to several metres, are sharply truncated at the base of the overlying foliated cataclasites (Fig. 3). This indicates that the phyllonites and calcite-mytonites formed early, were dismembered and isolated by movement across the footwall faults, and were then superseded by deformation accommodated within the foliated cataclasites (Smith *et al.* 2007). Thirdly, calcite hydrofracture veins (Collettini *et al.* 2006a) that cross-cut the fault-rock sequence are sometimes truncated by shear surfaces within the foliated fault gouges, suggesting that the gouges were the latest fault-rock unit to develop at Punta di Zuccale. The gouges also contain clasts of sandstone derived from the immediate hanging wall, not found in any of the underlying fault-rock units.

## Fault-rock microstructures at the type locality: Punta di Zuccale

### *Amphibole schists*

Large (up to 1000 µm) fractured clasts of actinolite lie within a strongly foliated, fine-grained matrix containing actinolite grains 10–20 µm in length (Fig. 5a, b). Apatite, chlorite, biotite and a platy K-Al-silicate phase are minor constituents of the matrix. Amphibole compositions became progressively more Fe-rich over time. For example, relatively Fe-rich actinolite was precipitated in intragranular fractures and in the strain shadow regions of large clasts (Fig. 5a, b). In addition, the matrix is cross-cut by numerous cataclastic shears up to 100 µm thick that contain fractured and rotated grains of relatively Fe-rich actinolite (Fig. 5b).

### *Phyllonites and calcite-ultramylonites*

*Phyllonites.* The phyllonites occur in close association with pods (up to tens of centimetres in diameter) of heavily fractured dolostone, representing the main protolith (Figs 2 & 6a). The dolostone consists of equigranular dolomite grains approximately 100 µm in diameter that are replaced by calcite along grain boundaries, and are cross-cut by fractures filled by calcite and fibrous talc (Fig. 6a, b) (Collettini *et al.* 2009b). The boundaries between dolomite and calcite are sharp and typically have a lobate morphology (Fig. 6b). Talc also occurs as randomly oriented grains 100–200 µm long dispersed throughout the dolostone protolith, where it is clearly associated with small intergranular fractures.

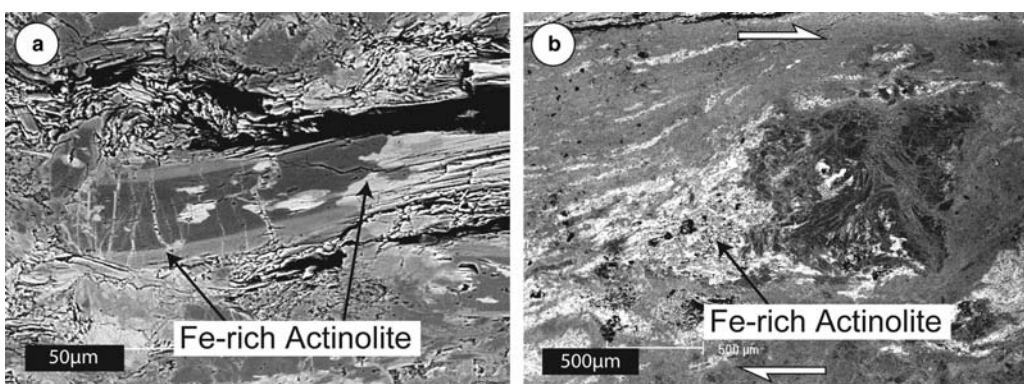


**Fig. 5.** Amphibole schists. (a) SEM image of a fractured amphibole grain, showing thin fractures in-filled by Fe-rich actinolite. (b) SEM image showing a large, fractured porphyroblast surrounded by a strain shadow of Fe-rich actinolite. Throughout the manuscript, the following abbreviations are used in the figures: Ca, calcite; Do, dolomite; Qtz, quartz; Tc, talc; Tr, tremolite.

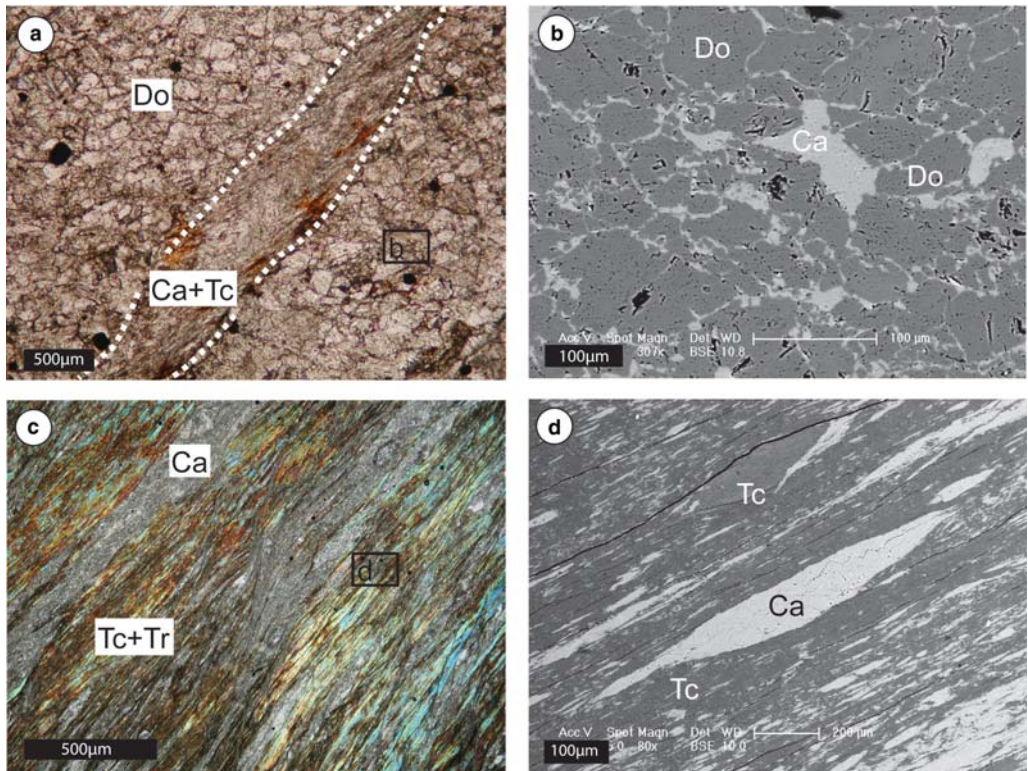


**Fig. 6.** Phyllonites. (a) Photomicrograph in plane-polarized light showing a fracture cross-cutting the dolostone protolith. The fracture contains calcite and fibrous talc. (b) SEM image of dolostone aggregates being replaced by calcite. (c) Photomicrograph in cross-polarized light showing layers of calcite-mylonite interbanded with layers of fibrous talc and tremolite. (d) Detailed SEM image of talc-rich foliation planes, and elongate porphyroclasts of calcite.

In high-strain areas (Fig. 6c, d) adjacent to the fractured pods of dolostone, the phyllonitic foliation is defined by a preferred orientation of elongate talc and tremolite grains up to 200 μm in length, and a compositional banding of talc-, tremolite- and calcite-rich layers up to several hundreds of μm wide (Fig. 6c, d). In these areas dolomite was completely replaced by calcite and talc. Calcite occurs in elongate polycrystalline ribbons, and as rounded clasts (Fig. 6d) (Collettini *et al.* 2009b). Talc dominates the matrix (see Collettini *et al.* 2009b for details), together with minor amounts of tremolite, and both host numerous thin (<1000 μm) calcite veins that formed parallel to the main foliation.

**Calcite-ultramylonites.** The calcite-ultramylonites typically occur as lenses or layers up to a few centimetres thick within the surrounding phyllonites (Fig. 2). Foliation in the ultramylonites is defined by a compositional banding of calcite and tremolite layers up to 1000 μm thick, and also by grain size variations within the calcite matrix (Fig. 7a).

Calcite occurs as: (1) fine-grained (8–10 μm) homogenous aggregates that dominate the mylonitic matrix (e.g. Fig. 7a, b); and (2) relatively coarse-grained veins that typically cross-cut the mylonitic foliation at high angles (Fig. 7c). The veins are between 100 and 1000 μm in width, and were progressively sheared into concordance with the foliation in the surrounding fine-grained matrix (Fig. 7c), associated with a marked reduction in grain size.

EBSM analysis reveals that vein calcite contains numerous subgrain boundaries across which there is 2°–5° of crystallographic misorientation, while matrix calcite is characterized by grain boundaries across which there is more than 25° of crystallographic misorientation, indicating that the matrix experienced pervasive dynamic recrystallization (Fig. 7c). Subgrains within the vein calcite are often of a similar size to grains in the surrounding matrix (8–10 μm). The texture of matrix calcite is characterized by a *c*-axes (0001) maxima that is broadly perpendicular to the main foliation,

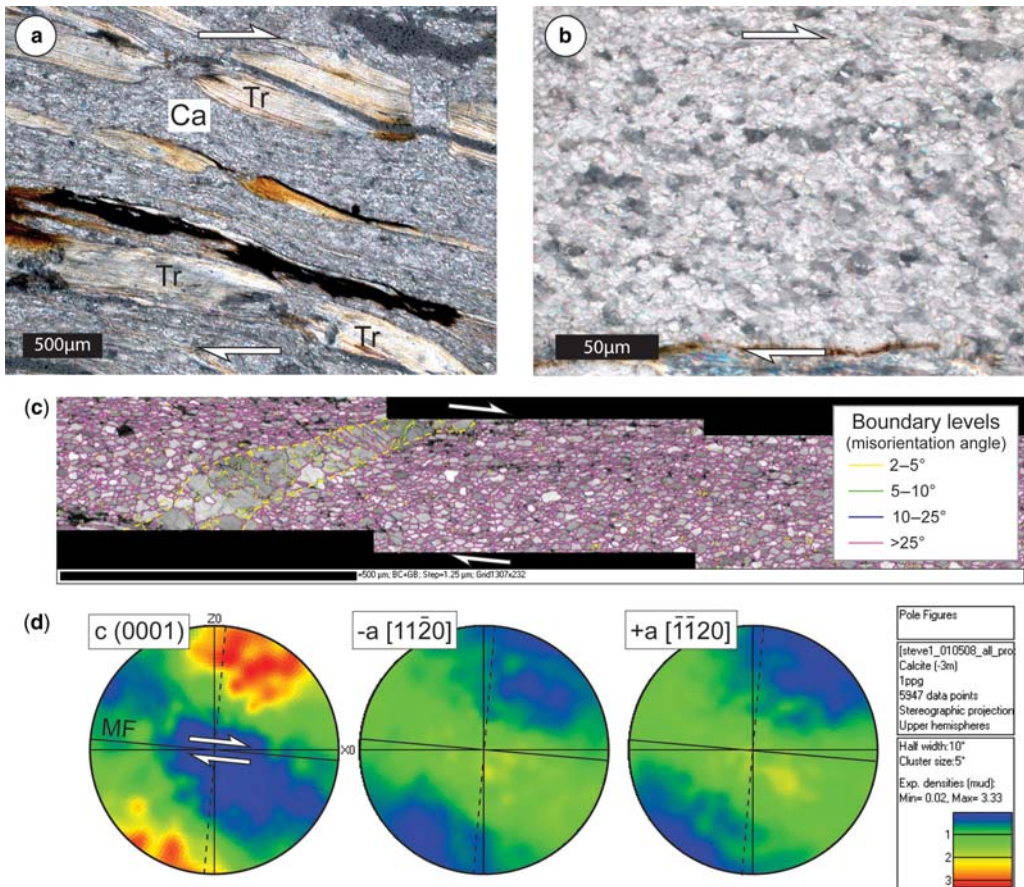


**Fig. 7.** Calcite ultramylonites. (a) Photomicrograph in crossed-polarized light highlighting the compositional banding of calcite and tremolite layers. (b) Photomicrograph in crossed-polarized light of fine-grained, recrystallized calcite matrix. (c) EBSD band contrast map overprinted with subgrain and grain-boundary misorientation levels. Boundary levels are detected by analysing the crystallographic misorientation of pairs of grains. Note the presence of numerous low-angle subgrain boundaries in the calcite vein, whilst the matrix grains are generally separated by high-angle boundaries. (d) Crystallographic preferred orientation data from the fine-grained matrix of the calcite ultramylonites determined by EBSD analysis. The data are presented as pole figures (equal-area, upper-hemisphere stereoplots) constructed by using one point per grain ( $n = 5947$ ). MF, mylonitic foliation; the dashed line represents a plane lying orthogonal to the mylonitic foliation.

although there is a small rotation ( $c. 15^\circ$ ) of the  $c$ -axes in a synthetic direction with respect to the top-to-the-east shear sense (Fig. 7d).

#### Foliated cataclasites

Subrounded to subangular clasts of dolomite sit within a matrix of fine-grained ( $<50 \mu\text{m}$ ) quartz, dolomite, apatite, Fe-oxide and a K-Al-silicate clay phase (Fig. 8a, b). The dolomite clasts frequently have a blocky–elongate morphology and exhibit a diffuse chemical zoning, suggesting derivation from pre-existing dolomite veins or

cements. Matrix phases show clear evidence of fracturing and progressive grain-size reduction. The foliated cataclasites are cross-cut by numerous discrete shear surfaces that are enriched in fine-grained ( $<50 \mu\text{m}$ ) quartz and broadly parallel the margins of the fault core (e.g. Fig. 8a).

The foliated cataclasites host networks of syntectonic dolomite veins that often account for more than 90% of the fault rock (Fig. 8c, d). Veins are typically 200–1000  $\mu\text{m}$  thick, closely spaced, and interconnected (Fig. 8c, d). These vein networks parallel the dominant foliation that lies at  $25^\circ$ – $30^\circ$  to the margins of the fault core (Fig. 8c, d) (i.e. in

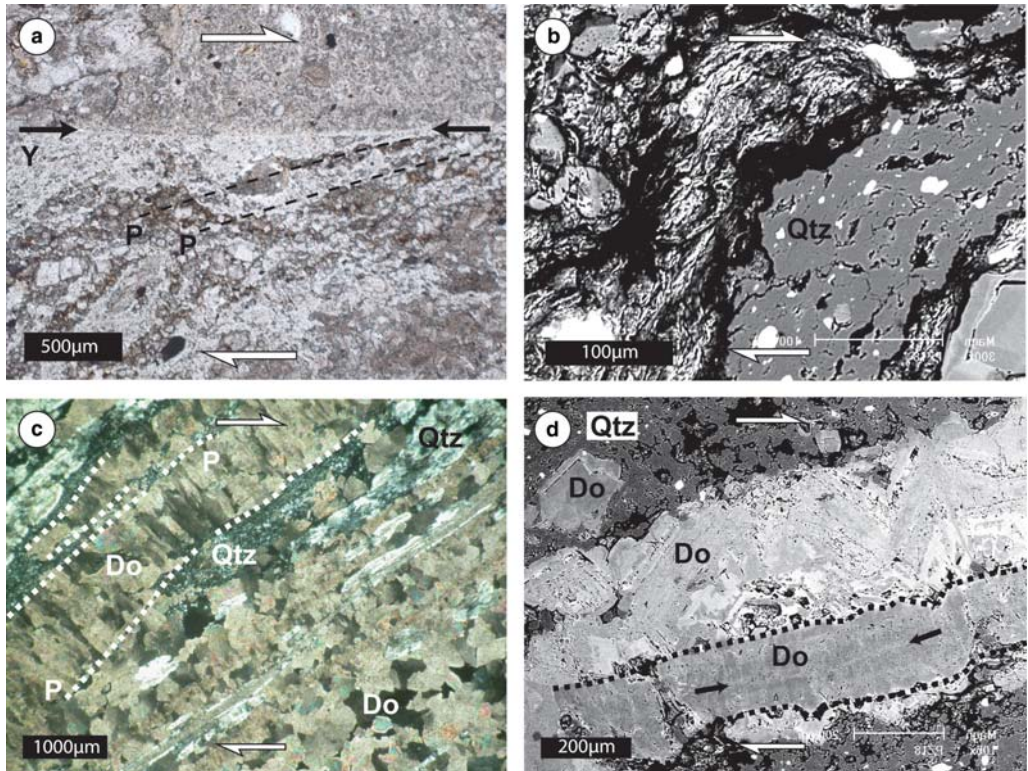


**Fig. 8.** Foliated cataclasites. (a) Photomicrograph in plane-polarized light showing the dominant foliation defined by a compositional banding of quartz- and dolomite-rich layers, and a preferred orientation of large survivor grains. The P-foliation is cross-cut by discrete Y-shears (between black arrows) that are enriched in fine-grained quartz. (b) SEM image showing a preferred orientation of quartz, Fe-oxides and clay in the matrix of the foliated cataclasites. (c) Photomicrograph in crossed-polarized light highlighting the geometry of dolomite vein networks. (d) SEM image showing a dolomite vein with a central core that is relatively poor in Fe, flanked by wide rims of Fe-rich dolomite.

a P-orientation: Chester *et al.* 1985). Most dolomite veins display a central area that contains blocky or elongate-blocky grain morphologies, surrounded by rims of coarse-grained euhedral dolomite that is relatively enriched in Fe and most probably grew post-tectonically (Fig. 8d). Elongate-blocky grains are typically oriented perpendicular to vein margins, and are 100–200 μm long and up to 100 μm wide. However, it is rare to find evidence of multiple growth episodes within individual veins, such as crack-seal banding.

#### Fault breccias

The breccias are characterized by clasts of the underlying foliated cataclasites that are set within a well-cemented and fine-grained matrix of quartz, dolomite and calcite (Fig. 9a). Syntectonic dolomite cement was precipitated within irregular inter- and intragranular fractures 500–2000 μm thick, and

also within irregular vein networks surrounding large clasts (Fig. 9a). Dolomite was then replaced by both syn- and post-tectonic calcite (Fig. 9b). Calcite initially replaced dolomite along grain boundaries and along specific growth zones, eventually leading to the complete replacement of dolomite aggregates (Fig. 9b).

#### Fault gouges

The fault gouges contain 5–15% survivor grains at the hand-specimen scale, mainly of dolomite, quartz, calcite and grains of sandstone derived from the immediate hanging wall. The matrix contains dolomite, quartz, calcite, minor chlorite and a K-Al clay phase (Fig. 10a). Dolomite occurs as fine-grained (<10 μm), rounded–subrounded grains that are often elongate and aligned parallel to the P-foliation (Chester *et al.* 1985). In the lower fault gouges dolomite occurs as a syntectonic

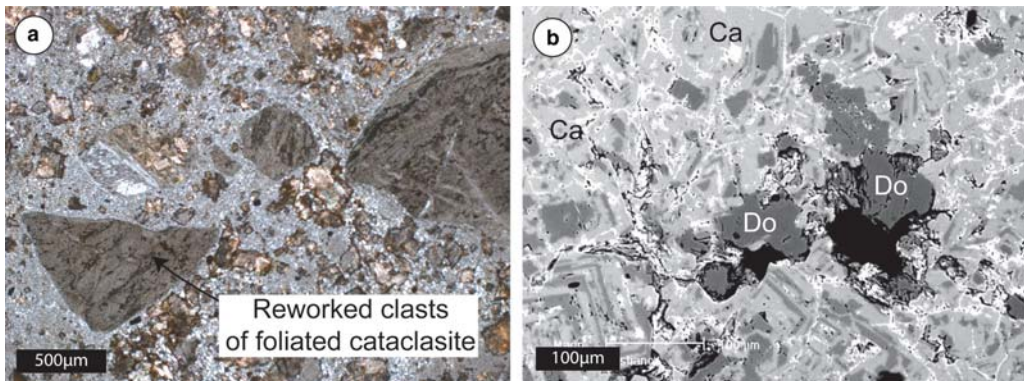


**Fig. 9.** Fault breccias. (a) Photomicrograph in crossed-polarized light showing angular clasts of foliated cataclasite sitting within a fine-grained matrix of quartz, chlorite and dolomite. (b) SEM image showing an aggregate of euhedral, post-tectonic dolomite replaced by calcite.

cement precipitated in thin tensile veins (<1 mm) around the margins of survivor grains, and also in intergranular fractures. In the upper fault gouges, dolomite is widely replaced by calcite (50–95% replacement), which is also precipitated in thin (<100 μm) shear veins that parallel the margins of the fault core (Fig. 10b).

## Discussion

Like many examples of regional-scale fault zones, including other low-angle normal faults, the Zuccale Fault preserves a diverse assemblage of fault rocks, most of them foliated and organized into a series of shallowly dipping layers or lenticular zones orientated broadly parallel to the margins of the core (Figs 2 & 3). The fault rocks preserve

microstructural evidence for the operation of different deformation mechanisms, including: (1) fracturing and cataclastic grain-size reduction in the amphibole schists, dolomite pods within the talc-phyllonites, foliated cataclasites, breccias and fault gouges; (2) fluid-assisted mass transfer and dissolution–precipitation creep in the amphibole schists, talc-bearing phyllonites and, perhaps, along the clay-bearing shears in the fault gouges; and (3) crystal-plasticity, most probably by dislocation creep (e.g. De Meer *et al.* 2002; Bestmann & Prior 2003), in the calcite-ultramylonites. In some cases, these deformation mechanisms overlapped in time or were active broadly contemporaneously. For example, the calcite-ultramylonites are cross-cut by veins that were progressively sheared into concordance with the surrounding foliation, indicating that plastic deformation alternated with brittle

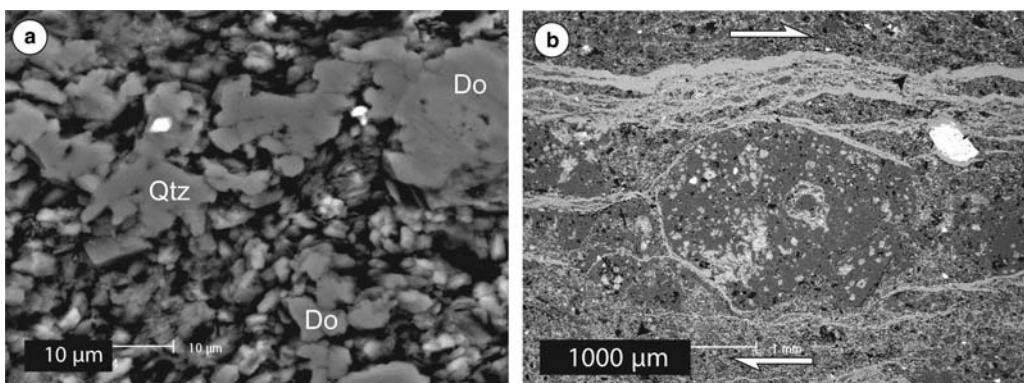
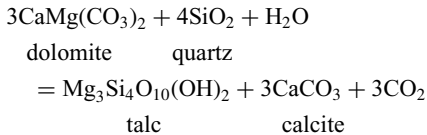


**Fig. 10.** Fault gouges. (a) SEM image of the matrix, showing quartz and dolomite grains with platy clays in the interstices. (b) SEM image of a rounded calcite and quartz survivor grain, surrounded by a thin calcite vein. The matrix also contains thin calcite veins.

fracture. In addition, Collettini *et al.* (2009b) suggested that brittle fracture of the dolomite pods embedded within the talc-phylloites allowed an influx of silica-bearing fluids, leading to the formation of calcite and talc by the reaction (e.g. Gordon & Greenwood 1970):



The fibrous nature of calcite and talc, and the observation that talc was commonly precipitated in strain shadows around clasts of calcite, indicates that growth occurred by fluid-assisted diffusive mass-transfer processes (Rutter 1976; Andreani *et al.* 2005). Once talc had formed a through-going, interconnected network, deformation was accommodated in part by frictional sliding along talc foliation planes (Collettini *et al.* 2009b).

Deformation along through-going, interconnected layers of talc is likely to result in a very low frictional strength. Talc has an experimentally determined frictional strength,  $\mu$ , of  $<0.2$  over a wide range of pressures and temperatures (Moore & Lockner 2008), and also exhibits inherently stable sliding behaviour that favours fault creep as the dominant slip mechanism (Moore & Lockner 2008; Collettini *et al.* 2009a). In contrast, the foliated cataclasites, fault breccias and fault gouges contain dolomite, calcite and quartz as dominant minerals, all of which have higher frictional strengths in the range  $0.5 < \mu < 0.8$  (Weeks & Tullis 1985; Mair & Marone 1999; Morrow *et al.* 2000). These minerals are characterized in some instances by inherently unstable sliding behaviour that can lead to fracture nucleation and propagation (e.g. Marone 1998; Mair & Marone 1999). More generally, the diverse mineralogy within the Zuccale Fault, coupled with the clear availability of fluids, has significant implications for the mechanisms and possible interactions of fault-zone-weakening processes. These weakening processes include reaction softening due to changes in mineralogy (e.g. growth of talc), the onset of grain-size-sensitive solution–precipitation creep and other diffusive mass-transfer mechanisms, and the localized, cyclic development of high pore-fluid pressures due to the trapping of fluids in the fault zone. It is clear in the Zuccale Fault that each of the deformation processes leading to weakening were profoundly influenced by one another. For example, the onset of diffusive-creep mechanisms and mineralogical alteration processes was triggered by fluid influx following initial cataclasis. The resulting

development of foliated, phyllosilicate-rich fault rocks led to a greater capacity for fault sealing, which in turn allowed fluid pressures to build up.

The fault-rock sequence at Punta di Zuccale formed during progressive exhumation of the fault zone, and is also determined to some extent by the position and lithology of the pre-existing thrust nappes. We envisage the fault-rock sequence as forming during progressive down-dip movement of various hanging wall lithologies (fault-rock protoliths), which were sequentially placed in contact with the basement schists and quartzites that form the footwall at Punta di Zuccale. Considering Figure 1c, the tremolite schists at the base of the fault core are likely to have been derived from thrust nappe IV, the talc-phylloites and calcite-ultramylonites from thrust nappes II and III, the foliated cataclasites from thrust nappes II and III, and the fault gouges from thrust nappe V that currently forms the local hanging wall at Punta di Zuccale. In addition to this diversity of hanging-wall lithologies, cross-cutting relationships preserved in the fault core at Punta di Zuccale indicate that deformation was localized first within fault rocks at the base of the fault core (tremolite schists, phylloites/calcite-ultramylonites), and later within fault rocks towards the top of the fault core (foliated cataclasites, breccias, fault gouges). A critical question to address is what controlled this migration, and specifically, why did deformation not simply continue to localize within the talc-phylloites once they had formed, given that the phylloites represent an extremely weak horizon capable of accommodating low-angle movements?

We suggest that grain-scale weakening effects due to interconnected talc were limited by changes to the internal geometry of the Zuccale Fault and the distribution of fault rocks over time. Specifically, Smith *et al.* (2007) documented using field observations that the talc-phylloites were progressively dismembered into a series of isolated fault-rock lenses, up to tens of metres in length, due to broadly synchronous movement on networks of subsidiary footwall faults (Fig. 3). This is significant because even if the talc-phylloites had at one time formed a continuous fault-rock horizon, progressive dismemberment meant that ultimately they were not interconnected on length scales greater than a few metres, and hence were unable to transmit grain-scale weakening effects up to the fault-scale. At that point, deformation was inevitably accommodated by other, more continuous fault-rock horizons, such as the foliated cataclasites that are currently preserved as a 3–4 m-thick well-connected layer.

A similar question is why deformation was transferred from the foliated cataclasites to the fault breccias (dominated by reworked clasts from

the underlying foliated cataclasites) and ultimately to the foliated fault gouges (containing clasts of the local hanging wall). In the field, the foliated cataclasites are rich in dolomite veins, very few of which preserve evidence of multiple episodes of vein opening and sealing. This indicates that once the veins had formed, and dolomite was precipitated, the veins were sealed and hardened, so that the following episode of high fluid pressures generated a new vein. In addition, the matrix of the foliated cataclasites is well cemented by dolomite, a mineral with an experimentally determined frictional strength of approximately 0.5–0.8 (Weeks & Tullis 1985; De Paola *et al.* 2011). We suggest that the foliated cataclasites were ultimately strengthened and underwent ‘precipitation-hardening’ due to the widespread growth of dolomite, leading to migration of deformation into the fault breccias and foliated fault gouges. Similar occurrences of reaction- or precipitation-hardening, followed by a migration of deformation away from the sites of mineral precipitation, have been documented in fault zones that experienced widespread syntectonic growth of epidote and K-feldspar (e.g. Di Toro & Pennacchioni 2005; Stoetz *et al.* 2007).

The complex distribution of fault rocks within the core of the Zuccale Fault, coupled with the range of observed deformation mechanisms, leads us to suggest that the Zuccale Fault accommodated deformation by a range of diverse slip mechanisms. Let us consider the talc-phyllonites and calcite-ultramylonites as an example, and assume that these fault-rock units at one point formed a well-connected horizon within the fault core (Smith *et al.* 2007). Both of them are likely to have accommodated strain by stable creep, and indeed their strengths may adequately explain slip at low angles over a wide range of depths in the upper crust (Collettini *et al.* 2009b). Over time, however, the geometry of the fault core, and the distribution of fault rocks within the fault core, were modified by interactions with subsidiary footwall (and hanging wall) normal faults, leading to dismemberment of the talc-phyllonites and calcite-ultramylonites, until eventually they were isolated as a series of fault-rock lenses. At this stage, deformation was mainly accommodated within well-connected layers of cataclasite, breccia and gouge, possessing high frictional strengths and potentially unstable frictional behaviour. Notwithstanding the possibility that other weakening mechanisms such as high fluid pressures may have been active, unstable deformation can result in fracture nucleation and propagation, and stick-slip-type behaviour. The discrete shear surfaces enriched in fine-grained quartz locally cutting the foliated cataclasites (Fig. 8a) are a potential indication of instability and slip localization.

In recent years, high-resolution GPS and seismological data have revealed that many tectonic faults, including active low-angle normal faults (Chiarioluce *et al.* 2007; Hreinsdottir & Bennett 2009), exhibit a spectrum of complex fault-slip behaviours, including earthquake rupture, repeating earthquakes and slow slip phenomena (e.g. Waldhauser *et al.* 2004; Fagereng & Sibson 2010; Perfettini *et al.* 2010). The physical processes responsible for this slip diversity are poorly understood, but our field and microstructural observations from the Zuccale Fault indicate that they may have their origins in the complexity of fault-zone structure and fault-rock distribution, and in mechanically diverse deformation mechanisms that are often active broadly contemporaneously.

## Conclusions

Fault rocks within the core of the Zuccale Fault preserve microstructural evidence for a range of deformation processes, at times active broadly contemporaneously, including cataclasis and brittle fracture, dissolution–precipitation creep and crystal-plasticity. These deformation processes, coupled with the diverse mineralogy, were responsible for a range of potential slip mechanisms, from stable creep at low friction within the talc-bearing phyllonites, to potentially unstable slip within the dolomite-, quartz- and calcite-bearing foliated cataclasites, breccias and gouges. The observed fault-rock zonation formed as a result of the structural juxtaposition of different fault rocks derived from pre-existing, lithologically heterogeneous thrust nappes, as well as the reworking of fault rocks during displacement. Deformation was first localized within the talc-bearing phyllonites before being progressively transferred to a unit of foliated cataclasites, and, ultimately, to fault breccias and foliated fault gouges. Although the talc-phyllonites were capable of accommodating low-angle movements, grain-scale weakening effects due to interconnected layers of talc were ultimately limited by changes to the structure of the fault core, resulting in stretching and dismemberment of the phyllonites to the extent that they were no longer able to cause fault-scale weakening. Similarly, accommodation of slip within the foliated cataclasites was limited by widespread precipitation of dolomite, leading to precipitation hardening. The spectrum of fault-slip behaviours identified along many tectonic faults in recent years may reflect both the complexity of fault-zone structure and fault-rock distribution, as well as the interplay of diverse deformation mechanisms.

S. Smith was supported by a Durham University Postgraduate Fellowship, and is currently supported by

European Research Council Starting Grant no. 205175 (USEMS). R. Holdsworth acknowledges receipt of a Leverhulme Fellowship to support his research. X-Ray diffraction analysis was carried out by A. Calder at the Materials Analysis Service, St Andrews University, Scotland. Thorough reviews by C. Rowe and N. Hayman, and comments by Å. Fagereng, helped us to focus and improve the manuscript considerably. A review of an earlier version of the manuscript by N. Mancktelow is also gratefully acknowledged. S. Smith thanks J. Imber and D. Faulkner for stimulating discussions during the course of his PhD.

## References

- ALVAREZ, W. 1972. Rotation of Corsica–Sardinia microplate. *Nature*, **235**, 103–105.
- ANDREANI, M., BOULLIER, A. M. & GRATIER, J. P. 2005. Development of schistosity by dissolution–crystallization in a Californian serpentinite gouge. *Journal of Structural Geology*, **27**, 2256–2267.
- AXEN, G. J. 2004. Mechanics of Low-Angle Normal Faults. *Rheology and Deformation of the Lithosphere at Continental Margins*. Margins: Theoretical and Experimental Earth Science Series. Columbia University Press, New York, 46–91.
- BARCHI, M. R., MINELLI, R. & PIALLI, G. 1998. The CROP 03 profile: a synthesis of results on deep structures of the northern Apennines. *Memorie della Società Geologica Italiana*, **52**, 383–400.
- BESTMANN, M. & PRIOR, D. J. 2003. Intragranular dynamic recrystallisation in naturally deformed calcite marble: diffusion accommodated grain boundary sliding as a result of subgrain rotation recrystallisation. *Journal of Structural Geology*, **25**, 1597–1613.
- BORTOLOTTI, V., FAZZUOLI, M., PANDELI, E., PRINCIPI, G., BABBINI, A. & CORTI, S. 2001. Geology of central and eastern Elba Island, Italy. *Ophioliti*, **26**, 97–150.
- BYERLEE, J. 1978. Friction of rocks. *Pure and Applied Geophysics*, **116**, 615–626.
- CAINE, J. S., EVANS, J. P. & FORSTER, C. B. 1996. Fault zone architecture and permeability structure. *Geology*, **24**, 1025–1028.
- CARMIGNANI, L. & KLIBFIELD, R. 1990. Crustal extension in the northern Apennines – the transition from compression to extension in the alpi apuane core complex. *Tectonics*, **9**, 1275–1303.
- CHESTER, F. M. & CHESTER, J. S. 1998. Ultracataclasite structure and friction processes of the Punchbowl fault, San Andreas system, California. *Tectonophysics*, **295**, 199–221.
- CHESTER, F. M., EVANS, J. P. & BIEGEL, R. L. 1993. Internal structure and weakening mechanisms of the San Andreas Fault. *Journal of Geophysical Research*, **98**, 771–786.
- CHESTER, F. M., FRIEDMAN, M. & LOGAN, J. M. 1985. Foliated cataclasites. *Tectonophysics*, **111**, 139–146.
- CHIARALUCE, L., CHIARABBA, C., COLLETTINI, C., PICCININI, D. & COCCO, M. 2007. Architecture and mechanics of an active low-angle normal fault: Alto Tiberina Fault, northern Apennines, Italy. *Journal of Geophysical Research – Solid Earth*, **112**, B10310, doi: 10.1029/2007JB005015.
- CHILD, C., WATTERSON, J. & WALSH, J. J. 1996. A model for the structure and development of fault zones. *Journal of the Geological Society, London*, **153**, 337–340.
- CLADOUHOS, T. T. 1999. Shape preferred orientations of survivor grains in fault gouge. *Journal of Structural Geology*, **21**, 419–436.
- COLLETTINI, C. & BARCHI, M. R. 2002. A low-angle normal fault in the Umbria region (Central Italy): a mechanical model for the related microseismicity. *Tectonophysics*, **359**, 97–115.
- COLLETTINI, C. & HOLDSWORTH, R. E. 2004. Fault zone weakening and character of slip along low-angle normal faults: insights from the Zuccale fault, Elba, Italy. *Journal of the Geological Society*, **161**, 1039–1051.
- COLLETTINI, C. & SIBSON, R. H. 2001. Normal faults, normal friction? *Geology*, **29**, 927–930.
- COLLETTINI, C., DE PAOLA, N. & GOULTY, N. R. 2006a. Switches in the minimum compressive stress direction induced by overpressure beneath a low-permeability fault zone. *Terra Nova*, **18**, 224–231.
- COLLETTINI, C., DE PAOLA, N., HOLDSWORTH, R. E. & BARCHI, M. R. 2006b. The development and behaviour of low-angle normal faults during Cenozoic asymmetric extension in the Northern Apennines, Italy. *Journal of Structural Geology*, **28**, 333–352.
- COLLETTINI, C., NIEMEIJER, A., VITI, C. & MARONE, C. J. 2009a. Fault zone fabric and fault weakness. *Nature*, **462**, 907–910.
- COLLETTINI, C., VITI, C., SMITH, S. A. F. & HOLDSWORTH, R. E. 2009b. Development of interconnected talc networks and weakening of continental low-angle normal faults. *Geology*, **37**, 567–570.
- CONEY, P. J. 1980. Cordilleran metamorphic core complexes: a review. In: CRITTENDEN, M. D., CONEY, P. J. & DAVIS, G. H. (eds) *Cordilleran Metamorphic Core Complexes*. Geological Society of America, Memoirs, **153**, 7–31.
- COWAN, D. S., CLADOUHOS, T. T. & MORGAN, J. K. 2003. Structural geology and kinematic history of rocks formed along low-angle normal faults, Death Valley, California. *Geological Society of America Bulletin*, **115**, 1230–1248.
- DANIEL, J. M. & JOLIVET, L. 1995. Detachment faults and pluton emplacement – Elba Island (Tyrrenian Sea). *Bulletin de la Societe Geologique de France*, **166**, 341–354.
- DAVIS, G. A. 1980. Structural characteristics of metamorphic core complexes, southern Arizona. In: CRITTENDEN, M. D., CONEY, P. J. & DAVIS, G. H. (eds) *Cordilleran Metamorphic Core Complexes*. Geological Society of America, Memoirs, **153**, 35–77.
- DAVIS, G. A. 1987. A shear-zone model for the structural evolution of metamorphic core complexes in south-eastern Arizona. In: COWARD, M. P., DEWEY, J. F. & HANCOCK, P. L. (eds) *Continental Extensional Tectonics*. Geological Society, London, Special Publications, **28**, 247–266.
- DE MEER, S., DRURY, M. R., DE BRESSER, J. H. P. & PENNOCK, G. M. 2002. Current issues and new developments in deformation mechanisms, rheology and tectonics. In: DE MEER, S., DRURY, M. R., DE

- BRESSER, J. H. P. & PENNOCK, G. M. (eds) *Deformation Mechanisms, Rheology and Tectonics: Current Status and Future Perspectives*. Geological Society, London, 1–27.
- DE PAOLA, N., HIROSE, T., MITCHELL, T., DI TORO, G., VITI, C. & SHIMAMOTO, T. 2011. Fault lubrication and earthquake propagation in thermally unstable rocks. *Geology*, **39**, 35–38.
- DINI, A., INNOCENTI, F., ROCCHI, S., TONARINI, S. & WESTERMAN, D. S. 2002. The magmatic evolution of the late Miocene laccolith–pluton–dyke granitic complex of Elba Island, Italy. *Geological Magazine*, **139**, 257–279.
- DI TORO, G. & PENNACCHIONI, G. 2005. Fault plane processes and mesoscopic structure of a strong-type seismogenic fault in tonalites (Adamello batholith, Southern Alps). *Tectonophysics*, **402**, 55–80.
- DOGLIONI, C., HARABAGLIA, P., MERLINI, S., MONGELLI, F., PECCERILLO, A. & PIROMALLO, C. 1999. Orogenes and slabs vs. their direction of subduction. *Earth Science Reviews*, **45**, 167–208.
- ELTER, P., GIGLIA, G., TONGIORGI, M. & TREVISAN, L. 1975. Tensional and compressional areas in recent (Tortonian to present) evolution of the northern Apennines. *Bollettino di Geofisica Teorica e Applicata*, **17**, 3–18.
- ENGELDER, J. T. 1974. Cataclasis and the generation of fault gouge. *Geological Society of America Bulletin*, **85**, 1515–1522.
- FAGERENG, Å. & SIBSON, R. H. 2010. Melange rheology and seismic style. *Geology*, **38**, 751–754.
- FAULKNER, D. R., LEWIS, A. C. & RUTTER, E. H. 2003. On the internal structure and mechanics of large strike-slip fault zones: field observations of the Carboneras fault in southeastern Spain. *Tectonophysics*, **367**, 235–251.
- GORDON, T. M. & GREENWOOD, H. J. 1970. The reaction: dolomite + quartz + water = talc + calcite + carbon dioxide. *American Journal of Science*, **268**, 225–242.
- HAYMAN, N. W. 2006. Shallow crustal fault rocks from the Black Mountain detachments, Death Valley, CA. *Journal of Structural Geology*, **28**, 1767–1784.
- HAYMAN, N. W., HOUSEN, B. A., CLADOUHOS, T. T. & LIVI, K. 2004. Magnetic and clast fabrics as measurements of grain-scale processes within the Death Valley shallow crustal detachment faults. *Journal of Geophysical Research – Solid Earth*, **109**, B05409, doi: 10.1029/2003JB02902.
- HOLDSWORTH, R. E. 2004. Weak faults – Rotten cores. *Science*, **303**, 181–182.
- HOLDSWORTH, R. E., VAN DIGGELEN, E. W. E., SPIERS, C. J., DE BRESSER, J. H. P., WALKER, R. J. & BOWEN, L. 2011. Fault rocks from the SAFOD core samples: implications for weakening at shallow depths along the San Andreas Fault, California. *Journal of Structural Geology*, **33**, 132–144.
- HREINSDÓTTIR, S. & BENNETT, R. A. 2009. Active aseismic creep on the Alto Tiberina low-angle normal fault, Italy. *Geology*, **37**, 683–686.
- IMBER, J., HOLDSWORTH, R. E., BUTLER, C. A. & LLOYD, G. E. 1997. Fault-zone weakening processes along the reactivated Outer Hebrides Fault Zone, Scotland. *Journal of the Geological Society*, **154**, 105–109.
- IMBER, J., HOLDSWORTH, R. E., BUTLER, C. A. & STRACHAN, R. A. 2001. A reappraisal of the Sibson–Scholz fault zone model: The nature of the frictional to viscous ('brittle-ductile') transition along a long-lived crustal-scale fault, Outer Hebrides, Scotland. *Tectonics*, **20**, 601–624.
- JEFFERIES, S. P., HOLDSWORTH, R. E., SHIMAMOTO, T., TAKAGI, H., LLOYD, G. E. & SPIERS, C. J. 2006. Origin and mechanical significance of foliated cataclastic rocks in the cores of crustal-scale faults: examples from the Median Tectonic Line, Japan. *Journal of Geophysical Research – Solid Earth*, **111**, B12303, doi: 10.1029/2005JB004205.
- JOLIVET, L., FACCENNA, C. ET AL. 1998. Midcrustal shear zones in postorogenic extension: example from the northern Tyrrhenian Sea. *Journal of Geophysical Research – Solid Earth*, **103**, 12 123–12 160.
- KELLER, J. V. A. & COWARD, M. P. 1996. The structure and evolution of the Northern Tyrrhenian Sea. *Geological Magazine*, **133**, 1–16.
- KELLER, J. V. A. & PIAILLI, G. 1990. Tectonics of the island of Elba: a reappraisal. *Bollettino della Società Geologica Italiana*, **109**, 413–425.
- KELLER, J. V. A., MINELLI, G. & PIAILLI, G. 1994. Anatomy of late orogenic extension – the northern Apennines case. *Tectonophysics*, **238**, 275–294.
- KNIPE, R. J. 1989. Deformation mechanisms – recognition from natural tectonites. *Journal of Structural Geology*, **11**, 127–146.
- KUMERICUS, C., RING, U., BRICHAU, S., GLODNY, J. & MONIE, P. 2005. The extensional Messaria shear zone and associated brittle detachment faults, Aegean Sea, Greece. *Journal of the Geological Society, London*, **162**, 701–721.
- LISTER, G. S. 1984. Metamorphic core complexes of Cordilleran type in the Cyclades, Aegean Sea, Greece. *Geology*, **12**, 221–225.
- LISTER, G. S. & DAVIS, G. A. 1989. The origin of metamorphic core complexes and detachment faults formed during Tertiary continental extension in the northern Colorado River region, U.S.A. *Journal of Structural Geology*, **11**, 65–94.
- MAIR, K. & MARONE, C. 1999. Friction of simulated fault gouge for a wide range of velocities and normal stresses. *Journal of Geophysical Research*, **104**, 28 899–28 914, doi: 10.1029/1999JB900279.
- MALINVERNO, A. & RYAN, W. B. F. 1986. Extension in the Tyrrhenian Sea and shortening in the Apennines as result of Arc migration driven by sinking of the lithosphere. *Tectonics*, **5**, 227–245.
- MANATSCHAL, G. 1999. Fluid- and reaction-assisted low-angle normal faulting: evidence from rift-related brittle fault rocks in the Alps (Err Nappe, eastern Switzerland). *Journal of Structural Geology*, **21**, 777–793.
- MANATSCHAL, G., MARQUER, D. & FRUH-GREEN, G. L. 2000. Channelized fluid flow and mass transfer along a rift-related detachment fault (Eastern Alps, southeast Switzerland). *Geological Society of America Bulletin*, **112**, 21–33.
- MARONE, C. 1998. Laboratory-derived friction laws and their application to seismic faulting. *Annual Review of Earth and Planetary Sciences*, **26**, 643–696.
- MEHL, C., JOLIVET, L. & LACOMBE, O. 2005. From ductile to brittle: evolution and localization of deformation

- below a crustal detachment (Tinos, Cyclades, Greece). *Tectonics*, **24**, TC4017, doi: 10.1029/2004TC001767.
- MILLER, M. G. 1992. Brittle faulting induced by ductile deformation of a Rheologically Stratified Rock sequence, badwater turtleback, Death-Valley, California. *Geological Society of America Bulletin*, **104**, 1376–1385.
- MOORE, D. E. & LOCKNER, D. A. 2008. Talc friction in the temperature range 25–400°C: relevance for fault-zone weakening. *Tectonophysics*, **449**, 120–132.
- MOORE, D. E. & RYMER, M. J. 2007. Talc-bearing serpentinite and the creeping section of the San Andreas fault. *Nature*, **448**, 795–797.
- MORROW, C. A., MOORE, D. E. & LOCKNER, D. A. 2000. The effect of mineral bond strength and adsorbed water on fault gouge frictional strength. *Geophysical Research Letters*, **27**, 815–818, doi: 10.1029/1999GL008401.
- PAUSELLI, C., BARCHI, M. R., FEDERICO, C., MAGNANI, M. B. & MINELLI, G. 2006. The crustal structure of the Northern Apennines (central Italy): an insight by the CROP03 seismic line. *American Journal of Science*, **306**, 428–450.
- PERFETTINI, H., AVOUAC, J.-P. ET AL. 2010. Seismic and aseismic slip on the central Peru megathrust. *Nature*, **465**, 78–81.
- PERUGINI, D. & POLI, G. 2007. Tourmaline nodules from Capo Bianco aplite (Elba Island, Italy): an example of diffusion limited aggregation growth in a magmatic system. *Contributions to Mineralogy and Petrology*, **153**, 493–508.
- PRIOR, D. J., BOYLE, A. P. ET AL. 1999. The application of electron backscatter diffraction and orientation contrast imaging in the SEM to textural problems in rocks. *American Mineralogist*, **84**, 1741–1759.
- ROCCHI, S., WESTERMAN, D. S., DINI, A., INNOCENTI, F. & TONARINI, S. 2002. Two-stage growth of laccoliths at Elba Island, Italy. *Geology*, **30**, 983–986.
- ROSENBAUM, G. & LISTER, G. S. 2004. Neogene and Quaternary rollback evolution of the Tyrrhenian Sea, the Apennines, and the Sicilian Maghrebides. *Tectonics*, **23**, TC1013, doi: 10.1029/2003TC001518.
- ROSSETTI, F., FACCENNA, C., JOLIVET, L., FUNICIELLO, R., TECCE, F. & BRUNET, C. 1999. Syn- versus post-orogenic extension: the case study of Giglio Island (Northern Tyrrhenian Sea, Italy). *Tectonophysics*, **304**, 71–93.
- RUTTER, E. H. 1976. Kinetics of rock deformation by pressure solution. *Philosophical Transactions of the Royal Society of London Series A – Mathematical Physical and Engineering Sciences*, **283**, 203–219.
- SCHOLZ, C. H. 2002. *The Mechanics of Earthquakes and Faulting*. 2nd edn. Cambridge University Press, Cambridge.
- SIBSON, R. H. 1977. Fault rocks and fault mechanisms. *Journal of the Geological Society, London*, **133**, 191–213.
- SMITH, S. A. F. & FAULKNER, D. 2010. Laboratory measurements of the frictional properties of the Zuccale low-angle normal fault, Elba Island, Italy. *Journal of Geophysical Research*, **115**, B02407, doi: 10.1029/2008JB006274.
- SMITH, S. A. F., COLLETTINI, C. & HOLDSWORTH, R. E. 2008. Recognizing the seismic cycle along ancient faults: CO<sub>2</sub>-induced fluidization of breccias in the footwall of a sealing low-angle normal fault. *Journal of Structural Geology*, **30**, 1034–1046.
- SMITH, S. A. F., HOLDSWORTH, R. E. & COLLETTINI, C. 2011. Interactions between low-angle normal faults and plutonism: insights from the Island of Elba, Italy. *Geological Society of America Bulletin*, **123**, 329–346.
- SMITH, S. A. F., HOLDSWORTH, R. E., COLLETTINI, C. & IMBER, J. 2007. Using footwall structures to constrain the evolution of low-angle normal faults. *Journal of the Geological Society, London*, **164**, 1187–1191.
- STOESZ, E., WINTSCH, R. P. & SCHIEBER, J. 2007. Textural evidence for reaction hardening by feldspar precipitation in mylonites. Paper presented at the 42nd Annual Meeting of the Northeastern Section, GSA, 12–14 March, University of New Hampshire, Durham, NH. *Geological Society of America Abstracts with Programs*, **39**, 97.
- TANELLI, G., BENVENUTI, M. ET AL. 2001. The iron mineral deposits of Elba Island: state of the art. *Ophioliti*, **26**, 239–248.
- TREVISAN, L., MARINELLI, G. ET AL. 1967. *Carta Geologica dell'Isola d'Elba, Consiglio Nazionale delle Ricerche. Gruppo di Ricerca per la Geologia dell'Appennino centro-settentrionale e della Toscana*. Pisa.
- TULLIS, T. E., BURGMANN, R. ET AL. 2007. Group report: rheology of fault rocks and their surroundings. In: HANDY, M. R., HIRTH, G. & HOVIUS, N. (eds) *Tectonic Faults: Agents of Change on a Dynamic Earth*. MIT Press, Cambridge, MA, 183–204.
- WALDHAUSER, F., ELLSWORTH, W. L., SCHAFF, D. P. & COLE, A. 2004. Streaks, multiplets, and holes: high-resolution spatiotemporal behaviour of Parkfield seismicity. *Geophysical Research Letters*, **31**, L18608, doi: 10.1029/2004GL020649.
- WATTS, L. M., HOLDSWORTH, R. E., SLEIGHT, J. A., STRACHAN, R. A. & SMITH, S. A. F. 2007. The movement history and fault rock evolution of a reactivated crustal-scale strike-slip fault: the Walls Boundary Fault Zone, Shetland. *Journal of the Geological Society, London*, **164**, 1037–1058.
- WEEKS, J. D. & TULLIS, T. E. 1985. Frictional sliding of dolomite: a variation in constitutive behaviour. *Journal of Geophysical Research*, **90**, 7821–7826, doi: 10.1029/JB090fb09P07821.
- WIBBERLEY, C. A. J., YIELDING, G. & DI TORO, G. 2008. Recent advances in the understanding of fault zone internal structure: a review. In: WIBBERLEY, C. A. J., KURZ, W., IMBER, J., HOLDSWORTH, R. E. & COLLETTINI, C. (eds) *The Internal Structure of Fault Zones: Implications for Mechanical and Fluid Flow Properties*. Geological Society, London, Special Publications, **299**, 5–33.



# Diverse habitats of pseudotachylytes in the Alpine Fault Zone and relationships to current seismicity

VIRGINIA G. TOY\*, SAMUEL RITCHIE & RICHARD H. SIBSON

*Geology Department, University of Otago, PO Box 56, Dunedin 9054, New Zealand*

\*Corresponding author (e-mail: [virginia.toy@otago.ac.nz](mailto:virginia.toy@otago.ac.nz))

**Abstract:** Pseudotachylytes are ubiquitous within New Zealand's Alpine Fault Zone, occurring as: (i) thin fault veins parallel to existing hanging wall mylonitic foliation; (ii) thicker fault and injection veins around and within metabasite lenses in hanging wall fault rocks and on the footwall–hanging wall boundary; (iii) chaotic injected masses within footwall-derived, granitoid mylonites; and (iv) chaotic injected masses into cataclasites within the fault core.

Overall, pseudotachylytes are not volumetrically dominant enough to have formed during all increments of earthquake slip on the Alpine Fault. We propose they were mostly generated during regular moderate magnitude events or during foreshock and aftershock sequences to larger earthquakes. The largest volume pseudotachylytes occur in footwall-derived mylonites (type (iii)). This may indicate that high-stress, anhydrous seismic slip is most common in the footwall. Most types (i), (ii) and (iii) pseudotachylytes formed at or near the base of the seismogenic zone, at temperatures up to 350 °C and at depths of 7–10 km or more. Ductilely overprinted pseudotachylytes represent the down-dip termination of large fault ruptures in a zone that would usually fail by aseismic creep. Type (iv) pseudotachylytes were formed at shallower depths (4–7 km) in a damage zone around the fault principal slip surface. Rare amygdalites indicate that the fault zone locally contained free fluids.

**Supplementary material:** Table of host, rock and pseudotachylyte major and minor oxide proportions is available at <http://www.geolsoc.org.uk/SUP18490>.

## *Friction melts as evidence of past seismic events*

Frictional heating during seismic slip can lead to the formation of pseudotachylytes, provided that other dynamic weakening mechanisms or thermal pressurization do not operate (Shand 1916; Jehu & Craig 1932; Jeffreys 1942; Sibson 1975; Sibson & Toy 2006). From these unequivocally earthquake-generated rocks (Cowan 1999), it may be possible to determine where, and under what conditions, seismic slip occurs within fault zones. Furthermore, pseudotachylytes can provide information about the stress levels and energy budget during earthquake faulting in optimal situations, such as when total slip and rupture area can be measured (e.g. Di Toro *et al.* 2005), and can be used to date palaeoseismicity (Warr & van der Pluijm 2005).

Pseudotachylytes occur in many exhumed active and ancient fault zones (e.g. Sibson 1975; Swanson 1998; Boullier *et al.* 2001 and many others – see Sibson & Toy 2006 for a comprehensive review of known occurrences), including New Zealand's active Alpine Fault Zone (Fig. 1) (Wallace 1976; Sibson *et al.* 1979; Seward & Sibson 1985; Bossiere 1991; Warr & van der Pluijm 2005). This structure could be considered the prime example

of plate-boundary fault zones transecting quartz-feldspathic crust worldwide. However, the Alpine Fault-related pseudotachylytes so far described are mostly from a small number of popular locations, which may not be characteristic of the fault zone as a whole.

In this contribution, we comprehensively describe the diverse geological host units and structural settings of pseudotachylytes in the Alpine Fault Zone, and make estimates of the conditions under which they formed; in other words, we define the pseudotachylytes' *habitats*. We differentiate four main habitats, between which we have not observed any cross-cutting relationships. The pseudotachylytes we describe have demonstrably been through a melt phase, as described later. We favour the interpretation that the different habitats reflect an extended history of friction melt generation in multiple earthquakes within a long-lived and complex fault structure. These data are then discussed in the context of the modern record of seismicity around the fault zone.

We focus on the well-exposed section of the fault between Hokitika and Haast, where a significant component of dip-slip has resulted in the exhumation of fault rocks from depth. However, similar observations of pseudotachylyte can be made in

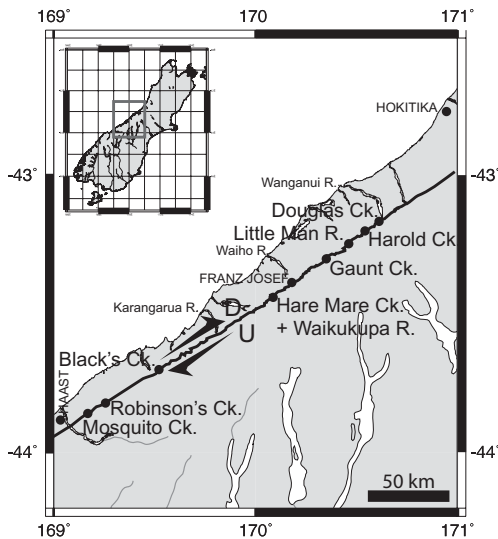


**Fig. 1.** Map of the west coast of the South Island, New Zealand, indicating locations of creeks (Ck.) and rivers (R.) mentioned in the text. The Alpine Fault is marked by a black line with shear sense indicated. Towns are labelled in capitals; major rivers that are not mentioned in the text are in smaller type. D and U refer to sense of dip slip across the Alpine Fault. Inset shows the entire South Island, with the area of the main figure in the box.

outcrops further to the south. Most observations were made in exposures within the beds of rivers and creeks (Fig. 1) that run orthogonal to the trace of the fault.

#### *Geological and tectonic setting of the fault zone*

The Alpine Fault Zone is a dextral reverse structure that accommodates around 70% of the relative motion between the Pacific and Australian plates through the central South Island of New Zealand. Best estimates from geological and geophysical data suggest that the fault zone dips 40°–60° to the SE at depth (Sibson *et al.* 1979; Scherwath *et al.* 2003). A sequence of hanging wall rocks, including an approximately 1 km-thick mylonite zone, have been exhumed from depths of  $\leq 35$  km in the last 5–8 Ma (Norris & Cooper 2007; Toy *et al.* 2008).

In most Alpine Fault outcrops, a basal overthrust, with centimetre(s) thick finely comminuted gouge (the principal slip surface), is immediately overlain by mint green cataclasites, which may contain abundant chlorite, quartz veins and disseminated pyrite. This hydrothermally altered zone extends for a variable distance from the principal slip surface, dying out in either cataclasites (e.g. Gaunt Creek, Robinson's Creek) or more intact mylonites (e.g. Hare Mare Creek). Overlying the

hydrothermally altered zone are partially cataclasized dark-grey, black, bottle or olive-green ultramylonites, which become less densely fractured with increasing distance from the fault. Above these lie planar-foliated, medium-grey mylonites that are mostly derived from a quartzofeldspathic, metasedimentary protolith, although there are other minor lithological constituents, such as metabasite, meta-chert, marble and very rare ultramafic rock. More detailed mylonite descriptions are included in Toy (2007). Before incorporation into the fault zone, the hanging wall lithologies experienced a two-phase deformation history under greenschist- and amphibolite-facies metamorphic conditions (Grapes 1995; Little *et al.* 2002). The initial phase resulted from accretion and crustal thickening during the Jurassic–Cretaceous, and culminated with a temperature–pressure ( $T$ – $P$ ) maximum as the orogenic belt was rifted from Australia in the late Cretaceous. The latter event is a consequence of renewed crustal thickening in the modern tectonic regime.

The fault footwall is composed of a variety of Western Province lithologies, including Palaeozoic granites and gneisses, Greenland Group metasediments and Cretaceous granitoids (Bradshaw 1993). Pieces of the footwall have been incorporated into the fault zone and exhumed at some locations (e.g. Harold Creek, Gaunt Creek; Fig. 1); for the most part, these crop out discontinuously as less than kilometre-scale ‘lozenges’ intercalated with hanging wall-derived material (Toy 2007). These footwall-protolith mylonites can be distinguished from more typical hanging wall-derived lithologies by the presence of abundant allanite and rare potassium feldspar porphyroclasts. They also generally have a more hydrated greenschist-facies mineral assemblage developed during low-grade regional metamorphism compared with the hanging wall lithologies that have been exhumed from the relatively anhydrous lower crust.

#### **Characteristics of Alpine Fault pseudotachylites**

##### *Host rocks and pseudotachylite morphology*

The Alpine Fault pseudotachylites can be subdivided into the following four habitat groups: (i) foliation-parallel pseudotachylites in hanging wall mylonites; (ii) pseudotachylites on lithological boundaries; (iii) pseudotachylites in footwall-derived mylonites; and (iv) pseudotachylites within cataclasites. Characteristics of the various groups are presented in tables to facilitate comparison. Typical host rock characteristics and structural settings are summarized in Table 1. Microscopic characteristics are summarized in Table 2 (see, in

**Table 1.** Host-rock types and structural characteristics of Alpine Fault pseudotachylytes

	Host rock type	Relationship to foliation	Fault and injection vein characteristics	Typical vein thickness	Relationship to cataclasite	Other characteristics
Type (i): Foliation-parallel in hanging wall mylonites	Medium grey Alpine Schist-derived quartzofeldspathic mylonite with amphibolite facies mineralogy of quartz+oligoclase+biotite+muscovite+opacites; locally a retrograde assemblage with chlorite after biotite (e.g. rare 5cm thick layers at Gaunt Creek; more pervasive at Little Man River). Pseudotachylytes most common in less micaceous lithologies. Micaceous mylonite parts easily along foliation.	Fault veins mostly parallel to host mylonite foliation (Fig.2a)	Injection into wedges bounded by Riedel shears common (Fig.3d). Rare injection veins at high angles to fault plane with low aspect ratios (Fig.3e).	Mostly mm-thick; cm-thick veins result from melt migration into lenticular dilatational jogs (Fig.4)	Mixed cataclasite-pseudotachylyte veins common (Fig.4b); thin, parallel cataclasite layers in sequence probably coeval (Fig.3)	Arrays of subparallel veins and sidewall rip-outs common (Swanson, 1989)
A: Foot wall-hanging-wall	Boundaries between purple-grey Alpine Schist-derived ultramylonite with amphibolite-facies mineralogy and brown-green footwall-derived ultramylonite with greenschist-facies mineralogy	Host rock is only weakly foliated; no consistent relationship observed	Mostly fault, rather than injection, veins; multiple overprinting veins common	Typically cm-thick	Some veins have been subsequently cataclasized but cataclasite is not common within or parallel to veins	Difficult to find in outcrop; common in float
B: Amphibolites	Boundaries between medium grey Alpine Schist-derived quartzofeldspathic mylonite and intercalated metabasic mylonite, both with amphibolite-facies mineralogy (as previously, but with hornblende in metabasites). Some pseudotachylytes entirely hosted within metabasites belong to the same structural setting.	Mylonitic foliation typically converges towards one side of pseudotachylyte vein, but parallels it on the other; implying these are bounding faults of foliation boudinage structures (Fig.5). Convergent foliations mostly strike more N-S than average Alpine Fault mylonite foliation (Fig. 6b).	Injection veins < 30 cm long, tapering from 1-0 cm thick, at low angles to generating surface (Fig.5). Fault-bounded and low aspect ratio injection veins visible in thin section.	Range up to 1 cm thick and are thickest where the bounding foliations are most oblique (Fig.5)	Variably associated with cataclasite; one notable mixed pseudotachylyte-cataclasite vein was observed at Mosquito Creek (Fig. 1); gradation from cataclasite to pseudotachylyte across veins also observed (Fig. 6)	Coeval foliation boudinage structures have quartz+carbonate veins in boudin necks; Extensive networks of sub-parallel veins with linking structures possible
Type (ii): On lithologic boundaries	Brown-green footwall granitoid-derived ultramylonite with greenschist-facies assemblage of quartz+albite//orthoclase+chlorite+chloritised amphibole+epidote; mm-diameter feldspar augen and allanite porphyroblasts common. Foliated but cohesive along foliation planes. Foliation-oblique quartz veins common, but cross-cutting relationships with pseudotachylyte veins not apparent.	No consistent orientation relationship to the mylonitic foliation observed in outcrop, but measured orientations are generally more E-W striking than the average mylonite foliation (Fig.2c)	Injection breccias and networks bounded by fault veins common (e.g. Fig.7); cross-cutting injection veins (Fig.7); low aspect ratio injection veins at high angles to generating surface in thin section (Fig.8d)	mm-thick fault veins; injection veins < 2.5 cm thick and 30 cm long (Fig.7)	Rarely overprint cataclasites; may be overprinted by cataclasite or chlorite veins (Fig.6g)	Pseudotachylyte veins are abundant in float and difficult to find in outcrop
Type (iii): Pseudotachylites in footwall-derived mylonites	Hydrothermally-altered, mint green cataclasites with abundant chlorite, quartz veins and disseminated pyrite that immediately overlie the principal slip surface (p.s.s.) of the Alpine Fault. Also in partially cataclasized dark grey, black, bottle or olive green ultramylonites overlying the hydrothermally-altered cataclasites; the latter become less densely fractured with increasing distance from the fault p.s.s. Pseudotachylytes are relatively more common on boundaries between host rock of different mineralogy (e.g. around quartz/feldspar pods, or at the boundary between olive green and black cataclasites)	Fault veins strike parallel to main foliation in host cataclasites. Injection veins generally dip to the NW, orthogonal to the fault veins (Fig.2d)	Fault veins are rarely observed; most veins have irregular boundaries and are inferred to be injected masses (e.g. Fig.9a)	Fault veins typically < 1mm thick; injected masses range up to 5cm thick	Commonly overprint cataclastic textures in the host, and formed coevally with other cataclasites; patches of pseudotachylyte may also be entrained in overprinting cataclasites	Pseudotachylytes within the hydrothermally-altered host are typically blue-grey, orange-brown or red-brown in colour, rather than a more typical black or dark brown.
Type (iv): Pseudotachylites within cataclasites						

**Table 2.** Microscopic characteristics of Alpine Fault pseudotachylites

	Matrix characteristics	Clast characteristics	Other features of interest	
Type (i): Foliation-parallel in hanging wall mylonites	Cryptocrystalline; opaque-rich; may be aphytic; commonly composed of a felted mass of sericite with shape-preferred orientation oblique to vein boundaries	Dominantly quartz; minor feldspar	-	
Type (ii): On lithologic boundaries	A: Foot wall-hanging wall  B: Amphibolites	Flow banded, typically orange-brown  Colour ranges from black through medium brown to transparent (Fig.6f,g) - the latter are probably masses of sericite; cryptocrystalline or microspherulitic; banding parallel to margins common	Rare, rounded quartz and feldspar clasts  Reasonably rare, rounded quartz and 'resorbed' or angular feldspar clasts; some lithic clasts	-  Progressive overprinting of pseudotachylite fabric by mylonitic fabric (Fig.6a, b, c)
Type (iii): Pseudotachylites in footwall-derived mylonites		Black to brown and cryptocrystalline; commonly opaque; colour-banded parallel to vein margins; microspherulites with Fe-oxide stained rims occur in the centres of the thickest veins; entire matrix can be replaced by chlorite	Feldspar and quartz clasts; larger clasts have interlobate boundaries with matrix (Fig.8a, b); calcite clasts common, as are calcite-bearing lithic clasts	Quartz-carbonate amygdalules occasionally observed (Fig.8c)
Type (iv): Pseudotachylites within cataclasites		Typically dirty brown, cryptocrystalline and isotropic in places; may contain disseminated carbonate; some felted masses of oriented sericite and biotite (Fig.10b) observed	May be absent, where present they are rounded quartz and angular, altered feldspars	Some veins contain flattened, quartz+carbonate amygdalules (Fig.10a); and carbonate+quartz in cross-cutting fractures.

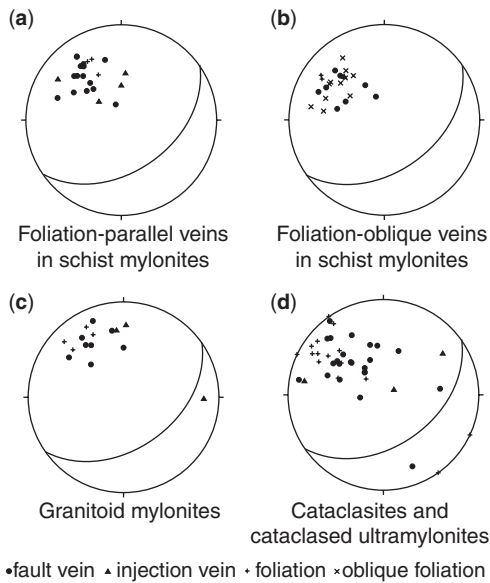


**Fig. 2.** Equal-area lower-hemisphere projections of poles to pseudotachylyte fault and injection veins, and to host rock foliations. Great circles represent the average Alpine Fault plane.

addition, Figs 2–9). Representative field and microstructural relationships are also illustrated in Figures 3–10.

From these summaries, key differences between the four habitat groups are apparent. In particular, type (i) pseudotachylytes are hosted in foliated and, therefore, strongly anisotropic hanging wall Alpine Schist-derived mylonite. They formed along foliation planes, are commonly only millimetres in thickness, are intimately associated with cataclasite and have low melt:clast ratios. They rarely form extensive injection networks. Type (ii) pseudotachylytes exploit lithological boundaries and are commonly associated with foliation boudinage structures. They are variably thicker than the preceding group, have reasonably high melt:clast ratios and friction melt was injected some distance off from the generating surface. Type (iii) pseudotachylytes may have reasonably high melt:clast ratios, and generally form extensive injection networks and breccias; these are the most voluminous friction melts observed in the fault zone. We emphasize that these pseudotachylytes occur in a peculiar host rock type, and do not exemplify solidified friction melts typically found in the rest of the Alpine Fault Zone. Type (iv) pseudotachylytes are the only group to cross-cut well-developed cataclasite fabrics. Injection veins and masses are common. Quartz–carbonate mineralization was

coeval with, and post-dated, the generation of these pseudotachylytes.

#### *Chemical relationships between pseudotachylytes and host rocks*

The bulk chemistries of pseudotachylyte host rocks were determined by X-ray fluorescence (XRF), using a Phillips PW2400 X-ray fluorescence spectrometer. Chemical make-up of the pseudotachylytes were determined by energy dispersive spectrometry (EDS), using a JEOL JXA-8600 Superprobe, with a defocused, 15–20  $\mu\text{m}$  diameter beam in order to sample the bulk chemistry of the matrix, which is commonly clast-bearing, and may now be composed of fine alteration assemblages. Between two and six spot analyses were averaged for each sample. Both instruments are housed at the University of Otago. Analytical methods were outlined by Ritchie (2009), and the major oxide proportions and minor element concentrations are presented as Supplementary publication table SUP18490.

In summary, we find that type (i) pseudotachylytes are silica and alkali deficient, but enriched in  $\text{Al}_2\text{O}_3$  and  $\text{TiO}_2$  with respect to their hosts. Type (iii) pseudotachylyte are only slightly lower in silica, iron and magnesium than their hosts, but significantly lower in potassium (Ritchie 2009). This may be explained by the fact the host rocks are cross-cut by adularia veins (Toy 2007), which would have been included in bulk chemical analyses. Type (iv) pseudotachylytes are lower in silica and calcium, but enriched in alkalis (potassium, sodium) than their host rocks. No analyses were performed on type (iii) pseudotachylytes.

#### **Environments of pseudotachylyte formation**

##### *Type (i): foliation-parallel pseudotachylytes in hanging wall mylonites*

At Gaunt Creek (Fig. 1), one of a swarm of pseudotachylyte and ultracataclasite veins (Fig. 3) is cross-cut by, and offset along, a quartz vein with the BLG–SGR regime boundary defined by quartz microstructures characteristic of Stipp *et al.* (2002) (Fig. 6d). These should develop at temperatures ranging from around 400 to 450 °C for the steady-state shear strain rates of  $10^{-11}$ – $10^{-12}\text{ s}^{-1}$  within the fault zone proposed by Norris & Cooper (2003), and at about 350 °C at a slower shear strain rate of  $10^{-13}\text{ s}^{-1}$ . The latter rate is more appropriate for post-seismic creep around a discrete shear surface that experienced episodic brittle failure. This is a reasonable, although very

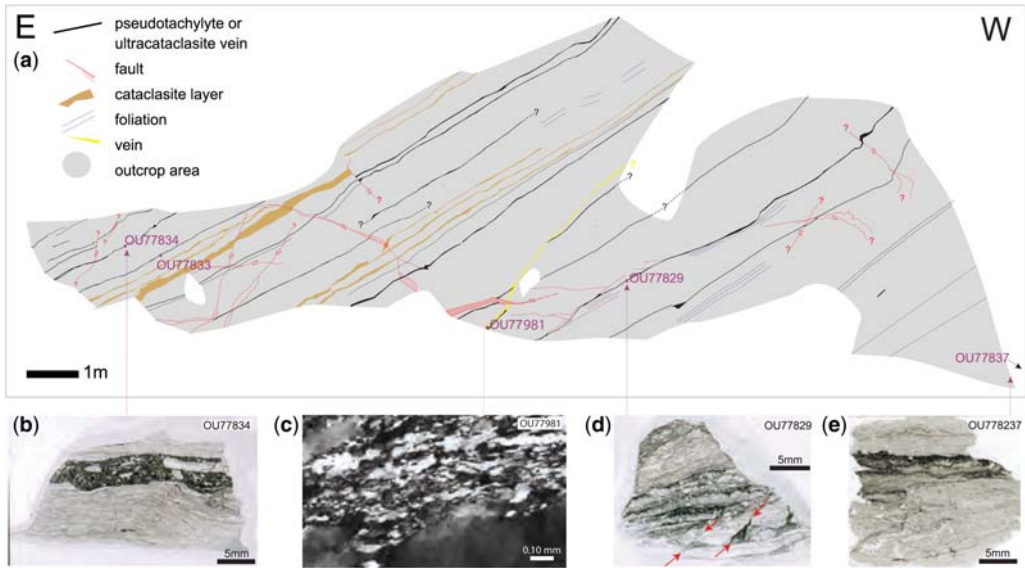


**Fig. 3.** Mylonite section in lower Gaunt Creek, around NZ Map Grid 2293100E 5762200N, illustrating numerous thin mixed pseudotachylite and ultracataclasite veins subparallel to the mylonitic foliation. The diagram is of a subvertical face. The locations of veins were positioned on photographs in the field, and these were stitched together to form the final diagram. Foliation-parallel cataclasite zones, cross-cutting faults and veins are also indicated. Scans of thin sections cut from selected pseudotachylite and cataclasite layers are shown at the base of the diagram (b, d, e). Note the injection wedges bounded by Riedel shears (arrowed) near the base of the pseudotachylite in (d) and injection veins on the upper surface of the pseudotachylite in (e). (c) is a photomicrograph from a quartz vein that cross-cuts a pseudotachylite vein towards the centre of (a). The quartz displays a BLG/SGR microstructure of Stipp *et al.* (2002) indicating that it experienced dislocation creep.

approximate, lower bounding estimate of the host rock temperatures during formation of the pseudotachylite–ultracataclasite veins.

#### Type (ii): pseudotachylites on lithological boundaries

We are unable to estimate the depth at which seismic slip occurred between hanging wall- and footwall-derived mylonites. Some of these pseudotachylites in ultramylonites of both lithologies have been replaced by chlorite or are cross-cut by dilational chlorite veins (Toy *et al.* 2008). Unfortunately, this observation does not provide a precise constraint on formation conditions.

Toy *et al.* (2010) analysed fluid inclusions in quartz–carbonate veins trapped in the necks of some foliation boudinage structures in metabasic layers within the mylonites. Pseudotachylite is also observed on boudin-bounding faults, but only those without quartz–carbonate veins (Fig. 2); presumably pseudotachylite formed when fluids were not present during this phase of deformation. The fluid-inclusion microthermometric data suggest that these structures formed at temperatures

of about 325 °C and fluid pressures of approximately 40 MPa, which Toy *et al.* (2010) interpreted to reflect formation from relatively light ( $\rho \geq 500 \text{ kg m}^{-3}$ ) mixed CO<sub>2</sub>–H<sub>2</sub>O fluids under hydrostatic pressure conditions at depths of  $\leq 8$  km. Furthermore, some quartz in the quartz–carbonate veins in boudin necks has been dynamically recrystallized, suggesting fluctuating brittle–viscous conditions, in the temperature range of 300–350 °C.

Pseudotachylites of this type exposed at Mosquito Creek are notable for two reasons.

- They are hosted in mylonite that is microstructurally distinct from most ‘normal’ Alpine Fault mylonites because foliation-parallel quartz ribbons within it are made up of atypically very fine (<15 µm) subgrains (Fig. 2d). This indicates that transiently high stresses were experienced, possibly during post-seismic creep.
- The pseudotachylites here are composed of dirty brown, sometimes isotropic, cryptocrystalline material, with some paler patches, possibly composed of very fine alteration assemblages (Fig. 6a). Patches of the mylonite are also

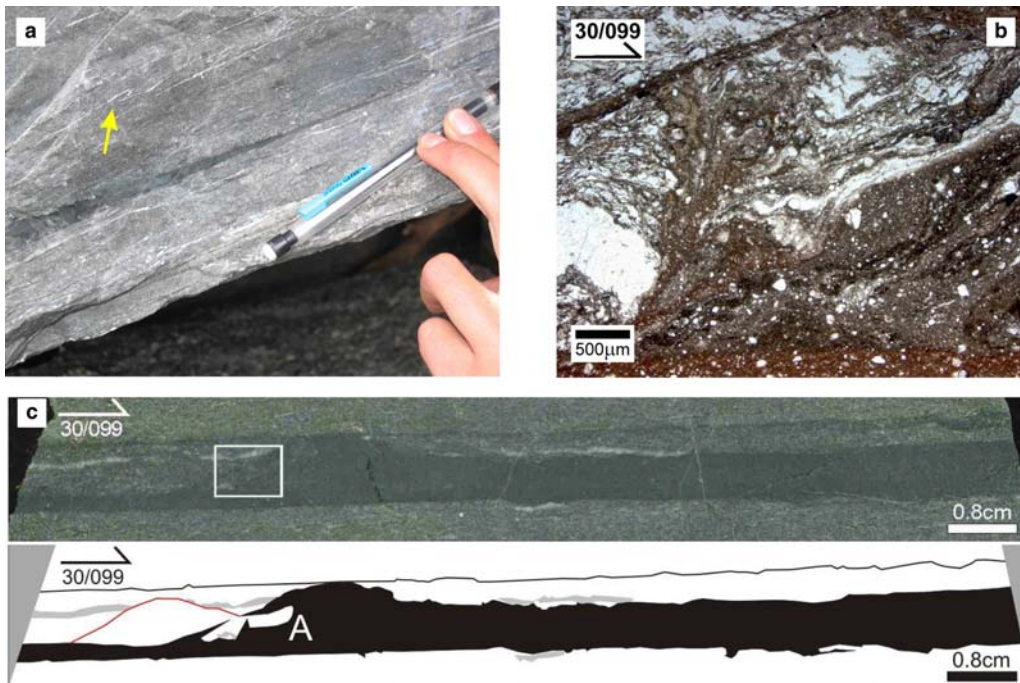


**Fig. 4.** Foliation-parallel pseudotachylytes in quartzfeldspathic schist-derived mylonite, Little Man River. (a) Three parallel mm-thick pseudotachylyte veins are present within 10 cm of one another. One of these veins thickens into a lens 1 cm thick at bottom left of the photograph. The other veins also thicken into lenses beyond the limits of the photograph. A similar thickness of protocataclasite occurs below the fault vein. An asymmetrically folded quartz vein in the host mylonite is indicated by the yellow arrow. Elsewhere, similar folded veins are cross-cut by planar pseudotachylyte fault veins indicating folding predicated friction melting. (c) OU78143. Foliation 036/26SE. Hand sample of the pseudotachylyte in (a). Photograph and tracing of photograph. The thickest pseudotachylyte is developed along the lower slip surface. This vein thickens into an aphorophysis that almost meets the adjacent slip surface. A 'sidewall ripout' in the region between the two main shear surfaces is outlined in red. At A, the mylonite was only partially assimilated by the pseudotachylyte, as shown in the photomicrograph in (b), which corresponds to the white box on the hand sample photograph. A layer of protocataclasite approximately 2 mm thick occurs beneath the upper slip surface.

composed of quartz or feldspar porphyroclasts in a dirty brown, isotropic matrix. The fabric in this material is smeared out and anastomosing, while intercalated patches of quartz and chlorite are ductilely folded (Fig. 6b). Short, stubby injection veins feed off from one of the foliation surfaces in this material (Fig. 6c). We infer the latter represent remylonitized pseudotachylytes.

Both observations suggest that this location was subject to brittle, seismogenic failure, followed by a period of aseismic creep accommodated by ductile mechanisms, initially at high stress. The seismogenic faulting that produced these pseudotachylytes, and type (ii) pseudotachylytes elsewhere, probably occurred near and just below the base of the typical seismogenic part of the fault zone.

#### Type (iii): pseudotachylytes in footwall-derived mylonites

Pseudotachylytes in retrograde mylonites with a probable Western Province protolith cross-cut a mylonitic fabric containing quartz, albite, chlorite, epidote and chloritized amphibole; broadly a greenschist-facies assemblage. They are, in turn, cross-cut by chlorite and unrecrystallized quartz veins, and the pseudotachylyte is sometimes replaced by chlorite. The lack of recrystallization in quartz suggests that the veins were formed at temperatures below about 300 °C (cf. Voll 1976), at which conditions chlorite could also be expected to precipitate. Calcite grains in clasts in OU77702 are mostly dynamically recrystallized, which occurs above around 250 °C (Ferrill *et al.* 2004). However, large calcite clasts within this pseudotachylyte have

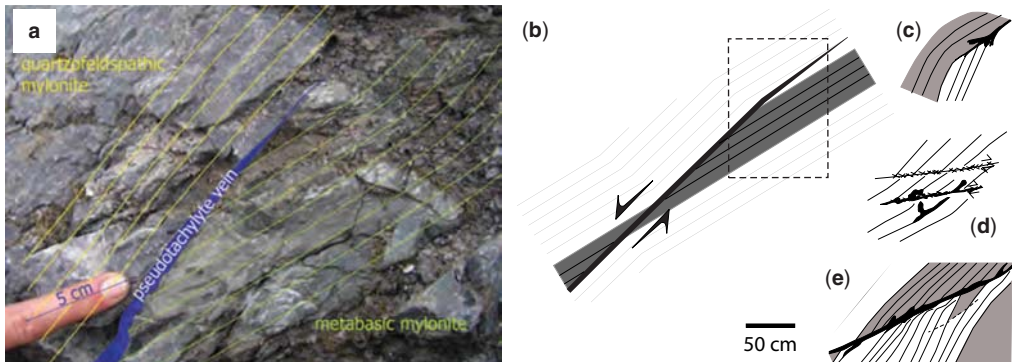


**Fig. 5.** Illustrations of typical orientation of mylonitic foliation around pseudotachylite veins that occur on the boundaries of metabasite units. (a) Gaunt Creek. Pseudotachylite fault vein at the contact between quartzofeldspathic and metabasic mylonites. The foliation in the metabasite converges towards the vein towards the bottom of the photograph. The pseudotachylite vein is thickest adjacent to this convergence of foliation and tapers towards the top of the photograph as the foliations in the metabasic and quartzofeldspathic mylonites become parallel. (b) Schematic illustration of the larger-scale boudinage structure that the relationship observed in (a) is inferred to be part of. (a) is thought to be equivalent to the area within the dashed box. (c)–(e) Field sketches illustrating the relationships between pseudotachylite veins (filled black areas), and foliations in the host quartzofeldspathic (grey) and metabasic (white) mylonites. All sketches are orientated to give a view towards the south; all are represented at the same scale.

relatively narrow, cross-hatched e-twins, indicating at least some of the calcite in the protolith before frictional melting was deformed at lower temperatures. Alternatively (and more likely), plastic strains post-dating deposition of that particular calcite were very small. These observations indicate that these pseudotachylites were formed at various temperatures ranging up to 300 °C.

#### Type (iv): pseudotachylites within cataclasites

The quartz/feldspar pods, which commonly have blue-tinged pseudotachylite on their margins, are not present in the protolith mylonite. We infer that they originated as extension veins in the early stages of cataclastic deformation. Subsequently, they would have presented a rheological contrast promoting localization of seismic slip to their margins. The blue pseudotachylite post-dates the formation of quartz pods so cannot be the first stage of cataclastic deformation (cf. Warr & Cox 2001). Instead, it appears that pseudotachylite forms within the ‘middle’ parts of the continually exhuming cataclasite zone. Furthermore, this interpretation suggests that fluids were present in the cataclasite zone before frictional melting occurred.

Calcium deficiency of pseudotachylite matrices with respect to the protolith catalasites suggests that most of the carbonate now observed in both the pseudotachylites and the host rock was introduced into the rock after frictional melting, and was preferentially deposited in the cataclasite, perhaps

because the solidified pseudotachylite was relatively impermeable.

The calcite observed in the cataclastic matrix of OU77868 (Fig. 10a) is composed of small crystals with interlobate boundaries, indicating that it was dynamically recrystallized above temperatures of 250 °C (Ferrill *et al.* 2004). Larger single crystals in amygdules contain relatively narrow cross-hatched e-twins. Comparison with the calcite twin geothermometer of Ferrill *et al.* (2004) suggests that the observed twin width (*c.* 2–6 µm) and intensity (*c.* 50–150 twins mm<sup>-1</sup>) in amygdule-fill is characteristic of temperatures in the range 170–200 °C (note that it is very difficult to measure twin widths of this size precisely in normal 30 µm-thickness sections without a universal stage). This pseudotachylite must therefore have formed at temperatures exceeding 170 °C and possibly greater than 250 °C.

The pseudotachylites also cross-cut and therefore post-date ultramylonitic fabrics that include quartz, which was deformed by dislocation creep; a process which should not occur below about 300 °C (Voll 1976). This is therefore an upper temperature limit for formation of these pseudotachylites.

## Discussion

### Proof of melt origin

Pseudotachylite studies have been plagued by the need to prove a ‘melt origin’. Not all black flinty or aphanitic rocks observed in the field are

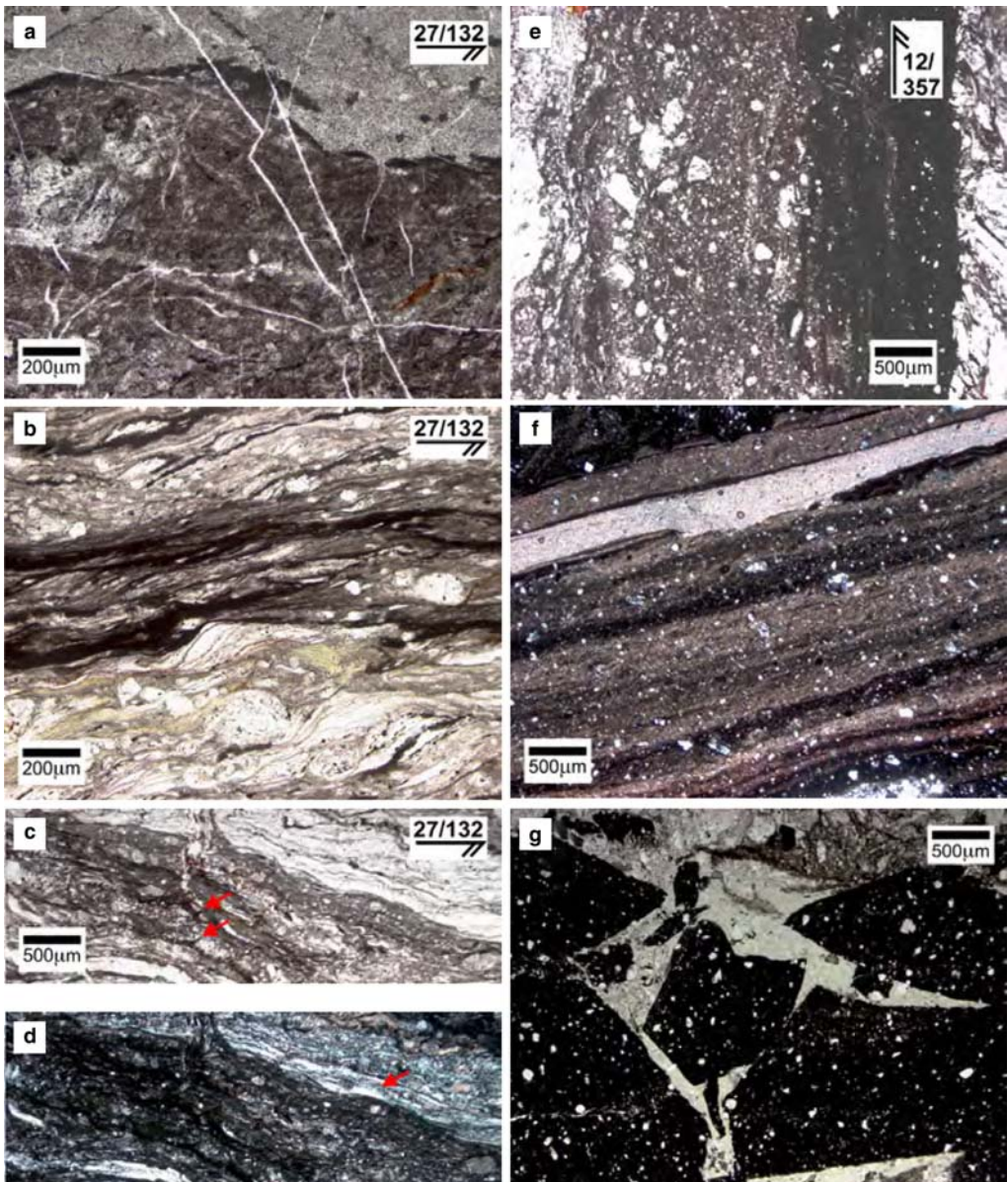


**Fig. 6.** Photomicrographs illustrating pseudotachylite microtextures. Sections cut perpendicular to foliation; lineation direction is marked. Pseudotachylites from Mosquito Creek at varying stages of remobilization (OU78175). (a) Undeformed pseudotachylite with variable proportion of an opaque phase. Plane-polarized light (PPL). (b) Bands of very opaque-rich ultramylonite, lacking quartzofeldspathic clasts suggesting derivation from pseudotachylite. PPL. (c) Layers of dirty brown, cryptocrystalline pseudotachylite smeared along the foliation, intercalated with gently folded quartz ribbons. Pseudotachylite injection veins are preserved in a cataclasite layer (arrowed). PPL. (d) Crossed-polars (XPL) version of the photomicrograph in (c), illustrating quartz ribbons composed of finely recrystallized grain and subgrains (arrowed). Pseudotachylites in metabasic lithologies (Harold Creek). (e) OU77739. A thin fault vein is composed of cataclasite grading to pseudotachylite from left to right of the image. Amphiboles in the wall rock have been altered to a brownish colour. (f) OU77804. There are layers of material with different matrix colours, and proportions of sericite, parallel to the vein margins. The most sericite-rich layer through the centre of the photomicrograph is transparent in PPL. (g) OU77811. This opaque-matrix pseudotachylite is cross-cut by numerous chlorite-filled fractures.

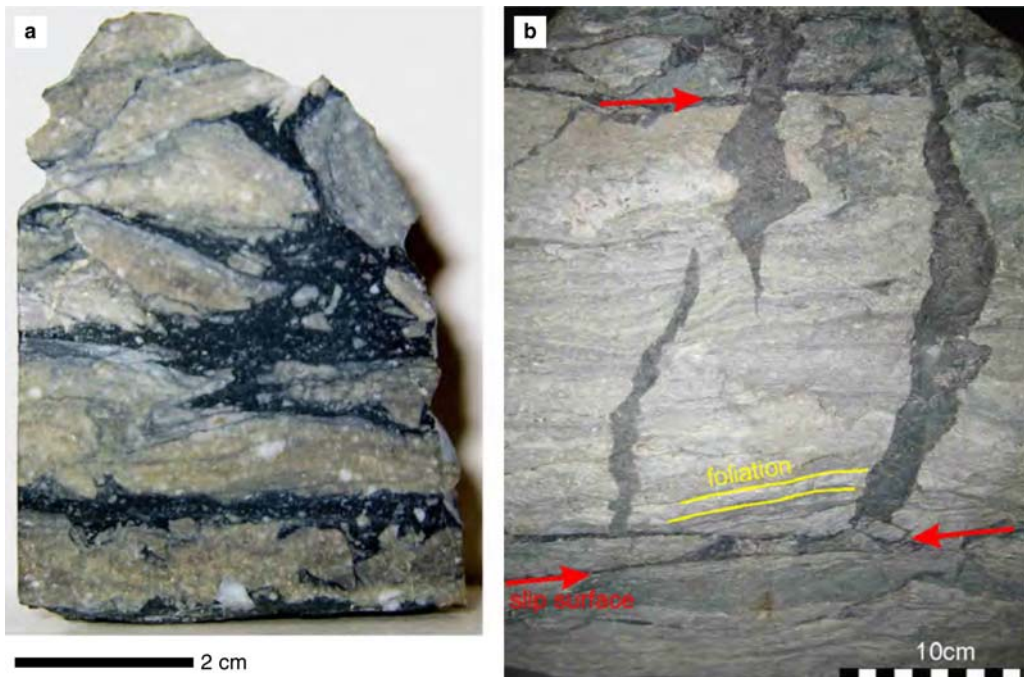


**Fig. 7.** Examples of pseudotachylytes hosted in mylonites with granitoid (i.e. footwall) protoliths. Both samples are from Harold Creek. (a) Hand specimen OU77702. The sample has been cut perpendicular to the Alpine Fault slip vector. Host mylonite foliation is disrupted and has been locally folded. (b) Boulder. Injection veins <2.5 cm wide and 30 cm long project near orthogonally off a fault vein (labelled 'slip surface'), cross-cutting the mylonite foliation and an earlier fault vein.

pseudotachylytes; some are also ultracataclasites or ultramylonites (Sibson 1975; Maddock 1992; Magloughlin & Spray 1992), which may have formed at subseismic slip rates (Cowan 1999). Some authors do not think that pseudotachylytes have to have been through a melt phase (Lin 2008). However, we consider evidence of frictional melting as a key criterion in applying the term pseudotachylyte and in linking the rocks to seismic events. Consequently, we provide a list of evidence for a melt origin observed in a few samples of each type of pseudotachylyte hosted within the Alpine Fault Zone in Table 3. The criteria are discussed in a general sense here.

The most unequivocal evidence that frictional melting has occurred on a fault plane is the presence of glass, which could be expected to form from a rapidly quenched melt. Unfortunately, glass rapidly becomes hydrated (Stevenson *et al.* 1998) or devitrified to fine-grained granular crystalline aggregates (Gifkins *et al.* 2005), and so is not usually preserved when pseudotachylyte is exposed at the surface. Glass is particularly rare in Alpine Fault pseudotachylytes. In part this may be because many Alpine Fault pseudotachylytes crystallized

minerals directly from the melt, rather than glass (as observed in the samples described in detail by Warr *et al.* 2003; Warr & van der Pluijm 2005).

In experimentally produced friction melts of a quartzofeldspathic protolith (Spray 1987), the surviving clasts are quartz and less commonly feldspar, mostly because mechanical break-down processes precede melting. Similar clast compositions have been observed in many natural pseudotachylytes (e.g. McNulty 1995; Macaudiere & Brown 1998; Fabbri *et al.* 2000; Barker 2005 and many others). Consequently, we consider the presence of angular quartz and rounded feldspar clasts, but absence of mica clasts, within a pseudotachylyte as a good indicator of a melt origin (Passchier & Trouw 1996). These relationships are observed in many of our samples (Table 3), as is occasional embayment of micas in the wall rocks (cf. Shaw *et al.* 2001). Previously determined Alpine Fault pseudotachylyte matrix chemistries (e.g. Warr *et al.* 2003; Warr & van der Pluijm 2005) and our data are also consistent with this sort of clast distribution. Most pseudotachylyte matrices are silica deficient with respect to the host rock – pseudotachylyte types (i), (ii), and (iv). Type (i) pseudotachylytes are also

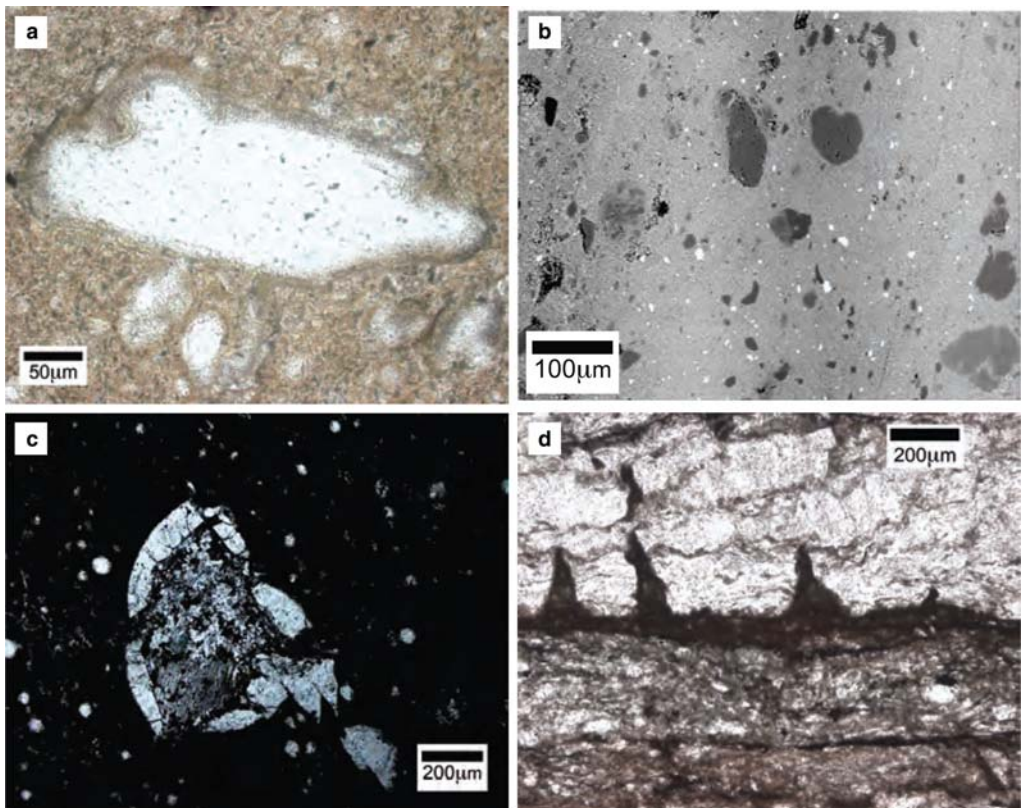


**Fig. 8.** Textural features indicating a melt origin. (a) Photomicrograph of partially resorbed feldspar clast. OU78154 from Little Man River. (b) Backscattered electron image illustrating embayed and resorbed quartz (dark grey) and feldspar (lighter grey) clasts in pseudotachylite hosted in cataclasite at Gaunt Creek. OU80610. (c) Amygdule with quartz and calcite fill in Western Province-derived mylonite from Harold Creek. OU77805. (d) Less than 100  $\mu\text{m}$ -thick pseudotachylite observed in thin sections of granitoid-derived ultramylonites. Injection veins project at high angles into the adjacent mylonite. The pseudotachylite vein occurs along the boundary between cataclasite (brown) and host mylonite. OU77714.

enriched in aluminium and titanium, both of which would be derived from the preferential melting of biotite over quartz and feldspar (Ritchie 2009).

Other evidence for a melt origin includes the presence of microlites (e.g. Sibson 1975; Allen 1979), quenched vein margins (e.g. Di Toro & Pennacchioni 2004), vesicles and amygdules (e.g. Boullier *et al.* 2001; Craddock & Magloughlin 2005), flow textures (e.g. Braathen *et al.* 2004), embayed clasts (e.g. Sibson 1975; Caggianelli *et al.* 2005), the presence of newly crystallized minerals that are not stable in the host rock (e.g. Shaw *et al.* 2001) or a texture that could have resulted from melting and is very different from textures in the host rock (broadly after Magloughlin & Spray 1992). These features are variably developed in the Alpine Fault pseudotachylites (Table 3).

In the past, fault-injection vein relationships were considered to be diagnostic of pseudotachylite (Magloughlin & Spray 1992). However, Lin (1996) showed that injection veins could also form during cataclastic deformation in the absence of melting if the gouge becomes fluidized. Because of this uncertainty in origin, fault and injection vein habits alone are not considered sufficient evidence that the material on a fault plane has been through a melt episode.

#### Estimation of formation depth

Estimation of the depths at which Alpine Fault Zone pseudotachylites formed would enable determination of confining pressures and magnitudes of shear stress on the fault surfaces for static (pre-failure) conditions. Previously, formation depths

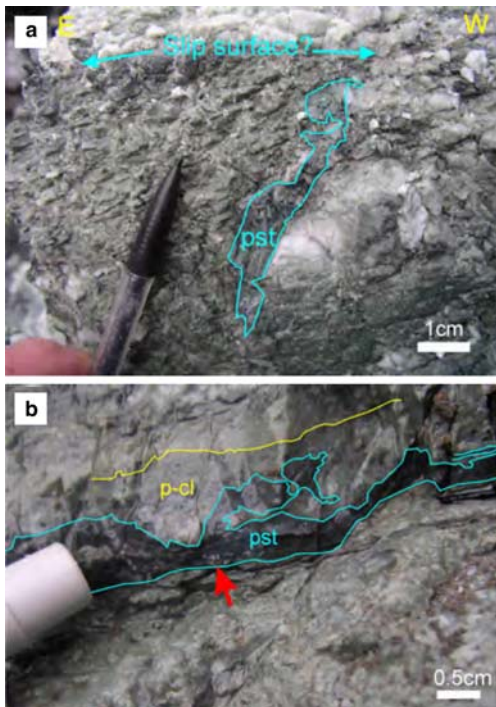


**Fig. 9.** Pseudotachylytes in mint-green cataclasites, Gaunt Creek. (a) Pseudotachylyte vein (outlined in cyan; labelled ‘pst’) with erratic habit and small aspect ratio, which is probably an injection vein. There is no associated fault vein but a possible generating slip surface is indicated. (b) Subhorizontal 0.5–1 cm-thick pseudotachylyte vein (outlined in cyan; labelled ‘pst’). The pseudotachylyte contains numerous rounded clasts less than 0.5 mm in diameter and local larger fragments of cataclasite (indicated by the red arrow). The vein is overlain by a layer of weakly banded, cemented cataclasite (labelled ‘p-cl’) containing rounded clasts less than 1 mm in diameter and then by more structureless cataclasite. The association with a parallel layer of cataclasite indicates that this may be a fault vein.

for Alpine Fault pseudotachylytes have been estimated based on their ages and average uplift rates. For example, Warr *et al.* (2007) used  $^{40}\text{Ar}/^{39}\text{Ar}$  methods to estimate that pseudotachylytes from Harold Creek (probably hosted in footwall-derived mylonites) were formed at about 570 ka, giving formation depths of approximately 3–5.5 km for average uplift rates of 6–9 mm year $^{-1}$ . However, age and uplift rate data are sparse, and the latter vary significantly along-strike of the Alpine Fault (Adams 1981; Seward & Sibson 1985; Norris & Cooper 2001; Little *et al.* 2005).

To estimate formation depths for the wide variety of pseudotachylytes described here, we compare estimated host rock temperatures to the

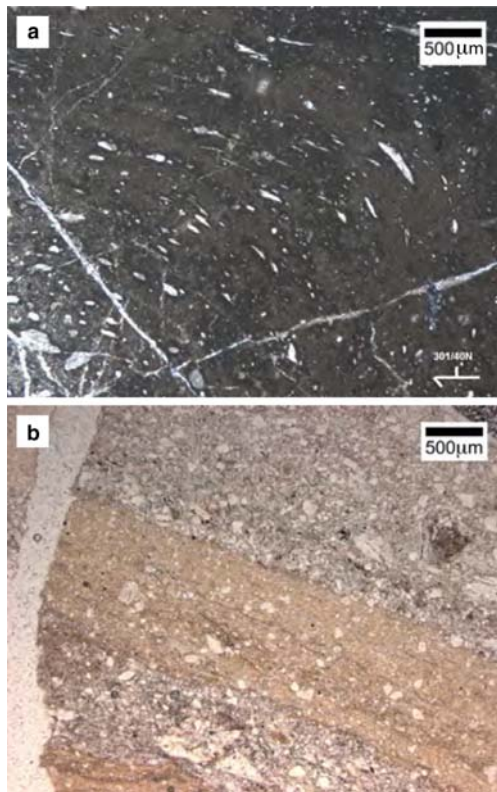


**Fig. 10.** (a) Photomicrograph of pseudotachylyte in OU77868 illustrating flattened carbonate amygdalites. (b) OU77879. Pseudotachylyte veins, composed of clasts of quartz and feldspar in a matrix of felted sericite cross-cut a cataclastic host. PPL.

uplift path  $P-T$  profile determined by Toy *et al.* (2010), on the assumption that the  $P-T$  profile is similar to the geothermal gradient at depth (Table 4). We recognize this is not a very precise method by which to estimate the depth at which pseudotachylytes were formed, and stress that the estimates should be viewed with caution.

#### Other factors influencing pseudotachylyte formation

By far the most voluminous pseudotachylytes in the Alpine Fault Zone are those hosted in footwall-derived mylonites. Factors that are likely to influence production of greater volumes of friction melt in this setting include the following.

- The host rock has a greenschist-facies mineralogy with abundant hydrated mineral phases such as chlorite and epidote. When these phases start to melt during shear heating they release

**Table 3.** Features suggesting a melt origin for Alpine Fault pseudotachylytes, and examples of locations from which samples containing these features have been collected

Feature suggesting a melt origin	Alpine Schist-derived mylonite host: foliation-parallel veins	Alpine Schist-derived mylonite host: foliation-oblique veins	Cataclastic or cataclasped ultramylonite host	Western Province granitoid-derived mylonite host
• Embayed micas in wall rock	Gaunt Creek, Little Man River	Gaunt Creek	–	Harold Creek
• Resorbed, rounded or embayed feldspar clasts	Little Man River, Gaunt Creek	Gaunt Creek	–	Harold Creek, Douglas Creek (Waitaha River)
• Glass patches	Little Man River	–	Gaunt Creek	–
• Feldspar microlites	Little Man River	–	–	–
• Microspherulites	Gaunt Creek, Little Man River	Mosquito Creek	–	–
• Felted sericite matrix	Hare Mare Creek	Gaunt Creek	Gaunt Creek	–
• Flow textures	Gaunt Creek, Little Man River	Mosquito Creek	Gaunt Creek	Harold Creek, Douglas Creek (Waitaha River)
• Chilled margins	Gaunt Creek, Little Man River	–	Gaunt Creek	Harold Creek
• Quartz and feldspar clasts only	Gaunt Creek, Little Man River, Blacks Creek (Paringa area)	Mosquito Creek	Gaunt Creek	Harold Creek
• Altered palagonite matrix	Gaunt Creek, Little Man River	Gaunt Creek	Harold Creek	
• Fault and injection vein relationships	Gaunt Creek, Blacks Creek	Gaunt Creek	Gaunt Creek	Harold Creek
• Brown, cryptocrystalline matrix	–	–	Gaunt Creek	–
• Flattened calcite and quartz-filled amygdalules	–	–	Gaunt Creek	Harold Creek
• Isotropic matrix	–	Mosquito Creek	–	Harold Creek

**Table 4.** Estimates of temperatures and approximate depths of formation of pseudotachylytes in the Alpine Fault Zone

Pseudotachylyte type	T <sup>*</sup> <sub>host</sub> (°C)		Depth of formation (km)	
	Min.	Max.	Min.	Max.
Type (i): Alpine Schist-derived mylonite host; foliation-parallel	350	?	10	?
Type (ii): Alpine Schist-derived mylonite host; foliation-oblique	300	350	7	10
Type (iii): Western Province granitoid-derived mylonite host		≤300		≤7
Type (iv): Cataclastic host	170	300	4	7

\*Temperature of host rock at the time of frictional melting.

water, which lowers the melting point of the rock, promoting greater volumes of melt for comparable amounts of frictional heat compared to more anhydrous host rocks.

- The host rock is also relatively isotropic, unlike the strongly layered hanging wall-derived mylonite. In the latter, injection veins are generally short (millimetres long) and stubby, and do not contain abundant melt. Fracture strength is demonstrably much greater for parting parallel to foliation than perpendicular to it in anisotropic rocks (Lockner 1995). Consequently, in strongly anisotropic rocks where slip occurs parallel to foliation, it is difficult to create fractures at high angles to the foliation that allow melt to be ‘tapped’ off the fault plane. In this situation, friction melt lubricates that fault plane, reducing shear resistance and therefore further pseudotachylyte production. However, if melt can be tapped from a fault plane, frictional resistance probably remains high and pseudotachylyte continues to be generated throughout faulting.

The second most voluminous pseudotachylytes are those that occur on lithological boundaries, particularly where the generating surface is oblique to foliation in the host rock. These pseudotachylytes are testament to the importance of rheological contrasts (e.g. between metabasite and quartzofelspathic mylonite), which provide stress and/or strain-rate heterogeneities sufficient to promote brittle failure during bulk ‘ductile’ shearing. In the Alpine Fault Zone these provide rupture sites for pseudotachylyte-producing slip events. Similar effects have been proposed in other deforming zones (e.g. Sibson 1980; Fagereng & Sibson 2010).

The presence of amygdules, which are common in type (iv) pseudotachylytes (Fig. 10a) but are also observed in type (iii) pseudotachylytes (Fig. 8c), further suggests that fluid was present, particularly in the cataclasite zone, at the time of frictional melting. It has been suggested that vesicles may form in melt by exsolution of volatiles, but, as argued by Dixon & Dixon (1989), it is unlikely that exsolution can occur in the few short minutes for which pseudotachylytes are molten. Frictional melting should be inhibited in impermeable host rocks saturated in free fluids (Sibson 1973). The Alpine Fault cataclasites probably have permeabilities of  $10^{-19} \text{ m}^2$  or less under moderate lithostatic load from preliminary tests on these materials (Toy unpublished data), consistent with measurements in other similar fault rocks (Wibberley & Shimamoto 2003). At these conditions, thermal pressurization should occur if free fluids are present (Lachenbruch 1980). We suggest that fluids are variably present in the Alpine Fault cataclasite zone, both in time and space. One can easily envisage a situation where

melting occurs at asperity contacts along a heterogeneous rupture plane. The melt may subsequently mingle with fluids present at other sites on the fault plane, forming vesicles that are filled by later fluid flux through the rock mass.

## Relationship to present-day seismicity

We have illustrated that pseudotachylyte is widely distributed in the Alpine Fault Zone. However, is it the normal product of seismic slip in these rocks? In the absence of feedback mechanisms lowering kinetic shear resistance during slip, melting would be expected during most seismic events, provided that the slip is well localized (Sibson 2003). As noted by Toy (2007), the Alpine Fault Zone has probably experienced tens of thousands of  $M_w < 8$  earthquakes in its roughly 5 Ma convergence phase. If each  $> 8 \text{ m}$  slip event produced pseudotachylyte on a new slip surface, the total integrated thickness of pseudotachylyte within the fault rocks should be around 1 km. Such cumulative thicknesses of pseudotachylyte are never observed in Alpine Fault outcrops. Why not? Is it because there are problems preserving and recognizing the pseudotachylyte? Pseudotachylyte in the cataclasite zone at Gaunt Creek has been altered almost beyond recognition, but this sort of alteration is not pervasive within the fault rocks so should not prevent recognition of the material elsewhere, hence we do not favour this interpretation.

Alternatively, it may be that other dynamic weakening mechanisms such as thermal pressurization (Sibson 1973; Lachenbruch 1980), elastohydrodynamic lubrication (Brodsky & Kanamori 2001) or granular fluidization (Brodsky *et al.* 2008) operated during seismic slip so that frictional heating was insignificant. This seems the most likely explanation based on our observations that granular fluidized materials (to be described in a separate publication) are also present in the fault zone. In addition, fluids were transiently (in both space and time) present during frictional melting since hydrous mineral assemblages both pre- and post-date friction melt generation, and amygdules are present in some pseudotachylytes. These weakening mechanisms are likely to be associated with the nucleation and propagation of large earthquake ruptures through the fault zone.

At present, comparatively few moderate magnitude ( $3 < M_w < 6$ ) earthquakes are convincingly located in the down-dip projection of the Alpine Fault Zone (Fig. 11). However, if we assume that the exhumed sequence is representative of one ‘slice’ through the seismogenic zone, the pseudotachylytes presently exposed could have been generated at any time during exhumation of that

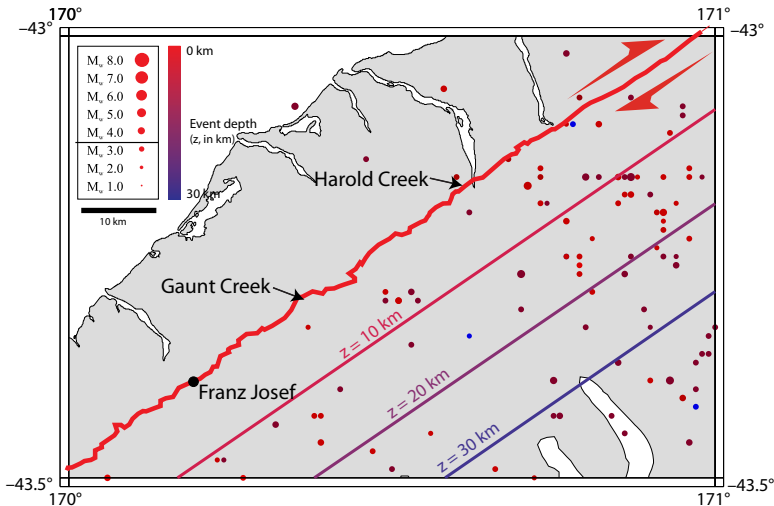


**Fig. 11.**  $M_w > 3.5$  seismic events recorded by the New Zealand National Seismic Network (NZNSN) in the vicinity of the central Alpine Fault, in the period 1989–2009. The down-dip projection of the Alpine Fault, assuming a 45° dip, is also indicated. Both earthquake epicentres and the fault-plane contours are coloured for depth, so that it is possible to see that most of the hypocentres (foci) lie in the hanging wall crust above the Alpine Fault Zone.

sequence through the brittle regime. At uplift rates of 9 mm year<sup>-1</sup> (Little *et al.* 2005), exhumation of an 8 km-thick seismogenic zone occurs in approximately 90 000 years; 30 000 times the period of observation illustrated in Figure 11. This seems ample time for the small number of pseudotachylytes observed in outcrop to have been generated by the moderate-sized earthquakes recorded historically.

Unfortunately, there is insufficient information to estimate the magnitudes of earthquakes responsible for the generation of the observed pseudotachylytes. Moment magnitude ( $M_w$ ) depends on rupture area, which cannot be constrained as outcrop areas are small, and average coseismic slip increment, which cannot be constrained because of a lack of offset markers, particularly in cases where failure occurred parallel to the mylonitic foliation. However, the pseudotachylytes' habits and structural settings provide some clues about how they are related to large 'characteristic' Alpine Fault earthquakes.

In the section we have examined (approximately Haast–Hokitika) (Fig. 1), the Alpine Fault juxtaposes quite different hanging wall and footwall lithologies. Some type (ii) pseudotachylytes do occur at and around lithological boundaries that could be the main principal slip surface of the fault at depth. These pseudotachylytes may well have formed during large Alpine Fault ruptures either on the main rupture plane or as part of a damage zone surrounding it. However, most of the pseudotachylytes are hosted on fault surfaces within one lithology or lithological group (e.g. metabasite layers within quartzofeldspathic, Alpine Schist-derived

mylonites). We recognize that it is possible that large fault ruptures do not always exploit pre-existing lithological boundaries, but infer that these surfaces mostly do not represent the principal slip surface of the Alpine Fault at depth.

This inference is supported by the structural style of the pseudotachylyte-hosting structures. Field observations of mature faults, defined as faults that have accommodated large displacements, possibly by numerous increments of slip (Cowie & Scholz 1992), indicate these structures develop distinct internal fabrics and well-developed, localized zones of cataclasite (Chester & Logan 1987; Frost *et al.* 2009). They may also have relatively wide zones of associated damage (Faulkner *et al.* 2008). Conversely, most Alpine Fault pseudotachylytes are hosted on relatively simple faults, lacking evidence of well-developed associated damage zones or overprinting relationships, indicating that they result from numerous increments of slip. We suggest these are single-jerk structures formed by shear failure of cohesive rock, rather than the principal slip surface of a mature plate-boundary structure.

Type (iv) pseudotachylytes are different because they occur within a well-developed zone of cataclastic damage surrounding the principal slip surface of the Alpine Fault. It is likely they were formed during large 'characteristic' Alpine Fault earthquakes, but again not on the principal slip surface of the major fault.

It is estimated that most Alpine Fault pseudotachylytes were formed in the depth range of 4–10 km or greater, while most historical earthquakes

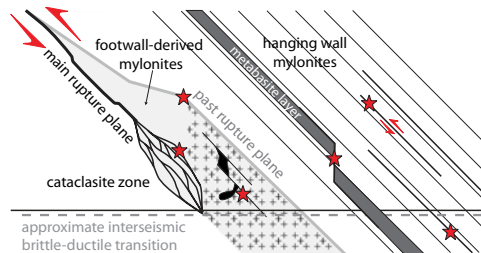


**Fig. 12.** Schematic illustration of the various habitats of pseudotachylyte in the Alpine Fault Zone. Red stars illustrate possible sites of pseudotachylyte generation. Viewed towards the NE.

(Fig. 11) have hypocentres (foci) at depths of 10 km or less (also see Leitner *et al.* 2001). Thus, pseudotachylytes formed at the shallower estimated depths could have formed during moderate magnitude events similar to those illustrated in Figure 11. However, type (i) and (ii) pseudotachylytes display evidence of formation at or below the base of the contemporary seismogenic zone as they are overprinted by ductile structures (recrystallized quartz veins) or remylonitized. These pseudotachylytes may represent splay-type faults at the down-dip termination of large earthquake ruptures.

## Conclusions

Pseudotachylyte occurs in four major settings in New Zealand's Alpine Fault Zone (Fig. 12). These are:

- (i) in strongly foliated, quartzofeldspathic hanging wall mylonites – the thin fault veins mostly lie parallel to the mylonitic foliation, and injection structures are uncommon;
- (ii) on lithological boundaries, particularly between footwall- and hanging wall-derived mylonites, and at the boundaries of metabasic layers and lozenges – most fault veins are up to 1 cm in thickness;
- (iii) in mylonites derived from a footwall protolith – in this setting, voluminous pseudotachylytes occur in injection structures;
- (iv) within the cataclasites that make up the fault core – fluids were variably present coeval with frictional melting in this setting.

Pseudotachylytes were formed in the approximate depth range of 4–10 km or greater. The deeper limiting depth is at and below the ‘brittle–ductile’ transition indicated by hanging wall seismicity distributions, and which would be found from

examination of the fault’s thermal structure. This illustrates that some earthquake ruptures may propagate into this zone, which has implications for estimates of the seismic moment potential of the fault (cf. Sutherland *et al.* 2007, who estimated that the fault is capable of generating  $M_w$  7.6–7.9 earthquakes assuming the fault rupture stretches 12 km down-dip; i.e. to a depth of c. 8.5 km).

The most voluminous pseudotachylytes within the fault rocks occur in settings (ii) and (iii). In setting (iii), this is related to the composition of the host rock, which contains abundant hydrous minerals, and to their relatively anisotropic nature. Alternatively, we could interpret that pseudotachylyte formation in this fault zone is most common in the immediate footwall, and around the brittle–ductile transition in the hanging wall. In setting (ii), rheological heterogeneities play a major role in localizing seismic slip.

Although widely distributed, it is unlikely that pseudotachylytes were generated and preserved during every Alpine Fault earthquake. It is possible that most of the observed pseudotachylytes were generated in the period between large earthquakes on the fault, during the sparse moderate magnitude ( $3 < M_w < 6$ ) events that are recorded by the New Zealand National Seismic Network. During large earthquakes, we infer that other coseismic weakening mechanisms, particularly thermal pressurization and granular fluidization, are more important. We cannot rule out that the pseudotachylytes formed during foreshock and aftershock sequences at the down-dip termination of larger fault ruptures or in the damage zone surrounding the principal slip surface of the Alpine Fault during large ‘characteristic’ earthquakes.

V. G. Toy acknowledges financial support from a University of Otago post-graduate scholarship during the early stages of this research. J. Scott provided helpful comments on a draft, and detailed reviews by L. Warr and an anonymous reviewer helped us to substantially improve the manuscript.

## References

- ADAMS, C. J. 1981. Uplift rates and thermal structure in the Alpine Fault Zone and Alpine Schists, Southern Alps, New Zealand. *In: McCRAY, K. R. & PRICE, N. J. (eds) Thrust and Nappe Tectonics*. Geological Society, London, Special Publications, **9**, 211–222.
- ALLEN, A. R. 1979. Mechanism of frictional fusion in fault zones. *Journal of Structural Geology*, **1**, 231–243.
- BARKER, S. L. L. 2005. Pseudotachylyte-generating faults in Central Otago, New Zealand. *Tectonophysics*, **397**, 211–223.

- BOSSIÈRE, G. 1991. Petrology of pseudotachylites from the Alpine Fault of New Zealand. *Tectonophysics*, **196**, 173–193.
- BOULLIER, A.-M., OHTANI, T., FUJIMOTO, K., ITO, H. & DUBOIS, M. 2001. Fluid inclusions in pseudotachylites from the Nojima fault, Japan. *Journal of Geophysical Research*, **106**, 21 965–21 977.
- BRAATHEN, A., OSMUNDSEN, P. T. & GABRIELSEN, R. H. 2004. Dynamic development of fault rocks in a crustal-scale detachment; an example from western Norway. *Tectonics*, **23**, 21.
- BRADSHAW, J. 1993. A review of the Median Tectonic Zone: terrane boundaries and terrane amalgamation near the Median Tectonic Line. *New Zealand Journal of Geology and Geophysics*, **36**, 117–125.
- BRODSKY, E. E. & KANAMORI, H. 2001. Elastohydrodynamic lubrication of faults. *Journal of Geophysical Research*, **106**, 16 367–16 374.
- BRODSKY, E., ROWE, C., MENGHINI, F. & MOORE, J. 2008. A geological fingerprint of low-viscosity fault fluids mobilized during an earthquake. *Journal of Geophysical Research*, **114**, B01303, doi: 10.1029/2008JB005633.
- CAGGIANELLI, A., DE LORENZO, S. & PROSSER, G. 2005. Modeling the heat pulses generated on a fault plane during coseismic slip: inferences from the pseudotachylites of the Copanello cliffs (Calabria, Italy). *Tectonophysics*, **405**, 99–119.
- CHESTER, F. & LOGAN, J. 1987. Composite planar fabric of gouge from the Punchbowl Fault, California. *Journal of Structural Geology*, **9**, 621–634.
- COWAN, D. S. 1999. Do faults preserve a record of seismic slip? A field geologist's opinion. *Journal of Structural Geology*, **21**, 995–1001.
- COWIE, P. & SCHOLZ, C. 1992. Growth of faults by accumulation of seismic slip. *Journal of Geophysical Research*, **97**, 11 085–11 095.
- CRADDOCK, J. P. & MAGLOUGHIN, J. F. 2005. Calcite strains, kinematic indicators, and magnetic flow fabric of a Proterozoic pseudotachylite swarm, Minnesota River valley, USA. *Tectonophysics*, **402**, 153–168.
- DI TORO, G. & PENNACCHIONI, G. 2004. Superheated friction-induced melts in zoned pseudotachylites within the Adamello tonalites (Italian Southern Alps). *Journal of Structural Geology*, **26**, 1783–1801.
- DI TORO, G., PENNACCHIONI, G. & TEZA, G. 2005. Can pseudotachylites be used to infer earthquake source parameters? An example of limitations in the study of exhumed faults. *Tectonophysics*, **402**, 3–20.
- DIXON, J. E. & DIXON, T. H. 1989. Vesicles, amygdales, and similar structures in fault-generated pseudotachylites – comment. *Lithos*, **131**, 225–229.
- FABBRI, O., LIN, A. & TOKUSHIGE, H. 2000. Coeval formation of cataclasite and pseudotachylite in a Miocene forearc granodiorite, southern Kyushu, Japan. *Journal of Structural Geology*, **22**, 1015–1025.
- FAGERENG, A. & SIBSON, R. H. 2010. Mélange rheology and seismic style. *Geology*, **38**, 751–754, doi: 10.1130/G30868.1.
- FAULKNER, D. R., MITCHELL, T. M., RUTTER, E. H. & CEMBRANO, J. 2008. On the structure and mechanical properties of large strike-slip faults. In: WIBBERLEY, C., KURZ, W., IMBER, J., HOLDSWORTH, R. & COLLET-TINI, C. (eds) *The Internal Structure of Fault Zones: Implications for Mechanical and Fluid-flow Properties*. Geological Society, London, Special Publications, **299**, 139–150.
- FERRILL, D. A., MORRIS, A. P., EVANS, M. A., BURKHARD, M., GROSCHONG, R. H., JR. & ONASCH, C. M. 2004. Calcite twin morphology: a low-temperature deformation geothermometer. *Journal of Structural Geology*, **26**, 1521–1529.
- FROST, E., DOLAN, J., SAMMIS, C., HACKER, B., COLE, J. & RATSBACH, L. 2009. Progressive strain localization in a major strike-slip fault exhumed from mid-seismogenic depths: structural observations from the Salzach–Ennstal–Mariazell–Puchberg fault system, Austria. *Journal of Geophysical Research*, **114**, B04406, doi: 10.1029/2008JB005763.
- GIFKINS, C., HERRMAN, W. & LARGE, R. (eds) 2005. *Altered Volcanic Rocks: A Guide to Description and Interpretation*. Centre for Ore Deposit Research, University of Tasmania, Hobart.
- GRAPES, R. H. 1995. Uplift and exhumation of Alpine Schist, Southern Alps, New Zealand: thermobarometric constraints. *New Zealand Journal of Geology and Geophysics*, **38**, 525–533.
- JEFFREYS, H. 1942. On the mechanics of faulting. *Geological Magazine*, **79**, 291–295.
- JEHU, T. & CRAIG, R. 1932. Geology of the Outer Hebrides. Part V – North Harris and Lewis. *Transactions of the Royal Society of Edinburgh*, **57**, 839–874.
- LACHENBRUCH, A. H. 1980. Frictional heating, fluid pressure, and the resistance to fault motion. *Journal of Geophysical Research*, **85**, 6097–6112.
- LEITNER, B., EBERHART-PHILLIPS, D., ANDERSON, H. & NABELEK, J. L. 2001. A focussed look at the Alpine Fault, New Zealand: seismicity, focal mechanisms, and stress observations. *Journal of Geophysical Research*, **106**, 2193–2220.
- LIN, A. 1996. Injection veins of crushing-originated pseudotachylite and fault gouge formed during seismic faulting. *Engineering Geology*, **43**, 213–224.
- LIN, A. 2008. *Fossil Earthquakes: The Formation and Preservation of Pseudotachylites*. Lecture Notes in Earth Sciences, **111**. Springer, New York.
- LITTLE, T. A., COX, S., VRY, J. K. & BATT, G. 2005. Variations in exhumation level and uplift rate along the oblique-slip Alpine Fault, central Southern Alps, New Zealand. *Geological Society of America Bulletin*, **117**, 707–723.
- LITTLE, T. A., HOLCOMBE, R. J. & ILG, B. R. 2002. Ductile fabrics in the zone of active oblique convergence near the Alpine Fault, New Zealand: identifying the neotectonic overprint. *Journal of Structural Geology*, **24**, 193–217.
- LOCKNER, D. 1995. Rock failure. In: AHRENS, T. J. (ed.) *Rock Physics and Phase Relations: A Handbook of Physical Constants*. American Geophysical Union, Washington, DC, 127–147.
- MACAUDIERE, J. & BROWN, W. L. 1998. Progressive fracturing and twinning related to pseudotachylite generation. In: SNOKE, A. W., TULLIS, J. & TODD, V. R. (eds) *Fault-related Rocks: A Photographic*

- Atlas*. Princeton University Press, Princeton, NJ, 108–111.
- MADDOCK, R. H. 1992. Effects of lithology, cataclasis and melting on the composition of fault-generated pseudotachylites in Lewisian gneiss, Scotland. *Tectonophysics*, **204**, 261–278.
- MAGLOUGHIN, J. F. & SPRAY, J. G. 1992. Frictional melting processes and products in geological materials: introduction and discussion. *Tectonophysics*, **204**, 197–206.
- MCNULTY, B. A. 1995. Pseudotachylite generated in the semi-brittle and brittle regimes, Bench Canyon shear zone, central Sierra Nevada. *Journal of Structural Geology*, **17**, 1507–1521.
- NORRIS, R. J. & COOPER, A. F. 2001. Late Quaternary slip rates and slip-partitioning on the Alpine Fault, New Zealand. *Journal of Structural Geology*, **23**, 507–520.
- NORRIS, R. J. & COOPER, A. F. 2003. Very high strains recorded in mylonites along the Alpine Fault, New Zealand: implications for the deep structure of plate boundary faults. *Journal of Structural Geology*, **25**, 2141–2157.
- NORRIS, R. J. & COOPER, A. F. 2007. The Alpine Fault, New Zealand: Surface geology and field relationships. In: OKAYA, D., STERN, T. & DAVEY, F. (eds) *A Continental Plate Boundary: Tectonics at South Island, New Zealand*. American Geophysical Union, Geophysical Monograph, **175**, 159–178.
- PASSCHIER, C. W. & TROUW, R. A. J. 1996. *Micro-tectonics*. Springer, Berlin.
- RITCHIE, S. 2009. *Alpine Fault Pseudotachylites*. BSc(Hons) thesis, University of Otago.
- SCHERWATH, M., STERN, T., DAVEY, F., OKAYA, D., HOLBROOK, W. S., DAVIES, R. & KLEFFMANN, S. 2003. Lithospheric structure across oblique continental collision in New Zealand from wide-angle P wave modelling. *Journal of Geophysical Research*, **108**, 2566.
- SEWARD, D. & SIBSON, R. H. 1985. Fission-track age for a pseudotachylite from the Alpine Fault Zone, New Zealand. *New Zealand Journal of Geology and Geophysics*, **28**, 553–557.
- SHAND, S. 1916. The Pseudotachylite of Parijs (Orange Free State) and its relation to ‘Trap-Shotten gneiss’ and ‘flinty crush-rock’. *Quarterly Journal of the Geological Society, London*, **72**, 198–210.
- SHAW, C. A., KARLSTROM, K. E., WILLIAMS, M. L. & JERCINOVIC, M. J. 2001. Electron-microprobe monazite dating of ca. 1.71–1.63 Ga and ca. 1.45–1.38 Ga deformation in the Homestake shear zone, Colorado; origin and early evolution of a persistent intracontinental tectonic zone. *Geology*, **28**, 739–742.
- SIBSON, R. H. 1973. Interactions between temperature and pore-fluid pressure during earthquake faulting – a mechanism for partial or total stress relief. *Nature Physical Sciences*, **234**, 66.
- SIBSON, R. H. 1975. Generation of pseudotachylite by ancient seismic faulting. *Geophysical Journal of the Royal Astronomical Society (now Geophysical Journal International)*, **43**, 775–794.
- SIBSON, R. H. 1980. Transient discontinuities in ductile shear zones. *Journal of Structural Geology*, **2**, 165–171.
- SIBSON, R. H. 2003. Thickness of the seismic slip zone. *Bulletin of the Seismological Society of America*, **93**, 1169–1178.
- SIBSON, R. H. & TOY, V. G. 2006. The habitat of fault-generated pseudotachylite: presence vs absence of friction melt. In: ABERCROMBIE, R., MCGARR, A., KANAMORI, H. & DI TORO, G. (eds) *Radiated Energy and the Physics of Faulting*. American Geophysical Union, Geophysical Monograph, **170**, 153–166.
- SIBSON, R. H., WHITE, S. H. & ATKINSON, B. K. 1979. Fault rock distribution and structure within the Alpine Fault zone: a preliminary account. *Royal Society of New Zealand Bulletin*, **18**, 55–65.
- SPRAY, J. G. 1987. Artificial generation of pseudotachylite using friction welding apparatus: simulation of melting on a fault plane. *Journal of Structural Geology*, **9**, 49–60.
- STEVENSON, C. M., MAZER, J. J. & SCHEETZ, B. E. 1998. Laboratory obsidian hydration rates. In: SHACKLEY, M. S. (ed.) *Archeological Obsidian Studies*. Plenum Press, New York, 181–204.
- STIPP, M., STEUNITZ, H., HEILBRONNER, R. & SCHMID, S. M. 2002. The eastern Tonale fault zone: a ‘natural laboratory’ for crystal plastic deformation of quartz over a temperature range from 250 to 700 °C. *Journal of Structural Geology*, **24**, 1861–1884.
- SUTHERLAND, R., EBERHART-PHILLIPS, D. ET AL. 2007. Do great earthquakes occur on the Alpine Fault in central South Island, New Zealand? *Geophysical Research Abstracts*, **9**, 03148.
- SWANSON, M. T. 1989. Sidewall ripouts in strike-slip faults. *Journal of Structural Geology*, **11**, 933–948.
- SWANSON, M. T. 1998. Pseudotachylite-bearing strike-slip faults in mylonitic rocks. In: SNOKE, A. W., TULLIS, J. & TODD, V. R. (eds) *Fault-related Rocks: A Photographic Atlas*. Princeton University Press, Princeton, NJ, 104–107.
- TOY, V. G. 2007. *Rheology of the Alpine Fault mylonite zone: deformation processes at and below the base of the seismogenic zone in a major plate boundary structure*. PhD thesis, University of Otago.
- TOY, V. G., CRAW, D., COOPER, A. & NORRIS, R. 2010. Thermal regime in the central Alpine Fault zone, New Zealand: constraints from microstructures, biotite chemistry, and fluid inclusion data. *Tectonophysics*, **485**, 178–192.
- TOY, V. G., PRIOR, D. J. & NORRIS, R. J. 2008. Quartz textures in the Alpine fault mylonites: influence of pre-existing preferred orientations on fabric development during progressive uplift. *Journal of Structural Geology*, **30**, 602–621; doi: 10.1016/j.jsg.2008.01.001.
- VOLL, G. 1976. Recrystallization of quartz, biotite and feldspars from Erstfeld to the Leventina nappe, Swiss Alps, and its geological significance. *Schweizerische Mineralogische und Petrographische Mitteilungen*, **56**, 641–647.
- WALLACE, R. C. 1976. Partial fusion along the Alpine Fault Zone, New Zealand. *Geological Society of America Bulletin*, **87**, 1225–1228.
- WARR, L. N. & COX, S. C. 2001. Clay mineral transformations and weakening mechanisms along the Alpine Fault, New Zealand. In: HOLDSWORTH, R. E., STRACHAN, R. A., MAGLOUGHIN, J. F. & KNIFE, R. J. (eds) *The Nature and Tectonic Significance of Fault*

- Zone Weakening*. Geological Society, London, Special Publications, **186**, 85–101.
- WARR, L. N. & VAN DER PLUIJM, B. A. 2005. Crystal fractionation in the friction melts of seismic faults (Alpine Fault, New Zealand). *Tectonophysics*, **402**, 111–124.
- WARR, L. N., VAN DER PLUIJM, B. A., PEACOR, D. R. & HALL, C. M. 2003. Frictional melt pulses during a ~1.1 Ma earthquake along the Alpine Fault, New Zealand. *Earth and Planetary Science Letters*, **209**, 39–52.
- WARR, L., VAN DER PLUIJM, B. & TOURSCHER, S. 2007. The age and depth of exhumed friction melts along the Alpine Fault, New Zealand. *Geology*, **35**, 603–606.
- WIBBERLEY, C. A. J. & SHIMAMOTO, T. 2003. Internal structure and permeability of major strike-slip fault zones: the Median Tectonic Line in Mie Prefecture, Southwest Japan. *Journal of Structural Geology*, **25**, 59–78.



# Seismogenic structure of a crystalline thrust fault: fabric anisotropy and coeval pseudotachylite–mylonitic pseudotachylite in the Grizzly Creek Shear Zone, Colorado

JOSEPH L. ALLEN<sup>1</sup>\* & COLIN A. SHAW<sup>2</sup>

<sup>1</sup>*Department of Physical Sciences, Concord University, Athens, WV 24712-1000, USA*

<sup>2</sup>*Department of Earth Sciences, Montana State University, Bozeman, MT 59717, USA*

\*Corresponding author (e-mail: allenj@concord.edu)

**Abstract:** Field and microstructural observations from the Proterozoic Grizzly Creek Shear Zone suggest that crustal-scale fabric anisotropy exerted a significant control on earthquake rupture propagation during deformation at mid-crustal depths. The shear zone developed in amphibolite-facies supracrustal gneisses and granitoids, and consists of a 0.4–0.7 km-wide zone of high-strain rocks with foliation transposed to 256°/51°NW and top-to-the-south kinematics. The shear zone is overprinted by hundreds of veins of pseudotachylite, mylonitic pseudotachylite and ultramylonite. Field observations and whole-rock geochemical data suggest that pseudotachylite fault veins formed as a result of first-generation rupture through intact rock. Pseudotachylites are preferentially localized in as many as nine decametre-scale rupture zones dispersed across the width of the shear zone, concordant to foliation. We present a conceptual model for the asymmetric development of anisotropic fabric in a thrust-related fault zone in crystalline metamorphic rocks. Progressive tectonic exhumation of hanging wall rocks during thrusting results in the development of a crustal-scale anisotropic fabric that provides a preferentially weakened zone that could accommodate the propagation of earthquake ruptures from the seismogenic zone into the middle crust.

Pre-existing, crustal-scale structures are known to guide tectonic inheritance on continental scales and serve as a focus for seismicity (e.g. Sykes 1978; Thomas 2006; Albaric *et al.* 2009). Within felsic continental crust, metamorphic fabrics in basement rocks that formed in the lower and middle crust appear to be a significant factor controlling brittle fault development when the rocks are exhumed and reactivated in the upper crust (Beacom *et al.* 2001; Watts *et al.* 2007; Butler *et al.* 2008). As fabric anisotropy in basement rocks can influence faulting, it follows that anisotropy may also serve as a focus for earthquake rupture propagation, either as a fault develops or during brittle reactivation.

The continental fault-zone model of Sibson (1977) accounts for the development of pseudotachylite by seismogenic frictional melting within and above the brittle–plastic transition (Fig. 1); in the former setting, it may be synkinematic with mylonite (Sibson 1980). In the plastic regime, mylonites result from crystal-plastic processes leading to viscous flow at much lower, aseismic strain rates (Sibson 1977). The presence of mutually overprinting pseudotachylite and mylonite therefore indicates a deformational environment in which seismogenic rupture and aseismic creep occurred cyclically. This suggests strain rates must have fluctuated across at

least 10 orders of magnitude ( $c. 10^{-2}$ – $10^{-12} \text{ s}^{-1}$ ), dependent upon the thickness and rate of the aseismically creeping layer. Unequivocal preservation of this extreme contrast in strain rates is uncommon and has only been documented in a handful of locations around the world (see Sibson & Toy 2006, and more recent examples documented by Shaw & Allen 2007; Chattopadhyay *et al.* 2008; Moecher & Steltenpohl 2009).

Sibson's fault-zone model and subsequent modifications (Sibson 1986; Scholz 1988, 2002) predict that deformation zones should widen with depth. Seismically active faults may be rooted within broad mylonite–ultramylonite zones in the lower crust in order to accommodate high strain rates in the upper crust (Whitmeyer & Simpson 2003). Earthquake ruptures are interpreted from seismological data and modelling to occur below the seismogenic regime from the downward propagation of large ruptures (Das & Scholz 1983; Strehlau 1986), consistent with observations of coeval pseudotachylite and mylonite in exhumed faults (e.g. Lin *et al.* 2005). Such occurrences offer an opportunity to examine the internal seismogenic structure of a fault zone and evaluate whether mid-crustal earthquakes are randomly dispersed or systematically distributed. Most studies of coeval mylonites and pseudotachylites have focused on geochemical and

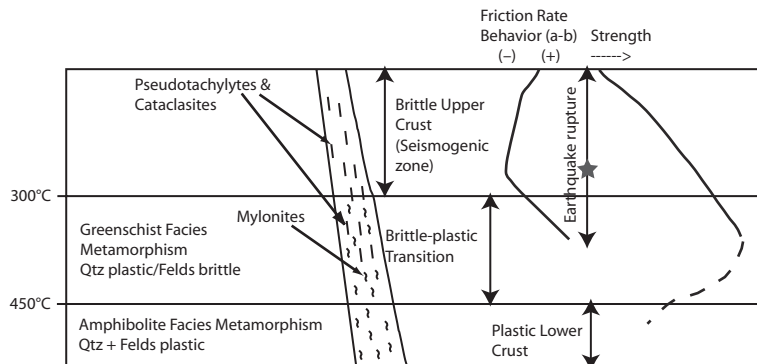


**Fig. 1.** Conceptual model for a fault zone (adapted from Sibson 1977, 1986; Scholz 2002). Earthquakes nucleate in the seismogenic zone where friction rate is negative, resulting in velocity weakening (Scholz 1988). Rock strength increases linearly into the middle crust, which is interpreted to be the maximum rupture depth for a large earthquake nucleating near the base of the seismogenic zone (Das & Scholz 1983). In the middle crust, seismogenic pseudotachylites may be coeval with mylonites generated by crystal-plastic deformation. In this figure and throughout this paper, we use the shortened term ‘plastic’ to refer to crystal-plasticity as a deformation mechanism.

microstructural relationships; comparatively fewer studies have aimed to document these fault-rock associations at macroscopic scales (e.g. Passchier 1982a; Camacho *et al.* 1995; Lin *et al.* 2005; Shaw & Allen 2007). In this paper, we examine the relationship between pseudotachylite zones, mylonitic pseudotachylite and the crustal-scale structure of the newly described Grizzly Creek shear zone, which is preserved in amphibolite-facies supracrustal rocks in the Palaeoproterozoic basement of the southern Rocky Mountains. We document the geometry and kinematics of the system, and discuss the significance of the shear zone to understanding tectonic fabric controls on seismicity in the middle crust.

## Geological setting

The Grizzly Creek Shear Zone is exposed in two tributaries to Glenwood Canyon, Colorado, where the Colorado River is deeply incised into the southern margin of the White River uplift, a Laramide basement arch in the Rocky Mountain foreland (Fig. 2). Exposures in the canyons of Grizzly Creek and No Name Creek provide an outstanding cross-section of the shear zone with approximately 450 m of relief (Fig. 3). The shear zone cuts amphibolite-facies supracrustal metamorphic rocks and granitic plutons, with preliminary U–Pb ages between 1760 and 1740 Ma (Jones *et al.* 2007; Kirkham *et al.* 2008). The shear zone is truncated by the non-conformity beneath the Upper Cambrian Sawatch Formation and is offset by the Laramide-age Grizzly Creek Fault.

The Grizzly Creek Shear Zone lies within the Yavapai Province that was assembled to the southern

margin of Laurentia around 1750–1700 Ma (e.g. Karlstrom & Bowring 1988). Between approximately 1450 and 1350 Ma the lithosphere of the entire province was perforated by an extensive episode of A-type granitic plutonism (Silver *et al.* 1977; Anderson 1983) and affected by regional greenschist-facies metamorphism (Shaw *et al.* 1999, 2005). During this same interval of time a through-going system of NE-trending transpressional shear zones developed in central Colorado including the Homestake and Idaho Springs–Ralston shear zones (Shaw *et al.* 2001, 2002; McCoy *et al.* 2005). This Mesoproterozoic shear-zone system appears to have focused Mesozoic–Cenozoic mineralization into a 100 km-wide zone that cuts across the southern Rocky Mountains forming the Colorado Mineral Belt (Fig. 2) (Tweto & Sims 1963).

The observation that the Grizzly Creek and Homestake shear zones both comprise a similar assemblage of tectonites including mylonite, ultramylonite, and pseudotachylite suggests that the two shear zones may have formed under similar crustal conditions (Allen & Shaw 2007). Also, regional muscovite and biotite  $^{40}\text{Ar}/^{39}\text{Ar}$  data (Shaw *et al.* 2005) show that most exposed basement rocks in central Colorado cooled below 300 °C by about 1.35 Ga. As this is approximately the lower temperature limit for quartz ductility (van Daalen *et al.* 1999; Stipp *et al.* 2002), it is unlikely that either shear zone formed after about 1.35 Ga. Both of these observations support the hypothesis that the Grizzly Creek Shear Zone may be broadly contemporaneous with the approximately 1.4 Ga Colorado Mineral Belt Shear Zone System described by McCoy *et al.* (2005) that includes the Homestake Shear Zone (Shaw *et al.* 2001).

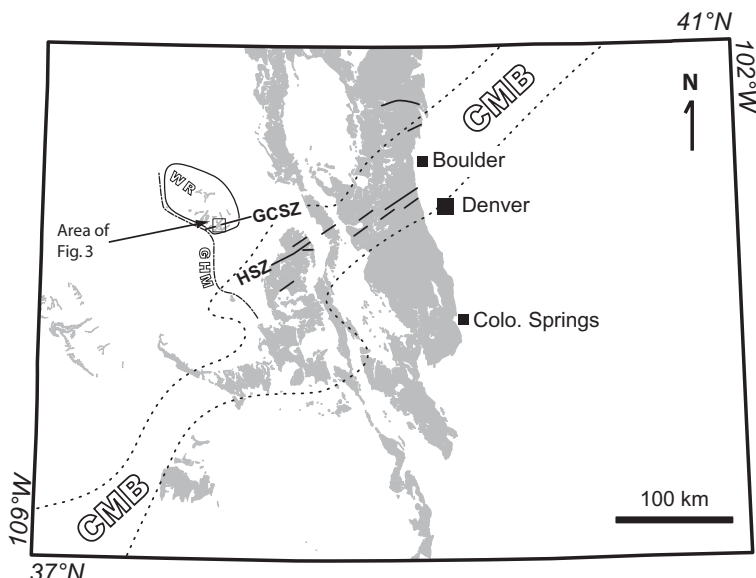


**Fig. 2.** Location map showing the distribution of exhumed Precambrian rocks (shaded) in the State of Colorado, USA. Phanerozoic features (outline text) include the Laramide White River uplift (WR), Grand Hogback monocline (GHB) and the Colorado mineral belt (CMB; Tweto & Sims 1963). Proterozoic features (bold text) include the Homestake Shear Zone (HSZ) and the Grizzly Creek Shear Zone (GCSZ) as well as numerous unlabelled shear zones within the Colorado mineral belt. Box shows the area of Figure 3.

The Grizzly Creek Shear Zone coincides with a left step in the Laramide Grand Hogback monocline, and bounds the margin of a late Cenozoic evaporite collapse basin (Fig. 2). This suggests that the shear zone represents a long-lived lithospheric weakness initiated during Mesoproterozoic intra-continental tectonism.

### Host rock lithology

We define the Grizzly Creek Shear Zone as a 400–700 m-thick zone of moderately NNW-dipping, high-strain fabrics and tectonites exposed in cross-section in the canyons of No Name Creek and Grizzly Creek (Fig. 3). The lateral extent of the shear zone is unknown because it is covered by Palaeozoic strata along strike to the east and west. The shear zone is hosted by three major lithological units; (i) supracrustal gneiss; (ii) megacrystic granite; and (iii) fine-grained, foliated granite.

#### Supracrustal gneiss

The supracrustal gneiss is a heterogeneous metamorphic rock unit that primarily consists of biotite–muscovite gneiss and mica schist. It is the most abundant rock unit in the vicinity of the shear zone. Supracrustal metamorphic rocks throughout Colorado range in age from more than 1750 Ma to

approximately 1650 Ma (Bickford 1988; Reed *et al.* 1993). We infer the age of the supracrustal gneiss to be greater than 1760 Ma on the basis of the age of granitoids that intrude the gneiss (Allen & Shaw 2007). The rock unit is typically composed of fine-grained quartz, alkali feldspar, plagioclase, and as much as 20–35% biotite and muscovite where the unit is schistose. The mineralogy locally includes garnet and fibrous sillimanite, especially within the hanging wall block. Locally, biotite is partially replaced by chlorite. Migmatitic leucosomes of quartz and alkali feldspar are present in cm-thick bands up to 1 m long.

The supracrustal gneiss is cut by 1–20 m-thick, tabular pegmatite and aplite bodies that are concordant with the enclosing NNW-dipping gneissic foliation. Within and near the shear zone, the pegmatite and aplite exhibit lower strain than surrounding rocks, and are composed of pink alkali feldspar, and lesser amounts of quartz, plagioclase, biotite and muscovite. An equigranular texture in the pegmatite and aplite bodies contrasts with well-developed gneissic foliation in the supracrustal host rocks.

#### Megacrystic granite

A megacrystic granite is present in the lower half of the Grizzly Creek Shear Zone and in the footwall

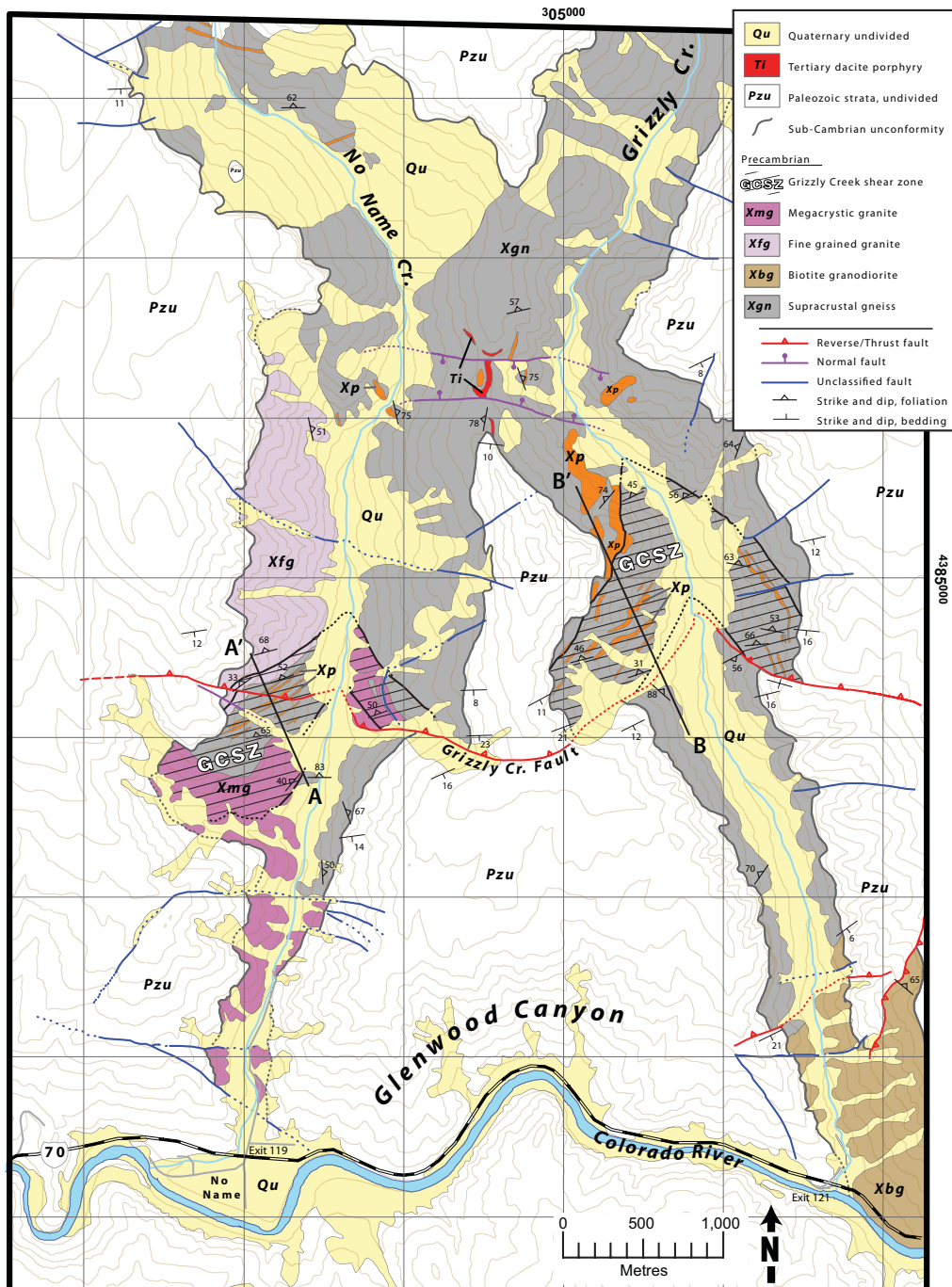


**Fig. 3.** Geological map of the Grizzly Creek Shear Zone and the Proterozoic rocks along the southern margin of the White River uplift (location shown on Fig. 2). A–A' shows the location of the line of section illustrated in Figure 4a; B–B' shows the location of the photograph in Figure 4b. Precambrian geological mapping by authors; Phanerozoic geology simplified from Kirkham *et al.* (2008). The topographical contour interval is 200 feet (61 m). 1000 m grid, UTM Zone 13N.

of the shear zone at No Name Creek. The rock unit shows discordant, intrusive relationships into the older supracrustal gneiss. The granite is distinctly bimodal with regards to grain size, and includes 2–8 cm tabular, euhedral phenocrysts of reddish-pink orthoclase dispersed within a coarse (0.1–1 cm) equigranular matrix of anhedral plagioclase (20–30%), orthoclase (25–35%), quartz (15–25%) and biotite (15–20%). In thin section, quartz is monocrystalline to coarsely polycrystalline, and has slightly to moderately undulose extinction. Orthoclase phenocrysts locally define a NW-striking, NE-dipping magmatic foliation and comprise as much as 20% of the rock unit.

In the footwall, solid-state deformation is apparent up to 100 m below the shear zone, where orthoclase phenocrysts are stretched and drawn out into irregularly shaped augen that are locally replaced by a fine-grained micaceous aggregate. Within the shear zone, the granite commonly exhibits higher-strain fabrics including protomylonite and a distinct solid-state gneissic foliation; phenocrysts are stretched into reddish-pink microfractured augen with aspect ratios exceeding 20:1. These high-strain fabrics are interspersed with 5–40 m-long macrolithons of relatively undeformed granite within protomylonitic granite that is locally difficult to distinguish from the biotite–muscovite gneiss. Preliminary LA-ICP-MS (Laser Ablation Inductively Coupled Plasma Mass Spectrometry) U–Pb and  $^{207}\text{Pb}/^{206}\text{Pb}$  ages for the megacrystic granite are  $1741 \pm 10$  Ma (Jones *et al.* 2007; Kirkham *et al.* 2008).

#### Fine-grained granite

A fine-grained granite crops out along the western slope of No Name Canyon where it is deformed in the upper part of the shear zone. The rock unit shows discordant, intrusive relationships into the older supracrustal gneiss. The texture is equigranular with a distinctive north-dipping, solid-state foliation. Primary mineral constituents include dynamically recrystallized grains of anhedral quartz, plagioclase, microcline, biotite and minor hornblende. A preliminary  $^{207}\text{Pb}/^{206}\text{Pb}$  age of  $1743 \pm 9$  Ma (Jones *et al.* 2007; Kirkham *et al.* 2008) suggests that the unit is coeval with intrusion of the megacrystic granite present in the footwall. The fine-grained granite is the primary host rock for mylonitic pseudotachylite and thin ultramylonite bands within the Grizzly Creek Shear Zone, as described in a subsequent section.

#### Structural features and tectonites in the Grizzly Creek Shear Zone

In cross-section, the Grizzly Creek Shear Zone consists of a thin, north- to NW-dipping mylonite

overlain by strongly foliated supracrustal gneisses and granitoid rocks cut by cataclasites and hundreds of pseudotachylite fault veins (Fig. 4). The foliation throughout the shear zone is moderately dipping  $256^\circ/51^\circ\text{NW}$ , in sharp contrast with steep foliations in the footwall and hanging wall (Fig. 5). An upper zone consisting of pseudotachylite, mylonitic pseudotachylite and ultramylonite is hosted by the fine-grained granite in the westernmost exposures of the shear zone at No Name Creek (Fig. 3).

#### Mylonite

A foliated and locally phyllonitic mylonite defines the base of the shear zone (Figs 4 & 6a). The mylonite is 10–20 m-thick, and represents approximately 2–3% of the volume of the shear zone. Submillimetre porphyroclasts consist of dynamically recrystallized quartz and brittley fractured feldspar in a very fine-grained, dusky-yellow to pale-olive micaceous matrix that dominates the composition of the rock. Evidence for solid-state strain and dynamic recrystallization in quartz includes undulose extinction, the development of subgrains and lattice-preferred orientation. Feldspars exhibit undulose extinction, fracturing and tiled microfaults; micas commonly show evidence of grain bending. Kinematic indicators are commonly monoclinic, and include sigma and delta mantled porphyroclasts visible in outcrop and thin section; observations parallel to lineation and perpendicular to foliation consistently show top-to-the-south displacement of the hanging wall relative to the footwall (Fig. 6b). Local *S*–*C* fabric and extensional shear bands (*C'*) also indicate top-to-the-south displacement. Minor fold axes and mineral stretching lineations preserved on foliation planes plunge down-dip to the north–NE ( $40^\circ \rightarrow 026^\circ$ ) (Fig. 5c).

#### Pseudotachylite

*Field relations.* In outcrop, pseudotachylite is greyish black to brownish black, and is in abrupt contact with host rocks (Fig. 6c). Pseudotachylite fault veins range from less than 0.5 mm to 15 cm thick, although veins ranging from 1 to 12 mm thick are most common. Thicker veins show lighter grey colour bands along the margins, suggestive of chilled margins discussed by others (e.g. Magloughlin 1989; Lin 2008). Host rocks are commonly intact and do not show evidence of a cataclastic precursor or retrogression, suggesting pseudotachylites are commonly first-generation ruptures. Offset markers in the host rock show cm-scale to dm-scale top-to-the-south kinematics, consistent with the kinematics exhibited by the basal mylonite. Injection veins are commonly

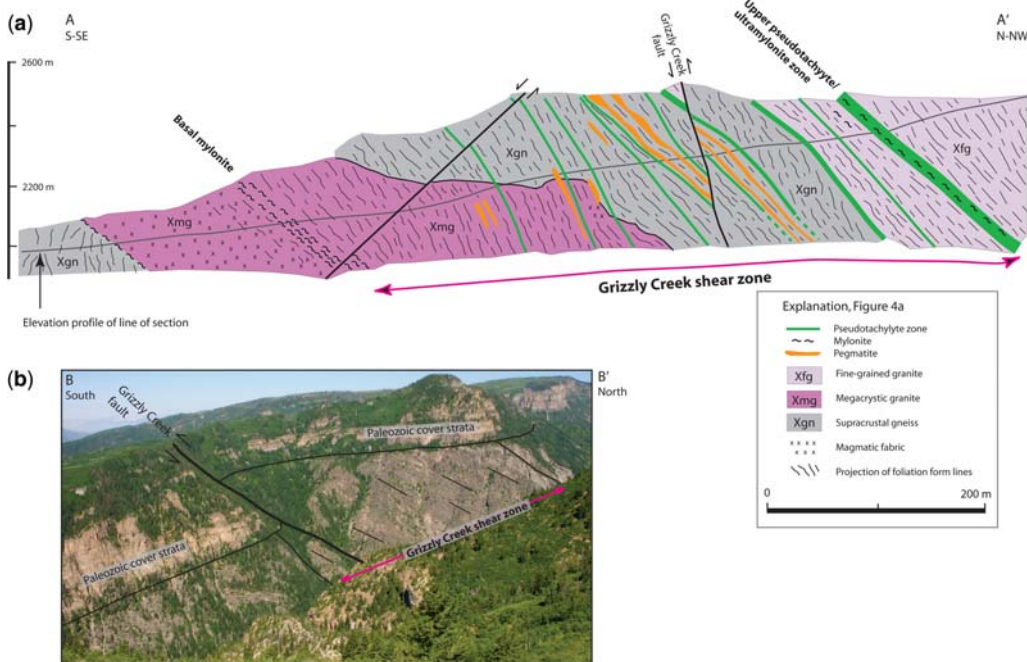


**Fig. 4.** (a) Cross-section across Grizzly Creek Shear Zone in the canyon of No Name Creek. The section shows foliation form surfaces, lithological units, mylonite and pseudotachylite rupture zones projected onto the line of section from detailed mapping in steep canyon exposures. Phanerozoic cover is omitted from the projection. View towards the WSW of an east-facing exposure in the canyon of No Name Creek. (b) Photograph across the Grizzly Creek Shear Zone in the canyon of Grizzly Creek illustrating the distinct north-dipping foliation within the shear zone (highlighted with black lines for clarity). View towards the NW of an east-facing exposure in the canyon of Grizzly Creek. In both (a) and (b), brittle faults are Laramide features post-dating Proterozoic pseudotachylite generation.

intensely fractured vein networks that are typically asymmetric about the fault vein and usually concentrated in the footwall of each fault vein. Less commonly, injection veins are solitary and orientated at high angles to fault veins. Pseudotachylite fault veins are commonly observed to cross-cut one another along strike or obliquely; steeper fault veins (dipping 45°–70°) are typically observed to be cut by lower-angle veins (dipping 20°–40°) (Fig. 6d). Steep veins are also cross-cut by thin, anastomosing cataclasite bands. The cataclasite bands are of mm-scale thickness and consist of 10–100 µm fractured quartz and feldspar clasts in a greyish orange–pink, very fine-grained micaceous matrix.

Pseudotachylites are mostly clustered into nine 4–20 m-thick zones representing the locus of repeated seismogenic rupture above the basal mylonite (Fig. 4). Each of these seismogenic rupture zones is concordant to the overall shear-zone foliation and consists of dozens of pseudotachylite fault veins. Within the seismogenic zones, fault veins are mostly concordant to foliation (or C-surfaces in the fine-grained granite in the upper

shear zone) (Fig. 6e). Where sufficiently exposed, discordant vein segments can locally be traced to concordant segments giving the impression of a south-climbing, stair-stepped geometry. Pseudotachylite is more widely dispersed between each of the mapped seismogenic rupture zones. Outside of the shear zone, only one pseudotachylite fault vein was observed in the footwall approximately 100 m below the basal mylonite. Although the seismogenic zones are mappable as continuous tectonic units, individual pseudotachylite fault veins typically cannot be traced more than a few metres due to a combination of local extent of exposure, complications associated with cross-cutting relationships and difficulty tracing individual veins in the predominantly dark-coloured supracrustal gneiss.

**Petrography.** In thin section, pseudotachylite consists of a black to light-brown cryptocrystalline matrix studded with relict lithic clasts inherited from the host rock (Fig. 6f). Lithic clasts include both mm-scale polymimetic fragments of the host rock, and smaller monomineralic fragments.

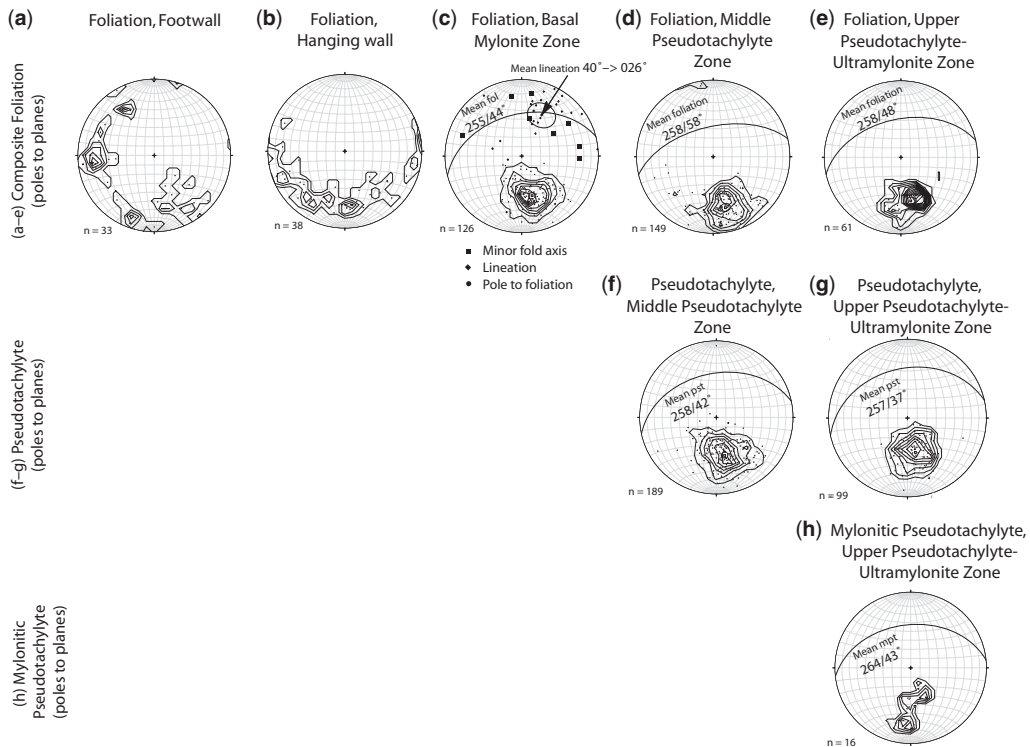


**Fig. 5.** (a)–(e) Equal-area stereograms showing foliations in footwall and hanging wall rocks (a and b) in comparison to the basal, middle and upper parts of the Grizzly Creek Shear Zone (c, d and e, respectively). (f)–(h) Equal-area stereograms showing pseudotachylite fault veins and mylonitic pseudotachylite fault veins. Contour interval 2% per 1% area, except for the mylonitic pseudotachylite data set (5% per 1% area). Lineations on foliation planes and minor fold axes are shown for the basal mylonite zone.

Clasts range from rounded and embayed to angular, and are dominated by monocrystalline and polycrystalline quartz, with lesser amounts of alkali feldspar and plagioclase. They represent up to 20–30% of the pseudotachylite by volume. Less abundant monomineralic clasts include magnetite, zircon, allanite, and fragments of biotite and hornblende. Petrographical observations indicate the presence of numerous features that are consistent with the rapid cooling of a melt (Sibson 1975; Maddock 1983; Magloughlin & Spray 1992; Swanson 1998; Lin 2008), including the presence of flow structures around relict lithic clasts, chilled vein margins, rounded embayments in lithic clasts, intracrystalline fractures in lithic clasts invaded by pseudotachylite and the presence of domains of spherulitic microlites.

**Geochemistry.** Pseudotachylites are commonly characterized by a bulk whole-rock chemistry that closely approximates that of the surrounding host rock (Maddock 1992; Magloughlin & Spray 1992;

Cosca *et al.* 2005; Lin 2008). The pseudotachylite chemical system often differs from other fault rocks, such as cataclasites and mylonites, which show chemical enhancement or depletion of some elements due to mass transfer during the introduction of external fluids in an open system (e.g. O’Hara & Blackburn 1989; Goddard & Evans 1995). Pseudotachylites generated on pre-existing fault planes lined with cataclasite may therefore chemically differ from host rock as chemical mass transfer along the fault plane may have occurred before melt generation. As an example, Di Toro & Pennacchioni (2005) measured increases in Fe, K, Rb, Ba and U, and a decrease in Si, Ca and Na in cataclasites and pseudotachylites compared to host rock, a relatively homogenous tonalite. In their study, pseudotachylites exhibited a chemical composition similar to the cataclasites, presumably because cataclasites were overprinted by pseudotachylite and their chemical signature was imparted upon the melt.

In order to characterize pseudotachylite from the Grizzly Creek Shear Zone, we compared the

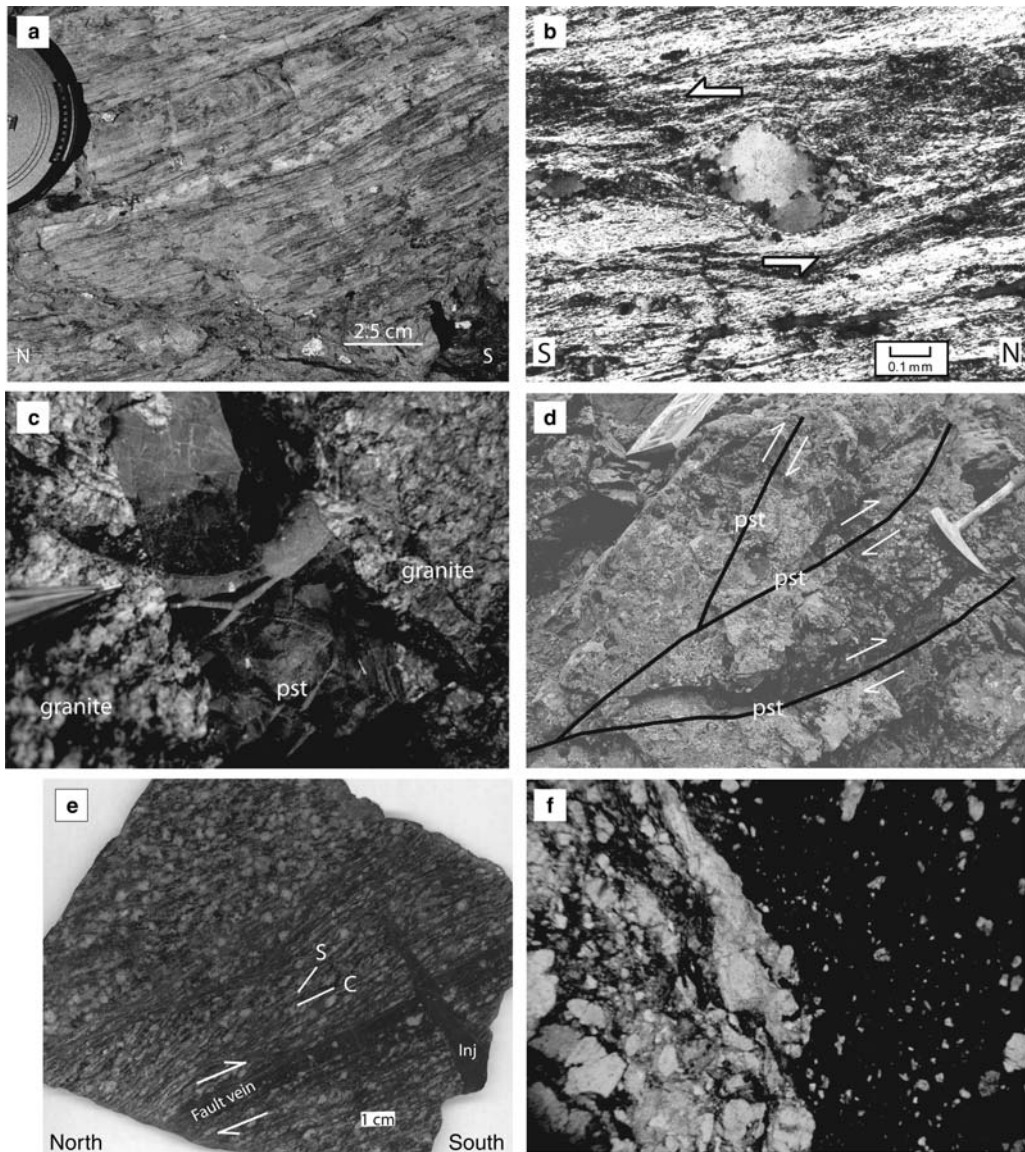


**Fig. 6.** (a) Outcrop photograph of the basal mylonite at Grizzly Creek. (b) Photomicrograph of asymmetric  $\sigma$ -quartz porphyroblast in micaceous matrix from the basal mylonite showing top-to-the-south sense of shear. (c) Outcrop photograph of pseudotachylite with macroscopic lithic clasts showing a sharp contact with fine-grained granite. Width of view is approximately 8 cm. (d) Outcrop photograph and sketch showing the cross-cutting relationships between three thin pseudotachylite fault veins. View towards east. (e) Polished slab of fine-grained granite showing  $S-C$  fabric. Locally, the mylonitic pseudotachylite fault vein follows the  $C$ -surface and is cut by a younger injection vein (Inj) that is not overprinted by mylonite. (f) Photomicrograph showing lithic clasts in a dark cryptocrystalline pseudotachylite matrix (right). The width of view is 6.2 mm.

whole-rock chemistry of bulk pseudotachylite and adjacent host rock from three sample pairs in the fine-grained granite. This rock is the finest-grained, and the most mineralogically and texturally homogenous lithological unit in the shear zone, which

should result in greater chemical similarity between pseudotachylite and host rock between samples. Approximately 40–60 g of pseudotachylite and 600–800 g of the immediately adjacent host rock were sampled from three host rock–pseudotachylite

pairs along three separate fault veins. Samples of host rock were cut from areas without obvious injection veins in order to minimize contamination by the pseudotachylyte. Bulk pseudotachylyte samples, including lithic clasts, were isolated from the host rock. All samples were powdered, mixed with Li tetraborate and fused into a disk. Major and trace elements were analysed by wavelength-dispersive X-ray fluorescence (XRF) spectrometry on a Bruker S4 PIONEER with a 4 kW X-ray tube at the Michigan State University XRF laboratory.

The results of major- and trace-element analyses of pseudotachylyte fault veins and their associated host rocks are presented in Table 1. The bulk chemistry of both are similar, and show only a slight decrease in silica, and minimal increases in iron and alumina in bulk pseudotachylyte compared to host rock. Variations in some trace elements, such as Zr, are likely owing to the heterogeneous distribution of accessory minerals such as zircon, monazite and allanite in the host rock, which would be influenced by sample size. We interpret the results to indicate that pseudotachylyte was derived from the immediately adjacent host rock in a closed chemical system. For these three locations, this further supports our field observations suggesting that pseudotachylyte formed during first-generation

ruptures through intact rock that had not been, and was not subsequently, altered by fluid activity.

#### *Mylonitic pseudotachylyte and ultramylonite*

Some pseudotachylytes in the Grizzly Creek Shear Zone are plastically deformed and exhibit a mylonitic fabric (Fig. 7a, b). Field observations indicate mylonitic pseudotachylyte is mostly restricted to the fine-grained granite in the westernmost exposures of the upper shear zone where some of the observed veins were recognized to be mylonitic; one mylonitic vein was observed in supracrustal gneisses in the upper shear zone at Grizzly Creek. Mylonitic pseudotachylyte is concordant with foliation and the mean orientation of measured fault veins is 264°/43°NW (Fig. 5).

Field and petrographical characteristics are similar to mylonitic pseudotachylytes from other shear zones (e.g. Passchier 1982b, 1984; Passchier *et al.* 1990a; Pennacchioni & Cesare 1997; White 1998; Takagi *et al.* 2000). The mylonitic pseudotachylyte is medium grey-greenish grey with a streaked appearance parallel to fault-vein boundaries. In outcrop, mylonitic pseudotachylyte is recognized by the presence of injection veins branching off plastically deformed and foliated fault veins (Fig. 7a).

**Table 1.** Major- and trace-element analyses for three host rock–pseudotachylyte sample pairs

Sample	Host I [IW-2b]	Pst I [IW-1b]	Host II [IW-2d]	Pst II [IW-2c]	Host III [IW-3c]	Pst III [IW-3b]
<i>Major elements (wt%)</i>						
SiO <sub>2</sub>	64.78	64.60	66.05	65.30	66.74	64.82
TiO <sub>2</sub>	0.47	0.49	0.46	0.44	0.44	0.51
Al <sub>2</sub> O <sub>3</sub>	14.82	15.48	15.26	15.42	15.16	15.37
Fe <sub>2</sub> O <sub>3</sub>	4.10	4.26	3.85	4.08	3.77	4.32
MnO	0.05	0.04	0.03	0.05	0.04	0.05
MgO	2.46	2.51	2.27	2.22	2.18	2.57
CaO	2.97	2.58	1.93	2.66	1.93	2.68
Na <sub>2</sub> O	3.64	3.45	3.78	4.13	3.85	3.82
K <sub>2</sub> O	3.48	3.59	3.39	3.02	3.44	3.37
P <sub>2</sub> O <sub>5</sub>	0.21	0.22	0.20	0.20	0.20	0.22
LOI*	2.54	2.55	2.54	2.24	2.01	2.01
Total	99.52	99.77	99.76	99.78	99.76	99.74
<i>Trace elements (ppm)</i>						
Ni	46	54	45	62	53	67
Zn	33	35	32	35	31	50
Rb	105	107	101	106	102	135
Sr	665	722	684	748	682	655
Y	28	29	23	7	32	36
Zr	173	172	168	262	177	191
Ba	1075	1179	1056	1008	1078	1372
Cr, Cu, Nb	below detection					

\*LOI, loss on ignition.

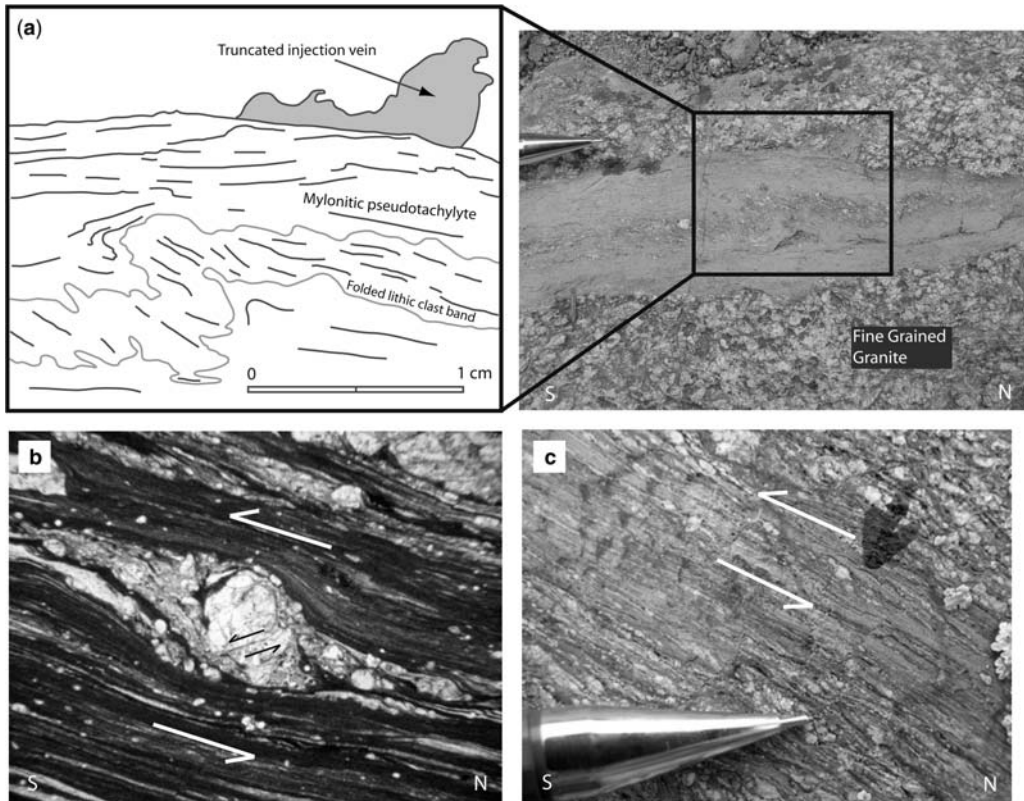


**Fig. 7.** (a) Outcrop photograph (right) and interpretive sketch (left) of mylonitic pseudotachylite fault vein and associated injection vein. Sketch illustrates the trend of foliation developed in mylonitic pseudotachylite and the outline of a folded band of lithic clasts. The injection vein is undeformed and truncated by plastic flow in the fault vein, suggesting that post-rupture aseismic creep was limited to the more spatially extensive planes formed by pseudotachylite fault veins parallel to subparallel to shear-zone foliation. (b) Photomicrograph of mylonitic pseudotachylite showing the mantled porphyroblast of feldspar. The asymmetry of tails in a mantling lithic clast and displacement on a brittle microfault (indicated by dark arrows) indicate top-to-the-south displacement. The width of view is 1.8 mm. (c) Outcrop photograph of an ultramylonite in fine-grained granite. The black arrow on the outcrop highlights a sigma porphyroblast, indicating top-to-the-south (left) kinematics.

Lithic clasts in injection veins may show little evidence of solid-state plastic deformation, except where the veins have been transposed into subparallelism with the parent fault vein. Mylonitic pseudotachylite veins are demonstrably cyclic, as undeformed pseudotachylite veins can be found cutting mylonitic pseudotachylite (Fig. 6e).

It is not clear why mylonitic pseudotachylite is restricted to the fine-grained granite and why it would be prevalent only at the top of the shear zone at a shallower crustal level. It may be that it is easier to recognize it in the light-coloured granite than in darker gneisses. Alternatively, the fine-grained granite is equigranular and, in comparison to the gneisses, it is less micaceous, thus suggesting that it may be more resistant to aseismic creep and plastic flow. Pseudotachylite generation resulted in

finer-grained zones that could serve as discontinuities favouring plastic flow. Passchier (1982b) suggested such a process for the generation of ultramylonite bands from pseudotachylite in France.

The fine-grained granite is locally cut by cm-scale veins of ultramylonite that are parallel to subparallel to the foliation. The ultramylonite exhibits a strong foliation and lineation with  $S-C$  fabric and sigma porphyroblasts (Fig. 7c). Quartz shows dynamic recrystallization to smaller subgrains, and feldspars exhibit brittle fractures and microfaults. Some ultramylonite could have formed as a result of obliteration of pseudotachylite veins during progressive mylonitization, although field confirmation of a pseudotachylite precursor for ultramylonite is difficult in the absence of low-strain injection veins.

## Discussion

Earthquakes characterize episodic brittle frictional deformation in the upper 15–18 km of continental crust in mature fault zones; the region defined as the seismogenic zone (Sibson 1982, 1983; Scholz 1988, 2002). The coeval generation of pseudotachylite and mylonitic pseudotachylite therefore poses a well-known paradox. As pseudotachylites are interpreted to be a result of seismogenic rupture, and mylonites represent deformation largely by intracrystalline plastic mechanisms, this suggests that melt-generating ruptures in the Grizzly Creek Shear Zone either (i) formed within the plastic regime or (ii) formed within the brittle–plastic transition because low temperatures above the transition would preclude the operation of mechanisms controlling intracrystalline deformation in quartz. In the following sections, we examine how progressive shear-zone development at the crustal scale provides an anisotropic fabric that favours localization of seismogenic ruptures.

### *Nature of cyclic pseudotachylite–mylonitic pseudotachylite*

Numerous mechanisms have been suggested to explain the generation of pseudotachylite below the seismogenic zone (also see the discussion by McNulty 1995). These include: (1) the development of transient plastic instabilities in mylonites (Sibson 1980; Hobbs *et al.* 1986; Hobbs & Ord 1988; White 1996, 1998); (2) stress amplification adjacent to or within rheologically rigid rock units (Sibson 1980; Koch & Masch 1992); and (3) dynamic propagation of earthquake ruptures from the seismogenic zone to greater depths (Sibson 1977, 1980; Strehlau 1986; Lin *et al.* 2003, 2005; Moecher & Steltenpohl 2009). The first two models suggest nucleation of ruptures in the plastic regime below the seismogenic zone. The latter model invokes nucleation of earthquake ruptures within the seismogenic zone.

Evidence supporting either the plastic instability model or the stress amplification model is not readily apparent in the Grizzly Creek Shear Zone. Plastic instabilities imply generation by a mechanism other than well-known models involving frictional wear and cataclasis, which are derived from extensive field observations, laboratory experiments and reconciliatory numerical models (e.g. Spray 1987, 1992, 1995; Swanson 1992; Di Toro *et al.* 2006, 2009). If transient ruptures occur in response to strain-rate fluctuations in natural mylonites, the development of features associated with frictional pseudotachylites from the shallow crust, including injection veins and lithic clasts, are not predicted (Moecher & Steltenpohl 2009). These features are present in pseudotachylites and mylonitic

pseudotachylites from the Grizzly Creek Shear Zone. Furthermore, the Grizzly Creek pseudotachylites neither occur within nor root within the basal mylonite, which accounts for only 2–3% of the shear zone. Rather, they are mostly localized within dispersed decametre-scale zones across the 700 m-thick shear zone (Fig. 4). Furthermore, at mid-crustal depths of approximately 15 km, thrust faults require high differential stresses ( $>1$  GPa) that are 2.6–4.3 times larger than strike-slip and normal faults in order to initiate failure on a pre-existing fault plane (Sibson 1974). Rupture of intact rock would require even higher differential stress. It is therefore unlikely that plastic instabilities generated in the basal mylonite could drive brittle rupture in high-strain rocks of the hanging wall.

The stress amplification model predicts nucleation of seismogenic ruptures around decametre-scale lozenges of rigid isotropic rock in response to either brittle frictional sliding or plastic instabilities below the seismogenic zone (Sibson 1980). Pseudotachylite zones in the Grizzly Creek Shear Zone are developed in both the supracrustal gneiss and fine-grained granite. Foliation-parallel pegmatites crop out within the shear zone, and these bodies are not pervasively deformed by ductile flow. The margins of some pegmatite units are locally cut by pseudotachylite, indicating that they were emplaced before the onset of brittle seismicity. However, there is no systematic spatial relationship between pseudotachylites and pegmatite, suggesting that they did not serve to amplify stress and trigger earthquake ruptures.

The hypocentres of large earthquakes in continental crust are located near the base of the seismogenic zone; downwards propagation to deeper crustal levels requires that ruptures penetrate stronger rock in the middle crust (Fig. 1), which slows rupture propagation significantly and inhibits deep propagation (Das & Scholz 1983; Scholz 1998). Therefore, models supporting propagation of a rupture within the middle crust would be aided by the presence of mechanical anisotropy parallel to the direction of crack propagation. In the next section, we explore how model (3), downwards rupture propagation, may be supported by the crustal-scale structure of the Grizzly Creek Shear Zone.

### *Seismogenic structure and anisotropy*

Seismogenic zones defined by pseudotachylite are systematically distributed throughout the Grizzly Creek Shear Zone. We propose a model that accounts for the development of fabric anisotropy at the crustal scale as a critical control on the distribution and preservation of pseudotachylite in the Grizzly Creek Shear Zone (Fig. 8). Progressive deformation in a crystalline thrust sheet rooted below the seismogenic

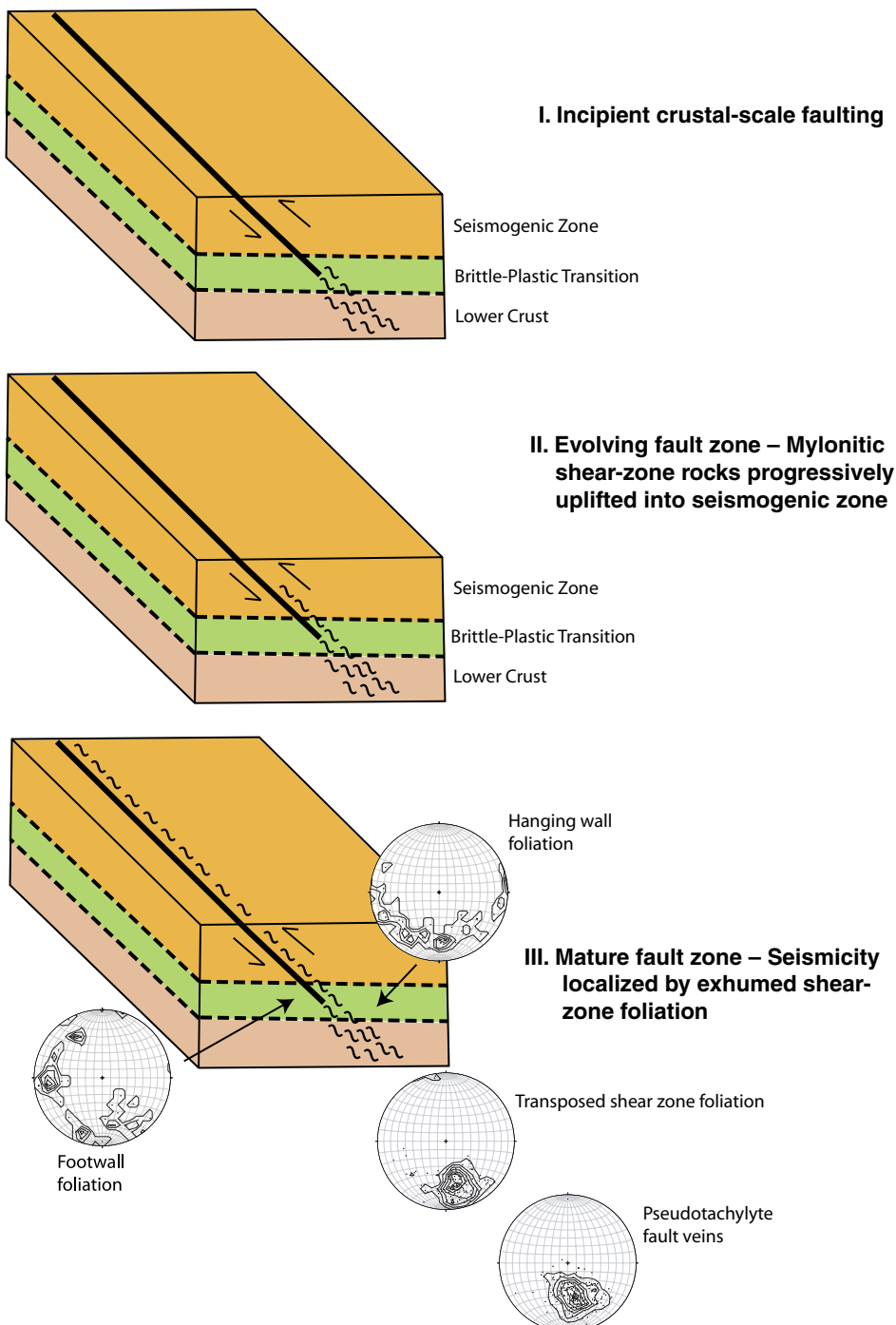


**Fig. 8.** Model for progressive asymmetric tectonic exhumation of mid-crustal rocks in a crustal-scale thrust. An incipient crustal-scale fault zone (I) evolves to translate high-strain, mid-crustal rocks up-dip through the base of the seismogenic zone (II), eventually resulting in progressive exhumation of the middle crust (III). Asymmetric anisotropy in the hanging wall could accommodate earthquake rupture propagation in the middle crust from downward propagation of large earthquakes nucleating at the base of the seismogenic zone.

zone would emplace mylonites and high-strain rocks into the upper crust (e.g. Grocott 1977). The distribution of mylonites and high-strain fabrics tectonically exhumed to the upper crust is predicted to be asymmetric and concentrated within the hanging wall of a crystalline thrust sheet (Passchier *et al.* 1990b). As experimental and field geological evidence indicates rocks are weaker parallel to fabric anisotropy in crystalline metamorphic rock (e.g. Donath 1961; Borg & Handin 1966; Baud *et al.* 2005; Butler *et al.* 2008), transposed north-dipping foliation and tabular pegmatite bodies in the Grizzly Creek Shear Zone provide a systematic grain to accommodate rupture propagation.

It is uncertain whether or not all of the pseudotachylite formed in the middle crust because only some of the veins in one lithological unit in the upper shear zone are mylonitic. However, the presence of mylonitic pseudotachylite indicates that the shear zone was located within the middle crust for at least part of the time in which pseudotachylite was generated. A possible mechanism for seismicity in this setting may include rupture nucleation in the seismogenic zone, followed by dynamic propagation along a crustal-scale anisotropic fabric into the middle crust, where some pseudotachylites were later overprinted by viscous flow in response to aseismic creep. Pseudotachylite fault veins that are not overprinted by mylonite may have formed in the middle crust coevally with mylonitic pseudotachylite and escaped viscous flow, presumably because they are hosted by micaceous rocks that could more readily have accommodated aseismic creep (e.g. Baud *et al.* 2005). Alternatively, some of them may have either (i) formed as the shear zone was exhumed during progressive deformation and uplift (through the mechanism described by Passchier 1982b) or (ii) formed at a later time. In either case, relict anisotropy was available to control their distribution in the upper crust.

How are mylonites spatially related to pseudotachylite in other fault systems? We have observed similar systematic relationships in the Homestake Shear Zone, a transpressional strike-slip system of pseudotachylite and mylonite 55 km SE of the Grizzly Creek Shear Zone (Fig. 2) (Allen 2005). At that location, subvertical pseudotachylite zones are located as far as 3 km strike-perpendicular from a subvertical mylonite zone (Shaw & Allen 2007). The presence of plastically deformed pseudotachylite within the mylonite (Shaw *et al.* 2001), and our recent observations of mutually overprinting pseudotachylite and mylonitic pseudotachylite within 200 m of the mylonite zone, suggest that the entire system may have represented partitioned aseismic creep localized in a mylonite zone, and episodic seismic rupture dispersed through the surrounding host rock. Pseudotachylite zones as

much as 25 m wide and containing up to 2% fault melt are clearly concordant to gneissic foliation in the host rock (Allen *et al.* 2002; Allen 2005).

In the Saint-Barthélemy Massif, pseudotachylite veins are mapped in the footwall beneath a 5–30 m-thick mylonite; the veins are generally concordant to foliation and are located within 250 m of the mylonite (Passchier 1982a). In the Woodroffe Thrust, a 1 km-thick zone consisting of 4% vol. pseudotachylite is localized in the hanging wall above a thick basal mylonite–ultramylonite (Camacho *et al.* 1995). Where exposed, pseudotachylites, mylonites and ultramylonites are shown to be concordant to foliation, which dips SSE in the hanging wall of the Woodroffe Thrust (Lin *et al.* 2005). Although pseudotachylite–mylonite relationships at the fault-zone scale are known only from a few studies at present, these observations suggest that seismogenic rupture associated with frictional melting is systematically distributed in mid-crustal shear zones. In a recent literature survey, Sibson & Toy (2006) estimated that 61% of pseudotachylites described in foliated rocks were reported to be concordant to foliation (presumably at mesoscopic scales). As a consequence, such fault zones may exhibit a systematic seismogenic structure that could be elucidated on a broader scale if carefully mapped.

Strehlau (1986) demonstrated that downwards propagation of earthquake ruptures below the base of the seismogenic zone is aided by a decrease in the static coefficient of friction ( $\mu$ ), a process that can be triggered by frictional melting and pseudotachylite generation (Di Toro *et al.* 2006). In micaceous crystalline rocks, anisotropy extending from the seismogenic zone through the middle crust would serve as an additional mechanism to decrease the coefficient of friction as micas have low values of  $\mu$  (0.3) compared to isotropic igneous rocks (where  $\mu = 0.7$ ) (Baud *et al.* 2005). Observations of asymmetric anisotropy and the systematic distribution of seismogenic pseudotachylites in the Grizzly Creek Shear Zone are analogous to indirect observations of crustal-scale seismicity beneath active fold-thrust belts (e.g. Berberian 1995; Lavecchia *et al.* 2003; Paul *et al.* 2006). In a crustal-scale thrust system in the Italian Apennines, Lavecchia *et al.* (2003) noted a relationship between fault geometry and down-dip seismicity. They suggested that earthquake ruptures either propagated from the base of the seismogenic zone into deeper crystalline rocks, or nucleated at depth due to plastic instabilities or pore-fluid overpressurization. Regardless of the focal depth and mechanism of rupture nucleation, the progressive development of anisotropy during the evolution of a basement-involved thrust belt provides a preferential path for rupture propagation.

## Conclusions

The results of this study indicate that the Grizzly Creek shear zone is a Proterozoic crystalline thrust that developed in the middle crust during top-to-the-south displacement along a 400–700 m-wide zone of mylonitic rocks and transposed foliation with a mean orientation of 256°/51°NW. The shear zone cuts three lithological units, including micaceous, amphibolite-facies supracrustal gneiss and schist, a megacrystic granite, and a fine-grained granite. Seismicity in the shear zone was systematically localized above a basal mylonite and largely concentrated into nine decametre-scale rupture zones that are concordant to shear-zone foliation. Chemical similarity between the bulk pseudotachylite and host rock, and sharp boundaries between pseudotachylite and unaltered host rock, suggest that frictional melting was generated during the propagation of individual seismogenic ruptures through intact rock. In westernmost exposures of the shear zone, the upper shear zone is characterized by the presence of mylonitic pseudotachylite within the fine-grained granite. These tectonites document cyclic frictional-plastic deformation, indicating that at least some of the seismicity occurred below the seismogenic zone.

The systematic seismogenic structure of the shear zone indicates that crustal-scale fabric anisotropy exerted a significant control on earthquake rupture propagation during deformation. Progressive deformation in a mid-crustal thrust results in the development of asymmetric anisotropy as hanging wall rocks are translated up-dip into the seismogenic zone (Fig. 8). The resulting structure provides an anisotropically weakened connection between the middle crust and the seismogenic zone that can favour downwards propagation of large earthquake ruptures from the base of the seismogenic zone into the stronger middle crust.

Research was supported by the National Science Foundation (EAR-0635894 and EAR-0635920), the donors of the American Chemical Society Petroleum Research Fund and the US Geological Survey EDMAP program. Numerous undergraduate students participated in fieldwork, including F. Ferri, M. Ganak, A. Graves, A. Johnson, S. Lyman, S. Mumma, J. Ofsa and J. Skeen. I. M. Ware participated in two field seasons of mapping, prepared samples and provided important scientific contributions to this study. A. Lin, D. P. Moecher and V. G. Toy provided helpful reviews that improved the manuscript.

## References

- ALBARIC, J., DÉVERCHÈRE, J., PETIT, C., PERROT, J. & LE GALL, B. 2009. Crustal rheology and depth distribution of earthquakes: insights from the central and southern East African Rift System. *Tectonophysics*, **468**, 28–41.
- ALLEN, J. L. 2005. A multi-kilometer pseudotachylite system as an exhumed record of earthquake rupture geometry at hypocentral depths (Colorado, USA). *Tectonophysics*, **402**, 37–54.
- ALLEN, J. L. & SHAW, C. A. 2007. Proterozoic geology and Phanerozoic reactivation of the newly recognized Grizzly Creek shear zone, Glenwood Canyon, Colorado. In: RAYNOLDS, R. G. (ed.) *Discovering the Rocky Mountains: Geological Field Trips*. Geological Society of America, Field Guide, **10**, 45–61.
- ALLEN, J. L., O'HARA, K. D. & MOECHER, D. P. 2002. Structural geometry and thermal history of pseudotachylite from the Homestake shear zone, Sawatch Range, Colorado. In: LAGESON, D. (ed.) *Science at the Highest Level. Geological Field Trips*. Geological Society of America, Field Guide, **3**, 17–32.
- ANDERSON, J. L. 1983. Proterozoic anorogenic granite plutonism of North America. In: MEDARIS, L. G. JR, BYERS, C. W., MICKELSON, D. M. & SHANKS, W. C. (eds) *Proterozoic Geology: Selected Papers from an International Proterozoic Symposium*. Geological Society of America, Memoirs, **161**, 133–154.
- BAUD, P., LOUIS, L., DAVID, C., RAWLING, G. C. & WONG, T.-F. 2005. Effects of bedding and foliation on mechanical anisotropy, damage evolution and failure mode. In: BRUHN, D. & BURLINI, L. (eds) *High Strain Zones: Structure and Physical Properties*. Geological Society, London, Special Publications, **245**, 223–249.
- BEACOM, L. E., HOLDSWORTH, R. E., McCAFFREY, K. J. W. & ANDERSON, T. B. 2001. A quantitative study of the influence of pre-existing compositional and fabric heterogeneities upon fracture-zone development during basement reactivation. In: HOLDSWORTH, R. E., STRACHAN, R. A., MAGLOUGHIN, J. F. & KNIFE, R. J. (eds) *The Nature and Tectonic Significance of Fault Zone Weakening*. Geological Society, London, Special Publications, **186**, 195–211.
- BERBERIAN, M. 1995. Master 'blind' thrust faults hidden under the Zagros folds: active basement tectonics and surface morphotectonics. *Tectonophysics*, **241**, 193–224.
- BICKFORD, M. E. 1988. The accretion of Proterozoic crust in Colorado: igneous, sedimentary, deformational, and metamorphic history. In: ERNST, W. G. (ed.) *Metamorphism and Crustal Evolution of the Western United States*. Prentice-Hall, Englewood Cliffs, NJ, 411–429.
- BORG, I. & HANDIN, J. 1966. Experimental deformation of crystalline rocks. *Tectonophysics*, **3**, 249–367.
- BUTLER, R. W. H., BOND, C. E., SHIPTON, Z. K., JONES, R. R. & CASEY, M. 2008. Fabric anisotropy controls on faulting in the continental crust. *Journal of the Geological Society, London*, **165**, 449–452.
- CAMACHO, A., VERNON, R. H. & FITZGERALD, J. D. 1995. Large volumes of anhydrous pseudotachylite in the Woodroffe Thrust, eastern Musgrave Ranges, Australia. *Journal of Structural Geology*, **17**, 371–383.
- CHATTOPADHYAY, A., KHASDEO, L., HOLDSWORTH, R. E. & SMITH, S. A. F. 2008. Fault reactivation and pseudotachylite generation in the semi-brittle and brittle regimes: examples from the Gavilgarh–Tan Shear Zone, central India. *Geological Magazine*, **145**, 766–777.

- COSCA, M. A., CABY, R. & BUSSY, F. 2005. Geochemistry and  $^{40}\text{Ar}/^{39}\text{Ar}$  geochronology of pseudotachylite with UHP whiteschists from the Dora Maria massif, Italy. *Tectonophysics*, **402**, 93–110.
- DAS, S. & SCHOLZ, C. H. 1983. Why large earthquakes do not nucleate at shallow depths. *Nature*, **305**, 621–623.
- DI TORO, G. & PENNACCHIONI, G. 2005. Fault plane processes and mesoscopic structure of a strong-type seismogenic fault in tonalites (Adamello batholith, Southern Alps). *Tectonophysics*, **402**, 55–80.
- DI TORO, G., HIROSE, T., NIELSEN, S., PENNACCHIONI, G. & SHIMAMOTO, T. 2006. Natural and experimental evidence of melt lubrication of faults during earthquakes. *Science*, **311**, 647–649.
- DI TORO, G., PENNACCHIONI, G. & NIELSEN, S. 2009. Pseudotachylites and earthquake source mechanics. In: FUKUYAMA, E. (ed.) *Fault-zone Properties and Earthquake Rupture Dynamics*. Elsevier, Amsterdam, 87–134.
- DONATH, F. A. 1961. Experimental study of shear failure in anisotropic rocks. *Geological Society of America Bulletin*, **72**, 986–990.
- GODDARD, J. V. & EVANS, J. P. 1995. Chemical changes and fluid–rock interaction in faults of crystalline thrust sheets, northwestern Wyoming, U.S.A. *Journal of Structural Geology*, **17**, 533–547.
- GROCOTT, J. 1977. The relationship between Precambrian shear belts and modern fault systems. *Journal of the Geological Society, London*, **133**, 257–262.
- HOBBS, B. E. & ORD, A. 1988. Plastic instabilities: implications for the origin of intermediate and deep focus earthquakes. *Journal of Geophysical Research*, **93**, (B9), 10 521–10 540.
- HOBBS, B. E., ORD, A. & TEYSSIER, C. 1986. Earthquakes in the ductile regime? *Pure and Applied Geophysics*, **124**, 309–336.
- JONES, J. V. III, SHAW, C. A., GOODFELLOW, R. E. & HOUSH, T. 2007. U–Pb zircon age constraints on Proterozoic granitic magmatism and shear zone development in the Glenwood Springs area, Colorado. *Geological Society of America Abstracts with Programs*, **39**, 334.
- KARLSTROM, K. E. & BOWRING, S. A. 1988. Early Proterozoic assembly of tectonostratigraphic terranes in southwestern North America. *Journal of Geology*, **96**, 561–576.
- KIRKHAM, R. M., STREUFERT, R. K., CAPPA, J. A., SHAW, C. A., ALLEN, J. L. & JONES, J. V. 2008. *Geologic Map of the Glenwood Springs Quadrangle, Garfield County, Colorado*. Colorado Geological Survey, Map Series, **MS-38**.
- KOCH, N. & MASCH, L. 1992. Formation of Alpine mylonites and pseudotachylites at the base of the Silvretta nappe, eastern Alps. *Tectonophysics*, **204**, 289–306.
- LAVECCHIA, G., BONCIO, P. & CREATI, N. 2003. A lithospheric-scale seismogenic thrust in central Italy. *Journal of Geodynamics*, **36**, 79–94.
- LIN, A. 2008. *Fossil Earthquakes: The Formation and Preservation of Pseudotachylites*. Springer, Berlin.
- LIN, A., MARUYAMA, T., AARON, S., MICHIBAYASHI, K., CAMACHO, A. & KANO, K. 2005. Propagation of seismic slip from brittle to ductile crust: evidence from pseudotachylite of the Woodroffe thrust, central Australia. *Tectonophysics*, **402**, 21–35.
- LIN, A., SUN, Z. & YANG, Z. 2003. Multiple generations of pseudotachylite in the brittle to ductile regimes, Quinling–Dabie Shan ultrahigh-pressure metamorphic complex, central China. *The Island Arc*, **12**, 440–452.
- MADDOCK, R. L. 1983. Melt origin of fault-generated pseudotachylites demonstrated by textures. *Geology*, **11**, 105–108.
- MADDOCK, R. L. 1992. Effects of lithology, cataclasis and melting on the composition of fault-generated pseudotachylites in Lewisian gneiss, Scotland. *Tectonophysics*, **204**, 261–278.
- MAGLOUGHLIN, J. F. 1989. The nature and significance of pseudotachylite from the Nason terrane, North Cascades Mountains, Washington. *Journal of Structural Geology*, **11**, 907–917.
- MAGLOUGHLIN, J. F. & SPRAY, J. G. 1992. Frictional melting processes and products in geological materials: introduction and discussion. *Tectonophysics*, **204**, 197–204.
- MCCOY, A. M., KARLSTROM, K. E., SHAW, C. A. & WILLIAMS, M. L. 2005. The Proterozoic ancestry of the Colorado mineral belt: 1.4 Ga shear zone system in central Colorado. In: KARLSTROM, K. E. & KELLER, G. R. (eds) *The Rocky Mountain Region: An Evolving Lithosphere*. American Geophysical Union, Geophysical Monograph, **154**, 71–90.
- MCNULTY, B. A. 1995. Pseudotachylite generated in the semi-brittle and brittle regimes, Bench Canyon shear zone, central Sierra Nevada. *Journal of Structural Geology*, **17**, 1507–1521.
- MOECHER, D. P. & STELTENPOHL, M. G. 2009. Direct calculation of rupture depth for an exhumed paleoseismic fault from mylonitic pseudotachylite. *Geology*, **37**, 999–1002.
- O'HARA, K. & BLACKBURN, W. 1989. Volume-loss model for trace-element enrichments in mylonites. *Geology*, **17**, 524–527.
- PASSCHIER, C. W. 1982a. *Mylonitic Deformation in the Saint-Barthélemy Massif, French Pyrenees, with Emphasis on the Genetic Relationship Between Ultramylonite and Pseudotachylite*. GUA Papers of Geology, Series 1, no. 16.
- PASSCHIER, C. W. 1982b. Pseudotachylite and the development of ultramylonite bands in the Saint-Barthélemy Massif, French Pyrenees. *Journal of Structural Geology*, **4**, 69–79.
- PASSCHIER, C. W. 1984. The generation of ductile and brittle shear bands in a low-angle mylonite zone. *Journal of Structural Geology*, **6**, 273–281.
- PASSCHIER, C. W., HOEK, J. D., BEKENDAM, R. F. & DE BORDER, H. 1990a. Ductile reactivation of Proterozoic brittle fault rocks; an example from the Vestfold Hills, East Antarctica. *Precambrian Research*, **47**, 3–16.
- PASSCHIER, C. W., MYERS, J. S. & KRÖNER, A. 1990b. *Field Geology of High-Grade Gneiss Terrains*. Springer, Heidelberg.
- PAUL, A., KAVIANI, A., HATZFELD, D., VIERGNE, J. & MOKHTARI, M. 2006. Seismological evidence for crustal-scale thrusting in the Zagros mountain belt (Iran). *Geophysical Journal International*, **166**, 227–237.
- PENNACCHIONI, G. & CESARE, B. 1997. Ductile–brittle transition in pre-Alpine amphibolite facies mylonites during evolution from water-present to water-deficient

- conditions (Mont Mary nappe, Italian Western Alps). *Journal of Metamorphic Geology*, **15**, 777–791.
- REED, J. C. JR., BICKFORD, M. E. & TWETO, O. 1993. Proterozoic accretionary terranes of Colorado and southern Wyoming. In: REED, J. C. JR., BICKFORD, M. E., HOUSTON, R. S., LINK, P. K., RANKIN, D. W., SIMS, P. K. & VAN SCHMUS, W. R. (eds) *Precambrian: Conterminous U.S.* Geological Society of America, Boulder, Colorado, The Geology of North America **C-2**, 110–121.
- SCHOLZ, C. H. 1988. The brittle/plastic transition and the depth of seismic faulting. *Geologische Rundschau*, **77**, 319–328.
- SCHOLZ, C. H. 1998. Earthquakes and friction laws. *Nature*, **391**, 37–42.
- SCHOLZ, C. H. 2002. *The Mechanics of Earthquakes and Faulting*. 2nd edn. Cambridge University Press, New York.
- SHAW, C. A. & ALLEN, J. L. 2007. Field rheology and structural evolution of the Homestake shear zone, Colorado. *Rocky Mountain Geology*, **42**, 31–56.
- SHAW, C. A., HEIZLER, M. T. & KARLSTROM, K. E. 2005.  $^{40}\text{Ar}/^{39}\text{Ar}$  thermochronologic record of 1.45–1.35 Ga intracontinental tectonism in the southern Rocky Mountains: Interplay of conductive and advective heating with intracontinental deformation. In: KARLSTROM, K. E. & KELLER, G. R. (eds) *The Rocky Mountain Region: An Evolving Lithosphere*. American Geophysical Union, Geophysical Monograph, **154**, 163–184.
- SHAW, C. A., KARLSTROM, K. E., MCCOY, A., WILLIAMS, M. L., JERCINOVIC, M. J. & DUEKER, K. 2002. Proterozoic shear zones in the Colorado Rocky Mountains: from continental assembly to intracontinental reactivation. In: LAGESON, D. (ed.) *Science at the Highest Level*. Geological Society of America, Field Guide, **3**, 102–117.
- SHAW, C. A., KARLSTROM, K. E., WILLIAMS, M. L., JERCINOVIC, M. J. & MCCOY, A. M. 2001. Electron-microprobe monazite dating of ca. 1.71–1.63 Ga and ca. 1.45–1.38 Ga deformation in the Homestake shear zone, Colorado: origin and early evolution of a persistent intracontinental tectonic zone. *Geology*, **29**, 739–742.
- SHAW, C. A., SNEE, L. W., SELVERSTONE, J. & REED, J. C. JR. 1999.  $^{40}\text{Ar}/^{39}\text{Ar}$  thermochronology of Mesoproterozoic metamorphism in the Colorado Front Range. *Journal of Geology*, **107**, 49–67.
- SIBSON, R. H. 1974. Frictional constraints on thrust, wrench and normal faults. *Nature*, **249**, 542–544.
- SIBSON, R. H. 1975. Generation of pseudotachylite by ancient seismic faulting. *Geophysical Journal of the Royal Astronomical Society*, **133**, 191–213.
- SIBSON, R. H. 1977. Fault rocks and fault mechanisms. *Journal of the Geological Society, London*, **133**, 192–214.
- SIBSON, R. H. 1980. Transient discontinuities in ductile shear zones. *Journal of Structural Geology*, **2**, 165–171.
- SIBSON, R. H. 1982. Fault zone models, heat flow, and the depth distribution of earthquakes in the continental crust of the United States. *Bulletin of the Seismological Society of America*, **72**, 151–163.
- SIBSON, R. H. 1983. Continental fault structure and the shallow earthquake source. *Journal of the Geological Society, London*, **140**, 741–761.
- SIBSON, R. H. 1986. Earthquakes and rock deformation in crustal fault zones. *Annual Review of Earth and Planetary Sciences*, **14**, 149–175.
- SIBSON, R. H. & TOY, V. G. 2006. The habitat of fault-generated pseudotachylite: Presence vs. absence of friction melt. In: ABERCROMBIE, R., MCGARR, A., DI TORO, G. & KANAMORI, H. (eds) *Earthquakes: Radiated Energy and the Physics of Faulting*. American Geophysical Union, Geophysical Monograph, **170**, 153–166.
- SILVER, L. T., BICKFORD, M. E., VAN SCHMUS, W. R., ANDERSON, J. L., ANDERSON, T. H. & MEDARIS, L. G. JR. 1977. The 1.4–1.5 b.y. transcontinental anorogenic plutonic perforation of North America. *Geological Society of America Abstracts with Programs*, **9**, 1176–1177.
- SPRAY, J. G. 1987. Artificial generation of pseudotachylite using friction welding apparatus: simulation of melting on a fault plane. *Journal of Structural Geology*, **9**, 49–60.
- SPRAY, J. G. 1992. A physical basis for the frictional melting of some rock-forming minerals. *Tectonophysics*, **204**, 205–221.
- SPRAY, J. G. 1995. Pseudotachylite controversy: fact or friction? *Geology*, **23**, 1119–1122.
- STIPP, M., STUENITZ, H., HEILBRONNER, R. & SCHMID, S. M. 2002. The eastern Tonale fault zone; a “natural laboratory” for crystal plastic deformation of quartz over a temperature range from 250 to 700°C. *Journal of Structural Geology*, **24**, 1861–1884.
- STREHLAU, J. 1986. A discussion of the depth extent of rupture in large continental earthquakes. In: DAS, S., BOATWRIGHT, J. & SCHOLZ, C. H. (eds) *Earthquake Source Mechanics*. American Geophysical Union, Geophysical Monograph, **37**, 131–146.
- SWANSON, M. T. 1992. Fault structure, wear mechanisms and rupture processes in pseudotachylite generation. *Tectonophysics*, **204**, 223–242.
- SWANSON, M. T. 1998. Pseudotachylite-bearing strike-slip faults in mylonitic rocks. In: SNOKE, A. W., TULLIS, J. & TODD, V. R. (eds) *Fault-related Rocks: A Photographic Atlas*. Princeton University Press, Princeton, NJ, 104–107.
- SYKES, L. R. 1978. Intraplate seismicity, reactivation of preexisting zones of weakness, alkaline magmatism, and other tectonism postdating continental fragmentation. *Reviews of Geophysics and Space Physics*, **16**, 621–688.
- TAKAGI, H., GOTO, K. & SHIGEMATSU, N. 2000. Ultramylonite bands derived from cataclasite and pseudotachylite in granites, northeast Japan. *Journal of Structural Geology*, **22**, 1325–1339.
- THOMAS, W. A. 2006. Tectonic inheritance at a continental margin. *GSA Today*, **16**–**2**, 4–11.
- TWETO, O. & SIMS, P. K. 1963. Precambrian ancestry of the Colorado mineral belt. *Geological Society of America Bulletin*, **74**, 991–1014.
- VAN DAALEN, M., HEILBRONNER, R. & KUNZE, K. 1999. Orientation analysis of localized shear deformation in quartz fibres at the brittle–ductile transition. *Tectonophysics*, **303**, 83–107.
- WATTS, L. M., HOLDSWORTH, R. E., SLEIGHT, J. A., STRACHAN, R. A. & SMITH, S. A. F. 2007. The

- movement history and fault rock evolution of a reactivated crustal-scale strike-slip fault: the Walls Boundary Fault Zone, Shetland. *Journal of the Geological Society, London*, **164**, 1037–1058.
- WHITE, J. C. 1996. Transient discontinuities revisited: pseudotachylite, plastic instability and the influence of low pore pressure on deformation processes in the mid-crust. *Journal of Structural Geology*, **18**, 1471–1486.
- WHITE, J. C. 1998. Coeval mylonites and pseudotachylite. In: SNOKE, A. W., TULLIS, J. & TODD, V. R. (eds) *Fault-related Rocks: A Photographic Atlas*. Princeton University Press, Princeton, NJ, 98–103.
- WHITMEYER, S. J. & SIMPSON, C. 2003. High strain-rate deformation fabrics characterize a kilometers-thick Paleozoic fault zone in the Eastern Sierras Pampeanas, central Argentina. *Journal of Structural Geology*, **25**, 909–922.



# Microstructure and petrology of a Calabrian garnet-bearing pseudotachylyte – a link to lower-crustal seismicity

U. ALTENBERGER<sup>1\*</sup>, G. PROSSER<sup>2</sup>, M. RUGGIERO<sup>2</sup> & C. GÜNTNER<sup>1</sup>

<sup>1</sup>Institute of Earth and Environmental Sciences, University of Potsdam,  
Karl-Liebknecht-Strasse 24, D-14476 Potsdam-Golm, Germany

<sup>2</sup>Dipartimento di Scienze Geologiche, Università della Basilicata,  
Via dell'Ateneo Lucano, 10-85100 Potenza, Italy

\*Corresponding author (e-mail: [uwe@geo.uni-potsdam.de](mailto:uwe@geo.uni-potsdam.de))

**Abstract:** A pseudotachylyte vein enclosed in tilted Hercynian lower crust of the Calabrian Serre Massif provides information on the source of a fossil seismic event. The pseudotachylyte contains euhedral garnet that formed by direct crystallization from a frictional melt and not during a later metamorphic overprint. Pseudotachylyte formation started with grain-size reduction caused by ductile deformation and brittle deformation. Subsequent frictional melting affected almost all phases including quartz but excluding monazite. After rapid cooling, chilled margins composed of glass and iron sulphide droplets formed. The central part of the vein solidified as biotite, and plagioclase crystallized directly from the frictional melt. Garnet occurs in three different grain-size classes; there are significant differences between very small garnets in the chilled margins and larger garnets in the central part of the pseudotachylyte vein. This proves that garnet rapidly crystallized from the pseudotachylyte melt after the seismic event. Garnet composition is used to define the depth of garnet growth, implying that the seismogenic zone was located at a depth of about 21–23 km. The melt temperature was between approximately 1515 and 2040 °C, representing the melting points of  $\beta$ -quartz and monazite, respectively.

This study supports the interpretation from seismic data that lower-crustal seismicity occurs and affirms, by direct observation, that the classical jelly sandwich model of the lithosphere is not always appropriate for crustal sections. In contrast to well-known regions with dry and very strong lower crusts (e.g. the Caledonides), the studied part of the Hercynian lower crust contains significant amounts of biotite, which release aqueous fluids during frictional melting. In addition, fluid inclusions in quartz fragments within the pseudotachylyte indicate that fluids probably played an important role during fault-zone evolution at the time of frictional melting.

Tectonically induced, seismic failure along faults at crustal and upper-mantle depths produces strong permanent effects on the active fault plane. The damage on the fault plane corresponds predominantly to brittle and/or ductile deformation. During seismic failure at slip velocities of more than  $10 \text{ cm s}^{-1}$  up to 90% of the energy released is dissipated as heat and, depending on the seismic efficiency, only a minor component is radiated as seismic energy (Sibson 2003). Frictional heating can cause localized melting on parts of the active fault.

Fault rocks formed by frictional melting on seismogenic faults are called pseudotachylytes. They are the most conclusive petrological and petrophysical evidence of palaeo-seismicity in exhumed rocks.

Pseudotachylytes mostly consist of fine-grained dark material (Shand 1916), formed predominantly by frictional melting. Melting follows seismic failure and brittle grain-size reduction (e.g. Magloughlin 1992; Magloughlin & Spray 1992;

Lin 1994; Hetzel *et al.* 1996; Sibson 2003) or hydrofracturing (Austrheim & Boundy 1994; Lund & Austrheim 2003).

Most examples of pseudotachylytes are described from the brittle upper crust. However, pseudotachylytes can also form in deep-crustal orogenic roots taken to eclogite-facies conditions by continental subduction (e.g. Austrheim & Boundy 1994; Lund & Austrheim 2003; John & Schenk 2006) or at mid-crustal levels during exhumation (e.g. Lin 1994; Handy & Brun 2004). Brittle structures and the evidence of short-lived periods of increased deformation rate in the intermediate–lower crust have been connected to seismic events (Kruhl *et al.* 2006). Lower-crustal seismicity is neglected by the classical ‘jelly-sandwich model’, which describes the lower crust as an aseismic and weak layer between a strong seismic upper crust and a seismic upper mantle (Chen & Molnar 1983). This model has been challenged in the last decade since accurate reinterpretations of seismic

data have revealed seismic activity in some lower-crustal parts of the continental lithosphere (Maggi *et al.* 2000a, b; Emmerson *et al.* 2006; Jackson *et al.* 2008). This is consistent with experimental results indicating that strength in the lower crust is strongly influenced by small amounts of aqueous fluids (Jackson 2002). Consequently, strength and seismicity of the lower crust should derive mostly from its dry granulite-facies composition. However, petrographical evidence of pseudotachylites in granulite-facies lower-crustal rocks has only been described in a few cases to date (e.g. in Australia: Lin 2008a).

Pseudotachylites in granulite-facies rocks may have formed during earthquakes that occurred at deep-crustal conditions. However, seismicity may have also taken place during the exhumation of the high-grade rocks at intermediate- to upper-crustal levels; as, for example, described from the southern Alps, Italy (Techmer *et al.* 1992). For this reason, one of the important questions is how to determine the crustal levels of the ancient seismogenic zone. Independent of the depth of formation, pseudotachylites are almost always fine-grained, dark, with rock and mineral fragments, flow textures, chilled margins and fine-grained new minerals (Magloughlin & Spray 1992). Therefore, in this study we have concentrated on two questions. (1) In the absence of textural variations – how can we estimate the depth of the seismic source of palaeo-earthquakes? (2) Is it possible to distinguish a syntectonic from a post-tectonic metamorphic origin for new minerals in pseudotachylites that are not observed in the host rock, particularly garnet? In order to obtain reliable indicators of the depth in the crust from which frictional melts are derived, the present study will focus on the petrology and microfabrics of a garnet-bearing pseudotachylite enclosed in felsic lower-crustal granulites from Calabria (southern Italy).

## Geological setting

The high-grade rocks containing the pseudotachylites are part of the Calabria terrane (Bonardi *et al.* 2001), representing an exotic crustal block, mainly made up of metamorphic and intrusive rocks, inserted between the NW-trending Southern Apennines and the east-trending Sicilian Maghrebides (Fig. 1). Incorporation of the Calabria terrane into the Apennine–Maghrebian chain is related to the processes responsible for the formation of the Tyrrhenian Basin since the late Miocene time (Gueguen *et al.* 1998). The main metamorphism of the Calabria basement rocks occurred during the late stages of the Hercynian orogeny, as peak metamorphism has been dated at

299–304 Ma (Graessner *et al.* 2000; Langone *et al.* 2010).

In the Serre Massif (Fig. 1), the Calabria basement consists of three superposed nappes that can be distinguished on the basis of the different Hercynian and Alpine overprint (Amadio Morelli *et al.* 1976; Langone *et al.* 2006). The lower and intermediate nappes mainly consist of low-grade phyllites, and medium-grade orthogneisses and paragneisses, respectively. The upper nappe (the Sila Nappe of Festa *et al.* 2004) makes up the main part of the Calabria basement. It consists of a nearly complete section of the continental crust (Schenk 1990), comprising granulite-facies rocks at the base, thick granitoid sheets in the intermediate part, and micaschists and phyllites in the upper part. An Alpine metamorphic overprint of Eocene age (Schenk 1980) can be recognized in the lower and intermediate nappes; whereas, in the Sila nappe, the late Hercynian fabrics and mineral assemblages are still well preserved. The Sila and the intermediate nappes are separated by an important shear zone of Alpine age (the Curinga–Girifalco line), whose development is related to the SE-directed thrusting of the upper nappe with respect to the intermediate and lower nappes (Langone *et al.* 2006). Later tilting towards the SE affects the Sila nappe; consequently, in the northwestern sector of the Serre Massif, the lowermost portions of the crustal section are exposed. Tilting has occurred since the Oligocene, when the Calabria terrane underwent extension and rapid exhumation (Thomson 1994).

In the Curinga area the base of the Sila nappe, which consists of metagabbros, felsic and mafic granulites, and spinel-bearing peridotites, is widely exposed (Schenk 1984). However, the Curinga–Girifalco line does not crop out because it is offset by young north-trending fault that dissects the Calabria nappe structure. For this reason the Alpine overprint is weak and strongly localized, and the Hercynian tectonic setting is almost preserved.

At the base of the exposed crustal section, metagabbros form a huge body showing preserved primary layering (Moresi *et al.* 1979). Above the metagabbros there are mafic and felsic granulites, with minor bodies of fine-grained peridotites. Pressure–temperature ( $P$ – $T$ ) evolution during the Hercynian metamorphism can be reconstructed based on the analysis of corona textures developed around metamorphic garnet in metagabbros and mafic granulites. According to Schenk (1984), peak metamorphism took place at  $P = 0.75$  GPa and  $T = 800$  °C. More recent analyses (Acqua-fredda *et al.* 2008) indicate peak  $P$ – $T$  conditions of 1.1 GPa and 900 °C. However, decompression along the retrograde path led to  $P$ – $T$  conditions of 750–650 °C and 0.7–0.8 GPa at the end of the

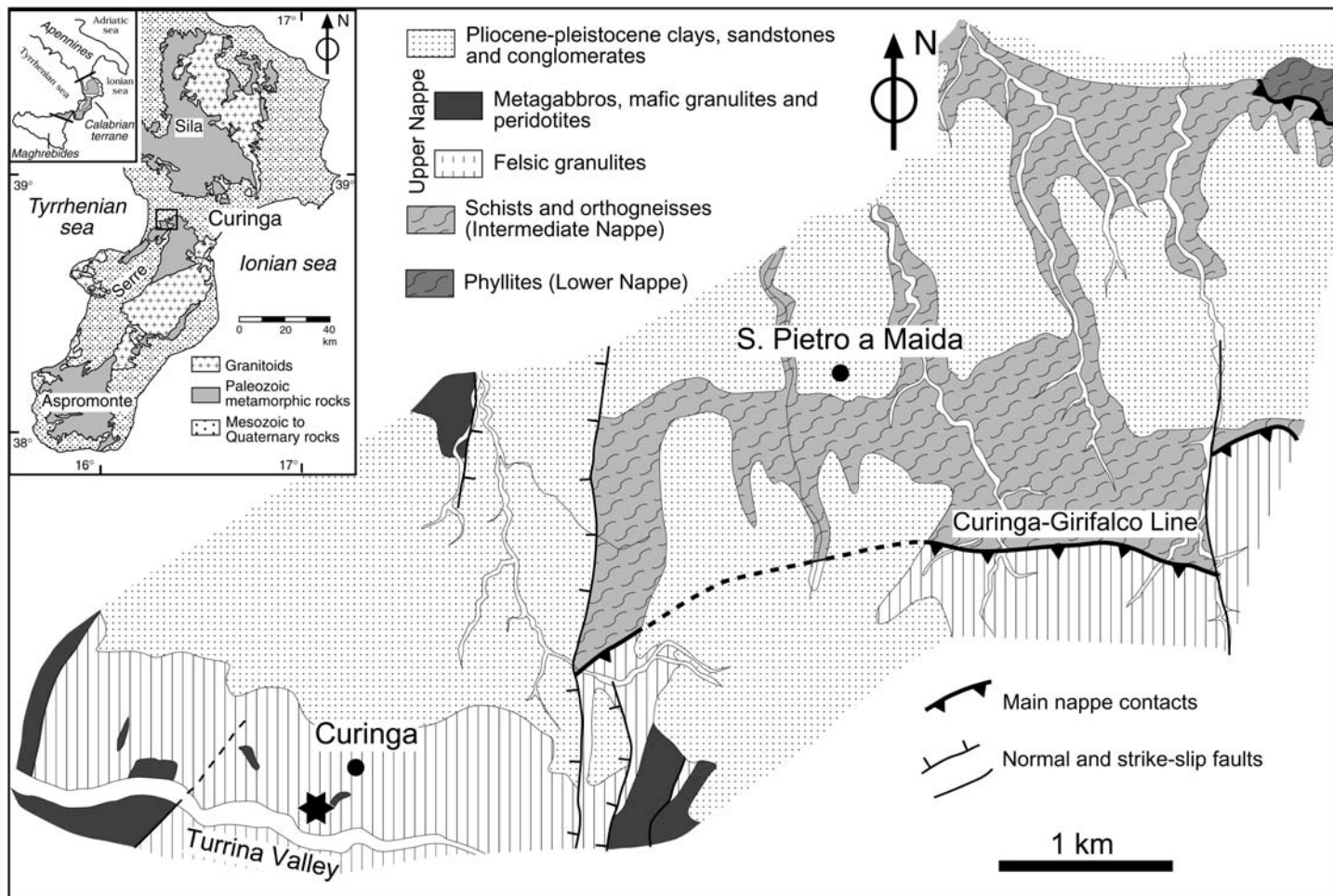


**Fig. 1.** Geological sketch map of the sample location (asterisk). Insets in the upper left show the geology of the Calabrian terrane and its location in the Apennine–Maghrebide chain. Modified after Paglionico & Piccarreta (1976), Schenk (1980, 1990), Bonardi *et al.* (2001), Langone *et al.* (2006), and Prosser and coworkers (unpublished).

Hercynian evolution. Decompression was synchronous with the activation of high-temperature shear zones with top-to-the-NW shearing (Altenberger & Kruhl 2000).

In the Curinga area (Fig. 1) pseudotachylites are frequently associated with fault planes cross-cutting all of the lithologies of the lower crust. Poor outcrop conditions frequently hinder precise description of the relationships between fault planes and pseudotachylite veins. However, there are a few exposed faults that strike from  $40^\circ$  to  $130^\circ$  with shallow dip angles and show extensional kinematics. This is particularly evident at the contact between felsic granulites and a peridotite sheet, where the orientation of pseudotachylite injected into en echelon dilatant cracks indicates a normal shear sense (Fig. 2). The studied pseudotachylites formed as fault and injection veins within felsic granulites. Faults and related pseudotachylites are mostly observed in loose blocks where clear relationships between major fault planes and synthetic Riedel shears can be detected. The maximum thickness of pseudotachylites, as observed in injection veins and at the junction between Riedel shears and the main fault plane, is less than 1 cm.

### Analytical methods

Major element concentrations were determined with wavelength dispersive spectrometry using a Jeol JXA 830 electron microprobe operating at an accelerating voltage of 15 kV and a beam current of 20 nA. Backscattered electron (BSE) images and areal bulk composition analyses were obtained with a SEM JSM 6510 combined with an Oxford

Incax-act analytical EDX (energy dispersive X-ray spectroscopy) system.

### The pseudotachylite

We describe detailed petrographical, textural and geochemical analysis of a system composed of wall rocks and the pseudotachylite, with its matrix, fragments of the wall rock and newly formed mineral phases, to characterize this remnant of a seismic event.

### Wall rocks

The host rock of the pseudotachylite shows a well-defined foliation defined by shape- (and crystal-) preferred orientation of quartz, biotite and feldspars. The rock is a coarse-grained gneiss, interpreted as a granulite-facies metapelite (Schenk 1984). It is composed of anhedral K-feldspar, plagioclase, quartz, garnet, biotite, sillimanite and subhedral garnet as its major constituents. Accessory minerals are apatite, rutile and monazite.

Quartz infrequently occurs as lens-shaped large single grains and, more commonly, as partially recrystallized grains or polygonized grains (subgrains). The large grains or aggregates show an elongate shape with maximum and minimum diameters of 0.8 and 0.2 cm, respectively. Recrystallized grains reach a size of approximately 10–15% of the diameter of the aggregate. Subgrains are of a similar size as the recrystallized grains and indicate dynamic recrystallization via subgrain rotation. In addition, close to the pseudotachylites a second generation of recrystallized grains appears. These have maximum diameters of around 10  $\mu\text{m}$  and are therefore significantly smaller than the first type. The small grain sizes, and the highly sutured grain boundaries between the host grain and the recrystallized grains, suggest that these grains were generated by bulging recrystallization, reflecting the relatively low temperatures or fast strain rates for crystal-plasticity to dominate as a deformation mechanism (Stipp *et al.* 2002).

Feldspars have a diameter of about 0.2 mm, whereas garnets are notably larger with a maximum diameter of about 0.5 cm. K-feldspar has thin perthitic exsolutions and shows microcline twinning at the rim or in smaller grains, indicating that in these regions the K-feldspar was completely ordered, probably enhanced by deformation. Myrmekitic structures are frequently observed at the K-feldspar rim.

Biotite crystals are up to 0.5 cm in length; close to the pseudotachylite they are extremely deformed by small kink bands. Prismatic sillimanite occurs in two grain-size groups: one group has a maximum size of up to  $200 \times 800 \mu\text{m}$ ; the second group is

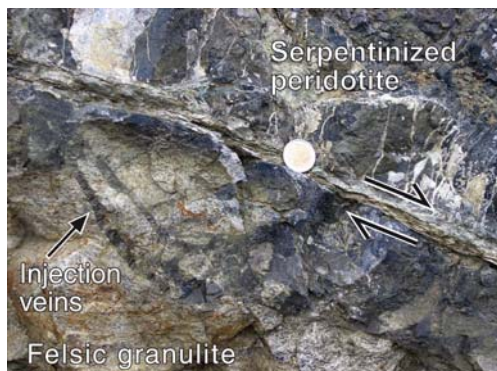


**Fig. 2.** Injection veins close to the sample locality (arrow) developed along a fault separating serpentinized peridotites and felsic granulites in the Turrina Valley area (see Fig. 1). The orientation of the injection veins is coherent with extensional kinematics along the fault plane.

more scarce and is around 3–4 times larger. Small anhedral rutile and subhedral monazites, ranging from 200 to 300 µm, also occur.

### The pseudotachylite

The pseudotachylite vein cuts across almost perpendicular to the foliation of the wall rocks. The

mean thickness is about 1 cm. It forms a planar vein-like structure with a dark and fine-grained matrix enclosing clasts composed of mineral, as well as rock fragments (Fig. 3a). The rock clasts occur as subangular objects a few millimetres thick, with their smallest diameter oblique to the vein boundaries. In addition, injection veins a few millimetres thick (apophyses) and up to 0.7 cm in length are

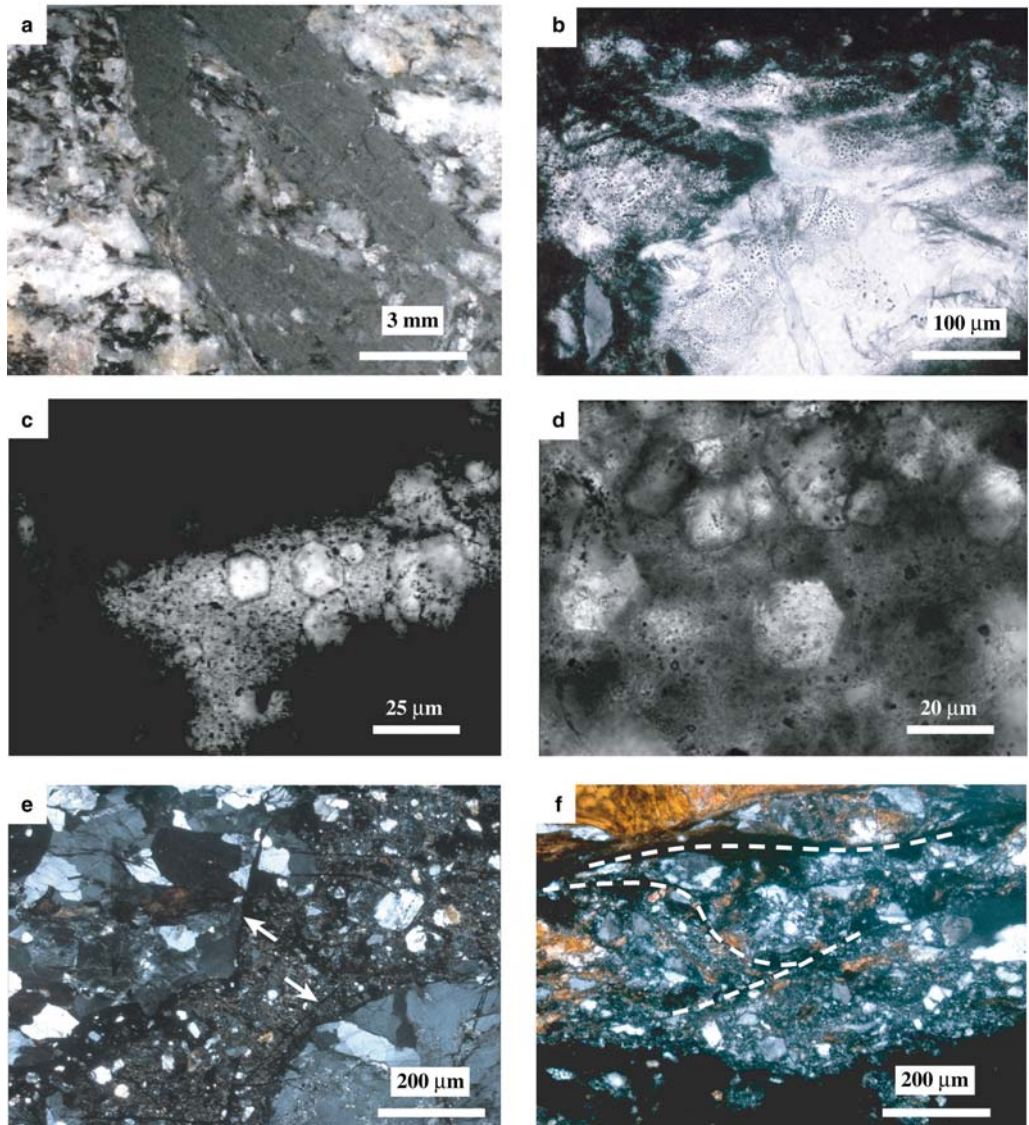


**Fig. 3.** (a) Digital camera image of parts of the central pseudotachylite vein with a clast of the wall rock. (b) Quartz clast with concentrated zones of fluid inclusions (dark dots). (c) & (d) Newly grown euhedral garnet in a dark matrix. (e) Chilled margins (arrows) at the contact with the wall rock (left) and a rock fragment (right) within the pseudotachylite vein. (f) Brittlely deformed zone with  $S-C$  structures close to the contact with the wall rock. Photomicrographs (c) and (d) with parallel polars; (b), (e) and (f) with crossed polars.

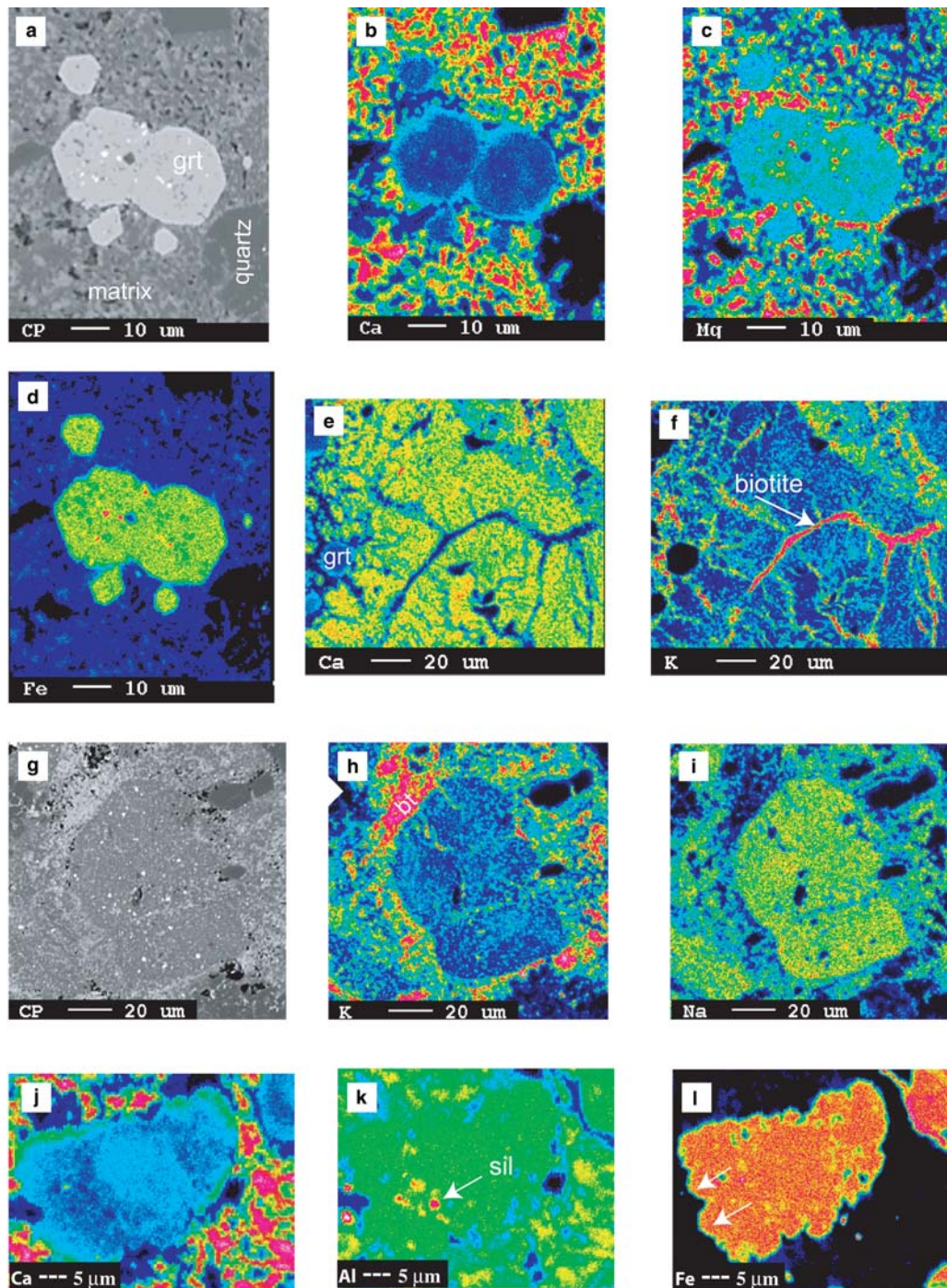


**Fig. 4.** (a) BSE image and (b)–(d) element maps of newly grown euhedral garnets (grt) and pseudotachylite matrix. Note the Ca- and Mg-rich matrix, indicating the intergrowth of plagioclase and biotite. Garnets show a Ca-enriched rim. Small Fe-sulphide-rich inclusions in the core of the garnets are shown as light dots in the BSE and red dots in the Fe-element images. Element concentration increases in the order black–blue–green–yellow–red. (e) & (f) Ca-rich

orientated perpendicular to oblique to the central vein.

#### *Rock fragments in pseudotachylite veins*

The majority of clasts in the central parts of the veins are wall-rock fragments or monomineralic quartz grains. Quartz fragments are rounded, elongate to subspherical and have sizes from a few up to 1000 µm. The larger clasts commonly contain significant amounts of fluid inclusions, either with irregularly to patchy distribution or concentrated as (fracture-induced?) fluid-inclusion trails (Fig. 3b). Their concentration is significantly higher than in the host rock. Scanning electron microscopy (SEM) imaging illustrates that quartz clasts have deep embayments, resembling resorption structures, and therefore the quartz grains were in disequilibrium (Fig. 3a). Quartz grains in rock fragments have very small recrystallized grains (5–10 µm) at the margin of the pseudotachylite. Recrystallization features and grain size are similar to those of the wall rock at the margin of the pseudotachylite. In contrast, monomineralic feldspar clasts are extremely rare and have a limited grain size of about 400–500 µm. SEM images illustrate that there are no feldspar clasts smaller than 400 µm. In addition, there is no evidence of biotite fragments in the pseudotachylite.

Scarce monomineralic sillimanite clasts that have been detected by electron dispersive spectroscopy (EDS) techniques in the scanning electron microscope are smaller than 5 µm. They also occur as inclusions in newly crystallized phases (Fig. 4d). Some irregular sillimanite crystals with embayed grain boundaries are also detectable. Monazites are subhedral and show fractures, suggesting that brittle deformation occurred during pseudotachylite formation.

#### *Matrix and new phases*

Optical and electron microscopy, as well as electron microprobe studies (EMS), indicate that the *matrix* of the pseudotachylite is composed of different domains. Under the optical microscope, the matrix is nearly opaque to dark brown in colour in thin sections of 30 µm thickness. In a few regions, lighter brownish zones and blebs with small garnets can be detected (Fig. 3c, d).

The central vein shows up to 50 µm-thick chilled margins at the interface with the wall rock or wall-rock fragments (Fig. 3e). In the chilled margins, the grain-size decreases to less than 5 µm. However, in some parts of the central pseudotachylite vein the ‘chilled areas’ truncate thin cataclastic layers or fragments (Fig. 3f). The cataclastic zone is close to the wall-rock contact and consists mostly of brittlely deformed feldspars, kinked biotites and quartz with similar textures and composition to the host rock. In addition, the brittle zone shows evidence of S–C-like fabric (Fig. 3f), indicating concentrated simple-shear deformation. These textures are not visible in the wall rock outside the pseudotachylite.

Newly formed microlitic phases are the dominant grains observed in the matrix of the central vein. Microlites can be easily distinguished from clasts because they make up intergrowths of anhedral–subhedral biotite and euhedral–subhedral plagioclase laths of up to 5 µm (Fig. 5a). Biotite microlites are mostly smaller than the plagioclase. However, larger biotite grains are concentrated around nuclei of fragmented and rounded quartz clasts. The latter sometimes display textures indicative of resorption (Fig. 5a).

Optical microscopic observations of the injection veins reveal isotropic to weakly anisotropic spheres or oval drop-like features, which look like glass (Fig. 5b, c). The spheres or ‘drops’ have diameters of less than 80 µm and are separated by a thin network of a more transparent matrix. SEM and back-scattered-electron imaging reveals that these rounded to spherical and optically nearly isotropic bodies are composed of intergrowths of two major phases/materials. These phases show very small grain sizes, mostly in the range 0.5–2 µm, but ranging up to 5 µm towards the rims of the spheres (Figs 4g & 5b). Both minerals/phases are anhedral and isometric, and subhedral lath-shaped grains occur in only a few cases. Small inclusions of highly reflective opaque minerals occur (these appear light in BSE images; Figs 4g & 5b). Close to the rims of the spheres and in cracks of the spheres, ‘ordinary’ fine-grained, anhedral–ehedral biotite appears to have grown (Fig. 4f, h). The network of sphere–drop-like structures are embedded in a biotite-dominated matrix (Fig. 4f–i). In addition, in these parts clasts of quartz occur. The spheres, embedded in a more biotite-rich network, resemble perlitic structures in acid volcanic rocks.

**Fig. 4.** (*Continued*) chilled margin of the injection vein transected by biotite-filled cracks. Note the radiating cracks on the left, also filled by biotite. (g)–(i) Sphere in the chilled margin of the injection vein, composed of tiny biotite- and plagioclase-like (glassy?) areas, surrounded by a rim of biotite (bt). (j) & (k) Anhedral garnet showing straight grain surfaces on the left (arrows) and weak Fe-zoning. Note that the Al-rich inclusions (sil is sillimanite) are outside of the inner Fe-enriched core.

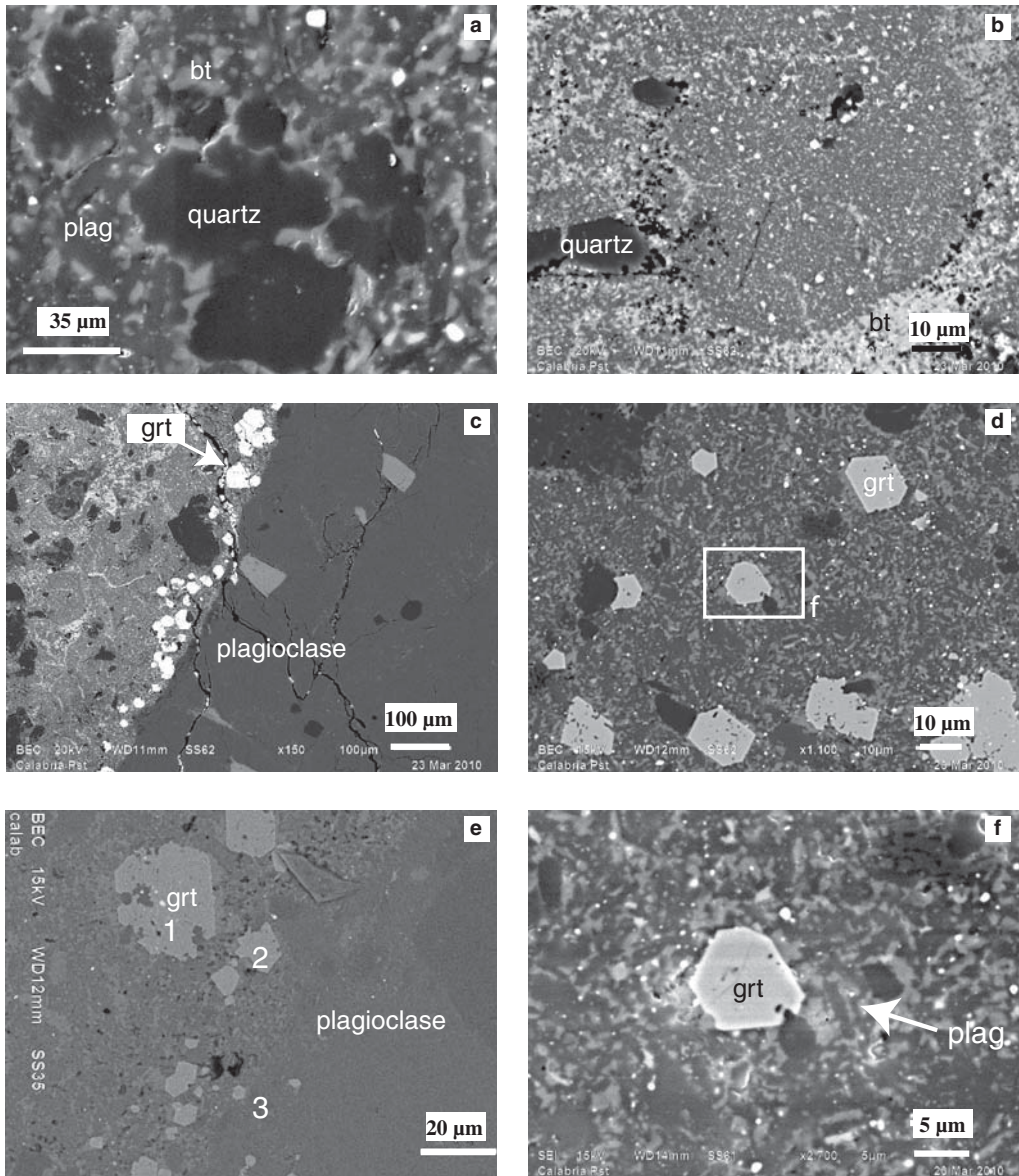


**Fig. 5.** BSE and SEM images of the pseudotachylite. (a) Amoeboid quartz clasts (black) surrounded by intergrowths of biotite (bt) and plagioclase (plag, partly subhedral). Quartz shows embayments indicating resorption. The very small light grains are Fe-sulphides. (b) Ca–Na-rich (glassy?) sphere in the chilled margin of the injection vein. The very small light grains are Fe-sulphides, the middle grey areas consists of K–Mg-rich (glassy?) material. The sphere is surrounded by a biotite-rich zone (bt). (c) Euhedral garnet at the chilled margin of the injection vein. Dark spheres (which are nearly isotropic when viewed using standard optical microscopy) and quartz fragments (black). Plagioclase occurs in the wall rock to the right. (d) Garnets in a matrix of plagioclase–biotite. The newly grown minerals are anhedral–euhedral (see also a). The box indicates the location of (f). (e) Garnet (grt) of three different grain sizes: the largest grain (1) has serrated boundaries, small grains at the rim of the wall rock (2) and tiny grains within plagioclase grains in the wall rock (3) very close to the pseudotachylite. (f) SEM image, enlargement of (a), displaying newly grown euhedral plagioclase (dark) in the matrix of the central vein ‘embedded’ in biotite (light grey). The euhedral garnet shows zoning, reflected by the brighter grey-shade at the grain rim.

Newly formed euhedral garnet occurs frequently (Figs 3c, d, 4a–d, j–l & 5c–f). Most garnets are found in the pseudotachylite matrix, but rarely they are also found in plagioclases of the outermost 10–20 µm of wall-rock fragments and in the wall rock itself. They appear in three grain-size classes, which vary according to the location in which they grew: 3–4 µm at the margin of the whole rock or in whole-rock clasts; 7–9 µm at the chilled margins; and 15–25 µm in the centre of the pseudotachylite vein (Fig. 5e). In the chilled margins of the injection veins, radiating cracks occur around some fine-grained garnets (Fig. 4e, f). This points to a difference in the coefficient of thermal expansion between garnet and the matrix.

The larger garnets contain tiny inclusions of highly reflecting opaque minerals, similar to those in the ‘isotropic spheres’. Some garnets have slightly irregular forms with sutured grain boundaries (lower left and lower right of Fig. 5d). In addition, electron microscopic images reveal garnets with highly sutured grain boundaries and rarer straight grain boundaries. Two adjacent boundaries show interfacial angles close to 110°–120°. This means euhedral shapes started to develop (Fig. 4j–l), suggesting that the new garnet overgrew garnet clasts. The shapes are dissimilar to ‘classical’ rectangular fracture systems that are commonly preserved in brittlely deformed rocks.

## Mineral and matrix chemistry

### *Biotite*

Electron-microprobe analyses indicate that biotite grains that nucleated around quartz grains and in the plagioclase–biotite matrix are significantly richer in  $\text{FeO}_{\text{total}}$  and poorer in  $\text{MgO}$  than those of the wall rocks (Table 1). In addition, biotite that formed at the rims of quartz grains or in cracks of the spheres is significantly richer in  $\text{TiO}_2$  than any other analysed biotite in the host rock or pseudotachylite (Table 1).

### *Plagioclase*

The newly formed plagioclase, analysed in the matrix of the central vein, shows only minor differences in composition from the large grains of the granulite wall rock (Table 1).

### *Garnet*

Garnet microlites are generally richer in Fe and poorer in Mg than garnet in the surrounding granulite. The composition of the microlites is  $\text{Alm}_{71–75}, \text{Prp}_{19–22}, \text{Sps}_2, \text{And}_{2–4}$  (Table 1). Garnet composition in the surrounding granulite is  $\text{Alm}_{66–67}, \text{Prp}_{19–20},$

$\text{Sps}_{1–3}, \text{And}_{4–6}$ . Garnet microlites show a zoning pattern where the rims are enriched in Ca, but a similar zoning is also observed in the granulite host rock (Fig. 4b).

Higher Fe–Mg ratios in pseudotachylite garnets, compared to wall-rock garnets, generally indicates higher crystallization temperatures (e.g. Spear 1993). The tiny inclusions in garnet microlites are composed of iron sulphides, sillimanite or quartz, as proven by EMS (Fig. 4a, k).

The subhedral garnets, interpreted as fragments formed by cataclastic processes with some newly grown crystal faces (Fig. 4j–l), show a weak and cloudy zonation in the core, best indicated by X-ray maps of Ca. The differences in Mg and Fe concentrations, however, are not as high as in Ca. Surrounding a Ca-poor core, small sillimanite clasts or ‘drops’ occur. This suggests that the fragmented core was a nucleus that was overgrown by new garnet, which contained sillimanite clasts/drops.

Radiating cracks around some small garnets are healed by biotite (Fig. 4f). These garnets have a similar composition and zonation to those without cracks.

### ‘Isotropic’ spheres

Bulk-rock and EMS and EDS mineral analyses of the nearly isotropic spheres, along with examination of the BSE images, reveals that the fine intergrowth is predominantly composed of a Ca–Na-rich and a K–Mg–Fe-rich phase (Table 1) as well as iron sulphide droplets. (Tables 1 & 2, Fig. 4g–i). These two dominant phases have compositions similar to plagioclase and biotite, each with elements that typically occur in the other phase; for example, plagioclase with Fe and Mg, and biotite with Ca and Na. The Ca–Na-rich plagioclase-like phase dominates (Fig. 4i). We can exclude analytical overlap as we made frequent point analyses with relatively consistent results. Both minerals/phases are anhedral with equant and sometimes lath shapes. Small inclusions of highly reflecting opaque minerals also occur. The bulk composition of the spheres is relatively poor in  $\text{SiO}_2$  compared to garnet-rich parts of the pseudotachylite but similar to the chilled margins of the central vein (Fig. 4, Table 2).

### *Chilled margin and matrix of the central vein*

The bulk composition of the chilled margin differs in proportions of  $\text{SiO}_2$ , alkalies and  $\text{FeO}$  from the matrix in the central vein (Fig. 6, Table 2). The chilled margin of the central vein and the spheres in the injection veins have lower  $\text{SiO}_2$  concentrations than the ‘normal’ (i.e. garnet-poor) parts of the pseudotachylite. This could be best explained

**Table 1.** Mean composition of the major phases of the host rock and pseudotachylite (electron microprobe data)

	Garnet				Biotite		Plagioclase		Isotropic spheres	
	Host rock		Pseudotachylite		Host rock centre	pst centre	Host rock centre	pst centre		
	Core	Rim	Core	Rim						
SiO <sub>2</sub>	37.86	38.08	37.60	37.46	SiO <sub>2</sub>	37.71	38.56	SiO <sub>2</sub>	60.39	
TiO <sub>2</sub>	0.03	0.09	0.06	0.03	TiO <sub>2</sub>	4.67	2.05	Al <sub>2</sub> O <sub>3</sub>	25.49	
Al <sub>2</sub> O <sub>3</sub>	22.39	21.96	22.12	22.08	Al <sub>2</sub> O <sub>3</sub>	17.59	20.34	CaO	6.69	
FeO	31.70	31.61	34.11	33.81	FeO	13.06	15.80	Na <sub>2</sub> O	7.58	
MgO	6.76	6.95	4.82	5.10	MgO	14.81	9.96	K <sub>2</sub> O	0.37	
MnO	0.87	0.76	1.12	1.08	MnO	0.00	1.92		u.d.l	
CaO	1.62	1.59	1.29	1.51	Na <sub>2</sub> O	0.08	u.d.l		0.52	
Na <sub>2</sub> O					K <sub>2</sub> O	9.85	8.86		12.15	
K <sub>2</sub> O									2.63	
Cr <sub>2</sub> O <sub>3</sub>			0.00	0.00					0.06	
Yb <sub>2</sub> O <sub>3</sub>			0.03	0.00					4.23	
Total	101.24	101.05	101.13	101.08		97.77	97.49		100.0	
Si	5.8	5.909	5.9	5.9	Si	2.67	2.76	Si	1.01	
Al	4.1	4.016	4.1	4.1	Ti	0.25	0.11	Al	0.48	
Cr	0.0	0	0.0	0.0	Al <sup>3+</sup>	1.47	1.72	Ca	0.12	
Fe <sup>2+</sup>	3.9	3.936	4.4	4.3	Fe <sup>2+</sup>	0.41	0.64	Na	0.24	
Fe <sup>3+</sup>	0.2	0.166	0.1	0.2	Mn		0.12	K	0.01	
Mn	0.1	0.1	0.1	0.1	Mg	1.56	1.06		0.00	
Mg	1.6	1.608	1.1	1.2	Na	0.01		An	67.93	
Ca	0.3	0.265	0.2	0.3	K	0.89	0.81	Ab	29.93	
Fe <sup>2+</sup> /Mg			3.9	3.6	Fe <sup>3+</sup>	0.36	0.30	Or	29.14	
Pyrope	26.3	27.2	19.1	20.3					0.00	
Almandine	65.9	66.6	74.7	72.9						
Grossular	0.0	0.3	1.9	0.5						
Spessartine	1.9	1.7	2.5	2.4						
Andradite	5.9	4.2	1.8	3.8						

**Table 2.** Mean composition of the major pseudotachylyte domains (EDX data)

	Isotropic spheres			Chilled margin	Matrix	Matrix
	Injection veins			Central vein	Central vein	Central vein
	Phase A bt-like	Phase B plag-like	Bulk	Garnet-poor	Garnet-poor	Garnet-rich
SiO <sub>2</sub>	46.63	57.84	54.73	56.65	61.78	56.79
TiO <sub>2</sub>	1.76	2.05	2.53	1.14	0.99	1.39
Al <sub>2</sub> O <sub>3</sub>	18.57	21.99	18	19.97	17.53	17.17
FeO	17.47	4.71	10.93	5.51	5.78	9.71
MgO	6.12	2.05	4.03	3.63	3.39	4.67
CaO	2.61	4.99	5.93	4.28	3.18	2.89
Na <sub>2</sub> O	3.77	5.88	4.3	4.76	4.72	3.1
K <sub>2</sub> O	2.88	1.39	3.06	2.9	2.48	2.87
Sum	100.04	100.97	103.51	98.84	99.85	98.59

by noting that the melt-clast proportion at the chilled margins is lower than in the centre of the pseudotachylyte. The garnet-rich parts of the pseudotachylyte are richer in FeO than the garnet-poor parts and the chilled margins. Interestingly, most bulk analyses have very similar K<sub>2</sub>O concentrations, ranging from 2.6 to 3.6 wt%. Only one analysis in the garnet-poor region shows values of about 1.9 wt%, suggesting that the distribution of biotite or phases similar to biotite is relatively homogeneous. In contrast, garnet is preferentially observed (and therefore preferentially grew) in the regions with higher FeO (Fig. 6, Table 2).

## Discussion and conclusion

The garnet-bearing pseudotachylyte that we have described shows clear evidence of a melt origin, namely chilled margins, resorption textures and new biotite that crystallized on quartz clasts, as well as newly crystallized plagioclase and biotite in the matrix. This indicates that the texture of the pseudotachylyte results from melting, subsequent crystallization and, possibly, solid devitrification. The microstructures also suggest that crushing to extremely fine grain sizes, and subsequent fluidization and injection (e.g. Wenk 1978; Lin 2008b), was of little importance.

The studied pseudotachylyte developed during a transition from ductile to brittle deformation. Fine-grained, dynamically recrystallized quartz with S-C-like structures indicates ductile deformation, while fractured plagioclase-dominated zones at the pseudotachylyte rim derive from brittle deformation. These may indicate increasing strain rate resulting in brittle fragmentation, grain-size reduction, increase in grain surface (Hetzell *et al.*

1996) and onset of frictional melting. Similar microstructures may also form at a constant strain rate in a temperature range of about 300–500 °C. However, these brittle structures in plagioclase will not form at ‘normal’ tectonic strain rates (cf. Pfiffner & Ramsay 1982) and temperatures significantly higher than 500 °C, at which dynamic recrystallization of plagioclase occurs (e.g. Altenberger *et al.* 1987; Prysor 1993). Therefore, the presence of these microstructures in lower-crustal rocks indicates an (abrupt?) increase in strain rate.

While the central vein is almost completely crystallized, the chilled margins in the injection veins are composed of optically isotropic and chemically anisotropic spheres. The spheres may have originated as glassy material with different chemical compositions affected by incipient devitrification. The spheres were later transected by thin, biotite-rich veins (Fig. 4f) that probably originate from a later metamorphic/fluid-controlled reaction along cooling fractures.

Theoretically, the newly formed Fe-rich garnets can be generated by two different mechanisms: by metamorphic recrystallization; or by direct crystallization from a melt. In the studied pseudotachylyte we conclude that the garnets primarily crystallized from a melt. A strong argument in favour of this interpretation is the significant grain-size contrast between the garnets in the central vein and the chilled margin; indicating that the rate of cooling controlled the size of the garnets. At the chilled margin the nucleation rate or nucleation/growth rate was significantly higher than in the central vein, as typically seen in magmatic systems (Vernon 2004). Direct crystallization from melt is also indicated by the fact that the garnets contain inclusions like iron sulphides and sillimanite clasts, which are prominent in the melt but do not

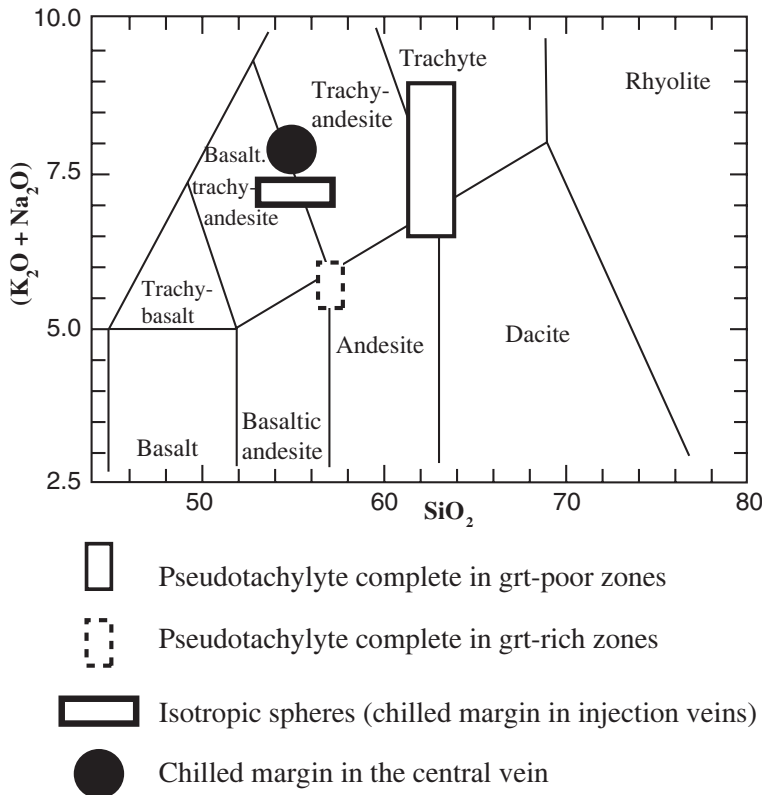


**Fig. 6.** Diagram of total alkali v. silica for volcanic rocks (after Middlemost 1994), showing the bulk compositions of different domains of the pseudotachylite. The dark line separates subalkaline and alkaline melts. Chemical data are the result of EDX areal analyses ( $400\text{--}500\,000\,\mu\text{m}^2$ ).

contain matrix minerals such as biotite or plagioclase. The very small new garnets in the plagioclase of the wall rock, very close to the pseudotachylite, formed due to the drastic increase in the local temperature during frictional melting or due to melt transport through a very fine fracture network.

The habit of garnet is, in most cases, euhedral. However, some larger garnets reveal a more irregular shape. These shapes resemble the cauliflower-like garnets crystallized from pseudotachylite melts in the Norwegian Caledonides, interpreted as disequilibrium texture indicative of undercooling and rapid quenching (Austrheim & Boundy 1994; Austrheim *et al.* 1996) (Fig. 7). However, the Caledonian pseudotachylites differ greatly from the example shown in the present study because: (i) frictional melt formed in the eclogite facies, as shown in kyanite microlites and omphacite pyroxene included in the garnet; (ii) the grain size is significantly larger; and (iii) the wall rocks are nearly anhydrous, lacking (OH)-bearing minerals. The shapes of the smaller euhedral garnets and the very small garnets in the chilled margins are probably of

primary crystallization origin. However, the zoning patterns, revealed by the element maps, are due to later metamorphic diffusion as this metamorphic zoning is observed in both in the country rock and the pseudotachylite.

Frictional melting in fault zones is an extremely rapid processes compared to anatetic melting in metamorphic regions. The detailed analysis of the pseudotachylite matrix shows that there is no newly grown K-feldspar or quartz as could be expected from eutectic melts of gneisses of 'granodioritic' composition. Therefore, eutectic melts were probably not formed. As melting was non-eutectic, the melt composition differs from the precursor in a way not expected by equilibrium thermodynamics. Temperature estimates for pseudotachylite formation can be roughly bracketed based on the composition of consumed or newly formed minerals (Spray 1992; Austrheim *et al.* 1996) because fast non-equilibrium melting implies that individual minerals participated in melting processes. In the studied pseudotachylite K-feldspar, plagioclase, quartz, biotite, garnet and, probably sillimanite

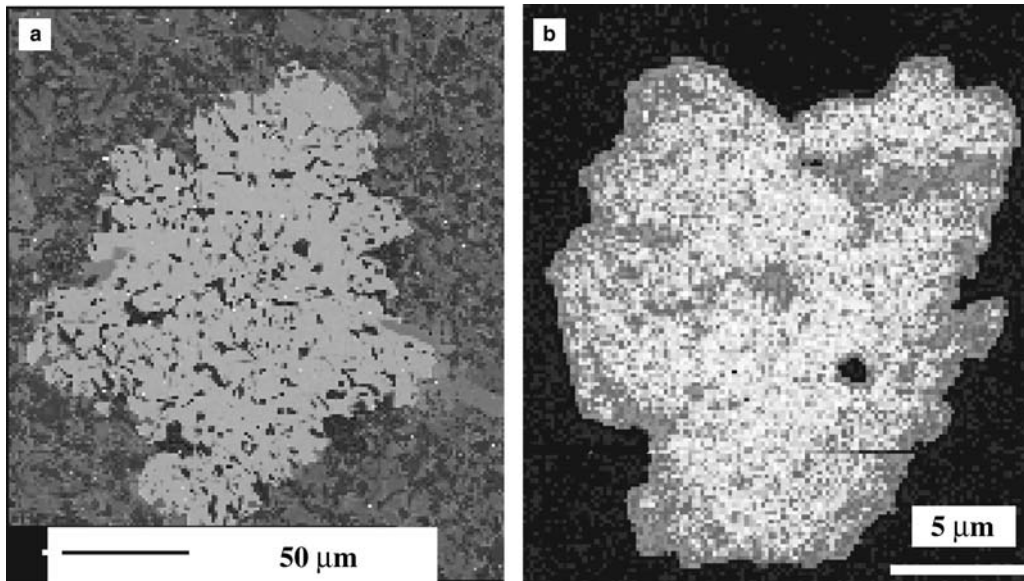


**Fig. 7.** Comparison of a cauliflower garnet from: (a) eclogite-facies frictional melts (BSE image, Adnefjell, Caledonides, Bergen Arcs, Norway); and (b) from this study (element-map image in grey scale).

were melted. Monazite remained stable or was fractured. The melting point, or ‘breaking point’, in the study by Spray (1992), for (OH)-bearing minerals is lower in frictional melts than in static melting. This is explained by ‘disequilibrium flash melting’ of those mineral phases possessing the lower shear yield strengths, fracture toughnesses and thermal conductivities rather than by eutectic melting that would have otherwise generated equilibrium minimum melts indicative of igneous processes (Spray 1992). Based on this study, biotite breaks down at temperatures of approximately 650 °C in pseudotachylites. The mineral with the highest melting point in the studied sample is quartz, which melts at a minimum of about 1515 °C ( $\beta$ -quartz). Although the melting point of  $\beta$ -quartz is 1750 °C, it is well known that rapid melting reduces the melting point down to about 1515 °C (Petzold & Hinz 1976). The upper temperature limit attained by the friction melt is given by the stability of monazite, which should melt at 2040 °C but does not show any evidence of melting. The granodioritic–dacitic composition of the protolith produces an andesitic melt plus quartz clasts. From the andesitic melt, Fe-sulphides, plagioclase, garnet and biotite crystallize. According to Magloughlin (2005), Fe-sulphide droplets indicate evidence of molten pyrrhotite, low O-fugacity and immiscibility of the Fe-sulphide droplets with the silicate melt, suggesting minimum temperatures of about 1200 °C.

According to recent reinterpreted geophysical data about the distribution of earthquake focal depths in continental lithosphere, seismicity occurs in the wet upper crust, the high-temperature granulite-facies lower crust and in the upper mantle if  $T$  is less than 600 °C (Priestley *et al.* 2008). The studied pseudotachylite, located within a granulite-facies wall rock, could therefore have originated in the lower or upper crust. The pressure, and therefore nucleation depth of the pseudotachylite, is difficult to estimate. No feasible barometer exists for the studied melt–matrix composition. However, the existence of almandine-rich garnet in silicate melts is restricted to higher pressures. A number of experimental studies (Green & Ringwood 1968; Allen *et al.* 1975; Eggler & Burnham 1973; Conrad *et al.* 1988; Green 1992) and studies in natural systems (Harangi *et al.* 2001; Barnes & Allen 2006) have defined the lower stability of garnet in melts of andesitic and dacitic composition. These studies consistently show that for moderate–high  $H_2O$  concentrations, igneous garnet is formed at pressures of greater than 0.7–0.8 GPa. These minimum pressures only weakly correlate with temperature. Also, Ca and Mn in garnet seem to correlate positively (Ca) or negatively (Mn) with pressure. However, Ca and Mn concentrations in garnet also depend strongly on the source rock–melt composition. In the studied pseudotachylite, garnets are low in Mn and Ca. Lin (2008b) interpreted that one of the rare known garnet-bearing

pseudotachylytes from Central Australia ha formed at a pressure of around 0.8 GPa. Petrological analyses of granulite-facies wall rocks from the Sila Nappe, from which the sample is taken, provide maximum  $P-T$  conditions of about 0.75 GPa and 800 °C (Schenk 1984), indicating that a formation depth exceeding 25 km is unlikely. Therefore, a garnet growth probably occurred at the limit of lower stability of garnet in andesitic melts (*c.* 0.7 GPa) and the estimated pressure conditions of the wall rock (about 0.75 GPa). A depth of formation for the documented pseudotachylyte, and therefore the seismic zone, of approximately 21–23 km is likely.

In contrast to the unusual strength of very dry lower-crustal rocks of the Scandinavian Caledonides, which suffered frictional melting followed by ductile deformation at eclogite-facies conditions, the studied pseudotachylyte was generated in relatively hydrous wall rocks. Here, fluids were stored in significant amounts of biotite and were subsequently released at the beginning of the seismic event by biotite breakdown. Excess (aqueous) fluids, which were not dissolved by the melt and not consumed for the crystallization of new biotite, are probably documented by fluid inclusions in quartz. Therefore, the presence of free volatiles during the seismic event was likely, although not provable. Furthermore, in contrast to the Caledonian pseudotachylytes, the microstructures of the studied samples show evidence that brittle deformation followed ductile deformation. This can be easily explained by a local increase in strain rate. Alternatively, fluids under near-lithostatic pressure may have caused a decrease in the effective stress on pre-existing faults and thus allowed brittle failure to occur at depths where, under dry conditions, only ductile deformation would be expected (e.g. Deichmann 1992). Another model to explain the shift from ductile to brittle deformation involves increasing the resistance to ductile flow, as known from auriferous deposits in ductile shear zones of the lower crust in which hydrothermal fluids and diffusion creep lead to significant sealing and a reduction in the ductility (Kolb 2008). In summary, the studied pseudotachylyte was formed in fluid-present conditions, although a direct link between an increase in fluid pressure and the triggering of a seismic event can not be proven.

We would like to thank B. Fabian for her tireless help in preparing the graphics and C. Fischer for excellent thin section preparation. H. Rhede and O. Appelt assisted by sharing their experience in electron microprobe work, and R. Oberhaensli is thanked for the installation and easy access to the institute's laboratories. We thank J.H. Kruhl, M. Bjørnerud and V.G. Toy for their very constructive reviews, and A. Fagereng for editorial handling. Funding by the PRIN project (year 2007) is acknowledged.

## References

- ACQUAFREDDA, P., FORNELLINI, A., PICCARRETA, G. & PASCAZIO, A. 2008. Multi-stage dehydration-decompression in the metagabbros from the lower crustal rocks of the Serre (southern Calabria, Italy). *Geological Magazine*, **145**, 397–411.
- ALLEN, J. C., BOETTCHER, A. L. & MARLAND, G. 1975. Amphiboles in andesite and basalt: I. Stability as a function of  $P-T-fO_2$ . *American Mineralogist*, **60**, 1069–1085.
- ALTENBERGER, U. & KRÜHL, J. H. 2000. The long life of a thin and dry high-temperature shear zone in the Hercynian lower crust of Calabria (S.Italy). *Periodico di Mineralogia*, **69**, 125–142.
- ALTENBERGER, U., HAMM, N. & KRÜHL, J. H. 1987. Movements and metamorphism north of the Insubric Line between Val Loana and Val d'Ossola, N.Italy. *Jahrbuch der Geologischen Bundesanstalt Wien*, **130**, 365–374.
- AMODIO MORELLI, L., BONARDI, G. ET AL. 1976. L'Arco Calabro-Peloritano nell'Orogeno Appenninico-Maghrebide. *Memorie della Società Geologica Italiana*, **17**, 1–60.
- AUSTRHEIM, H. & BOUNDY, T. 1994. Pseudotachylytes generated during seismic faulting and eclogitization of the deep crust. *Science*, **265**, 82–83.
- AUSTRHEIM, H., ERAMBERT, M. & ENGVIK, A. K. 1996. Garnets recording deep crustal earthquakes. *Earth and Planetary Science Letters*, **139**, 223–238.
- BARNES, C. G. & ALLEN, C. M. 2006. Depth of origin of late Middle Jurassic garnet andesite, southern Klamath Mountains, California. *Geological Society of America, Special Papers*, **410**, 269–286.
- BONARDI, G., CAVAZZA, W., PERRONE, V. & ROSSI, S. 2001. Calabria-Peloritani terrane and northern Ionian sea. In: VAI, G. B. & MARTINI, I. P. (eds) *Anatomy of an Orogen: The Apennines and Adjacent Mediterranean Basins*. Kluwer Academic, Dordrecht, 287–306.
- CHEN, W.-P. & MOLNAR, P. 1983. Focal depths of intracontinental and intraplate earthquakes and their implications for the thermal and mechanical properties of the lithosphere. *Journal of Geophysical Research*, **88**, 4183–4214.
- CONRAD, W. K., NICHOLLS, I. A. & WALL, V. J. 1988. Water-saturated and undersaturated melting of meta-luminous and peraluminous crustal compositions at 10 kb: evidence for the origin of silicic magmas in the Taupe volcanic Zone, New Zealand and other occurrences. *Journal of Petrology*, **29**, 765–803.
- DEICHMANN, N. 1992. Structural and rheological implications of lower-crustal earthquakes below northern Switzerland. *Physics of the Earth and Planetary Interniors*, **69**, 270–280.
- EGGLER, D. H. & BURNHAM, C. W. 1973. Crystallization and fractionation trends in the system andesite-H<sub>2</sub>O-CO<sub>2</sub>-O<sub>2</sub> at pressures to 10 kb. *Geological Society of America Bulletin*, **84**, 2517–2532.
- EMMERSON, B., JACKSON, J., MCKENZIE, D. & PRIESTLEY, K. 2006. Seismicity, structure and rheology of the lithosphere in the Lake Baikal region. *Geophysical Journal International*, **167**, 1233–1272.
- FESTA, V., MESSINA, A., PAGLIONICO, A., PICCARRETA, G. & ROTTURA, A. 2004. Pre-Triassic history recorded in

- the Calabria-Peloritani segment of the Alpine chain, southern Italy. An overview. *Periodico di Mineralogia*, **73**, 57–71.
- GRAESSNER, T., SCHENK, V., BRÖCKER, M. & MEZGER, K. 2000. Geochronological constraints on the timing of granitoid magmatism, metamorphism and post metamorphic cooling in the Hercynian crustal cross-section of Calabria. *Journal of Metamorphic Geology*, **18**, 409–421.
- GREEN, T. H. 1992. Experimental phase equilibrium studies of garnet-bearing I-type volcanics and high-level intrusives from Northland, New Zealand. *Transactions of the Royal Society of Edinburgh: Earth Sciences*, **83**, 429–438.
- GREEN, T. H. & RINGWOOD, A. E. 1968. Origin of the garnet phenocrysts in calc-alkaline rocks. *Contributions to Mineralogy and Petrology*, **65**, 59–67.
- GUEGUEN, E., DOGLIONI, C. & FERNANDEZ, M. 1998. On the post-25 Ma geodynamic evolution of the western Mediterranean. *Tectonophysics*, **298**, 259–269.
- HANDY, M. R. & BRUN, J. P. 2004. Seismicity, structure and strength of the continental lithosphere. *Earth and Planetary Science Letters*, **223**, 427–441.
- HARANGI, S. Z., DOWNES, H., KÓSA, L., SZABÓ, C. S., THIRLWALL, M. F., MASON, P. R. D. & MATTEY, D. 2001. Almandine garnet in calc-alkaline volcanic rocks of the Northern Pannonian Basin (Eastern-Central Europe): geochemistry, petrogenesis and geodynamic implications. *Journal of Petrology*, **42**, 1813–1843.
- HETZEL, R., ALTENBERGER, U. & STRECKER, M. R. 1996. Structural and chemical evolution of pseudotachylites during seismic events. *Mineralogy & Petrology*, **58**, 33–50.
- JACKSON, J. 2002. Strength of the continental lithosphere: time to abandon the jelly sandwich? *Geological Society of America (GSA) Today*, **12**, 4–10.
- JACKSON, J., MCKENZIE, D., PRIESTLEY, K. & EMMERON, B. 2008. New views on the structure and rheology of the lithosphere. *Journal of the Geological Society*, **165**, 453–465.
- JOHN, T. & SCHENK, V. 2006. Interrelations between intermediate-depth earthquakes and fluid flow within subducting oceanic plates: Constraints from eclogite facies pseudotachylites. *Geology*, **34**, 557–560.
- KOLB, J. 2008. The role of fluids in partitioning brittle deformation and ductile creep in auriferous shear zones between 500 and 700°C. *Tectonophysics*, **446**, 1–15.
- KRUHL, J. H., ERDMANN, S. & BÜTTNER, S. 2006. Brittle–ductile microfabrics in naturally deformed cordierite: evidence for significant short-term strain-rate variations. *Journal of Structural Geology*, **29**, 355–374.
- LANGONE, A., GODARD, G., PROSSER, G., CAGGIANELLI, A., ROTTURA, A. & TIEPOLO, M. 2010. P–T–t path of the Hercynian low-pressure rocks from the Mandatoriccio complex (Sila Massif, Calabria, Italy): new insights for crustal evolution. *Journal of Metamorphic Geology*, **28**, 137–162.
- LANGONE, A., GUEGUEN, E., PROSSER, G., CAGGIANELLI, A. & ROTTURA, A. 2006. The Curinga-Girifalco fault zone (northern Serre, Calabria) and its significance within the Alpine tectonic evolution of the western Mediterranean. *Journal of Geodynamics*, **42**, 140–158.
- LIN, A. 1994. Glassy pseudotachylite veins from the Fuyun fault zone, northwest China. *Journal of Structural Geology*, **16**, 71–84.
- LIN, A. 2008a. Seismic Slip in the Lower Crust Inferred from Granulite-related pseudotachylite in the Woodroffe Thrust, Central Australia. *Pure & Applied Geophysics*, **165**, 215–233.
- LIN, A. 2008b. *Fossil Earthquakes: Formation and Preservation of Pseudotachylites*. Springer, Berlin.
- LUND, M. G. & AUSTRHEIM, H. 2003. High-pressure metamorphism and deep-crustal seismicity. *Tectonophysics*, **372**, 59–83.
- MAGGI, A., JACKSON, J., MCKENZIE, D. & PRIESTLEY, K. 2000a. Earthquake focal depths, effective elastic thickness, and the strength of the continental lithosphere. *Geology*, **28**, 495–498.
- MAGGI, A., JACKSON, J., PRIESTLEY, K. & BAKER, C. 2000b. A re-assessment of focal depth distribution in southern Iran, the Tien Shan and northern India: do earthquakes really occur in the continental mantle? *Geophysical Journal International*, **143**, 629–661.
- MAGLOUGHLIN, J. F. 1992. Microstructural and chemical changes associated with cataclasis and frictional melting at shallow crustal levels: the cataclasite–pseudotachylite connection. *Tectonophysics*, **204**, 243–260.
- MAGLOUGHLIN, J. F. 2005. Immiscible sulfide droplets in pseudotachylite: evidence for high temperature (>1200°C) melts. *Tectonophysics*, **402**, 81–91.
- MAGLOUGHLIN, J. F. & SPRAY, J. G. 1992. Frictional melting processes and products in geological materials: introduction and discussion. *Tectonophysics*, **204**, 197–204.
- MIDDLEMOST, E. A. K. 1994. Naming materials in the magma/igneous rock system. *Earth Science Reviews*, **37**, 215–224.
- MORESI, M., PAGLIONICO, A., PICCARRETA, G. & ROTTURA, A. 1979. The deep crust in Calabria (Polia Copanello Unit): a comparison with the Ivrea–Verbano zone. *Memorie della Società Geologica Padova*, **33**, 233–242.
- PAGLIONICO, A. & PICCARRETA, G. 1976. Le Unità del Fiume Pomo e di Castagna nelle Serre Settentrionali (Calabria). *Bullettino della Società Geologica Italiana*, **95**, 27–37.
- PETZOLD, A. & HINZ, W. 1976. *Silikatchemie*. VEB, Leipzig.
- PFIFFNER, O. A. & RAMSAY, J. G. 1982. Constraints on geological strain rates: arguments from finite strain states of naturally deformed rocks. *Journal of Geophysical Research*, **87**, 311–322.
- PRIESTLEY, K., JACKSON, J. & MCKEENZIE, D. 2008. Lithospheric structure and deep earthquakes beneath India, the Himalaya and southern Tibet. *Geophysical Journal International*, **172**, 345–362.
- PRYER, L. L. 1993. Microstructures in feldspars from a major crustal thrust zone: the Grenville Front, Ontario, Canada. *Journal of Structural Geology*, **15**, 21–36.
- SCHENK, V. 1980. U–Pb and Rb–Sr radiometric dates and their correlation with metamorphic events in the granulite-facies basement of the Serre, southern Calabria (Italy). *Contributions to Mineralogy and Petrology*, **73**, 23–38.

- SCHENK, V. 1984. Petrology of felsic Granulites, metapelites, metabasics, ultramafics, and metacarbonates from Southern Calabria (Italy): Prograde Metamorphism, Uplift and Cooling of a Former Lower Crust. *Journal of Petrology*, **25**, 255–296.
- SCHENK, V. 1990. The exposed crustal cross section of southern Calabria, Italy: structure and evolution of a segment of Hercynian crust. In: SALISBURY, M. H. & FOUNTAIN, D. M. (eds) *Exposed Cross-sections of the Continental Crust*. Kluwer, Dordrecht, The Netherlands, 21–42.
- SHAND, S. J. 1916. The pseudotachylite of Parijs (Orange Free State). *Quarterly Journal of the Geological Society, London*, **72**, 198–221.
- SIBSON, R. H. 2003. Thickness of the seismic slip zone. *Bulletin of the Seismological Society of America*, **93**, 1169–1178.
- SPEAR, F. S. 1993. *Metamorphic Phase Equilibria and Pressure–Temperature–Time Paths*. Mineralogical Society of America, Monographs, **1**.
- SPRAY, J. G. 1992. A physical basis for the frictional melting of some rock-forming minerals. *Tectonophysics*, **204**, 205–221.
- STIPP, M., STÜNITZ, H., HEILBRONNER, R. & SCHMID, S. M. 2002. The eastern Tonale fault zone: a ‘natural laboratory’ for crystal plastic deformation of quartz over a temperature range from 250 to 700°C. *Journal of Structural Geology*, **24**, 1861–1884.
- TECHMER, K. S., AHRENDT, H. & WEBER, K. 1992. The development of pseudotachylite in the Ivrea-Verbano zone of the Italian Alps. *Tectonophysics*, **204**, 307–322.
- THOMSON, S. N. 1994. Fission track analysis of the crystalline basement rocks of the Calabrian Arc, southern Italy: evidence of Oligo-Miocene late-orogenic extension and erosion. *Tectonophysics*, **238**, 331–352.
- VERNON, R. 2004. *A Practical Guide to Rock Microstructures*. Cambridge University Press, Cambridge.
- WENK, H. R. 1978. Are pseudotachylites products of fraction or fusion? *Geology*, **6**, 507–511.

# Petrological evidence for co-seismic slip in extending middle–lower continental crust: Heier’s zone of pseudotachylite, north Norway

D. P. MOECHER<sup>1\*</sup> & M. G. STELTENPOHL<sup>2</sup>

<sup>1</sup>*Department of Earth and Environmental Sciences, University of Kentucky,  
101 Sloane Building, Lexington, KY 40506-0053, USA*

<sup>2</sup>*Department of Geology and Geography, Auburn University, 210 Petrie Hall,  
Auburn, AL 36849-5305, USA*

\*Corresponding author (e-mail: moker@uky.edu)

**Abstract:** Multiple generations of pseudotachylite occur in the normal, shallowly dipping ( $30^{\circ}$ NW) Eidsfjord and Fiskfjord shear zones, northern Norway, which developed during late-to-post-Caledonian crustal extension of Precambrian crystalline basement. Garnet-bearing amphibolite-facies mineral assemblages occur in metamorphosed pseudotachylite and in sheared meta-anorthosite. Similar mineral assemblages (+clinopyroxene) occur in mylonitized pseudotachylite cut by normal shear bands at Fiskfjord. These assemblages permit calculation via geothermobarometry of pressure and temperature for the crustal level at which pseudotachylite was repeatedly generated by co-seismic slip during crustal extension. Equilibration conditions at Eidsfjord of  $700 \pm 50$  MPa and  $650 \pm 25$  °C correspond to  $z = 22\text{--}29$  km; conditions for Fiskfjord of  $950 \pm 200$  MPa and  $640 \pm 50$  °C correspond to  $z = 30\text{--}40$  km. Both ranges are significantly greater than the standard depth of the seismogenic zone. Creep at depth in the normal fault accumulated elastic strain in the shallower levels of the fault, which upon release initiated rupture downwards into the ductile regime at high strain rates resulting in frictional sliding and the generation of pseudotachylite. Garnet-bearing ultramylonitic pseudotachylites attest to a return to steady-state creep following co-seismic slip at depths well below the standard seismogenic zone.

The seismogenic potential (frequency and magnitude) of normal faults compared to thrust and strike-slip faults has been a point of discussion for decades (Jackson 1987; Wernicke 1995; Axen 2007). The overall lower frequency of normal-fault earthquakes and the relative rarity of large magnitude ( $M > 6.5$ ) earthquakes in extending continental crust (Jackson & White 1989) is mirrored by the relative rarity of pseudotachylite in normal-fault systems compared to thrust and strike-slip occurrences (Sibson & Toy 2006). An additional unusual aspect of normal-fault seismicity is that some of the deepest continental intraplate earthquakes occur in extensional rift settings (East African and Baikal rift systems: Foster & Jackson 1998; Déverchère *et al.* 2001; Albaric *et al.* 2009) at depths 10–25 km greater than the approximate 15–20 km cutoff of focal depths for the majority of continental seismicity (Sibson 1982). However, the evidence for the widespread development of seismicity on ancient and modern shallow-dipping normal faults is now convincing (Wernicke 1995; Abers *et al.* 1997; Brozzetti *et al.* 2009). The problem remains to explain the seismicity, as it is also well known that shallow-dip normal faults do not conform to

standard Coulomb–Anderson–Byerlee mechanisms for co-seismic faulting (Axen 2004).

This study describes the distribution, style of brittle and ductile deformation, and mineralogy and petrology of fault rocks and wall rocks in ‘Heier’s zone’, an approximately  $150\text{ km}^2$  region of pseudotachylite exposed on Langøya and Hinnøya in Vesterålen (northern Norway) (Fig. 1). The pseudotachylite is associated primarily with a shallow-dipping ( $c. 30^{\circ}$ ) ductile normal-fault system that is a manifestation of post-Caledonian, late Palaeozoic–Mesozoic extension of the Norwegian rifted passive margin during the opening of the North Atlantic. Heier’s zone is defined primarily by a high concentration of pseudotachylite associated with the Eidsfjord ductile normal fault on Langøya, and more scattered occurrences of pseudotachylite associated with the Fiskfjord ductile fault on Hinnøya (Fig. 1). In addition to providing an insight into the link between upper- and lower-crustal seismicity, the study area provides a rare, well-exposed record of seismicity on a shallow normal fault. Finally, Heier’s zone is noteworthy as there exist multiple generations of pseudotachylite that have been overprinted by mylonites and

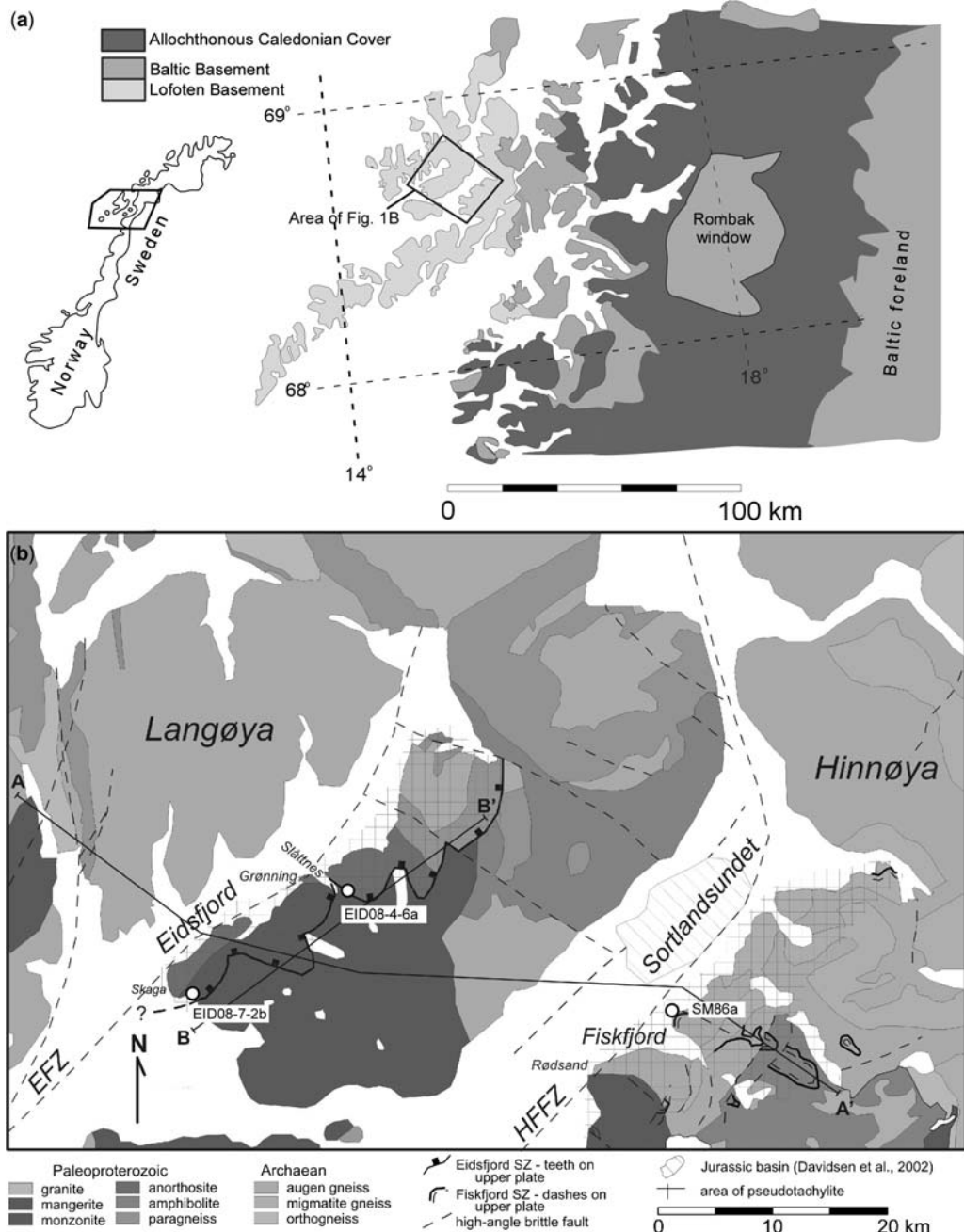


**Fig. 1.** (a) Location and geological setting of study area, northern Norway. (b) Schematic geological map of the area of the Eidsfjord and Fiskfjord shear zones on the islands of Langøya and Hinnøya, respectively (Steltenpohl *et al.* 2011).

metamorphosed at amphibolite-facies conditions. These samples permit determination of depth–temperature conditions of the palaeoseismic rupture zone. The unusual occurrence of abundant

pseudotachylite in mylonitic rocks is relevant to unconventional models for continental strength and co-seismic rupture in ductile rocks (e.g. Hobbs *et al.* 2002; Regenauer-Lieb *et al.* 2008; John

*et al.* 2009). Other aspects of the system point to potentially significant hydrothermal fluid–rock interaction during early development of the ductile normal-fault system.

### Geological setting

The system of fault pseudotachylyte studied here occurs within the most outboard exposures of the extended northern Norwegian continental margin (Fig. 1a). Reflection seismic surveys across the rifted Norwegian margin reveal that crustal extension and extreme attenuation are accommodated largely by displacement and rotation of 5–10 km-scale crustal blocks along low-angle detachments that cut the entire continental crust (Osmundsen *et al.* 2002; Osmundsen & Ebbing 2008), a spectacular example of deformation partitioning. The primary onshore manifestation of this extension is Mesozoic–Cenozoic brittle fracture and faulting, and is expressed in the controls on landscape evolution by such structures (Løseth & Tveten 1996; Bergh *et al.* 2007). However, the earliest extensional structures are late Palaeozoic ductile normal faults such as those described here (Osmundsen *et al.* 2002).

Løseth & Tveten (1996) first reported pseudotachylyte associated with a zone of brittle and ductile faults on Langøya along Eidsfjord in the Vesterålen area in the area of bedrock originally mapped by Heier as part of his ground-breaking studies on granulites (in 1960) (Fig. 1b). Løseth & Tveten (1996) mapped additional brittle and ductile faults on Hinnøya, as part of the same zone that as a whole constitutes ‘Heier’s zone of pseudotachylyte’ (Ball *et al.* 2008). Archaean and Proterozoic continental basement rocks (anorthosite, mangerite, monzonite and granitic migmatite) were metamorphosed at granulite- to upper-amphibolite-facies conditions at 1.8–1.7 Ga (Griffin *et al.* 1978; Corfu 2004). Despite its internal orogenic position and occurrence structurally beneath the stack of Caledonian allochthons that overrode it toward the east, Caledonian metamorphic and deformational effects in Lofoten are strictly limited to shear zones (Tull 1978; Bartley 1982; Hames & Andresen 1996; Klein *et al.* 1999; Steltenpohl *et al.* 2004). The Lofoten window lies roughly along strike of the WGR and, likewise, is considered to be the western edge of Baltica (today’s co-ordinates; Fig. 1a) that was deeply subducted beneath Laurentia during the Caledonian orogeny (Hodges *et al.* 1982; Steltenpohl *et al.* 2004). Some previous studies describe the fault as a thrust (e.g. Heier 1960; Markl 1998; Plattner *et al.* 2003), and early thrust motion is possible, but the preponderance of structural and petrological evidence (Løseth & Tveten 1996; Ball *et al.* 2008;

this study) demonstrates that the most recent motion is normal.

### Eidsfjord shear zone

Heier’s zone was examined in detail on the SE coast of Eidsfjord on Langøya (herein the Eidsfjord Shear Zone) (Fig. 2). Ductile and brittle fault rocks associated with the Eidsfjord Shear Zone are best exposed along the SE coast of Eidsfjord, with the main detachment exposed at Slåttne and Grønning (Figs 1b & 2). Mylonites and extensional structures in meta-anorthosite, mangerite and monzonite gneiss also occur discontinuously to the SW end of Langøya at Skaga (Fig. 1b).

The Eidsfjord Shear Zone is a 200 m-thick zone of mylonite displaying top-down-to-the-west normal-slip movement. Strike of mylonitic foliation in the shear zone is roughly N50°E, with dip ranging from 7° to 35°NW and the detachment surface dipping 25°–30°NW (Fig. 2). The hanging wall is predominantly massive, coarse-grained, grey, pyroxene-bearing granulite-facies anorthosite that grades downwards into altered gneissic–mylonitic

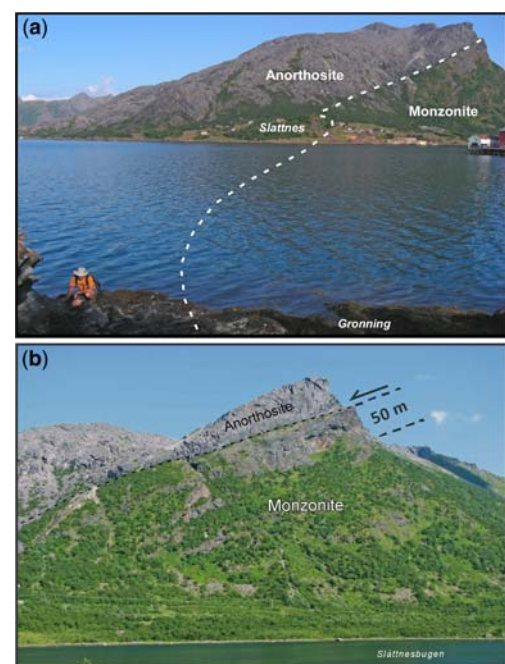


**Fig. 2.** Views of exposures of Eidsfjord Shear Zone near Slåttne. (a) View of Eidsfjord Shear Zone near Slåttne from Gronning. The trace of the highest strain rocks in the shear zone is shown by the white dashed line. (b) Vertical lithological relations in the most continuous exposure of Eidsfjord Shear Zone; the arrow shows the displacement sense.

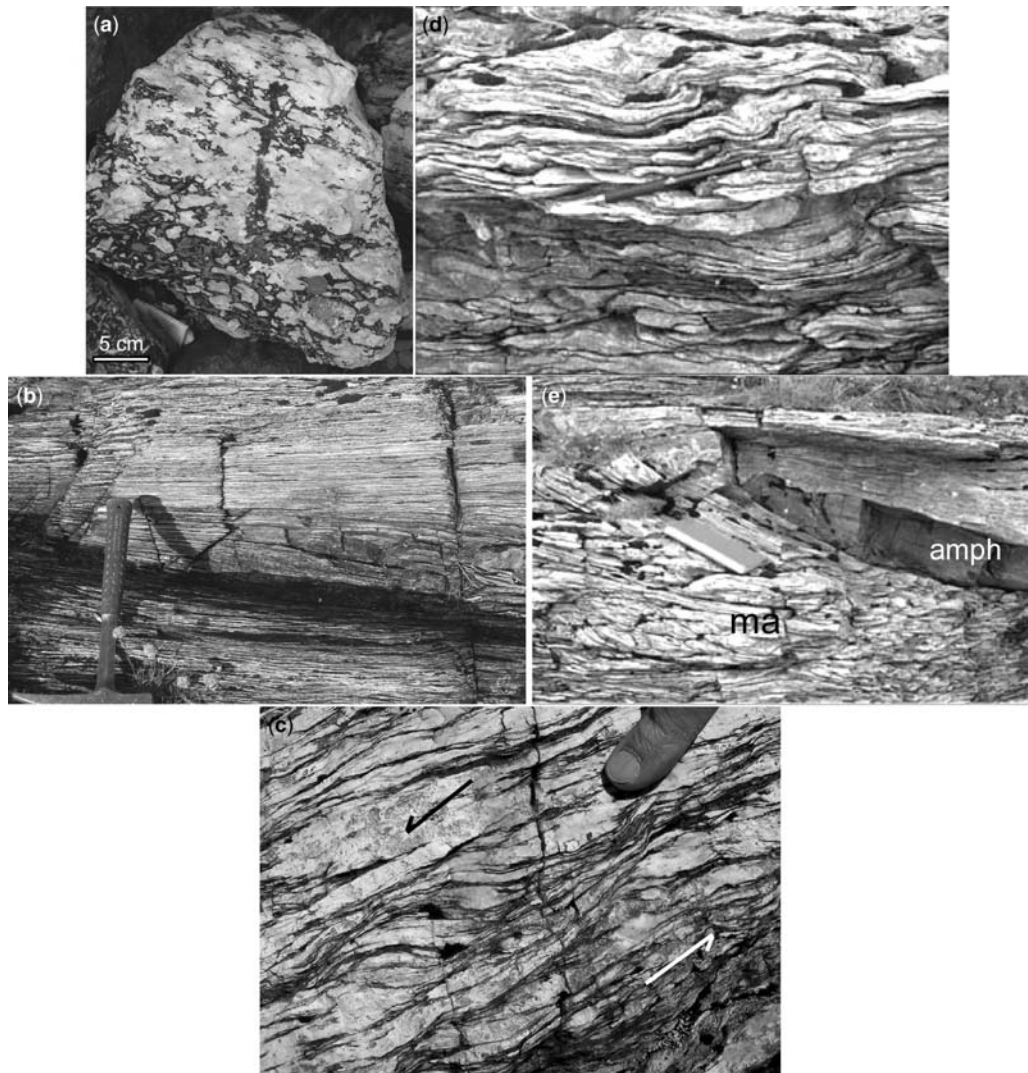


**Fig. 3.** Mesoscopic structures demonstrating normal-sense ductile displacement. (a) Unfoliated bleached meta-anorthosite protolith in the Eidsfjord Shear Zone. Dark clots are hornblende + biotite aggregates (after clinopyroxene) in white, coarse-grained, recrystallized plagioclase. (b) Mylonitic meta-anorthosite. (c) Normal shear bands cutting foliation in meta-anorthosite (finger for scale). (d) Asymmetric (NW-vergent) folds of foliation in meta-anorthosite (pen for scale). (e) Amphibolite-cored, NW-vergent sheath fold (book for scale) in mylonitic meta-anorthosite (ma).

meta-anorthosite in the shear zone. The footwall is coarse-grained, light-grey granulite-facies biotite–monzonite and ferrodiorite that grades upwards towards the detachment zone into monzonitic mylonitic gneiss with metre-scale lenses of amphibolite. Pseudotachylite is also developed in migmatitic granulite-facies granitic gneiss NE of the cutoff of the Eidsfjord Shear Zone (Fig. 1b).

Mylonites within the Eidsfjord Shear Zone and shear zones to the SW end of Langøya record a

non-coaxial simple-shear deformation history with abundant shear-sense indicators that consistently record top-to the-west, normal-slip shear bands (Fig. 3) (Ball *et al.* 2008; Steltenpohl *et al.* 2011). Mylonitic foliation and normal-slip shear bands,  $S-C$  fabrics and asymmetric folds above the main detachment surface develop sharply downwards in the meta-anorthosite over a distance of 1–2 m. Mylonitic foliation is in part compositional, defined by alternating biotite + hornblende- and

plagioclase-rich layers, and partly by preferred orientation of biotite and hornblende. Anastomosing networks of ultramylonite that encapsulate lenses of weakly deformed anorthosite characterize the detachment zone. Mylonitized monzonite in the footwall contains abundant sigma and delta porphyroclasts, broken-displaced grains, shear bands and  $S-C$  fabrics with top-to-the-west normal-slip shear sense. Mylonites disappear approximately 200 m structurally downwards into the monzonite by way of anastomosing shears that surround weakly deformed lenses, which finally give way to centimetre-thick shears along the margins of competent mafic bodies. The detachment surface is narrow and remarkably planar (Fig. 2). Anorthosite is locally observed in direct contact with monzonite but more commonly a thin (metre-scale) zone of densely spaced, domino-style, top-to-the-west, brittle normal faults mixed with cataclasite, ultracataclasite and pseudotachylite mark the detachment. Although the history of displacement is complex and strains were high (e.g. formation of sheath folds: Steltenpohl *et al.* 2011), and offset markers are absent, there does not appear to be significant offset across the Eidsfjord Shear Zone as granulite-facies mineral assemblages are preserved in Palaeoproterozoic metaplutonic rocks in the footwall and hanging wall. This contrasts with other areas of post-Caledonian extension in central and southern Norway that exhibit marked contrast in lithology and palaeodepth across the detachment (e.g. Nordfjord–Sogn detachment: Andersen & Jamtveit 1990). It is also uncertain whether the dip of the shear zone was originally steeper and subsequently rotated into its present orientation. Seismic reflection data for offshore regions of the rifted Norwegian margin reveal that rotation of continental crust occurred along listric detachments (Osmundsen *et al.* 2002) with inboard dips similar to the Eidsfjord Shear Zone. Syn- and/or post-detachment faulting have excised the Eidsfjord detachment to the NE (Fig. 1b). Its trace beneath Eidsfjord to the SW and NW is unknown, although seismic sections suggest that it may correlate with extensional faults in the subsurface (Osmundsen *et al.* 2002).

#### *Timing of ductile deformation at Eidsfjord*

Plattner *et al.* (2003) carried out laser heating  $^{40}\text{Ar}/^{39}\text{Ar}$  analysis of various components of pseudotachylite in anorthosite in the hanging wall. The  $^{40}\text{Ar}/^{39}\text{Ar}$  systematics were complex, with multiple Precambrian age components present, but the youngest ages are consistent with Devonian pseudotachylite formation.

Steltenpohl *et al.* (2011; see also Ball *et al.* 2008) present  $^{40}\text{Ar}/^{39}\text{Ar}$  laser heating analyses on six

fabric-forming muscovite-bearing samples collected from ultramylonitic meta-anorthosite within the Eidsfjord detachment. Single-crystal total fusion (SCTF) analyses of muscovite (c. 10 per sample) yield age probability distributions with a dominant mode at about 405 Ma. Laser incremental heating analyses for fine-grained, recrystallized fabric-forming muscovite yield plateau ages with a combined mean of  $403.6 \pm 1.1$  Ma (95% confidence level, *mean square weighted deviation* (MSWD) = 2.0). The age of  $403.6 \pm 1.1$  Ma for the fine-grained muscovite is interpreted to represent the age of recrystallization and argon isotopic re-equilibration in the Eidsfjord detachment. This Devonian age is also identical to  $^{40}\text{Ar}/^{39}\text{Ar}$  muscovite ages reported from the same structural position along the Nordfjord–Sogn detachment (Berry *et al.* 1995; Walsh *et al.* 2007).

#### **Fiskfjord Shear Zone**

We have made a preliminary petrological examination of fault rocks on Hinnøya (the Fiskfjord Shear Zone) (Fig. 1b) (also see Mager 2006; Ball *et al.* 2008). Compared to the Eidsfjord Shear Zone, the Fiskfjord Shear Zone is a thinner (c. 20 m) less well-defined zone of tectonites, with mylonites and pseudotachylite in the hanging wall. At its exposed southeastern limit, the top of the footwall is fine-grained, plagioclase-rich biotite–amphibolite  $L-S$  tectonite and a leucocratic biotite–hornblende  $L-S$  tectonite. The most recent displacement on the Fiskfjord Shear Zone is normal. The base of the footwall is a leucocratic porphyroclastic granitic orthogneiss (foliation striking  $115^\circ$ , dipping  $45^\circ\text{N}$ ). However, steeply to moderately-dipping ( $60^\circ$ – $30^\circ$ ) normal ductile shear zones sole into the Fiskfjord Shear Zone proper, and many pseudotachylite veins exhibit evidence of ductile reactivation. The latter are the focus of this study.

#### **Petrology**

##### *Eidsfjord Shear Zone*

A variety of fault rock types, ranging from high-temperature mylonite to coherent cataclasite to pseudotachylite, contain microstructures and assemblages that reflect conditions of Caledonian and later deformation within the Eidsfjord Shear Zone. Markl (1998) documented the petrology and geochemistry of the granulite-facies, Proterozoic anorthosite and monzonite protoliths. Plattner *et al.* (2003) described the pseudotachylites of the Eidsfjord Shear Zone, which are typical fault pseudotachylites similar to other occurrences worldwide

(vein, reservoir and pseudobreccias: Sibson 1975). Plattner *et al.* (2003) presented detailed petrological descriptions, including evidence of a melt origin of the pseudotachylite (quench crystals of plagioclase and biotite in an aphanitic matrix, flow banding, variably melted mineral and lithic clasts, brown glass along grain boundaries in clasts). We observed the same features throughout anorthosite, mangerite and migmatite in the Eidsfjord area. However, transmission electron microscopy (TEM) studies documenting an amorphous pseudotachylite matrix phase (i.e. melt) have not yet been performed. Plattner *et al.* (2003) also presented major element geochemical systematics of pseudotachylite in vertical profiles through the base of the anorthosite hanging wall, focusing on chemical variations and ages of pseudotachylite. The volume proportion of pseudotachylite generally decreases in abundance upwards from the fault zone (50% near the fault to rare 30 m above the fault), and pseudotachylite compositions can be correlated with the enclosing rock compositions (Plattner *et al.* 2003). The present study focuses on the more unusual pseudotachylites and host rocks formed by ductile extensional deformation and metamorphism of rocks in the footwall and hanging wall.

In general, normal displacement mylonitization in the Eidsfjord Shear Zone hanging wall and footwall resulted in retrogression of granulite-facies assemblages developed in meta-igneous protoliths. Massive, coarse-grained (up to 5 cm-long plagioclase phenocrysts), grey, granulite-facies meta-anorthosites (plagioclase ± orthopyroxene ± clinopyroxene ± biotite ± hornblende ± quartz ± ilmenite) comprises the hanging wall on Langøya where the Eidsfjord Shear Zone is best exposed (Fig. 2). Anorthosites at the base of the hanging wall in the Eidsfjord Shear Zone (Figs 3a & 4a–d) becomes bleached white and variably recrystallized (in porphyroclastic protomylonite–mylonite) to amphibolite-facies assemblages of plagioclase ± hornblende ± biotite ± muscovite ± epidote ± scapolite ± garnet (Figs 5 & 6). The retrograde assemblage is variably foliated, but extremely so in *S* and *S*–*C* tectonites in the normal-sense shear zone defining the detachment (Figs 3b, f, g & 4f–h).

Not all bleached rocks are foliated. Coarse (1–5 cm) crystals of plagioclase in bleached meta-anorthosite exhibit recrystallization along transgranular fractures/shears and grain boundaries to form aggregates of fine-grained plagioclase and secondary minerals. Pyroxenes react to form symplectic aggregates of hornblende ± biotite ± quartz (Figs 3a, 4b–d & 6a). Bleached pseudotachylite veins and pseudobreccias occur in unfoliated bleached meta-anorthosite at the base of the hanging wall (Fig. 4b, c). These pseudotachylite veins and their enclosing rocks become progressively foliated and metamorphosed downwards over

approximately 5 m into the shear zone (Fig. 4e). The least transposed veins preserve relict lithic pseudotachylite clasts of fine-grained plagioclase in an amphibolites-facies matrix of plagioclase + hornblende ± biotite ± epidote ± scapolite ± garnet ± ilmenite (Fig. 5). However, relict clasts within pseudotachylite are identifiable even in strongly foliated meta-anorthosite (Figs 4e & 5b, c).

Mylonitic meta-anorthosite in the shear zone and mylonitic monzonite gneiss at the top of the footwall are cut by at least one generation of undeformed pseudotachylite veins. The thicker veins are oriented parallel to or at a low angle to foliation but have offshoots that fill 5 mm-wide extensional veins orientated at a high angle to the mylonitic foliation (Fig. 4f). Pseudotachylite breccias contain clasts of fine-grained mylonitic meta-anorthosite (Fig. 4g).

The thickest and greatest concentration of pseudotachylite is present in the most strongly foliated and mylonitic rocks at the top of the detachment at Grønning (Figs 1b & 7a), where pseudotachylite breccias consist of clasts of mylonitic–ultramylonitic meta-anorthosite in dark grey–black pseudotachylite (Fig. 7b). Several generations of pristine to strongly foliated, mylonitic and metamorphosed pseudotachylite cutting the ultramylonitic meta-anorthosite can be resolved. Folded mylonitic meta-anorthosite and pseudotachylite veins (Fig. 7c), some defining sheath folds, are also present.

Mylonitized pseudotachylite in anorthosite and mangerite occur in the hanging wall (Fig. 7e–1). Feldspars, pyroxenes and amphibole in wall rocks and in pseudotachylite clasts exhibit dynamic recrystallization at grain margins and along internal shear bands. Ultramylonitic pseudotachylite in meta-anorthosite, ferrodiorite and monzonite commonly contain strings of tiny garnet grains aligned parallel to the mylonitic foliation (Fig. 7e–2, e–3).

#### Fiskfjord Shear Zone

Pseudotachylite in coastal exposures of the hanging-wall mangerite of the Fiskfjord Shear Zone occurs as planar, centimetre-wide and tens of metres long veins and pseudobreccias (Fig. 8a). Pseudotachylite veins and hanging-wall gneisses are cut by narrow (metres wide) normal (top-to-the-NW) shear zones with orientations that parallel the roughly NE strike of the Eidsfjord Shear Zone, resulting in mylonitic and ultramylonitic pseudotachylite (Fig. 8b). Normal-sense shear bands strike 020° and dip 60°NW, with a lineation orientated obliquely (plunging 042° to 340°) to dip defined by feldspar and pseudotachylite streaks.

Undeformed (non-mylonitic) pseudotachylite veins in granulite-facies mangerite of the Fiskfjord

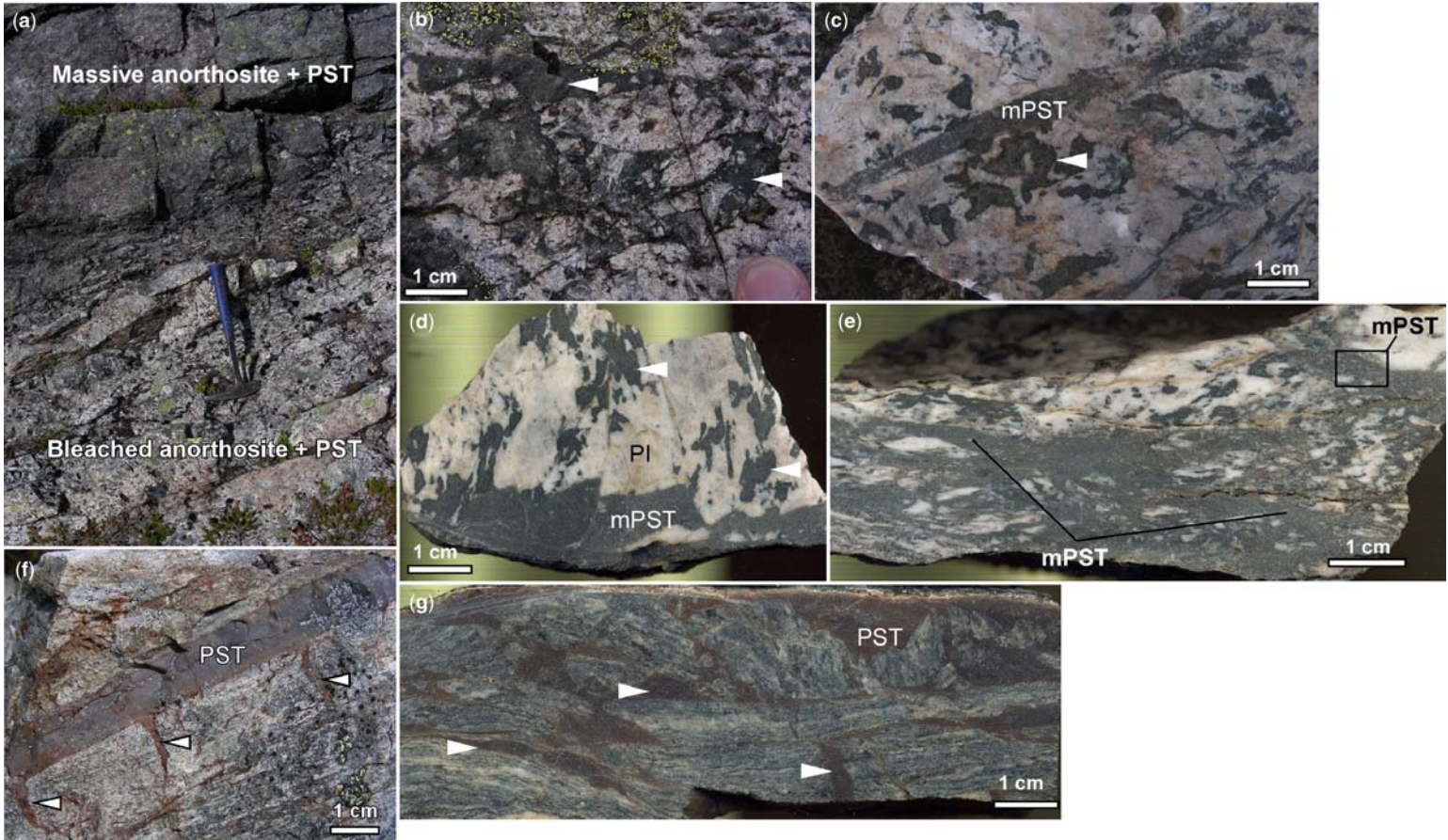


**Fig. 4.** Outcrop- and hand-sample-scale features of altered anorthosite and pseudotachylite at the base of the hanging wall of the Eidsfjord Shear Zone above Slåttnesbungen (Fig. 2). (a) Outcrop photograph showing dark-grey unaltered anorthosite (top) and light-grey bleached anorthosite, both containing pseudotachylite veins and pseudobreccias (not visible at the scale of the photograph). (b) Altered pseudotachylite breccia from the area of bleached meta-anorthosite containing light-coloured clasts of unfoliated meta-anorthosite in pseudotachylite (arrow heads). (c) Bleached unfoliated meta-anorthosite. Arrow denotes hornblende + biotite pseudomorph after clinopyroxene. (d) Bleached porphyroclastic meta-anorthosite cut by metamorphosed pseudotachylite (mPST), all cut by late brittle fractures. (e) Foliated meta-anorthosite with metamorphosed pseudotachylite veins (mPST); sample EID08-4-6a (also see Fig. 6). (f) Undeformed pseudotachylite cutting foliated meta-anorthosite. (g) Pseudotachylite breccia containing clasts of mylonitic meta-anorthosite in a dark matrix of pseudotachylite (PST and white arrow heads).

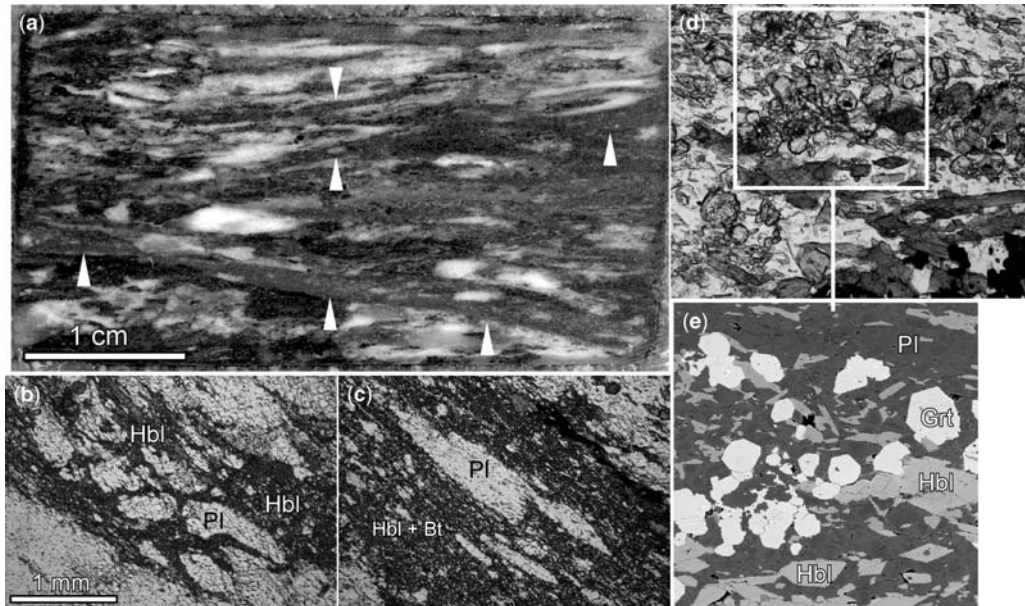


**Fig. 5.** Microstructures and mineral assemblages of pseudotachylite-bearing meta-anorthosite (sample EID08-4-6a). (a) Thin-section chip showing pseudotachylite veins (white arrows) with relict plagioclase clasts. (b) & (c) Plane light photomicrographs showing recrystallized plagioclase clasts in a matrix of hornblende and biotite. (d) Plane light photomicrograph showing a cluster of garnets with hornblende and plagioclase. (e) Backscattered electron image of the box in (d) showing garnet, hornblende and plagioclase analysed by electron microprobe for thermobarometry.

Shear Zone contain clasts of mesoperthite in a statistically recrystallized matrix of extremely fine-grained K-feldspar + plagioclase + hornblende + garnet + ilmenite + clinopyroxene (Fig. 8d). Garnet occurs as clusters of numerous subgrains with inclusions of quartz (Fig. 8d-2b) and locally clinopyroxene. Mylonitized pseudotachylite veins and host rock cut by normal shear bands contain the same assemblage as undeformed/recrystallized pseudotachylite and recrystallized relict mesoperthite clasts. Garnet in mylonitic pseudotachylite consists of strings of garnet crystals aligned parallel to the fabric defined by the long axis of hornblende crystals and recrystallized mesoperthite clasts (Fig. 8d-3). Recrystallized mesoperthite and clinopyroxene in shear bands cutting the host rock contain garnet that nucleated on aggregates of clinopyroxene (Fig. 8d-1).

### Thermobarometry and depth of pseudotachylite formation

The middle–upper amphibolite-facies, garnet-bearing mineral assemblages in metamorphosed pseudotachylite and host rocks from the Eidsfjord and Fiskfjord shear zones afford the unusual

opportunity to measure the depth and temperature of the seismogenic zone via mineralogical thermobarometry. There are few instances in pseudotachylite-bearing systems where such mineral assemblages are present either within the pseudotachylite proper (Austrheim & Boundy 1994; Andersen & Austrheim 2006) or in shear bands that deform the pseudotachylite. The formation of garnet is a critical distinction of the Eidsfjord and Fiskfjord Shear Zone pseudotachylites compared to other instances of mylonitized pseudotachylite (e.g. Lin *et al.* 2005), as garnet is a key phase in mineralogical thermobarometers. Many pseudotachylites are developed in high-grade rocks but the pseudotachylites often formed at shallower depths and lower ambient temperatures than those corresponding to regional metamorphism of the wall rocks. Furthermore, pseudotachylites are usually much younger than the regional metamorphic event that formed the wall-rock assemblages, having formed by co-seismic slip during exhumation of the mid-crustal rocks in which the pseudotachylites occur (e.g. Allen 2005; Swanson 2006).

Mineral compositions (Table 1) were used to calculate the pressure and temperature ( $P-T$ ) locus of the following thermobarometric equilibria. The relevant equilibria for components in phases

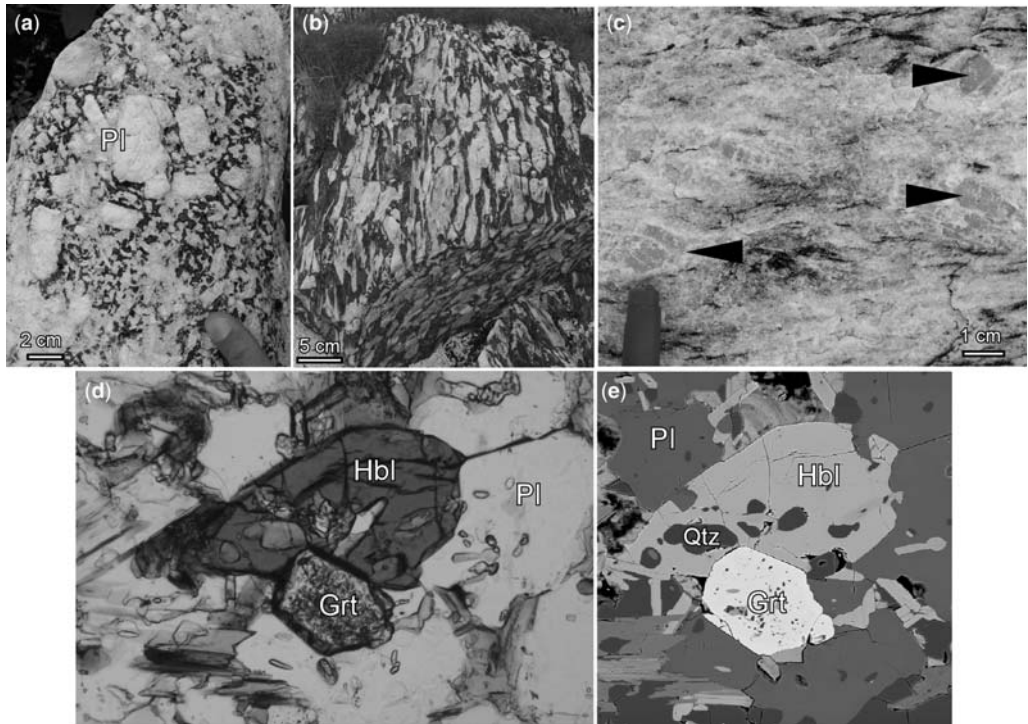
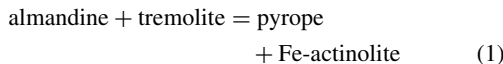
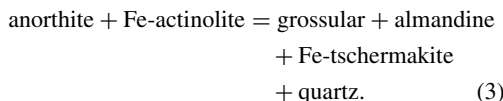
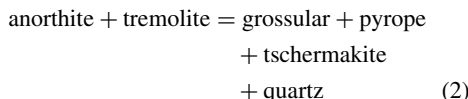


**Fig. 6.** Outcrop-, hand-sample- and thin-section-scale textures and mineral assemblages in meta-anorthosite sample from Skaga used for thermobarometry (EID08-7-2a). (a) Unfoliated, coarse-grained bleached meta-anorthosite protolith of mylonitic meta-anorthosite. (b) Foliated and lineated hornblende + biotite meta-anorthosite. Dark areas are elongated and flattened clusters of hornblende + biotite, and the white objects are deformed and recrystallized plagioclase. (c) Porphyroclastic meta-anorthosite with minor biotite and hornblende. (d) & (e) Plane light photomicrograph and backscattered electron image of representative area of garnet + hornblende + plagioclase + quartz analysed by electron microprobe.

defining the assemblage garnet–hornblende–plagioclase–quartz are the garnet–hornblende Fe–Mg exchange thermometer:

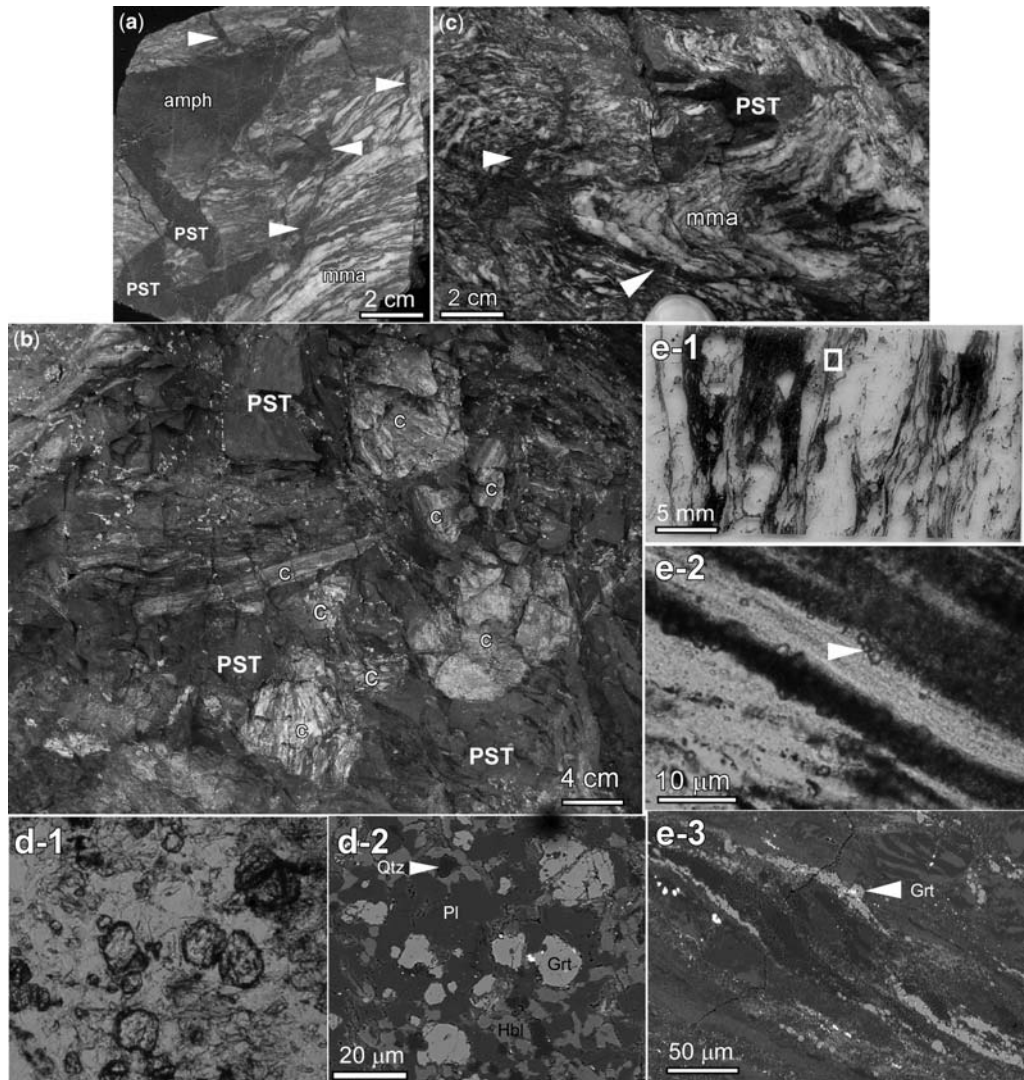


and net transfer reaction geobarometer:



We used the empirical calibrations of Graham & Powell (1984) for equilibrium (1) and Kohn & Spear

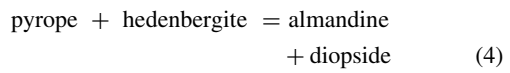
(1990) for equilibria (2) and (3). As such, they are not as thermodynamically rigorous as experimentally calibrated equilibria or those based on internally consistent thermodynamic datasets. However, their use permits direct comparison with results of thermobarometry in other crustal settings, and avoids the issue of quantifying  $\text{Fe}^{3+}/\text{Fe}^{2+}$  in hornblende, which has been shown to be notoriously inaccurate (Cosca *et al.* 1991). The minerals in the samples analysed here have compositions very similar to those in samples used to calibrate the relevant thermobarometers, which further reduces uncertainty in the use of empirical calibrations. The calibration of Graham & Powell (1984) was based on temperatures obtained from garnet–clinopyroxene Fe–Mg exchange thermometry (Ellis & Green 1979) for the same samples, so that comparisons can be made between the results for the hornblende-bearing, clinopyroxene-absent, assemblages in the Eidsfjord Shear Zone and the clinopyroxene-bearing assemblages of the Fiskfjord Shear Zone.



**Fig. 7.** Outcrop- and thin-section-scale features at Grønning coastal exposures of the Eidsfjord Shear Zone. (a) Mylonitic meta-anorthosite and amphibolite ('amph') cut by pseudotachylite ('PST' and white arrows). (b) Pseudotachylite breccia consisting of clasts ('c') of mylonitic meta-anorthosite in dark pseudotachylite ('PST'). (c) Folded mylonitic meta-anorthosite ('mma') and pseudotachylite ('PST', and white arrows). (d-1) & (d-2) Photomicrograph (plane light) and backscattered electron image of garnet-bearing mylonitic meta-anorthosite clast in pseudotachylite breccia. (e-1) Thin section from mylonitized pseudotachylite in mangerite. The small white box is the area shown in (e-2) photomicrograph of ultramylonite shear bands with strings of tiny garnets (white arrows). (e-3) backscattered electron image of area in (e-1) with an asymmetric mesoperthite clast surrounded by garnets nucleating during ductile deformation.

The results of thermobarometry in the Fiskfjord Shear Zone samples was presented by Moecher & Steltenpohl (2009), but are summarized here for comparison with the Eidsfjord Shear Zone. Relevant equilibria for the Fiskfjord Shear Zone samples are the garnet-clinopyroxene Fe-Mg

cation exchange geothermometer:



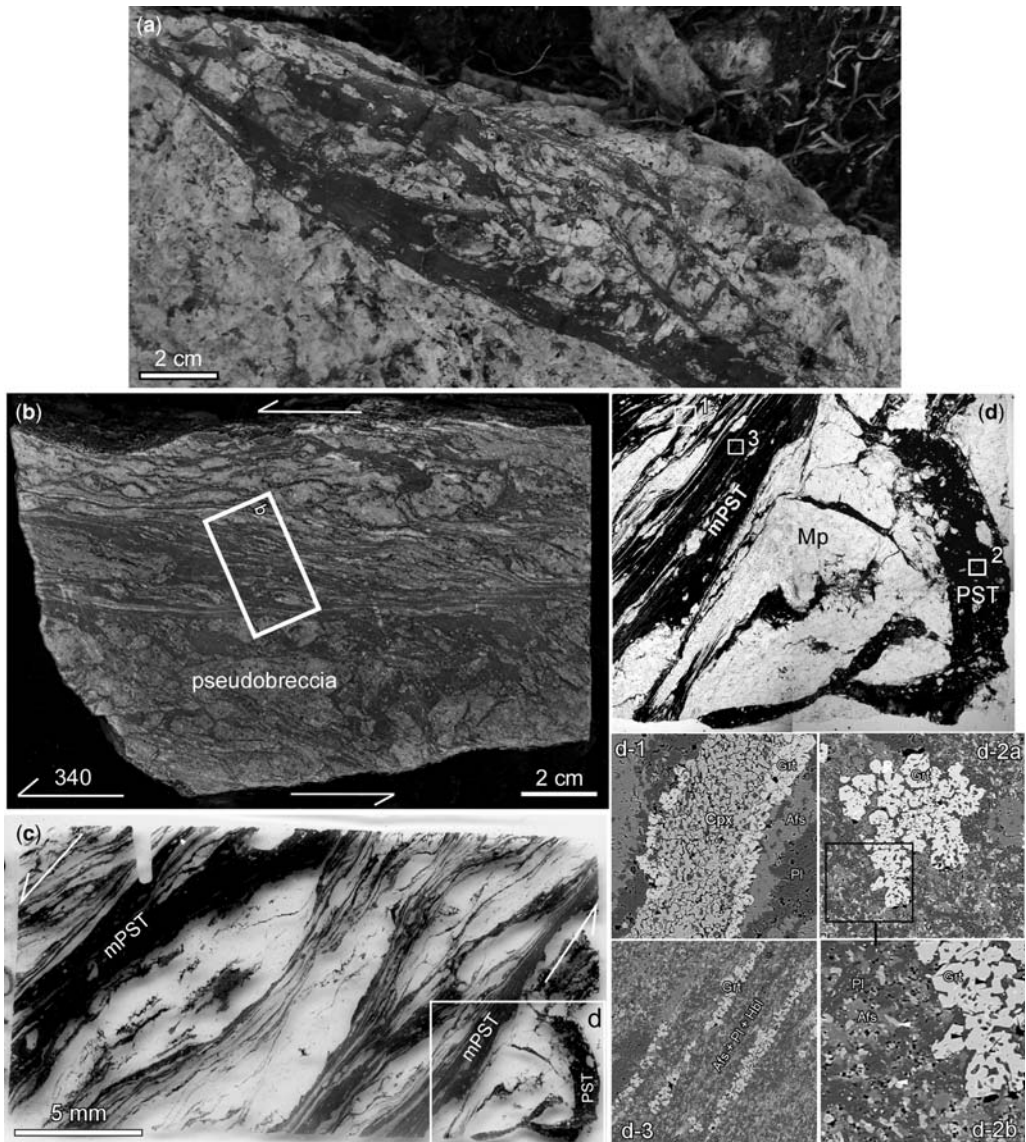
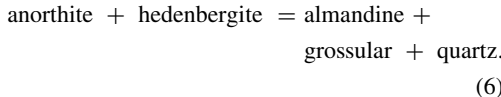
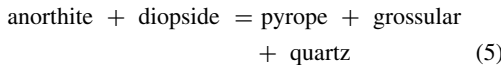


**Fig. 8.** Microstructures and mineral assemblages in mylonitized pseudotachylyte from the Fiskfjord Shear Zone. **(a)** Outcrop photograph of undeformed pseudobreccia. **(b)** Sawn orientated hand sample (bearing of the plunge of the lineation is  $340^\circ$ ) containing deformed pseudotachylyte veins and pseudobreccia, cut parallel to stretching lineation and perpendicular to mylonitic foliation. The white box shows the orientation of the thin section in **(c)**. **(c)** Oriented vertical thin section showing the normal-sense shear bands cutting pseudotachylyte ('PST') and forming mylonitic pseudotachylyte ('mPST'). The white box in the lower-right is the area of shown in the photograph in **(d)**. **(d)** Mesoperthite of mangerite cut by undeformed ('PST') and mylonitized pseudotachylyte ('mPST'). The small boxes are the areas of backscattered electron images shown in **(d-1)**, **(d-2)** and **(d-3)**. **(d-1)** dynamically recrystallized clinopyroxene, mesoperthite (now fine-grained alkali feldspar and plagioclase) with garnet nucleating on clinopyroxene. **(d-2a)** garnet cluster nucleating in undeformed PST. **(d-2b)** Matrix of the PST consisting of extremely fine-grained alkali feldspar, plagioclase, hornblende and ilmenite. **(d-3)** Garnets aligned parallel to the mylonitic foliation in mPST.

**Table 1.** Representative microprobe analyses

Plagioclase				Garnet				Hornblende						
EID08-4-6a		EID08-7-2b		EID08-4-6a		EID08-7-2b		EID08-4-6a		EID08-7-2b				
No.	8	20	36	43	No.	27	39	51	57	No.	13	24	28	38
SiO <sub>2</sub>	54.97	57.18	56.59	58.99	SiO <sub>2</sub>	37.46	37.19	37.16	36.93	SiO <sub>2</sub>	40.92	40.48	38.45	41.39
Al <sub>2</sub> O <sub>3</sub>	29.33	27.12	27.99	26.50	TiO <sub>2</sub>	0.06	0.06	0.06	0.04	TiO <sub>2</sub>	0.10	0.39	0.35	0.22
Fe <sub>2</sub> O <sub>3</sub>	0.56	0.53	0.16	0.06	Al <sub>2</sub> O <sub>3</sub>	21.18	20.78	21.38	21.18	Al <sub>2</sub> O <sub>3</sub>	17.95	18.04	17.08	17.28
CaO	10.44	8.85	9.72	7.47	FeO	28.73	27.59	27.61	29.35	FeO	16.91	17.68	17.40	17.31
Na <sub>2</sub> O	5.16	6.49	5.35	7.02	MnO	3.29	5.64	4.32	2.90	MnO	0.32	0.29	0.31	0.37
K <sub>2</sub> O	0.12	0.08	0.03	0.03	MgO	3.94	3.19	3.74	3.97	MgO	8.58	7.51	8.17	7.91
<b>Sum</b>	<b>100.59</b>	<b>100.24</b>	<b>99.83</b>	<b>100.06</b>	CaO	5.18	5.21	5.24	4.98	CaO	11.35	11.40	11.75	11.68
Si	2.463	2.562	2.538	2.626	<b>Sum</b>	<b>99.84</b>	<b>99.65</b>	<b>99.50</b>	<b>99.36</b>	Na <sub>2</sub> O	1.52	1.58	1.43	1.47
Al	1.549	1.432	1.479	1.390	Si	2.9831	2.988	2.970	2.962	K <sub>2</sub> O	0.47	0.67	0.62	0.60
Fe	0.021	0.020	0.006	0.002	Ti	0.003	0.003	0.004	0.002	Cl	0.26	0.39	0.25	0.23
Ca	0.501	0.425	0.467	0.356	Al	1.988	1.967	2.014	2.002	<b>Sum</b>	<b>98.37</b>	<b>98.42</b>	<b>95.80</b>	<b>98.46</b>
Na	0.449	0.564	0.465	0.606	Fe	1.913	1.854	1.846	1.968	Si	6.087	6.065	5.945	6.167
K	0.007	0.005	0.001	0.002	Mn	0.222	0.384	0.292	0.197	Ti	0.011	0.044	0.041	0.024
Ab	0.46	0.57	0.53	0.62	Mg	0.468	0.382	0.445	0.475	Al	3.146	3.186	3.112	3.035
An	0.54	0.43	0.47	0.38	Ca	0.442	0.448	0.449	0.428	Fe	2.103	2.215	2.249	2.157
					Gr	0.145	0.146	0.148	0.140	Mn	0.040	0.036	0.041	0.047
					Py	0.154	0.124	0.147	0.155	Mg	1.903	1.677	1.882	1.758
					Alm	0.628	0.604	0.609	0.641	Ca	1.809	1.830	1.946	1.864
					Sp	0.073	0.125	0.096	0.064	Na	0.439	0.458	0.428	0.425
					Mg#	0.196	0.171	0.194	0.194	K	0.089	0.128	0.123	0.113
										Cl	0.066	0.098	0.065	0.059

and garnet–clinopyroxene–plagioclase–quartz net transfer reaction geobarometers:



Calculation of the  $P$ – $T$  locus of equilibria (4)–(6) follows Berman (1991).

The compositions of the relevant minerals in each sample were determined by electron probe microanalysis using the CAMECA SX50 at the University of Kentucky. Representative data for the Eidsfjord Shear Zone samples are presented in Table 1, and data for the Fiskfjord Shear Zone appear in Moecher & Steltenpohl (2009). Several grains of each mineral within millimetre-scale textural domains of each thin section (e.g. Figs 5d, e & 6d, e) were analysed to assess homogeneity and evaluate the approach to equilibrium. Multiple combinations of each mineral composition were used to calculate  $T$  and/or  $P$ . Although the absolute values of calculated pressure and temperature are accurate to 100–200 MPa and  $\pm 50$  °C, differences in calculated values are more accurate and significant for comparing depth of deformation between the clinopyroxene- and hornblende-bearing assemblages in the Fiskfjord and Eidsfjord shear zones, respectively.

Garnet has been identified in numerous samples of mylonitic meta-anorthosite, mangerite and amphibolite within the Eidsfjord shear zone system. Two samples of meta-anorthosite from the Eidsfjord Shear Zone with the coarsest-grained and texturally best-equilibrated mineral assemblages were selected for analysis. One is from the top of the shear zone at Slåttnes and consists of metamorphosed pseudotachylite (Fig. 5). The second sample is from the Eidsfjord Shear Zone at the SW end of Langøya (Fig. 6). We have not found pseudotachylite within foliated meta-anorthosite proper (it is present in mangerite at Skaga), but the sample of meta-anorthosite from Skaga is from the same exposure as samples used for  $^{40}\text{Ar}/^{39}\text{Ar}$  geochronology.

## Results

For sample EID08-6a-2, four domains were analysed with 14 combinations of garnet, hornblende and plagioclase compositions that span a range of inferred equilibrium compositions (grains in contact). For an error of 50 °C and 100 MPa for each determination of  $T$  or  $P$  (based on propagation

of  $\pm 2$  mol.% of each component) the weighted average temperature is  $639 \pm 26$  ( $2\sigma$ ) °C. For sample EDI08-7-2b, three domains were analysed with 15 total combinations of garnet, hornblende and plagioclase compositions; the calculated temperature is  $666 \pm 25$  ( $2\sigma$ ) °C. Pressure for the Eidsfjord Shear Zone samples was calculated at 600, 650 and 700 °C for each of the combinations of plagioclase, garnet and hornblende compositions for both the Mg and Fe end-member reactions. The exceptionally shallow slope of the  $P$ – $T$  locus for the hornblende-bearing equilibria (10–20 MPa per 100 °C) minimizes the temperature dependence of the calculated pressure and thus translates into very precise estimates of the depth of metamorphism within the Eidsfjord Shear Zone during ductile extension. At 650 °C, the weighted average pressure for each sample is  $650 \pm 30$  and  $730 \pm 30$  MPa, respectively. The latter values equate to a depth interval of 25–28 km for formation of the garnet-bearing mineral assemblages in deformed pseudotachylites.

Pressure and temperature conditions for the pseudotachylite ductile recrystallization event in the Fiskfjord Shear Zone, calculated from garnet–clinopyroxene–plagioclase–quartz geobarometers and geothermometers, are  $950 \pm 150$  MPa at  $650 \pm 25$  °C (Moecher & Steltenpohl 2009) (Fig. 9). The calculated pressure interval corresponds to a depth interval of 30–40 km. These conditions correspond to minimum depths for formation of the pseudotachylites that are cut by normal-sense ductile shear bands.

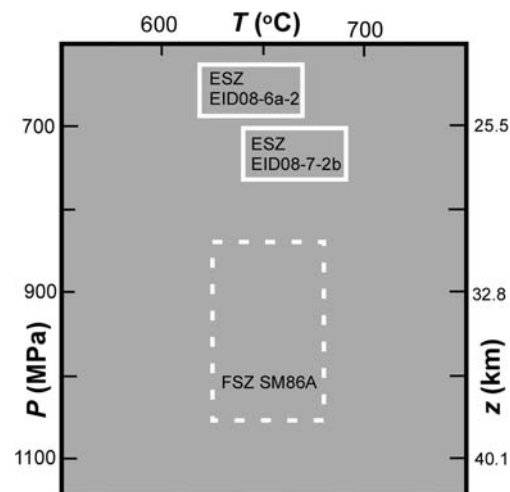


**Fig. 9.** Results of mineralogical thermobarometry on garnet-bearing assemblages from Eidsfjord Shear Zone (ESZ).  $P$ – $T$  conditions from Fiskfjord Shear Zone (FSZ) sample are from Moecher & Steltenpohl (2009).

The depth intervals calculated for the Eidsfjord and Fiskfjord shear zones correspond to those at which pseudotachylite formation, and presumably co-seismic slip, occurred at pressures of roughly 400 Ma in extending continental crust. The depths are well below the commonly cited lower limit of 15–20 km for the seismogenic zone of mature plate-boundary strike-slip faults and thrust faults (Sibson 1982; Scholz 1988), even considering that ‘roughness’ that might result from variations in heat production, differential strength of various middle crustal rock types and strain rate (Sibson 1984). Furthermore, the temperature at the calculated depths is about 200 °C greater than for the onset of crystal-plasticity in feldspars (Voll 1976), which is considered the primary control on the lower depth limit of seismogenesis.

### Relevance of pseudotachylite occurrences

Deformed and/or metamorphosed pseudotachylite occurs within the main fault or in splays from the Eidsfjord and Fiskfjord shear zones; pristine pseudotachylite occurs in undeformed hanging-wall crystalline rocks in the Eidsfjord Shear Zone. The timing of pseudotachylite formation in the former is constrained by the timing of the deformation in the Eidsfjord Shear Zone (pseudotachylite is deformed by and cuts the mylonitic foliations determined by  $^{40}\text{Ar}/^{39}\text{Ar}$  geochronology to be *c.* 400 Ma; see also Plattner *et al.* 2003). Pseudotachylite in the base of the hanging wall within metres of the detachment can be related to pseudotachylite in the Eidsfjord Shear Zone via proximity and cross-cutting relationships. However, we cannot yet definitively state that all pseudotachylite in the hanging wall is Devonian, considering the likelihood of Caledonian thrusting (Steltenpohl *et al.* 2004), and that Mesozoic brittle fracturing and faulting are widespread in coastal northern Norway (Bergh *et al.* 2007). However, the majority of pseudotachylite within the Eidsfjord Shear Zone can be linked structurally and petrologically to Devonian extensional structures and petrofabrics.

Two aspects of the deep pseudotachylite-bearing ductile fault system described here are unusual with regard to structural and crustal setting. First, following the conventional interpretation of the seismogenic significance of pseudotachylite (Sibson 1975; Scholz 2002), the presence of pseudotachylite is evidence that the Eidsfjord and Fiskfjord shear zones were seismically active during a ductile phase of normal displacement. The upper amphibolite-facies metamorphic mineral assemblages in the Eidsfjord Shear Zone and splays of the Fiskfjord Shear Zone were used to

directly calculate ambient temperature and depth of, presumably, the deeper part of the rupture plane. Both occurrences indicate that co-seismic slip occurred at depths and temperatures exceeding the standard lower limit of the seismogenic zone (*c.* 15 km,  $T = 350\text{--}450$  °C; Sibson 1982; Scholz 1988). Such deep earthquakes are not uncommon in the seismological record. Although located in a region exhibiting a different style of crustal extension, intraplate earthquakes with calculated focal depths of 30–40 km comprise 10–20% of the seismicity in the East African and Baikal rift systems (Déverchère *et al.* 2001; Albaric *et al.* 2009). These earthquakes have been accounted for by enhanced strength of a mafic lower crust or the reduced heat flow and geothermal gradient generated by mafic lower crust (Nyblade & Langston 1995). The East African and Baikal normal faulting earthquakes differ from the Eidsfjord and Fiskfjord shear zone system in that: (1) dips of nodal planes tend to cluster around 45°, so that few potential fault-plane solutions dip as shallowly as the current 30° dip of the Eidsfjord Shear Zone; (2) for earthquakes with observable surface rupture, the faults appear to be steeply dipping and not listric throughout the entire crust (Foster & Jackson 1998); and (3) East Africa and Baikal are intraplate rifts far removed from a recently extended continental margin and not previously related to a Caledonian-style continental collision zone. However, the congruence of calculated focal depths for modern seismicity in East Africa and Baikal with palaeo-focal depths in the study area (Moecher & Steltenpohl 2009) make a common mode of rupture possible.

The second unique aspect of Heier’s zone is that pseudotachylite cuts, and is subsequently deformed by, mylonites in a shallow normal fault, implying periodic strengthening for co-seismic slip during extension. Coeval pseudotachylite and mylonite have been reported from a number of ductile thrust and strike-slip systems (Sibson 1980; Hobbs *et al.* 1986; Camacho *et al.* 1995; Allen & Shaw 2007), with fewer reported occurrences in extensional settings (Davis *et al.* 1986; John 1987; Abers 2001; Barker 2005). However, never to our knowledge has pseudotachylite been described from a shallowly dipping, deep-crustal ductile normal-fault system such as Heier’s zone. The rarity of normal-fault pseudotachylite parallels the observation that seismicity in normal-fault systems is generally less frequent and of lower magnitude than thrust and strike-slip systems (Jackson 1987; Wernicke 1995; Axen 2007). Although active seismogenic low-angle normal faults are now recognized (Abers *et al.* 1997; Brozzetti *et al.* 2009), the simplest explanation for the low dip of the Eidsfjord Shear Zone is that it represents a reactivated

Caledonian ductile thrust. We see only minor evidence in the two shear zones for an early thrust history, but if reactivation occurred then any original thrust structures have been completely overprinted. As the Eidsfjord Shear Zone is a lithological contact, it is also possible that the shear zone took advantage of strength contrasts between two crystalline rock types. If fault reactivation did not occur, and the Eidsfjord Shear Zone is a newly formed rupture, then special conditions for failure in strong crystalline rocks must have developed.

### Implications for deep crustal seismicity

Mechanisms proposed to account for repeated pseudotachylite generation overprinted by mylonites (and vice versa), implying repeated seismicity in middle- to deep-crustal settings, include: (1) dynamic downwards rupture propagation into the ductile regime (Sibson 1980; Iio *et al.* 2002; Lin *et al.* 2005), which produces a rapid increase in strain rate of nearly 10 orders of magnitude (Jackson 1987); (2) local amplification of stress and strain rate at lithological contacts (Campbell 1978; Sibson 1980; Fagereng & Sibson 2010); and (3) shear heating phenomena such as plastic instabilities (Hobbs *et al.* 1986) and self-localizing thermal runaway (John *et al.* 2009). The Eidsfjord–Fiskfjord shear zone pseudotachylite system exhibits evidence consistent with the first two mechanisms: (1) the depth of co-seismic slip is well below the lower limit of the seismogenic zone; and (2) slip occurred in a ductile fault system that is also a major lithological contact in strong Mesoproterozoic Baltic basement, which experienced the entire Caledonian collision, thrusting and metamorphic history without undergoing penetrative deformation (Hames & Andresen 1996; Steltenpohl *et al.* 2004, 2006, 2011). We do not see the diagnostic field evidence predicted by models for formation of plastic instabilities or self-localizing thermal runaway; that is, centimetre-thick ductile shear zones cored by pseudotachylite (e.g. fig. 1 in John *et al.* 2009).

The critical outcome of the present study on models of crustal seismicity is the depth and thermal constraints imposed by the geothermobarometric calculations. Shear heating and plastic instabilities in anorthosite are predicted to form in a 1000 m-thick ductile shear zone cored by a thin zone of high shear strain (implied to be cm-scale: Hobbs *et al.* 1986) *below* a critical temperature ( $T_c$ ) of approximately 225 °C (Hobbs *et al.* 1986) at bulk strain rates of  $10^{-12} \text{ s}^{-1}$ . This  $T_c$  is well below the temperature documented in the Eidsfjord Shear Zone (c. 650 °C). A  $T_c$  of 650 °C for a

100 m-thick shear zone (approximate thickness at Eidsfjord) requires a strain rate of  $10^{-7} \text{ s}^{-1}$ . However, localized high strain rates are predicted by models of stress amplification within ductile fault zones (Sibson 1980; Fagereng & Sibson 2010), leading to strengthening and fracture within nominally ductile rocks. Dynamic thermal–mechanical feedback models predict stress localization and formation of ductile extensional detachment faults at mid-crustal depths corresponding to the conventional brittle–ductile transition for a quartz rheology (Regenauer-Lieb *et al.* 2006, 2008). Here, again, the Eidsfjord system is much deeper than predicted by the feedback model, and the quartz rheology used in the model is not applicable to the feldspar-dominated lithologies in the hanging wall and footwall at Eidsfjord.

Intraplate earthquakes in the elastic, seismogenic upper crust have been related to broad-scale, low average strain rate ( $10^{-15} \text{ s}^{-1}$ ) homogeneous ductile flow of the lower crust that generates regional stress and rupture of pre-existing weak faults or favourably oriented fractures in the upper crust (Sykes 1978; Hinze *et al.* 1988; Zoback 1992). An alternative interpretation is that stress is *localized* in the lower crust; that is, regional plate-scale stress is partitioned heterogeneously into ductile shear zones 1–100 m wide that locally experience higher strain rates ( $10^{-13}$ – $10^{-10} \text{ s}^{-1}$ ) (Iio & Kobayashi 2002, 2003; Regenauer-Lieb *et al.* 2006, 2008) and control the behaviour of the lithosphere (Regenauer-Lieb & Yuen 2003). In this model, seismogenic faults in the upper crust have downwards extensions in the ductile lower crust (Hobbs *et al.* 2002; Iio *et al.* 2002). Aseismic creep on the downwards extensions accumulates stress on the brittle, seismogenic segment of faults (Iio *et al.* 2002) that eventually slip according to standard frictional failure modes. Downwards dynamic rupture may propagate along the ductile fault zone, resulting in plastic failure, slip and melting to form pseudotachylites. If the fault is a through-going crustal discontinuity, as demonstrated for much of the Norwegian rifted margin (Osmundsen *et al.* 2002), then the slip may extend through the middle–lower crust. Aseismic ductile slip then resumes following rupture, deforming any newly generated pseudotachylite at the middle–lower crustal depth and generating mylonitized garnet-bearing pseudotachylite, as demonstrated by the Eidsfjord and Fiskfjord shear zone system.

A. Andresen of the University of Oslo provided logistical support for this research. The research was also supported by a Faculty Research Grant to D. P. Moecher from the University of Kentucky.

## References

- ABERS, G. A. 2001. Evidence for seismogenic normal faults at shallow dips in continental rifts. In: WILSON, R. C., WHITMARSH, R. B., TAYLOR, B. & FROITZHEIM, N. (eds) *Non-volcanic Rifting of Continental Margins: A Comparison of Evidence from Land and Sea*. Geological Society, London, Special Publications, **187**, 305–318.
- ABERS, G. A., MUTTER, C. Z. & FANG, J. 1997. Shallow dips of normal faults during rapid extension: earthquakes in the Woodlark-d'Entrecasteaux rift system, Papua New Guinea. *Journal of Geophysical Research*, **102**, 15,301–15,317.
- ALBARIC, J., DÉVERCHÈRE, J., PETIT, C., PERROT, J. & LE GALL, B. 2009. Crustal rheology and depth distribution of earthquakes: insights from the central and southern East African Rift System. *Tectonophysics*, **468**, 28–41.
- ALLEN, J. L. 2005. A multi-kilometer pseudotachylite system as an exhumed record of earthquake rupture geometry at hypocentral depths. *Tectonophysics*, **402**, 37–54.
- ALLEN, J. L. & SHAW, C. A. 2007. *Proterozoic Geology and Phanerozoic Reactivation of the Newly Recognized Grizzly Creek Shear Zone, Glenwood Canyon, Colorado*. Geological Society of America, Field Guide, **10**, 1–17.
- ANDERSEN, T. B. & AUSTRHEIM, H. 2006. Fossil earthquakes recorded by pseudotachylites in mantle peridotite from the Alpine subduction complex of Corsica. *Earth and Planetary Science Letters*, **242**, 58–72.
- ANDERSEN, T. B. & JAMTVEIT, B. 1990. Uplift of deep crust during orogenic extensional collapse: a model based on field studies in the Sogn-Sunnfjord region of western Norway. *Tectonophysics*, **9**, 1097–1111.
- AUSTRHEIM, H. & BOUNDY, T. M. 1994. Pseudotachylites generated during seismic faulting and eclogitization of the deep crust. *Science*, **265**, 82–83.
- AXEN, G. J. 2004. Mechanics of low-angle normal faults. In: KARNER, G., TAYLOR, B., DRISCOLL, N. & KOHLSTEDT, D. L. (eds) *Rheology and Deformation in the Lithosphere at Continental Margins*. Columbia University Press, New York, 46–91.
- AXEN, G. J. 2007. Research focus: significance of large-displacement low angle normal faults. *Geology*, **35**, 287–288.
- BALL, J., STELTENPOHL, M. G., MOECHER, D. P. & KEY, T. 2008. The development of pseudotachylites within Heier's shear zone, Lofoten-Vesterålen, North Norway, and implications for late- to post-Caledonian tectonics. *Geological Society of America Abstracts with Programs*, **40**, 147–146.
- BARKER, S. L. L. 2005. Pseudotachylite-generating faults in Central Otago, New Zealand. *Tectonophysics*, **397**, 211–223.
- BARTLEY, J. M. 1982. Limited basement involvement in Caledonian deformation, Hinnøy, North Norway, and tectonic implications. *Tectonophysics*, **83**, 185–203, doi: 10.1016/0040-1951(82)90018-X.
- BERGH, S. G., EIG, K., KLOVJAN, O. D., HENNINGSSEN, T., OLESEN, O. & HANSEN, J. -A. 2007. The Lofoten-Vesterålen continental margin: a multiphase Mesozoic–Paleogene rifted shelf as shown by offshore-onshore brittle fault-fracture analysis. *Norwegian Journal of Geology*, **87**, 29–58.
- BERMAN, R. G. 1991. Thermobarometry using multi-equilibrium calculations: a new technique with petrologic applications. *Canadian Mineralogist*, **29**, 833–855.
- BERRY, H. N., LUX, D. R., ANDRESEN, A. & ANDERSEN, T. B. 1995. Progressive exhumation during orogenic collapse as indicated by  $^{40}\text{Ar}/^{39}\text{Ar}$  cooling ages from different structural levels, southwest Norway. *Geoytt*, **22**, 20–21.
- BROZZETTI, F., BONCIO, P., LAVECCHIA, G. & PACE, B. 2009. Present activity and seismogenic potential of a low-angle normal fault system (Cita di Castello, Italy): constraints from surface geology, seismic reflection data and seismicity. *Tectonophysics*, **463**, 31–46.
- CAMACHO, A., VERNON, R. H. & FITZGERALD, J. D. 1995. Large volumes of anhydrous pseudotachylite in the Woodroffe thrust, central Musgrave Ranges, Australia. *Journal of Structural Geology*, **17**, 371–383.
- CAMPBELL, D. L. 1978. Investigation of the stress-concentration mechanism for intraplate earthquakes. *Geophysical Research Letters*, **54**, 477–479.
- CORFU, F. 2004. U-Pb geochronology of the Leknes Group: an exotic early-Caledonian metasedimentary assemblage stranded on Lofoten basement, northern Norway. *Journal of the Geological Society, London*, **161**, 619–627.
- COSCA, M. A., ESSENE, E. J. & BOWMAN, J. R. 1991. Complete chemical analyses of metamorphic hornblendes: implications for normalizations, calculated  $\text{H}_2\text{O}$  activities, and thermobarometry. *Contributions to Mineralogy and Petrology*, **108**, 472–484.
- DAVIS, G. A., LISTER, G. S. & REYNOLDS, S. J. 1986. Structural evolution of the Whipple and South mountains shear zones, southwestern United States. *Geology*, **14**, 7–10.
- DÉVERCHÈRE, J., PETIT, C., GILEVA, N., RADZIMINOVITCH, N., MELNIKOVA, V. & SAN'KOV, V. 2001. Depth distribution of earthquakes in the Baikal rift system and its implications for the rheology of the lithosphere. *Geophysical Journal International*, **146**, 714–730.
- ELLIS, D. J. & GREEN, D. H. 1979. An experimental study of the effect of Ca upon garnet-clinopyroxene Fe–Mg exchange equilibria. *Contributions to Mineralogy and Petrology*, **71**, 12–22.
- FAGERENG, Å. & SIBSON, R. H. 2010. Melange rheology and seismic style. *Geology*, **38**, 751–754.
- FOSTER, A. N. & JACKSON, J. A. 1998. Source parameters of large African earthquakes: implications for crustal rheology and regional kinematics. *Geophysical Journal International*, **134**, 422–448.
- GRAHAM, C. M. & POWELL, R. 1984. A garnet-hornblende geothermometer: calibration, testing, and application to the Pelona schist, southern California. *Journal of Metamorphic Geology*, **2**, 13–31.
- GRIFFIN, W. L., TAYLOR, P. N. ET AL. 1978. Archean and Proterozoic crustal evolution of Lofoten-Vesterålen, north Norway. *Journal of the Geological Society, London*, **135**, 629–647.
- HAMES, W. E. & ANDRESEN, A. 1996. Timing of orogeny and extension in the continental shelf of north-central Norway as indicated by laser  $^{40}\text{Ar}/^{39}\text{Ar}$  muscovite dating. *Geology*, **24**, 1005–1008.

- HEIER, K. S. 1960. Petrology and geochemistry of high-grade metamorphic and igneous rocks on Langøy, northern Norway. *Norges Geologiske Undersøkelse*, **207**, 1–246.
- HINZE, W. J., BRAILE, L. W., KELLER, G. R. & LIDIAK, E. G. 1988. Models for mid-continent tectonism: an update. *Reviews in Geophysics*, **26**, 699–717.
- HOBBS, B. E., ORD, A. & TEYSSIER, C. 1986. Earthquakes in the ductile regime? *Pure and Applied Geophysics*, **124**, 309–336.
- HOBBS, B. E., TANAKA, H. & IIO, Y. 2002. Acceleration of slip motion in deep extensions of seismogenic faults in and below the seismogenic region. *Earth Planets Space*, **54**, 1195–1205.
- HODGES, K. V., BARTLEY, J. M. & BURCHFIEL, B. C. 1982. Structural evolution of an A-type subduction zone, Lofoten Rombak area, northern Scandinavian Caledonides. *Tectonics*, **1**, 441–462.
- IIO, Y. & KOBAYASHI, Y. 2002. A physical understanding of large intraplate earthquakes. *Earth Planets Space*, **54**, 1001–1004.
- IIO, Y. & KOBAYASHI, Y. 2003. Is the plastic flow uniformly distributed below the seismogenic region? *Tectonophysics*, **364**, 443–453.
- IIO, Y., KOBAYASHI, Y. & TADA, T. 2002. Large earthquakes initiate by the acceleration of slips on the downward extensions of seismogenic faults. *Earth and Planetary Science Letters*, **202**, 337–343.
- JACKSON, J. A. 1987. Active normal faulting and crustal extension. In: COWARD, M. P., DEWEY, J. F. & HANCOCK, P. L. (eds) *Continental Extensional Tectonics*. Geological Society, London, Special Publications, **28**, 3–17.
- JACKSON, J. A. & WHITE, N. J. 1989. Normal faulting in the upper continental crust: observations from regions of active extension. *Journal of Structural Geology*, **11**, 15–36.
- JOHN, B. E. 1987. Geometry and evolution of a mid-crustal extensional fault system: Chemehuevi Mountains, southeastern California. In: COWARD, M. P., DEWEY, J. F. & HANCOCK, P. L. (eds) *Continental Extensional Tectonics*. Geological Society, London, Special Publications, **28**, 313–335.
- JOHN, T., MEDVEDEV, S., RÜPKE, L. H., ANDERSEN, T. B., PODLADCHIKOV, Y. Y. & AUSTREIM, H. 2009. Generation of intermediate-depth earthquakes by self-localizing thermal runaway. *Nature Geoscience*, **2**, 137–140, doi: 10.1038/NGEO419.
- KLEIN, A. C., STELTENPOHL, M. G., HAMES, W. G. & ANDRESEN, A. 1999. Ductile and brittle extension in the southern Lofoten archipelago, north Norway: implications for differences in tectonic style along an ancient collisional margin. *American Journal of Science*, **299**, 69–89.
- KOHN, M. J. & SPEAR, F. S. 1990. Two new geobarometers for garnet amphibolites, with applications to southeastern Vermont. *American Mineralogist*, **75**, 89–96.
- LIN, A., MARUYAMA, T., AARON, S., MICHIBAYASHI, K., CAMACHO, A. & KANO, K. 2005. Propagation of seismic slip from the brittle to ductile crust: evidence from pseudotachylite of the Woodroffe thrust, central Australia. *Tectonophysics*, **402**, 21–35.
- LOSETH, H. & TVETEN, E. 1996. Post-Caledonian structural evolution of the Lofoten and Vesterålen offshore and onshore areas. *Norsk Geologisk Tidsskrift*, **76**, 215–230.
- MAGER, S. 2006. *The late- to post-caledonian extensional history of northwest Hinnoy, North Norway*. MS thesis, Auburn University, Auburn, AL.
- MARKL, G. 1998. The Eidsfjord anorthosite, Vesterålen, Norway: field observations and geochemical data. *Norsk Geologisk Undersøkelses Bulletin*, **434**, 53–75.
- MOECHER, D. P. & STELTENPOHL, M. G. 2009. Direct calculation of rupture depth for an exhumed paleoseismic fault from mylonitic pseudotachylite. *Geology*, **37**, 999–1002.
- NYBLADE, A. A. & LANGSTON, C. A. 1995. East African earthquakes below 20 km depth and their implications for crustal structure. *Geophysical Journal International*, **121**, 49–62.
- OSMUNDSEN, P. T. & EBING, J. 2008. Styles of extension offshore mid-Norway and implications for mechanisms of crustal thinning at passive margins. *Tectonics*, **27**, TC6016, doi: 10.1029/2007TC002242.
- OSMUNDSEN, P. T., SOMMARUGA, A., SKILBREI, J. R. & OLESEN, O. 2002. Deep structure of the Mid Norway rifted margin. *Norwegian Journal of Geology*, **82**, 205–224.
- PLATTNER, U., MARKL, G. & SHERLOCK, S. 2003. Chemical heterogeneities of Caledonian (?) pseudotachylites in the Eidsfjord anorthosite, north Norway. *Contributions to Mineralogy and Petrology*, **145**, 316–338.
- REGENAUER-LIEB, K. & YUEN, D. A. 2003. Modeling shear zones in geological and planetary sciences: solid- and fluid-thermal-mechanical approaches. *Earth-Science Reviews*, **63**, 295–349.
- REGENAUER-LIEB, K., ROSENBAUM, G. & WEINBERG, R. F. 2008. Strain localization and weakening of the lithosphere during extension. *Tectonophysics*, **458**, 96–104.
- REGENAUER-LIEB, K., WEINBERG, R. F. & ROSENBAUM, G. 2006. The effect of energy feedbacks on continental strength. *Nature*, **442**, 67–70.
- SCHOLZ, C. H. 1988. The brittle–plastic transition and the depth of seismic faulting. *Geologische Rundschau*, **77**, 319–328.
- SCHOLZ, C. H. 2002. *The Mechanics of Earthquakes and Faulting*. Cambridge University Press, Cambridge.
- SIBSON, R. H. 1975. Generation of pseudotachylite by ancient seismic faulting. *Geophysical Journal of the Royal Astronomical Society*, **43**, 775–794.
- SIBSON, R. H. 1980. Transient discontinuities in ductile shear zones. *Journal of Structural Geology*, **2**, 165–171.
- SIBSON, R. H. 1982. Fault zone models, heat flow, and the depth distribution of earthquakes in the continental crust of the United States. *Bulletin of the Seismological Society of America*, **72**, 151–163.
- SIBSON, R. H. 1984. Roughness at the base of the seismogenic zone: contributing factors. *Journal of Geophysical Research*, **89**, 5791–5799.
- SIBSON, R. H. & TOY, V. G. 2006. The habitat of fault-generated pseudotachylite: Presence v. absence of friction-melt. In: ABERCROMBIE, R., McGARR, A., DI TORO, G. & KANAMORI, H. (eds) *Earthquakes: Radiated Energy and the Physics of Faulting*. American Geophysical Union, Geophysical Monograph, **170**, 153–166.

- STELTENPOHL, M. G., HAMES, W. E. & ANDRESEN, A. 2004. The Silurian to Permian history of a metamorphic core complex in Lofoten, northern Scandinavian Caledonides. *Tectonics*, **23**, 1–23, doi: 10.1029/2003TC001522.
- STELTENPOHL, M. G., KASSOS, G. & ANDRESEN, A. 2006. Retrograded eclogite-facies pseudotachylites as deep-crustal paleoseismic faults within continental basement of Lofoten, north Norway. *Geosphere*, **2**, 61–72.
- STELTENPOHL, M. G., MOECHER, D., ANDRESEN, A., BALL, J., MAGER, S. & HAMES, W. E. 2011. The Eidsfjord shearzone, Lofoten-Vesterålen, north Norway: An Early Devonian paleoseismogenic low-angle normal fault. *Journal of Structural Geology*, **33**, 1023–1043.
- SWANSON, M. T. 2006. Pseudotachylite-bearing strike-slip faults in mylonitic host rocks, Fort Foster brittle zone, Kittery, Maine. In: ABERCROMBIE, R., McGARR, A., DI TORO, G. & KANAMORI, H. (eds) *Earthquakes: Radiated Energy and the Physics of Faulting*. American Geophysical Union, Geophysical Monograph, **170**, 167–179.
- SYKES, L. R. 1978. Intraplate seismicity, reactivation of preexisting zones of weakness, alkaline magmatism, and other tectonism postdating continental fragmentation. *Reviews in Geophysics*, **16**, 621–688.
- TULL, J. F. 1978. *Geology and Structure of Vestvågøy, Lofoten, North Norway*. Norges Geologiske Undersøkelse, **42**.
- VOLL, G. 1976. Recrystallization of quartz, biotite, and feldspars from Erstfeld in the Levantina nappe, Swiss Alps, and geological implications. *Schweizerische Mineralogische und Petrographische Mitteilungen*, **56**, 641–647.
- WALSH, E. O., HACKER, B. R., GANS, P. B., GROVE, M. & GEHRELS, G. 2007. Protolith ages and exhumation histories of (ultra)high-pressure rocks across the Western Gneiss Region, Norway. *Geological Society of America Bulletin*, **119**, 289–301.
- WERNICKE, B. 1995. Low-angle normal faults and seismicity: a review. *Journal of Geophysical Research*, **100**, 20159–20174.
- ZOBACK, M. L. 1992. Stress field constraints on intraplate seismicity in eastern North America. *Journal of Geophysical Research*, **97**, 11761–11782.

# Mid-crustal controls on episodic stress-field rotation around major reverse, normal and strike-slip faults

JENS-ALEXANDER NÜCHTER<sup>1</sup>\* & SUSAN ELLIS<sup>2</sup>

<sup>1</sup>*Institut für Geologie, Mineralogie und Geophysik, Ruhr-Universität Bochum,  
Universitätsstraße 150, 44801 Bochum, Germany*

<sup>2</sup>*GNS Science, 1 Fairway Drive, Avalon, PO Box 30368, Lower Hutt, New Zealand*

\*Corresponding author (e-mail: [jens.nuechter@rub.de](mailto:jens.nuechter@rub.de))

**Abstract:** Numerical models are used to investigate the geometry of coseismic stress-field perturbation in the crust surrounding a reverse fault, a normal fault and a strike-slip fault. The results predict a coseismic stress drop in the upper crust and loading to high stress below the brittle–ductile transition (BDT) due to the taper-off in fault slip. Coseismic stress deflections occur for each fault type as a result of the coseismic stress redistribution and is at a maximum in the middle crust where fault slip tapers-off. The zone of high-stress deflection extends downwards to the base of the crust. During the post-seismic interval, the stress-field geometry recovers towards the pre-earthquake stress state, but simple stress-field geometries cannot be re-established. The numerical results indicate that: (1) stress deflection due to slip taper-off below the BDT is important for the stress perturbation throughout the crust; (2) predictions for coseismic stress deflection exclusively based on the fault-parallel shear-stress drop ratio systematically underestimate stress deflection in the entire crust; (3) stress rotation is persistent throughout the crust in seismically active regions; and (4) the geometry of secondary faults is expected to be affected by the perturbed stress field.

Quantifying the interaction between faults and regional tectonic stresses is critical to the reconstruction of ancient tectonic regimes from geological data and the assessment of hazard from fault reactivation. Compilations of fault geometry have been compared with predictions from simple fault mechanics in order to constrain fault properties and their relationship to regional stresses (e.g. Sibson & Xie 1998; Collettini & Sibson 2001; Lisle *et al.* 2006; Célérier 2008). Such regional compilations reveal intriguing discrepancies between theory and nature; for example, in terms of optimal dip of faults compared to predictions from simple Andersonian fault mechanics (Anderson 1905, 1951). In particular, fault mechanics theory predicts that once the fault is severely misoriented to the regional stress field, ‘lockup’ will occur and the fault will cease to move (Byerlee 1978; Sibson 1985). Discrepancies between theory and nature may result from the finite rotation and deformation of originally optimally oriented faults; the weakening of faults by a local increase in pore fluid pressure; and/or the evolution in rheology and stresses of the fault and surrounding rocks (e.g. Rice 1992; Lockner & Byerlee 1993; Collettini & Sibson 2001; Faulkner *et al.* 2006; Healy 2008, 2009; Fagereng *et al.* 2010). Healy *et al.* (2006) proposed that juvenile faults grow with an orientation diverging

from Anderson’s predictions owing to the elastic interaction between tensile microfractures during their coalescence. Stresses may be deflected on a regional scale by weak low-angle decoupling zones in the middle and lower crust (Lister & Davis 1989; Melosh 1990; Westaway 1999), and transient thermal disequilibria in the lower crust (Westaway 2005). On a local scale, stress refraction may result from zones of high pore fluid pressure (Bradshaw & Zoback 1988), and from intrusive bodies (Parsons & Thompson 1993). The relative influence of these factors will depend on the particular tectonic setting and evolution of a fault system, and thus we may expect a wide range in fault dips compared to the simple mechanical predictions.

In this paper, we focus on the complex interaction between the fault and changes in the regional or local stress regime over time, and estimate the resulting departure of measured fault dips from predictions based on the assumption of the presence of a uniform stress field during faulting. Stress changes around faults can occur gradually as a result of the reorientation of regional tectonic forcing and/or topographical loading (e.g. Heidbach *et al.* 2008); this will depend strongly on local tectonics (e.g. Fitzenz & Miller 2004). More generally, episodic stress perturbations are expected in regions close to a seismically active

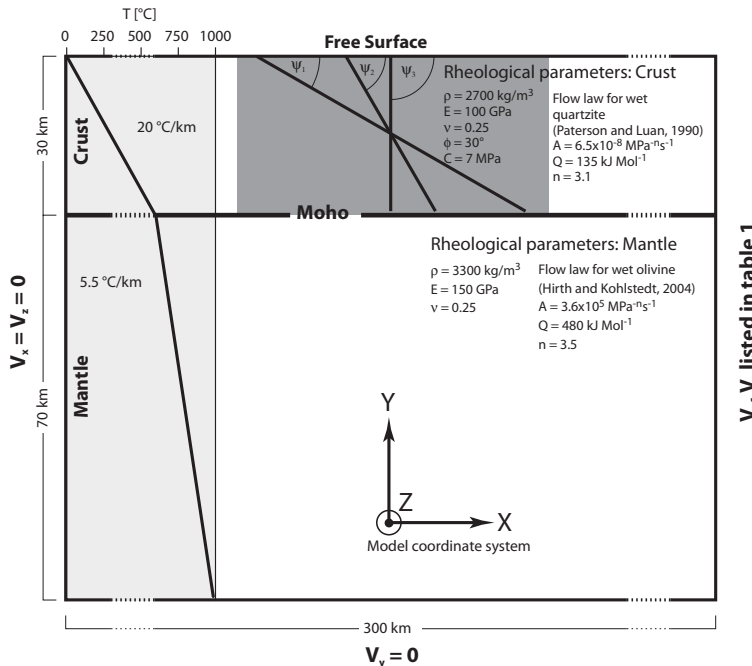
fault (e.g. Reid 1910; Rudnicki 1979; Sibson 1994; Yin & Rogers 1995; Küster & Stöckhert 1999; Trepmann & Stöckhert 2001; Nüchter & Stöckhert 2008). Coseismic slip can deflect the stress field in a wide crustal region surrounding the fault (i.e. Michael 1987; Hauksson & Jones 1988; Michael *et al.* 1990; Hauksson 1994; King *et al.* 1994; Yin & Rogers 1995; Hardebeck & Hauksson 2001; Healy *et al.* 2004), and these stress changes only partly recover during the subsequent post-seismic period (e.g. Nüchter & Ellis 2010). To-date, most analyses of such transient stress cycles have focused on coseismic stress changes around strike-slip faults and have only considered stress changes in the upper crust. Here, we use numerical models to examine the ability of transient slip along major faults to perturb regional stress directions and magnitudes. Our analysis includes

consideration of the change in rheology with depth and the commensurate tapering-off in fault slip near the brittle–ductile transition. We compare the orientations and magnitudes of coseismic and post-seismic stress perturbations for reverse, normal and strike-slip faults. We illustrate that significant stress rotations can occur in a large rock volume surrounding the fault, and that these rotations are strongly influenced by the taper-off in slip near the brittle–ductile transition.

## Numerical experiments

### Model set-up

Figure 1 outlines the simple model set-up used to test episodic stress cycling around a fault. All symbols are explained in Table 1. The set-up is



V<sub>x</sub>, V<sub>z</sub> listed in table 1

**Fig. 1.** The set-up of the numerical model using *Abaqus*/Standard finite element software. A 100 km-thick cross-section is used to represent the crust and mantle lithosphere, where axisymmetric elements with twist allow both in-plane and out-of-plane (transcurrent) motion. Kinematic boundary conditions are applied to represent: (1) compressional; (2) extensional; and (3) strike-slip tectonic settings. The kinematic boundary condition at the sides of the model does not change with depth. At the base of the model, frictionless slip is assumed in the horizontal direction. The rheologies of the crust and the mantle are modelled by a combination of elastic, frictional and ductile rheology. Ductile rheology is described by the parameters corresponding to extrapolations from laboratory tests on: (1) wet quartzite in the crust (Paterson & Luan 1990); and (2) wet olivine in the mantle (Hirth & Kohlstedt 2004). The profile to the left shows the increase of temperature with depth. The faults are represented by a contact surface down to 29.5 km depth, with a prescribed coefficient of friction,  $\mu$ , that varies from 0.12 (stress build-up phase and seismic phase) to 1.0 (interseismic, locked phase), which is when it is essentially locked. Initial fault dip is prescribed according to Andersonian predictions as  $\psi_1 = 30^\circ$  (reverse fault),  $\psi_2 = 60^\circ$  (normal fault) and  $\psi_3 = 90^\circ$  (strike-slip fault). The dark-grey square represents the analysed section of the crust.

**Table 1.** Symbols used in the text, kinematic boundary conditions applied to the models (Fig. 1) and sign convention

Symbol	Explanation
<i>Rheological parameters</i>	
$E, v$	Young's modulus; Poisson's ratio
$A, Q, R, n$	Pre-exponential constant, activation energy, gas constant, stress exponent
$\dot{\varepsilon}$	Strain rate
$C, \phi, \mu$	Cohesion, angle of internal friction, friction coefficient
$T$	Temperature
$\psi$	Fault dip angle
<i>Stresses</i>	
$\sigma_{xx}, \sigma_{yy}, \sigma_{zz}$	Normal components of cartesian stress tensor
$\sigma_{xy}, \sigma_{xz}, \sigma_{yz}$	Shear components of cartesian stress tensor
$\sigma_1, \sigma_2, \sigma_3$	Maximum, intermediate and minimum compressive stresses
$\sigma_d, \tau_f$	Differential stress ( $\sigma_d = \sigma_1 - \sigma_3$ ), fault parallel shear stress
$\Delta$	Prefix to indicate coseismic stress change
$\Delta\tau_f/\tau_f$	Fault-parallel shear-stress drop ratio (Yin & Rogers 1995)
<i>Kinematic boundary conditions applied to the models (Fig. 1)</i>	
Normal fault	$V_x = 4.5 \text{ cm year}^{-1}, V_z = 0$
Reverse fault	$V_x = -4.5 \text{ cm year}^{-1}, V_z = 0$
Strike slip fault	$V_z = 4.5 \text{ cm year}^{-1}, V_x = 0$
<i>Sign convention</i>	
Stresses	Compressive stresses are denoted by positive values
Rotation	Rotation in clockwise direction denoted by positive values
Stress drop	Stress drops are denoted by negative values (we acknowledge that it is commonplace to denote coseismic fault-parallel shear-stress drops by positive values but we do not adopt this convention)

similar to that used in Ellis & Stöckhert (2004a, b), Ellis *et al.* (2006) and Nüchter & Ellis (2010). The numerical models consists of a 300 km-wide and 30 km-thick crust underlain by a 70 km-thick mantle section. A linear geothermal gradient of  $20^\circ\text{C km}^{-1}$  in the crust and of  $5.5^\circ\text{C km}^{-1}$  in the mantle is prescribed. The crustal section contains a fault represented by a contact surface that extends to a depth of 30 km with a dip,  $\psi$ , dependent on the investigated tectonic regime. For the reverse-fault and normal-fault models, we assume two-dimensional (2D) geometry and stress state, so that the intermediate principal stress is assumed to be the out-of-plane component, and equal to the arithmetic mean of maximum and minimum principal compressive stresses,  $\sigma_1$  and  $\sigma_3$  (e.g. Lisle *et al.* 2006). For the strike-slip case, a 2D section across a vertical strike-slip fault is considered assuming no variations along-strike; that is, where out-of-plane velocity derivatives in  $x$  and  $y$  are permitted but not in the  $z$  direction; in this case,  $\sigma_1$  will be oriented at an angle to the 2D plane.

We use a combination of elastic, frictional and ductile rheology to describe the mechanical behaviour of the model crust and upper mantle (Fig. 1). In the brittle upper crust, the yield strength is

described by the Mohr–Coulomb criterion for optimally oriented slip:

$$\frac{\sigma_1 - \sigma_3}{2} = (P - P_f) \cdot \sin(\phi) + C \cdot \cos(\phi). \quad (1)$$

Where the temperature is sufficiently high, thermally activated creep relieves stresses to below the frictional yield. In the models, the transition from the brittle to the ductile regime is calculated to occur when the predicted creep stress is lower than the frictional yield stress. In the ductile region, maximum shear stress depends on temperature and strain rate:

$$\tau = G \left( \frac{\dot{\varepsilon}}{A} \right)^{1/n} e^{Q/(nRT)}. \quad (2)$$

The parameters describing thermally activated creep in the crust and the mantle correspond to values derived from laboratory creep experiments on wet quartzite (Paterson & Luan 1990) and wet olivine (Hirth & Kohlstedt 2004), respectively (Fig. 1). In the case of the dip-slip fault experiments, the geometric factor  $G$  is necessary for conversion

from triaxial creep laboratory data to shear strain (Ranalli 1987):

$$G = 3^{-(n+1)/2n} \cdot 2^{(1-n)/n}. \quad (3)$$

Throughout the experiments, the models are loaded by gravity and appropriate kinematic boundary conditions to simulate the respective tectonic regime (Fig. 1, Table 1). Prior to modelling seismic cycles we prescribe a 20 ka interval during which stresses are allowed to build up in two steps. During the first 10 ka the fault remains locked, and differential stress increases until the frictional yield in the upper crust is reached or thermally activated creep becomes active below the brittle–ductile transition (BDT). At the end of this step, all stresses are in steady state. Then, the fault is released for 10 ka to simulate the gradual ‘spin-up’ of the stress field, as previously described by Ellis & Stöckhert (2004a, b), Ellis *et al.* (2006), Hetland & Hager (2006), DiCaprio *et al.* (2008) and Nüchter & Ellis (2010). Afterwards, we run a series of model seismic cycles to simulate the associated stress perturbations. The depth to which the fault slips is self-determined by the contact algorithm in the model according to ambient stresses surrounding it; that is, the prescribed contact surface extends much deeper than the depth to which slip occurs. This is because ductile creeping below the mid-crust relieves stresses faster than they build up by the kinematic boundary conditions, so that low shear stress is available below the BDT to drive fault slip. This set-up allows the code to self-determine the depth of the transition from a frictional to a ductile rheological regime as a function of the prescribed temperature and the strain field.

Several important features of real fault cycles are neglected or simplified in the model, including: (1) the neglect of dynamic stress perturbations from the propagation of seismic waves, as we are considering much longer timescales than the seconds to minutes that a fault rupture usually takes; (2) no small-scale heterogeneities in fault geometry and strength; (3) no variations in fluid pressure gradients. (4) The power-law rheology used to model thermally activated creep below the BDT has been calibrated for steady-state deformation in the regime of dislocation creep (Paterson & Luan 1990). Such rheologies are frequently used in seismic cycle modelling, although the relevance of such creep laws is questionable for describing fast and, particularly, non-steady-state post-seismic creep. Furthermore, the evolution of microfabrics related to post-seismic creep preserved in metamorphic rocks indicates a shift in the deformation

regime from initially low-temperature plasticity when stresses are high towards dislocation creep, followed by static grain growth when stresses are relaxed to a large extent (Trepmann & Stöckhert 2003). (5) Note, however, that our chosen coefficient of fault friction is low compared to most estimates from intact rocks (e.g. Brace & Kohlstedt 1980); we are implicitly including assumptions about weakened fault rheology from elevated pore pressure, and the development of clay minerals and gouge. An additional simplification concerns our choice of fault dip according to the predictions from Andersonian mechanics, although, as we have noted in the first section of this paper, real faults do not always display simple geometries and dips. Our argument is that by considering stress perturbations, even for faults dipping at optimum predicted angles, we can gauge whether stress rotations around the fault are likely to cause any additional nearby faults to develop at different dips.

#### *Stress perturbations during the coseismic interval*

Following the set-up phase described in the previous subsection, the fault is locked for 1000 years (1 ka) to simulate a long interseismic period. It is then released to a low coefficient of friction of  $\mu = 0.12$  for a short interval that allows slip along it, which represents the static effects of an earthquake. In Figure 2, a summary of the coseismic changes in differential stress magnitudes (a–c) and orientations (d–g) is presented for each assumed mechanism. Plots of the coseismic changes in the Cartesian stress components v. depth along the faults in the hanging walls and the footwalls are presented in Figure 3.

As expected, a differential stress drop (Fig. 2a–c) occurs in the upper crust around each fault as elastic strain related to fault slip relieves some of the regional stress that has been built up by application of steady velocities at the boundaries. The geometry of stress drop depends on the fault mechanism and is only symmetric for the strike-slip fault. At shallow depths, the stress change is complicated by interaction with the free surface. In the experiments, slip tapers-off over a depth interval between approximately 11–15 (strike-slip and normal faults) and 8–16 km (reverse fault) (Fig. 4a) in the middle crust. The related deformation of the surrounding crust leads to a differential stress increase of up to 60 MPa near the lower fault termination (Fig. 2a–c) (Ellis & Stöckhert 2004a; Ellis *et al.* 2006; Nüchter & Ellis 2010). Note that the comparison with similar models for compressive (Ellis & Stöckhert 2004a) and

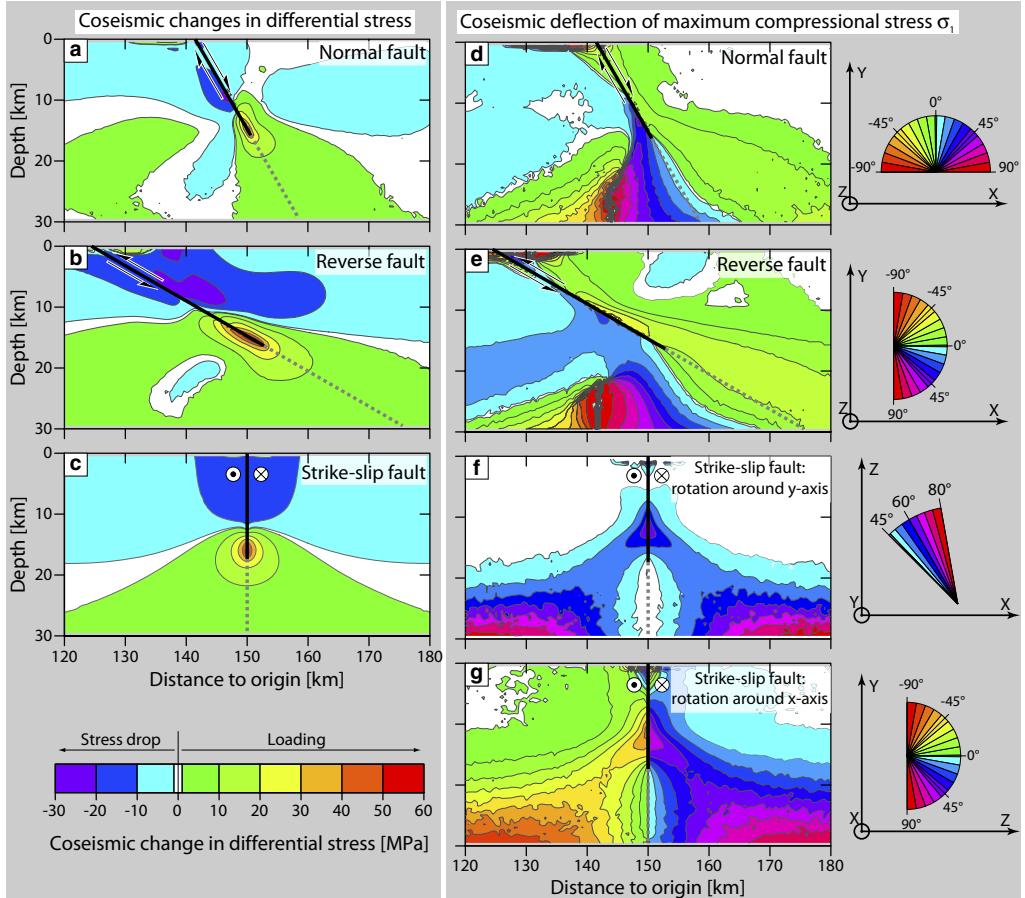


**Fig. 2.** Results of numerical models for coseismic stress perturbations. Panels (a) & (d) normal fault; (b) & (e) reverse fault; and (c), (f) & (g) strike-slip fault. (a)–(c) Coseismic change in differential stress. (d)–(g) Deflection of the maximum principal stress  $\sigma_1$  from the predictions of Anderson's theory of faulting. (d) & (e) Results for rotation around the  $z$ -axis (out-of-plane horizontal axis) in dip-slip fault experiments. (f) & (g) Results for rotation around the  $y$ -axis (vertical axis) and the  $x$ -axis (in-plane horizontal axis) in the strike-slip fault experiment. The model co-ordinate system is depicted in Figure 1. Bold solid black lines represent the part of the contact surfaces with coseismic slip. Dashed grey lines indicate the extent of the contact surfaces below the slip termination depth (Fig. 4a).

extensional tectonic settings (Nüchter & Ellis 2010) shows that the magnitude of coseismic loading scales with the coseismic drop in fault friction.

The right-hand panels of Figure 2d–g illustrate how coseismic stress changes perturb the orientation of the principal stresses near the fault. In each case, the local angle of the principal compressive stress is plotted with colour contours representing the departure from the expected angles predicted by Anderson's theory of faulting (white colour denote regions where Andersonian stress orientations prevail). Figure 2d, e show how the predicted principal stress orientations are rotated away and towards the fault normal in the normal fault model and the thrust fault model in the

upper crust, respectively. The senses of the rotation agree with the predictions of Yin & Rogers (1995). By far the biggest stress rotation occurs at the lower tip of the fault on the footwall side. Nüchter & Ellis (2010) showed how principal stress rotations at the lower tip of normal faults result from fault-parallel compression and extension in the hanging wall and the footwall, respectively. In the case of the strike-slip fault,  $\sigma_1$  rotates around both the  $y$ - (Fig. 2f) and the  $x$ -axis (Fig. 2g) (i.e. in 3D). Rotation around the  $y$ -axis is the result of elastic deformation related to coseismic stress release, and the associated change in  $\sigma_{xz}$  (Fig. 3d). Stress rotation around the  $x$ -axis results from changes in  $\sigma_{yz}$  (Fig. 3d) related to the

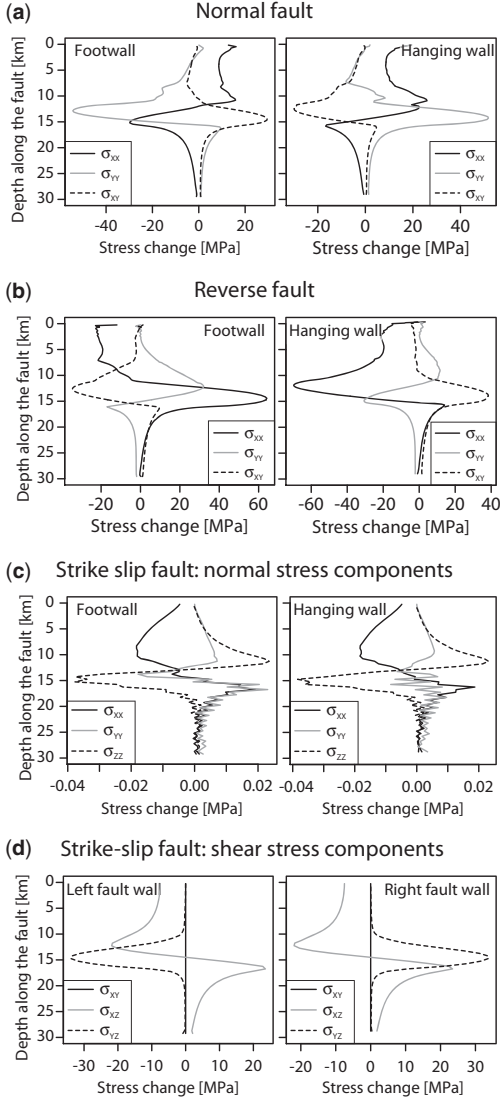


**Fig. 3.** Profiles of coseismic changes in Cartesian stress components along the contact surface with depth in the hanging walls and the footwalls. Stresses represent averages of the fault elements; that is, represent the stresses at approximately 150 m distance to the fault. Results for (a) normal fault, (b) reverse fault and (c) & (d) strike-slip fault. (c) Normal-stress components & (d) shear-stress components. The model co-ordinate system is depicted in Figure 1.

increase in the simple-shear deformation along near-horizontal planes with depth due to the taper-off in fault slip. Coseismic stress rotation around the  $y$ -axis is predicted by Yin & Rogers (1995), while rotation around the  $x$ -axis is not, as their

analysis does not include stress changes related to gradients in fault slip. In all experiments, the most significant stress rotations occur close to the fault termination (Fig. 2d–g). Coseismic stress deflection from the predictions of Anderson's theory of faulting is the result of changes in the Cartesian shear-stress components (Fig. 3) due to elastic strain in the crust imposed by fault slip (Nüchter & Ellis 2010).

Yin & Rogers (1995) correlated the magnitude of coseismic stress deflection with the fault-parallel shear-stress drop ratio  $\Delta\tau_f/\tau_f$  (here  $\tau_f$  denotes the pre-earthquake fault-parallel shear stress). The plots of  $\Delta\tau_f/\tau_f$  v. depth are roughly consistent for the three experiments (Fig. 4b). The downwards decrease in  $\Delta\tau_f/\tau_f$  at shallow depth shows that  $\Delta\tau_f$  is approximately constant in the upper crust, whereas the total fault-parallel shear stress,  $\tau_f$ , increases. Within the depth interval between 5 and 10 km,  $\Delta\tau_f$  roughly scales with the increase in  $\tau_f$  towards the base of the upper crust, and  $\Delta\tau_f/\tau_f$  has roughly constant values close to 0.5 (Fig. 4b). In the middle crust, where shear-stress drop gives way to coseismic loading,  $\Delta\tau_f/\tau_f$  drops to zero and becomes negative throughout the middle and lower crust (Fig. 4b). The downwards increase in  $\Delta\tau_f$  is consistent with observations of shear-stress drop distributions during the 1992  $M$  7.3 Landers, the 1994  $M$  6.9 Kobe and the 1994  $M$  6.7 Northridge earthquakes (Fletcher & McGarr 2006).

#### Stress recovery during the post-seismic interval

Following each coseismic interval, the faults are locked for a further 1000 years and the post-seismic stress recovery is analysed. Below the BDT, differential stress relaxes during an episode of post-seismic creep at initially high, but decreasing, strain rates (Fig. 5). Concomitantly, the upper crust containing the fault is gradually reloaded by far-field extension and by stress transfer from the lower crust due to post-seismic creep (Fig. 5) (Thatcher 1983; Huc *et al.* 1998; Kenner 2004; Lin & Freed 2004; Freed 2005; Freed *et al.* 2006; Nüchter & Ellis 2010). The related relaxation of the Cartesian shear-stress components causes rotation in principal stresses near the fault back towards their pre-earthquake configurations (Figs 6 & 7). However, even after 1000 years, stresses near the fault have not attained an Andersonian stress state (Figs 6 & 7). This illustrates how a fault perturbs regional stresses at all times, although the maximum deviation from simple theory is predicted during the coseismic period.

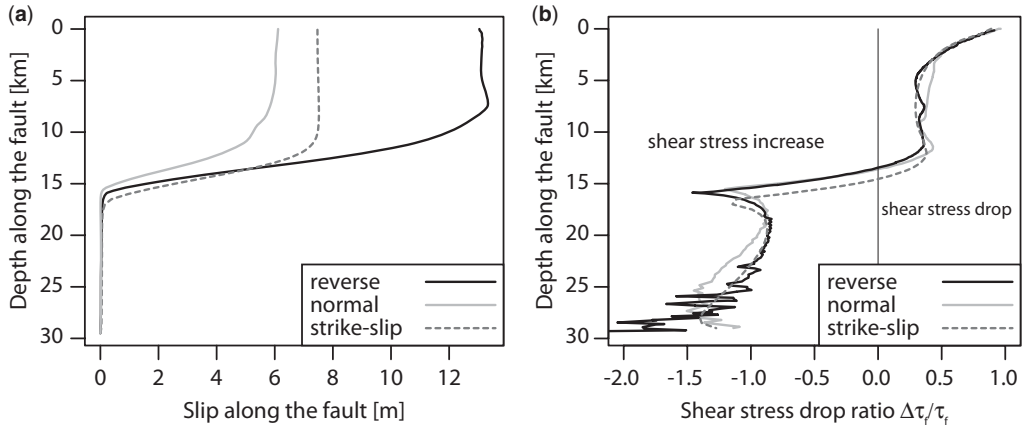


**Fig. 4.** (a) Slip along the contact surface as a function of depth in the normal fault, reverse fault and strike-slip fault experiment. (b) Shear stress ratio,  $\Delta\tau_f/\tau_f$ , in the normal fault, reverse fault and strike-slip fault experiments.

## Discussion

*Are stress rotations in the upper crust during the seismic cycle significant enough to perturb regional stress fields? Comparison to theoretical analysis of Yin & Rogers (1995) and to observations*

Yin & Rogers (1995) predicted stress rotations caused by a prescribed stress drop for reverse, normal and strike-slip faults using simple geometric analyses and assuming pressure-sensitive Coulomb yield relations between principal stress components. They showed that for a stress drop ratio of 0.5 (0.1) – and assuming that the fault was oriented optimally with respect to the regional stress field – rotations in principal stress axes of about  $+30^\circ$  ( $+3^\circ$ ) (reverse fault),  $-15^\circ$  ( $-3^\circ$ ) (normal fault) and  $0^\circ$  (strike-slip, assuming a stress ratio of 0.5) may be expected. Yin & Rogers (1995) denoted principal stress rotation towards and away from the fault normal by positive and negative signs, respectively. As we consider clockwise and anticlockwise rotations by positive and negative signs (Table 1), respectively, the stress deflections of  $-10^\circ$ ,  $-30^\circ$  and  $5^\circ$ , respectively, observed in the upper crusts of our models (Fig. 2d–g) are in qualitative agreement to the predictions of Yin & Rogers (1995). However, the comparison of our numerical results to the predictions of Yin & Rogers (1995) is complicated by the facts that: (1) the stress drop ratio is not constant in our models, but decreases from close to 1 (shallow crust) to 0 (mid-crust) (Fig. 4b); and (2) stress changes due to gradients in fault slip are considered in our models. According to Yin & Rogers (1995), a decrease in  $\Delta\tau_f/\tau_f$  with depth (Fig. 4b)

results in a decrease in the magnitude of stress deflection with depth. Significantly more stress deflection should prevail in the upper crust, where  $\Delta\tau_f/\tau_f$  ranges between 0.5 and 1 compared to the middle crust where  $\Delta\tau_f/\tau_f$  drops to 0 (Fig. 4b). However, the main observation from our models is that stress rotation increases with depth in all experiments and is highest (up to  $\pm 30^\circ$ – $50^\circ$  depending on the fault kinematics) in the mid-crust close to the lower fault termination (Fig. 2d–g); that is, in a depth interval not considered in the analysis of Yin & Rogers (1995). In this region, stress perturbation is predominantly controlled by deformation related to the tapering-off in fault slip (Ellis & Stöckhert 2004a, b; Nüchter & Ellis 2010), while the shear-stress drop ratio decays and becomes negative (Fig. 4b); that is, fault-parallel shear stress increases during the earthquake. These zones of high stress rotation extend downwards into the ductile lower crust (Fig. 2d–g). Here, pre-existing stresses are low, and small changes in stress may cause large rotations of the principal stresses. The resulting stress field is expected to affect the geometry of the creep strain field during the post-seismic period.

Yin & Rogers (1995) did not make any predictions concerning the horizontal width over which stresses would be perturbed by the fault. Experiments with models like those shown in Figure 2 but for different friction coefficients show that the stress perturbation width in the upper crust depends on the stress drop ratio. For the moderate stress drops modelled here, stresses are perturbed over horizontal length scales approximately equal to the total depth of the fault.

Many observational studies have tried to quantify whether rotations in principal stresses occur

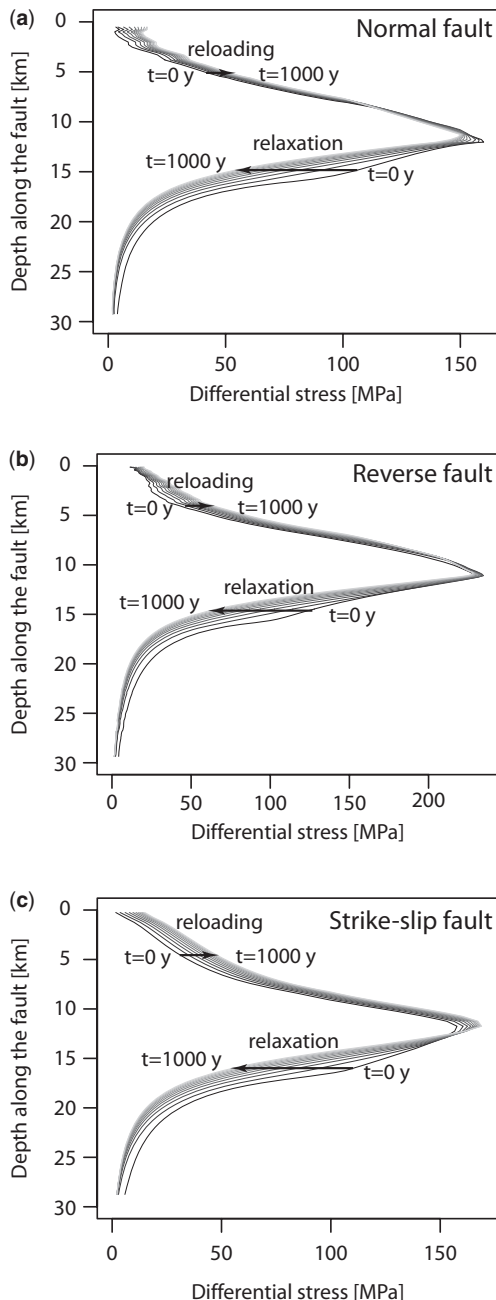


**Fig. 5.** Profiles of differential stress,  $\sigma_d$ , along the contact surface in the hanging wall immediately after the earthquake (black lines), and in 100 year steps during the post-seismic period (grey lines). Differential stress is calculated for the average of the fault elements; that is, represents the stress at approximately 150 m distance to the fault. Results for the (a) normal fault experiment, (b) reverse fault experiment and (c) strike-slip fault experiment.

during major earthquakes. Collettini & Trippetta (2007) analysed focal mechanisms of aftershocks following the Colfiorito (Italy) and ChiChi (Taiwan) earthquakes, and concluded that major stress rotations did not result from these events; that is, that aftershock slip planes were well orientated with respect to the predicted stress fields. This suggests that stress drop ratios were very small or that stress perturbations around the faults were localized – although the authors acknowledged that some ruptures were not optimally oriented, especially for the ChiChi earthquake. In contrast, other studies have suggested significant stress rotations following major earthquakes; for example, Bohnhoff *et al.* (2006) reported rotations in the angle of  $\sigma_1$  with respect to the North Anatolian Fault Zone of up to  $8^\circ$  following the 1999 Izmit earthquake (also based on aftershock focal mechanisms). Such comparisons are hampered by the facts that: (1) many faults have significant complexity in geometry and slip; and (2) inferences on the natural stress-field geometry that can be tested against the model predictions are only available in areas that are brought close to failure and are therefore more likely to fail seismically by aftershocks. According to our numerical experiments, the most significant stress rotations are predicted to occur in the mid-crust where stick-slip behaviour on seismic timescales gives way to slow after-slip and creep. Observations of stress changes following major earthquakes may therefore significantly underestimate stress rotations in the middle and lower crust. In the models shown here, slip extends all the way to the surface, but in nature slip often tapers off at shallow levels owing to the reduced strength of near-surface materials and/or topographical loading. If this is the case, significant stress rotations may also occur at shallow depths causing changes in near-surface fault dip and/or secondary shallow faults.

#### *Do different fault kinematics (reverse, normal, strike-slip) produce different amounts of stress rotation?*

In the case of dip-slip faults, Yin & Rogers (1995) predicted the same magnitude of stress deflection during normal and reverse fault earthquakes when the stress drop ratio is the same. However, in our numerical results, reverse faults seem to produce the most intense stress rotations (Fig. 2e), although the stress drop ratios are roughly consistent for all experiments (Fig. 4b). Comparison between Figure 2d and e shows that the highest differences in the magnitude of stress deflection between the dip-slip faults occurs at and below the base of the upper crust, and that the differences in stress

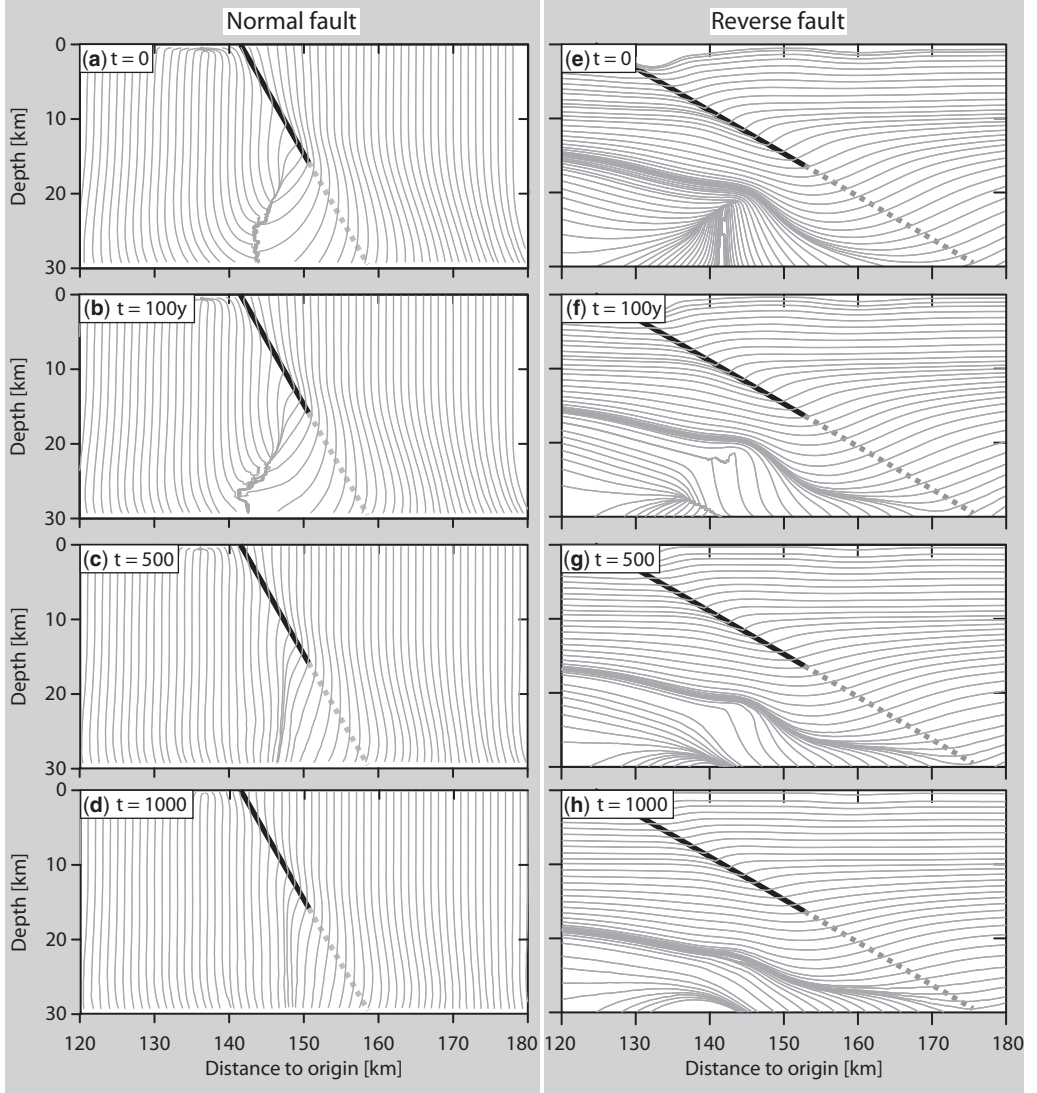


**Fig. 6.** Trajectories of the maximum principal stress,  $\sigma_1$ , indicate the residual stress deflection during the post-seismic period. (a)–(d) Normal fault experiment and (e)–(h) reverse fault experiment.  $\sigma_1$  trajectories: (a) & (e) immediately after the earthquake at  $t = 0$ ; (b) & (f) after 100 years; (c) & (g) after 500 years; and (d) & (h) after 1000 years. Tangled trajectories in the deep footwalls result from interpolation. Bold solid black lines represent the part of the contact surfaces with coseismic slip. Dashed grey lines indicate the extent of the contact surfaces below the slip termination depth (Fig. 4).

rotation decreases towards the surface. For the strike-slip fault, Yin & Rogers (1995) predicted no significant stress rotation for the stress ratio ( $\sigma_2 - \sigma_3$ )/( $\sigma_1 - \sigma_3$ ) of 0.5 that prevails throughout the model crust resulting from the axisymmetric assumptions made in our experiments. However, the results of our strike-slip fault experiment show that stress rotation also occurs throughout the

crust, though the magnitude of deflection is less compared to the dip-slip experiments (Fig. 2d–g). Rotation around the  $x$ -axis is not predicted by Yin & Rogers (1995) at all, but is persistent throughout the crust in our experiment (Panel 2g). Stress rotations near the lower end of the fault are still high for the strike-slip case (Fig. 2f, g) despite the fact that we modelled the fault as a 2D slice; that

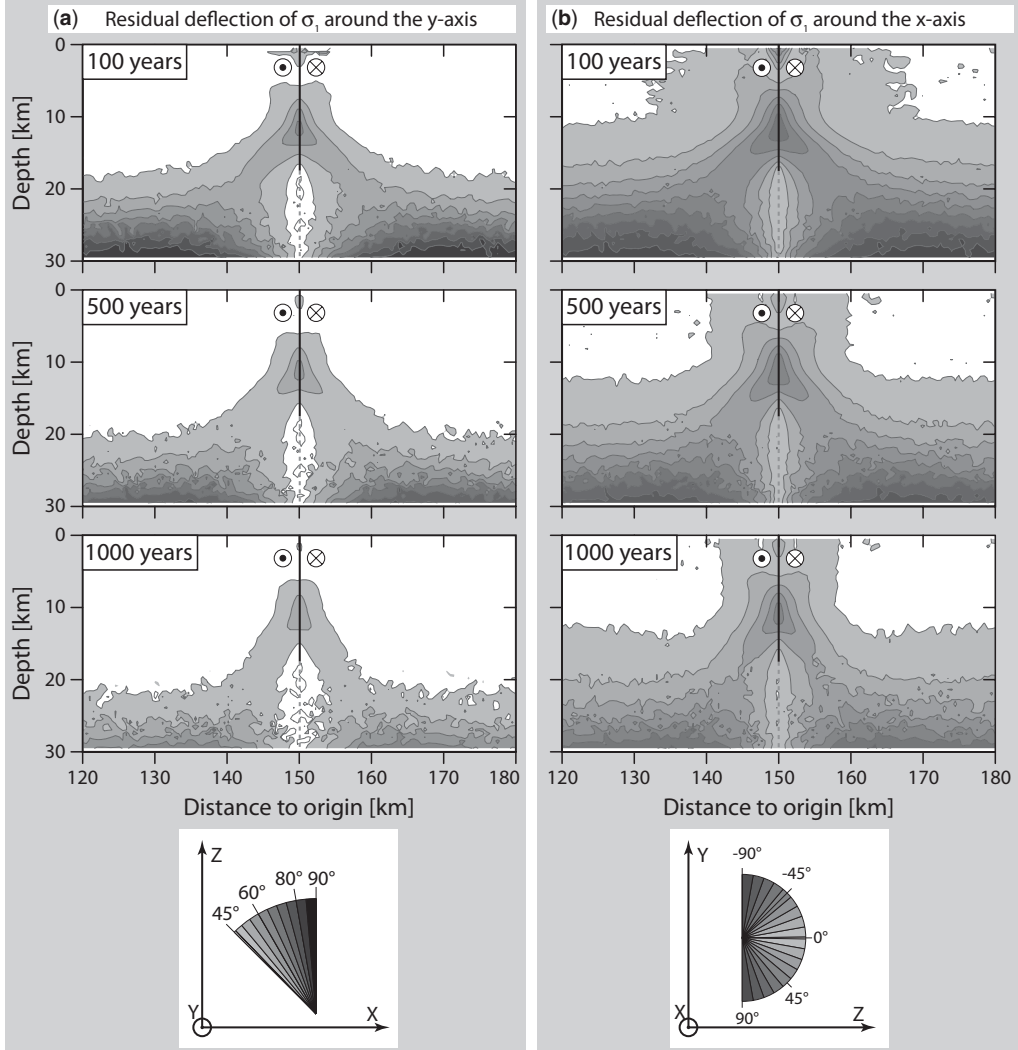


**Fig. 7.** Magnitude of the residual stress deflection in the strike-slip fault experiment 100, 500 and 1000 years after the earthquake step. Residual deflection of the maximum compressional stress component,  $\sigma_1$ : (a) around the y-axis (vertical axis); and (b) around the x-axis (in-plane horizontal axis). The model co-ordinate system is depicted in Figure 1. Bold solid black lines represent the part of the contact surfaces with coseismic slip. Dashed grey lines indicate the extent of the contact surfaces below the slip termination depth (Fig. 4).

is, the tapering-off in slip that would occur at the along-strike terminations of the fault was not considered.

The facts that we observe (1) an increase in the magnitude of stress deflection towards depth in all experiments (Fig. 2d–g) even though the stress drop ratios decrease (Fig. 4b); and (2) stress rotation around two orthogonal axes throughout the crust in the strike-slip experiments demonstrate the importance of slip tapering at depth for the

coseismic changes in the stress-field geometry throughout the crust. The model results imply that the importance of the stress-rotation mechanism proposed by Yin & Rogers (1995) decreases with depth. Instead, stress changes related to the slip tapering-off become the dominant mechanism that controls coseismic stress deflection at and below the base of the upper crust. If so, the termination in fault slip near the BDT is the predominant factor that controls the coseismic perturbation

within a depth range typical for focal depths of major earthquakes. In all experiments, the intensity of stress-field perturbation depends on depth and on the position relative to the fault, and, in the case of dip-slip faults, stress rotation differs in the footwall v. the hanging wall (Fig. 2d, e). The complexity of the coseismic stress field has to be taken into account when: (1) comparing aftershock focal mechanisms with predictions of stress rotation; and (2) plotting and interpreting maps displaying coseismic Coulomb stress changes restricted to a single depth level (e.g. King *et al.* 1994).

### *Stress rotations near weak strike-slip faults*

The maximum principal horizontal stress  $\sigma_H$  lies at high angles ( $68^\circ \pm 7^\circ$ : Hickman & Zoback 2004; Townend & Zoback 2004) or at intermediate angles ( $40^\circ$ – $60^\circ$ : Provost & Houston 2003;  $50^\circ \pm 22^\circ$ : Hardebeck & Michael 2004) to the strike of the San Andreas Fault (SAF) in central California. This has been taken as evidence that the SAF must have a low strength so that stress drop ratios are almost 1, although some other studies contradict this interpretation (e.g. Scholz 2000). High angles have also been observed in the  $\sigma_H$  orientations derived from seismology for the Marlborough Fault System (MFS), a series of dextral strike-slip faults located at the northern end of the Alpine Fault, New Zealand (Balfour *et al.* 2005). In comparison, in our strike-slip fault model, we predict only a modest change in the angle that  $\sigma_1$  makes to the fault in the upper crust (Fig. 2f). However, Yin & Rogers (1995) showed that, for a strike-slip fault, stress rotations depend not only on the stress drop ratio but also on the angle between the initial  $\sigma_1$  axis and the fault. For a stress ratio of 0.5 and a maximum principal stress initially oriented at  $45^\circ$  to the fault (as modelled here), the model of Yin & Rogers (1995) predicts no stress rotation at all in the upper crust. However, the SAF and MFS have regional upper-crustal stresses orientated at considerably higher angles to the faults, and in this case, for finite stress drop ratios Yin & Rogers (1995) predict that an earthquake will rotate  $\sigma_1$  towards the fault-normal direction.

Rotation of  $\sigma_1$  during an earthquake, combined with the non-Andersonian stress state resulting from perturbation associated with the fault, may cause  $\sigma_1$  to (in general) occur at a high angle to the fault in the upper crust. At mid-crustal depths, the results of our study additionally suggest that amplification of coseismic stress deflection along the SAF and the MFS due to slip taper-off at depth should be taken into consideration when addressing fault strength based on recent stress-field orientations.

### *Predictions for modification in the dip of faults developing near major faults*

We have examined stress changes around mature faults with prescribed fault geometries. However, it is instructive to consider what would happen if a fault was growing at its lower termination or was causing secondary faulting to develop. How would the extending segments of the fault dip, and how would this depend on the perturbation in the regional stress field caused by the (already-slipping) fault patches? To answer these questions fully, models of fault evolution are needed. As a first approximation, Figure 2d–g suggests that new fault segments would propagate into a perturbed non-Andersonian stress field. If the propagating fault segments follow the optimum Coulomb angle to  $\sigma_1$ , we would expect the development of significant deviations from simple fault geometries predicted by Anderson's theory of faulting (Anderson 1905, 1951). As  $\sigma_1$  is rotated anticlockwise in the hanging walls of both dip-slip faults (Fig. 2d, e) (as predicted by Mandl 1988), we expect any secondary antithetic faults to steepen as they approach the main fault. However, near the surface such faults should exhibit typical dips, as predicted from the regional stress field. Conversely, the anticlockwise deflection of the stress field at the lower tip of the reverse fault (Fig. 2e) implies that new fault segments should shallow in dip with depth. In the case of the normal fault, the fault terminates in a region where anticlockwise and clockwise stress-field rotation prevails in the hanging wall and the footwall. If new-formed fault segments develop in the footwall, a downwards steepening of the fault is expected. If fault propagation continues in the hanging wall, we would expect a similar decrease in the dip angle as predicted for the reverse fault.

The timing at which secondary faults develop could be important as regards the optimum dip angle at which they might form. For example, splay faults are most likely to propagate in close temporal association with slip along the primary fault, because it is at this stage that shear stresses are highest at the mid-crustal fault termination. The geometry of the new-formed fault segments is expected to be significantly affected by the perturbed stress field, and complex fault geometries may develop. Secondary antithetic faults that respond to the regional stress field will be suppressed during the immediate post-seismic phase after the major faults have slipped, as a stress shadow is present close to these faults. Such faults may start to reassert themselves near the main fault later in the interseismic period. At this stage the local stresses still exhibit a perturbation with respect to regional stresses, but not so great as those immediately

post-earthquake (Figs 6 & 7). Therefore, late-stage secondary faults are more likely to obey predictions from Andersonian mechanics. These results imply that dip-slip faults with a shallower dip angle than predicted by Anderson's theory of faulting should be more frequent than faults with higher dip angles. This prediction is consistent with the significant peak in global active normal fault dips occurring at  $45^\circ \pm 2.5^\circ$  found by Jackson & White (1989) and Collettini & Sibson (2001).

We caution that, in nature, fault orientations are unlikely to follow such simple predictions, because faults typically develop as a coalescence of many small fault segments, often with mode I or hybrid mechanisms (Reches & Dieterich 1983; Lockner *et al.* 1991; Healy *et al.* 2006; Blenkinsop 2008). In addition, a non-uniform 3D stress field favours the development of discontinuous, segmented slip surfaces (e.g. Mandl 1987); as we predict heterogeneous stress orientations near the fault, subsidiary faulting is likely to start out as many small segments with differing dips dependent on location.

#### *Preservation of stress-field perturbation effects in the geological record*

We predict maximum stress rotations associated with tapering-off in slip as a fault penetrates the mid-crust. The models do not distinguish between seismic and aseismic fault slip because we only model static stress changes. We expect that, in many cases, the lower region of the fault will slip at subseismic rupture velocities. As a result, the stress changes and stress rotations in this region may not be measured by seismology, but are most likely to be observed when the lower tips of ancient faults are exhumed at the surface. Since exhumation depends on the fault mechanism, the geological record of exhumed metamorphic rock should preferentially record stress cycles related to seismic activity around the lower tip of normal and reverse faults rather than strike-slip faults.

Evidence for cycles of coseismic loading to high differential stress followed by episodes of post-seismic relaxation by creep has been isolated from the geological record of metamorphic rocks exhumed in a compressional tectonic setting in the Sesia zone, European Alps (Trepmann & Stöckhert 2001, 2002, 2003), and in extensional tectonic settings in south Evia, Greece (Nüchter & Stöckhert 2007, 2008) and on Rugsundøya Island, Norway (Birtel & Stöckhert 2008). Based on the results of the present study, we predict that these rocks experienced post-seismic creep within an initially perturbed, but recovering, stress-field geometry. The results of the present experiments (Fig. 5) and previous numerical models (Ellis & Stöckhert 2004a)

show that post-seismic creep rate decays during the post-seismic interval owing to continuous stress relaxation. Therefore, we expect that most of the post-seismic creep strain recorded by metamorphic rocks is accumulated during a short interval in an early stage of the post-seismic period. During this interval, stress-field reorientation (Figs 6 & 7) is expected to be too low to leave a detectable imprint in the geological record of the metamorphic rocks.

#### **Conclusions**

We have used numerical models to compare the orientations and magnitudes of coseismic and post-seismic stress perturbations for normal, reverse and strike-slip fault kinematics. Significant stress rotations can occur in a large rock volume surrounding the fault, particularly for normal and reverse faults. Stress rotations are strongly influenced by the taper-off in slip near the brittle–ductile transition, which we find to be more significant than the stress rotations caused by changes in the fault shear stress predicted in earlier theoretical analyses (e.g. Yin & Rogers 1995). These results imply that enhanced information about the background stress level and the magnitude of coseismic stress perturbation at and below the BDT is required to make inferences about stress rotations at typical focal depth levels of major earthquakes. In the present study, we have shown that:

- the characteristics of stress deflection depend on the type of faulting;
- stress rotation is persistent throughout the crust in a large rock volume surrounding the fault;
- the magnitude of rotation strongly depends on the amount of slip, and the depth and distance to the fault;
- stress changes caused by the taper-off in slip in the mid-crust can influence changes in stress-field geometry up to shallow levels and downwards beneath the brittle–ductile transition;
- predictions for coseismic stress deflection exclusively based on the fault-parallel shear stress drop ratio systematically underestimate stress deflection in the entire crust;
- the geometry of secondary faults is expected to be affected by the perturbed stress field.

The present study is funded by the 'Deutsche Forschungsgemeinschaft', DFG to J. A. Nüchter and PGSF 'Geological Hazards and Society' contract C05X0804 to S. Ellis. This work benefits from discussions with B. Stöckhert, R. H. Sibson, and A. Freed. The constructive comments by D. Healy, O. Heidbach, V. G. Toy and A. Fagereng are gratefully acknowledged. We acknowledge use of the software package R, with which the stresses were calculated and plotted (R Development Core Team 2009).

## References

- ANDERSON, E. M. 1905. The dynamics of faulting. *Transactions of the Edinburgh Geological Society*, **8**, 387–402.
- ANDERSON, E. M. 1951. *The Dynamics of Faulting*. 2nd edn. Edinburgh, Oliver & Boyd.
- BALFOUR, N. J., SAVAGE, M. K. & TOWNSEND, J. 2005. Stress and crustal anisotropy in Marlborough, New Zealand: evidence for low fault strength and structure-controlled anisotropy. *Geophysics Journal International*, **163**, 1073–1086.
- BIRTEL, S. & STÖCKHERT, B. 2008. Quartz veins record earthquake-related brittle failure and short term ductile flow in the deep crust. *Tectonophysics*, **457**, 53–63.
- BLENKINSOP, T. G. 2008. Relationships between faults, extension fractures and veins, and stress. *Journal of Structural Geology*, **30**, 622–632.
- BOHNHOFF, M., GROSSER, H. & DRESEN, G. 2006. The 2004 release of the world stress map. *Geophysics Journal International*, **166**, 373–385.
- BRACE, W. F. & KOHLSTEDT, D. L. 1980. Limits on lithospheric stress imposed by laboratory experiments. *Journal of Geophysical Research*, **85**, 6248–6252.
- BRADSHAW, G. A. & ZOBACK, M. D. 1988. Listric normal faulting, stress refraction, and the state of stress in the Gulf Coast basin. *Geology*, **16**, 271–274.
- BYERLEE, J. D. 1978. Friction of rocks. *Pure and Applied Geophysics*, **116**, 615–626.
- CÉLÉTIER, B. 2008. Seeking Anderson's faulting in seismicity: a centennial celebration. *Reviews of Geophysics*, **46**, RG4001.
- COLLETTINI, C. & SIBSON, R. H. 2001. Normal faults, normal friction? *Geology*, **29**, 927–930.
- COLLETTINI, C. & TRIPPIETTA, F. 2007. A slip tendency analysis to test mechanical and structural control on aftershock rupture planes. *Earth and Planetary Science Letters*, **255**, 402–413.
- DiCAPRIO, C. J., SIMONS, M., KENNER, S. J. & WILLIAMS, C. A. 2008. Post-seismic reloading and temporal clustering on a single fault. *Geophysics Journal International*, **172**, 581–592.
- ELLIS, S. & STÖCKHERT, B. 2004a. Elevated stresses and creep rates beneath the brittle–ductile transition caused by seismic faulting in the upper crust. *Journal of Geophysical Research*, **109**, B05407, doi: 10.1029/2003JB002744.
- ELLIS, S. & STÖCKHERT, B. 2004b. Imposed strain localization in the lower crust on seismic timescales. *Earth Planets Space*, **56**, 1103–1109.
- ELLIS, S., BEAVAN, J., EBERHART-PHILLIPS, D. & STÖCKHERT, B. 2006. Simplified models of the Alpine Fault seismic cycle: stress transfer in the mid-crust. *Geophysics Journal International*, **166**, 386–402.
- FAGERENG, A., REMITTI, F. & SIBSON, R. H. 2010. Shear veins observed within anisotropic fabric at high angles to the maximum compressive stress. *Nature Geoscience*, **3**, 482–485.
- FAULKNER, D. R., MITCHELL, T. M., HEALY, D. & HEAP, M. J. 2006. Slip on 'weak' faults by the rotation of regional stress in the fracture damage zone. *Nature*, **444**, 922–925.
- FITZENZ, D. D. & MILLER, S. A. 2004. New insights on stress rotations from a forward regional model of the San Andreas fault system near its Big Bend in southern California. *Journal of Geophysical Research*, **109**, B08404, doi: 10.1029/2003JB002890.
- FLETCHER, J. B. & MCGARR, A. 2006. Distribution of stress drop, stiffness, and fracture energy over earthquake rupture zones. *Journal of Geophysical Research*, **111**, B03312, doi: 10.1029/2004JB003396.
- FREED, A. M. 2005. Earthquake triggering by static, dynamic, and postseismic stress transfer. *Annual Reviews of Earth and Planetary Science*, **33**, 335–367.
- FREED, A. M., BÜRGMANN, R., CALAIS, E. & FREYMUELLER, J. 2006. Stress-dependent power-law flow in the upper mantle following the 2002 Denali, Alaska, earthquake. *Earth and Planetary Science Letters*, **252**, 481–489.
- HARDEBECK, J. L. & HAUSSON, E. 2001. Crustal stress field in southern California and its implications for fault mechanics. *Journal of Geophysical Research*, **106**, 21 859–21 882.
- HARDEBECK, J. L. & MICHAEL, A. J. 2004. Stress orientations at intermediate angles to the San Andreas fault, California. *Journal of Geophysical Research*, **109**, B11303, doi: 10.1029/2004JB003239.
- HAUSSON, E. 1994. State of stress from focal mechanisms before and after the 1992 Landers earthquake sequence. *Bulletin of the Seismological Society of America*, **84**, 917–934.
- HAUSSON, E. & JONES, L. M. 1988. The July 1986 Oceanside (ML = 5.3) earthquake sequence in the continental borderland, southern California. *Bulletin of the Seismological Society of America*, **78**, 1885–1906.
- HEALY, D. 2008. Damage patterns, stress rotations and pore fluid pressures in strike-slip faults. *Journal of Geophysical Research*, **113**, B12407, doi: 10.1029/2008JB005655.
- HEALY, D. 2009. Anisotropy, pore fluid pressure and low angle normal faults. *Journal of Structural Geology*, **31**, 561–574.
- HEALY, D., JONES, R. E. & HOLDSWORTH, R. E. 2006. Three-dimensional brittle shear fracturing by tensile crack interaction. *Nature*, **439**, 64–67.
- HEALY, D., YIELDING, G. & KUSZNIR, N. 2004. Fracture prediction for the 1980 El Asnam, Algeria earthquake via elastic dislocation modeling. *Tectonics*, **23**, TC6005, doi: 10.1029/2003TC001575.
- HEIDBACH, O., IAFFALDANO, G. & BUNGE, H. P. 2008. Topography growth drives stress rotations in the central Andes: observations and models. *Geophysical Research Letters*, **35**, L08301, doi: 10.1029/2007GL032782.
- HETLAND, E. A. & HAGER, B. H. 2006. Interseismic strain accumulation: spin-up, cycle invariance, and irregular rupture sequences. *Geochemistry Geophysics Geosystems*, **7**, Q05004, doi: 10.1029/2005GC001087.
- HICKMAN, S. H. & ZOBACK, M. 2004. Stress orientations and magnitudes in the SAFOD pilot hole. *Geophysical Research Letters*, **31**, L15S12, doi: 10.1029/2004GL020043.
- HIRTH, G. & KOHLSTEDT, D. 2004. Rheology of the upper mantle and the mantle wedge: a view from the experimentalists. In: EILER, J. (ed.) *The Subduction Factory*.

- American Geophysical Union, Geophysical Monograph, **138**, 83–105.
- HUC, M., HASSANI, R. & CHÉRY, J. 1998. Large earthquake nucleation associated with stress exchange between middle and upper crust. *Geophysical Research Letters*, **25**, 551–554.
- JACKSON, J. A. & WHITE, N. J. 1989. Normal faulting in the upper continental crust: observations from regions of active extension. *Journal of Structural Geology*, **11**, 15–36.
- KENNER, S. J. 2004. Rheological controls on fault loading rates in northern California following the 1906 San Francisco earthquake. *Geophysical Research Letters*, **31**, L01606, doi: 10.1029/2003GL018903.
- KING, G. C. P., STEIN, R. S. & LIN, J. 1994. Static stress changes and the triggering of earthquakes. *Bulletin of the Seismological Society of America*, **84**, 935–953.
- KÜSTER, M. & STÖCKHERT, B. 1999. High differential stress and sublithostatic pore fluid pressure in the ductile regime – microstructural evidence for short-term post-seismic creep in the Sesia Zone, Western Alps. *Tectonophysics*, **303**, 263–277.
- LIN, J. & FREED, A. M. 2004. Time-dependent viscoelastic stress transfer and earthquake triggering. In: CHEN, Y. J. (ed.) *Environment, Natural Hazards, and Global Tectonics of the Earth. Advances in Earth Sciences, Monograph*, **2**, 21–38.
- LISLE, R. J., ORIFE, T. O., ARLEGUI, L., LIESA, C. & SRIVASTAVA, D. C. 2006. Favoured states of palaeostress in the Earth's crust: evidence from fault-slip data. *Journal of Structural Geology*, **28**, 1051–1066.
- LISTER, G. S. & DAVIS, G. A. 1989. The origin of metamorphic core complexes and detachment faults formed during Tertiary continental extension in the northern Colorado River region, USA. *Journal of Structural Geology*, **11**, 65–93.
- LOCKNER, D. A. & BYERLEE, J. D. 1993. How geometrical constraints contribute to the weakness of mature faults. *Nature*, **363**, 250–252.
- LOCKNER, D. A., BYERLEE, J. D., KUSENKO, V., PONOMAREV, A. & SIDORIN, A. 1991. Quasi static fault growth and shear fracture energy in granite. *Nature*, **350**, 39–42.
- MANDL, G. 1987. Discontinuous fault zones. *Journal of Structural Geology*, **9**, 105–110.
- MANDL, G. 1988. *Mechanics of Tectonic Faulting – Models and Basic Concepts*. Elsevier, Amsterdam.
- MELOSH, H. J. 1990. Mechanical basis for low-angle normal faulting in the Basin and Range province. *Nature*, **343**, 331–335.
- MICHAEL, A. J. 1987. Stress rotation during the Coalinga aftershock sequence. *Journal of Geophysical Research*, **92**, 7963–7979.
- MICHAEL, A. J., ELLSWORTH, W. L. & OPPENHEIMER, D. H. 1990. Coseismic stress changes induced by the 1989 Loma Prieta, California earthquake. *Geophysical Research Letters*, **17**, 1441–1444.
- NÜCHTER, J.-A. & ELLIS, S. 2010. Complex states of stress during the normal-faulting seismic cycle: Role of mid-crustal postseismic creep. *Journal of Geophysical Research – Solid Earth*, **115**, B12411, doi: 10.1029/2010JB007557.
- NÜCHTER, J.-A. & STÖCKHERT, B. 2007. Vein quartz microfabrics indicating progressive evolution of fractures into cavities during postseismic creep in the middle crust. *Journal of Structural Geology*, **29**, 1445–1462.
- NÜCHTER, J.-A. & STÖCKHERT, B. 2008. Coupled stress and pore fluid pressure changes in the middle crust: vein record of coseismic loading and postseismic stress relaxation. *Tectonics*, **27**, TC 1007, doi: 10.1029/2007TC002180.
- PATRICK, T. & THOMPSON, G. A. 1993. Does magmatism influence low-angle normal faulting? *Geology*, **21**, 247–250.
- PATERSON, M. S. & LUAN, F. C. 1990. Quartzite rheology under geological conditions. In: KNIFE, R. J. & RUTTER, E. H. (eds) *Deformation Mechanisms, Rheology and Tectonics*. Geological Society, London, Special Publications, **54**, 299–307.
- PROVOST, A. S. & HOUSTON, H. 2003. Stress orientations in northern and central California: evidence for the evolution of frictional strength along the San Andreas plate boundary system. *Journal of Geophysical Research*, **108**, 2175, doi: 10.1029/2001JB001123.
- R DEVELOPMENT CORE TEAM 2009. *R: A Language and Environment for Statistical Computing*. R Foundation for Statistical Computing, Vienna, Austria. uri: <http://www.R-project.org>.
- RANALLI, G. 1987. *Rheology of the Earth*. Chapman & Hall, London.
- RECHES, Z. & DIETERICH, J. H. 1983. Faulting of rocks in three-dimensional strain fields I. Failure of rocks in polyaxial, servo-control experiments. *Tectonophysics*, **95**, 111–132.
- REID, H. F. 1910. *The California Earthquake of April 18, 1906: The Mechanics of the Earthquake*, Volume 2. Carnegie Institut, Washington, DC.
- RICE, J. R. 1992. Fault stress states, pore pressure distributions, and the weakness of the San Andreas Fault. In: EVANS, B. & WONG, T. (eds) *Fault Mechanics and Transport Properties of Rocks; A Festschrift in Honor of W. F. Brace* International Geophysics Series, **51**, 475–503.
- RUDNICKI, J. W. 1979. Rotation of principal stress axes caused by faulting. *Geophysical Research Letters*, **6**, 135–138.
- SCHOLZ, C. H. 2000. Evidence for a strong San Andreas Fault. *Geology*, **28**, 163–166.
- SIBSON, R. H. 1985. A note on fault reactivation. *Journal of Structural Geology*, **7**, 751–754.
- SIBSON, R. H. 1994. An assessment of field evidence for Byerlee friction. *Pure and Applied Geophysics*, **142**, 645–662.
- SIBSON, R. H. & XIE, G. Y. 1998. Dip range for intracontinental reverse fault ruptures: truth not stranger than friction? *Bulletin of the Seismological Society of America*, **88**, 1014–1022.
- THATCHER, W. 1983. Nonlinear strain buildup and the earthquake cycle on the San Andreas fault. *Journal of Geophysical Research*, **88**, 5893–5902.
- TOWNSEND, J. & ZOBACK, M. D. 2004. Regional stress near the San Andreas fault in central and southern California. *Geophysical Research Letters*, **31**, L15S11, doi: 10.1029/2003GL018918.

- TREPMLANN, C. A. & STÖCKHERT, B. 2001. Mechanical twinning of jadeite; an indication of synseismic loading beneath the brittle–plastic transition. *International Journal of Earth Sciences*, **90**, 4–13.
- TREPMLANN, C. A. & STÖCKHERT, B. 2002. Cataclastic deformation of garnet; a record of synseismic loading and postseismic creep. *Journal of Structural Geology*, **24**, 1845–1856.
- TREPMLANN, C. A. & STÖCKHERT, B. 2003. Quartz microstructures developed during non-steady state plastic flow at rapidly decaying stress and strain rate. *Journal of Structural Geology*, **25**, 2035–2051.
- WESTAWAY, R. 1999. The mechanical feasibility of low-angle normal faulting. *Tectonophysics*, **308**, 407–443.
- WESTAWAY, R. 2005. Active low-angle normal faulting in the Woodlark extensional province, Papua New Guinea: a physical model. *Tectonics*, **24**, TC6003, doi: 10.1029/2004TC001744.
- YIN, Z. M. & ROGERS, G. C. 1995. Rotation of the principal stress directions due to earthquake faulting and its seismological implications. *Bulletin of the Seismological Society of America*, **85**, 1513–1517.



# Evolution of fluid chemistry and fluid-flow pathways during folding and faulting: an example from Taemas, NSW, Australia

SHAUN L. L. BARKER\* & STEPHEN F. COX

*Research School of Earth Sciences, The Australian National University, Canberra,  
ACT 0200, Australia*

*Present address: Department of Earth and Ocean Sciences, University of British Columbia,  
Vancouver, BC, Canada V6T 1Z4*

\*Corresponding author (e-mail: [sbarker@eos.ubc.ca](mailto:sbarker@eos.ubc.ca))

**Abstract:** In the Taemas area, New South Wales, Australia, a swarm of hydrothermal calcite and quartz veins is hosted in upright, open to close folded limestones and shales. Overprinting relationships and vein geometries demonstrate that the vein swarm formed progressively during fold growth and associated reverse faulting. Textures preserved in veins reveal that veins formed via hundreds to thousands of individual dilation and mineral precipitation events. Bedding-parallel flexural slip during fold growth was associated with laminated vein development, and limb-parallel stretching during fold growth was associated with the formation of bedding-orthogonal extension veins. The presence of subhorizontal extension fractures and severely misoriented reverse faults imply that fluid pressures exceeded lithostatic levels, at least transiently, during the development of the vein swarm.

Vein  $\delta^{18}\text{O}$  compositions increase upwards through the Murrumbidgee Group in response to a progressive reaction of an externally derived, upwards-flowing low- $\delta^{18}\text{O}$  fluid (of probable meteoric origin) with host limestones. Vein  $\delta^{18}\text{O}$  and  $^{87}\text{Sr}/^{86}\text{Sr}$  compositions vary spatially and temporally within the same outcrop, and within individual veins. These variations are inferred to be caused by the ascent of packages of fluid along constantly changing flow pathways caused by multiple permeability creation–destruction cycles associated with fault slip and fault sealing. Vein trace and rare earth element (REE) concentrations are more variable, probably reflecting rapid rock buffering along fluid pathways on length scales of less than 10 m. Our results indicate that fluid-flow pathways change dynamically during crustal shortening, with pathways switching between states of low and high permeability during episodic fault slip and associated fracture development.

**Supplementary material:** Two appendices are available at <http://www.geolsoc.org.uk/SUP18492>.

Syntectonic veins record information on spatial and temporal variations in the composition of fluids migrating through the crust during progressive deformation and associated vein growth (e.g. Dietrich *et al.* 1983; Rye & Bradbury 1988). Exhumed vein systems potentially contain a record of where fluid flow was localized, how flow has influenced the mechanical behaviour of the crust, and the nature of chemical reactions between rocks and fluids along fluid-flow pathways. Vein chemistry may also provide constraints on the nature of fluid reservoirs contributing to fluid flow during crustal deformation.

An extensive fold- and fault-related vein network (hereafter called the ‘Taemas Vein Swarm’ or TVS) composed mainly of calcite veins is developed throughout much of an interbedded limestone and shale sequence (the Murrumbidgee Group) in the Taemas area of southeastern NSW. The vein

swarm is localized mainly within an area of approximately 20 km<sup>2</sup>. Vein development and folding were synchronous, with a variety of bedding-discordant fault veins, bedding-parallel fault veins and extension veins developed. Laminated veins related to bedding-parallel slip are common, particularly in thinly interbedded limestone–mudstone units. Bedding-discordant faults, fault-related extension veins and extension veins related to flexural flow and bedding-parallel stretching of fold limbs are also found (Cox 2007).

As externally sourced fluids react with rocks, they become progressively rock-buffered along fluid-flow pathways. Many studies have been carried out exploring how fluid flow and fluid–rock reaction processes may affect the chemical and isotopic composition of host rocks and hydrothermal veins (e.g. Bickle & McKenzie 1987; Lassey & Blattner 1988; Rye & Bradbury 1988; Bowman *et al.* 1994;

Gerdes *et al.* 1995; McCaig *et al.* 1995; DePaolo & Getty 1996; Abart & Sperb 1997; Eppel & Abart 1997; Steefel & Lichtner 1998; Abart & Pozzorini 2000; McCaig *et al.* 2000; Badertscher *et al.* 2002; Knoop *et al.* 2002; Matthäi 2003; Steefel *et al.* 2005; DePaolo 2006; Cox 2007; Zack & John 2007). Many of these studies have assumed 'steady state' or essentially continuous fluid flow, without considering the influence that dynamic changes in permeability, with both time and space, will have on resulting fluid and vein compositions.

In addition to isotopic compositions of calcite, we present trace element compositions from hydrothermal calcite veins. Calcite commonly contains appreciable concentrations of Mg, Mn and Fe, and lesser amounts of Sr and Ba (Deer *et al.* 1962, 1992; Mucci & Morse 1990). In general, there are little available experimental data addressing the trace element composition of calcite precipitated at temperatures above 50 °C. The concentration of trace elements in calcite will reflect a variety of factors in the fluid from which the calcite precipitated. These factors include the concentration of substituting elements in solution, temperature, pH, other aspects of fluid composition (e.g. concentrations of other species such as  $\text{CO}_3^{2-}$ ) and oxidation state. The major factors controlling trace element partitioning between calcite and fluid are the size of the cation site and the ionic radius of the substituting element (Garrels & Christ 1982; Mucci & Morse 1990; Zhong & Mucci 1995). The reviews of Mucci & Morse (1983) and Wasylenski *et al.* (2005) found a strong temperature control on the incorporation of both Mg and Sr into calcite. Faster precipitation rates also lead to higher concentrations of both Sr and Mg in calcite (Mucci & Morse 1990). Fe and Mn concentrations in calcite are controlled by the concentration of Fe and Mn in solution, as well as the temperature and precipitation rate of calcite (Dromgoole & Walter 1990). In hydrothermal fluids, rare earth element (REE) fractionation is a function of: (a) sorption and desorption of REEs during migration of fluids along particle surfaces; and (b) coprecipitation (Bau & Moller 1992).

The aim of this chapter is to use spatial and temporal variations in vein isotopic and trace element composition to explore controls on fracturing, fluid flow, and fluid–rock reaction, in a fracture-controlled hydrothermal system that was active during progressive crustal shortening.

## Geological setting of the Taemas Vein Swarm

The Taemas area is located SW of Yass, in the Eastern Belt of the Lachlan Orogen, in southeastern New South Wales, Australia (Glen 1992). Here, a

major fold triplet (Wee Jasper Syncline, Narrangullen Anticline and Taemas Synclinorium) forms the larger Black Range Synclinorium (c. 180 km long × 25 km wide). The Taemas Synclinorium is a doubly-plunging synclinorial structure approximately 5 km wide (Cramsie *et al.* 1975) (Fig. 1). Within the Taemas Synclinorium, sedimentary rocks of the Murrumbidgee Group (Table 1) have been folded into upright, open to close folds (wavelengths varying from tens-of-metres- to kilometre-scale), which have a predominant NNW trend, and steep axial surfaces (Fig. 2). The synclinorium is to the west of the major, steeply-dipping, Warroo and Deakin– Devil's Pass Fault System. Here, Silurian volcanics overthrust the Murrumbidgee Group sediments (Cramsie *et al.* 1975). Within the Taemas Synclinorium, the Murrumbidgee Group is approximately 1 km thick, and is composed of several limestone and shale formations that were deposited during the Early Devonian (Browne 1958) (see Table 1 for stratigraphy and formation name abbreviations).

At the base of the sedimentary sequence (in the Sugarloaf Creek Formation, SLC and the underlying volcanic basement) bedding dips are low (typically <20°) and bedding is gently folded, with fold wavelengths of the order of hundreds of metres to more than 1 km. Higher in the sequence, particularly in the Cavan Bluff Limestone (CBL), Spirifer yassensis Limestone (SYL) and Bloomfield Limestone (BFL), close to tight folds occur, with shorter fold wavelengths (from tens to hundreds of metres: see Figs 2 & 3). The shorter fold wavelength in the interbedded limestone–shale units (SYL and BFL), compared with the thicker, more competent underlying and overlying units (Majurgong Formation (MJF) and Receptaculites Limestone, RCL) reflects a strong control of thickness of competent stratigraphical units on fold wavelength. The changes in fold wavelength and strains accommodated by folding through the Murrumbidgee Group require detachment accommodated by faulting where major changes in fold wavelength occur.

Cleavage is strongly developed in the MJF, and in shale-rich beds in the SYL and BFL. Within sandstone beds in the MJF, cleavage fans strongly around outcrop-scale folds, and is typically at a high angle to bedding. This implies that layer-parallel shortening occurred early during fold growth, with the subsequent buckling of bedding (Ramsay & Huber 1987). In general, shales have a penetrative slaty cleavage, whereas limestone beds are internally relatively unstrained or contain a weak pressure-solution cleavage. Total strain, calculated using bed lengths of internally unstrained limestone sequences, is in the range of 20–50%. Given geological strain rates of the order of  $10^{-14}$ – $10^{-15} \text{ s}^{-1}$  (Pfiffner & Ramsay 1982;

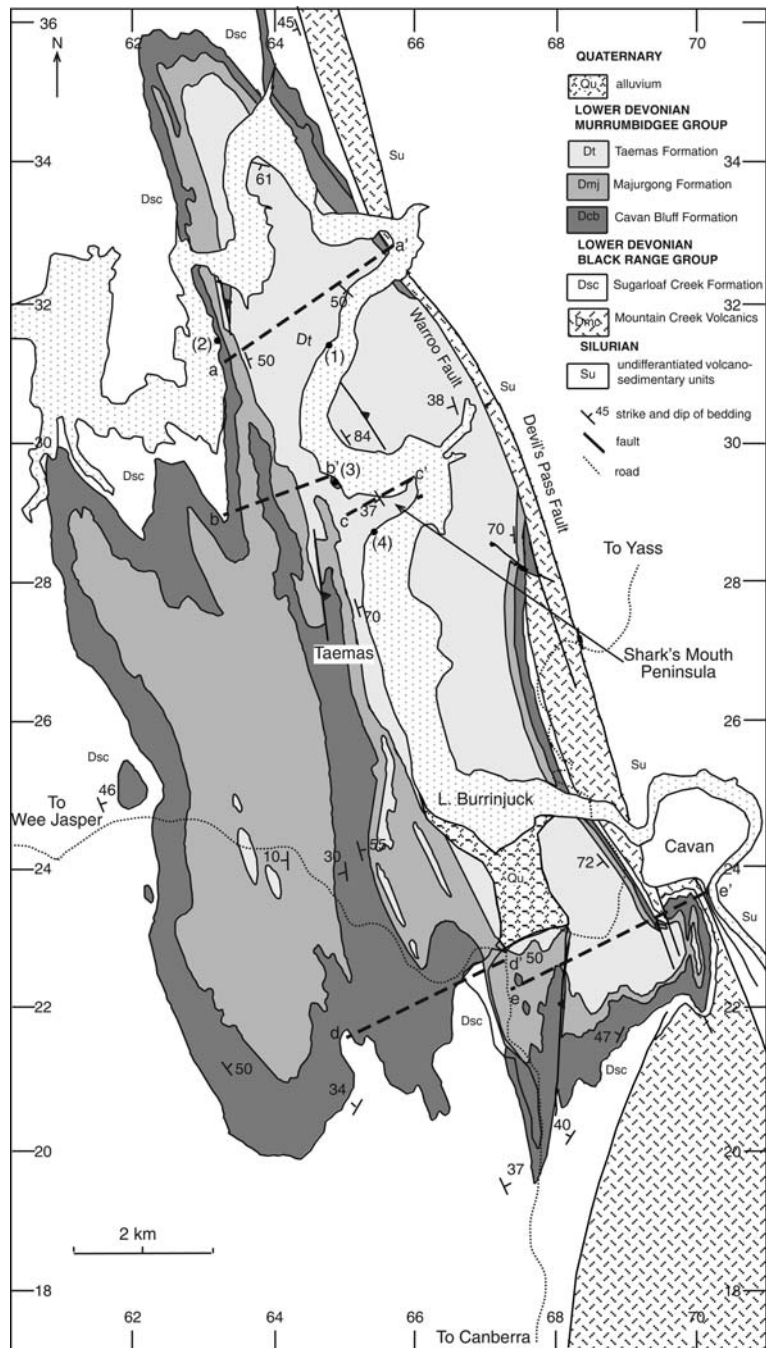


**Fig. 1.** Simplified geological map of the Taemas area (modified from Cox 2007), showing representative bedding orientations and major outcrop locations (locality numbers in parentheses) documented in this chapter. Map grid is Australian Geodetic Datum (1984). Figure 4 is at locality 2, Figure 5 is at locality 1. Other locations are noted in text. Cross sections (a-a'; b-b', c-c', d-d', e-e') are shown in Figure 2.

**Table 1.** Stratigraphy and brief description of host rocks for the Taemas Vein Swarm\*

Group	Formations	Members
Murrumbidgee Group	Taemas Formation: massive to interbedded limestones, shale, shaly limestones, variably fossiliferous	Crinoidal Limestone: calcarenite with prominent crinoid ossicles Warroo Limestone: shaly, thinly bedded, very fossiliferous limestone Receptaculites Limestone (RCL): Massive, grey limestone with similar appearance to Currajong Limestone Bloomfield Limestone (BFL): thinly interbedded limestone and shale Currajong Limestone (CJL): Massive, grey ls, prominently outcropping Spirifer yassensis Limestone (SYL): thinly interbedded limestone and shale
	Majurgong Formation (MJF): thin to well-bedded red sandstone beds, thin-interbedded limestones at bottom and top of formation.	
	Cavan Bluff Limestone (CBL): thinly bedded flaggy limestones with interbedded shale	
Black Range Group	Sugarloaf Creek Formation (SLC): tuff, shale, tuffaceous silstone, rhyolite, agglomerate	
	Rhyolite, andesite, dacite, agglomerate, tuff	

\*Note the abbreviations for host rocks used in the text. See Browne (1958) and Cramsie *et al.* (1975) for further details.

Mueller *et al.* 2000), this would imply that folding occurred over a period of 0.5–15 Ma.

## The Taemas Vein Swarm

Veins occur as:

- fault veins – veins that form as dilatant zones within faults, which cut across and displace bedding;
- bedding-parallel veins (BPV) – veins that are concordant to bedding and show evidence of shear, such as laminations and slickenfibres;
- extension veins – veins that have no evidence of shear displacement.

### Fault veins

Shear veins, occurring as both bedding-discordant and bedding-parallel structures, are found throughout the Taemas Vein Swarm. Fault veins cross-cut and displace bedding, and are found in several

outcrops. Fault veins are dominantly calcite, with minor quartz and rare fluorite. Extension veins are common around bedding-discordant faults. Nearly all fault veins are hosted by reverse faults that, with respect to the inferred stress field at the time of faulting, range from optimally oriented to severely misoriented (cf. Sibson 1985). In addition, some minor subvertical, apparently late, strike-slip faults cut bedding. Displaced marker beds and the size of dilatational jogs indicate that the majority of fault veins have net slip of the order of centimetres to a few metres. Within the Murrumbidgee Group, only four mapped faults have displacements larger than a few tens of metres.

Commonly, bedding-parallel and bedding-discordant fault veins are connected. Some of the thickest calcite veins found to date in the TVS occur where a bedding-parallel fault becomes bedding-discordant and displaces two anticlines against one another, generating a dilatant jog with a strike length of several tens of metres (Fig. 1, locality 2; see the detailed outcrop photograph in

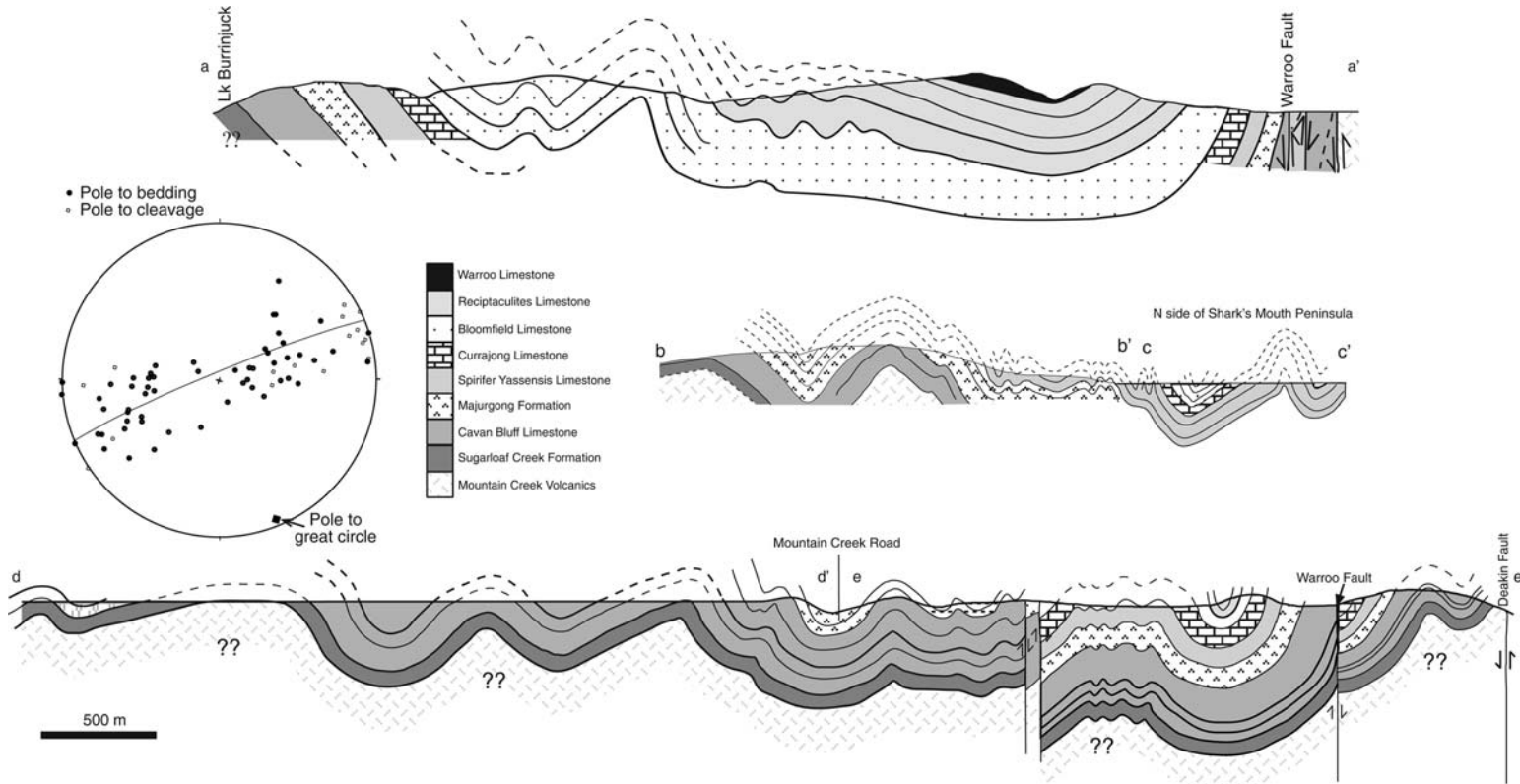


**Fig. 2.** Cross-sections constructed from field mapping, aerial photographs and pre-dawn infrared images, showing the fold style in the Black Range and Murrumbidgee groups. Fold wavelengths tend to be longer (*c.* km scale) in the Black Range Group, and decrease to wavelengths of 100 m or less in the Spirifer *yassensis* and Bloomfield members of the Taemas Limestone. For clarity, some units that do not crop out are not shown on sections. The equal-area stereonet shows poles to bedding (circles) and cleavage (squares) throughout the Taemas area. Plotted is a best-fit great circle, indicating a NNW–SSE trend for the Taemas Synclinorium, with a very gentle south plunge.

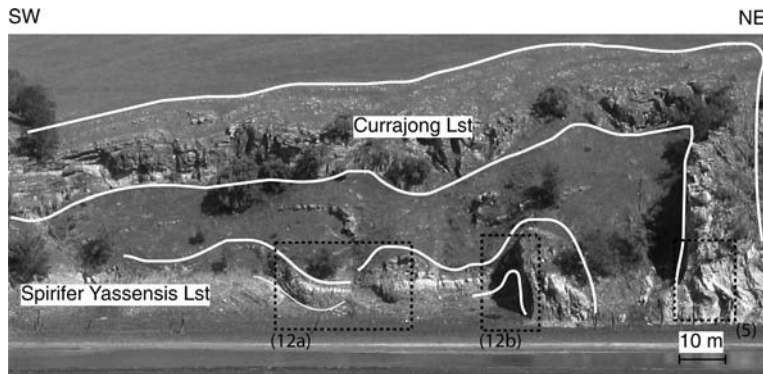


**Fig. 3.** Folded Spirifer yassensis and Currajong Limestone beds at Kangaroo Flat (locality 1 on Fig. 1). Note the decoupling that must occur between and within SYL and C JL limestones to allow observed fold geometries. Black rectangles mark the locations of the two outcrops shown in Figure 12 and the outcrop shown in Figure 5 (as indicated by numbers in parentheses in the figure).

Fig. 4), which would have been a zone of high palaeo-permeability (cf. Cox 2005).

#### *Bedding-parallel veins*

Bedding-parallel veins commonly contain tens to hundreds of mesoscopic grey-brown laminations, which lie subparallel to the vein margins. Laminations are usually striated, with striations generally subperpendicular to the plunge of fold hinges. However, the trend of striations on low-angle bedding-parallel veins at Shark's Mouth Peninsula (Fig. 2, locality 4) varied over 55° on different laminae in the same vein. Most veins have dips of 40°–60°.

The laminated, bedding-parallel veins are analogous to those described previously, where slickenfibres and slickenlines found on laminations in the bedding-parallel veins record the slip vector (Gaviglio 1986; Tanner 1989; Jessell *et al.* 1994; Fowler 1996 and references therein). Some BPV may be traced around fold hinges. The presence of BPV in fold-hinge zones, and asymmetrically folded laminations within BPV on fold limbs, suggest that ongoing fold growth post-dated initial flexural slip. It seems likely that during the initial stages of folding, significant strain was accommodated via slip along bedding. However, as bedding dips increased during folding, frictional lock-up occurred (Ramsay 1974). During ongoing fold tightening, new bedding-discordant faults have formed. The occurrence of small saddle reefs indicates that dilation occurred at some fold hinges during fold amplification by flexural slip.

#### *Extension veins*

Fold limbs rotated into steep orientations have undergone limb-parallel stretching, resulting in

incipient bedding boudinage and formation of associated subhorizontal extension veins (Fig. 5). Extension veining of this type is most prevalent in the C JL. This is likely owing to the high competence of this unit relative to the surrounding interbedded limestone–shale of the SYL and BFL.

Generally, extension veins overprint cleavage development and are generally later than bedding-parallel slip veins. At locality 3 in Figure 1, calcite extension veins cut cleavage at a high angle on fold limbs. A bedding-parallel vein between the two anticlines is cut by extension veins, which dip east (342°/37°E). The bedding-parallel vein is interpreted to be the result of flexural slip during folding. The high angle of calcite extension veins to cleavage within folds is consistent with some veins formed as beds deformed via flexural flow (Ramsay & Huber 1987). Extension veins cross-cutting the bedding-parallel vein imply that strain may be accommodated via flexural-flow folding after bedding-parallel slip ceases due to the frictional lock-up of beds (Ramsay 1974). It is noted that en echelon arrays of veins related to flexural flow form only in semi-competent and incompetent beds, and do not form within more competent massive limestone beds.

Extension veins can also show mutually overprinting relationships with cleavage (in shale-rich beds) and stylolites (in more massive limestones), and folded veins are rare. This implies that extension vein formation and folding were contemporaneous. Extension veins sometimes show mutually overprinting relationships (Fig. 5c, e), implying that the orientation of  $\sigma_3$  (at least sometimes) changed dynamically over time.

In summary, various vein types formed throughout crustal shortening. Thus, vein chemistry may be used to track variations in fluid composition

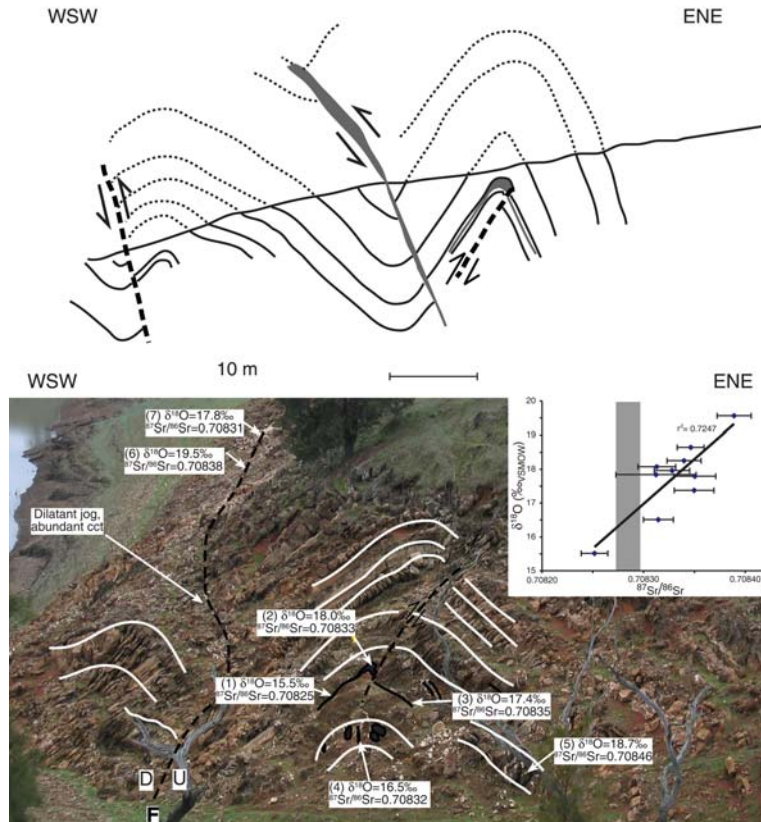


**Fig. 4.** Faults and veins within the Cavan Bluff Limestone at a fault–fold complex at location 2 in Figure 1. The top panel is a cross-section through the outcrop shown in the photograph in the lower panel. On the photograph white lines mark bedding, black lines mark faults. Shown are O and Sr isotope compositions for different vein types (numbered below) contained within the outcrop: (1) bed-parallel vein; (2) saddle-reef; (3) bed-parallel vein; (4) hinge extension vein; (5) flexural-flow extension vein; (6) laminated fault vein; and (7) fault vein dilatant jog. Inset graph shows the relationship between  $\delta^{18}\text{O}$  and  ${}^{87}\text{Sr}/{}^{86}\text{Sr}$  ( $\pm 2$  SE) for different veins. (SE, standard error.)

( $\delta^{18}\text{O}$ ,  ${}^{87}\text{Sr}/{}^{86}\text{Sr}$ , trace and rare earth elements), not just during growth of individual veins but also as the TVS evolved from early fold growth to later fold tightening, cleavage development and associated reverse faulting.

#### Vein textures

Veins dominantly have fibrous (Fig. 6a), massive (Fig. 6b), laminated (Fig. 6c) and fibrous (Fig. 6d) textures, with elongate-blocky and crustiform textures also occurring (Bons 2000; Oliver & Bons 2001). Bedding-parallel and discordant fault veins have massive and laminated textures, with fibrous textures preserved in some parts of fault and bedding-parallel veins (Fig. 6b). Conversely, extension veins have massive, elongate-blocky or fibrous textures (Fig. 6a, d). It is emphasized here that the particular textures are not isolated to specific host lithologies,

and textural variations are present among veins within the same outcrop, as well as within individual veins (Fig. 6b). Notably, veins may contain both fibrous and massive calcite; massive and fibrous extension veins also show mutually overprinting relations (Fig. 6b).

Laminated textures in bedding-parallel slip veins have been classified according to the terminology of Koehn & Passchier (2000). *Inclusion bands* are thin, dark bands parallel to the vein margins. *Crack–seal bands* are thin, dark bands between parallel inclusion bands, which, in this study, are typically inclined at angles of  $20^\circ$ – $35^\circ$  to inclusion bands (Figs 6c & 7). Crack–seal bands are typically separated by distances of 100  $\mu\text{m}$ –2 mm in laminated veins (Fig. 6c), and hundreds of crack–seal bands may occur in an interval of around 10 cm along one calcite lamina (Fig. 6c). Crack–seal bands are inferred to have formed along dilatational

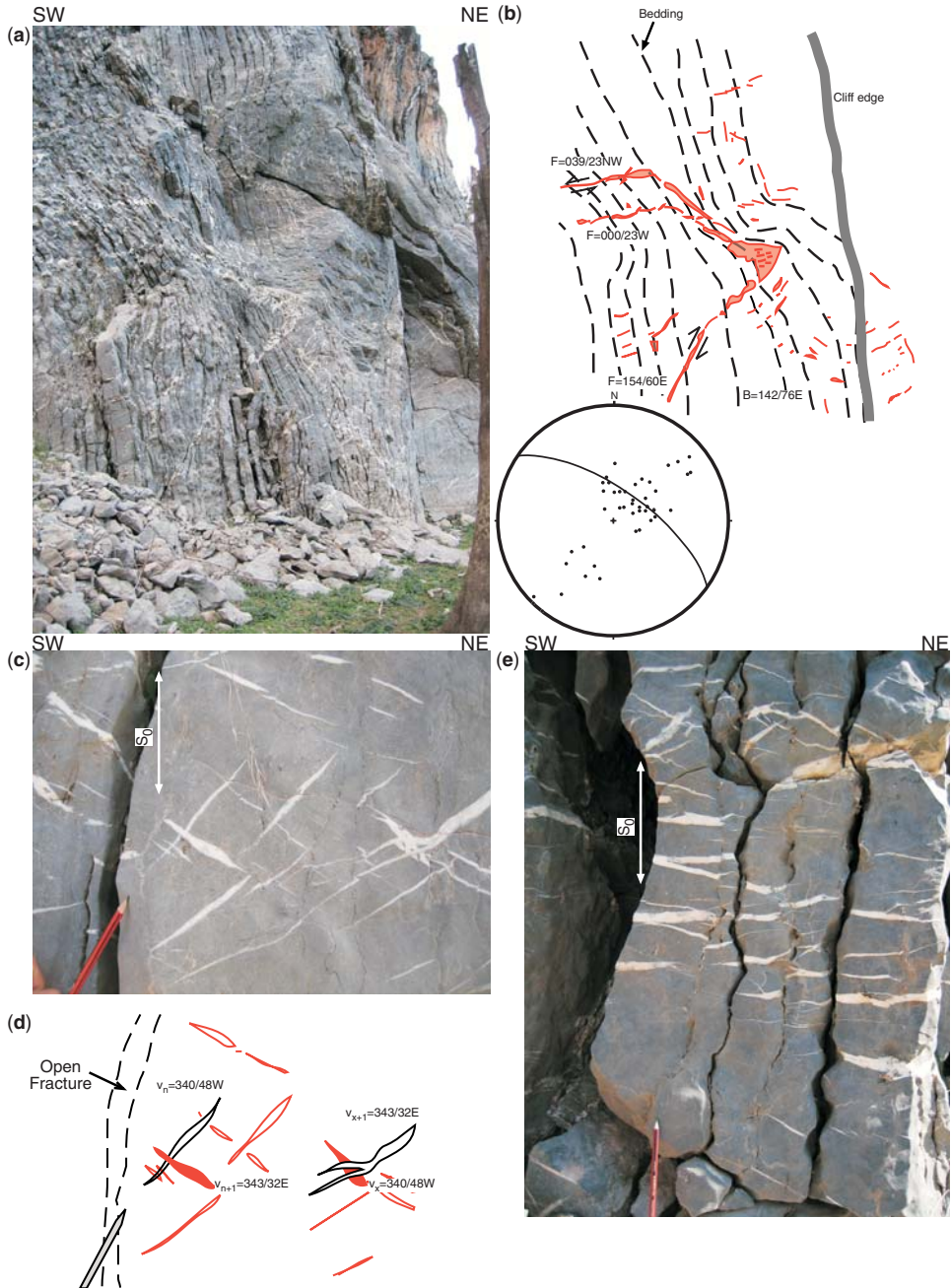


**Fig. 5.** (a) Photograph of Currajong Limestone with extension veins in subvertical bedding at ‘Kangaroo Flat’ on the eastern side of Taemas Peninsula (locality 1 in Fig. 1, and locality 5 in Fig. 3). (b) Interpretative sketch of (a). Bedding is dashed black, calcite veins are red. Representative fault and bedding orientations are shown. Equal-area stereonet shows the average orientation of bedding (great circle) and poles to veins (note the higher density of veins at approximately  $90^\circ$  to bedding). The outcrop is approximately 10 m wide. (c) Photograph of calcite extension veins from limestone on the right-hand side of photograph (a). Pencil tip (10 cm) for scale. (d) Interpretative sketch of (c). Note that vein sets ( $v_n$  and  $v_x$ ) with similar orientations show mutually overprinting relations. Styolites are approximately parallel to bedding. Some veins cross-cut stylolites, while other veins are truncated against stylolites. (e) Boudinaged limestone beds and extension veins on the upper transition of CJL to BFL. Note the pencil (15 cm) for scale.

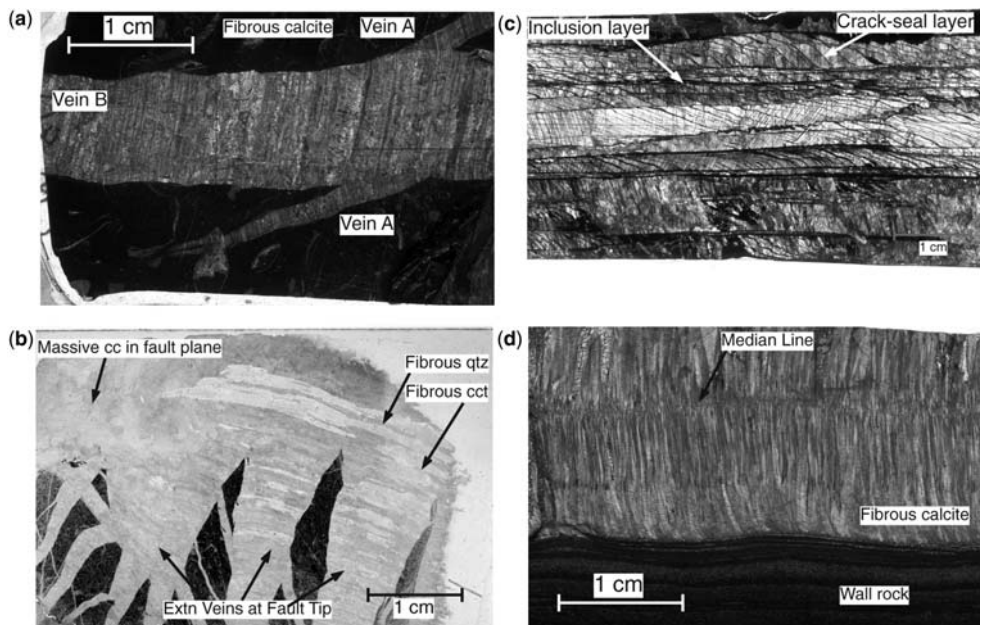


**Fig. 6.** (a) Thin section photomicrograph of a fibrous stretched-crystal calcite vein (Vein B) cross-cutting earlier fibrous calcite vein (Vein A) within the Cavan Bluff Limestone. (b) Thin section photomicrograph of fibrous calcite–quartz textures preserved within extension veins at the tip of a fault with massive calcite preserved within the fault plane. (c) Thin section photomicrograph showing part of a laminated bedding-parallel vein. Note the obvious crack–seal layers between inclusion bands (Koehn & Passchier 2000). (d) Antitaxial fibrous calcite vein collected from the Cavan Bluff Limestone. Note the median growth line.

sites during slip along laminations on the BPV (Koehn & Passchier 2000).

## Geochemical methods

### Sample collection

The position and structural relationships of veins were recorded in the field prior to sample collection (see Supplementary material SUP18492 for

sampling locations and complete analytical results). Unaltered host rock (at distances of more than 50 m from any visible veins) was collected from the Cavan Bluff, Spirifer yassensis, Currajong, Bloomfield and Receptaculites limestones.

### Stable isotope analysis

Oxygen and carbon isotope ratios for carbonates were measured on a Finnigan MAT251 mass

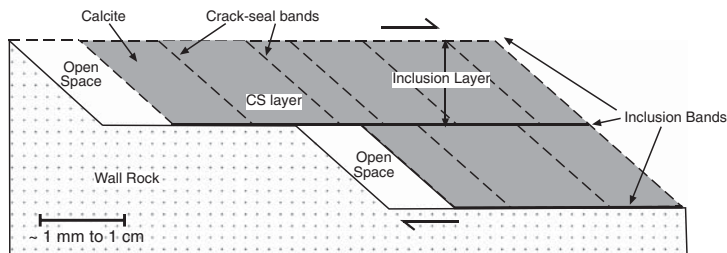


**Fig. 7.** Schematic diagram showing the growth mechanism and resulting microstructures during the formation of inclusion and crack–seal bands during bedding-parallel slip. Crack–seal bands and layers are produced in dilational jogs, while inclusion bands are produced on the shear planes along which slip is occurring. After Koehn & Passchier (2000).

spectrometer. For each sample,  $200 \pm 20 \mu\text{g}$  of carbonate powder was dissolved in 103%  $\text{H}_3\text{PO}_4$  at 90 °C in an automated carbonate (Kiel) device. Carbon isotope ratios are reported relative to Vienna PeeDee Belemnite (VPDB). Oxygen isotope results are reported relative to Vienna Standard Mean Ocean Water (VSMOW), and were converted from VPDB values, where:

$$\delta^{18}\text{O}_{\text{VSMOW}} = 1.03091 * \delta^{18}\text{O}_{\text{VPDB}} + 30.91.$$

(Coplen *et al.* 1983).

Isotope results have been normalized on the VSMOW and VPDB scales so that analyses of:

$$\text{NBS} - 19 \delta^{18}\text{O}_{\text{VPDB}} = -2.20\text{\textperthousand};$$

$$\delta^{18}\text{O}_{\text{SMOW}} = +28.64\text{\textperthousand} \text{ and } \delta^{13}\text{C}_{\text{VPDB}} = +1.95\text{\textperthousand}$$

$$\text{NBS} - 18 \delta^{18}\text{O}_{\text{VPDB}} = -23.0\text{\textperthousand};$$

$$\delta^{18}\text{O}_{\text{SMOW}} = +7.2\text{\textperthousand} \text{ and } \delta^{13}\text{C}_{\text{VPDB}} = -5.0\text{\textperthousand}.$$

The standard deviation ( $2\sigma$ ) for the 50 replicate NBS-19 standards used during the analysis of these samples was 0.02‰ for  $\delta^{13}\text{C}$  and 0.06‰ for  $\delta^{18}\text{O}$ .

Quartz oxygen isotope ratios were measured at the University of New Mexico. Quartz samples were separated from calcite (the calcite was stored for oxygen isotope analysis, as outlined earlier), and the quartz chips were placed into a 1 M HCl solution until all effervescence had ceased and calcite was removed.

The resulting quartz separates were examined using a binocular microscope, and clear quartz pieces were selected for analysis by laser fluorination (following the method of Sharp 1990). An internal laboratory standard (Lausanne-1) was analysed to determine the reproducibility of analyses ( $\pm 0.2\text{\textperthousand}$ ).

### *Strontium isotope analyses*

*Host rock.* Sr isotope compositions of host-rock carbonate were measured by thermal ionizing mass spectrometry (TIMS). Approximately 1 kg of each of two samples from each limestone member (10 samples in total) was crushed using a tungsten carbide swing mill. Around 0.06–0.11 g of rock powder was placed into a clean Teflon® screw-cap vial. To separate only the carbonate component of the limestones, 1 ml of distilled 1 M acetic acid was added to each beaker, resulting in immediate, gentle effervescence. The beakers were allowed to rest for 2 h at room temperature, and a further 1 ml of acetic acid was added, after which

effervescence ceased. The resulting mixture of solution and sediment was centrifuged in clean tubes, and the liquid was drawn off and dried on hot plates. The samples were then taken up in  $\text{HNO}_3$  for loading onto cation-exchange columns, where Sr was separated from other matrix elements. Rubidium was not collected or analysed as Rb concentrations in carbonate are generally very low (Faure & Powell 1972), and were confirmed to be very low (<1 ppm) by laser ablation multi-collector inductively coupled plasma mass spectrometry (LA-MC-ICP-MS) analyses (see later).

Purified Sr was loaded in  $\text{H}_3\text{PO}_4$  on Ta filaments and analysed on a Finnigan Mat261 mass spectrometer. All filaments were out-gassed for 30 min prior to loading. Sr isotope values were normalized to  $^{86}\text{Sr}/^{88}\text{Sr} = 0.1194$ . The NIST SRM-987 Sr isotope standard analysed had a  $^{87}\text{Sr}/^{86}\text{Sr}$  value of  $0.71023 \pm 0.00001$ .

*Carbonate veins.* Sr isotope compositions of vein calcite were analysed on the same samples on which trace element analyses were conducted. Analyses were made using *in situ* LA-MC-ICP-MS, and the results of the vein analyses are reported in Supplementary material SUP18492. Analyses were carried out using a HelEx ArF excimer laser ablation system, interfaced to a Finnigan MAT Neptune MC-ICP-MS (see Egginis *et al.* 1998, 2005 for details). Analyses were performed using a single-spot approach (with a laser spot diameter of 137–233  $\mu\text{m}$ ). Laser pulse rates of 5 Hz in combination with a laser fluence of  $5 \text{ J cm}^{-2}$ , short laser wavelength ( $\lambda = 193 \text{ nm}$ ) and aperture imaging optics were used to attain controlled calcite ablation ( $c. 1 \mu\text{m s}^{-1}$ ) in a He ablation medium (Egginis *et al.* 1998).

The gas flow and electrostatic lens settings were optimized for maximum Sr sensitivity and peak shape while ablating a modern *Tridachna* clam shell, which has a measured  $^{87}\text{Sr}/^{86}\text{Sr}$  value of  $0.709143 \pm 15$  (Woodhead *et al.* 2005). *Tridachna* was additionally used to monitor instrument reproducibility and accuracy. For 22 analyses of *Tridachna*, the average  $^{87}\text{Sr}/^{86}\text{Sr}$  ratio was  $0.709149 \pm 38$  ( $2\sigma$ ). Further details of analytical procedures are given in Barker *et al.* (2006).

### *Trace element analyses*

*Host rock.* The trace element compositions of the carbonate component of limestone host rocks were measured by solution collector inductively coupled plasma mass spectrometry (ICP-MS). A known amount of approximately 50–60 mg of rock powder was placed into a clean Teflon® screw-cap vial. To separate only the carbonate component of the limestones, 1 ml of distilled 1 M acetic acid

was added to each beaker resulting in immediate, gentle effervescence. The beakers were allowed to rest for 2 h at room temperature, and a further 1 ml of acetic acid was added, after which effervescence ceased. The resulting mixture of solution and sediment was centrifuged in clean tubes, and the liquid was drawn off, dried on hot plates and taken up in around 100 ml of 2% HNO<sub>3</sub> for analysis. Trace elements were measured using a quadrupole ICP-MS (Agilent 7500s) running in solution mode. Multiple major and trace elements (<sup>9</sup>Be, <sup>23</sup>Na, <sup>25</sup>Mg, <sup>29</sup>Si, <sup>31</sup>P, <sup>45</sup>Sc, <sup>49</sup>Mn, <sup>57</sup>Fe, <sup>75</sup>As, <sup>85</sup>Rb, <sup>86</sup>Sr, <sup>89</sup>Y, <sup>115</sup>In, <sup>137</sup>Ba, <sup>139</sup>La, <sup>140</sup>Ce, <sup>141</sup>Pr, <sup>146</sup>Nd, <sup>147</sup>Sm, <sup>151</sup>Eu, <sup>158</sup>Gd, <sup>163</sup>Dy, <sup>165</sup>Er, <sup>166</sup>Er, <sup>174</sup>Yb, <sup>175</sup>Lu, <sup>185</sup>Re, <sup>208</sup>Pb, <sup>209</sup>Bi, <sup>232</sup>Th, <sup>238</sup>U) were analysed, with multiple internal standards (Be, As, In, Re, Bi) to monitor instrument performance and drift.

**Carbonate veins.** Veins were analysed for trace element compositions using a multiple-spot analysis, laser ablation ICP-MS approach. Samples were analysed using a pulsed ArF Excimer laser ( $\lambda = 193$  nm) and a quadrupole ICP-MS (Agilent 7500s; Eggins *et al.* 1998). Samples were pre-cleaned with ethanol. Every vein sample was analysed between three and 10 times using a 70  $\mu\text{m}$  laser spot, and an average composition was determined (results reported in Supplementary material SUP18492). This approach has some drawbacks, particularly regarding zoning of trace elements within individual crystals in carbonate veins. However, this approach was chosen to: (a) avoid inclusions within veins; (b) minimize sample preparation time; and (c) allow veins with complex internal fabrics to be documented more completely. Multiple major and trace elements (<sup>23</sup>Na, <sup>24</sup>Mg, <sup>29</sup>Si, <sup>43</sup>Ca, <sup>44</sup>Ca, <sup>45</sup>Sc, <sup>49</sup>Mn, <sup>57</sup>Fe, <sup>85</sup>Rb, <sup>88</sup>Sr, <sup>89</sup>Y, <sup>138</sup>Ba, <sup>139</sup>La, <sup>140</sup>Ce, <sup>141</sup>Pr, <sup>146</sup>Nd, <sup>147</sup>Sm, <sup>153</sup>Eu, <sup>158</sup>Gd, <sup>163</sup>Dy, <sup>166</sup>Er, <sup>174</sup>Yb, <sup>208</sup>Pb, <sup>232</sup>Th, <sup>238</sup>U) were simultaneously analysed during laser sampling by repeated, rapid sequential peak hopping, with a mass spectrometer cycle time of 0.65 s. Data reduction followed established protocols for time-resolved analysis (Longerich *et al.* 1996), with NIST 612 standard (values of Pearce *et al.* 1997), analysed before and after every six samples, and <sup>43</sup>Ca was used as an internal standard. Laser pulse rates of 5 Hz in combination with a laser fluence of 5 J cm<sup>-2</sup>, short laser wavelength ( $\lambda = 193$  nm) and aperture imaging optics were used to attain controlled calcite ablation (*c.* 1  $\mu\text{m s}^{-1}$ ) in a He ablation medium (Eggins *et al.* 1998).

### Vein and wall-rock chemistry

Characterizing the isotopic and trace element composition of a heterogeneous host rock is a challenging problem. For example, it is difficult to

determine the overall oxygen or strontium isotope composition of a calcareous shale because small variations in the proportion of carbonate:silicate minerals may cause significant changes in Sr or O isotope ratios. In addition, it is not feasible to characterize each individual bed in an interbedded limestone–shale unit and then produce an ‘average’ isotopic composition. The majority of veins in the Taemas Vein Swarm are calcite, with minor quartz. Cox (2007) found that the siliciclastic Majorgong Formation had no effect on the oxygen isotope composition of fluids migrating through this unit. Therefore, it was decided to characterize only the *carbonate* component of host rocks via weak acid extraction of carbonate. In particular, extracting only the Rb-poor carbonate component of host rocks means that no age correction is required to determine <sup>87</sup>Sr/<sup>86</sup>Sr values at the time of hydrothermal vein growth (Faure & Powell 1972).

Distal limestone samples (more than 50 m from significant veining) have  $\delta^{18}\text{O}$  between 23 and 25‰,  $\delta^{13}\text{C}$  of  $-0.5$  to  $+3.0\text{\textperthousand}$  (Cox 2007), and <sup>87</sup>Sr/<sup>86</sup>Sr ratios between 0.70815 and 0.70828 (Table 2), which are consistent with sea-water values for the Early Devonian (Veizer *et al.* 1999). Host rocks measured within about 1 mm–1 cm of vein margins have a broader range of  $\delta^{18}\text{O}$ , varying between 14 and 24‰ (Cox 2007). Depleted  $\delta^{18}\text{O}$  margins are usually a few centimetres wide, except around a fault zone at the bottom of the Cavan Bluff Limestone (Fig. 4), where  $\delta^{18}\text{O}$ -depleted zones are several metres wide (Cox 2007).

A few veins (less than 10) have  $\delta^{13}\text{C}$  values up to 11‰ lower than is typical for the unaltered host rocks. Vein carbonate  $\delta^{18}\text{O}$  values have significant variation, from roughly 0 to 25‰. <sup>87</sup>Sr/<sup>86</sup>Sr in vein calcite typically varies between 0.70820 and 0.70865. This range is significantly greater than the range for <sup>87</sup>Sr/<sup>86</sup>Sr in host-rock calcite (0.70815–0.70830). In general, Sr isotope ratios show no systematic relationship to  $\delta^{18}\text{O}$  (Fig. 8) or  $\delta^{13}\text{C}$

**Table 2.** Host-rock carbonate Sr isotope ratios (and associated errors) as measured by TIMS

Sample	<sup>87</sup> Sr/ <sup>86</sup> Sr	$\pm 2\sigma$
Cavan Bluff host rock 1	0.70828	0.00003
Cavan Bluff host rock 2	0.70828	0.00002
Spirifer yassensis host rock 1	0.70826	0.00003
Spirifer yassensis host rock 2	0.70826	0.00001
Currajong host rock 1	0.70821	0.00002
Currajong host rock 2	0.70815	0.00003
Bloomfield host rock 1	0.70825	0.00002
Bloomfield host rock 2	0.70826	0.00003
Receptaculites host rock 1	0.70821	0.00002
Receptaculites host rock 2	0.70819	0.00001

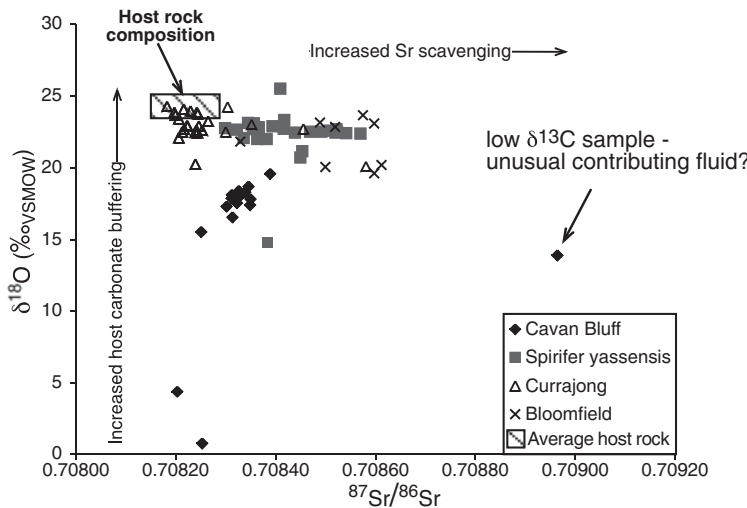


**Fig. 8.** Graph of Sr v. oxygen isotope compositions for veins in different stratigraphical units. The striped box represents the compositional range of the host-rock carbonate.

values, although, in individual localities, correlations are observed between  $\delta^{18}\text{O}$  and Sr isotope ratios (Fig. 4).

Oxygen isotope compositions from calcite and quartz inferred to have grown in equilibrium (i.e. intergrown fibrous quartz and calcite) suggest fluid temperatures of between 100 and 250 °C (Table 3 and Fig. 9) (thermometer of Zheng 1993).

Host-rock carbonates have variable Mg concentrations, particularly in the Cavan Bluff Limestone (see Table 4 for calcite trace element compositions in host rocks). In general, the CBL has higher concentrations of Mg, Mn, Sc, Y and the REEs. Sr concentrations are relatively constant throughout

the Murrumbidgee Group (1000–2000 ppm). The massive Currajong and Receptaculites limestones generally have lower concentrations of most trace elements in comparison to the interbedded limestone–shale members (Cavan Bluff, Spirifer yassensis and Bloomfield limestones). Host-rock REE, Y and Sc concentrations, and REE patterns, are similar to those measured in Devonian limestones by Nothdurft *et al.* (2004).

Vein calcites have Mn concentrations (50–800 ppm) that are similar to those of host limestone calcite (50–900), whereas Sr concentrations (1000–15 000 ppm) are generally higher than those of host-rock carbonates, particularly for veins within

**Table 3.** Oxygen isotope ratios ( $\delta^{18}\text{O}$ , VSMOW) for coexisting quartz and calcite fibres from two different samples

Sample	Qtz $\delta^{18}\text{O}_{(\text{VSMOW})}$	Cct $\delta^{18}\text{O}_{(\text{VSMOW})}$
CL12-7	26.8	24.1
CL12-5	27.1	23.8
CL12-4	25.8	24.0
Cjcrk-C3	26.0	23.8
Cjcrk-C4	26.1	23.8
Cjcrk-C5	26.9	23.9
Cjcrk-C6	27.1	23.8
Cjcrk-C7	26.9	25.0
Cjcrk-J1	27.1	23.9
Cjcrk-J2	25.5	23.9
Cjcrk-Ka	26.1	23.6
Cjcrk-Kb	27.1	23.6

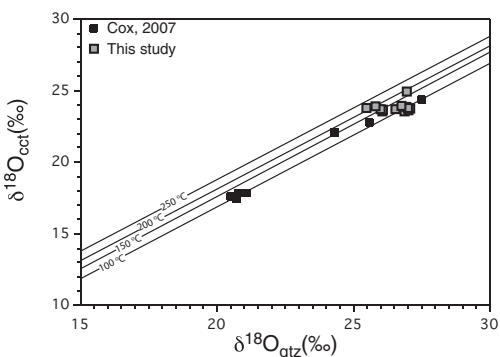


**Fig. 9.** Quartz–calcite oxygen isotope pairs ( $\delta^{18}\text{O}$ , relative to VSMOW) plotted on temperature contours derived from Zheng (1993). Black squares are data from Cox (2007); grey squares are data from this study.

**Table 4.** Host-rock carbonate trace element composition for selected trace elements (concentrations given in parts per million, ppm)

Element	CBHR1	CBHR2	SP1	SP2	CJ1	CJ2	BL1	BL2	RCP1	RCP2
Mg	57 783	9767	7165	4931	3395	5821	2526	1921	2529	1848
Sc	4.29	2.67	1.47	1.59	0.61	0.40	1.72	1.50	1.28	0.90
Mn	1026	821	312	118	63	47	284	476	154	160
Fe	1264	1805	2500	3500	2105	2014	2326	2183	1848	1593
Rb	1.10	0.54	0.60	0.63	0.13	0.15	0.63	0.52	0.50	0.42
Sr	1556	1478	1123	1647	1078	2182	1805	1808	1057	910
Y	20.13	19.34	5.77	3.86	2.40	1.09	5.31	6.17	2.93	2.36
Ba	39.21	38.13	10.21	8.18	6.10	6.61	9.51	8.70	6.81	5.81
La	16.86	19.43	5.43	3.93	1.46	1.00	4.94	4.18	3.10	2.25
Ce	37.63	42.39	12.33	8.95	3.33	1.98	11.17	10.56	6.71	4.93
Pr	4.04	4.48	1.51	1.12	0.36	0.21	1.46	1.47	0.79	0.59
Nd	16.99	18.08	6.19	4.57	1.48	0.84	6.19	6.70	3.19	2.36
Sm	4.02	3.94	1.32	0.91	0.33	0.19	1.27	1.50	0.62	0.47
Eu	0.98	0.89	0.29	0.20	0.08	0.04	0.36	0.62	0.16	0.11
Gd	4.17	4.01	1.26	0.83	0.38	0.18	1.16	1.38	0.58	0.45
Tb	0.65	0.61	0.19	0.12	0.06	0.03	0.17	0.20	0.09	0.07
Dy	3.88	3.55	1.09	0.69	0.37	0.17	0.97	1.12	0.50	0.41
Ho	0.77	0.70	0.21	0.13	0.08	0.04	0.20	0.21	0.10	0.08
Er	2.03	1.83	0.54	0.35	0.21	0.09	0.49	0.51	0.27	0.21
Yb	1.69	1.40	0.42	0.30	0.18	0.08	0.41	0.37	0.21	0.18
Lu	0.23	0.20	0.06	0.04	0.03	0.01	0.06	0.05	0.03	0.02
Pb	3.79	2.81	1.23	0.89	0.75	0.24	1.06	1.26	0.66	0.62
Th	1.24	1.56	0.62	0.83	0.31	0.15	0.71	0.89	0.34	0.25
U	0.38	0.64	1.99	1.38	1.51	0.75	0.49	0.24	0.62	1.12

CBHR, Cavan Bluff Limestone; SP1 and SP2, Spirifer yassensis Limestone; CJ1 and CJ2, Currajong Limestone; BL1 and BL2, Bloomfield Limestone; RCP1 and RCP2, Receptaculites Limestone.

the CBF. Vein carbonate has highly variable Sc, Y and REE concentrations.

#### Chemical variations in vein composition with stratigraphical position

Vein  $\delta^{18}\text{O}$  increases with stratigraphical height through the Murrumbidgee Group (Fig. 10). However, variations in vein  $\delta^{18}\text{O}$  values are seen at any one stratigraphical level, with veins (exceptionally) having approximately 10%  $\delta^{18}\text{O}$  variation. Veins in the Currajong Limestone have slightly lower  $^{87}\text{Sr}/^{86}\text{Sr}$  ratios than veins in the interbedded limestone–shale units (Fig. 10). Below the Cavan Bluff Limestone, vein carbonate  $^{87}\text{Sr}/^{86}\text{Sr}$  is slightly lower than CBL  $^{87}\text{Sr}/^{86}\text{Sr}$  host-rock carbonate compositions. However, within the CBL, vein carbonate is slightly higher, or in equilibrium with, the host-rock carbonate with respect to  $^{87}\text{Sr}/^{86}\text{Sr}$ .

Within the SYL, veins have higher  $^{87}\text{Sr}/^{86}\text{Sr}$  (0.7083–0.7086) than host-rock carbonate (0.70826).  $^{87}\text{Sr}/^{86}\text{Sr}$  decreases with increasing stratigraphical height towards the Currajong Limestone. Within the CJL, vein calcites have  $^{87}\text{Sr}/^{86}\text{Sr}$  ratios (0.70817–0.7083) that are generally close to equilibrium with those of host-rock

carbonate ( $^{87}\text{Sr}/^{86}\text{Sr} = 0.70815\text{--}0.70821$ ). However, veins in the interbedded limestones and shales of the immediately overlying Bloomfield Limestone have calcite  $^{87}\text{Sr}/^{86}\text{Sr}$  values (0.7083–0.7087) elevated above those of host-rock carbonate ( $^{87}\text{Sr}/^{86}\text{Sr} = 0.70825$ ).

In the interbedded limestone–shale lithologies, veins have the most variable trace element concentrations, particularly in the Cavan Bluff Limestone (Fig. 11). Generally, trace element concentrations in vein carbonate decrease with increasing stratigraphical height (except for Mg). Vein carbonate Sr concentrations are generally significantly higher (around 2000–10 000 ppm) than host-rock carbonate Sr concentrations (*c.* 1000–3000 ppm). Pb concentrations in veins are consistently lower than Pb concentrations in host-rock carbonate. Sc, Y and heavy REE (HREE) concentrations are generally similar, or lower, than host-rock carbonate. Light REE (LREE) concentrations decrease with increasing stratigraphical height, whereas the HREEs show a more limited concentration decrease with increasing stratigraphical height. Chondrite-normalized (values of McDonough & Sun 1995) REE patterns in Cavan Bluff veins are generally LREE-enriched, whereas veins higher in

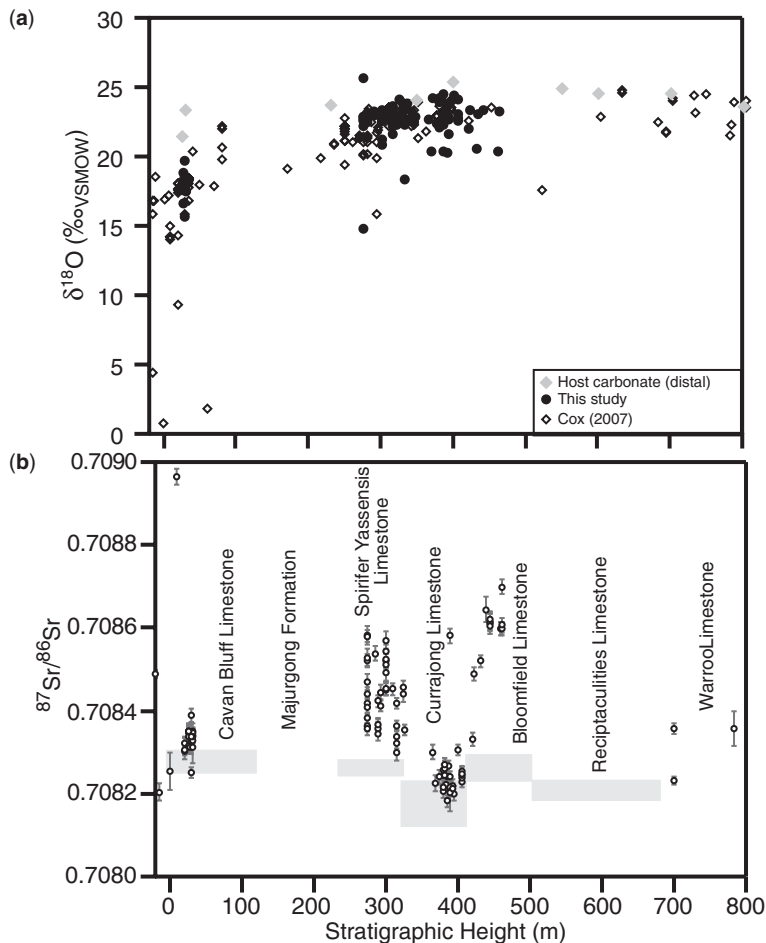


**Fig. 10.** (a) Host-rock carbonate (grey data points: Cox 2007) and vein carbonate (open squares are data from Cox 2007; black symbols, this study)  $\delta^{18}\text{O}$  values with stratigraphical height through the Murrumbidgee Group and (b)  $^{87}\text{Sr}/^{86}\text{Sr}$  as a function of stratigraphical height through the Murrumbidgee Group.

stratigraphy in the SYL and C JL become relatively depleted in LREE.

#### *Chemical variations within and between outcrops*

Veins were assessed on an outcrop-by-outcrop, as well as within-outcrop, scale to examine how fluid–rock reaction varies between veins in a similar host rock. Figure 4 shows the location, vein type and isotopic compositions of different veins (fault, bedding-parallel and extension) from a fold–fault complex in the CBL. Notable is that  $\delta^{18}\text{O}$  varies by approximately 5‰, and  $^{87}\text{Sr}/^{86}\text{Sr}$  varies between 0.70825 and 0.70846. A small

extension vein isolated within a single limestone bed (probably formed during flexural flow) shows higher  $^{87}\text{Sr}/^{86}\text{Sr}$  and  $\delta^{18}\text{O}$ , whereas bedding-parallel and fault veins show some of the lowest  $\delta^{18}\text{O}$  values and  $^{87}\text{Sr}/^{86}\text{Sr}$  ratios.

Figure 12a, b illustrates the structural setting, and Sr and O isotope ratios, of veins from distinct but closely spaced outcrops of folded *Spirifer yassensis* Limestone at Kangaroo Flat (locality 1 in Fig. 1, which is also shown in Fig. 3). These outcrops represent one of the few locations in which the chemistry of veins from the same stratigraphical level, but different structural settings, may be compared (see highlighted regions in Fig. 3). Site A (Fig. 12a) has a bedding-parallel vein developed within an asymmetrical syncline–anticline pair.

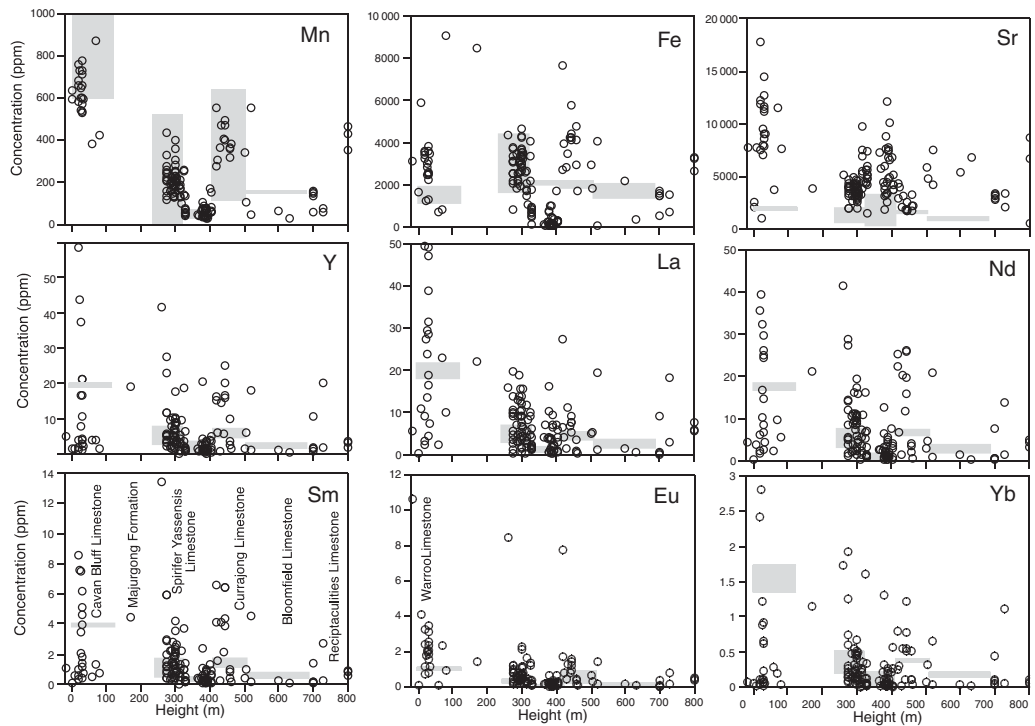


**Fig. 11.** Mg, Mn, Fe, Sr, Y, La, Ce, Nd, Sm, Eu, Gd and Yb concentrations in host-rock carbonate (grey squares) plotted as the range determined for the two samples analysed from each limestone member (see Table 3), and carbonate veins (black circles) with stratigraphical height through the Murrumbidgee Group (see Supplementary Appendix 2). Limestone formations and members are the same as in Figure 10.

Site B (Fig. 12b) is at the hinge zone of an upright, close fold containing predominantly bedding-parallel veins, with several small dilatational jogs and late bedding-perpendicular extension veins inferred to be related to limb-parallel stretching.

Within both outcrops, vein carbonate  $\delta^{18}\text{O}$  varies between 20 and 25‰ for most veins (except for a late strike-slip fault vein: 14.7‰), and vein  $\delta^{18}\text{O}$  values for the two outcrops are statistically indistinguishable at the 95% confidence level ( $P$  value = 0.63, Mann–Whitney test). However, the vein cluster at ‘Site A’ (Fig. 12a) has consistently lower  $^{87}\text{Sr}/^{86}\text{Sr}$  ratios than the ‘Site B’ (Fig. 12b) vein cluster ( $^{87}\text{Sr}/^{86}\text{Sr}$   $P$  value = 0.016) (Fig. 13). These two different vein clusters also have significantly different concentrations of Mn, Fe, Sr and Eu. Veins at ‘Site A’ have higher Mn, Fe and Eu concentrations, and lower Sr concentrations ( $P$  values for Mann–Whitney test: Mn = <0.0001, Fe = <0.0001, Sr = 0.0009, Eu = 0.0133) (Fig. 13). For normalized REE patterns, both outcrops have LREE-enriched patterns, with veins at ‘Site A’ having a more positive Eu anomaly than veins at ‘Site B’.

#### Vein-type variations

Approximately 80 different bedding-parallel, extension and fault veins were analysed from the Spirifer yassensis and Currajong limestones. Within the SYL,  $\delta^{18}\text{O}$  in vein calcite varies between 14.7 and 25.2‰, with the majority of veins having  $\delta^{18}\text{O}$  values of between 22 and 25‰. There is no apparent relationship between O isotope composition and vein type. Strontium isotope values ( $^{87}\text{Sr}/^{86}\text{Sr}$ ) show no relationship to the vein type (Fig. 14). Similarly, all veins within the CJL have  $\delta^{18}\text{O}$  values of 20–25‰, with the majority of values clustering between 22 and 24‰. However,  $^{87}\text{Sr}/^{86}\text{Sr}$  values systematically vary according to vein type, with extension veins having lower  $^{87}\text{Sr}/^{86}\text{Sr}$  values than most fault or bedding-parallel veins (Fig. 14).

Similar trends are observed for trace elements, with veins in the SYL having a broad range of trace element compositions, with no relationship observed between vein type and trace element concentration (Fig. 15). In comparison, extension veins within the CJL have lower concentrations of most

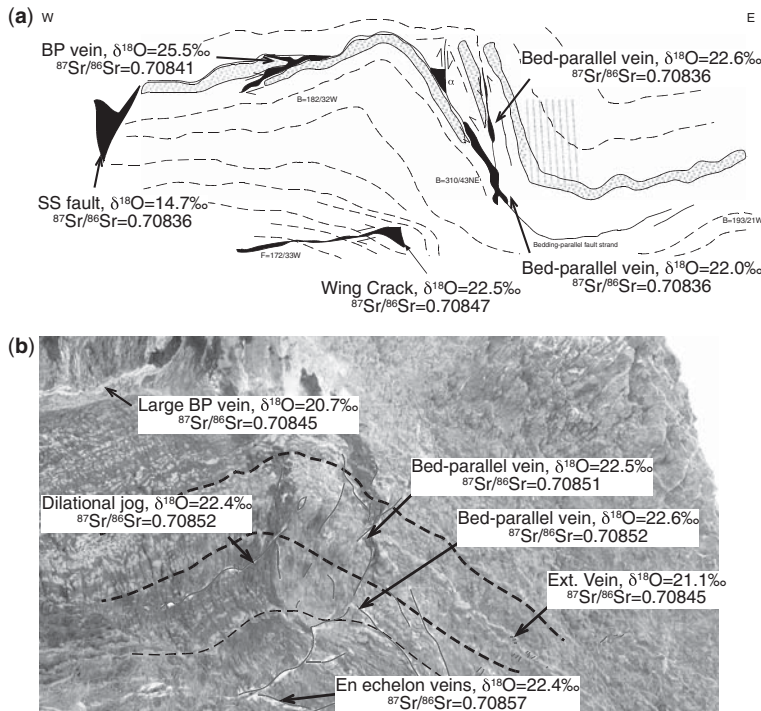


**Fig. 12.** Photograph panorama and interpretative sketch showing a bedding-parallel vein and other faults at 'Kangaroo Flat' on the eastern side of Taemas Peninsula (locality 1 on Fig. 1). **(a)** Outcrop at location (12a) in Figure 3. The outcrop is approximately 40 m wide. Bedding traces are dashed lines, and a dolomitic marker bed is shown as hatched grey. The faults are solid black lines, and regions of calcite mineralization are thicker zones of solid black. Note the decoupled bedding and associated wing crack (bottom of the sketch). Note that the  $\delta^{18}\text{O}$  and  ${}^{87}\text{Sr} / {}^{86}\text{Sr}$  compositions of specific veins are marked. **(b)** Outcrop at location (12b) in Figure 3, showing an antitcline in *Spirifer yassensis* Limestone containing multiple bedding-parallel and extension veins. The  $\delta^{18}\text{O}$  and  ${}^{87}\text{Sr} / {}^{86}\text{Sr}$  compositions of specific veins are marked.

trace elements compared to fault or bedding-parallel veins (Fig. 16). In particular, REE concentrations are lower in extension veins than in bedding-parallel or fault veins.

Extension veins in the Currajong Limestone have Sr isotope and trace element compositions that are most similar to host-rock carbonate compositions. In comparison, all veins in the SYL have a broad range of Sr isotope ratios and trace element concentrations, which are generally elevated above host-rock carbonate compositions. Many extension veins in the CJL are related to fold limb-parallel stretching. In comparison, most extension veins in the *Spirifer yassensis* Limestone are associated with bedding-discordant fault zones. The fluid that migrated through late extension veins in the CJL was apparently significantly more influenced by local host rock than the fluid from which fault veins or bedding-parallel veins formed.

## Discussion

The isotopic and trace element composition of hydrothermal calcite veins found within fault–fracture systems will reflect a variety of factors, including changes in fluid source, fluid-flow pathways, and the intensity of fluid–rock reaction in both time and space. The veins of the Taemas Vein Swarm record spatial and temporal variations in the composition of hydrothermal fluids responsible for the formation of the vein swarm.

### Fluid sources

If it is assumed that calcite precipitated in equilibrium with the parent fluid, and the fluid temperature can be estimated, then the  $\delta^{18}\text{O}$  of vein calcite may be used to determine the isotopic composition of the parent fluid. Quartz–calcite oxygen isotope pairs (see Fig. 10) (Cox 2007) suggest fluid

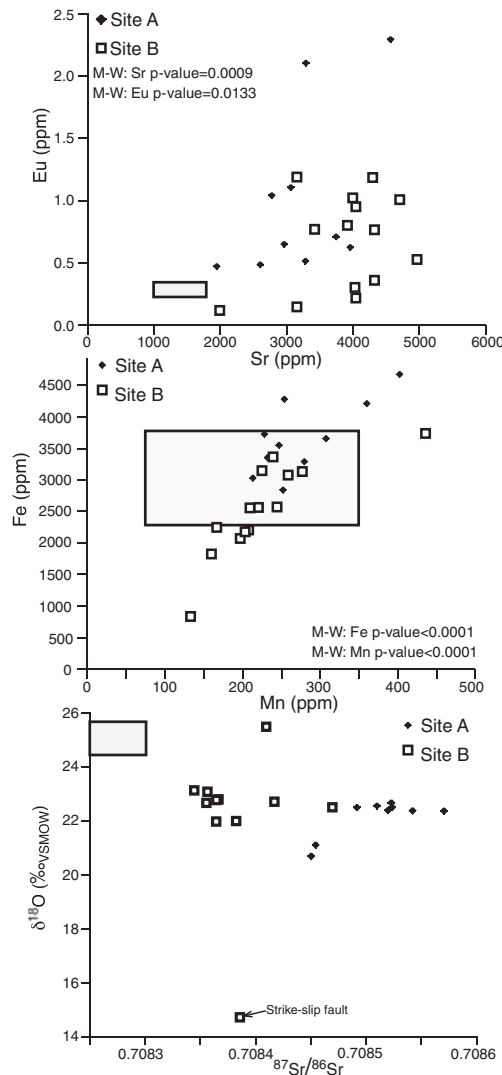


**Fig. 13.** Comparison of  $\delta^{18}\text{O}$  and  $^{87}\text{Sr}/^{86}\text{Sr}$ , and Sr, Eu, Mn and Fe concentrations for two vein clusters at the same stratigraphical level in the *Spirifer yassensis* Limestone (see also Figs 3 & 12). Rectangles show range of host rock compositions.

temperatures of 100–250 °C, with the presence of illite implying temperatures of less than 200 °C (Cox 2007). Minimum  $\delta^{18}\text{O}$  values measured in veins at the base of the Cavan Bluff Limestone are about 0 to +2‰ (Cox 2007). At temperatures of 100–200 °C, this implies that fluid  $\delta^{18}\text{O}$  was between –14 and –8‰ (Zheng 1999). Such low  $\delta^{18}\text{O}$  values are consistent with a meteoric fluid source (Sheppard 1986). To form a meteoric fluid with these low  $\delta^{18}\text{O}$  values, the meteoric fluid

must have been sourced at either high latitude (*c.* 50–60°), or significant altitude (2–4 km) (Bowen & Wilkinson 2002).

Several veins, or sections of individual veins have unusual  $^{87}\text{Sr}/^{86}\text{Sr}$  and  $\delta^{13}\text{C}$  values compared to the majority of veins in the TVS (e.g. sample C2a; see Supplementary material SUP18492). Barker *et al.* (2006) and Cox (2007) attributed localized negative- $\delta^{13}\text{C}$  values to the oxidation of organic matter during fluid–rock reaction. The coupling of elevated  $^{87}\text{Sr}/^{86}\text{Sr}$  and depleted  $\delta^{18}\text{O}$  values implies that a second fluid ‘source’ may have been present. This fluid may have been a residual interstitial pore fluid, which underwent enhanced fluid–rock reaction with iron oxides (causing oxidation of organic carbon) and  $^{87}\text{Sr}$ -enriched clay minerals (i.e. Majurgong Formation or the SYL) prior to mixing with the invading meteoric fluid.

#### Implications of isotopic and trace element data for fluid flow

Assuming that calcite deposition in veins was an equilibrium process, then the  $\delta^{18}\text{O}$  of vein carbonate changes in response to the  $\delta^{18}\text{O}$  of pore fluid, as pore fluid and wall rock undergo progressive reaction (Fig. 17). The conceptual model presented in Figure 17 emphasizes that veins within the same outcrop could have considerably different isotopic compositions (compare vein pair 1 and 3, and vein pair 6 and 7 in Fig. 4), depending on the length of the pathways along which those fluids flow. If a fluid migrates along a tortuous (i.e. long) fluid-flow pathway, then it will have greater opportunity to react with the country rock than fluids that migrate along more direct (i.e. shorter) fluid-flow pathways (see Fig. 17). In addition, fluid-flow pathways may change during deformation as permeability is created and destroyed. Variations in the isotopic composition of different vein types within the same outcrop in the Currajong Limestone indicate that fluids that precipitated calcite in fault and bedding-parallel veins underwent less interaction with host rocks than fluids forming extension veins. This is probably related to the length of fluid-flow pathways, with fault and bedding-parallel veins having (relatively) short flow pathways, causing fluids to undergo less reaction with host rock than fluids that formed extension veins (see Figs 16 & 17). This suggests that bedding-parallel and fault veins act as high-permeability pathways along which fluid could migrate.

The transition from the SYL to CJL is marked by a change from mixed shale–limestone lithology to only limestone, and a coincident decrease in vein  $^{87}\text{Sr}/^{86}\text{Sr}$  ratio. The carbonate content of SYL limestone determined in the laboratory (estimated from loss of weight after acetic acid leaching) is

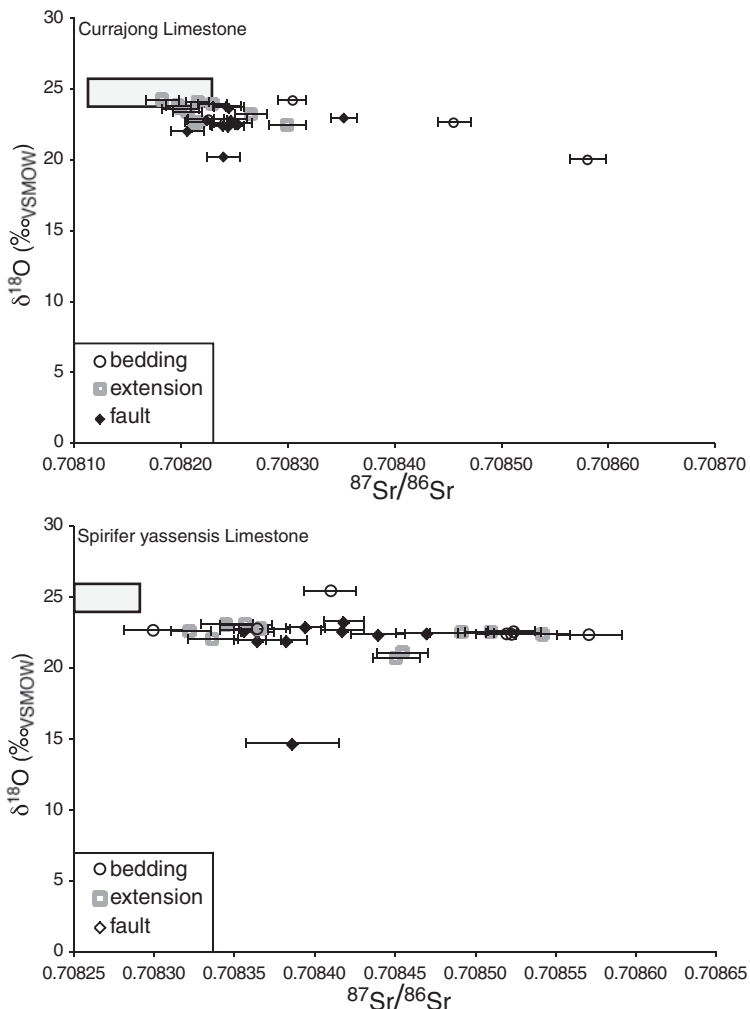


**Fig. 14.**  $\delta^{18}\text{O}$  and  $^{87}\text{Sr}/^{86}\text{Sr}$  isotope composition of extension, bedding-parallel and fault vein in the Currajong and Spirifer Yassensis Limestones. Sr isotope analyses are  $\pm 2$  SE. Rectangles show range of host rock compositions.

85–90% carbonate, while C JL limestones are 97–98% carbonate. The decrease in  $^{87}\text{Sr}/^{86}\text{Sr}$  from the SYL to the C JL is interpreted to be a result of decreasing amounts of other minerals being available for fluid–rock reaction (i.e. increasing amounts of carbonate to buffer fluids). As in the SYL, calcite veins in the Bloomfield Limestone (interbedded limestone–shale immediately above the Currajong Limestone) have  $^{87}\text{Sr}/^{86}\text{Sr}$  values elevated significantly above host-rock calcite, even as little as about 10 m stratigraphically above the Currajong Limestone. This implies that fluids have scavenged trace elements from the surface of other minerals such as layer silicates, and/or feldspars, over relatively short reactive path lengths during

fluid flow. The lack of mineral specific Sr isotope data, and the uncertainty regarding the timing of hydrothermal activity (see Barker *et al.* 2009), make this hypothesis difficult to test further.

During this study a relatively small number of host rocks were analysed. In particular, analyses of shales were not carried out during this study. The consistent isotopic and trace element composition of limestone carbonate throughout the stratigraphical sequence suggests that average carbonate compositions do not vary by a significant degree (except, perhaps, for Mg concentrations), particularly compared to the degree of variation in trace element concentrations in veins. The study of Cox (2007) demonstrated that fluids dominantly

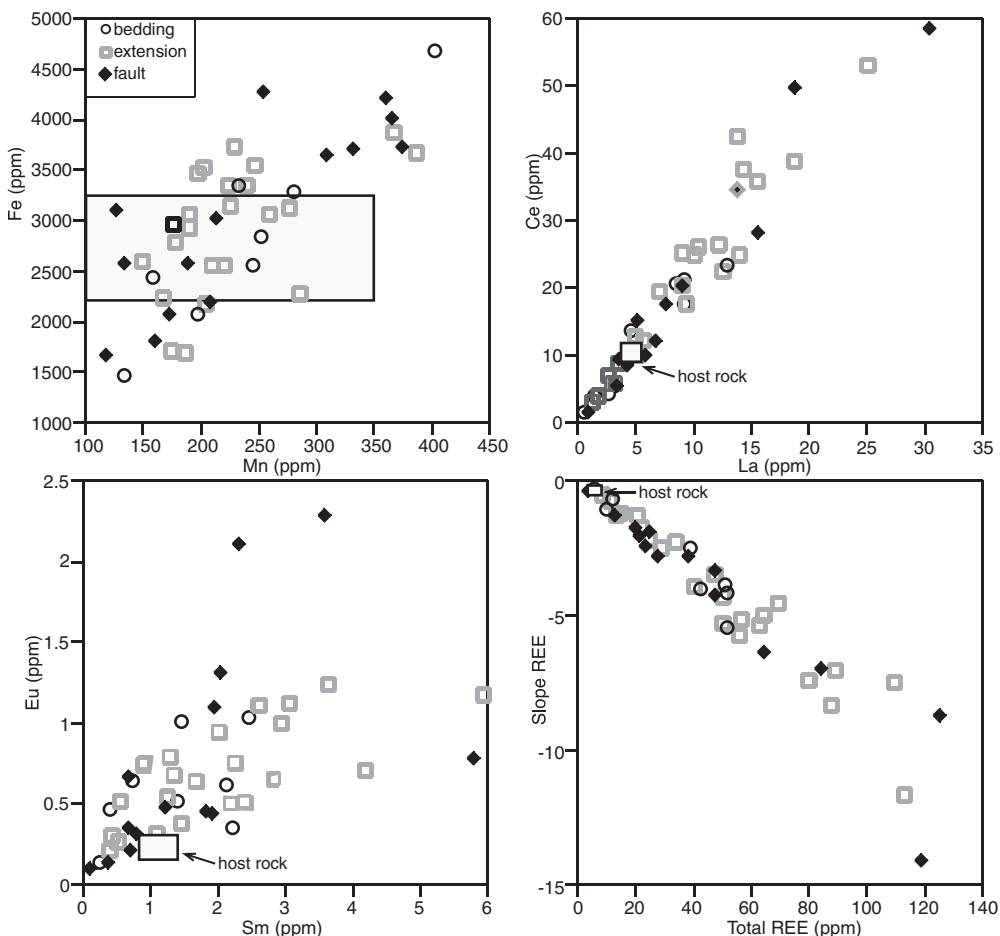


**Fig. 15.** Trace element composition of extension (grey squares), bedding-parallel (black circles) and fault veins (black diamonds) in the *Spirifer yassensis* Limestone. Rectangles show range of host rock compositions.

interacted with carbonate with respect to  $\delta^{18}\text{O}$ . Thus, comparing only vein calcite with only host-rock carbonate minerals allows other controls on vein chemistry (such as the interaction with other minerals and changes in physicochemical conditions) to be assessed.

Trace element concentrations in hydrothermal calcite veins may be affected by several factors, including (Lassey & Blattner 1988; Moller *et al.* 1991; Bau & Moller 1992; DePaolo & Getty 1996; Steefel & Lichtner 1998; Hecht *et al.* 1999; DePaolo 2006):

- spatial and temporal variations in the composition of infiltrating (source) fluid;
- interaction of infiltrating fluid with matrix fluid;
- dissolution of host-rock minerals, releasing lattice-bound trace and minor elements; that is, host carbonate being dissolved;

- scavenging by fluids of trace elements loosely bound to mineral surfaces, particularly layer silicates, releasing adsorbed elements. In addition, shales generally have well-developed cleavages, indicating that layer silicates have deformed and recrystallized, implying that chemical species associated with these minerals would be available for infiltrating fluids during deformation;
- precipitation of hydrothermal minerals (e.g. calcite) leading to coprecipitation of other trace elements, removing those elements from solution;
- sorption of trace elements onto mineral surfaces during fluid migration, removing trace elements from fluids;
- changes in physicochemical conditions (e.g. temperature, pressure, pH, complexing species), which may affect trace element fractionation fluids and vein-forming minerals.

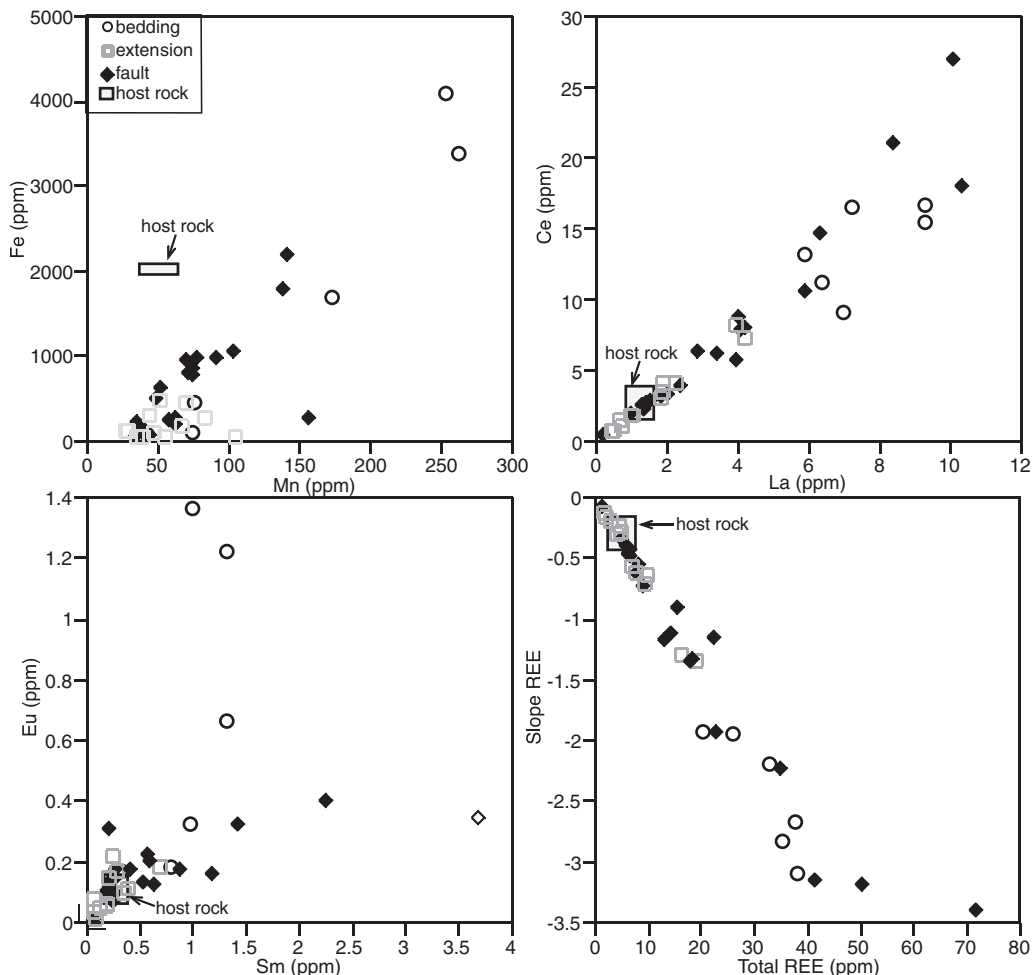


**Fig. 16.** Trace element composition of extension (grey squares), bedding-parallel (black circles) and fault veins (black diamonds) in the Currajong Limestone. Labelled rectangles show range of host rock compositions.

Steefel & Lichtner (1998) and DePaolo (2006) provided models addressing the chemical interaction of host rock, ‘matrix fluid’ and ‘fracture fluid’ during fracture-controlled fluid flow. As fluid migrates through a fracture, diffusion of trace elements occurs between that fluid and the rock matrix. The position of alteration fronts will be dependent on the temperature, fluid-flow rate, diffusion rate, kinetics of reactions and the reactive surface area of minerals. Along any one fracture, these factors will change depending on the fracture aperture, fracture roughness and wall-rock composition. For example, a small cataclastic fault zone, containing pulverized host rock with a high reactive surface area, will react in a different manner to a smooth-sided extension fracture through the same host rock.

Trace element concentrations are highest in veins in the lowest stratigraphical units; that is, those contained within the Cavan Bluff Limestone. This implies that the fluid which infiltrated the base of the Murrumbidgee Group was already enriched in trace elements. Presumably, the trace element composition of fluids infiltrating the base of the CBF reflects fluid–rock interaction that occurred with underlying rocks (i.e. volcanic sediments of the Black Range Group). Notable in some veins within the Cavan Bluff Limestone are elevated Sr concentrations, and veins with extremely positive Eu anomalies that could be produced by the dissolution of Ca-feldspar, which has appreciable concentrations of both Sr and Eu (Schnetzler & Philpotts 1970).

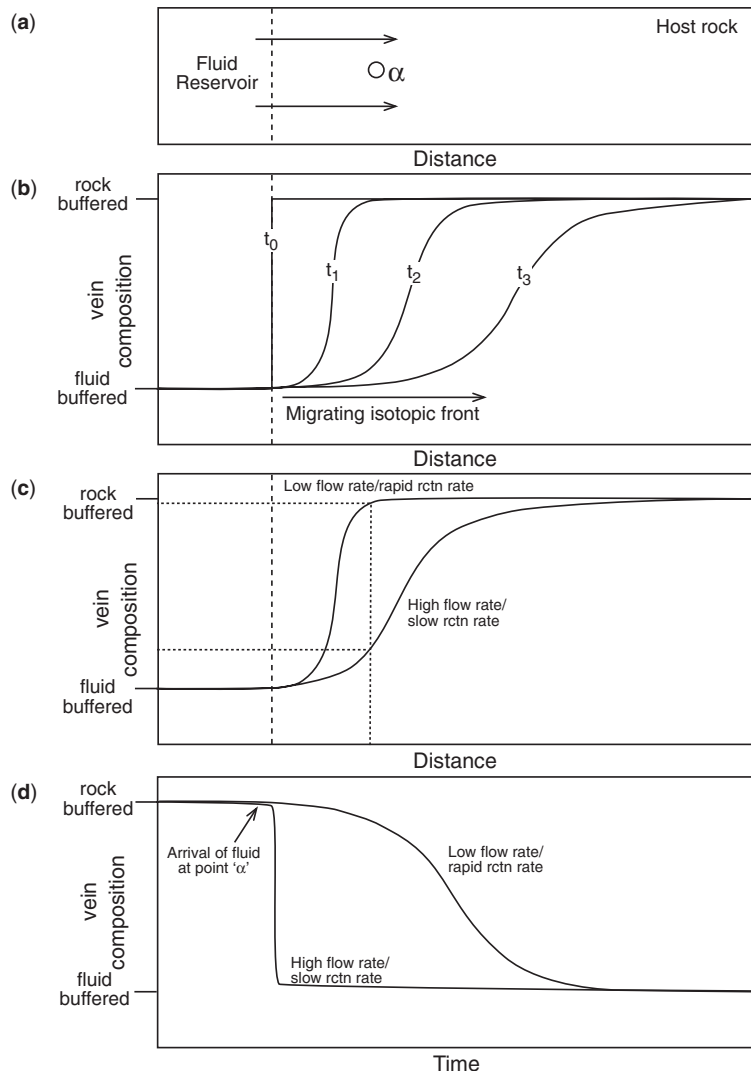


**Fig. 17.** Schematic diagrams showing evolution of vein  $\delta^{18}\text{O}$  compositions with time and space during progressive fluid–rock reaction (modified after Cox 2007). (a) Fluid from a fluid reservoir with a depleted  $\delta^{18}\text{O}$  composition advects through a rock sequence with a less depleted  $\delta^{18}\text{O}$  composition. (b) Evolution of vein  $\delta^{18}\text{O}$  compositions with time ( $t_0, t_1, t_2, t_3$ ) as a low  $\delta^{18}\text{O}$  advects through the rock mass. (c) Illustration of how a vein at the same distance along a fluid-flow pathway could have a markedly different  $\delta^{18}\text{O}$  composition depending on the fluid flow and/or reaction rate between the rock and fluid. (d) Evolution of the  $\delta^{18}\text{O}$  composition of a vein with time at a single point 'α' in (a), depending on the fluid–rock reaction rate. With a more rapid reaction rate, fluid becomes more rapidly buffered by the host-rock carbonate.

When vein REE concentrations are normalized to chondrite values, it is apparent that REE patterns in Cavan Bluff veins are generally LREE-enriched, whereas veins higher in stratigraphy in the SYL and CJL become gradually depleted in LREE (Figs 11, 15 & 16). In hydrothermal fluids, REE fractionation is a function of: (a) sorption and desorption of REEs during the migration of fluids along particle

surfaces; and (b) co-precipitation (Bau & Moller 1992). Carbonate and hydroxyl ligands form stronger complexes with HREEs than LREEs (Bau & Moller 1992). In carbonate-dominated hydrothermal solutions (such as those that would be expected in limestones), calcite precipitating from solutions with relatively low  $\text{CO}_3^{2-}$  concentrations will have flatter chondrite-normalized REE patterns than

calcite precipitating from a solution with higher  $\text{CO}_3^{2-}$  concentrations, which will be relatively enriched in the LREEs. This is because in carbonate-poor solutions there will be little difference in the complexing of the light and heavy REEs (Bau 1991; Bau & Moller 1992). If this interpretation is correct, it is suggested that  $[\text{CO}_3^{2-}]$  decreased as fluids migrated upwards through the Murrumbidgee Group, consistent with decreasing fluid pressure as fluids ascended.

### *Implications for fluid-flow pathways and vein development during crustal shortening*

Important conclusions that may be drawn from this study, and the previous studies of the Taemas vein swarm (Barker *et al.* 2006; Cox 2007; Barker *et al.* 2009), are:

- veins formed over an extended period, from early folding until after fold lock-up and cleavage development;
- depleted  $\delta^{18}\text{O}$  ratios in vein carbonate relative to host-rock carbonate indicate that fluid was derived externally to the host rocks;
- reactive transport modelling of oxygen isotope variations by Cox (2007) demonstrate that the systematic increase in vein  $\delta^{18}\text{O}$  and marked O-isotope alteration front in the Taemas Vein Swarm was the result of the buffering of an infiltrating low- $\delta^{18}\text{O}$  fluid by progressive fluid–rock reaction. Fluid flow was restricted largely to fractures with no substantial lateral fluid flow into vein sidewalls;
- analyses of vein  $\delta^{18}\text{O}$  and  $^{87}\text{Sr}/^{86}\text{Sr}$  conducted during this study, and results reported in Barker *et al.* (2006) and Cox (2007), reveal that fluid-flow pathways, path lengths, and/or fluid-flow and fluid–rock reaction rates changed dynamically during the growth of individual veins, and between different veins in the same outcrop. This is probably related to the creation and destruction of permeability during repeated fracture opening and sealing events.

Dynamic switches in fluid-flow pathways are interpreted in terms of fluid flow through a fault–fracture mesh (Hill 1977; Sibson 2001). In such a mesh, it is predicted that fractures will be transiently permeable after fracturing (promoting rapid migration of fluids) and then this permeability will be destroyed (i.e. via hydrothermal mineral deposition), thus creating a dynamic fluid-flow environment.

According to the conditions for tensile failure, fluid pressure must exceed the least compressive stress and the tensile strength of the rock to cause extension fractures to form. In a contractional (i.e. reverse) faulting regime, gently dipping

extension veins imply that: (a) the least compressive stress was approximately vertical; and (b) that the fluid pressure (at least transiently) exceeded the lithostatic pressure (i.e.  $\lambda_v > 1.0$ : Sibson 2001). Additional evidence for transiently high fluid pressures is provided by steeply dipping bedding-parallel slip veins, and severely misoriented bedding-discordant reverse faults. The presence of folded and unfolded laminations in some of these veins suggests that slip continued on these veins throughout fold growth, with some vein dips exceeding  $70^\circ$ . For slip to continue at severe misorientation on incohesive reverse faults requires that fluid pressures exceed supralithostatic levels (Sibson 1985). This constraint must also be met for cohesive faults (Cox 2010). These factors indicate that the formation of the Taemas Vein Swarm was driven by overpressured fluids (cf. Cox 2007).

Differential stress levels must have varied significantly during deformation (at least on a local scale). Parts of the stratigraphy must have had low differential stress levels at the time of vein formation to form extension fractures. Mutually overprinting relationships between shear and extension fractures indicate that differential stress values oscillated between  $(\sigma_1 - \sigma_3) < 4T$  and  $(\sigma_1 - \sigma_3) > 5.66T$ , where T is the tensile strength of the rock (Secor 1965; Hancock 1985). Such differential stress variations could be related to the loading and stress release associated with repeated seismic slip events (Sibson 1989).

In active fold-and-thrust belts, strain is accommodated in sedimentary rocks by a combination of folding and thrust faulting (e.g. Shaw & Suppe 1994). Seismic reflection profiles and surface mapping suggest that actively growing folds are intimately related to seismically active faults (e.g. Namson & Davis 1988; Davis *et al.* 1989; Shaw & Suppe 1994). In the Taemas Vein Swarm, timing relationships between bedding-parallel slip veins and overprinting flexural flow and extension veins indicate that early during folding strain was accommodated via flexural-slip folding with associated fluid flow along bedding surfaces. Crack-seal textures in bedding-parallel veins at Taemas indicate that bedding-parallel slip was episodic, suggesting that fold growth occurred episodically. Episodic fold growth and associated faulting probably generate significant fracture permeability in actively deforming fold-thrust belts (Finkbeiner *et al.* 1997). Later in folding, once fold lock-up occurred, fluid flow may have localized more along bedding-discordant faults and extension vein networks associated with fold limb stretching, rather than being isolated along bedding planes. Where bedding-parallel veins linked with discordant fault veins (i.e. thrust faults cutting through fold hinges), it is likely that

some bedding-parallel veins remained active as faults, even though fold tightening had essentially ceased.

## Conclusions

The Taemas Vein Swarm preserves evidence of hydrothermal vein growth during fold growth. Vein formation was intimately related to space created during folding, with vein growth active from the early to the latest stages of fold growth. Mutually cross-cutting relationships between veins indicate that vein growth was intermittent, and that veins formed as localized stress fields underwent significant changes in both orientation and magnitude.

Subhorizontal extension fractures and severely misoriented faults indicate that fluid pressures intermittently exceeded lithostatic levels over (at least) local regions of the deforming crust. Individual veins grew incrementally and preserve a variety of textures (fibrous, massive and laminated), and indicate that vein opening and mineral deposition rates varied significantly. Mutually cross-cutting veins and incrementally developed vein textures imply that high-permeability fluid-flow pathways varied dynamically through time and space.

A progressive increase in vein  $\delta^{18}\text{O}$  with increasing height through the Murrumbidgee Group is attributed to progressive buffering of  $^{18}\text{O}$ -depleted fluids by reaction with host-rock carbonate. Vein  $\delta^{18}\text{O}$  values imply that the invading fluid had  $\delta^{18}\text{O}$  compositions consistent with a meteoric fluid source. The isotopic and trace element composition of hydrothermal veins is variable across stratigraphy, between outcrops, within individual outcrops and within individual hydrothermal veins. Variability in O and Sr isotope ratios within and between veins is attributed to variable fluid–rock reaction along dynamically changing fluid-flow pathways, caused by episodic failure, permeability enhancement and transitory fluid flow accompanying episodic slip events within a fault–fracture mesh.

The isotopic and trace element composition of syntectonic veins reflect different rates of fluid–rock reaction for different elements and isotopic systems during hydrothermal fluid flow. Strontium isotope ratios ( $^{87}\text{Sr}/^{86}\text{Sr}$ ) indicate that fluids react with host-rock carbonate, but also scavenge Sr from Sr-enriched minerals (e.g. illite), within shale beds over short reactive path lengths. Trace element concentrations generally decrease with increasing stratigraphical height. Rare earth element concentrations and patterns are influenced by progressive calcite precipitation and sorption along fluid-flow pathways, and changes in REE complexation in solution.

Thanks to K. and S. Kilpatrick for land access and their friendship. Thanks to M. Gagan for facilitating access to stable isotope analyses, and J. Cali and H. Scott-Gagan for providing able technical help with stable isotope mass spectrometry. S. Eggin and L. Kinsley provided assistance with Sr isotope analyses. Thanks to C. Allen, M. Shelley and C. Magee for assistance with trace element LA-ICP-MS, and M. Norman for help with solution ICP-MS analysis. The Mervyn and Katalin Paterson Fellowship allowed S. L. L. Barker to travel to UNM to carry out analytical work. Thanks to Z. Sharp and V. Atudorei for assistance with quartz stable isotope analysis, and V. Atudorei for hospitality. S. L. L. Barker acknowledges receipt of an Australian Postgraduate Award, and RSES and the ANU for additional scholarship support during his PhD studies. S. F. Cox acknowledges ARC grant DP 0452448. An anonymous reviewer and J. Urai are thanked for helpful reviews, and A. Fagereng is thanked for editorial guidance.

## References

- ABART, R. & POZZORINI, D. 2000. Implications of kinetically controlled mineral-fluid exchange on the geometry of stable-isotope fronts. *European Journal of Mineralogy*, **12**, 1069–1082.
- ABART, R. & SPERB, R. 1997. Grain-scale stable isotope disequilibrium during fluid–rock interaction. 1: series approximations for advective–dispersive transport and first-order kinetic mineral-fluid exchange. *American Journal of Science*, **297**, 679–706.
- BADERTSCHER, N., ABART, R., BURKHARD, M. & McCAGA, A. 2002. Fluid flow pathways along the Glarus Overthrust derived from stable and Sr-isotope patterns. *American Journal of Science*, **302**, 517–547.
- BARKER, S., BENNETT, V., COX, S., NORMAN, D. & GAGAN, M. 2009. Sm–Nd, Sr, C and O isotope systematics in hydrothermal calcite–fluorite veins: implications for fluid–rock reaction and geochronology. *Chemical Geology*, **268**, 58–66.
- BARKER, S., COX, S., EGGIN, S. & GAGAN, M. 2006. Microchemical evidence for episodic growth of antitaxial veins during fracture-controlled fluid flow. *Earth and Planetary Science Letters*, **250**, 331–344.
- BAU, M. 1991. Rare-earth element mobility during hydrothermal and metamorphic fluid–rock interaction and the significance of the oxidation state of europium. *Chemical Geology*, **93**, 219–230.
- BAU, M. & MOLLER, P. 1992. Rare earth element fractionation in metamorphogenic hydrothermal calcite, magnesite and siderite. *Mineralogy and Petrology*, **45**, 231–246.
- BICKLE, M. & MCKENZIE, D. 1987. The transport of heat and matter by fluids during metamorphism. *Contributions to Mineralogy and Petrology*, **95**, 384–392.
- BONS, P. 2000. The formation of veins and their microstructures. In: JESSELL, M. W. & URAI, J. L. (eds) *Stress, Strain and Structure, A Volume in Honour of W.D. Means. Journal of the Virtual Explorer*, 2.
- BOWEN, G. & WILKINSON, B. 2002. Spatial distribution of  $^{18}\text{O}$  in meteoric precipitation. *Geology*, **30**, 315–318.
- BOWMAN, J., WILLETT, S. & COOK, S. 1994. Oxygen isotopic transport and exchange during fluid flow:

- one-dimensional models and applications. *American Journal of Science*, **294**, 1–55.
- BROWNE, I. 1958. Stratigraphy and structure of the Devonian rocks of the Taemas and Cavan areas, Murrumbidgee River, south of Yass, N.S.W. *Journal and Proceedings of the Royal Society of New South Wales*, **4**, 115–128.
- COPLEN, T., KENDALL, C. & HOPPLE, J. 1983. Comparison of stable isotope reference samples. *Nature*, **302**, 236–239.
- COX, S. F. 2005. Coupling between deformation, fluid pressures and fluid flow in ore-producing hydrothermal systems at depth in the crust. *Economic Geology and the Bulletin of the Society of Economic Geologists*, **100**, 39–75.
- COX, S. F. 2007. Structural and isotopic constraints on fluid flow regimes and fluid pathways during upper crustal deformation: an example from the Taemas area of the Lachlan Orogen, south-eastern Australia. *Journal of Geophysical Research*, **112**, B08208, doi: 10.1029/2006JB004734.
- COX, S. F. 2010. The application of failure mode diagrams for exploring the roles of fluid pressure and stress states in controlling styles of fracture-controlled permeability enhancement in faults and shear zones. *Geofluids*, **10**, 217–233.
- CRAMSIE, J., POGSON, D. & BAKER, C. 1975. *Yass 1:100,000 Geological Sheet 8628*. Geological Survey of New South Wales, Sydney.
- DAVIS, T. L., NAMSON, J. & YERKES, R. F. 1989. A cross section of the Los Angeles area; seismically active fold and thrust belt, the 1987 Whittier Narrows earthquake, and earthquake hazard. *Journal of Geophysical Research*, **94**, 9644–9664.
- DEPAOLO, D. 2006. Isotopic effects in fracture-dominated reactive fluid–rock systems. *Geochimica et Cosmochimica Acta*, **70**, 1077–1096.
- DEPAOLO, D. & GETTY, S. 1996. Models of isotopic exchange in reactive fluid–rock systems: implications for geochronology in metamorphic rock. *Geochimica et Cosmochimica Acta*, **60**, 3933–3947.
- DEER, W., HOWIE, R. & ZUSSMANN, J. 1962. *Rock-forming minerals, Non-silicates*, Vol. 5, Longman, London.
- DEER, W., HOWIE, R. & ZUSSMANN, J. 1992. *An Introduction to the Rock-forming Minerals*. 2nd ed., Longman Scientific Technical, Harlow.
- DIETRICH, D., MCKENZIE, J. & SONG, H. 1983. Origin of calcite in syntectonic veins as determined from carbon–isotope ratios. *Geology*, **11**, 547–551.
- DROMGOOLE, E. & WALTER, L. 1990. Iron and manganese incorporation into calcite; effects of growth kinetics, temperature and solution chemistry. *Chemical Geology*, **81**, 311–336.
- EGGINS, S., GRUN, R. ET AL. 2005. In situ U-series dating by laser-ablation multi-collector ICPMS: new prospects for Quaternary geochronology. *Quaternary Science Reviews*, **24**, 2523–2538.
- EGGINS, S., KINSLEY, L. & SHELLEY, J. 1998. Deposition and element fractionation processes during atmospheric pressure laser sampling for analysis by ICP-MS. *Applied Surface Science*, **127–129**, 278–286.
- EPPEL, H. & ABART, R. 1997. Grain-scale stable isotope disequilibrium during fluid–rock interaction; 2, an example from the Penninic-Austroalpin tectonic contact in eastern Switzerland. *American Journal of Science*, **297**, 707–728.
- FAURE, G. & POWELL, J. 1972. *Strontium Isotope Geology*. Springer, New York.
- FINKBEINER, T., BARTON, C. & ZOBACK, M. 1997. Relationships among in-situ stress, fractures and faults, and fluid flow: Monterey formation, Santa Maria basin, California. *American Association of Petroleum Geologists*, **81**, 1975–1999.
- FOWLER, T. 1996. Flexural-slip generated bedding-parallel veins from central Victoria, Australia. *Journal of Structural Geology*, **18**, 1399–1415.
- GARRELS, R. & CHRIST, C. 1982. *Solutions, Minerals and Equilibria*. Freeman, Cooper and Co., San Francisco.
- GAVIGLIO, P. 1986. Crack-seal mechanism in a limestone; a factor of deformation in strike-slip faulting. *Tectonophysics*, **131**, 247–255.
- GERDES, M., BAUMGARTNER, L. & PERSON, M. 1995. One- and two-dimensional models of fluid flow and stable isotope exchange at an outcrop in the Adamello contact aureole, Southern Alps, Italy. *American Mineralogist*, **80**, 1004–1019.
- GLEN, R. 1992. Thrust, extensional and strike-slip tectonics in an evolving Palaeozoic orogen; a structural synthesis of the Lachlan Orogen of southeastern Australia. *Tectonophysics*, **214**, 341–380.
- HANCOCK, P. 1985. Brittle microtectonics: principles and practice. *Journal of Structural Geology*, **7**, 437–457.
- HECHT, L., FREIBERGER, R., GILG, H., GRUNDMANN, G. & KOSTITSYN, Y. 1999. Rare earth element and isotope (C, O, Sr) characteristics of hydrothermal carbonates: genetic implications for dolomite-hosted talc mineralization at Gopfersgrün (Fichtelgebirge, Germany). *Chemical Geology*, **155**, 115–130.
- HILL, D. 1977. A model for earthquake swarms. *Journal of Geophysical Research*, **82**, 1347–1352.
- JESSELL, M., WILLMAN, C. & GRAY, D. 1994. Bedding parallel veins and their relationship to folding. *Journal of Structural Geology*, **16**, 753–767.
- KNOOP, S., KENNEDY, L. & DIPPLE, G. 2002. New evidence for syntectonic fluid migration across the hinterland-foreland transition of the Canadian Cordillera. *Journal of Geophysical Research*, **107**, 2071, doi: 10.1029/2001JB000217.
- KOEHN, D. & PASSCHIER, C. 2000. Shear sense indicators in striped bedding-veins. *Journal of Structural Geology*, **22**, 1141–1151.
- LASSEY, K. & BLATTNER, P. 1988. Kinetically-controlled oxygen isotope exchange between fluid and rock in one-dimensional advective flow. *Geochimica et Cosmochimica Acta*, **52**, 2169–2175.
- LONGERICH, H., JACKSON, S. & GUNTER, D. 1996. Laser ablation inductively coupled plasma mass spectrometric transient signal data acquisition and analyte concentration calculation. *Journal of Analytical Atomic Spectrometry*, **11**, 899–904.
- MATTHÄI, S. 2003. Fluid flow and (reactive) transport in fractured and faulted rock. *Journal of Geochemical Exploration*, **78–79**, 179–182.
- MCCAIG, A., WAYNE, D., MARSHALL, J., BANKS, D. & HENDERSON, I. 1995. Isotopic and fluid inclusion studies of fluid movement along the Gavarnie

- Thrust, Central Pyrenees – reaction fronts in carbonate mylonites. *American Journal of Science*, **295**, 309–343.
- MCCAIG, A., WAYNE, D. & ROSENBAUM, J. 2000. Fluid expulsion and dilatancy pumping during thrusting in the Pyrenees: Pb and Sr isotope evidence. *Geological Society of America Bulletin*, **112**, 1199–1208.
- MCDONOUGH, W. & SUN, S. 1995. The composition of the Earth. *Chemical Geology*, **120**, 223–253.
- MOLLER, P., LUDERS, V., SCHRODER, J. & LUCK, J. 1991. Element portioning in calcite as a function of solution flow rate: a study of vein calcites from the Harz Mountains. *Mineralium Deposita*, **26**, 175–179.
- MUCCI, A. & MORSE, J. 1983. The incorporation of  $Mg^{2+}$  and  $Sr^{2+}$  into calcite overgrowths; influences of growth rate and solution composition. *Geochimica et Cosmochimica Acta*, **57**, 217–233.
- MUCCI, A. & MORSE, J. 1990. Chemistry of low-temperature abiotic calcites: experimental studies on coprecipitation, stability, and fractionation. *Review in Aquatic Sciences*, **3**, 217–254.
- MUELLER, W., AERDEN, D. & HALLIDAY, A. 2000. Isotopic dating of strain fringes. *Science*, **288**, 2195–2198.
- NAMSON, J. S. & DAVIS, T. L. 1988. Seismically active fold and thrust belt in the San Joaquin Valley, Central California. *Geological Society of America Bulletin*, **100**, 257–273.
- NOHTDURFT, L., WEBB, G. & KAMBER, B. 2004. Rare earth element geochemistry of Late Devonian reefal carbonates, Canning Basin, Western Australia: Confirmation of a seawater REE proxy in ancient limestones. *Geochimica et Cosmochimica Acta*, **68**, 263–283.
- OLIVER, N. & BONS, P. 2001. Mechanisms of fluid flow and fluid–rock interaction in fossil metamorphic hydrothermal systems inferred from vein–wallrock patterns, geometry and microstructure. *Geofluids*, **1**, 137–162.
- PEARCE, N., PERKINS, W., WESTGATE, J., GORDON, M., JACKSON, S., NEAL, C. & CHENERY, S. 1997. A compilation of new and published major and trace element data for the NIST SRM 610 and NIST SRM 612 glass reference materials. *Geostandards and Geoanalytical Research*, **21**, 115–144.
- PFIFFNER, O. & RAMSAY, J. 1982. Constraints on geological strain rates: arguments from finite strains in naturally deformed rocks. *Journal of Geophysical Research*, **87**, 311–321.
- RAMSAY, J. 1974. Development of chevron folds. *Geological Society of America Bulletin*, **85**, 1741–1753.
- RAMSAY, J. G. & HUBER, M. 1987. *The Techniques of Modern Structural Geology. Folds and Fracture*, Volume 2. Academic Press, London.
- RYE, D. & BRADBURY, H. 1988. Fluid flow in the crust: an example from a Pyrenean thrust ramp. *American Journal of Science*, **288**, 197–235.
- SCHNETZLER, C. C. & PHILPOTTS, J. A. 1970. Partition coefficients of rare-earth elements between igneous matrix material and rock-forming mineral phenocrysts – II. *Geochimica et Cosmochimica Acta*, **34**, 331–340.
- SECOR, D. T. 1965. Role of fluid pressure in jointing. *American Journal of Science*, **263**, 633–646.
- SHARP, Z. 1990. A laser-based microanalytical method for the in situ determination of oxygen isotope ratios of silicates and oxides. *Geochimica et Cosmochimica Acta*, **54**, 1353–1357.
- SHAW, J. & SUPPE, J. 1994. Active faulting and growth folding in the eastern Santa Barbara Channel, California. *Geological Society of America Bulletin*, **106**, 607–626.
- SHEPPARD, S. 1986. Characterization and isotopic variations in natural waters. In: VALLEY, J., TAYLOR, J. H. P. & O'NEIL, J. (eds) *Stable Isotopes in High Temperature Geological Processes*. Reviews in Mineralogy, **16**, 165–183.
- SIBSON, R. H. 1985. A note on fault reactivation. *Journal of Structural Geology*, **7**, 751–754.
- SIBSON, R. H. 1989. Earthquake faulting as a structural process. *Journal of Structural Geology*, **11**, 1–14.
- SIBSON, R. H. 2001. Seismogenic framework for hydrothermal transport and ore deposition. In: RICHARDS, J. P. & TOSDAL, R. M. (eds) *Structural Controls on Ore Genesis*. Reviews in Economic Geology, **14**, 25–50.
- STEEFEL, C. & LICHTNER, P. 1998. Multicomponent reactive transport in discrete fractures: I. Controls on reaction front geometry. *Journal of Hydrology*, **209**, 186–199.
- STEEFEL, C., DEPAOLO, D. & LICHTNER, P. 2005. Reactive transport modelling: an essential tool and a new research approach for the Earth sciences. *Earth and Planetary Science Letters*, **240**, 539–558.
- TANNER, P. 1989. The flexural-slip mechanism. *Journal of Structural Geology*, **11**, 635–655.
- VEIZER, J., ALA, D. ET AL. 1999.  $^{87}Sr/^{86}Sr$ ,  $\delta^{13}C$  and  $\delta^{18}O$  evolution of Phanerozoic seawater. *Chemical Geology*, **161**, 59–88.
- WASYLENKI, L., DOVE, P. & DE YOREO, J. 2005. Effects of temperature and transport conditions on calcite growth in the presence of  $Mg^{2+}$ : implications for paleothermometry. *Geochimica et Cosmochimica Acta*, **45**, 2311–2323.
- WOODHEAD, J., SWEARER, S., HERGT, J. & MAAS, R. 2005. In situ Sr-isotope analysis of carbonates by LA-MC-ICP-MS: interference corrections, high spatial resolution and an example from otolith studies. *Journal of Analytical Atomic Spectrometry*, **20**, 22–27.
- ZACK, T. & JOHN, T. 2007. An evaluation of reactive fluid flow and trace element mobility in subducting slabs. *Chemical Geology*, **237**, 5–22.
- ZHENG, Y. 1993. Calculation of oxygen isotope fractionation in anhydrous silicate minerals. *Geochimica et Cosmochimica Acta*, **57**, 1079–1091.
- ZHENG, Y. 1999. Oxygen isotope fractionation in carbonate and sulfate minerals. *Geochemical Journal*, **33**, 109–126.
- ZHONG, S. & MUCCI, A. 1995. Partitioning of rare earth element (REEs) between calcite and seawater solutions at 25°C and 1 atm, and high dissolved concentrations. *Geochimica et Cosmochimica Acta*, **59**, 443–453.



# Formation of fault-related calcite precipitates and their implications for dating fault activity in the East Anatolian and Dead Sea fault zones

P. NURIEL<sup>1\*</sup>, G. ROSENBAUM<sup>1</sup>, T. I. UYSAL<sup>2</sup>, J. ZHAO<sup>3</sup>, S. D. GOLDING<sup>1</sup>,  
R. WEINBERGER<sup>4</sup>, V. KARABACAK<sup>5</sup> & Y. AVNI<sup>4</sup>

<sup>1</sup>School of Earth Sciences, The University of Queensland, Brisbane, QLD 4072, Australia

<sup>2</sup>Queensland Geothermal Energy Centre of Excellence, The University of Queensland,  
Brisbane, QLD 4072, Australia

<sup>3</sup>Radiogenic Isotope Laboratory, CMM, The University of Queensland, Brisbane,  
QLD 4072, Australia

<sup>4</sup>Geological Survey of Israel, 30 Malkhe Israel Street, Jerusalem 95501, Israel

<sup>5</sup>Department of Geology, Eskişehir Osmangazi University, Eskişehir, 26040, Turkey

\*Corresponding author (e-mail: p.nuriel@uq.edu.au)

**Abstract:** Fault-related calcite precipitates taken from different segments along the East Anatolian (SE Turkey) and Dead Sea (Israel) fault zones were investigated structurally, geochemically and geochronologically. The results indicate major differences in the nature of calcite precipitates and temporal relationship to faulting. In the Düziçi Fault, calcite-filled veins and hydraulic fractures precipitated co-seismically during three consecutive faulting events. Calcite precipitated in veins at the Har Zefiyya Fault was controlled by near-surface karst processes. Initial opening of the veins occurred prior to about 500 ka and may represent the onset of an east–west contractional deformation. In the Carmel Fault Zone the calcite coating the fault plane precipitated by karst processes, with no evidence of subsequent deformation. Calcite fault gouge from the same site are a mix of host-rock gouge and newly formed authigenic calcite, and their overall geochemistry suggests pervasive fluid–rock interaction in the fault zone. In the Baraq Fault Zone the precipitation of calcite within syntectonic tension gashes and veins occurred prior to 540 ka by the pervasive infiltration of meteoric water into the fault zone. The results demonstrate that geochemical and structural analyses, combined with U–Th geochronology, can shed light on co-seismic and inter-seismic fault activity, and can potentially provide precise age constraints on the timing of brittle deformation.

Dating fault movements is essential for reconstructing plate tectonic processes and understanding seismic reoccurrence along active faults. Such data can provide valuable information on palaeoseismological activity and verify whether specific structures are likely to be seismically active (e.g. Grant *et al.* 1999). While absolute age dating of minerals from ductile shear zones is becoming a routine (see the review paper by Muller 2003), dating of minerals from brittle fault zones has remained a major challenge. This challenge arises from the incomplete isotopic homogenization of syntectonic minerals due to the low-temperature conditions of their formation.

A large number of studies have focused on the relationship between tectonics and fluid flow, and especially on the geochemistry of fault-related precipitates (e.g. Boles & Grivetti 2000; Labaume *et al.* 2004; Matsuda *et al.* 2004). However, there have

been only few attempts to directly constrain the age of fault activity by U–Th geochronology (Szabo & Rosenthal 1989; Flotte *et al.* 2001; Verhaert *et al.* 2003, 2004; Uysal *et al.* 2007, 2009, 2011). Carbonate minerals are particularly prone to solution–reprecipitation and/or recrystallization during diagenesis (Folk 1965), which may overprint the primary isotopic signature. This is even more likely to occur within fault zones, where pervasive fluid infiltration is influenced by fracturing. Furthermore, in order to directly relate U–Th ages of calcite precipitates to fault activity, one should demonstrate temporal relationships among faulting, fracturing, fluid circulation and calcite precipitation processes. This challenging task requires a careful utilization of U–Th geochronology combined with geochemical and microstructural studies.

Tension gashes, fault-gouge injection veins, and other syntectonic and co-seismic structures are

commonly used as indicators for brittle faulting (Boullier *et al.* 2004; De Paola *et al.* 2008). Microstructural studies provide information on the progressive development of veins, temporal changes in conditions of precipitation, and growth mechanisms (Ramsay 1980; Barker *et al.* 2006). In addition, seismological studies have suggested that earthquake-mobilized fluids commonly circulate in fault zones (Secor 1965; Hickman *et al.* 1995; Gratier *et al.* 2002; Miller *et al.* 2004) and such fluids can be responsible for syntectonic mineralization in co-seismic veins and fissures (Sibson 1987; Verhaert *et al.* 2003; Boullier *et al.* 2004), as well as fault-gouge formation (Lin 1996; Vroljik & Van der Pluijm 1999). The geochemistry of fault-related calcite precipitates can therefore provide important information on the fluids that are responsible for their precipitation (Pili *et al.* 2002; Verhaert *et al.* 2004). The type and source of fluids, their transport mechanism and residence

time in the system determine the time relationship between faulting, veining and fluid circulation.

This paper combines structural, geochemical and geochronological approaches to investigate fault-related calcite precipitation in the active East Anatolian and Dead Sea fault zones (e.g. Klinger *et al.* 2000; Begin *et al.* 2005). The study areas are respectively in SE Turkey and Israel (Fig. 1a), situated in an intra-continental tectonic setting with major seismic activity documented in historical and archaeological records (i.e. Marco *et al.* 2005; Nemer & Meghraoui 2006). We studied fault-related calcite precipitates in order to determine growth and formation mechanisms, and applied petrographical and cathodoluminescence (CL) approaches to reveal diagenetic processes. Using these methods, we can determine whether calcite precipitates have retained their original textures and chemical compositions. We used stable isotope and rare earth element (REE) geochemistry

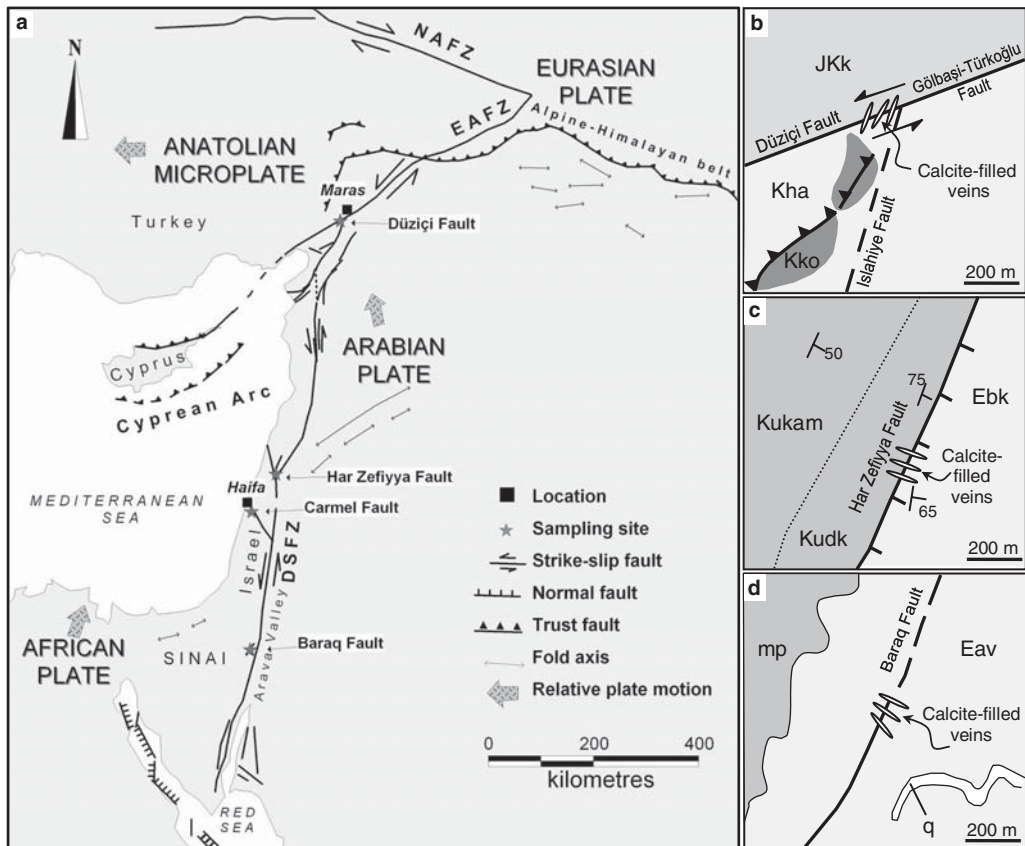


**Fig. 1.** (a) Regional tectonic map of the Eastern Mediterranean (modified after Karabacak *et al.* 2010), showing the locations of the Dead Sea, East Anatolian and North Anatolian fault zones (DSFZ, EAFZ and NAFZ, respectively). The stars mark the four study areas. Schematic maps with faults and veins orientations of (b) Düziçi Fault Zone; (c) Har-Zefiyya Fault and (d) Baraq Fault.

to constrain the origin of fluids and the conditions of precipitation. Here we compare the geochemical signatures of fault-related calcite minerals to those of the country rocks in order to achieve a better understanding of fluid residence time, fluid–rock interactions, and the role and mechanism of fluid mobilization in the fault zone. We performed U–Th dating of calcite minerals of the different types of fault-related precipitates by thermal ionization mass spectrometry (TIMS). We demonstrate and discuss the characteristics of the various types of fault-related calcite precipitates, and the implications of U–Th ages of fault-related precipitates in the context of the local and regional geology of the active strike-slip fault systems.

## Geology of the study areas

The study areas are located along an active plate boundary that has evolved since the Miocene owing to a northwards motion of the Arabian and African plates relative to the Eurasia plate (Fig. 1a). The East Anatolian Fault Zone (EAFZ) is a strike-slip fault associated with the westwards escape of the Anatolian block since the mid-Pliocene (Westaway & Arger 1996). The EAFZ is not directly connected to the Dead Sea Fault Zone (DSFZ); the two structures interact in a very complex triple junction near Maraş city in SE Turkey (Fig. 1a). The DSFZ is an approximately north–south-trending strike-slip fault that extends for more than 1000 km, and links the Red Sea divergent plate boundary with the convergent boundary of the Alpine–Himalayan belt in southeastern Turkey (Hempton 1987). It accommodates a sinistral relative plate motion between the Arabian and African plates (Joffe & Garfunkel 1987; Reilinger *et al.* 1997). Activity on the DSFZ commenced in the early–middle Miocene, based on the age of dykes that are offset by the fault zone (Eyal *et al.* 1981; Steinitz & Bartov 1991).

The DSFZ and EAFZ have been the subject of many geophysical and geological studies for several decades (see review papers by Westaway 1994; Garfunkel 1998; Bozkurt 2001; Skobelev *et al.* 2004; Taymaz *et al.* 2004; Mart *et al.* 2005). However, there is only a limited number of direct constraints on the timing of fault activities, most of which are based on palaeoseismological trenching studies involving  $^{14}\text{C}$  and optically stimulated luminescence (OSL) dating methods, which are both limited to relatively young events (Amit *et al.* 1999; Marco *et al.* 2005; Zilberman *et al.* 2005; Akyuz *et al.* 2006).

This study focuses on four segments along the EAFZ and DSFZ, which are (from north to south) the Düziçi, the Har Zefiyya, the Carmel and the

Baraq faults (Fig. 1a). In the southern part of the EAFZ, the Gölbaşı–Türkoğlu segment has accommodated left-lateral displacement of about 19 km since the Pliocene (4–3 Ma) (Westaway & Arger 1996). The southern continuation of the Gölbaşı–Türkoğlu Fault is the Düziçi Fault segment (Fig. 1b). Recent mapping in this area indicates that the Düziçi Fault is a NE–SW-trending sinistral strike-slip fault that juxtaposes the Upper Jurassic–Lower Cretaceous Karadağ limestone and Upper Triassic–Lower Jurassic Küreci dolomite (JKk in Fig. 1b) against rocks of the Hatay Ophiolites and Koçalı Complex (Kha and Kko in Fig. 1b) (Herece 2008). The Düziçi Fault is considered to be an active structure based on deflected young stream beds and faulted Quaternary deposits (Karabacak *et al.* 2010). However, the amount of displacement and the timing of fault activity are unknown.

The Har Zefiyya Fault is a NE–SW-trending fault in the DSFZ in northern Israel (Fig. 1c). The fault shows normal separation between the Bar Kokhba limestone (mid-Eocene; Ebk in Fig. 1c) in the hanging wall and the Deir Hanna Formation (Cenomanian; Kudk in Fig. 1c) in the footwall (Sneh & Weinberger 2003). Kinematic indicators suggest a younger reverse motion occurred along this fault (Weinberger *et al.* 2009). There are no age constraints on fault activity; however, calcite separates from fault-plane slickolites have been analysed by U–Th geochronology and found to be older than the age limit of the method, which suggests ages older than 500 ka (Bar-Matthews & Weinberger unpublished data).

The Carmel Fault Zone is a seismically active NW–SE-trending structure that crosses the city of Haifa and is therefore a potential source of seismic hazard (Ben-Menahem & Aboodi 1981; Shapira & Lea 1987; van Eck & Hofstetter 1990). The fault is considered to be a left-lateral strike-slip structure that branches from the DSFZ and transfers part of the left-lateral movement to the Levant continental margin (Rotstein *et al.* 2004; Schattner *et al.* 2006). In the section studied (Fig. 1a), the fault juxtaposes Upper Cenomanian–Turonian limestone (Muhraqa Formation) against Senonian chalk (Menuha Formation), and shows oblique normal and left-lateral sense of movement.

The Baraq Fault (Fig. 1d) is a NE–SW-trending fault that accompanies the western margin of the DSFZ in southern Israel. In the section studied (Fig. 1d), the fault shows normal separation within the Avedat Group (mid-Eocene; Eav in Fig. 1d). The onset of activity on the Baraq Fault is considered to have occurred during the Oligocene (Avni 1997). More recent activity, at 1–2 Ma, is responsible for approximately 100 m of displacement of the Pliocene Arava Formation. Neotectonic activity is known from the incision of rivers

following uplift of about 300–350 m of the Baraq Plateau relative to the Arava Valley (Fig. 1a), and is suggested to have occurred prior to 350 ka (Avni *et al.* 2001).

## Methodology

Orientations of fault planes, calcite-filled veins and other calcite precipitates were measured and documented in the field. Various types of fault-related calcite precipitates were collected from four sites (see Table 1), and a detailed petrographical investigation on orientated thin sections was performed with the aim of characterizing calcite crystal morphology and growth history. We used scanning electron microscopy (SEM) and CL microscopy in order to identify deformation and solution–reprecipitation and/or recrystallization diagenesis processes.

Samples were collected from four segments along the EAFZ and DSFZ. In each site, two or three sets of samples were analysed for REE and stable isotopes (Table 1). One set is composed of host-rock samples taken away from the fault zone (HR-8, HR-11 and HR-N2/N3) and is used to compare the composition of undeformed host rock to altered host rock in the fault zone. A second set of samples is composed of host rocks taken directly from vein walls, a few millimetres from calcite-filled vein (marked with HR and associated vein name in Table 1). These samples are used to compare the composition of altered host rock in the deformation zone to calcite-filled vein composition. A third set of samples was taken from calcite-filled veins, fault gouge, and fault planes. The samples were taken from the central part of the veins, excluding samples P7a and P7b that have two sub-samples from different distances from the vein wall. The compositions of this set of samples in comparison with the undeformed and deformed host rock help in determining the fluid composition and water–rock interaction processes.

Oxygen and carbon isotope analyses were carried out in the Stable Isotope Geochemistry Lab at the University of Queensland. The extraction of CO<sub>2</sub> was performed on a CO<sub>2</sub> extraction line for the host-rock samples (see Swart *et al.* 1991 for the procedure used) and using an on-line multi-prep microanalysis system for the calcite precipitates. Isotope measurements were obtained on an Isoprime Dual Inlet stable isotope ratio mass spectrometer (SIRMS) that was calibrated using NBS-18, NBS-19, and ANU-M2 carbonate standards. The δ<sup>13</sup>C and δ<sup>18</sup>O are compared to V-PDB (Vienna PeeDee Belemnite) and V-SMOW (Vienna Standard Mean Ocean Water), respectively, in per mil ‰ and have an analytical reproducibility better than ±0.1‰ (1σ error).

Rare earth elements were analysed on a Thermo X-series inductively coupled plasma mass spectrometry (ICP-MS) instrument with conditions as described in Lawrence & Kamber (2006). Calcite powders (with dilution factors of c. 3000 times, and only a minor <sup>43</sup>Ca isotope) were dissolved in a 2% nitric acid solution pre-mixed with internal standards consisting of <sup>6</sup>Li, <sup>61</sup>Ni, <sup>103</sup>Rh, <sup>115</sup>In, <sup>187</sup>Re, <sup>209</sup>Bi and <sup>235</sup>U (<sup>6</sup>Li, <sup>61</sup>Ni and <sup>235</sup>U are enriched isotopes) for internal correction of mass response drift following the protocol described in Eggins *et al.* (1997). Apart from internal drift correction, the raw data were also corrected for the low, but detectable blank, isobaric interferences from oxides and doubly charged species. The corrected raw data were then externally corrected for additional drift by repeated measurements of a matrix-matched drift-monitoring solution after every five–seven unknown samples being measured. The raw data were converted into concentrations in ppm using two independent digests of the USGS reference material W-2 as the calibration standards. The preferred elemental concentration values of W-2 are those reported in Lawrence & Kamber (2006). In addition, we use JCp-1 coral standard for cross-reference. Our measurements of the JCp-1 standard are in agreement with the values of Inoue *et al.* (2004). The ICP-MS results include measurements of Ca (major element), Mn, Fe and Mg (at ppm level), reported as ratios in Table 1, and yttrium (Y)-REE concentration (at ppm level; Table 2).

U-series dating was carried out in the Radiogenic Isotope Laboratory at the University of Queensland following the analytical procedures described in Zhao *et al.* (2001) and Yu *et al.* (2006). Calcite-powdered samples were completely dissolved in concentrated HNO<sub>3</sub> with a mixed <sup>229</sup>Th–<sup>233</sup>U–<sup>236</sup>U spike. After digestion, U and Th were co-precipitated with iron hydroxide, and then redissolved in nitric acid prior to purification using conventional anion-exchange column chemistry. The U and Th fractions were then loaded onto zone-refined rhenium filaments, sandwiched in between two graphite layers. Isotope ratios were measured in peak jumping mode on a Daly detector, with Th being measured manually and U automatically on a VG Sector-54 TIMS. The <sup>230</sup>Th/<sup>238</sup>U and <sup>234</sup>U/<sup>238</sup>U activity ratios were calculated using decay constants of Cheng *et al.* (2000). Non-radiogenic <sup>230</sup>Th correction has a minimal impact on the corrected <sup>230</sup>Th ages, as the <sup>230</sup>Th/<sup>232</sup>Th activity ratios are higher than 100 in most samples. The U–Th ages of all samples from this study are older than 400 ka, at the limit of the U-series dating technique (Ludwig 1991). As calculation of age errors using the usual first-derivative expansion are significantly inaccurate for samples

**Table 1.** Stable isotopes, mineralogy and general description of fault-related calcite precipitates

Sample	$\Delta^{13}\text{C}$ ‰ V-PDB	$\delta^{18}\text{O}$ ‰ V-SMOW	Mineralogy (XRD)	Mg/Ca	Mn/Fe	Sample type	Structure strike
(1) Düziçi Fault (strike 250°) – East Anatolian Fault Zone (SE Turkey)							
J1	-3.9	23.8	Calcite	0.009	0.047	Striated (horizontal) fault plane	250°
J2	-3.4	22.9	Calcite	0.008	0.062	Co-seismic vein	c. 210°
J3	-2.9	25.3	Calcite	0.007	0.058	Co-seismic vein	c. 200°
J4	-3.0	23.9	Calcite	0.009	0.045	Striated (horizontal) fault plane	c. 220°
HR-J2*	0.8	26.3	Calcite	0.072	0.010	Host-rock organic-rich limestone	
(2) Har Zefiyya Fault (strike 010°) – Dead Sea Fault Zone (north Israel)							
P7a_0.5–1.0	-11.2	24.3	Calcite	0.002	0.0005	Dilation vein – 0.75 cm from side A	290°
P7a_1.5–3.0	-11.0	24.9	Calcite			Dilation vein – 1.75 cm from side A	290°
P7b_0–0.5	-10.5	24.6	Calcite	0.002	0.0004	Dilation vein – 0.25 cm from side B	295°
P7b_1.5–2.0	-11.0	25.1	Calcite			Dilation vein – 1.75 cm from side B	295°
HR-P7a	-8.8	24.0	Calcite	0.004	0.012	P7a vein-wall host rock	
HR-P7b	-7.6	24.3	Calcite	0.010	0.031	P7b vein-wall host rock	
HR-P8*	-2.9	23.2	Calcite	0.013	0.036	Host-rock limestone (Bar Kokhba Formation)	
(3) Carmel Fault (strike 135°–145°) – Dead Sea Fault Zone (north Israel)							
N4	-9.8	26.1	Calcite	0.030	0.0069	Fault-plane coating	144°
N5	-8.6	24.5	Calcite	0.028	0.0006	Fault-plane coating	145°
N6	-10.0	26.2	Calcite	0.013	0.0002	Fault-plane coating	145°
N1	-2.8	30.8	Calcite-dolomite	0.245	0.040	Fault gouge	145°
HR-N2* (HW)	0.5	27.9	Calcite	0.007	0.001	Host-rock chalk (En-Zetim Formation)	
HR-N3* (FW)	1.6	30.1	Dolomite-calcite	0.481	0.012	Host-rock limestone (Muhraqa Formation)	
(4) Baraq Fault (strike 030°) – Dead Sea Fault Zone (south Israel)							
R6_2.0–3.0	0.0	29.0	Calcite	0.006	0.008	Fault-plane filling	296°
R8	-0.2	29.0	Calcite	0.004	0.011	Tension gashes	355°
R9_2.5–3.5	0.1	29.1	Calcite	0.005	0.007	Fault-plane filling	305°
HR-R6	0.1	25.1	Calcite	0.017	0.007	R6 vein-wall host rock	
HR-R8	-0.9	25.5	Calcite	0.074	0.009	R8 vein-wall host rock	
HR-R9	-0.2	24.4	Calcite	0.043	0.006	R9 vein-wall host rock	
HR-R11*	0.0	25.7	Calcite	0.026	0.006	Host-rock chalk (Mor Formation)	

\* Host-rock samples taken away from the fault zone

**Table 2.** Rare earth elements (+Y) concentration (ppm) of fault-related calcite precipitates and their host rocks

Sample	La	Ce	Pr	Nd	Sm	Eu	Gd	Tb	Dy	Y	Ho	Er	Tm	Yb	Lu
<b>Düzici Fault</b>															
J1	1.9882	2.7519	0.3954	1.6462	0.4133	0.1200	0.5710	0.0880	0.5132	4.9496	0.1071	0.2517	0.0278	0.1370	0.0171
J2	1.0564	1.5737	0.2291	1.0414	0.2806	0.0833	0.4214	0.0644	0.3943	3.5963	0.0821	0.1934	0.0213	0.1006	0.0122
J3	0.2441	0.2115	0.0256	0.1184	0.0273	0.0104	0.0582	0.0071	0.0446	0.6813	0.0096	0.0206	0.0017	0.0069	0.0006
J4	0.2814	0.3449	0.0488	0.2116	0.0467	0.0140	0.0737	0.0104	0.0590	0.6628	0.0133	0.0312	0.0032	0.0147	0.0020
HR-J2	3.9381	5.5806	0.8533	3.3952	0.6615	0.1598	0.6476	0.0964	0.5463	3.6688	0.1131	0.3178	0.0462	0.2712	0.0401
<b>Har Zefiyya Fault</b>															
P7a_0.5–1.0	0.1078	0.1421	0.0223	0.0817	0.0172	0.0037	0.0189	0.0026	0.0139	0.1084	0.0031	0.0096	0.0012	0.0069	0.0010
P7a_1.5–3.0															
P7b_0–0.5	0.0305	0.0581	0.0070	0.0280	0.0065	0.0014	0.0055	0.0009	0.0045	0.0386	0.0012	0.0032	0.0005	0.0024	0.0004
P7b_1.5–2.0															
HR-P7a	3.7332	6.3911	0.8345	3.2125	0.6422	0.1472	0.6073	0.0906	0.5238	3.5094	0.1115	0.3058	0.0460	0.2792	0.0410
HR-P7b	0.9989	1.7445	0.2109	0.8094	0.1577	0.0352	0.1438	0.0222	0.1321	0.8857	0.0294	0.0829	0.0129	0.0815	0.0122
HR-P8	0.6362	0.9229	0.1210	0.4625	0.0896	0.0221	0.0894	0.0138	0.0832	0.7046	0.0193	0.0545	0.0081	0.0496	0.0082
<b>Carmel Fault</b>															
N4	0.5873	0.6601	0.0912	0.3475	0.0682	0.0169	0.0733	0.0112	0.0727	0.7479	0.0168	0.0513	0.0081	0.0474	0.0078
N5	0.1454	0.2606	0.0213	0.0774	0.0148	0.0040	0.0143	0.0026	0.0156	0.1241	0.0037	0.0104	0.0016	0.0118	0.0018
N6	0.0178	0.0197	0.0028	0.0092	0.0019	0.0005	0.0019	0.0003	0.0017	0.0247	0.0004	0.0013	0.0003	0.0014	0.0002
N1	10.2472	10.2233	1.8517	7.3136	1.4509	0.3645	1.6055	0.2454	1.4683	12.7674	0.3329	0.9590	0.1451	0.8722	0.1321
HR-N2	6.1835	6.1489	1.0836	4.3775	0.8676	0.2223	0.9802	0.1474	0.9017	8.6924	0.2075	0.6163	0.0899	0.5341	0.0837
HR-N3	0.2180	0.3080	0.0373	0.1451	0.0313	0.0076	0.0338	0.0051	0.0297	0.2668	0.0062	0.0183	0.0025	0.0146	0.0022
<b>Baraq Fault</b>															
R6_2.0–3.0	0.1313	0.0524	0.0189	0.0849	0.0168	0.0067	0.0298	0.0047	0.0364	0.7874	0.0111	0.0414	0.0070	0.0448	0.0075
R8	0.0900	0.0290	0.0093	0.0361	0.0060	0.0028	0.0133	0.0025	0.0221	0.4283	0.0070	0.0273	0.0052	0.0374	0.0069
R9_2.5–3.5	0.3266	0.1083	0.0367	0.1392	0.0272	0.0103	0.0434	0.0076	0.0594	0.9776	0.0177	0.0649	0.0114	0.0826	0.0143
HR-R6	8.6647	4.4368	1.4550	6.1717	1.1927	0.3147	1.5955	0.2362	1.5332	14.9180	0.3732	1.1028	0.1656	1.0457	0.1608
HR-R8	13.4150	7.2136	2.1809	9.1167	1.7714	0.4658	2.4028	0.3638	2.4266	26.2840	0.6092	1.8569	0.2895	1.8034	0.2811
HR-R9	4.7660	2.9627	0.8261	3.4256	0.6668	0.1701	0.8588	0.1285	0.8084	7.7429	0.1949	0.5885	0.0923	0.6027	0.0973
HR-R11	6.0440	3.4535	1.0405	4.3813	0.8723	0.2202	1.0746	0.1582	1.0106	9.4518	0.2431	0.7240	0.1132	0.7405	0.1185

with ages of more than 300 ka, we therefore calculated the U/Th age errors by Monte Carlo simulation using Isoplot/Ex Version 2 Program (Ludwig 1991).

## Results

### Düziçi Fault

Several fault planes with horizontal slickenlines and associated veins are exposed within a small quarry about 20 km south of Maraş city in SE Turkey (Fig. 1a). Faults are subvertical and strike 250° (dipping 72°), with subhorizontal slickenlines pitching 7°E (Fig. 2a). This orientation is in agreement with recent mapping in the area that traced the Düziçi Fault along a NE–SW lineament (Herece 2008). Calcite-filled veins and fissures are distributed throughout the quarry with diverse orientations, and are emplaced in fine-grained, organic-rich limestone host rocks (sample HR-J2 in Table 1). We sampled two calcite-filled veins, which are oriented parallel to fault planes (samples J1 and J4). These veins are up to 100 mm thick and most probably formed by fluid infiltration into the fault zone as evidenced by the presence of slickenline morphology on calcite-filled veins and fault-plane interface (Fig. 2a). The penetrative slickenline morphology indicates that calcite precipitated either in-between faulting events or during faulting. We also sampled two calcite-filled veins from within the fault zone and with no slickenline morphology (sample J2 and J3). Sample J2 is part of a vein that is more than 20 m long and orientated roughly orthogonal to the fault plane. The overall structure of this vein resembles a tension-gash structure (Fig. 2b).

Calcite crystals from the Düziçi Fault are up to 8 mm in size and have a blocky texture. Grains are moderately deformed, and are characterized by twinning and sharp triple-junction grain boundaries (Fig. 3a). Grains do not show growth competition texture or hiatus, and vein filling is somewhat homogenous. Vein-wall host-rock limestone is strongly affected by thin calcite-filled hydraulic fractures with irregular orientation (F in Fig. 3a, b). In all veins, sharp fragments of host-rock material are incorporated into the vein filling and are surrounded by calcite-filled grains (HR in Fig. 3a, b).

X-ray diffraction (XRD) patterns and ICP-MS analyses confirm pure calcite mineralogy for all samples from this site (see Table 1). Petrographical and CL observations indicate high luminescence in both calcite-filled hydraulic fractures and veins (Fig. 3b), implying that both precipitated from similar fluids and with no significant modification by diagenesis. The  $\delta^{18}\text{O}$  (V-SMOW) and  $\delta^{13}\text{C}$  (V-PDB) average values of calcite precipitates

from this site are  $23.9 \pm 0.9$  and  $-3.9 \pm 0.4\text{\textperthousand}$ , respectively (Fig. 4a). A comparison of the  $\delta^{18}\text{O}$  and  $\delta^{13}\text{C}$  values of vein-wall host rocks with their calcite precipitates (linked with dashed lines in Fig. 4a) indicates that veins are depleted in both oxygen and carbon isotopes relative to the host rock (up to 3‰ in both; Fig. 4b). The REE patterns of the calcite-filled veins are similar to that of the host-rock sample (HR-J2; Fig. 5a). There is a slight depletion in the HREE composition of the calcite veins in comparison with the host-rock sample and a relatively high REE concentration in the veins in comparison to veins in other sites in this study (Fig. 5b–d). Reliable U–Th ages are obtained for two samples from this site: ages are  $405 \pm 15/13$  ka for sample J2; and  $501 \pm 44/32$  ka for sample J4-b (a replicate sample J4-a from the same vein was also analysed and yielded a similar age of  $525 \pm 50/38$  ka) (see Table 3 and Fig. 6).

### Har Zefiyya Fault

An approximately NNE-trending fault plane (dipping 50°) with dip-slip slickenlines, slickenfibres and breccia zone is well exposed. Approximately ESE–WNW-trending calcite-filled veins are distributed within 5 m from the fault plane. Samples P7-a and P7-b were taken from two sides of the same calcite vein (Fig. 2c); the vein is 0.1 m thick and can be traced for 1 m of vertical section. Calcite bands are consistently parallel to vein walls, which are highly brecciated (Fig. 2c). Sample HR-P8 is a relatively unaltered and undeformed limestone host rock of the Eocene Bar-Kokhba Formation, taken about 10 m away from the fault zone. Highly brecciated and altered host-rock samples were taken from both sides of P7 vein walls (HR-P7a and HR-P7b).

Calcite crystals of the Har Zefiyya veins show an elongate-blocky texture. The length to width ratio ranges between 5 and 30, and the maximum grain size is up to 30 mm in length (Fig. 3c). Calcite crystals appear to nucleate from microcrystalline carbonate of wall-rock material (Fig. 3c), and grains are arranged perpendicular to both vein wall and growth laminae (Fig. 3c). Growth competition texture (Kendall *et al.* 1993) is common, especially within the transition from vein wall and following hiatuses in vein growth. The calcite growth direction is inferred from an increase in size and width of crystals in the direction of vein growth (arrows in Fig. 3c). Calcite depositional hiatuses are common, and are characterized by steep-sided and truncated crystal termination. The hiatuses are parallel to growth laminae, and their spacing is between 1 and 10 mm. Fluid or solid inclusion trails, which are common features in veins that are

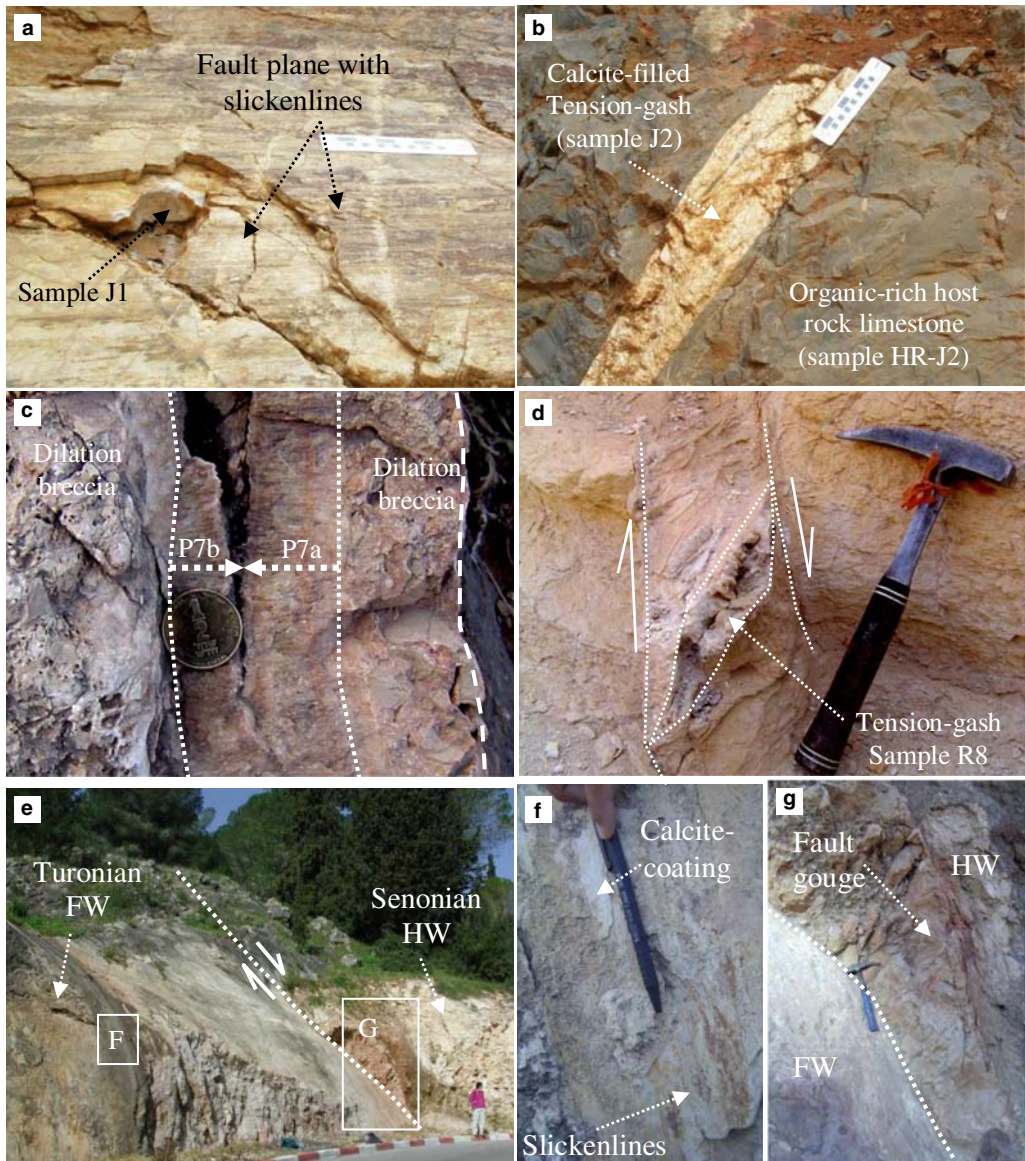


**Fig. 2.** Fault-related calcite precipitates at the four studied sites. (a) Calcite vein within a fault plane with slickenlines morphology taken from the Düzici Fault Zone. Location of sample J1 is marked (scale bar is 0.2 m). (b) Calcite-filled tension-gash vein (sample J2), and host-rock limestone (sample HR-J2). (c) Calcite-filled dilation vein in the Har-Zefiyya Fault Zone. (d) Calcite-filled tension-gash in the Baraq Fault Zone. (e) The Carmel Fault approximately 20 km SE of Haifa city. FW., footwall; HW, hanging wall. (f) Calcite-coating fault plane with slickenline morphology taken from the footwall (sample N4; see location in e). (g) Reddish-colour calcite fault gouge taken from the fault plane within the hanging wall (sample N1; see location on E).

built-up by successive incremental opening and filling episodes (Ramsay 1980), were not identified.

Vein-filling material was confirmed as pure calcite by XRD analyses (Table 1). Oxygen and carbon isotope ratio values of calcite precipitates

in this site are  $24.7 \pm 0.3$  and  $-11.2 \pm 0.2\text{\textperthousand}$ , respectively (Fig. 4a). Comparing the  $\delta^{18}\text{O}$  and  $\delta^{13}\text{C}$  values of vein-wall host rocks to their calcite precipitates indicates enrichment in oxygen and depletion in carbon isotopes in the veins (2 and

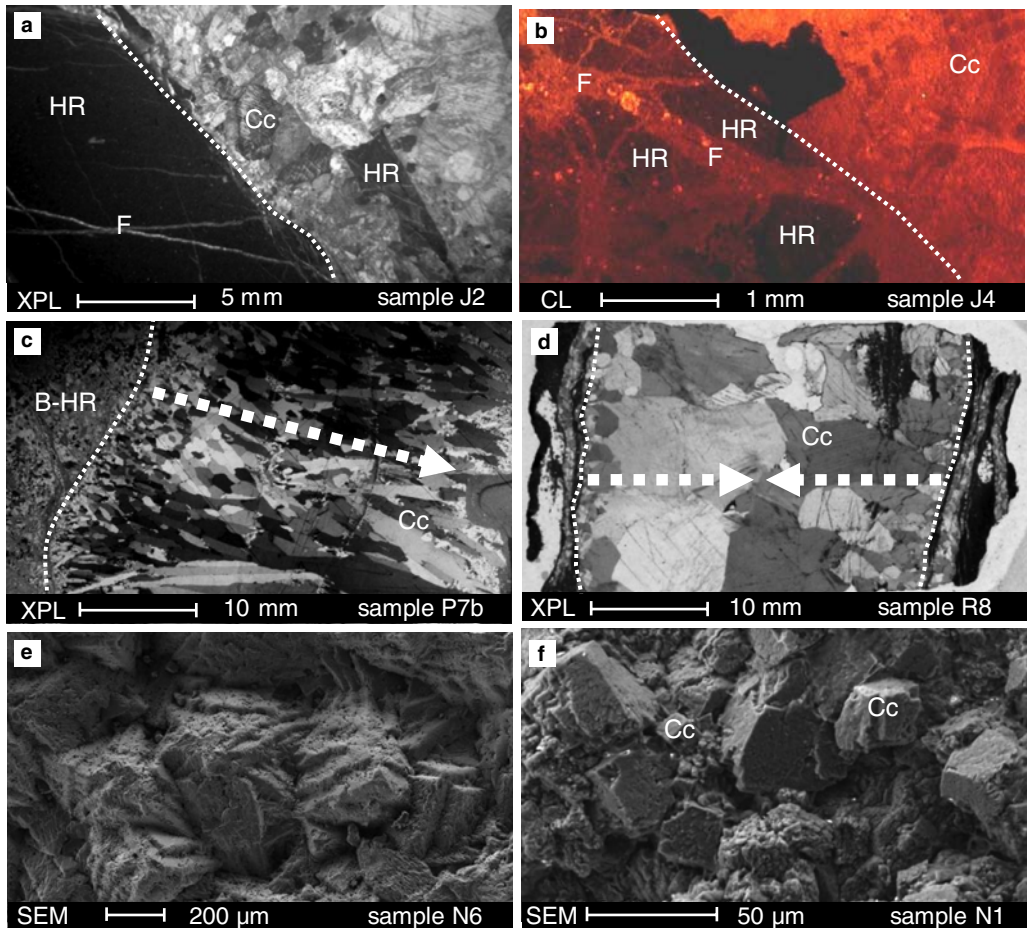


**Fig. 3.** Microstructures of fault-related calcite precipitates. (a) Sample J1 cross-polarized light (XPL). Note the host-rock fragments (HR) within calcite-filling vein (Cc). (b) Sample J4 in CL light. Calcite-filled vein (Cc) and fractures (F) showing high luminescence relative to host-rock fragments (HR). (c) Sample P7b in XPL. The transition from brecciated host rock (B-HR) to vein filling is marked with a dashed line, and the growth direction is shown with an arrow. (d) XPL image of sample R8, showing a growth competition texture from vein walls to vein centre (marked with an arrow). (e) SEM image of a calcite-coating fault plane (sample N6). (f) Calcite fault gouge (sample N1), showing well-crystallized calcite grains (Ca). SEM conditions: 15 kV, 6 spot size,  $\times 150$  and  $\times 1250$  magnification (e and f, respectively).

8‰ in oxygen and carbon, respectively; Fig. 4b). The REE pattern of calcite-filled veins is very similar to their host-rock samples, with Ce-negative and Gd- and Y-positive anomalies (Fig. 5b) that are typical of carbonates precipitated in the marine environment (Liu *et al.* 1988, Bolhar *et al.* 2004). The concentration, however, is considerably lower in comparison with the host rocks (Table 2). U–Th ages of subsamples taken close to vein wall in both sides of the vein are at the limit of the U–Th method (P7a\_0.5–1 and P7b\_0–0.5) and therefore have very large age errors. Two samples taken from the middle part of the vein (P7a\_1.5–3 and

P7b\_1.5–2) gave similar ages of  $510 \pm 86/58$  and  $551 \pm 110/67$  ka, respectively (Fig. 6 and Table 3).

#### Carmel Fault

A polished and wavy fault plane with slickenlines, breccia and fault gouge (Fig. 2e–g) is exposed about 20 km SE of Haifa city in northern Israel (Fig. 1a). The fault strikes roughly to the SE (dipping  $70^\circ$ ), and slickenlines measurements ( $64^\circ$ – $356^\circ$ , plunge-trend) indicate oblique normal and sinistral sense of movement. We collected a number of calcite samples taken directly from the

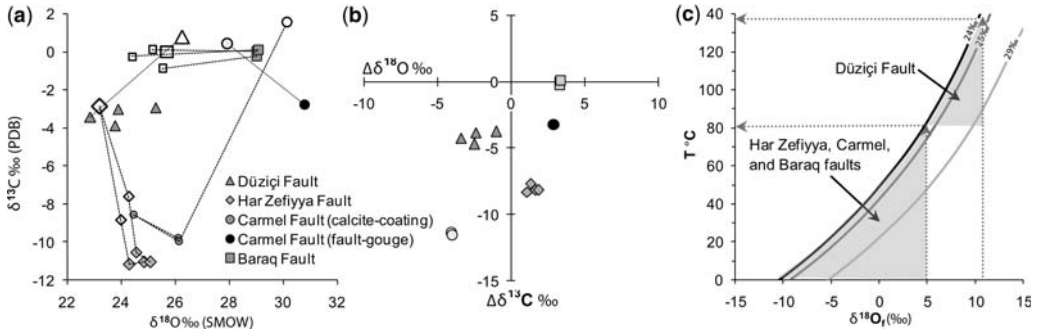


**Fig. 4.** Stable isotope data. (a) Stable isotope values ( $\delta^{18}\text{O}$  and  $\delta^{13}\text{C}$ ) of fault-related calcite precipitates and host-rock samples. The data of the various calcite precipitates samples taken from the four studied sites are shown in filled symbols (see the legend). Analyses of limestone and chalk host-rock samples (see Table 1) taken from each vein wall (linked with dashed line) are also shown (unfilled symbols), together with host-rock values away from fault zone (large unfilled symbols). (b)  $x$ - $y$  plot of  $\Delta\delta^{18}\text{O}$  and  $\Delta\delta^{13}\text{C}$  between vein and host-rock samples away from the fault zone. (c)  $\delta^{18}\text{O}$ -temperature plot for calcite-filled veins. The three curves represent the isotopic composition of calcite-filled veins in the Düziçi Fault, Har-Zefiyya and Carmel faults, and the Baraq Fault Zone (24, 25 and 29, respectively) in equilibrium with fluids [ $\delta^{18}\text{O}_f$  (‰)] from which the calcite precipitated. The curves have been constructed using the calcite- $\text{H}_2\text{O}$  (liquid) equation of (O'Neil *et al.* 1969). The equilibration temperature was estimated for isotopic composition of  $\text{H}_2\text{O}$  between -15 and 15‰.

fault plane (N4, N5 and N6 in Table 1). These samples are from thin calcite and calcite-dolomite layers that coat the fault plane (Fig. 2f). An SEM image indicates that calcite and dolomite crystals are undeformed and grew under open-space, fluid-fill conditions (Fig. 3e). We also collected a reddish fault gouge, composed of fine-grained calcite (Fig. 2g). An SEM image indicates that this fault gouge is composed of both host-rock crushed material and authigenic calcite minerals (Fig. 3f).

For comparison, we sampled a relatively undeformed and unaltered host-rock samples that were taken from the footwall (sample HR-N3) and hanging wall (sample HR-N2).

Calcite-coating fault-plane samples (N4, N5 and N6) and the host-rock sample HR-N2 are pure calcite, based on their XRD pattern and Mg/Ca ratios (Table 1). The host-rock sample HR-N3 and the fault-gouge sample N1 are dolomite-calcite and calcite-dolomite, respectively (Mg/Ca ratio of

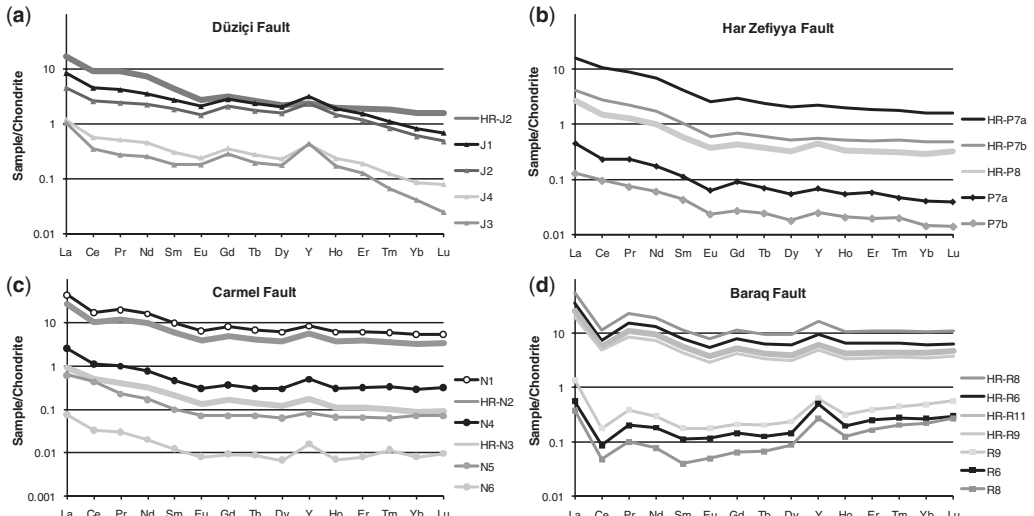


**Fig. 5.** Chondrite-normalized Y-REE patterns for fault-related calcite precipitates and host-rock samples. The (Y-REE)<sub>CN</sub> data are shown for each site: (a) Düziçi Fault Zone; (b) Har-Zefiyya Fault Zone; (c) Carmel Fault Zone; and (d) Baraq Fault Zone. Chondrite values from Sun & McDonough (1989).

**Table 3.** *U–Th age results (ka) of fault-related calcite precipitates*

Sample	U (ppm)	$^{232}\text{Th}$ (ppb)	$(^{230}\text{Th}/^{232}\text{Th})$	$(^{230}\text{Th}/^{238}\text{U})$	$\pm 2\sigma$	$(^{234}\text{U}/^{238}\text{U})$	$\pm 2\sigma$	U–Th age (ka)	+ $\sigma$	- $\sigma$	Initial $^{234}\text{U}/^{238}\text{U}$	+ $\sigma$	- $\sigma$
Düziçi Fault													
J1	0.179	5.07	111	1.0359	0.0057	1.0279	0.0033	>550	290	120	1.170	0.190	0.050
J2	0.095	2.34	133	1.0853	0.0037	1.0819	0.0012	405	15	13	1.260	0.010	0.009
J3	0.135	0.11	3891	1.0225	0.0068	1.0215	0.0014	>550	170	82	1.103	0.054	0.023
J4-a	0.338	7.16	147	1.0293	0.0033	1.0268	0.0012	525	50	38	1.120	0.016	0.011
J4-b	0.224	2.56	269	1.0157	0.0033	1.0185	0.0011	501	44	32	1.077	0.008	0.006
Har Zefiyya Fault													
P7a_0.5–1.0	0.406	15.63	80	1.0129	0.0057	1.0089	0.0019	>550	300	160	1.070	0.086	0.029
P7a_1.5–3.0	0.691	2.62	810	1.0107	0.0056	1.0146	0.0017	510	86	58	1.062	0.014	0.010
P7b_0–0.5	0.443	30.83	43	0.9973	0.0181	1.0092	0.0020	467	210	98	1.036	0.028	0.012
P7b_1.5–2.0	0.785	1.09	2226	1.0146	0.0037	1.0153	0.0025	>550	110	67	1.073	0.020	0.011
Carmel Fault													
N4	0.671	20.82	109	1.1102	0.0061	1.0250	0.0017	–	–	–	–	–	–
N5	0.325	3.04	349	1.0779	0.0046	1.0444	0.0021	–	–	–	–	–	–
N6	1.478	10.89	458	1.1124	0.0062	1.0596	0.0022	–	–	–	–	–	–
Baraq Fault													
R8	0.030	0.18	528	1.0081	0.0095	1.0076	0.0019	>550	260	140	1.046	0.047	0.018
R9_2.5–3.5	0.016	0.82	65	1.0752	0.0056	1.0721	0.0031	417	30	25	1.238	0.016	0.014

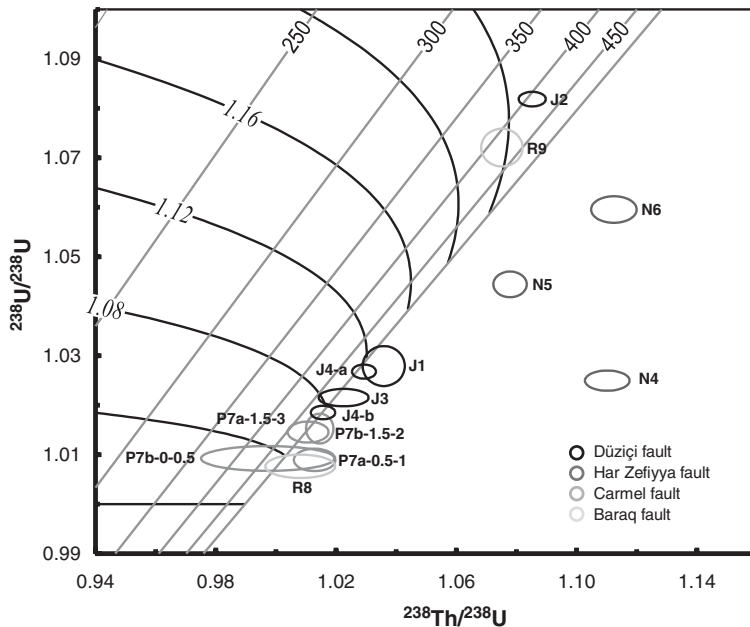


**Fig. 6.** Plot of activity ratios  $^{234}\text{U}/^{238}\text{U}$  against  $^{238}\text{Th}/^{238}\text{U}$  for fault-related calcite precipitates. Data-point error ellipses are  $2\sigma$  and are plotted for the Düzici, Har-Zefiyya, Carmel and Baraq fault zones. The U–Th ages results (in ka) are shown by subvertical grey isochron lines; the evolution curves for  $^{234}\text{U}/^{238}\text{U}$  are in subhorizontal black lines. Note that samples from the Carmel Fault plot outside of the permitted  $^{234}\text{U}/^{238}\text{U}$  evolution curves.

c. 0.5 and 0.25, respectively). Average  $\delta^{18}\text{O}$  and  $\delta^{13}\text{C}$  values of calcite precipitates in this site are  $25.6 \pm 0.8\text{\textperthousand}$  and  $-9.8 \pm 0.6\text{\textperthousand}$ , respectively. Calcite coating samples are depleted by up to 6 and 10‰ in their  $\delta^{18}\text{O}$  and  $\delta^{13}\text{C}$  values relative to their host rocks (Fig. 4b). In contrast, calcite fault gouge is enriched in oxygen and depleted in carbon isotopes (sample N1; up to 3‰ in both). The Y-REE pattern of calcite-coating fault-plane and calcite fault-gouge samples is similar to their host-rock sample (HR-N3 and HR-N2, respectively), with Ce-negative and Y-positive anomalies (Fig. 5c). The concentration in comparison to the host rock is either lower (N5 and N6) or slightly higher (N1 and N4). The  $^{230}\text{Th}/^{238}\text{U}$  and  $^{234}\text{U}/^{238}\text{U}$  activity ratios of calcite-bearing minerals in this site (Fig. 6) deviate from the predicted evolution of  $^{238}\text{U}$  decay series during ageing under close-system conditions (Ku 1965). This may suggest open-system conditions with respect to uranium isotopes, meaning that samples may have suffered partial uranium loss due to alteration. U–Th age determination is therefore not possible in this site.

#### Baraq Fault

Veins and tension gashes in the Baraq Fault Zone have varying orientations ( $206^\circ$ – $310^\circ$ ) and are

filled with gypsum, carbonate, and clay gouge. We sampled a calcite-filled tension-gash vein (sample R8; Fig. 2d), which is associated with two parallel normal faults (dipping  $60^\circ$ ). We also sampled two calcite-filled veins orientated parallel to other small-scale normal faults that strike approximately  $300^\circ$  (sample R9 and R6). The veins may have developed either during or after faulting. The host rock is chalk with interbedded chert layers of the lower Eocene Mor Formation. A relatively fresh host-rock sample was taken away from the fault zone for comparison (HR-R11). In addition, rather deformed host-rock samples were separated from vein walls of R6, R8 and R9 (HR-R6 and HR-R8 and HR-R9, respectively).

Calcite crystals are blocky, up to 16 mm long, with a length/width ratio of up to 2 and sharp grain boundaries (Fig. 3d). The transition from vein wall to calcite-vein filling is gradual and hiatuses are prominent close to the vein wall (Fig. 3d). With the exception of sample R9, growth competition textures are somewhat developed (e.g. sample R8; Fig. 3d), allowing the identification of growth direction. Calcite grains appear to nucleate and grow from both sides of the vein wall until the vein closure point at the centre.

All vein-filling material from this site are pure calcite with perfect XRD patterns and Mg/Ca

ratios of less than 0.01 (Table 1). The  $\delta^{18}\text{O}$  (V-SMOW) and  $\delta^{13}\text{C}$  (V-PDB) average values of calcite precipitates from this site are  $29.0 \pm 0.03$  and  $0.0 \pm 0.15\text{\textperthousand}$ , respectively (Fig. 4a). Stable isotope results indicate that vein-filling calcites are enriched in oxygen (up to 5‰) relative to their host-rock samples, with a very small (<1‰) change in carbon isotopes (Fig. 4b). REE concentrations of calcite-filled samples are much lower relative to their host rocks (Table 2). Their pattern, however, is very similar, with Ce-negative and Y-positive anomalies, and a slight enrichment in the HREE composition of calcite precipitates relative to their host rocks (Fig. 5d). U-Th ages were obtained for two samples R8 and R9; however, the age error for sample R8 is too large (Fig. 6). Therefore, only one sample from this site (R9) provided a reliable age of  $417 \pm 30/25$  ka (Table 3).

## Discussion

The microstructures and geochemistry of fault-related calcite precipitates from the four sites along the EAFZ and DSFZ suggest different formation mechanisms and varying conditions under which calcite precipitated (Fig. 7). We discuss the mechanisms of calcite precipitation and characterize the fluid source, transport, residence time and water–rock interaction. The U–Th ages of all samples from this study are close to the limit of the U-series technique so the age uncertainties are rather high (Fig. 6). However, U/Th ages were still obtained for three of the four sites. We address the implications of U–Th geochronology of the different types of calcite precipitates in terms of their temporal association with fault activity. Finally, we discuss the implications of the U–Th ages in terms of the local and regional geology in four studied segments along the EAFZ and DSFZ.

## Calcite precipitates in the Düziçi Fault

Calcite precipitates in the Düziçi Fault Zone are developed either as veins within the fault zone with slickenline morphology (sample J1 and J4) or linked to the fault zone by a calcite-filled hydraulic fracturing system (sample J2 and J3). The lack of internal structures and growth textures, and the presence of angular host-rock fragments within the veins and hydraulic fractures, indicate that precipitation of calcite in these structures was relatively rapid. The similar and rather high luminescence characteristic of calcite-filled veins and fractures, in comparison with the low luminescence of the host rock (Fig. 2b), suggest that both precipitated under similar conditions, from similar fluids, and possibly during the same event. The relative abundance of REE elements (up to 5 ppm; Table 2) and high Mn/Fe ratios (up to 0.06; Table 1) of all calcite-filled veins in this site may account for the observed high luminescence, indicating input of exotic or deep-seated fluids (rich in  $\text{Mn}^{2+}$  and trace elements) and precipitation under relatively reducing conditions, typical of deep meteoric or burial environments (Janssen *et al.* 2005, 2007).

The Y-REE concentrations in calcite precipitates at this site (Table 2) are much higher than other sites in this study. The fact that calcite precipitate Y-REE patterns preserve the Ce-negative anomaly suggests that fluids inherited their composition from the host rock with some input of exotic fluids. The observed depletion in HREE in the veins relative to the host rock can be explained by the carbonate complexation behaviour of HREE in the host rock. LREE/HREE fractionation can occur as a result of sorption and complexation processes. In the absence of complexing ligands (e.g. carbonate complexes, hydroxide) under acidic condition, fluid REE composition is controlled by sorption, the strength of which increases with decreasing ionic radius from La to Lu, leading to an enrichment of LREE in the fluids

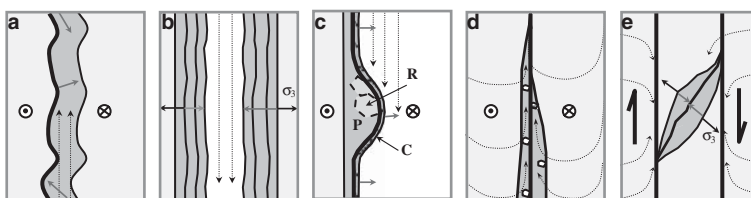


**Fig. 7.** Types of fault-related calcite precipitates. Calcite precipitation (a) in co-seismic veins along fault planes and by upwards-migrating fluids; (b) in dilation veins by karst process; (c) on fault planes by syntectonic crystallization (R), post-crystallization shear pressure (P) and coating pre-existing slickenlines by karst process (C); (d) in fault gouge by pervasive fluid flow; (e) in syntectonic tension gash structure and by groundwater infiltration in the fault zone. Fault planes are indicated by thick black lines; fault movement and orientation of tension  $\sigma_3$  are shown by black arrows. Grey arrows indicate the growth direction of calcite precipitates; black dashed lines indicate fluid circulation in the fault zone.

(Bau & Moller 1992). However, the stability of carbonate complexes of the REE in solution increases from La to Lu, resulting in the dominance of HREE in carbonic fluids. HREE depletion for the calcite veins in the Duzici Fault Zone may indicate that REE mobilization was controlled by sorption processes through the involvement of slightly acidic fluids that circulated deeply into a relatively high-temperature environment (Bau & Moller 1992).

Calcite veins show a conspicuous Y anomaly that provides further information on the fluid-flow event leading to the calcite precipitation. Under most magmatic and sedimentary conditions, Y behaves almost exactly like its geochemical twin Ho. However, under hydrothermal conditions, Y is known to be fractionated from Ho, resulting in suprachondritic Y/Ho ratios  $>27$ . For instance, Y/Ho ratios of up to 200 were reported for fluorine-rich medium-temperature hydrothermal fluids (Bau & Dulski 1999), in contrast to typical magmatic and sedimentary values of 24–34. In mildly acidic–mildly basic pH environments and slightly elevated temperatures ( $>100$  °C), fluoride complexes dominate over others (e.g. carbonate, chloride, sulphate, hydroxide) (Wood 1990). The anomalous behaviour of Y is derived from the higher stability of Y over REE complexes over a wide range of temperatures, pH and Eh conditions (Wood 1990). Elevated Y concentrations (Y/Ho up to 70) in the calcite samples can be interpreted as fractionation effects due to complexation during hydrothermal activity. Hydrothermal activity involving (bi)carbonate complexation as mobilizing agent is less likely, because hydrothermal carbonates typically show relative depletion of Y owing to the higher covalent contribution to complexation bonding (Bau & Dulski 1999). Fluoride complexation behaviour changes systematically with temperature. As temperature rises, the stability constants for fluoride (and carbonate) complexes increase for HREE. At the same time, Y also becomes progressively more stabilized as a fluoride complex (Wood 1990); hence, enrichment in Y and HREE is expected to increase with temperature in fluoro-bearing fluids.

Y-REE data in combination with CL examination of vein calcite indicate that fluids derived from deeper reservoirs may have been responsible for carbonate veining in the Duzici Fault Zone. Such deep-seated fluids are likely to have high  $\delta^{18}\text{O}$  composition relative to meteoric water origin (e.g. Janssen *et al.* 2005). The measured  $\delta^{18}\text{O}$  (V-SMOW) values of calcite veins in this site are 24‰ (Fig. 4c). Using the calcite–H<sub>2</sub>O (liquid) equation of O’Neil *et al.* (1969), and the estimated  $\delta^{18}\text{O}$  composition of fluids between 5 and 10‰, we can calculate the equilibration temperatures to be between 84 and 133 °C (Fig. 4c).

The calcite-filled hydraulic fractures at this site are similar to co-seismic structures documented in the Nojima Fault Zone in Japan (Boullier *et al.* 2004). Carbonate-filled hydraulic fractures and veins are interpreted to be the result of co-seismic upwards circulation of fluids in the fault zone, and fast nucleation of carbonates attributed to a sudden fluid or CO<sub>2</sub> partial pressure drop due to fracturing (Uysal *et al.* 2009). The above results suggest that calcite in the Düziçi Fault Zone has precipitated co-seismically by a similar mechanism, involving deep-seated fluids migrating upwards in the fault zone during the seismic cycle (Fig. 7a). This notion is supported by the following observations: (1) microstructural evidence for fast growth of calcite-filled veins, incorporated with angular host-rock fragments and precipitation within hydraulic fractures; (2) high Mn/Fe ratio and REE content; and (3) Y-anomaly and  $\delta^{18}\text{O}$  composition indicative of elevated temperatures (84–133 °C) during precipitation. Thus, U–Th ages seem to provide a good estimation for faulting events, with at least three episodes of faulting indicated by the results. The first generation of vein formation was associated with a calcite-filled fault zone (sample J4). This implies that faulting commenced prior to the precipitation of the calcite in the fault plane. A subsequent faulting event is associated with the co-seismic precipitation of veins in the fault zone. U–Th ages of these specimens (J4a, J4b) are 501–525 ka, implying that the faulting event occurred during that time. A third generation of co-seismic vein formation occurs at 405 ka (sample J2), possibly in association with the formation of post-crystallization fault striae morphology on existing veins.

### *Calcite precipitates in the Har Zefiyya Fault*

Calcite precipitates in the Har Zefiyya Fault Zone are different in their nature and formation mechanism from calcite precipitates in the Düziçi Fault Zone (Fig. 7b). Dilation breccia within vein walls (Fig. 2c) suggests that vein opening was associated with Mode I dilation. The geochemistry of calcite-filled veins indicates near-surface precipitation by karst processes. This view is supported by: (1) significant depletion in carbon isotopes (up to 8‰) with respect to the adjacent host rocks (sample HR-P8; Fig. 4a, b), indicating CO<sub>2</sub>-rich fluids, such as meteoric water enriched by C<sub>3</sub>-type Mediterranean vegetation (Bar-Matthews *et al.* 1997); (2) stable isotope compositions of calcite dilation veins that are comparable to measured values of oxygen and carbon isotopes in speleothems from the nearby ‘Peqi’ in cave’ (Bar-Matthews *et al.* 2003), suggesting similar conditions of precipitation by

meteoric water at the near-surface and low-temperature environment (Fig. 4c); (3) Y-REE patterns of calcite precipitates (Fig. 5b) which indicate that no major fractionation occurred during precipitation of calcites and that the REE composition of the fluid was mainly controlled by local fluid–rock interaction.

Initiation and opening of Mode I dilation veins may be linked directly to faulting. The east–west orientation of the Har Zefiyya dilation veins reflects a local north–south extension. This deformation is not consistent with normal dip-slip or reactivated reverse movement along the SE-dipping Har Zefiyya Fault (Weinberger *et al.* 2009). However, the formation of such a dilation vein system may represent a stage in deformation that was associated with a regional approximately north–south extension and roughly east–west contraction, as evident in other sites along this sector of the DSFZ (Weinberger *et al.* 2009). Calcite-filling dilation veins have precipitated both a short or a long time after the initial opening, and are most probably controlled by the local hydraulic system. Thus, U–Th ages of calcite precipitate in the veins, especially those obtained close to veins wall, may be regarded as the minimum age for the vein formation. The U–Th age results, although close to the limit of the method, indicate that the initial opening of the vein occurs prior to 550 ka, with continued calcite growth until 510–550 ka. Weinberger *et al.* (2009) suggested that a significant component of east–west regional shortening, normal to the DSFZ, occurred during the late Pleistocene. It is possible that the onset of this deformation stage, prior to 550 ka, is represented by the formation of dilation veins in the Har Zefiyya Fault Zone.

### *Calcite precipitates in the Carmel Fault*

The formation of calcite precipitates on fault plane with slickenline morphology can be attributed to three main mechanisms (Fig. 7c). The first and the most directly associated with faulting is syntectonic crystallization due to pressure solution and reprecipitation processes during faulting. In this case, the U–Th ages correspond to the time of precipitation, which is also the time at which the formation of the slickenlines occurred. The second mechanism is post-crystallization shear pressure (Eyal *et al.* 1992), implying that the formation of slickenlines post-date the formation of the host rock that is affected by them (P in Fig. 7c). The third mechanism is associated with the coating of calcite precipitation along pre-existing grooves within the fault plane (C in Fig. 7c). For the last two mechanisms, U–Th ages only provide minimum age constraints for fault activity.

The distinction between the three mechanisms discussed above can be made based on characteristic microstructures. Syntectonic and post-crystallization formation are characterized by a preferred orientation and/or deformed calcite-grain morphology. In contrast, calcite-coating precipitates simply mimic pre-existing slickenlines morphology and calcite grains are undeformed. SEM images taken both from the top and the bottom views of the calcite layer (less than 5 mm thick) reveal perfect euhedral calcite crystals (Fig. 3e). This observation suggests that calcite samples (N4, N5 and N6) are coating the fault plane, and are precipitated under open-space and fluid-filled conditions. Therefore, these calcite grains were not subjected to subsequent deformation associated with fault slip. The stable isotope composition of calcite coating is very similar to calcite-filled dilation veins in the Har Zefiyya Fault Zone (Fig. 4a), suggesting that calcite precipitated by karst processes, involving CO<sub>2</sub>-rich fluids migrating downwards in the fault zone. The U–Th ages of the calcite-coating precipitates may provide a minimum age constraint on the timing of fault activity, as calcite coating post-dated the formation of fault-related slickenlines. However, the U/Th activity ratios of samples from this site (Table 3, Fig. 6) suggest open-system conditions and potential post-formation alteration processes. U–Th age determination is therefore not possible.

Fault gouge is predominantly associated with the mechanical recycling of protolith host rock but can also involve fault-related mineralization (Van der Pluijm *et al.* 2001; Yan *et al.* 2001; Uysal *et al.* 2006). The fault-gouge sample from the Carmel Fault Zone (sample N1) is composed of a calcite and dolomite mixture (Table 1), and the SEM image indicates that a large part of the fault gouge is, in fact, newly grown euhedral calcite grains (Fig. 3f). However, because the two cannot be physically separated, the geochemical results are of a mixed host-rock gouge and authigenic calcite. The similarity of Y-REE patterns of the fault gouge (sample N1, Fig. 3f) and the host rock (sample HR-N2), suggests that the Y-REE composition was dominated by the marine carbonate host rock with the absence of an external fluid. However, unlike the other fault-related precipitates, the calcite fault gouge is enriched in REE relative to the host rock. A range of factors can affect fluid REE characteristics, including pH, release from host minerals and the compositional make-up of the source rock, as well as surface complexation by Fe–Mn oxyhydroxides (Choi *et al.* 2009). Influence of the latter can be seen in the relationship between REE levels in the veins (a proxy to the efficiency of REE scavenging from the fluid into the precipitating carbonate) and the presence of

oxyhydroxide, as approximated by Mn concentrations (108 ppm) and Mn/Fe ratio (0.04; Table 1). Variability in REE concentrations in some veins or fault gouges can be attributed partly to the effect of FeMn-oxyhydroxide scavenging. We proposed that fault gouge in the Carmel Fault Zone is enriched with REE due to pervasive fluid flow and REE scavenged by the calcite fault gouge, as found elsewhere (Pili *et al.* 2002). This is supported by the fact that the Ce-negative and Y-positive anomalies inherited from the sea-water carbonate host rocks is well preserved in the fault gouge sample (Fig. 5c), indicating that fluid was probably equilibrated with the carbonate sequence.

### *Calcite precipitates in the Baraq Fault*

In the Baraq Fault Zone, calcite precipitates are found as tension gashes and veins along fault planes (Fig. 7d). Calcite precipitates are characterized by a growth-competition texture (Fig. 3d), which indicates that vein precipitation occurred over a longer timescale. The REE pattern is similar to the host-rock samples (Fig. 5d), but is two orders of magnitude more depleted, with HREE enrichment in the veins (Table 2). The observed HREE enrichment can be due to complexation processes that are common within shallow groundwater systems (Johannesson *et al.* 1999; Johannesson & Hendry 2000). The rather high  $\delta^{18}\text{O}$  compositions of calcite-filled veins in this site (29‰; Fig. 4a) are similar to reported values in speleothems from southern Israel (Vaks *et al.* 2010). The increase in  $\delta^{18}\text{O}$  values in speleothems is considered to reflect the relatively heavy  $\delta^{18}\text{O}$  composition of rainwater in southern Israel compared with central and northern Israel due to the low amount of precipitation and intense evaporation processes (Vaks *et al.* 2003). Alternatively, the increase in  $\delta^{18}\text{O}$  values may represent deposition during glacial period (Vaks *et al.* 2010); however, the U–Th age uncertainties are too high to distinguish between glacial and interglacial intervals (sample R9 with  $417 \pm 30/25$  ka). In addition,  $\delta^{13}\text{C}$  values of speleothems usually reflect both the vegetation type and soil–water–rock interaction (e.g. Bar-Matthews *et al.* 1997). At this site, the  $\delta^{13}\text{C}$  values are relatively high (*c.* 0.02‰; Fig. 4a) and the  $\Delta\delta^{13}\text{C}$  vein-host rock values are close to zero (Fig. 4b), indicating the very small contribution made by vegetation (mostly C4 type) in this hyper-arid climate of southern Israel (Vaks *et al.* 2010). The results suggest that the fluid source is meteoric water or groundwater (rather than exotic or deep-seated fluid types) with a negligible component of  $\text{CO}_2$ , and precipitation in the near-surface, low-temperatures environment (Fig. 4c).

The structural observations indicate that tension gashes and fault-parallel fractures are syntectonic fault-driven structures. However, calcite precipitation occurred over a long period of time and during pervasive fluid infiltration into the fault zone. Estimation for calcite growth rate in fissures at near-equilibrium conditions range from 0.12 to 0.22 mm ka<sup>-1</sup> (Ford *et al.* 1993; Plummer *et al.* 2000). Thus, the U–Th ages can only provide an average age for calcite precipitation in the veins. Considering that an approximately 30 mm-thick calcite vein (sample R9) evolved over a time period of at least 150–250 ka, a calcite average age of  $417 \pm 30/25$  ka would suggest a maximum age for calcite precipitation of around 540 ka. Age constraint on the youngest activity along the Baraq Fault is considered to be prior to 350 ka. This age is based on estimation of the timing of erosion following major tectonic movement along the fault (Avni *et al.* 2000). It is possible that the formation of the syntectonic vein structures is associated with the youngest activity along the Baraq Fault.

### **Conclusions**

The microstructures and geochemistry of fault-related calcite precipitates indicate different conditions under which calcite precipitate in fault zones. Our conclusions from the four studied sites are as follows.

- In the Düzici Fault Zone, calcite-filled veins and hydraulic fractures precipitated co-seismically from deep-seated fluids that migrated upwards into the fault zone during the seismic cycle. The precipitation was associated with the fast nucleation of carbonates attributed to a sudden fluid or  $\text{CO}_2$  partial pressure drop caused by fracturing. The U–Th ages in this site indicate at least three consecutive faulting events: prior to 525 ka; during 525–501 ka; and at approximately 405 ka.
- In the Har Zefiyya Fault Zone, the geochemistry of calcite-filled dilation veins indicates that precipitation of calcite occurred by karst processes in the near-surface environment. The U–Th ages indicate that initial opening of the vein occurred prior to about 550 ka. This age is temporally associated with east–west contractional deformation phase documented along this sector of the DSFZ.
- In the Carmel Fault Zone, calcite precipitated directly onto the fault plane under open-space and fluid-filled conditions. The coating shows no subsequent deformation by repeated slip along the fault. Stable isotope composition suggests precipitation by karst processes, which involved  $\text{CO}_2$ -rich fluids migrating downwards

- in the fault zone. Calcite fault-gouge precipitates in the Carmel Fault Zone are a mixture of host-rock gouge and authigenic calcite, and their overall geochemistry suggests pervasive fluid–rock interaction in the fault zone.
- In the Baraq Fault Zone, calcite precipitated within syntectonic tension gashes and veins. This occurred over a long period of time and during a pervasive fluid infiltration in the fault zone. The U–Th ages provide an average age of  $417 \pm 30/25$  ka, with a maximum age of 540 ka. This age is in agreement with the youngest known activity along this fault zone.

We wish to thank Dr Y. Feng for providing technical assistance with U–Th TIMS analyses. Dr W.-P. (Sunny) Hu is thanked for her assistance with ICP-MS analyses. Ms K. Baublys is thanked for her kind help with stable isotope mass spectrometry and D. Thiede is thanked for his help with cathodoluminescence (CL) microscopy. The manuscript benefited from constructive reviews by S. Barker and an anonymous reviewer.

## References

- AKYUZ, H. S., ALTUNEL, E., KARABACAK, V. & YALCINER, C. C. 2006. Historical earthquake activity of the northern part of the Dead Sea Fault Zone, southern Turkey. *Tectonophysics*, **426**, 281–293.
- AMIT, R., ZILBERMAN, E., PORAT, N. & ENZEL, Y. 1999. Relief inversion in the Avrona Playa as evidence of large-magnitude historical earthquakes, Southern Arava Valley, Dead Sea Rift. *Quaternary Research*, **52**, 76–91.
- AVNI, Y. 1997. *Geological Evolution of the Central and Southern Negev as an Indicator of the Evolution of the Dead Sea Transform Western Margin in the Late Neogene and Quaternary*. PhD, Hebrew University.
- AVNI, Y., BARTOV, Y., GARFUNKEL, Z. & GINAT, H. 2000. Evolution of the Paran drainage basin and its relation to the Plio-Pleistocene history of the Arava Rift western margin, Israel. *Israel Journal of Earth Sciences*, **49**, 215–238.
- AVNI, Y., BARTOV, Y., GARFUNKEL, Z. & GINAT, H. 2001. The Arava Formation-A Pliocene sequence in the Arava Valley and its western margin, southern Israel. *Israel Journal of Earth Sciences*, **50**, 101–120.
- BAR-MATTHEWS, M., AYALON, A., GILMOUR, M., MATTHEWS, A. & HAWKESWORTH, C. J. 2003. Seaward oxygen isotopic relationships from planktonic foraminifera and speleothems in the Eastern Mediterranean region and their implication for paleorainfall during interglacial intervals. *Geochimica et Cosmochimica Acta*, **67**, 3181–3199.
- BAR-MATTHEWS, M., AYALON, A. & KAUFMAN, A. 1997. Late Quaternary paleoclimate in the eastern mediterranean region from stable isotope analysis of speleothems at Soreq Cave, Israel. *Quaternary Research*, **47**, 155–168.
- BARKER, S. L. L., COX, S. F., EGGINIS, S. M. & GAGAN, M. K. 2006. Microchemical evidence for episodic growth of antitaxial veins during fracture-controlled fluid flow. *Earth and Planetary Science Letters*, **250**, 331–344.
- BAU, M. & DULSKI, P. 1999. Comparing yttrium and rare earths in hydrothermal fluids from the Mid-Atlantic Ridge: implications for Y and REE behaviour during near-vent mixing and for the Y/Ho ratio of proterozoic seawater. *Chemical Geology*, **155**, 77–90.
- BAU, M. & MOLLER, P. 1992. Rare-earth element fractionation in metamorphic hydrothermal calcite, magnesite and siderite. *Mineralogy and Petrology*, **45**, 231–246.
- BEGIN, Z. B., STEINBERG, D. M., ICHINOSE, G. A. & MARCO, S. 2005. A 40,000 year unchanging seismic regime in the Dead Sea rift. *Geology*, **33**, 257–260.
- BEN-MENAHEM, A. & ABOODI, E. 1981. Micro- and macroseismicity of the Dead Sea rift and off-coast eastern Mediterranean. *Tectonophysics*, **80**, 199–233.
- BOLES, J. R. & GRIVETTI, M. 2000. Calcite cementation along the Refugio/Carneros fault, Coastal California: a link between deformation, fluid movement and fluid–rock interaction at a basin margin. *Journal of Geochemical Exploration*, **69–70**, 313–316.
- BOLHAR, R., KAMBER, B. S., MOORBATH, S., FEDO, C. M. & WHITEHOUSE, M. J. 2004. Characterisation of early Archaean chemical sediments by trace element signatures. *Earth and Planetary Science Letters*, **222**, 43–60.
- BOULLIER, A.-M., FUJIMOTO, K. ET AL. 2004. Textural evidence for recent co-seismic circulation of fluids in the Nojima fault zone, Awaji island, Japan. *Tectonophysics*, **378**, 165–181.
- BOZKURT, E. 2001. Neotectonics of Turkey – a synthesis. *Geodinamica Acta*, **14**, 3–30.
- CHENG, H., EDWARDS, R. L., HOFF, J., GALLUP, C. D., RICHARDS, D. A. & ASMEROM, Y. 2000. The half-lives of uranium-234 and thorium-230. *Chemical Geology*, **169**, 17–33.
- CHOI, H. S., YUN, S. T., KOH, Y. K., MAYER, B., PARK, S. S. & HUTCHISON, I. 2009. Geochemical behavior of rare earth elements during the evolution of CO<sub>2</sub>-rich groundwater: a study from the Kangwon district, South Korea. *Chemical Geology*, **262**, 334–343.
- DE PAOLA, N., HOLDSWORTH, R. E. & COLLETTINI, C. 2008. The internal structure of dilatational stepovers in regional transtension zones. *International Geology Review*, **50**, 291–304.
- EGGINS, S. M., WOODHEAD, J. D. ET AL. 1997. A simple method for the precise determination of  $\geq 40$  trace elements in geological samples by ICPMS using enriched isotope internal standardisation. *Chemical Geology*, **134**, 311–326.
- EYAL, M., EYAL, Y., BARTOV, Y. & STEINITZ, G. 1981. The tectonic development of the western margin of the Gulf of Elat (Aqaba) rift. *Tectonophysics*, **80**, 39–66.
- EYAL, Y., KAUFMAN, A. & BAR-MATTHEWS, M. 1992. Use of 230Th/U ages of striated carnötites for dating fault displacements. *Geology*, **20**, 829–832.
- FLOTTE, N., PLAGNES, V., SOREL, D. & BENEDICTO, A. 2001. Attempt to date Pleistocene normal faults of the Corinth-Patras Rift (Greece) by U/Th method, and tectonic implications. *Geophysical Research Letters*, **28**, 3769–3772.
- FOLK, R. L. 1965. Some aspects of recrystallization in ancient limestones. In: PRAY, L. C. & MURRAY, R. C.

- (eds) *Dolomitization and Limestones Diagnosis*. SEPM, Special Publications, **13**, 14–48.
- FORD, D. C., LUNDBERG, J., PALMER, A. N., PALMER, M. V., DREYBRODT, W. & SCHWARCZ, H. P. 1993. Uranium-series dating of the draining of an aquifer; the example of Wind Cave, Black Hills, South Dakota; with Suppl. Data 9302. *Geological Society of America Bulletin*, **105**, 241–250.
- GARFUNKEL, Z. 1998. Constraints on the origin and history of the Eastern Mediterranean basin. *Tectonophysics*, **298**, 5–35.
- GRANT, L. B., MUELLER, K. J., GATH, E. M., CHENG, H., EDWARDS, R. L., MUNRO, R. & KENNEDY, G. L. 1999. Late Quaternary uplift and earthquake potential of the San Joaquin Hills, southern Los Angeles basin, California. *Geology*, **27**, 1031–1034.
- GRATIER, J. P., FAVREAU, P., RENARD, F. & PILI, E. 2002. Fluid pressure evolution during the earthquake cycle controlled by fluid flow and pressure solution crack sealing. *Earth, Planets and Space*, **54**, 1139–1146.
- HEMPTON, M. R. 1987. Constraints on Arabian plate motion and extensional history of the Red Sea. *Tectonics*, **6**, 687–705.
- HERECE, E. 2008. *Geological Map along East Anatolian Fault-İslahiye Segment*. General Directorate of Mineral Research and Exploration, Ankara, Turkey.
- HICKMAN, S. H., SIBSON, R. & BRUHN, R. 1995. Introduction to special section: mechanical involvement of fluids in faulting. *Journal of Geophysical Research*, **100**, 15 441–15 449.
- INOUE, M., NOHARA, M., OKAI, T., SUZUKI, A. & KAWAHATA, H. 2004. Concentrations of trace elements in carbonate reference materials Coral JCp-1 and Giant Clam Jct-1 by inductively coupled plasma-mass spectrometry. *Geostandards and Geoanalytical Research*, **28**, 411–416.
- JANSSEN, C., ROMER, R. L., HOFFMANN-ROTHE, A., MINGRAM, B., DULSKI, P., MÖLLER, P. & AL-ZUBI, H. 2005. The role of fluids in faulting deformation: a case study from the Dead Sea Transform (Jordan). *International Journal of Earth Sciences*, **94**, 243–255.
- JANSSEN, C., ROMER, R. L., PLESSEN, B., NAUMANN, R., HOFFMANN-ROTHE, A. & MATAR, A. 2007. Contrasting fluid regimes along the Dead Sea Transform. *Geofluids*, **7**, 275–291.
- JOFFE, S. & GARFUNKEL, Z. 1987. Plate kinematics of the circum Red Sea-a re-evaluation. *Tectonophysics*, **141**, 5–22.
- JOHANNESSEN, K. H., FARNHAM, I. M., GUO, C. & STETZENBACH, K. J. 1999. Rare earth element fractionation and concentration variations along a groundwater flow path within a shallow, basin-fill aquifer, southern Nevada, USA. *Geochimica et Cosmochimica Acta*, **63**, 2697–2708.
- JOHANNESSEN, K. H. & HENDRY, M. J. 2000. Rare earth element geochemistry of groundwaters from a thick till and clay-rich aquitard sequence, Saskatchewan, Canada. *Geochimica et Cosmochimica Acta*, **64**, 1493–1509.
- KARABACAK, V., AKYÜZ, S., KIYAK, N. G., ALTUNEL, E., MEGHRAOUI, M. & YÖNLÜ, Ö. 2010. Late Quaternary activity of the East Anatolian Fault Zone between *Gölbaşı* (Adiyaman) and *Karataş* (Adana). TÜBITAK (The Scientific and Technological Research Council of Turkey) Project (109Y043), First Annual Report.
- KENDALL, A. C., GONZALEZ, L. A., CARPENTER, S. J. & LOHMANN, K. C. 1993. Columnar calcite in speleothems: discussion and reply. *Journal of Sedimentary Petrology*, **63**, 550–552.
- KLINGER, Y., AVOUAC, J. P., DORBATH, L., KARAKI, N. A. & TISNERAT, N. 2000. Seismic behaviour of the Dead Sea fault along Araba valley, Jordan. *Geophysical Journal International*, **142**, 769–782.
- KU, T.-L. 1965. An evaluation of the  $U^{234}/U^{238}$  method as a tool for dating pelagic sediments. *Journal of Geophysical Research*, **70**, 3457–3474.
- LABAUME, P., CARRIO-SCHAFFHAUSER, E., GAMOND, J.-F. & RENARD, F. 2004. Deformation mechanisms and fluid-driven mass transfers in the recent fault zones of the Corinth Rift (Greece). *Comptes Rendus Geosciences*, **336**, 375–383.
- LAWRENCE, M. G. & KAMBER, B. S. 2006. The behaviour of the rare earth elements during estuarine mixing-revisited. *Marine Chemistry*, **100**, 147–161.
- LIN, A. 1996. Injection veins of crushing-originated pseudotachylite and fault gouge formed during seismic faulting. *Engineering Geology*, **43**, 213–224.
- LIU, Y. G., MIAH, M. R. U. & SCHMITT, R. A. 1988. Cerium: a chemical tracer for paleo-oceanic redox conditions. *Geochimica et Cosmochimica Acta*, **52**, 1361–1371.
- LUDWIG, K. R. 1991. *ISOPLOT: A Plotting and Regression Program for Radiogenic-isotope Data*; version 2.2. US Geological Survey, Reston, VA.
- MARCO, S., ROCKWELL, T. K., HEIMANN, A., FRIESLANDER, U. & AGNON, A. 2005. Late Holocene activity of the Dead Sea Transform revealed in 3D palaeoseismic trenches on the Jordan Gorge segment. *Earth and Planetary Science Letters*, **234**, 189–205.
- MART, Y., RYAN, W. B. F. & LUNINA, O. V. 2005. Review of the tectonics of the Levant Rift system: the structural significance of oblique continental breakup. *Tectonophysics*, **395**, 209–232.
- MATSUDA, T., OMURA, K. ET AL. 2004. Fracture-zone conditions on a recently active fault: insights from mineralogical and geochemical analyses of the Hirabayashi NIED drill core on the Nojima fault, southwest Japan, which ruptured in the 1995 Kobe earthquake. *Tectonophysics*, **378**, 143–163.
- MILLER, S. A., COLLETTINI, C., CHIARALUCE, L., COCCO, M., BARCHI, M. & KAUS, B. J. P. 2004. Aftershocks driven by a high-pressure  $\text{CO}_2$  source at depth. *Nature*, **427**, 724–727.
- MULLER, W. 2003. Strengthening the link between geochronology, textures and petrology. *Earth and Planetary Science Letters*, **206**, 237–251.
- NEMER, T. & MEGHRAOUI, M. 2006. Evidence of coseismic ruptures along the Roum fault (Lebanon): a possible source for the AD 1837 earthquake. *Journal of Structural Geology*, **28**, 1483–1495.
- O'NEIL, J. R., CLAYTON, R. N. & MAYEDA, T. K. 1969. Oxygen isotope fractionation in divalent metal carbonates. *Journal of Chemical Physics*, **51**, 5547–5558.
- PILI, É., POITRASSON, F. & GRATIER, J.-P. 2002. Carbon–oxygen isotope and trace element constraints on how fluids percolate faulted limestones from the San

- Andreas Fault system: partitioning of fluid sources and pathways. *Chemical Geology*, **190**, 231–250.
- PLUMMER, L. N., BUSENBERG, E. & RIGGS, A. C. 2000. In-situ growth of calcite at Devils Hole, Nevada: comparison of field and laboratory rates to a 500,000 year record of near-equilibrium calcite growth. *Aquatic Geochemistry*, **6**, 257–274.
- RAMSAY, J. G. 1980. The crack-seal mechanism of rock deformation. *Nature*, **284**, 135–139.
- REILINGER, R. E., MCCCLUSKY, S. C. ET AL. 1997. Global positioning system measurements of present-day crustal movements in the Arabia–Africa–Eurasia plate collision zone. *Journal of Geophysical Research*, **102**, 9983–9999.
- ROTSTEIN, Y., SHALIV, G. & RYBAKOV, M. 2004. Active tectonics of the Yizre’el valley, Israel, using high-resolution seismic reflection data. *Tectonophysics*, **382**, 31–50.
- SCHATTNER, U., BEN-AVRAHAM, Z., RESHEF, M., BAR-AM, G. & LAZAR, M. 2006. Oligocene–Miocene formation of the Haifa basin: Qishon–Sirhan rifting coeval with the Red Sea–Suez rift system. *Tectonophysics*, **419**, 1–12.
- SECOR, D. T. 1965. Role of fluid pressure in jointing. *American Journal of Science*, **263**, 633–646.
- SHAPIRA, A. & LEA, F. 1987. Microseismicity of three locations along the Jordan Rift. In: BEN-AVRAHAM, Z. (ed.) *Sedimentary Basins within the Dead Sea and Other Rift Zones*. *Tectonophysics*, **141**, 89–94.
- SIBSON, R. H. 1987. Earthquake rupturing as a mineralizing agent in hydrothermal systems. *Geology*, **15**, 701–704.
- SKOBELEV, S. F., HANON, M., KLERKX, J., GOVOROVA, N. N., LUKINA, N. V. & KAZMIN, V. G. 2004. Active faults in Africa: a review. *Tectonophysics*, **380**, 131–137.
- SNEH, A. & WEINBERGER, R. 2003. Geology of the Metulla quadrangle, northern Israel: implications for the offset along the Dead Sea Rift. *Israel Journal of Earth Sciences*, **52**, 123–138.
- STEINITZ, G. & BARTOV, Y. 1991. The Miocene–Pleistocene history of the Dead Sea segment of the Rift in the light of K–Ar of basalts. *Israel Journal of Earth Sciences*, **40**, 199–208.
- SUN, S.-S. & McDONOUGH, W. F. 1989. Chemical and isotopic systematics of oceanic basalts: implications for mantle compositions and processes. In: SAUNDERS, A. D. & NORRY, M. J. (eds) *Magmatism in the Ocean Basins*. The Geological Society, London, Special Publications, **42**, 313–345.
- SWART, P. K., BURNS, S. J. & LEDER, J. J. 1991. Fractionation of the stable isotopes of oxygen and carbon in carbon dioxide during the reaction of calcite with phosphoric acid as a function of temperature and technique. *Chemical Geology*, **86**, 89–96.
- SZABO, B. J. & ROSHOLT, J. N. 1989. Uranium-series nuclides in the Golden fault, Colorado, U.S.A.: dating latest fault displacement and measuring recent uptake of radionuclides by fault-zone materials. *Applied Geochemistry*, **4**, 177–182.
- TAYMAZ, T., WESTAWAY, R. & REILINGER, R. 2004. Active faulting and crustal deformation in the Eastern Mediterranean region. *Tectonophysics*, **391**, 1–9.
- UYDAL, I. T., MUTLU, H., ALTUNEL, E., KARABACAK, V. & GOLDING, S. D. 2006. Clay mineralogical and isotopic (K–Ar,  $\delta^{18}\text{O}$ , 8D) constraints on the evolution of the North Anatolian Fault Zone, Turkey. *Earth and Planetary Science Letters*, **243**, 181–194.
- UYDAL, I. T., FENG, Y. ET AL. 2007. U-series dating and geochemical tracing of late Quaternary travertine in co-seismic fissures. *Earth and Planetary Science Letters*, **257**, 450–462.
- UYDAL, I. T., FENG, Y.-X., ZHAO, J.-X., ISIK, V., NURIEL, P. & GOLDING, S. D. 2009. Hydrothermal CO<sub>2</sub> degassing in seismically active zones during the late Quaternary. *Chemical Geology*, **265**, 442–454.
- UYDAL, I. T., FENG, Y.-X. ET AL. 2011. Seismic cycles recorded in late Quaternary calcite veins: geochronological, geochemical and microstructural evidence. *Earth and Planetary Science Letter*, **303**, 84–96.
- VAKS, A., BAR-MATTHEWS, M. ET AL. 2003. Paleoclimate reconstruction based on the timing of speleothem growth and oxygen and carbon isotope composition in a cave located in the rain shadow in Israel. *Quaternary Research*, **59**, 182–193.
- VAKS, A., BAR-MATTHEWS, M., MATTHEWS, A., AYALON, A. & FRUMKIN, A. 2010. Middle–Late Quaternary paleoclimate of northern margins of the Saharan–Arabian Desert: reconstruction from speleothems of Negev Desert, Israel. *Quaternary Science Reviews*, **29**, 2647–2662.
- VAN DER PLUIJM, B. A., HALL, C. M., VROLIJK, P. J. & PEVEAR, D. R. 2001. The dating of shallow faults in the Earth’s crust. *Nature*, **412**, 172–175.
- VAN ECK, T. & HOFSTETTER, A. 1990. Fault geometry and spatial clustering of microearthquakes along the Dead Sea–Jordan rift fault zone. In: KOVACH, R. L. & BEN-AVRAHAM, Z. (eds) *Geologic and Tectonic Processes of the Dead Sea Rift Zone*. *Tectonophysics*, **180**, 15–27.
- VERHAERT, G., MUCHEZ, P. ET AL. 2004. Origin of palaeofluids in a normal fault setting in the Aegean region. *Geofluids*, **4**, 300–314.
- VERHAERT, G., MUCHEZ, P., SINTUBIN, M., SIMILOX-TOHON, D., VANDYCKE, S. & WAELKENS, M. 2003. Reconstruction of neotectonic activity using carbonate precipitates: a case study from the northwestern extremity of the Isparta Angle (SW Turkey). *Journal of Geochemical Exploration*, **78–79**, 197–201.
- VROLIJK, P. J. & VAN DER PLUIJM, B. A. 1999. Clay gouge. *Journal of Structural Geology*, **21**, 1039–1048.
- WEINBERGER, R., GROSS, M. R. & SNEH, A. 2009. Evolving deformation along a transform plate boundary: example from the Dead Sea Fault in northern Israel. *Tectonics*, **28**, doi:10.1029/2008TC002316.
- WESTAWAY, R. 1994. Present day kinematics of the Middle East and Eastern Mediterranean sea. *Journal of Geophysical Research*, **99**, 12 072–12 096.
- WESTAWAY, R. & ARGYR, J. 1996. The Golbasi basin, southeastern Turkey: a complex discontinuity in a major strike-slip fault zone. *Journal of the Geological Society, London*, **153**, 729–744.
- WOOD, S. A. 1990. The aqueous geochemistry of the rare-earth elements and yttrium. I. Review of available low-temperature data for inorganic complexes and the

- inorganic REE speciation of natural-waters. *Chemical Geology*, **82**, 159–186.
- YAN, Y., VAN DER PLUIJM, B. A. & PEACOR, D. R. 2001. Deformation microfabrics of clay gouge, Lewis Thrust, Canada: a case for Fault weakening from clay transformation. In: HOLDSWORTH, R. E., STRACHAN, R. A., MAGLOUGHLIN, J. F. & KNIPE, R. J. (eds) *The Nature and Tectonic Significance of Fault Zone Weakening*. Geological Society, London, Special Publications, **186**, 103–112.
- YU, K.-F., ZHAO, J.-X., SHI, Q., CHEN, T.-G., WANG, P.-X., COLLERSON, K. D. & LIU, T.-S. 2006. U-series dating of dead Porites corals in the South China sea: evidence for episodic coral mortality over the past two centuries. *Quaternary Geochronology*, **1**, 129–141.
- ZHAO, J.-X., HU, K., COLLERSON, K. D. & XU, H. 2001. Thermal ionization mass spectrometry U-series dating of a hominid site near Nanjing, China. *Geology*, **29**, 27–30.
- ZILBERMAN, E., AMIT, R., PORAT, N., ENZEL, Y. & AVNER, U. 2005. Surface ruptures induced by the devastating 1068 AD earthquake in the southern Arava valley, Dead Sea Rift, Israel. *Tectonophysics*, **408**, 79–99.

# Controls on fluid flow in transpressive orogens, Taiwan and New Zealand

P. UPTON<sup>1</sup>\*, D. CRAW<sup>2</sup>, B. YU<sup>3</sup> & Y.-G. CHEN<sup>4</sup>

<sup>1</sup>GNS Science, PO Box 30368, Lower Hutt 5040, New Zealand

<sup>2</sup>Geology Department, University of Otago, PO Box 56, Dunedin 9054, New Zealand

<sup>3</sup>National Taipei University of Technology, Taipei, Taiwan

<sup>4</sup>Geosciences Department, National Taiwan University, Taipei, Taiwan

\*Corresponding author (e-mail: [p.upton@gns.cri.nz](mailto:p.upton@gns.cri.nz))

**Abstract:** Taiwan and the Southern Alps of New Zealand are both young transpressive orogens characterized by rapid uplift and exhumation, high heat flow and vigorous surface processes. However, the distribution of heat flow, hot springs and veins in the two orogens is different. Taiwan has higher heat flow, distributed hot springs and localized veining. The Southern Alps has a narrow heat-flow anomaly, localized warm springs and widespread veining. Both orogens have two fluid-flow systems centred about the drainage divide. Shallow topographically driven meteoric water is restricted to the top 2–4 km. Deep flow is dominated by mineralizing rock-exchanged fluids. Extensional deformation occurs in the divide region of both orogens. At depth, vertical stretching produces subhorizontal veins. At shallower levels, stretching is horizontal and veins are steep. Veins in Taiwan are rare with zones of intense veining where flow has been localized into one site during exhumation from metamorphic to near-surface conditions. Fracturing and veining of the initially weak Slate Belt rocks causes a rheological change, increasing the tensile strength and making it more prone to fracturing, thus focusing fluid flow into the same locale. More uniform rheology in the Southern Alps leads to distributed veining.

Orogen-wide fluid generation and flow are an inevitable consequence of collisional-related deformation in all convergent mountain belts, both ancient and modern (Yardley *et al.* 1991; Dipple & Ferry 1992; Cox 2005). Fluids at depth can have a significant impact on tectonic processes, as the presence of fluid, especially at high pore fluid pressures, affects rheology, seismicity, metamorphism and the structural evolution of rocks within the orogen (Dipple & Ferry 1992; Sibson 2000; Cox 2005; Upton & Koons 2007). Much of the evidence for fluid flow is ephemeral, and it is difficult to trace fluid processes in ancient mountain belts because such transient features are lost when tectonic processes cease. Veins and associated fluid inclusions are the most tangible fluid-related features preserved, but the conditions under which veins formed – including strain rates, heat flow distribution and topography – are difficult to deduce in ancient mountain belts. To better understand fluid flow in collisional orogens it is necessary to examine active mountain belts where transient fluid features are present along with active exhumation of young vein systems. These natural laboratories provide well-constrained snapshots of tectonically driven fluid-flow processes. Taiwan is one of the youngest and best-constrained collisional

mountain belts on Earth (Suppe 1980; Ho 1986; Byrne & Liu 2002; Simoes *et al.* 2007), and provides a unique view into an active tectonic–hydrothermal fluid-flow system (Fig. 1).

Hot-spring systems are the most obvious ephemeral tectonic fluid-flow features in active mountain belts, and these give indications of the distribution and magnitude of near-surface fluid mobility and heat flow within the orogen (Chen 1985). At greater depth, geophysical techniques such as seismic tomography (Wu *et al.* 1997, 2007; Wang *et al.* 2010) and magnetotelluric determination of resistivity (Bertrand *et al.* 2009) provide insight into fluid distribution on a crustal scale. In this study, we combine available information on these fluid features with newly acquired observations on vein distribution at outcrop and orogen scale to deduce the scale and nature of fluid-flow processes within the main mountain range of Taiwan.

All active collisional mountain belts have associated fluid-flow systems that have been operating since the inception of the orogens (Craw *et al.* 2002; Cox 2005). However, each of these orogens has unique features that affect the fluid flow, limiting the value of generalized observations on fluid flow in orogenic processes. Hence, comparisons between different orogens are useful for seeing

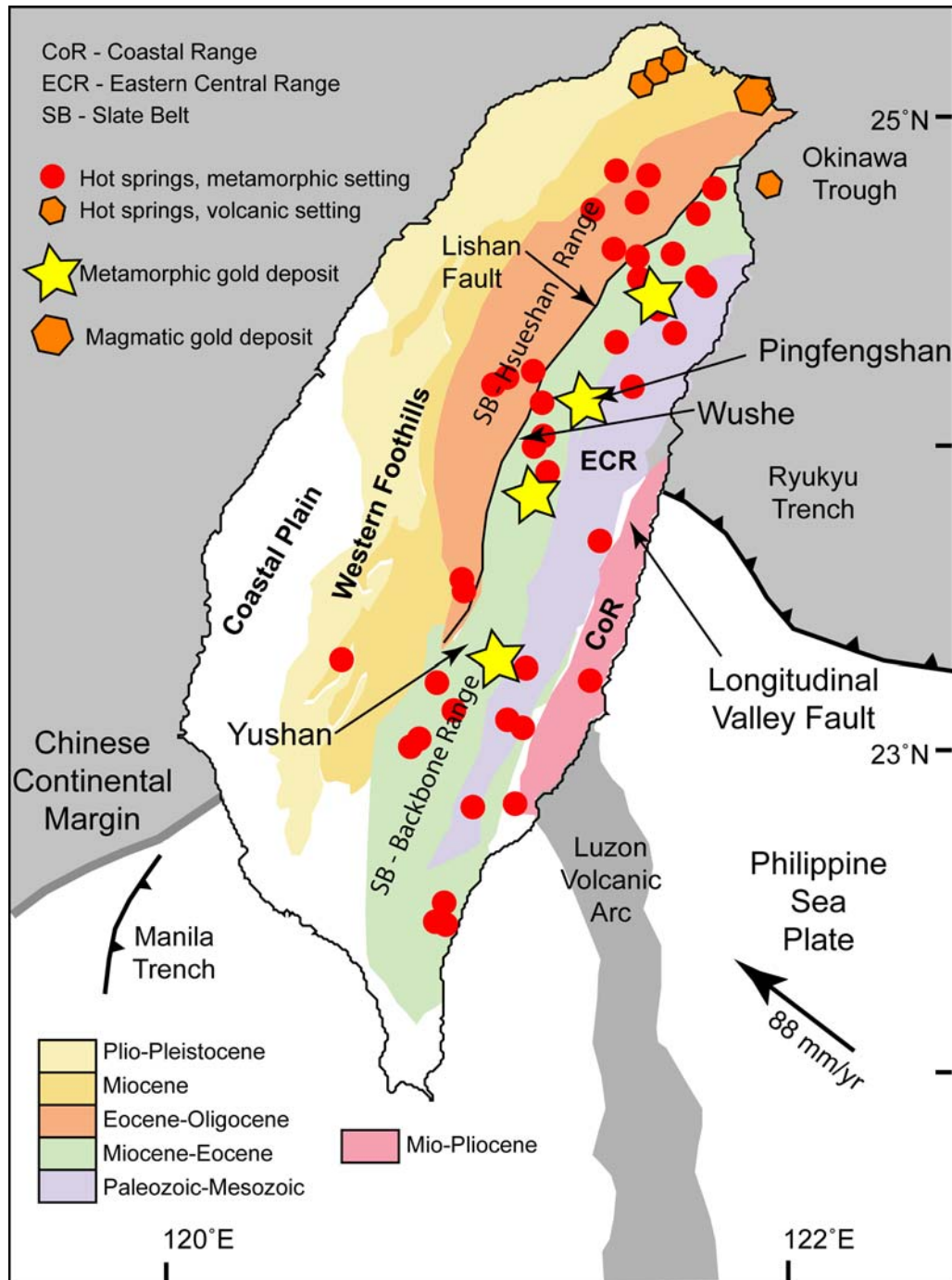


**Fig. 1.** Geology and tectonic setting of Taiwan. Also shown are hot springs and gold deposits within Taiwan.

past the various local effects to more general processes of collision-driven fluid flow. In this study, we make extensive comparisons between Taiwan

and the Southern Alps of New Zealand, which share many orogenic and fluid-flow features (Table 1). In particular, the relative youth and the

**Table 1.** Comparison of tectonic–hydrothermal fluid-flow systems in mountains of Taiwan and South Island (SI), New Zealand

		Taiwan	New Zealand SI
Tectonics	Plate boundary	Eurasia–Philippine	Pacific–Australia
	Motion	Oblique collision	Oblique collision
	Obliquity	20° from perpendicular <sup>a</sup>	70° from perpendicular <sup>a</sup>
	Rate	88 mm year <sup>-1</sup> <sup>a</sup>	37 mm year <sup>-1</sup> <sup>a</sup>
	Initiation	Pliocene	Pliocene
	Magmatism	Volcanism above the subduction zone at the northern tip of the orogen	Volcanism above the subduction zones to the north and south of the orogen
Mountains	Altitude	Maximum 3952 m	Maximum 3754 m
	Gradient	c. 30 km sea level to the Main Divide on the inboard side (east)	c. 30 km sea level to Main Divide on the inboard side (west)
	Profile	Asymmetrical, outboard basins and foothills (west)	Asymmetrical, outboard basins and foothills (east)
	Rocks	Pre-Tertiary basement; Cenozoic sediments, minor basement; outboard Pliocene–Recent molasse	Mesozoic basement; outboard Cenozoic cover and Pliocene–Recent molasse
Climate	Weather patterns	Subtropical, summer monsoon, typhoons	Temperate maritime + alpine; prevailing W wind, orographic
	Rainfall	1–5 m year <sup>-1</sup> <sup>b</sup>	0.5–12 m year <sup>-1</sup> <sup>c</sup>
	Rain distribution	Symmetrical across mountains	Asymmetrical, maximum on inboard (western) side, rain shadow to the east
Warm/hot springs	Distribution	Throughout mountains	Along plate boundary
	Temperature	Up to 99 °C <sup>d</sup>	Maximum of 56 °C <sup>e</sup>
	Water source	Meteoric <sup>d</sup>	Meteoric <sup>e</sup>
Major vein systems (fluid-flow zones)	Inboard	Focused vein swarms	Fracture-controlled; dispersed <sup>f,g</sup>
	Outboard	Lishan Fault; locally focused zones in mountains	Outboard faults <sup>h,j</sup>
	Fluid source	Mainly shallow meteoric; some deep-sourced brines	Mainly shallow meteoric; some basinal water; some deep-sourced <sup>h,j</sup>
Gold	Vein types	Mainly ankeritic; some late metamorphic	Mainly ankeritic; some late metamorphic <sup>k</sup>
	Distribution	Focussed zones near Main Divide	Widely dispersed near Main Divide <sup>l</sup>
	Fluid source	Deep, rock-exchanged brines	Deep, rock-exchanged low-salinity water <sup>l,m</sup>

<sup>a</sup>DeMets *et al.* (2010); <sup>b</sup>Galewsky *et al.* (2006); <sup>c</sup>Hicks *et al.* (1996); <sup>d</sup>Chen (1985); <sup>e</sup>Barnes *et al.* (1978); <sup>f</sup>Craw (1988); <sup>g</sup>Craw *et al.* (2002); <sup>h</sup>Templeton *et al.* (1998); <sup>i</sup>Templeton *et al.* (1999); <sup>j</sup>Upton *et al.* (2003); <sup>k</sup>Craw *et al.* (2010); <sup>l</sup>Becker *et al.* (2000); <sup>m</sup>Craw *et al.* (1994).

absence of magmatism from the main part of the orogens are important common features in both of these active collisional mountain belts (Table 1). These comparisons elucidate some general features of tectonic–hydrothermal systems that are probably common to all collisional mountain belts, but may be obscured by later overprinting of other features such as magmatism. There is a comprehensive published literature on the Southern Alps fluid-flow system, summarized in Table 1, which we draw on for our comparison. However, there is relatively little integrated information on tectonically driven fluid-flow and vein systems in Taiwan, so we focus the first part of this paper on fluid flow within the Taiwanese orogenic belt.

## Tectonic setting and regional geology of Taiwan

The island of Taiwan is a convergent tectonic belt developing during collision of the Eurasian continental margin and the Luzon volcanic arc on the Philippine Sea plate (Fig. 1) (Ho 1986). Convergence is oblique, and is occurring at about 88 mm year<sup>-1</sup> (Fig. 1) (DeMets *et al.* 2010). Convergence began in the Pliocene in the north of the island, and the locus of collision has migrated progressively southwards (Chi *et al.* 1981; Suppe 1981; Ho 1986). North of the Ryukyu Trench, extensional deformation is being imposed on the mature orogen, and some magmatic activity accompanies that extension (Ho 1986). Magmatism has induced some localized epithermal mineralization at the northern tip of the island, and the largest gold deposits occur in that region (Wang *et al.* 1999). However, there is no evidence of magmatic activity in the main orogen to the south of this zone. The Coastal Range Province of the island consists of accreted material from the northern portion of the Luzon Arc (Fig. 1) (Page & Suppe 1981; Ho 1986; Shyu *et al.* 2005).

From west to east, the Taiwan collisional orogen consists of three main components: the Western Foothills, a classic fold and thrust belt; the Slate Belt (Hseuhshan Range and Backbone Range), and the Eastern Central Range, which consists of overthrust basement rocks (Figs 1 & 2) (Ho 1986; Fisher *et al.* 2002). The fold and thrust belt deforms a thick (up to 10 km) pile of mainly marine sandstones, siltstones and mudstones formed on the passive and/or rifting Eurasian continental margin between Eocene and Miocene time (Suppe 1981; Ho 1986; Moutherneau *et al.* 2002). Continued deformation, uplift and erosion since the Miocene has resulted in incorporation of up to 5 km of Plio-Pleistocene molasse sediments into the deforming sedimentary pile (Moutherneau *et al.*

2002). The Slate Belt (Fig. 1) consists of finer-grained distal equivalents of the Eocene–Miocene sedimentary sequence that has been more complexly deformed and variably metamorphosed. The fold and thrust belt of the Western Foothills is being deformed above a regional décollement structure at 5–10 km depth (Suppe 1981, 2007; Carena *et al.* 2002). Pre-Tertiary basement rocks, including metasedimentary schists, marble and plutonic rocks, have been thrust onto the Slate Belt from the east and incorporated into the Pliocene–Recent orogen (Fig. 1) (Ho 1986; Lo & Onstott 1995; Fisher *et al.* 2002).

The Slate Belt consists of interlayered mudstones (slates), siltstones and sandstones that have been variably metamorphosed and texturally reconstituted. Some of the slates contain carbonaceous matter that becomes graphitized with increasing metamorphic grade (Beyssac *et al.* 2007). The degree of metamorphic reconstitution varies widely within and between outcrops, but there is a general progression in metamorphic grade from west to east. Metamorphic grade ranges from subgreenschist to lowest greenschist facies in the western part of the Slate Belt to upper greenschist facies (about 350 °C) (Beyssac *et al.* 2007) in the eastern part of the belt. Greenschist-facies foliation of probable Pliocene age is imposed on both the Slate Belt rocks and the overthrust basement rocks at the eastern margin of the Slate Belt (Lo & Onstott 1995; Fisher *et al.* 2002; Beyssac *et al.* 2007). Primary (sedimentary) porosity has been destroyed during metamorphic recrystallization, accompanied by several stages of creation and destruction of local (mm-scale) extension sites during cleavage development (Fisher *et al.* 2002).

Bedding is folded into tight and locally overturned folds that mainly face to the west (Ho 1986; Fisher *et al.* 2002). These folds of bedding have a well-defined fold-axial surface fabric that generally dips moderately to the east. The axial-surface fabric becomes progressively better developed towards the east, where the fabric is a fully recrystallized metamorphic foliation. Most outcrops on the western side of the belt are dominated by bedding, with weak cleavage in slates. Outcrops further east become dominated by the metamorphic foliation, which is best developed in the slates. The foliation has been deformed by kink folds on the 1–10 cm scale, with widespread development of steeply dipping fold-axial surface fractures.

The Lishan Fault stands out as a major topographical feature within Taiwan's mountain ranges. Active extension is occurring across the fault at its northeastern end, associated with stretching and the opening of the Okinawa Trough (Fig. 1). The Lishan Fault juxtaposes Slate Belt rocks against weakly deformed Eocene–Oligocene sedimentary

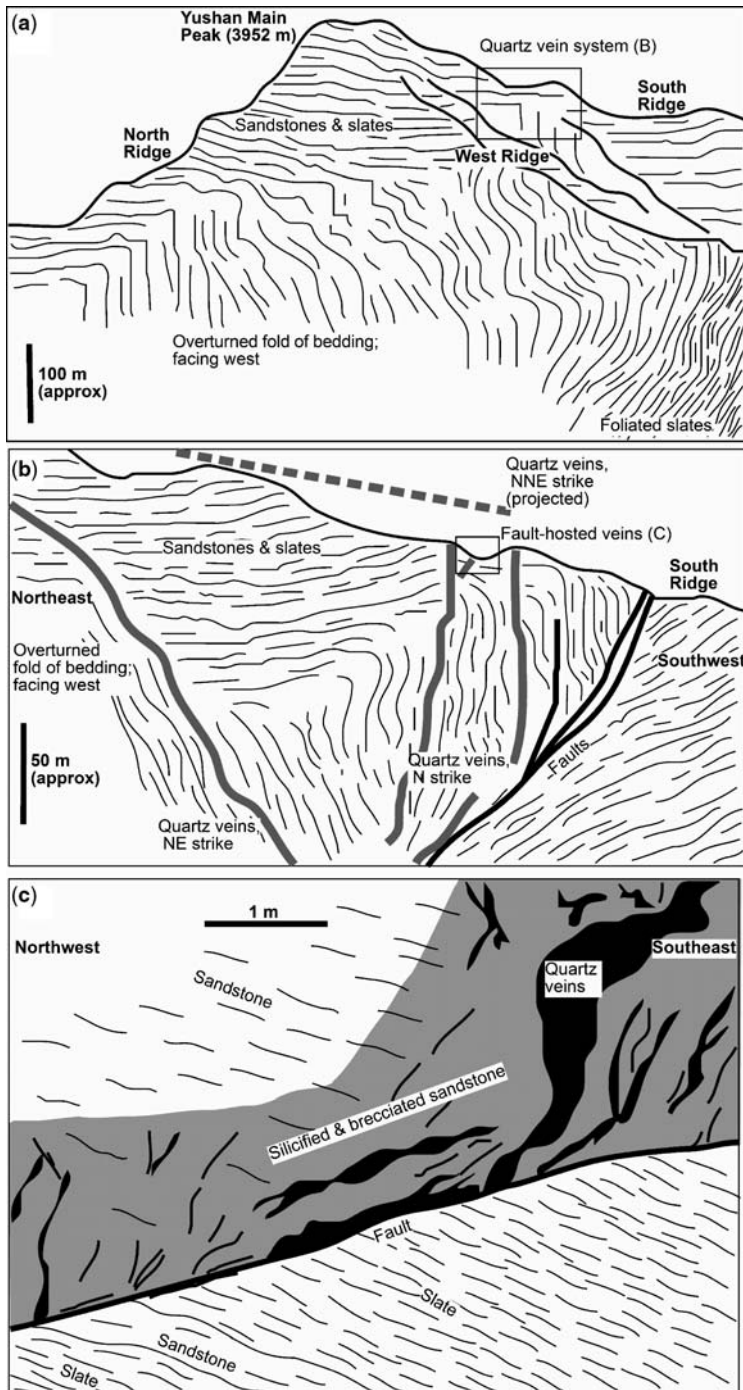


**Fig. 2.** Field sketches (from photographs) of structure and veins at Yushan in the core of the southern Slate Belt (Fig. 1). (a) Yushan Main Peak in the hinge of an overturned fold of bedding. (b) Parasitic fold hinge in the South Ridge of Yushan Main Peak, with cross-cutting quartz vein swarm. (c) Outcrop of quartz veins and silicification zone adjacent to a fault on the South Ridge of Yushan Main Peak.

rocks of the fold and thrust belt (Fig. 1). The fault becomes topographically indistinct at its southern end, near the Main Divide in the Yushan area, where it merges with the Chaochou Fault (Fig. 1). Calcite in Lishan Fault veins has  $\delta^{18}\text{O}$  values of +16.7 to +17.0‰. These values are similar to metamorphic veins at Pingfengshan gold mine, which formed from deep fluids in isotopic equilibrium with the rock (Fig. 1) (Craw *et al.* 2010)

## Field studies on vein systems

The general geology of the Taiwan Slate Belt has been well established from previous work (see the previous section), but there are few published observations on the structure and distribution of vein systems. Further, there is no integrated account of the nature and distribution of tectonic–hydrothermal fluid flow within the Slate Belt and associated rocks. Hence, as part of this study, we examined vein systems at a range of localities through the central mountains of Taiwan in order to link the fluid-flow system with the established geological framework. Fieldwork was focused on the Central Cross-island Highway and linking roads, the Pingfengshan gold mine area (Fig. 1) (Craw *et al.* 2010), the Lishan Fault zone and the high mountain area around Yushan (Fig. 1).

The steep mountains and rapid erosion rates ensure that outcrop is generally poor in all but the highest mountains and deepest gorges. Middle and lower slopes of the ranges are mantled by active landslides that commonly extend to river level. Hence, while it is generally possible to make observations on the mineralogical nature of veins and their relationships with their immediate host rocks, detailed structural analysis of vein geometry is fraught with uncertainties and has not been attempted in this study. Instead, we have focused on: (a) the general distribution pattern of vein systems on a regional scale; and (b) comparison of these Taiwan vein systems with those in the Southern Alps of New Zealand.

## Veins and gold deposits

Veins are rare in the Slate Belt and adjacent rocks to the east and west. Most outcrops are devoid of veins at all metamorphic grades from subgreenschist-facies rocks dominated by bedding to pervasively foliated upper-greenschist-facies rocks. Scattered thin (mm-scale) veinlets occur in some sandstone beds and cm-scale tension gashes occur locally in schists, especially those derived from sandstones. In contrast to the general paucity of veins, there are localized zones in which veins are abundant, and veins can dominate some outcrops in these

zones. The veined zones range from  $10\text{ m}^2$  to  $1\text{ km}^2$ , and vein orientations can vary widely within these zones, depending on the types of localized structural features that have controlled vein emplacement.

A spectacular set of veins on the slopes of Yushan Mountain (Figs 1 & 2) is intimately linked to fractures and faults formed during tight folding of bedding in a largely non-schistose part of the Slate Belt (Fig. 2). This vein system is especially notable because it occurs in a large volume of unusually well-exposed rock (several  $\text{km}^3$ ; Fig. 2a) that is unveined apart from rare scattered cm-scale tension gashes. Quartz veins up to 3 m across cut steeply through a parasitic fold on the steepened limb of a km-scale overturned fold of bedding (Fig. 2a, b). The veins appear to emanate from a moderately dipping fault zone in the hinge zone of the folds of bedding, but the largest veins cut across all structures (Fig. 2b). Small veins within a fault splay mimic this geometry at the outcrop scale (Fig. 2c). Veins consist of 10 cm- to metre-scale massive quartz, breccia zones from 10 cm to 10 m across, and silicified host rocks that extend up to 20 m from vein zones (Fig. 2b, c). The veins and silicified zones contain minor hydrothermal calcite and chlorite, in addition to quartz.

Veined zones in schistose parts of the Slate Belt to the east of the Main Divide have large numbers of small (10 cm-scale) veins that are commonly mutually cross-cutting. These zones, like that at Yushan (above), occur within large volumes of generally unveined schist. Some of these veins are parallel or subparallel to the pervasive foliation, and many of these have been boudinaged to some extent during synmetamorphic deformation of the foliation. Most of the veins clearly cut across the foliation, at a variety of angles, commonly forming stockworks and breccias. Veins in metamorphosed sandstones typically cut the foliation at a high angle, whereas veins in schistose slates are more nearly parallel to the foliation. All these veins, like those at Yushan, are dominated by quartz, with minor chlorite and calcite, and these minerals commonly merge into the greenschist-facies metamorphic fabric that contains the same minerals. These vein sets formed during, or in the latter stages of, the metamorphism of the host rocks.

A later set of veins containing ankeritic carbonate (ferroan dolomite) and rare albite, but no chlorite, is locally developed within the Slate Belt, and this cuts moderately to steeply across the foliation and any syn-late-metamorphic veins that are present. Ankeritic veins occur only rarely in the Yushan area. East of the Main Divide, ankeritic veins are mainly hosted by steeply dipping kink fold-axial surface fractures. These veins are rare or absent throughout most of the schist rock mass,

and occur in localized swarms. The ankeritic veins are particularly common in rocks that already contain abundant syn- to late-metamorphic veins (Craw *et al.* 2010).

Late-stage prismatic quartz veins (commonly called ‘fissure veins’ in other mountain belts) have formed in fractures in pre-existing quartz veins within well-defined vein zones (Craw *et al.* 2010). These late-stage veins contain prismatic quartz crystals (mm–cm scale) that extend into open cavities. These crystals are accompanied by bladed calcite crystals, a texture characteristic of boiling water, and rare adularia and chlorite (Simmons & Christenson 1994).

A zone of variable but locally intense vein emplacement occurs along the Lishan Fault (Figs 1 & 3). Some of these veins are concentrated in sandstones, with accompanying breccias and silicified host rock (Chan *et al.* 2005). The veins are dominated by quartz with subordinate chlorite and calcite. A wide (> 100 m) zone of slates at Wushe (Fig. 1) has anomalously well-developed foliation and veins (Fig. 3a, b) compared to adjacent rocks (Fig. 3c). Most of these veins consist of quartz with minor calcite and chlorite, and scattered ankerite along their margins. Some of the ankerite replaces hydrothermal chlorite and calcite that accompanied the early-formed veins in the swarm.

Four non-magmatic gold deposits occur within the Slate Belt of Taiwan (Fig. 1) (Tan *et al.* 1991). One of these, Pingfengshan, has been described in detail by Tan *et al.* (1991) and Craw *et al.* (2010). The Pingfengshan deposit occurs in a highly veined zone (> 1 km<sup>2</sup>) surrounded by largely unveined lower-greenschist-facies schist host rock. Foliation-parallel synmetamorphic veins are unmineralized, but late-metamorphic veins that transgress the foliation are mineralized with pyrrhotite, pyrite, arsenopyrite and gold (Tan *et al.* 1991; Craw *et al.* 2010). These veins are cut by auriferous ankeritic veins in kink fold-axial surfaces, and it is these veins that controlled historic mine development (Craw *et al.* 2010).

## Fluid sources and hot springs

Meteoric water is the most common near-surface fluid in the Taiwan orogen (Fig. 4). All springs are derived from meteoric water that has circulated through rocks with high geothermal gradients (Chen 1985; Lee & Cheng 1986). The stable isotopic signature of meteoric water is affected by precipitation altitude, with highest altitudes having a low  $\delta^{18}\text{O}$  value of approximately –13‰ (Shieh *et al.* 1983). Most springs consist of waters derived from a range of altitudes, although a spring near to Yushan, the highest mountain (Fig. 1), has the most depleted isotopic signature (Shieh *et al.* 1983). Waters emanating from some

springs in the eastern part of the fold and thrust belt have undergone some isotopic exchange with host-rock oxygen, so these waters have relatively high  $\delta^{18}\text{O}$  values (up to +4‰) and do not lie on the Taiwan meteoric water line (Shieh *et al.* 1983). Hot springs, with temperatures reaching 99 °C, are found throughout the Central and Hsuehsian Ranges of Taiwan (Fig. 1) (Chen 1985).

Oxygen isotopic exchange between meteoric water and host rocks becomes progressively more pronounced with increasing temperature of interaction (Fig. 4). Calcite deposited from hydrothermal fluids intersected in geothermal drillholes near to hot spring systems show increasing amounts of oxygen exchange with increasing depth and temperature (Yui *et al.* 1993). Significant exchange with the rock occurs at temperatures of 185–225 °C (Yui *et al.* 1993). Likewise, meteoric waters discharged from active fault zones in the fold and thrust belt have undergone some oxygen isotopic exchange with host sedimentary rocks (Fig. 4) (Yui *et al.* 1993).

Gold-bearing quartz veins near the Main Divide in the Slate Belt were deposited from fluids that had high  $\delta^{18}\text{O}$  values of around 10‰ (Fig. 4) (Tan *et al.* 1991). This high  $\delta^{18}\text{O}$  value is the same as that of a fluid in isotopic equilibrium with the greenschist-facies host rocks under metamorphic conditions (Tan *et al.* 1991). Gold mineralization was caused by passage of metamorphic brines (up to 5 wt% NaCl equivalent) from greenschist-facies slates into overlying rocks at 5–10 km depth (Craw *et al.* 2010). Some input from less saline meteoric water occurred in the auriferous ankeritic veins, and possibly the deeper-formed late-metamorphic veins as well (Craw *et al.* 2010).

The magnetotelluric data for the Taiwan orogen show a broad zone of low resistivity coincident with the fold and thrust belt (Bertrand *et al.* 2009). Such high conductivities are almost certainly a result of the presence of interconnected brines that make up the connate water in these dominantly marine sedimentary rocks. In contrast, the Slate Belt has relatively low conductivity in the magnetotelluric profile. This high resistivity is probably a result of: (a) the relatively small extent and highly focused nature of the fluid-flow systems that characterize the Slate Belt; (b) reduced porosity due to prograde metamorphism; and (c) the lower salinity of meteoric and diluted metamorphic fluids that dominate the Slate Belt. In addition, permeability for formation of vein systems was strongly structurally controlled and was probably transient and driven by seismic activity (Sibson 1996).

## Heat flow

Heat flow in regions such as Taiwan, with its mountainous terrain and high rainfall, is difficult to

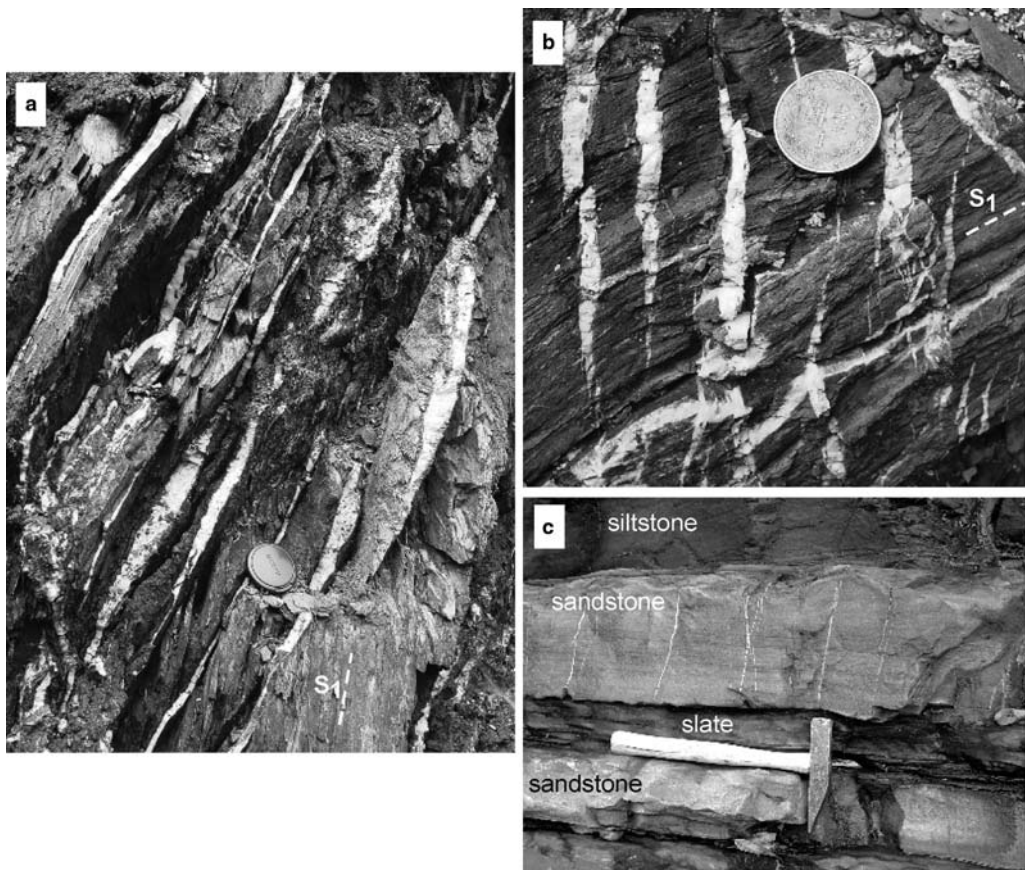


**Fig. 3.** Outcrop photographs of veined rocks in the vicinity of the Lishan Fault. (a) Schist from the Lishan Fault zone, with weak vertical foliation ( $S_1$ , dashed) and a swarm of quartz–carbonate veins (white) subparallel to the foliation. View to the south. (b) Schist from the Lishan Fault zone, with well-developed pervasive foliation ( $S_1$ , dashed), some foliation-parallel quartz–calcite–chlorite veins, and a swarm of steeply dipping quartz–ankerite veins filling vertical fractures. View to the south. (c) Bedded sedimentary rocks 4 km east of the Lishan Fault, with thin extensional veins in sandstone. Rocks are unfoliated apart from a weak cleavage in slate beds. View to the east.

constrain. Near-surface measurements of heat flow by Lee & Cheng (1986) show that heat flow is broadly associated with topographical relief, with the highest heat flows found in the Central Range between  $23^\circ$  and  $24^\circ\text{N}$ . Heat flow on the Coastal Plain is less than  $100 \text{ mW m}^{-2}$ . Heat flow estimates, determined from temperature measurements, increase from west to east, reaching approximately  $250 \text{ mW m}^{-2}$  in the Central Range (Lee & Cheng 1986).

There is no geological evidence for magmatic activity or igneous bodies at depth in the Slate Belt. Instead, the high heat flow arises from rapid exhumation and advection of hot rocks from depth towards the surface (Koons 1987; Lin 2000). In order to estimate the heat flow across the island of Taiwan, we ran simple three-dimensional (3D)

models (Fig. 5) using the thermo-mechanical modelling code FLAC<sup>3D</sup> (Cundall & Board 1988). These models were constrained by published estimates of exhumation rates (Dadson *et al.* 2003; Fuller *et al.* 2006a) and rock trajectories through the orogen (Carena *et al.* 2002; Gourley *et al.* 2007). Rock trajectories have exhumation from 25 km beneath the Eastern Central Range and from 12 km beneath the Slate Belt (Fig. 5b) (Beyssac *et al.* 2007; Craw *et al.* 2010). As the Luzon Arc is no longer active and only shows evidence of shallow hydrothermal activity,  $T = 60^\circ\text{C}$  (Chen 1985), we ignore any contribution to the heat flow from the Coastal Range. It should be noted that these basic models also ignore the effect of groundwater percolation (Whipp Jr & Ehlers 2007).

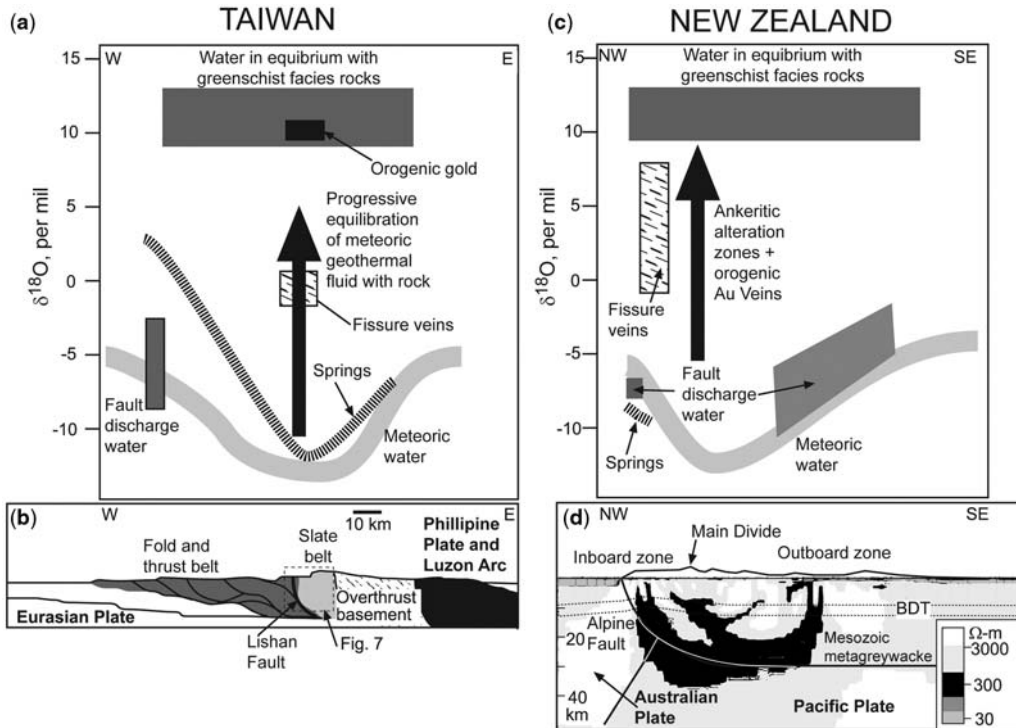


**Fig. 4.** Comparison of Taiwan and Southern Alps fluids. (a) Variation in  $\delta^{18}\text{O}$  of fluids in Taiwan from west to east showing the interaction between meteoric water and deeper water in equilibrium with greenschist-facies rocks occurring largely in the Slate Belt. (b) Schematic cross-section of Taiwan. (c) Variation in  $\delta^{18}\text{O}$  of fluids in the Southern Alps from west to east showing the interaction between meteoric water and deeper water in equilibrium with greenschist-facies rocks. Note that the fissure veins are found between the Alpine Fault and the Main Divide. (d) Cross-section of the Southern Alps showing high conductivity at depth beneath the mountains (Wannamaker *et al.* 2002).

Model estimates of heat flow range from  $300 \text{ mW m}^{-2}$  for an exhumation rate of  $5 \text{ mm year}^{-1}$  down to around  $115 \text{ mW m}^{-2}$  in the Central Ranges for the lower exhumation rates (Fig. 5d). In all models, the modelled high heat flow does not extend as far west as the estimated values of Lee & Cheng (1986). In order to model heat flow of  $240 \text{ mW m}^{-2}$  up to  $60 \text{ km}$  west of the Longitudinal Valley Fault, exhumation rates from depths of  $25 \text{ km}$  at that distance from the Longitudinal Valley Fault would have to be of the order of  $4\text{--}6 \text{ mm year}^{-1}$ . While Dadson *et al.* (2003) calculates an average exhumation rate of  $5 \text{ mm year}^{-1}$  across the whole island, most studies show a decrease in the exhumation rate from east to west across the island (Fig. 5a). Most models of rock trajectories do not have exhumation from more than  $15 \text{ km}$  beneath the Slate Belt (Fuller *et al.* 2006b). It is likely that the estimated heat flow values in the Slate Belt are biased towards higher heat flow as measurements were largely taken near hot springs and, thus, reflect zones where hot water is coming up from

depth, increasing the local heat flow (Song & Ma 2002). Our results (Fig. 5d) are similar to those of Zhou *et al.* (2003) who used two-dimensional (2D) thermal models to constrain the rheological structure across Taiwan. They show that rapid exhumation of hot rock is the dominant control on the value of the surface heat flow.

#### Distribution of strain regimes and seismicity across Central Taiwan and implications for permeability structure

An examination of the 3D strain rates within Taiwan provides an insight as to the permeability structure at depth. The strain-rate tensor is defined by the three principal strain rates,  $\dot{\epsilon}_1$ ,  $\dot{\epsilon}_2$  and  $\dot{\epsilon}_3$ , and their orientations, where  $\dot{\epsilon}_1$  is the maximum contraction rate (shortening),  $\dot{\epsilon}_2$  is the intermediate strain rate and  $\dot{\epsilon}_3$  is the minimum contraction or maximum elongation rate (stretching). Mouthereau *et al.* (2009) analysed the present-day 3D seismogenic

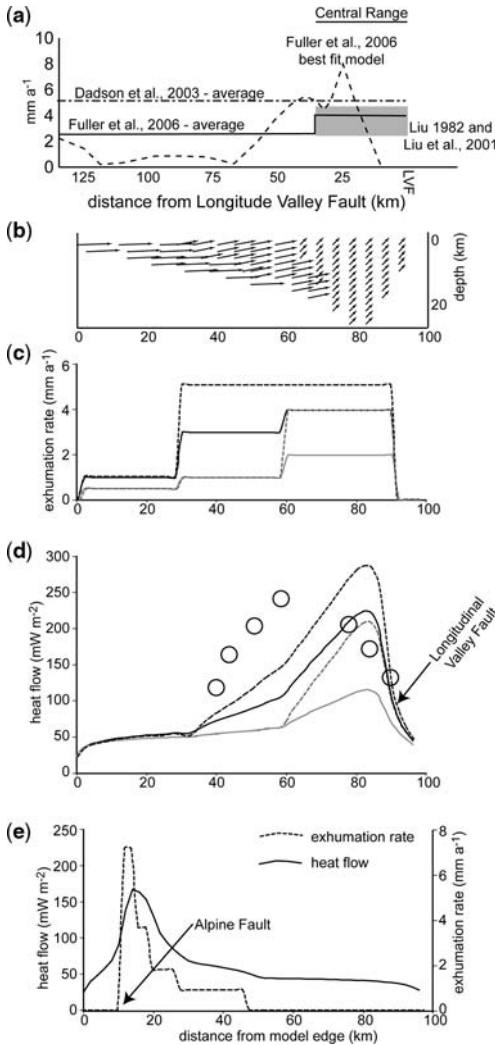


**Fig. 5.** Input and results from thermal models. (a) Summary of estimates of exhumation rate across Taiwan (Liu 1982; Liu *et al.* 2001; Dadson *et al.* 2003; Fuller *et al.* 2006b). (b) Velocity vectors used in the model. (c) Exhumation rates input into the thermal models of heat flow in Taiwan. (d) Modelled heat flow across Taiwan based on the exhumation rates shown in (c). Open circles are heat-flow measurements on a section through central Taiwan [Lin (2000), based on Lee & Cheng (1986)]. (e) Exhumation rates and modelled heat flow for the Southern Alps of New Zealand.

deformation field of Taiwan using more than 1000 earthquake events from 1995 to 2005. They divided Taiwan into four domains, distinguished by variable strain-rate fields. Their domain III, which comprises the Eastern and Western Central Ranges, east of the Lishan Fault, incorporates our area of interest. Analysis of geodetic measurements

shows that surface strain in domain III is extensional, with the maximum extension direction ranging from NNE–SSW to NE–SW (Fig. 6a) (Mouthereau *et al.* 2009). Extension of the Central Range persists to depths of more than 15 km (Fig. 6b). The rate ranges from  $10^{-8}$ – $10^{-9}$  year $^{-1}$  and is slightly larger than the contraction rate (Mouthereau *et al.* 2009). The principal strain axis,  $\dot{\epsilon}_1$ , is contractional and is subparallel to the relative plate motion between the two plates. A somewhat larger  $\dot{\epsilon}_3$  is near vertical,  $\dot{\epsilon}_2$  is generally subhorizontal and extensional (Fig. 6b). At the surface  $\dot{\epsilon}_2$  and  $\dot{\epsilon}_3$  have swapped, so that the maximum elongation axis,  $\dot{\epsilon}_3$ , is subhorizontal and orogen-parallel, and  $\dot{\epsilon}_2$  is vertical (Fig. 6a). While most earthquakes in Taiwan are thrust faulting or strike-slip, a significant number of normal events are recorded in the Slate Belt (Fig. 6c) (Crespi *et al.* 1996; Mouthereau *et al.* 2009).

The 3D strain-rate field suggests that, at depth within the orogen, extension fractures will be subhorizontal (vertical elongation) and closer to the surface (top 4–6 km), extension fractures will be near-vertical, with fractures striking approximately parallel to the relative plate-motion vector (Fig. 7).

## Discussion

### Fluid-flow regimes in the Taiwanese mountains

Two flow regimes exist in the Slate Belt, one dominated by meteoric water ( $\delta^{18}\text{O} < 0\text{\textperthousand}$ ) and the other by deep brines, with  $\delta^{18}\text{O} > 10\text{\textperthousand}$  (Fig. 7). Oxygen isotope signatures of the veins suggest that there is little vertical spatial overlap of these two regimes (Fig. 7), with some deeper fluids leaking upwards into the shallow flow regime (Upton & Craw 2009). The flow regimes stay approximately fixed in position as the orogen develops, rocks are uplifted and eroded, and new rocks are added laterally at depth. Rocks that have been affected by the deep fluid regime are progressively uplifted over time into and through the shallow fluid regime, to the surface, as evidenced by rock-buffered veins being overprinted by meteoric-derived veins. The uplift trajectory for rocks currently at the surface in the Slate Belt has been well defined temporally, from Pliocene to Recent, by a range of thermochronological tools (summarized by Beyssac *et al.* 2007).

Shallow fluid flow is driven by topography. In the upper 2–4 km of the crust, the rock is highly permeable with ubiquitous fractures allowing penetration of meteoric fluid beneath the mountains. The fluid is heated at depths of 2–4 km and returns to the surface in valleys, often focused as hot springs. The extensional strain and associated

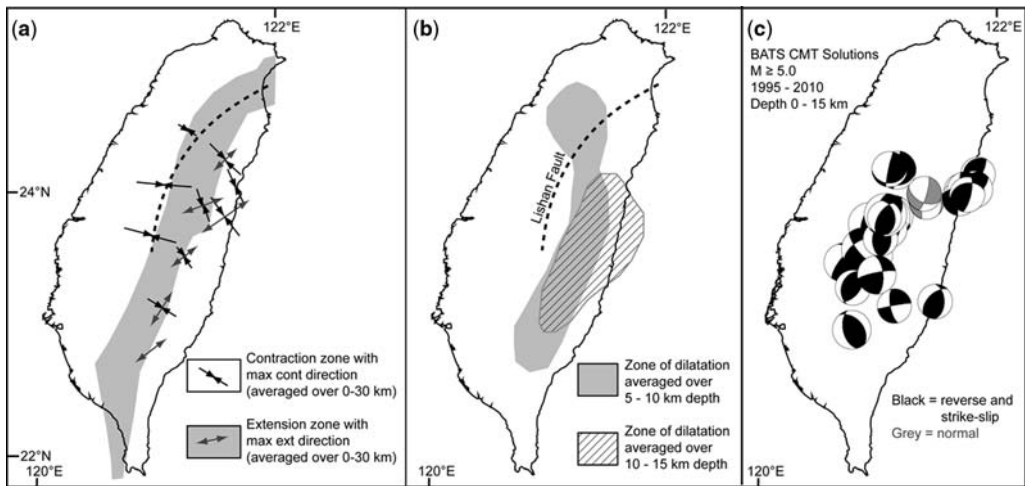


**Fig. 6.** Strain rates summarized by Moutheau *et al.* (2009). (a) Extent of regional extension as determined from geodetic measurements and current maximum strain directions based on earthquakes and averaged over the whole crust (0–30 km depth). (b) Extent of regional extension from 5 to 10 km depth (grey) and from 10 to 15 km depth (strips) as determined from earthquakes. (c) Representative focal mechanisms from a box 23°–24°30'N by 120°–122°30'E over the period 1995–2009 (BATS catalogue). Normal focal mechanisms are shown in grey.

normal faulting that occurs in the Central Ranges (Fig. 6a, c) enhances the permeability of the upper crust. The fractures that make up this permeability will be dominated by steep structures as they form in a regime with an orogen-parallel elongation direction (Fig. 6a).

The deep-flow regime involves brines that have equilibrated with the host rocks (Craw *et al.* 2010). The passive margin sediments that make up the Slate Belt originally contained connate brines with  $\delta^{18}\text{O}$  values of around 0‰, but a reduction in porosity during recrystallization ensures that connate brines form an extremely small proportion of the rock and are no longer recognizable isotopically. The fluid is probably a mixture of any remaining connate fluids and the product of metamorphic dehydration reactions (Chen 1985; Craw *et al.* 2010). At the centimetre–metre scale, there is widespread evidence for localized fluid flow through the Slate Belt rocks during metamorphism, including crack–seal mineral growth and pressure–shadow infilling (Fisher *et al.* 2002). The transition from sedimentary rocks to slates and schists, which has occurred and is still occurring in the Taiwan mountains, results in abundant fluid at depth. This fluid facilitates rock weakening and ductile folding of the rock mass.

The distribution of metamorphic and late-metamorphic veins suggests that the deep-flow regime is highly localized. Most of the rocks in the Slate Belt have no veins, or only small rare veins, implying little large-scale fluid movement in the belt. Where veins do occur, such as at

Yushan and the Lishan Fault (Figs 2 & 3), as well as at the Pingfengshan gold mine (Craw *et al.* 2010), several vein generations are present. This suggests that there has been continued focusing of fluid into the same region over an extended period of time during uplift. At depth within the Slate Belt, the elongation direction is vertical, which results in subhorizontal extension fractures. The late-metamorphic veins are largely subhorizontal shear-related fault veins and reflect the strain regime at depth calculated by Moutheau *et al.* (2009). Some late-metamorphic veins, such as those at Yushan (Fig. 2) and along the Lishan Fault (Chan *et al.* 2005), are steeply dipping and represent conduits that channel deep brines to shallower levels in the Slate Belt (Fig. 7). Ankeritic veins have formed as pure extensional veins within fold-axial surfaces. They are steeply dipping, and occur in fracture zones where deep brines rise through the rock mass and are chemically out of equilibrium with the host-rock minerals while retaining oxygen isotopic equilibrium. The ankeritic veins occur at levels where the elongation direction has flipped from vertical to horizontal, orientated approximately NNE–SSW, perpendicular to the plate-boundary convergence direction.

At Wushe, the Lishan Fault shows evidence of high strains with both ductile (foliation development) and brittle (veins and fractures within the foliation) deformation having occurred within the fault zone (Chan *et al.* 2005). The wide ( $>100$  m) zone of foliated rocks with extensive veining (Figs 1 & 3) suggests that the Lishan Fault hosts

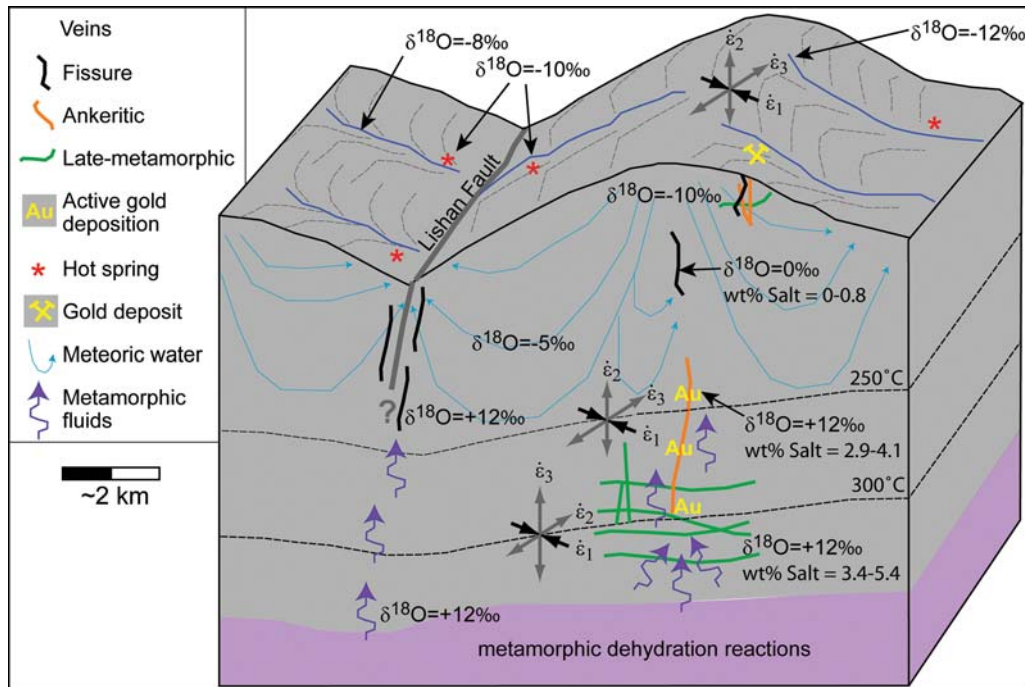


**Fig. 7.** Summary of upper-crustal fluid-flow regimes beneath the Central Ranges of Taiwan. Veins are shown in the depth range of their formation with an example at the surface showing the overprinting relationships of the three vein sets.  $\delta^{18}\text{O}$  values shown refer to the composition of the water component of the fluid phase.

an active fluid-flow system with substantially more fluid moving through this zone than has moved through rocks more than 1 km either side of the fault zone. The fluids within the Lishan Fault are metamorphic brines that have equilibrated with greenschist-facies rocks (Chan *et al.* 2005). Fluid flow in the Lishan Fault has encouraged further deformation within these rocks, producing a well-developed pervasive foliation in the fault zone. Ductile strain at depth has been focused onto the Lishan Fault, with seismically driven fluid flow at shallower levels (Chan *et al.* 2005). We suggest that fluid flow and deformation are coupled within the Lishan Fault zone and that fluid incursion, driven by seismic activity, is the key to focusing deformation into this zone.

We also suggest that veins in the Slate Belt are spatially localized because of a rheological change caused by the initial localized metamorphic veining events. The majority of Slate Belt rocks are fissile slates and shales with well-developed planes of weakness that deform in a ductile manner under greenschist-facies conditions with abundant fluid (above). However, if fracturing does occur and veining results, then the tensile strength of the rock is increased by the presence of the quartz veins,

which then makes the veined rock more prone to refractioning (Upton *et al.* 2008). The result is isolated polyphase stockwork vein systems, with metamorphic and late-metamorphic veins overprinted by ankeritic veins. Late-stage prismatic quartz veins have been further superimposed at the Pingfengshan gold mine (Craw *et al.* 2010). Through the whole of the uplift and exhumation sequence, fluids have been repeatedly focused into the same narrow region (Figs 7 & 8).

#### Comparison between Taiwan and the Southern Alps

The Southern Alps of New Zealand is an oblique collisional orogenic belt that has many similarities to Taiwan (Table 1). However, despite broad similarities in the dynamics and form of the mountain ranges, the heat and fluid-flow systems of the Southern Alps and Central Taiwan have some important differences (Fig. 8). In particular, the tectonic–hydrothermal vein systems in the Southern Alps are found mainly in the inboard zone, between the Main Divide and the Alpine Fault. The vein systems formed beneath the Main Divide and have

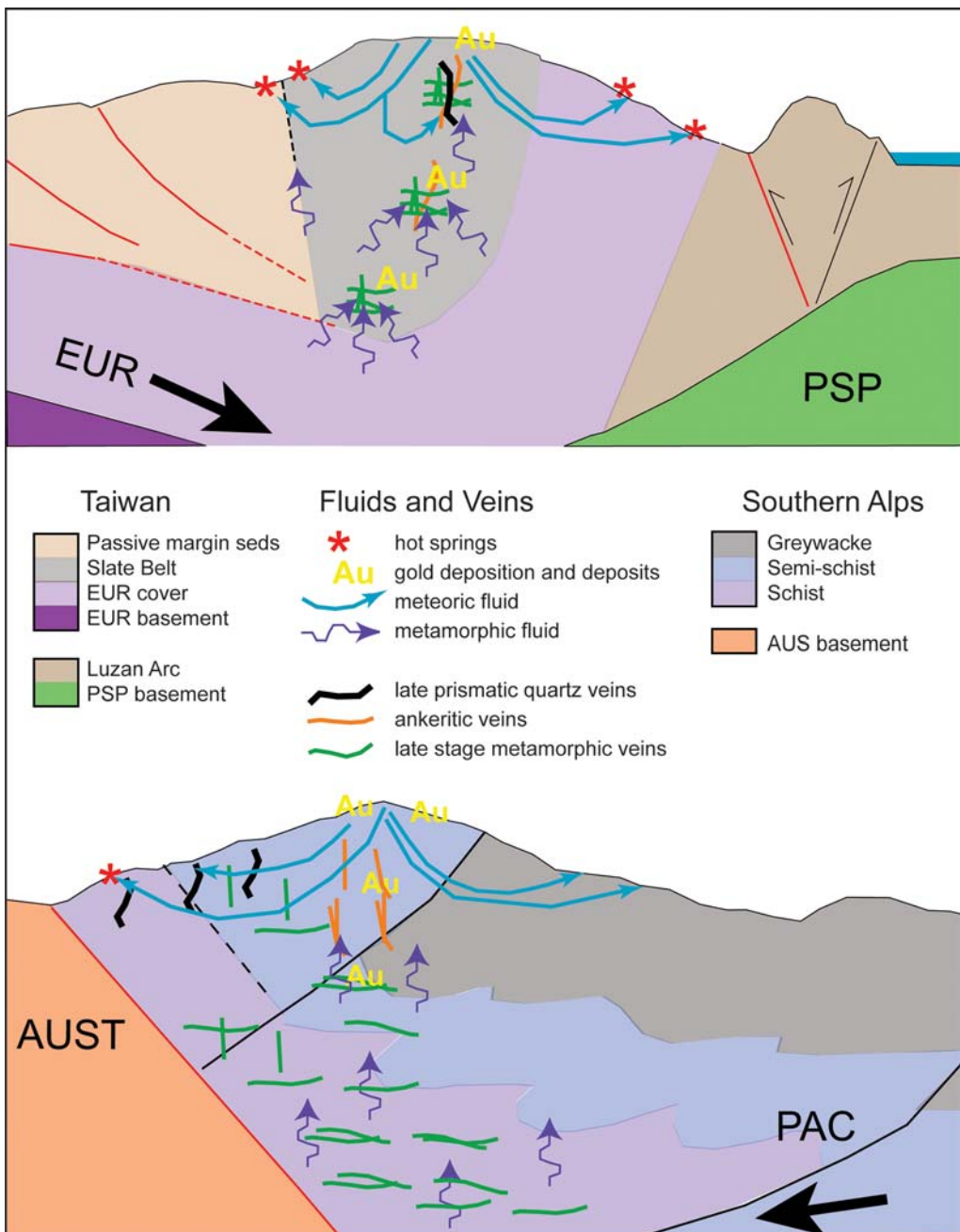


**Fig. 8.** Cartoon showing the different flow regimes in Taiwan (top) and the Southern Alps (bottom). Active faults are shown in red. In Taiwan flow is localized into discrete zones formed initially by late-metamorphic fault-related shear veins. Gold is focused into these regions. Meteoric water penetrates the top 2–4 km of the crust, it is heated and results in hot springs and late-stage prismatic quartz veins. In the Southern Alps, late-metamorphic veining and later fluid flow are much more distributed, and discrete zones of overprinting veins are not found. Ankeritic veining and gold deposition are localized around the Main Divide, while hot springs and late-stage prismatic quartz veins are found closer to the Alpine Fault.

moved towards the Alpine Fault during their exhumation (Craw *et al.* 2009). The hot springs of the Southern Alps are located close to the plate boundary, rather than throughout the mountains as in Taiwan, and Southern Alps springs are cooler (maximum = 56 °C; Table 1).

In the Southern Alps, the overall heat flow is considerably less than in Taiwan, with the region of high heat flow and hot springs localized close to the Alpine Fault. We have run thermal models of the Southern Alps of New Zealand for comparison with those of Taiwan (Fig. 5e). In the Southern Alps, a narrow band of hot rocks is being uplifted extremely rapidly (Fig. 5e) (Simpson *et al.* 1994; Norris & Cooper 2001). However, because the zone of rock experiencing the high uplift rates is narrow (<10 km), the majority of the heat is dissipated laterally (Koons 1987) and the maximum modelled heat flow is approximately 260 mW m<sup>-2</sup>. This value is consistent with the narrow band of hot springs and the relatively cool temperatures found in the Southern Alps. Even though Taiwan's exhumation rates are approximately half the exhumation rate at the Alpine Fault, there is much greater heat flow in Taiwan because the high exhumation rates extend across much of the island (Fig. 5).

The spatial distribution of veins in the Southern Alps is quite different from that which we observed in Taiwan (Fig. 8). In the Southern Alps, veins occur throughout the Main Divide region rather than being localized within the same narrow region, and multiple generation of veins in one locale are uncommon. The different distribution of veins in the two otherwise very similar orogens suggests to us that rheology plays a part in controlling where veins form in the two mountain belts. We suggest that the rocks making up the Slate Belt are initially rheological weaker than those currently being incorporated into the Southern Alps. Unlike the rocks of the Southern Alps, the rocks making up the Slate Belt of Taiwan have not previously experienced a deformational event. The slates and shales of the Slate Belt contain abundant phyllosilicates and metamorphic fluid. In contrast, the Southern Alps are made up of relatively brittle metasedimentary rocks that were partially dehydrated in the Mesozoic (Table 1). For example, the Slate Belt is folding in a ductile manner, whereas the greywacke of the Southern Alps is undergoing brittle faulting and very little folding (Upton *et al.* 2004). Fluid flow and vein formation in the Southern Alps greywackes was more dispersed than is currently occurring in Taiwan, resulting in a rock with widespread Mesozoic quartz veins. The presence of widespread veining in the Southern Alps metasedimentary rocks enhance its brittle nature and prevent the localized embrittlement that occurs in Taiwan.

Instead of being controlled by the rheology, the position of vein swarms in the Southern Alps is largely a result of the dynamics of the mountain range (Upton & Koons 2007). Veins that are forming at and above the brittle–ductile transition are found in low-grade schists around the Main Divide. The strain regime in the upper and mid-crust of the Southern Alps is predicted by 3D mechanical models to be in extension (Koons *et al.* 1998; Upton & Koons 2007). A small number of earthquakes with normal fault solutions have been recorded in this region (Anderson *et al.* 1993; Leitner *et al.* 2001) that are consistent with this region undergoing extension. Fluid and minor gold move into these structures (Craw *et al.* 1994; Upton & Koons 2007). As the active Main Divide is carried further west into the orogen, the rocks move out of the extensional strain regime and they no longer experience extension or focused fluid flow. Instead, that deformation is now focused on the new Main Divide (Craw *et al.* 2010). It is the position of the rocks within the deformation regime that determines whether or not a rock in the Southern Alps will be fractured and veined. As the rocks move through the system, refracturing and overprinting by several generations of veins is uncommon.

## Conclusions

Comparison of orogenic fluid flow in Taiwan and the Southern Alps is instructive in determining what are local effects v. what are more general processes that operate in young transpressive orogens. The two orogens are broadly similar, with oblique convergence, high rock uplift rates, high exhumation rates, high heat flow and no magmatism associated with collision. However, the distribution of the heat flow, hot springs and veins in the two orogens are quite different.

Taiwan has high heat flow throughout the high mountains and hot springs, where temperatures of up to 90 °C are common. The Southern Alps heat-flow anomaly and hot springs are restricted to a narrow zone parallel to the Alpine Fault. Taiwan's higher heat flow compared to the Southern Alps results from a much wider zone of material being exhumed at relatively rapid rates.

Two fluid-flow systems exist in both the central Southern Alps and Taiwan. Shallow flow is driven by topography and dominated by meteoric water. In the upper 2–4 km of the crust, fracture permeability allows penetration of surface water beneath the mountains to be heated and then returned to the surface in valleys. A deeper flow regime is dominated by brines in equilibrium with the host rocks. This fluid is preserved in the

metamorphic, late-metamorphic and ankeritic veins in both orogens.

Unlike in the central Southern Alps, where veins are relatively common and well dispersed, veins are rare in the Slate Belt of Taiwan. In contrast, there are localized sites, including the Pingfengshan mine and Yushan Mountain, where veins are abundant. These zones commonly have multiple generations of cross-cutting veins that formed at conditions ranging from metamorphic to near-surface. From oldest to youngest the vein styles are: (1) un-mineralized metamorphic veins; (2) late-metamorphic veins containing quartz with minor chlorite, calcite and minor mineralization; (3) ankeritic veins with rare albite and gold; and (4) late-stage prismatic quartz veins with bladed calcite crystals, and rare adularia and chlorite. Intense veining also occurs in a zone approximately 100 m wide that is centred on the Lishan Fault, where deformation is also enhanced due to the presence of fluids.

Extensional deformation is occurring in the Main Divide region of both the Southern Alps and the Taiwan Slate Belt. At depth, the elongation direction is near-vertical and subhorizontal fractures form. At shallower depths, the strain regime changes and the elongation direction becomes orogen-parallel such that fractures are steep and subparallel to the convergence direction. In the Southern Alps, veins form beneath the Main Divide and then are moved through the orogen towards the Alpine Fault with exhumation, while new veins form beneath the present-day Main Divide. In Taiwan, the distribution of veins suggests that fluid flow from depth is highly localized.

The rocks making up the Slate Belt have not undergone a previous deformational event. They are weak rheologically because of abundant phyllosilicates and metamorphic fluid. We suggest that fracturing and veining causes a rheological change, increasing the tensile strength of the rock, which makes the veined rock more prone to refractioning. The result is isolated stockwork vein systems with metamorphic and late-metamorphic veins overprinted by ankeritic veins and, at some locations, late-stage fissile veins.

Funding for this research was provided by the National Taiwan University, the University of Otago, and the NZ Foundation for Research, Science & Technology. Field assistance by L.-H. Chung greatly facilitated the research. Reviews by E. Bertrand, G. Caldwell, B. Yardley and one anonymous reviewer improved the clarity of the manuscript.

## References

- ANDERSON, H., WEBB, T. & JACKSON, J. 1993. Focal mechanisms of large earthquakes in the South Island of New Zealand: implications for the accommodation of Pacific-Australia plate motion. *Geophysical Journal International*, **115**, 1032–1054.
- BARNES, I., DOWNES, C. J. & HULSTON, J. A. 1978. Warm springs, South Island, New Zealand, and their potential to yield laumontite. *American Journal of Science*, **278**, 1412–1427.
- BECKER, J. A., CRAW, D., HORTON, T. & CHAMBERLAIN, C. P. 2000. Gold mineralisation near the Main Divide, upper Wilberforce valley, Southern Alps, New Zealand. *New Zealand Journal of Geology and Geophysics*, **43**, 199–215.
- BERTRAND, E., UNSWORTH, M. ET AL. 2009. Magnetotelluric evidence for thick-skinned tectonics in central Taiwan. *Geology*, **37**, 711–714.
- BEYSSAC, O., SIMOES, M., AVOUAC, J. P., FARLEY, K. A., CHEN, Y. G., CHAN, Y. C. & GOFFE, B. 2007. Late Cenozoic metamorphic evolution and exhumation of Taiwan. *Tectonics*, **26**, TC6001, doi: 10.1029/2006TC002064.
- BYRNE, T. B. & LIU, C. S., 2002. Preface: Introduction to the geology and geophysics of Taiwan. In: BYRNE, T. B. & LIU, C. S. (eds) *Geology and Geophysics of an Arc-Continent Collision, Taiwan*. Geological Society of America, Special Paper, **358**, v–viii.
- CARENNA, S., SUPPE, J. & KAO, H. 2002. Active detachment of Taiwan illuminated by small earthquakes and its control of first-order topography. *Geology*, **30**, 935–938.
- CHAN, Y. C., OKAMOTO, K., YUI, T.-F., IIZUKA, Y. & CHU, H. T. 2005. Fossil fluid reservoir beneath a duplex fault structure within the Central Range of Taiwan: implications for fluid leakage and lubrication during earthquake rupturing process. *Terra Nova*, **17**, 493–499.
- CHEN, C.-H. 1985. Chemical characteristics of thermal waters in the Central Range of Taiwan, R.O.C. *Chemical Geology*, **49**, 303–317.
- CHI, W. R., NAMSON, J. & SUPPE, J. 1981. Stratigraphic record of plate interactions in the coastal range of eastern Taiwan. *Memoir, Geological Society of China*, **4**, 155–194.
- COX, S. F. 2005. Coupling between deformation, fluid pressures and fluid flow in ore-producing hydrothermal systems at depth in the crust. In: HEDENQUIST, J. W., THOMPSON, J. F.H., GOLDFARB, R. J. & RICHARDS, J. (eds) *Economic Geology; One Hundredth Anniversary Volume, 1905–2005*. Society of Economic Geologists, Littleton, CO, 39–75.
- CRAW, D. 1988. Shallow-level metamorphic fluids in a high uplift rate metamorphic belt; Alpine Schist, New Zealand. *Journal of Metamorphic Geology*, **6**, 1–16.
- CRAW, D., RATTENBURY, M. S. & JOHNSTONE, R. D. 1994. Structures within greenschist facies Alpine Schist, central Southern Alps, New Zealand. *New Zealand Journal of Geology and Geophysics*, **37**, 101–111.
- CRAW, D., KOONS, P. O., HORTON, T. & CHAMBERLAIN, C. P. 2002. Tectonically driven fluid flow and gold mineralisation in active collisional orogenic belts: comparison between New Zealand and western Himalaya. *Tectonophysics*, **348**, 135–153.
- CRAW, D., UPTON, P. & MACKENZIE, D. J. 2009. Hydrothermal alteration styles in ancient and modern

- orogenic gold deposits, New Zealand. *New Zealand Journal of Geology and Geophysics*, **52**, 11–26.
- CRAW, D., UPTON, P., YU, B.-S., HORTON, T. & CHEN, Y.-G. 2010. Young orogenic gold mineralisation in active collisional mountains, Taiwan. *Mineralium Deposita*, **45**, 631–646, doi: 10.1007/s00126-010-0297-4.
- CRESPI, J. M., CHAN, Y. C. & SWAIM, M. S. 1996. Synorogenic extension and exhumation of the Taiwan hinterland. *Geology*, **24**, 247–250.
- CUNDALL, P. & BOARD, M. 1988. A microcomputer program for modelling of large-strain plasticity problems. In: *Sixth International Conference on Numerical Methods in Geomechanics*, Innsbruck, Austria. A.A. Balkema, Rotterdam, 101–108.
- DADSON, S. J., HOVIUS, N. ET AL. 2003. Links between erosion, runoff variability and seismicity in the Taiwan orogen. *Nature*, **426**, 648–651.
- DEMETS, C., GORDON, R. G. & ARGUS, D. F. 2010. Geologically current plate motions. *Geophysical Journal International*, **181**, 1–80, doi: 10.1111/j.1365-246X.2009.04491.x.
- DIPPLE, G. M. & FERRY, J. M. 1992. Metasomatism and fluid flow in ductile fault zones. *Contributions to Mineralogy and Petrology*, **112**, 149–164.
- FISHER, D. M., LU, C. & CHU, H. T. 2002. Taiwan Slate Belt: insights into the ductile interior of an arc–continent collision. In: BYRNE, T. & LIU, C. S (eds) *Geology and Geophysics of an Arc–Continent Collision, Taiwan*. Geological Society of America, Special Paper, **358**, 93–106.
- FULLER, C. W., WILLETT, S. D. & BRANDON, M. T. 2006a. Formation of forearc basins and their influence on subduction zone earthquakes. *Geology*, **34**, 65–68.
- FULLER, C. W., WILLETT, S. D., FISHER, D. & LU, C. Y. 2006b. A thermomechanical wedge model of Taiwan constrained by fission-track thermochronometry. *Tectonophysics*, **425**, 1–24.
- GALEWSKY, J., STARK, C. P., DADSON, S., WU, C. C., SOBEL, A. H. & HORNG, M. J. 2006. Tropical cyclone triggering of sediment discharge in Taiwan. *Journal of Geophysical Research*, **111**, doi: 10.1029/2005JF000428.
- GOURLEY, J. R., BYRNE, T., CHAN, Y. C., WU, F. & RAU, R. J. 2007. Fault geometries illuminated from seismicity in central Taiwan: implications for crustal scale structural boundaries in the northern Central Range. *Tectonophysics*, **445**, 168–185.
- HICKS, D. M., HILL, J. & SHANKAR, U. 1996. Variation of suspended sediment yields around New Zealand: the relative importance of rainfall and geology. In: WALLING, D. E. & WEBB, B. W. (eds) *Erosion and Sediment Yield: Global and Regional Perspectives*. IAHS, Wallingford, Publ. no. **236**, 149–156.
- HO, C. S. 1986. A synthesis of the geological evolution of Taiwan. *Tectonophysics*, **125**, 1–16.
- KOONS, P. O. 1987. Some thermal and mechanical consequences of rapid uplift: an example from the Southern Alps, New Zealand. *Earth and Planetary Science Letters*, **86**, 307–319.
- KOONS, P. O., CRAW, D., COX, S. C., UPTON, P., TEMPLETON, A. S. & CHAMBERLAIN, C. P. 1998. Fluid flow during active oblique convergence: a Southern Alps model from mechanical and geochemical observations. *Geology*, **26**, 159–162.
- LEE, C. R. & CHENG, W. T. 1986. Preliminary heat flow measurements in Taiwan. In: *Transactions of the Fourth Circum-Pacific Energy and Mineral Resources Conference: August 17–22, 1986, Singapore*. AAPG, Tulsa, OK, 31–36.
- LEITNER, B., EBERHART-PHILLIPS, D., ANDERSON, H. & NABELEK, J. L. 2001. A focused look at the Alpine fault, New Zealand: seismicity, focal mechanisms, and stress observations. *Journal of Geophysical Research B – Solid Earth*, **106**, 2193–2220.
- LIN, C.-H. 2000. Thermal modeling of continental subduction and exhumation constrained by heat flow and seismicity in Taiwan. *Tectonophysics*, **324**, 189–201.
- LIU, T. K. 1982. Tectonic implication of fission track ages from the Central Range, Taiwan. *Proceedings of the Geological Society of China*, **25**, 22–37.
- LIU, T. K., HSEIH, S., CHEN, Y.-G. & CHEN, W.-S. 2001. Thermo-kinematic evolution of the Taiwan oblique-collision mountain belt as revealed by zircon fission track dating. *Earth and Planetary Science Letters*, **186**, 45–56.
- LO, C. H. & ONSTOTT, T. C. 1995. Rejuvenation of K–Ar systems for minerals in the Taiwan Mountain Belt. *Earth and Planetary Science Letters*, **131**, 71–98.
- MOUTHEREAU, F., DEFFONTAINES, B., LACOMBE, O. & ANGELIER, J. 2002. Variations along the strike of the Taiwan thrust belt: Basement control of structural style, wedge geometry and kinematics. In: BYRNE, T. & LIU, C. S (eds) *Geology and Geophysics of an Arc–Continent Collision, Taiwan*. Geological Society of America, Special Paper, **358**, 35–58.
- MOUTHEREAU, F., FILLON, C. & MA, K. F. 2009. Distribution of strain rates in the Taiwan orogenic wedge. *Earth and Planetary Science Letters*, **284**, 361–385.
- NORRIS, R. J. & COOPER, A. F. 2001. Late Quaternary slip rates and slip partitioning on the Alpine Fault, New Zealand. *Journal of Structural Geology*, **23**, 507–520.
- PAGE, B. & SUPPE, J. 1981. The Pliocene Lichi melange of Taiwan: its plate tectonic and olistostromal origin. *American Journal of Science*, **281**, 193–227.
- SHIEH, Y.-N., CHERNG, F.-P. & HOERING, T. C. 1983. Oxygen and hydrogen isotope studies of meteoric and thermal waters in Taiwan. *Memoir, Geological Society of China*, **5**, 127–140.
- SHYU, J. B. H., SIEH, K., CHEN, Y. G. & LIU, C. S. 2005. Neotectonic architecture of Taiwan and its implications for future large earthquakes. *Journal of Geophysical Research B – Solid Earth*, **110**, 1–33.
- SIBSON, R. H. 1996. Structural permeability of fluid-driven fault-fracture meshes. *Journal of Structural Geology*, **18**, 1031–1042.
- SIBSON, R. H. 2000. Fluid involvement in normal faulting. *Journal of Geodynamics*, **29**, 469–499.
- SIMMONS, S. F. & CHRISTENSON, B. W. 1994. Origins of calcite in a boiling geothermal system. *American Journal of Science*, **294**, 361–400.
- SIMOES, M., AVOUAC, J. P., BEYSSAC, O., GOFFE, B., FARLEY, K. A. & CHEN, Y. G. 2007. Mountain building in Taiwan: a thermokinematic model. *Journal of Geophysical Research B – Solid Earth*, **112**, B11405, doi: 10.1029/2006JB004824.

- SIMPSON, G. D. H., COOPER, A. F. & NORRIS, R. J. 1994. Late Quaternary evolution of the Alpine Fault zone at Paringa, south Westland, New Zealand. *New Zealand Journal of Geology & Geophysics*, **37**, 49–58.
- SONG, T. R. A. & MA, K. F. , 2002. Estimation of thermal structure of a young orogenic belt according to a model of whole-crust thickening. In: BYRNE, T. & LIU, C. S (eds) *Geology and Geophysics of an Arc–Continent Collision, Taiwan*. Geological Society of America, Special Paper, **358**, 121–136.
- SUPPE, J. 1980. A retrodeformable cross section of northern Taiwan. *Proceedings of the Geological Society of China*, **23**, 46–55.
- SUPPE, J. 1981. Mechanics of mountain building and metamorphism in Taiwan. *Memoir of the Geological Society of China (Taiwan)*, **4**, 67–89.
- SUPPE, J. 2007. Absolute fault and crustal strength from wedge tapers. *Geology*, **35**, 1127–1130.
- TAN, L. P., CHEN, C. H., YEH, T. K. & TAKEUCHI, A. 1991. Tectonic and geochemical characteristics of Pleistocene gold deposits in Taiwan. In: JONES, M. & COSGROVE, J. (eds) *Neotectonics and Resources*. Bellhaven Press, London, 290–305.
- TEMPLETON, A. S., CHAMBERLAIN, C. P., KOONS, P. O. & CRAW, D. 1998. Stable isotopic evidence for mixing between metamorphic fluids and surface-derived waters during recent uplift of the Southern Alps, New Zealand. *Earth and Planetary Science Letters*, **154**, 73–92.
- TEMPLETON, A. S., CRAW, D., KOONS, P. O. & CHAMBERLAIN, C. P. 1999. Near-surface expression of a young mesothermal gold mineralizing system, Sealy Range, Southern Alps, New Zealand. *Mineralium Deposita*, **34**, 163–172.
- UPTON, P. & CRAW, D. 2009. Mechanisms of strain-rate- and reaction-dependent permeability in the mid-crust of the Southern Alps: insight from three-dimensional mechanical models. *Geofluids*, **9**, 287–302.
- UPTON, P. & KOONS, P. O. 2007. Three-dimensional geodynamic framework for the Central Southern Alps, New Zealand: Integrating geology, geophysics and mechanical observations. In: OKAYA, D., STERN, T. & DAVEY, F. (eds) *Geotectonic Investigation of a Modern Continent–Continent Collisional Orogen: Southern Alps, NZ*. American Geophysical Union, Geophysical Monograph, **175**, 255–272.
- UPTON, P., CRAW, D. ET AL. 2003. Upper crustal fluid flow in the outboard region of the Southern Alps, New Zealand. *Geofluids*, **3**, 1–12.
- UPTON, P., CRAW, D., JAMES, Z. & KOONS, P. O. 2004. Structure and late Cenozoic tectonics of the southern Two Thumb Range, mid Canterbury, New Zealand. *New Zealand Journal of Geology and Geophysics*, **47**, 141–153.
- UPTON, P., BEGBIE, M. & CRAW, D. 2008. Numerical modelling of mechanical controls on coeval steep and shallow dipping auriferous quartz vein formation in a thrust zone, Macraes mine, New Zealand. *Mineralium Deposita*, **43**, 23–35.
- WANG, Y., SASAKE, M., SASADE, M. & CHEN, C. H. 1999. Fluid inclusion studies of the Chinkuashih high sulfidation gold-copper deposits in Taiwan. *Chemical Geology*, **154**, 155–167.
- WANG, Y. J., MA, K. F., MOUTHEREAU, F. & EBERHART-PHILLIPS, D. 2010. Three-dimensional Qp- and Qs-tomography beneath Taiwan orogenic belt: implications for tectonic and thermal structure. *Geophysical Journal International*, **180**, 891–910.
- WANNAMAKER, P. E., JIRACEK, G. R., STODT, J. A., CALDWELL, T. G., GONZALEZ, V. M., MCKNIGHT, J. D. & PORTER, A. D. 2002. Fluid generation and pathways beneath an active compressional orogen, the New Zealand Southern Alps, inferred from magnetotelluric data. *Journal of Geophysical Research B – Solid Earth*, **107**, 2117, doi: 10.1029/2001JB000186.
- WHIPP, D. M., JR. & EHLERS, T. A. 2007. Influence of groundwater flow on thermochronometer-derived exhumation rates in the central Nepalese Himalaya. *Geology*, **35**, 851–854.
- WU, F. T., RAU, R. J. & SALZBERG, D. 1997. Taiwan orogeny: thin-skinned or lithospheric collision? *Tectonophysics*, **274**, 191–220.
- WU, Y.-M., CHANG, C.-H. ET AL. 2007. Seismic tomography of Taiwan: Improved constraints from a dense network of strong motion stations. *Journal of Geophysical Research*, **112**, B08312, doi: 10.1029/2007JB004983.
- YARDLEY, B., BOTTRELL, S. H. & CLIFF, R. A. 1991. Evidence for a regional-scale fluid loss event during mid-crustal metamorphism. *Nature*, **349**, 151–154.
- YUI, T.-F., LIU, K.-K. & SHIEH, Y.-N. 1993. Stable isotope systematics of argillite/slate from a deep well in the Chenshui geothermal field, Taiwan. *Chemical Geology*, **103**, 181–191.
- ZHOU, D., YU, H.-S., XU, H.-H., SHI, X.-B. & CHOU, Y.-W. 2003. Modeling of thermo-rheological structure of lithosphere under the foreland basin and mountain belt of Taiwan. *Tectonophysics*, **374**, 115–134.



# Reproduction of thermal pressurization and fluidization of clay-rich fault gouges by high-velocity friction experiments and implications for seismic slip in natural faults

KOHTARO UJIIE<sup>1,2\*</sup>, AKITO TSUTSUMI<sup>3</sup> & JUN KAMEDA<sup>4</sup>

<sup>1</sup>*Doctoral Program in Earth Evolution Sciences, Graduate School of Life and Environmental Sciences, University of Tsukuba, Tsukuba 305-0006, Japan*

<sup>2</sup>*Institute for Research on Earth Evolution, Japan Agency for Marine-Earth Science and Technology, Yokosuka 237-0061, Japan*

<sup>3</sup>*Division of Earth and Planetary Sciences, Graduate School of Science, Kyoto University, Kyoto 606-8502, Japan*

<sup>4</sup>*Department of Earth and Planetary Science, Graduate School of Science, University of Tokyo, Tokyo 113-0033, Japan*

\*Corresponding author (e-mail: kijiie@geol.tsukuba.ac.jp)

**Abstract:** We examine the frictional properties and microstructures of clay-rich fault gouges subjected to thermal pressurization and fluidization, generated in high-velocity friction experiments under dry and wet conditions. In the dry tests, slip weakening occurs by thermal pressurization, which is marked by a fault-gouge expansion associated with a water-phase transition from liquid to vapour. The water is derived from dehydration of clay minerals by frictional heating. The resulting microstructure in the gouge layer is a random distribution of spherical clay–clast aggregates in the matrix, and mixing of different gouge constituents without shear surfaces. In the wet tests, slip weakening is caused by pore-fluid pressurization resulting from shear-enhanced compaction of the water-saturated gouge and frictional heating. Compared to the dry tests, the wet tests show smaller dynamic stress drops and slip weakening distance. The steady-state shear stress in the wet tests is almost independent of normal stress, suggesting a fluid-like behaviour of the fault gouge during high-velocity shearing. The microstructures after the wet tests show that the foliated zone is accompanied by grain-size segregation in the gouge layer. The grain-size segregation is attributed to the Brazil-nut effect resulting from the difference in dispersive pressure in the granular-fluid shear flow at high shear rates, indicating a fluidization of fault gouge. Our results obtained at seismic slip rates imply that the propagation of an earthquake rupture can be enhanced by fluid pressurization and frictional heat, potentially leaving characteristic microstructures resulting from water vaporization by frictional heating or flow sorting at high slip rates.

The dynamic weakening of faults at coseismic slip rates is a key control of the fault shear strength, magnitude of strong ground motion and rupture propagation (Kanamori & Heaton 2000; Aagard *et al.* 2001). The possible mechanisms of the dynamic weakness include thermal pressurization and fluidization. Thermal pressurization is the transient fluid pressurization and reduction of effective normal stress caused by the thermal expansion of the fluid from frictional heating in the fault (Sibson 1973). There have been numerous numerical and theoretical studies on thermal pressurization, which have predicted earthquake processes related to the dynamic propagation of rupture and stress drop (e.g. Lachenbruch 1980; Mase & Smith 1987; Andrews 2002; Rice 2006). Fluidization is a

phenomenon in which the grains in a suspension move with a mean free path. The fluidization of fault gouge may be caused by normal interface vibration (Monzawa & Otsuki 2003) or the fluid pressurization associated with frictional heat (Ujiie *et al.* 2007a; Boullier *et al.* 2009). Whatever the cause of the fluidization, this phenomenon is inferred to reduce the dynamic shear strength of a fault. However, the natural and experimental evidence of thermal pressurization and fluidization has been limited. In contrast to the frictional melting recorded as pseudotachylites in natural faults with various tectonic settings (Sibson 1975; Sibson & Toy 2006; Ujiie *et al.* 2007b), the identification of thermal pressurization and fluidization from natural faults has been difficult.

High-velocity friction experiments on rocks have successfully reproduced frictional melting and demonstrated the melt lubrication of faults in crystalline rocks (e.g. gabbro and tonalite) (Tsutsumi & Shimamoto 1997; Di Toro *et al.* 2006) or the viscous strengthening of faults in argillite (a sedimentary rock mainly composed of clay minerals) (Ujiie *et al.* 2009). Similarly, reproducing thermal pressurization and fluidization by high-velocity friction experiments would allow us to obtain invaluable information on the frictional properties, physical processes, and resulting microstructures associated with thermal pressurization and fluidization. Thus, we recently conducted high-velocity friction experiments on clay-rich fault gouges and examined the resulting microstructures, which are briefly reported in Ujiie & Tsutsumi (2010). This chapter presents a detailed review of these results with additional experimental, microstructural and X-ray diffraction data, and then correlates the experimentally generated microstructures with those from natural faults in which fluidization has been recorded with evidence for frictional heating. Our results may be applicable to coseismic slip processes in mature faults because these commonly contain a considerable amount of clay minerals in their core (Faulkner *et al.* 2010).

## Experimental procedure

### Sample collection

Samples for high-velocity friction experiments were collected from the shallow portion of the megasplay fault in the Nankai accretionary prism, offshore of the Kii Peninsula, in SW Japan (Fig. 1). Detailed seismic reflection surveys and theoretical studies have suggested that the propagation of earthquake rupture occurred repeatedly along the megasplay fault during great subduction earthquakes such as the 1944 Tonankai earthquake (moment magnitude 8.1) (Park *et al.* 2002; Kame *et al.* 2003; Moore *et al.* 2007). Thus, high-velocity friction experiments on the megasplay fault material will be useful not only for an experimental investigation of the thermal pressurization and fluidization of fault gouges but also for determining the frictional response associated with rupture propagation from depths.

Integrated Ocean Drilling Program (IODP) Expedition 316 drilled into the shallow portion of the megasplay fault zone at depths of 258–308 mbsf (metres below sea floor) at Site C0004 (Expedition 316 Scientists 2009) (Fig. 1a, b). The megasplay fault zone is composed of fractured and brecciated mudstone and volcanic ash deposits. In this fault zone, the slip is localized along thin (*c.* 10 mm-thick) dark fault gouges in the microbreccia (Fig. 1c). The relatively high vitrinite reflectance in

this gouge zone with respect to the microbreccia may represent the generation of frictional heat at temperatures of approximately 400 °C along the thin gouge zone (Sakaguchi *et al.* 2011). Samples were taken from the microbrecciated mudstone immediately below (*c.* 5 cm) the dark fault gouge at 271 mbsf; these samples consist mainly of quartz, plagioclase, smectite, illite, chlorite and calcite. The total clay mineral content in the megasplay fault zone ranges from 52.9 to 65.4% (Expedition 316 Scientists 2009).

### Experimental method

The experiments were conducted using the rotary shear, intermediate- to high-velocity frictional testing apparatus at Kyoto University (Hayashi & Tsutsumi 2010). Although the basic design of this apparatus is similar to the apparatus introduced by Shimamoto & Tsutsumi (1994), the orientations of revolution axes are different: the former, used in this study, revolves along a vertical axis, while the latter revolves along a horizontal one. Samples were disaggregated by pestle, and sieved to obtain diameters of less than 0.17 mm. The gouge samples were then oven-dried at 60 °C for 24 h. In the dry tests, 0.5 g of gouge was placed between a pair of solid-cylindrical granite specimens. These specimens were 25 mm in diameter, and their end surfaces had been ground with #80 SiC powders to prevent slip along the interfaces between the gouge and granite specimens. The weight of the fault gouge was half of that considered in previous high-velocity friction experiments on fault gouges (e.g. Mizoguchi *et al.* 2007, 2009; Boutareaud *et al.* 2008, 2010; Brantut *et al.* 2008) in order to produce a relatively thin gouge layer. Thus, the achievement of higher temperatures in the fault gouge caused by a higher heat production rate could be expected in our experiments. In the wet tests, 0.2 ml of distilled water was added to the gouge to fulfill the water-saturated condition. A hollow-cylindrical Teflon sleeve was placed around the fault gouge to prevent gouge extrusion during shearing. The assembly composed of the fault gouge, granite specimens and Teflon sleeve was set in the apparatus, within which the upper cylinder remained stationary while the lower one was rotated by a servomotor (Fig. 2). The rotation of the motor was transmitted to the specimen through an electromagnetic clutch. The axial force, torque and axial displacement were measured with a force gauge, torque gauge and displacement transducer, respectively. In order to determine the temperature distribution in the gouge layer during shearing, we measured the temperature on the stationary side 9.5 mm from the interface between the fault gouge and granite specimen using a

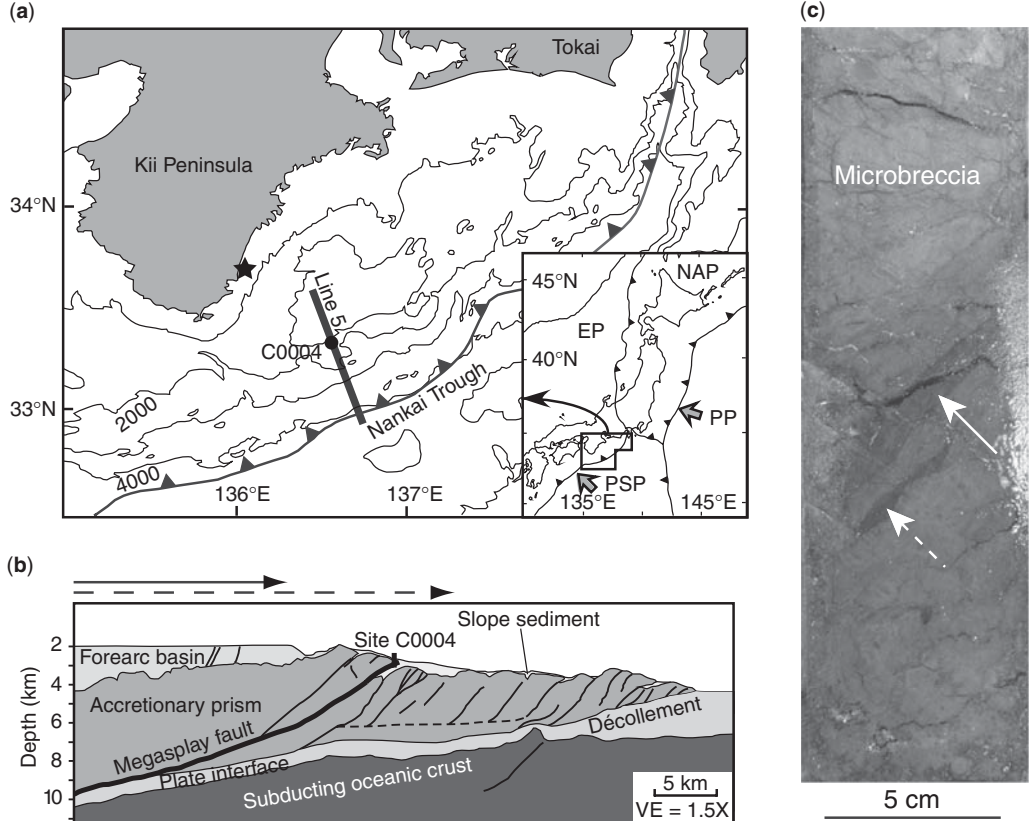


**Fig. 1.** Megasplay fault in Nankai subduction zone. (a) Map of the Nankai accretionary margin offshore of the Kii Peninsula showing the location of drill site C0004 and the epicentre of the 1944 Tonankai earthquake (star). In the inset: PSP, Philippine Sea plate; EP, Eurasian plate; PP, Pacific plate; NAP, North American plate. (b) Profile of the megasplay fault along Line 5 in (a) showing drilling site C0004. The solid and broken arrows indicate the extent of the 1944 Tonankai earthquake coseismic rupture from tsunami and seismic waveform inversions, respectively. (c) Photograph of the split core showing dark gouge (white arrow) and fragment of dark gouge (broken white arrow) in microbreccia.

thermocouple (Fig. 2). We monitored the change in humidity in the vicinity of the gouge layer (i.e. c. 2 cm from the Teflon sleeve) at room humidity using a moisture sensor.

Given the configuration of the solid-cylindrical specimen, the rotation velocity ( $V$ ) varies as a function of the distance from the centre of the rotation axis, and can be expressed as follows:

$$V = \frac{2\pi rR}{60} \quad (1)$$

where  $r$  and  $R$  are the radius of the solid cylindrical specimen and the revolution rate of the motor ( $1459 \text{ rotations m}^{-1}$ ), respectively. Thus,  $V$  varies from  $0 \text{ m s}^{-1}$  at the centre to the maximum at the edge. We used an equivalent slip rate ( $V_e$ ), which

is defined such that  $V_e$  multiplied by the sliding surface area ( $S$ ) provides the rate of frictional work, assuming a constant shear stress over  $S$ .  $V_e$  is given by (Shimamoto & Tsutsumi 1994):

$$V_e = \frac{4}{3} \pi r R. \quad (2)$$

Experiments were conducted at a  $V_e$  of  $1.27 \text{ m s}^{-1}$  and normal stresses ( $\sigma_n$ ) of  $0.6$ – $2.0 \text{ MPa}$  for dry and wet conditions. Before shearing, the sample assembly was consolidated for 30 min until the axial shortening became negligible at the same  $\sigma_n$  as that during shearing, for an initial gouge thickness of  $0.7$ – $0.8 \text{ mm}$ . The initial microstructures of the fault gouge before shearing are shown in Figure 3.

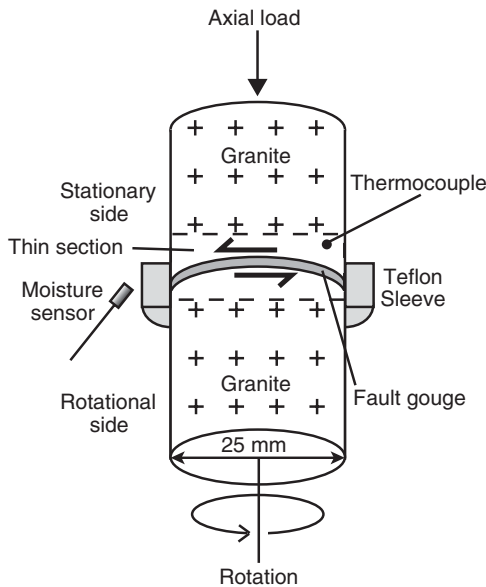


**Fig. 2.** Schematic sketch of the specimen assembly for high-velocity friction experiments on fault gouge showing positions of thermocouple, moisture sensor and the thin section (broken rectangular). The half arrows indicate the shear direction along a fault gouge during an experiment.

## Results

The high-velocity frictional properties, temperatures and microstructures of the clay-rich fault gouges are markedly different between the dry and wet tests.

### Experimental data

The dry tests show slip weakening. The peak friction is in the range of 0.6–0.7, which is followed by a decrease in friction with displacement toward the steady-state friction of 0.2–0.3 (Fig. 4a, b). The slip-weakening data from the dry tests can be fitted by the exponential decay curve (Mizoguchi *et al.* 2007):

$$\mu = \mu_{ss} + (\mu_p - \mu_{ss}) \exp\left(\frac{\ln(0.05) \cdot d}{D_c}\right) \quad (3)$$

where  $\mu_{ss}$  is the steady-state friction,  $\mu_p$  is the peak friction,  $d$  is the displacement after the peak friction and  $D_c$  is the slip weakening distance defined by the distance at which  $(\mu - \mu_{ss})$  is reduced to 0.05( $\mu_p - \mu_{ss}$ ).  $D_c$  ranges from 2.66 to 13.84 m and decreases with an increase in  $\sigma_n$  (Fig. 4b). The axial-displacement data indicate that the fault gouge was compacted immediately after the onset of shearing and then dilated (Fig. 4a). The end of slip weakening corresponds to the end of gouge dilation. The humidity increases with displacement (Fig. 4a).

There is a linear relationship between  $\sigma_n$  and the shear stresses (Fig. 4c), which is consistent with a Mohr–Coulomb type friction law:

$$\tau_p = 0.16 + 0.48\sigma_n \quad (4)$$

$$\tau_{ss} = 0.07 + 0.17\sigma_n \quad (5)$$

where  $\tau_p$  is the peak shear stress and  $\tau_{ss}$  is the steady-state shear stress. Equations (4) and (5) indicate that shear stresses are small but not zero when  $\sigma_n$  is 0 MPa. This would be due to the frictional resistance of the Teflon sleeve and/or weak van der Waals or hydrogen bonds between clay

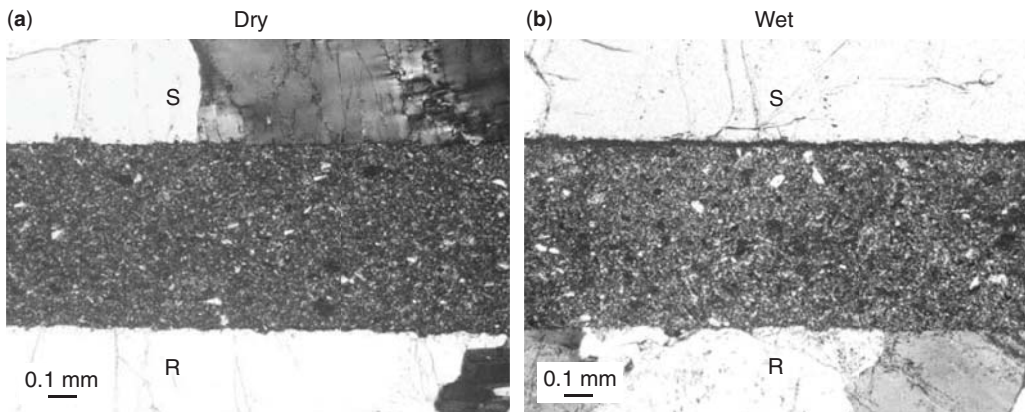


**Fig. 3.** Photomicrographs of initial gouge before shearing. S, stationary side; R, rotational side. (a) & (b) Dry and wet gouges under cross-polarized light, respectively. The dark band developed along the upper boundary between the gouge and the granite specimen in (b) is the crack impregnated with a low-viscosity epoxy resin that is formed during sample preparation.

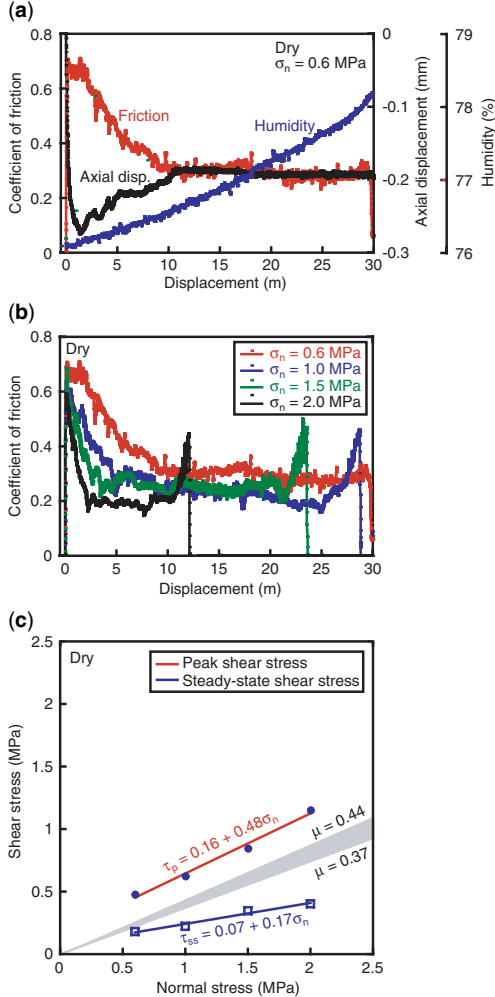


**Fig. 4.** Experimental results under dry conditions. (a) Coefficient of friction, axial displacement and humidity v. displacement at  $\sigma_n$  of 0.6 MPa. (b) Coefficient of friction v. displacement at different  $\sigma_n$ . (c) Peak shear stress ( $\tau_p$ ) and steady-state shear stress ( $\tau_{ss}$ ) v.  $\sigma_n$ . Steady-state stress is the average of the shear stresses during the last 5 s before clutch off. The frictional strength of the megasplay fault material at low slip rates ( $\leq 100 \mu\text{m s}^{-1}$ ) (Ikari *et al.* 2009) is plotted in grey.

particles (Mizoguchi *et al.* 2007; Brantut *et al.* 2008). Recently, Ikari *et al.* (2009) conducted friction experiments at low slip rates of less than  $100 \mu\text{m s}^{-1}$  under wet conditions using megasplay fault-zone material from the Nankai subduction zone. The best linear fit for the  $\tau_p$  data is above the friction strength lines from Ikari *et al.* (2009) (Fig. 4c). However, the best linear fit for the  $\tau_{ss}$  data is below the friction strength lines obtained at

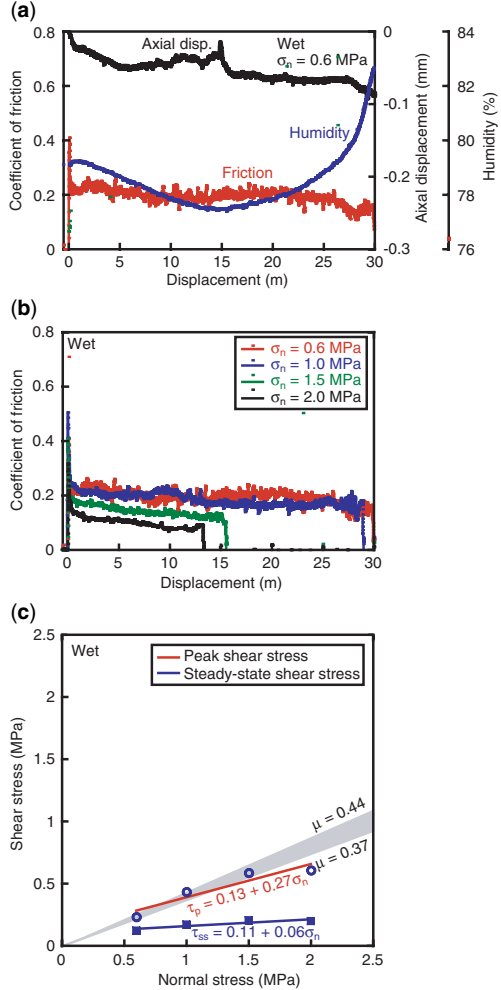


**Fig. 5.** Experimental results under wet conditions. (a) Coefficient of friction, axial displacement and humidity v. displacement at  $\sigma_n$  of 0.6 MPa. (b) Coefficient of friction v. displacement at different  $\sigma_n$ . (c) Peak shear stress ( $\tau_p$ ) and steady-state shear stress ( $\tau_{ss}$ ) v.  $\sigma_n$ . Steady-state stress is the average of the shear stresses during the last 5 s before clutch off. The frictional strength of the megasplay fault material at low slip rates ( $\leq 100 \mu\text{m s}^{-1}$ ) (Ikari *et al.* 2009) is plotted in grey.

low slip rates, demonstrating that the clay-rich fault gouge from the megasplay fault was weakened at high slip rates (Fig. 4c).

The wet tests show rapid slip weakening (Fig. 5a, b). The peak friction ranges from 0.3 to 0.5. A steady-state friction of 0.1–0.2 is established almost immediately. Thus,  $D_c$  shows very small values ( $< 0.2$ – $0.3$  m), regardless of  $\sigma_n$  (Fig. 5b). Under the same  $\sigma_n$ , the peak and steady-state

frictions in the wet tests are reduced with respect to those in the dry tests (Figs 4b & 5b). The axial displacement in the wet tests is smaller than that in the dry tests: after initial compaction, the compaction rate of the fault gouge is low until the end (the disengagement of the clutch) of the wet test (Fig. 5a). Transient gouge dilation is observed during the steady-state friction in the case of the wet tests at  $\sigma_n$  of 0.6 and 1.0 MPa, but this feature is absent in the case of the wet tests at  $\sigma_n$  of 1.5 and 2.0 MPa (see also Ujiie & Tsutsumi 2010). The humidity first decreases and then increases with displacement (Fig. 5a).

The best linear fit for the  $\tau_p$  data ( $\tau_p = 0.13 + 0.27\sigma_n$ ) is comparable to the friction strength lines at low slip rates (Fig. 5c). The best linear fit for the  $\tau_{ss}$  data ( $\tau_{ss} = 0.11 + 0.06\sigma_n$ ) is not only below the friction strength lines at low slip rates, but also below the best linear fit for the  $\tau_{ss}$  data under dry conditions (Figs 4c & 5c), displaying a very weak dependence of  $\tau_{ss}$  on  $\sigma_n$ .

#### *Temperature evolution and distribution in fault gouges*

Numerical modelling was conducted to determine the temperature evolution and distribution in a section of granite–gouge–Teflon sleeve by fitting the temperature measured by a thermocouple. We used the finite-element method (Kuroda 2001) for the calculation, which considers an axi-symmetric two-dimensional (2D) problem. We assume that all of the frictional work is converted to heat on the slip surface, and that the temperature changes are derived from heat production and heat loss due to conduction. The heat source term at a radial position is given by the shear stress multiplied by a slip rate at a radial position. The initial temperature in a section of granite–gouge–Teflon sleeve is 25 °C. The granite surface adjacent to the stainless-steel holder is assumed to be constant at 25 °C. A constant coefficient of heat transfer ( $10 \text{ W m}^{-2} \text{ K}^{-1}$ ) is assumed for the cooling of the granite surface that is in contact with the air and surface of the Teflon sleeve. The displacement v. shear stress curve was fitted by a stepwise-constant curve, with the shear stress at each step interval being the averaged value of shear stresses over the slip interval of each step (Fig. 6a). The parameter values used for the numerical modelling are shown in Table 1.

The temperature distributions at the end of the dry and wet tests reflect that the heat production is proportional to the slip rate at a radial position (Fig. 6b, c). In the dry tests, the temperature distribution tends to show high values when  $\sigma_n$  is increased from 0.6 to 2.0 MPa, while such a tendency is not recognized in the wet tests. Compared

to experiments under dry conditions, the temperatures in the fault gouge under wet conditions are reduced. Figure 6d, e shows the calculated temperature evolution at three points for the dry and wet tests at  $\sigma_n$  of 2.0 MPa: two points in the fault gouge, 3.75 and 11 mm from the revolution axis; and one point in the granite specimen where the thermocouple was placed. The calculated temperatures are consistent with the temperatures measured by a thermocouple. The temperatures in the fault gouge increase exponentially with displacement. The temperatures at the positions 3.75 and 11 mm from the revolution axis at the end of the dry tests are 249–343 and 375–572 °C, respectively; whereas the temperatures at these positions at the end of the wet tests are 136–210 and 248–326 °C, respectively.

#### *Microstructural and X-ray diffraction analyses*

After the experiments, the sample assembly was impregnated with a low-viscosity epoxy resin and dried in a vacuum evaporator. The sample was then cut through the axis of the cylinder to make a radial thin section that was perpendicular to the slip direction and gouge layer (Fig. 2). This radial thin section was useful for an observation of the microstructures that developed at various slip rates and displacements, ranging from a zero slip rate and displacement at the centre of the cylinder to the maximum slip rate and displacement at the edge of the cylinder. The pair of granite samples was separated by a 0.5–0.6 mm-thick gouge layer after the experiments. The microstructures of the fault gouges specimens were examined by optical microscope, scanning electron microscope (SEM) and transmission electron microscope (TEM).

The gouge has a light greyish colour before the experiments. After the dry tests, the colour of the gouge is changed to dark in the peripheral part of the cylinder, while the central part of the cylinder remains light grey (Fig. 7a). An X-ray diffraction (XRD) analysis was performed on bulk powders extracted from the gouge sample before the experiment, and on the light greyish and dark gouges after the experiment under the following setting: 40 kV and 20 mA, CuK $\alpha$  radiation, Ni filter, 1° divergence and scatter slits, 0.2 mm receiving slit, and 0.001 ° s $^{-1}$  scan speed. There are peaks from quartz, plagioclase, illite, chlorite and calcite in the XRD patterns of the gouge sample before the experiment and the light greyish gouge after the experiment, but the X-ray diffraction peaks for illite, chlorite and calcite are absent in the XRD patterns of the dark gouge (Fig. 7b). As described below, the microstructural features are different between the light greyish and dark gouges.

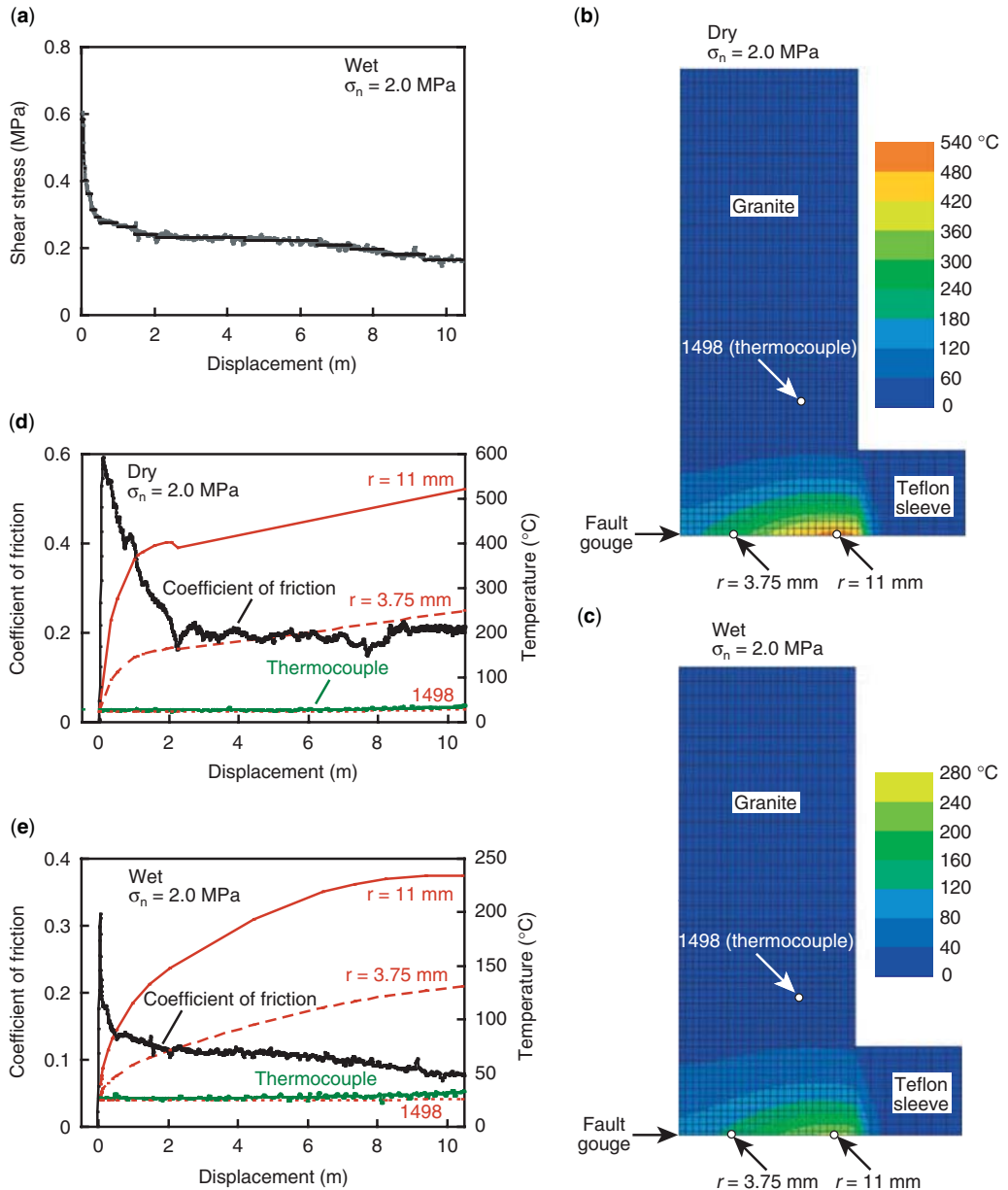


**Fig. 6.** Results of temperature analysis. (a) Shear stress (grey line) and average value of shear stresses used for the numerical calculation (black line) are plotted as a function of displacement. (b) & (c) Numerically calculated spatial distribution of temperature at the end of dry (b) and wet (c) tests at  $\sigma_n$  of 2.0 MPa. (d) & (e) Evolution of temperatures calculated by numerical modelling and measured using a thermocouple, along with coefficient of friction as a function of displacement under dry (d) and wet (e) conditions at  $\sigma_n$  of 2.0 MPa. The location of the thermocouple in the granite specimen and the radial position of the centre of the gouge layer are shown in (b) and (c).

The light greyish gouge is marked by the presence of angular–subrounded clasts of quartz, plagioclase and calcite in clay matrix. Under cross-polarized light, the clay minerals exhibit

interference colours but show no or only faint foliation, and their features are very similar to those of the starting material before shearing under dry conditions (Figs 3a & 8a). The dark gouge is

**Table 1.** Parameters and values used in numerical modelling

Property	Value
Density of fault gouge	$2000 \text{ kg m}^{-3}$
Heat capacity of fault gouge	$1000 \text{ J kg}^{-1} \text{ K}^{-1}$
Thermal conductivity of fault gouge	$1.5 \text{ W m}^{-1} \text{ K}^{-1}$
Density of granite	$2600 \text{ kg m}^{-3}$
Heat capacity of granite	$800 \text{ J kg}^{-1} \text{ K}^{-1}$
Thermal conductivity of granite	$2.0 \text{ W m}^{-1} \text{ K}^{-1}$

characterized by localized slip zone and a random distribution of rounded clasts in the matrix (Fig. 8b, c). The matrix of the dark gouge does not have interference colours and is optically isotropic under cross-polarized light. The dark gouge has irregular contact with the light greyish gouge, locally showing a region of mixing (Fig. 8d).

The matrices of the light greyish and dark gouge were observed under the TEM (JEOL FEM-2010) operated at 200 kV. TEM samples were prepared from thin sections by a focused ion beam (FIB) technique with a microsampling system (Hitachi FE-2100) using a Ga ion beam. Qualitative chemical analyses of the constituent minerals were performed by energy dispersive X-ray spectrometry (EDS) in the TEM (JEOL EX-24025JGT). The TEM image of the light greyish gouge matrix typically shows the presence of wavy flakes several hundreds nanometres in length (Fig. 9a), with their morphological features very similar to those of the smectite in marine sediments (Clauer *et al.* 1990; Bautier *et al.* 1992). The diffraction pattern from these flakes displays reciprocal lattice rows of  $10 \text{ \AA}$  spacing along  $c^*$ -like illite (inset in Fig. 9a), which is caused by the interlayer dehydration that occurs in the ultrahigh vacuum condition in the TEM. The EDS detected peaks for Si, Al, Mg, K, Ca and Fe from the flakes (Fig. 9b). These features indicate that the wavy flakes are smectite–illite mixed-layer clay. In contrast, the TEM image of the dark gouge matrix is marked by a random distribution of rounded grains with diameters smaller than 300 nm (Fig. 9c). The diffraction pattern from the rounded grains is characterized by amorphous rings (inset in Fig. 9c). The EDS analysis results demonstrate that the chemical composition of the rounded grains is the same as that of the wavy flakes in the light greyish gouge (Fig. 9d). These features reflect the amorphorization of the smectite–illite mixed-layer clay in the dark gouge.

The thickness of the localized slip zone (LSZ) in the dark gouge is less than 0.2 mm; this zone is developed along the boundaries between the gouge and the granite specimens (Figs 8b, d & 10). This

LSZ mainly occurs along the boundary with the granite specimen on the stationary side, but in some cases develops along the boundary with the specimen on the rotational side. There is no LSZ in the light greyish gouge from the central part of the cylinder. LSZ is rusty orange–dark brown under plane-polarized light and orange under cross-polarized light, showing the alignment of extremely fine-grained clay particles along the layer (Fig. 8b, d). In places, the LSZ is marked by anastomosed or undulated slip surfaces surrounding the non-foliated gouge (Fig. 10a). The upper and lower boundaries of these slip surfaces are gradual and sharp, respectively. In some cases, a composite planar fabric is developed in the LSZ, with its geometry similar to  $P-R_1$  fabric (Fig. 10b). The shear sense of the foliated gouge indicated by the composite planar fabric is consistent with the shear direction during the experiment. EDS–SEM element mapping of the LSZ reveals higher relative atomic densities of Al, Fe, Mg, Ca and K relative to those in the gouge matrix, indicating a concentration of smectite, illite and chlorite (Fig. 11). In places, sub-angular–rounded fragments composed of very fine-grained clay particles are included in the gouge matrix, which are probably derived from the LSZ along the gouge boundary (Fig. 10c).

The rounded clasts in the dark gouge are commonly defined by the central clasts of quartz and plagioclase that are surrounded by a cortex of concentric clay layers, including submicron fragments, with a texture very similar to that of accretionary lapilli (Fig. 12). These spherical aggregates were reported in high-velocity friction experiments on clay-rich (kaolinite and illite–smectite mixed layers) fault gouge (Boutareaud *et al.* 2008, 2010) and natural faults (Boullier *et al.* 2009), which were termed clay–clast aggregates (CCA). The EDS–SEM element mapping of the CCA shows that the cortex of the CCA has a higher relative atomic density of Al, Fe, Mg, Ca and K elements than those in the gouge matrix, representing the concentration of smectite, illite and chlorite in the cortex (Fig. 13). CCA rarely occur in the light greyish gouge from the central part of the cylinder.

After the wet tests, there is no visible change in the colour of the fault gouge, and a zone of preferred orientation of clay particles develops in the fault gouge (Fig. 14a) regardless of the radial position of the gouge layer. The clay particles in this zone are commonly orientated parallel to the gouge boundaries. Such a foliated zone is absent in the starting material before shearing under wet conditions (Fig. 3b). Compared to the LSZ developed in the experiments under dry conditions, the foliated zone formed under wet conditions is thick (0.25–0.45 mm in thickness), and the sizes of the clay particles in the foliated zone are large (i.e. the

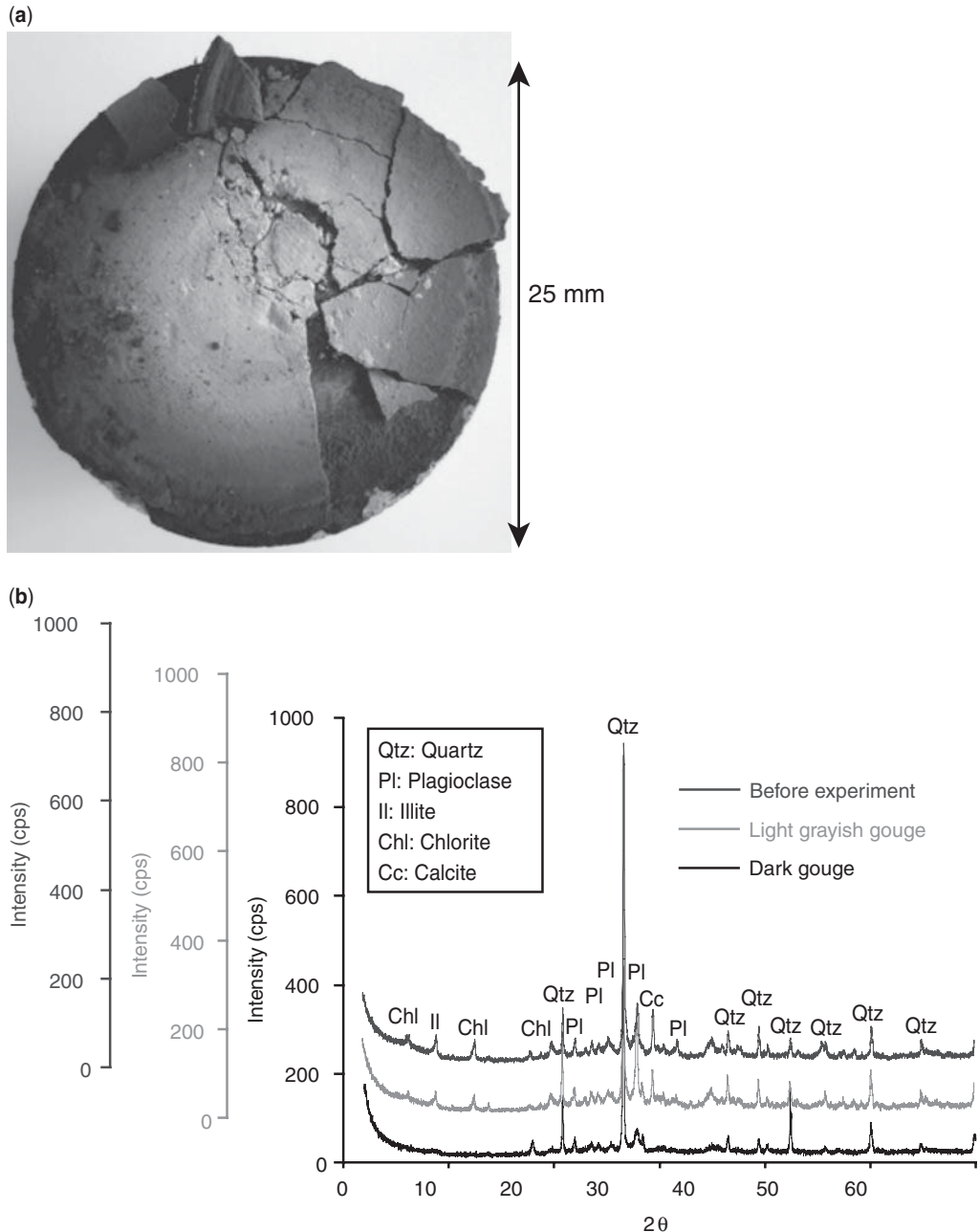


**Fig. 7.** Results of XRD analysis after the dry test at  $\sigma_n$  of 1.5 MPa. (a) A photograph of the fault gouge on the cylindrical granite specimen showing the distribution of the light greyish and dark gouges in the central and peripheral parts of the cylinder, respectively. (b) Bulk X-ray diffraction patterns of the gouge sample before the experiment, and the light greyish and dark gouges after the experiment.

pronounced particle-size reduction is lacking). The foliated zone develops in the upper part of the gouge layer in some cases, and within the gouge layer in others. The clay particles in the non-foliated

zone are randomly oriented with sizes similar to those of the starting material. Locally, intact foraminifera can be observed both in the foliated and in the non-foliated zones (Fig. 14b).

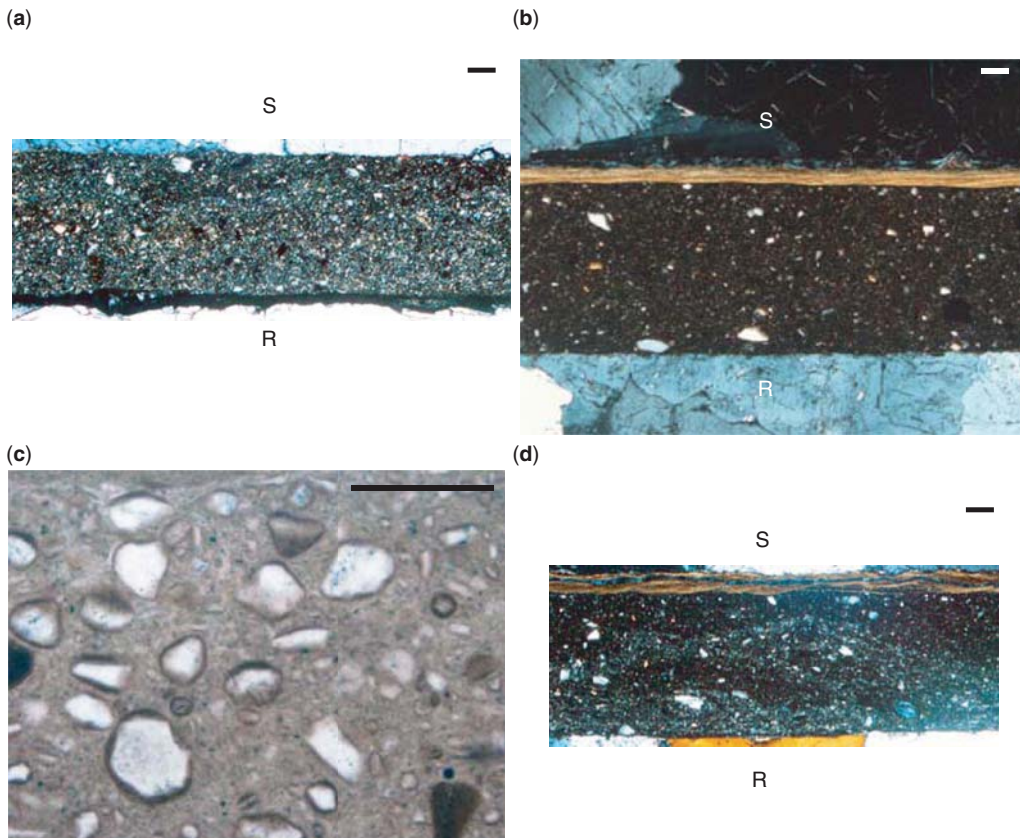


**Fig. 8.** Photomicrographs of gouge after dry tests. Scale bar: 0.1 mm. S, stationary side; R, rotational side. (a) The light greyish gouge under cross-polarized light. The dark band developed along the lower boundary between the gouge and the granite specimen represents the crack impregnated with a low-viscosity epoxy resin that is formed during sample preparation. (b) The localized slip zone (orange colour) developed along the upper boundary between the dark gouge and the granite specimen. Cross-polarized light. (c) The dark gouge under plane-polarized light. Note that rounded clasts are marked by central clasts surrounded by a dark brownish cortex of concentric clay minerals, representing clay-clast aggregates (CCA). (d) The mixing of the light greyish (bright colour) and dark gouges without shear surfaces. Note the development of the localized slip zone (orange colour) along the upper boundary of the gouge layer in which the crack (dark band) developed during sample preparation.

Another microstructural feature of the fault gouge after the wet tests is a concentration of large grains in the upper part of the gouge layer (Fig. 15). This grain-size segregation is observed in the peripheral part of the cylinder, where  $V$  is higher than  $0.62 \text{ m s}^{-1}$  according to Equation (1). The grain-size segregation tends to occur in the foliated zone (Fig. 15c).

## Discussion

### High-velocity weakening mechanisms of clay-rich fault gouges

The experimental data under dry conditions demonstrate that the slip weakening is closely related to the

gouge dilation and rapid temperature increase in the gouge: the end of the slip weakening corresponds to the end of gouge dilation and to the change in the increasing rate of gouge temperature in the peripheral part of the cylinder (Figs 4a & 6d). As  $D_c$  is inversely proportional to  $\sigma_n$ , the time for the slip weakening and gouge dilation is shorter for larger  $\sigma_n$ .

The calculated temperatures in the peripheral part of the cylinder during slip weakening under dry conditions are well above  $200^\circ\text{C}$ . These temperature values could be underestimated because the calculation does not consider the localized slip in the gouge layer (Fig. 8b). Under such increased temperatures, clay minerals (smectite, illite and chlorite) can release their absorbed and interlayer

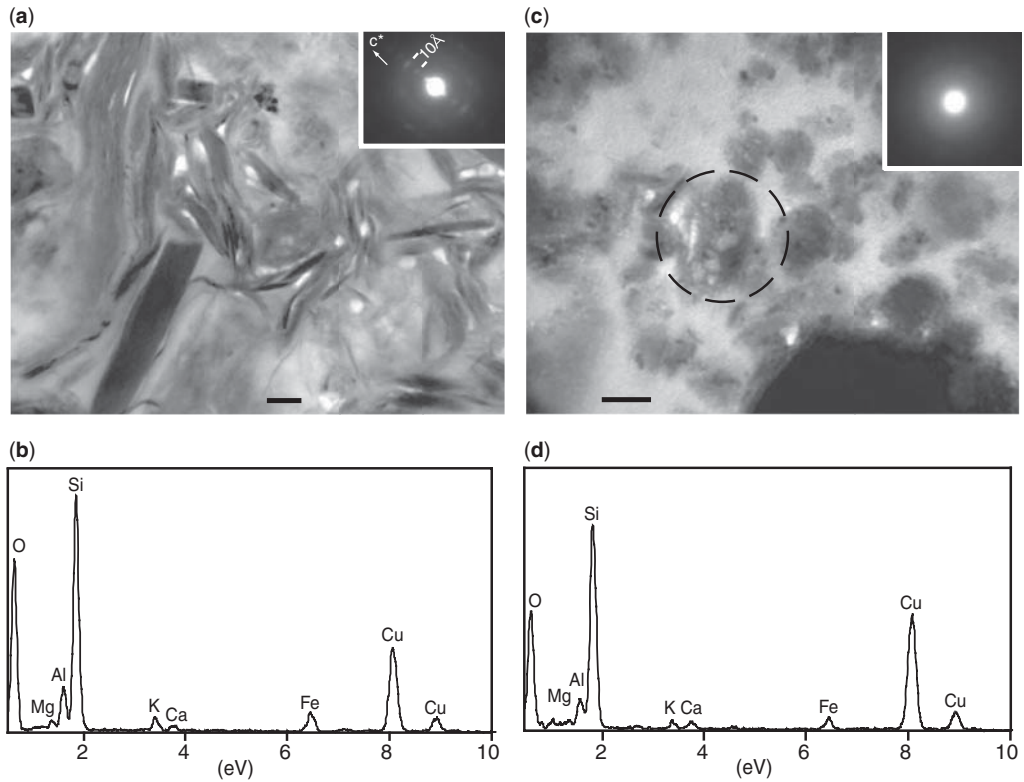


**Fig. 9.** TEM analysis of gouge after the dry test at  $\sigma_n$  of 1.0 MPa showing marked differences in morphologies and diffraction patterns between light greyish and dark gouges. Scale bar: 100 nm. (a) Bright-field TEM image of the light greyish gouge. Inset shows the diffraction pattern from the wavy flakes. (b) EDS signals from the wavy flakes. (c) Bright-field TEM image of the dark gouge. Inset shows the diffraction pattern from the rounded grains (dotted circle). (d) EDS signals from the rounded grains.

water (Grim & Bradley 1940; Deer *et al.* 1992; McConville & Lee 2005). Based on the water phase diagram (Fisher 1976), the temperatures for water vaporization at 0.6–2.0 MPa are estimated as 159–213 °C; thus, released water has to be vapourized. This water-phase transition induces a rapid increase in the volume of water by a factor of 10 (Lemmon *et al.* 2002), which would be accommodated by the fault-gouge dilation (Fig. 4a). However, the Teflon sleeve could not completely maintain the fluid pressure generated in the gouge layer, and the viscosity of vaporized water is of order of  $10^{-5}$  Pa s at the given pressure and temperature ranges (Lemmon *et al.* 2002). The increase in humidity during the dry tests is most likely to have been caused by leakage of the vaporized water from the gouge layer (Fig. 4a). Presumably, the production rate for the water vaporization is higher than the radial leakage rate of the vapour, resulting in the dilation of the gouge layer. Therefore, slip weakening during the dry tests is attributed

to the fault gouge expansion associated with water vaporization (i.e. thermal pressurization: Sibson 1973), which is caused by dehydration of the clay minerals due to frictional heating.

The disappearance of the X-ray diffraction peaks of illite, chlorite and calcite in the dark gouge distributed in the peripheral part of the cylinder (Fig. 7b) – along with the optically isotropic matrix of the dark gouge without any characteristic microstructures formed by the frictional melting of clay-rich materials (e.g. the presence of the clasts with corrosion rim, vesicles, Fe-rich spherules and mullite microlites in the glassy matrix) (Ujiie *et al.* 2007b, 2009) – may represent the thermal decomposition of the clay minerals and calcite. The TEM analysis indicates that amorphization of smectite–illite mixed-layer clay occurred in the matrix of dark gouge (Fig. 9c). This could be due to mechanical wear in the region of the high slip rates and large displacements, but may also represent the thermal decomposition of the smectite–illite

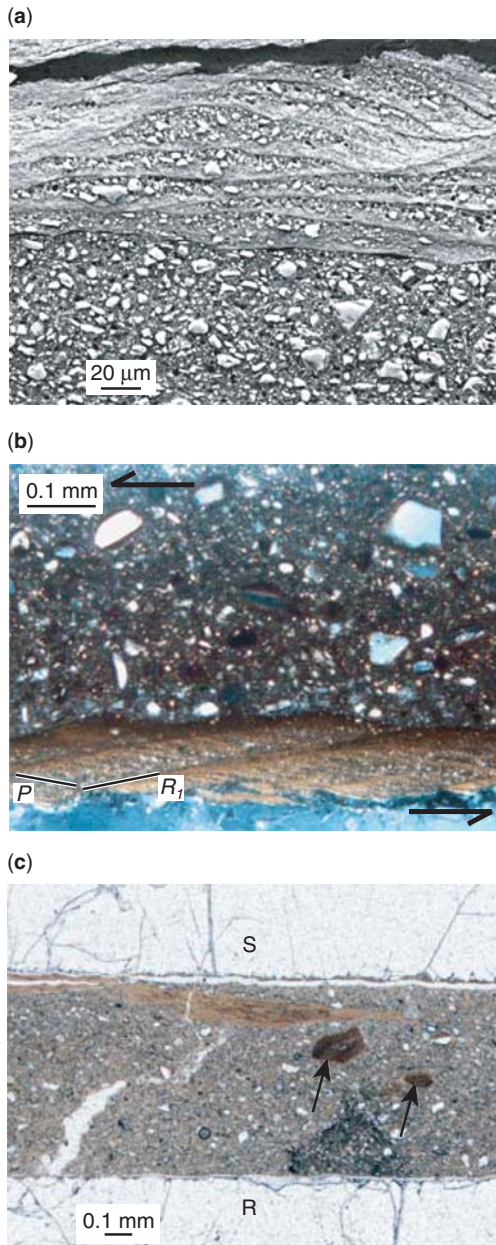


**Fig. 10.** Microstructural appearance of localized slip zone (LSZ) in dark gouge formed by dry tests. (a) BSE image of the LSZ composed of anastomosed slip surfaces. (b) The LSZ showing the composite planar fabric. The half arrows indicate the shear direction during an experiment. Cross-polarized light. (c) The dark brown fragments (arrows) in the matrix, probably derived from the LSZ. Note that the LSZ (rusty orange in the upper part of the gouge layer) is just incorporated into the gouge. Plane-polarized light. S, stationary side; R, rotational side.

mixed-layer clay by frictional heating. The thermal decomposition of the clay minerals and calcite occurs at temperatures of 720–850 °C (Grim & Bradley 1940; Deer *et al.* 1992; Sharp *et al.* 2003; McConville & Lee 2005). However, the temperature in the fault gouge in the peripheral part of the cylinder is less than 600 °C at the end of the dry tests. Such a discrepancy is likely to be due to the underestimation of the calculated temperatures. According to high-velocity friction experiments on marble, a steady-state friction of 0.06 is achieved in association with the thermal decomposition of calcite (Han *et al.* 2007). As the calcite abundance in the megasplay fault zone is less than 9 wt% (Expedition 316 Scientists 2009), the effect of calcite decomposition on the frictional property would be small: a majority of the slip weakening is attributed to the dehydration of clay minerals.

The axial shortening of the fault gouge during the rapid slip weakening in the wet tests is markedly smaller than that during the corresponding slip in the dry tests (Figs 4a & 5a). This may reflect the generation of fluid pressure caused by the shear-enhanced compaction of the water-saturated, low-permeability clay-rich gouge sandwiched between the pair of impermeable granite specimens. On the other hand, the rapid weakening of the fault gouge in the wet tests is synchronous with the rapid increase in gouge temperature (Fig. 6e). The calculated temperatures in the peripheral part of the cylinder during rapid weakening under wet conditions are lower than the temperatures for water vaporization at 0.6–2.0 MPa (i.e. 159–213 °C). Therefore, frictional melting, thermal decomposition of the clay minerals and calcite, dehydroxylation of the clay minerals, and water vaporization are unlikely to occur during rapid weakening. However, the temperature in the peripheral part of the gouge layer, the increase in humidity and the transient gouge dilation during the steady-state friction under wet conditions suggest the vaporization of pore water (Figs 5a & 6c, e). In summary, the rapid slip weakening of the fault gouge in the wet tests is caused by the pore-fluid pressurization due to a combination of shear-enhanced compaction and frictional heating.

#### Correlation between gouge microstructures, frictional heating, fluid pressurization and slip rates

In the dry tests, the LSZ occurs along the boundaries between the gouge and granite specimens in the peripheral part of the cylinder (Fig. 8b). This suggests that the development of the LSZ is dependent on the slip and/or slip rate. The pronounced size reduction of clay minerals within the LSZ appears

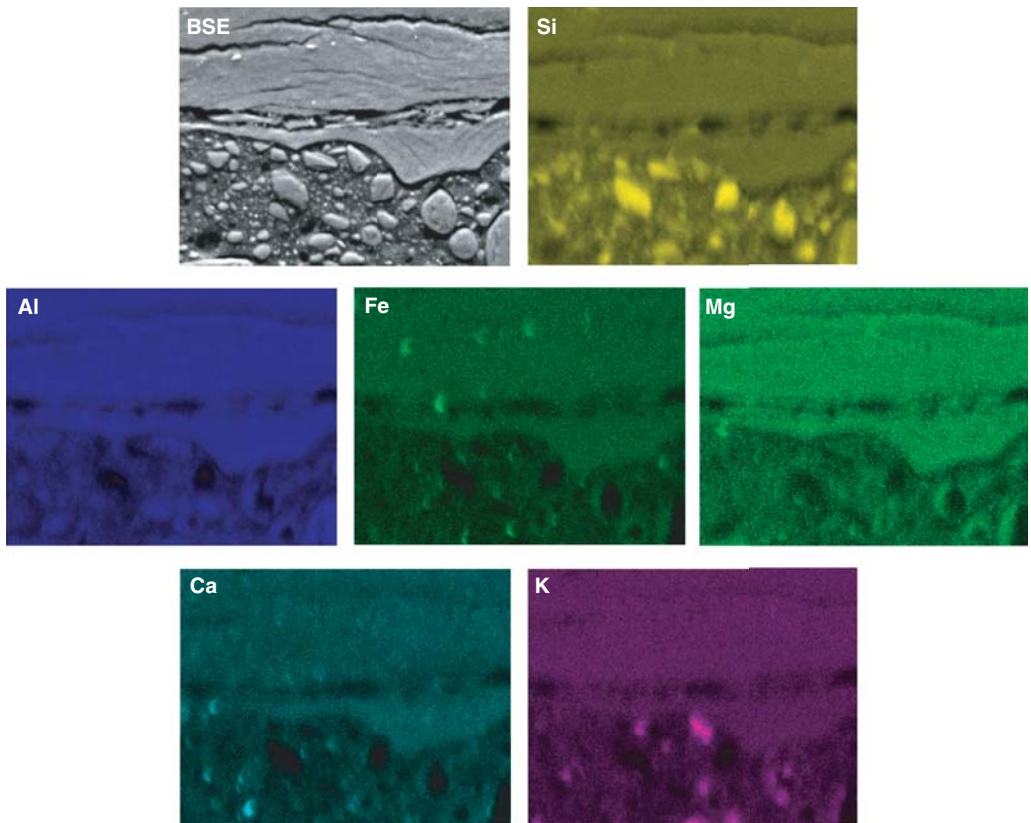


**Fig. 11.** EDS-SEM element mapping of localized slip zone. Brighter colours represent higher relative atomic density of elements.

to represent frictional wear. It is possible that the frictional heat is generated by the concentration of frictional slip along the thin (less than 0.2 mm in thickness) slip zone. The temperature rise associated

with the frictional heating would lead to the dehydration of clay minerals, which would cause the fault-gouge expansion associated with the water-phase transition from liquid to vapour. The dark and light greyish gouges are locally intermixed without shear surfaces and transecting fractures, demonstrating the mobilization of the materials derived from the central and peripheral parts of the cylinder (Fig. 8d). This texture produced by the flow mixing could reflect that the thermal expansion caused by the liquid–vapour transition of water leads to the fluidization of the fault gouge. The LSZ composed of extremely fine-grained clay minerals is locally fragmented and incorporated into the gouge matrix (Fig. 10c). Thus, the temporal relationship of the microstructures suggests that the frictional heating along the LSZ is followed by the thermal pressurization-induced fluidization of the fault gouge outside the LSZ.

Another characteristic microstructure formed during the dry tests is the presence of CCA in the gouge matrix (Fig. 12). By analogy with the mechanism for the formation of accretionary lapilli,

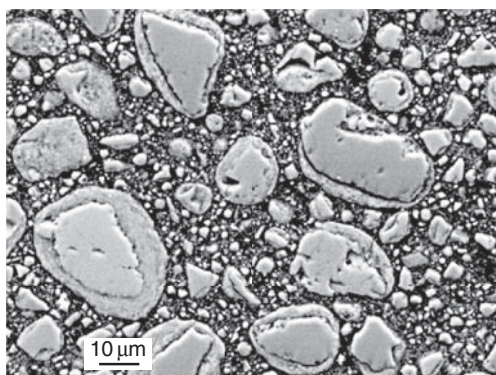


**Fig. 12.** Back-scattered electron (BSE) images of clasts after dry tests showing a random distribution of clay-clast aggregates in the matrix.

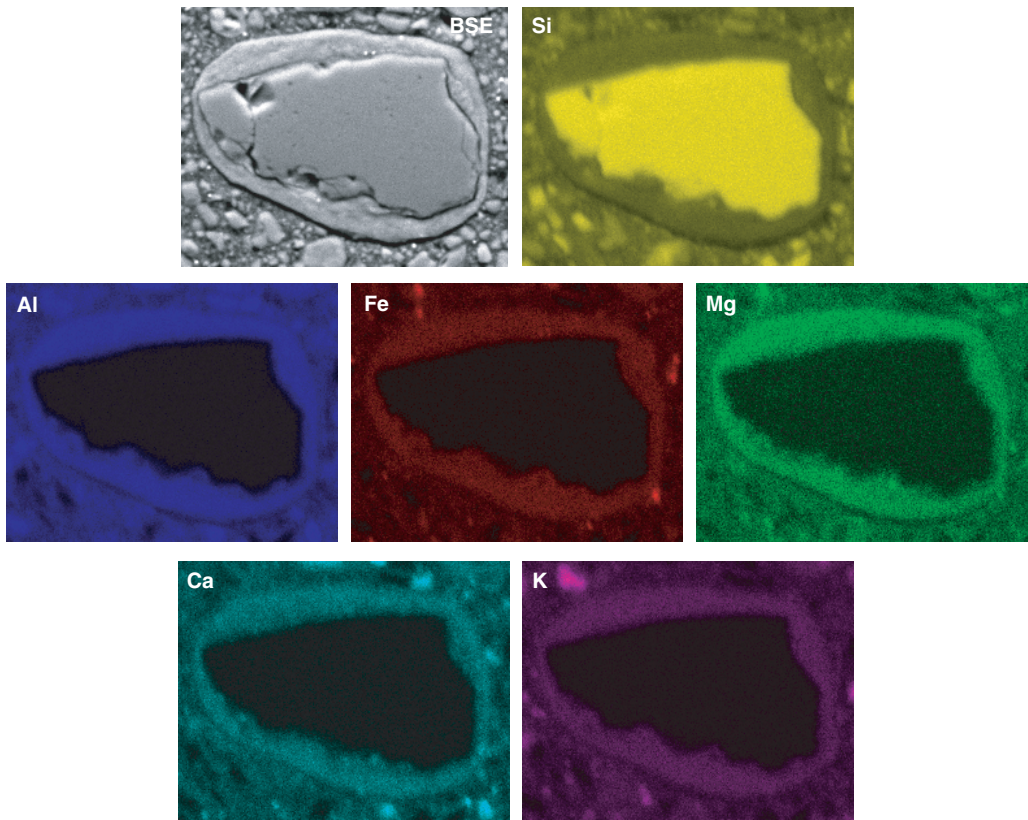


**Fig. 13.** EDS-SEM element mapping of clay-clast aggregates. Brighter colours represent higher relative atomic density of elements.

Boutareaud *et al.* (2008, 2010) argued that CCA are formed by adhesion of fine-grained clay particles around clasts, caused by a combination of electrostatic and capillary forces that occur in a critical

reactive liquid–vapour water medium. This is consistent with our experimental and numerical results, showing that gouge weakening is caused by thermal expansion associated with the water-phase

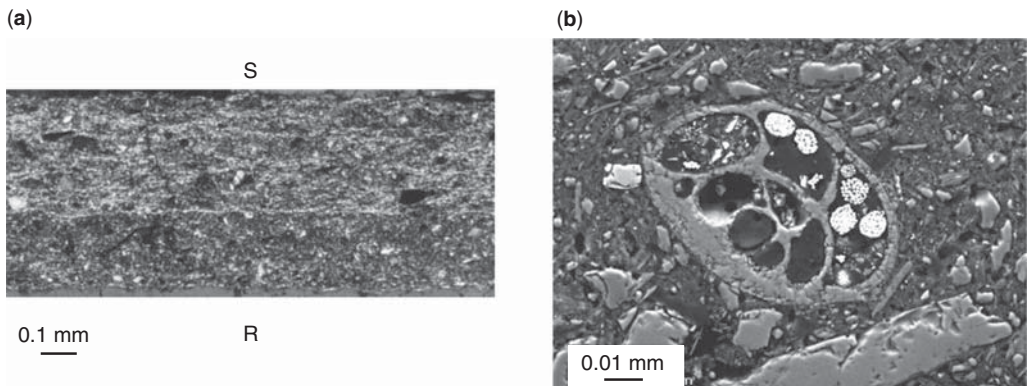


**Fig. 14.** Microstructures of gouge after wet tests. (a) The foliated zone developed in the upper part of the gouge layer showing the alignment of clay particles. Cross-polarized light. S, stationary side; R, rotational side. (b) BSE image showing the presence of intact foraminifera in the gouge.

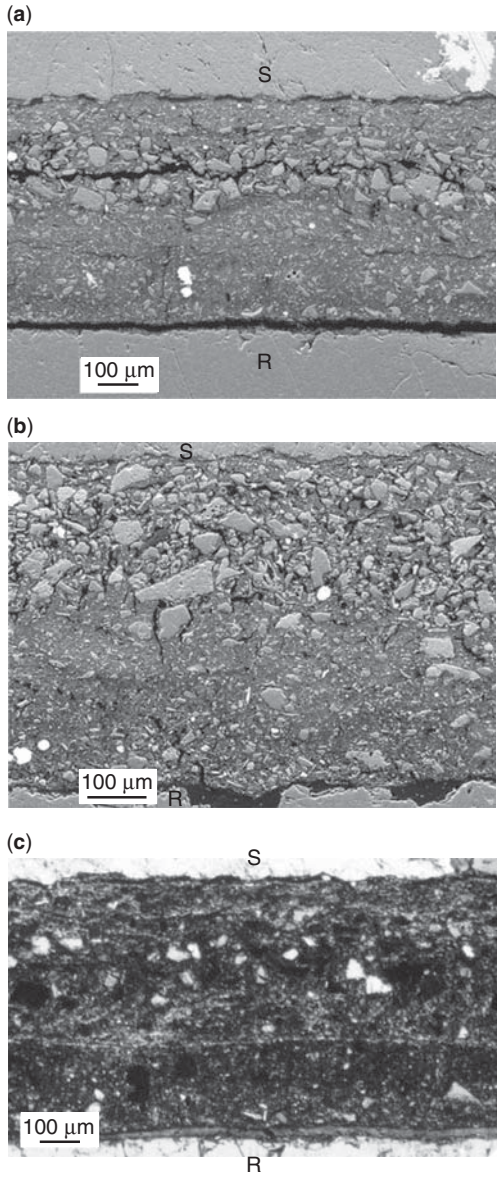


**Fig. 15.** Grain-size segregation in gouge after wet tests. S, stationary side; R, rotational side. (a) BSE image of the grain-size segregation in the gouge layer. (b) A close-up view of the grain-size segregation in the gouge. (c) The grain-size segregation in the foliated zone. Cross-polarized light.

transition from liquid to vapour. In this case, the CCA might be an indicator of the gouge weakening by thermal pressurization (Boutareaud *et al.* 2008, 2010). However, if the vapour production rate is lower than the rate of vapour escape from the gouge layer, the fault-gouge expansion and resulting

weakening would be limited or unlikely. The CCA may be an indicator of fault weakening by thermal pressurization. Additional friction experiments and a microstructural study on fault gouges with various clay content, using various ranges of slip rates, are required to test this hypothesis.

In the wet tests, the steady-state friction is established immediately after the peak friction, with a very small  $D_c$  value demonstrating that the fracture energy in the wet tests is very small relative to that in the dry tests (Figs 4b & 5b). This is consistent with the microstructural observations of the fault gouge after the wet tests, which show the absence of the pronounced particle-size reduction and the presence of intact foraminifera (Fig. 14). A very weak dependence of  $\tau_{ss}$  on  $\sigma_n$  under wet conditions suggests that the fault gouge behaves like a fluid (Fig. 5c). The foliated zone characterized by the alignment of clay particles (Fig. 14a) appears to represent that the flow textures developed in a fluid-like behaviour of the clay-rich gouge layer.

Grain-size segregation is commonly found in the peripheral part of the cylinder, where  $V$  is higher than  $0.62 \text{ m s}^{-1}$  (Fig. 15). Evidence of grain-size segregation is lacking in the fault gouge from the central part of the cylinder and from our preliminary experiments at the same displacement and  $\sigma_n$  but at a lower value of  $V_e$  of  $0.127 \text{ m s}^{-1}$  (i.e.  $V$  ranging from 0 to  $0.19 \text{ m s}^{-1}$ ) under wet conditions. These facts indicate that the grain-size segregation in the fault gouge reflects flow sorting at high slip rates. What physical processes were responsible for this texture? According to Bagnold's law (Bagnold 1954; Hanes & Inman 1985), the dispersive pressure ( $P$ ) generated by granular collision in a granular-fluid shear flow is proportional to the square of the shear rate ( $d\gamma/dt$ ):

$$P \propto \rho(\lambda D)^2 \left( \frac{d\gamma}{dt} \right)^2 \quad (6)$$

where  $\rho$  is the density of the granular-fluid materials,  $\lambda$  is the linear grain concentration defined by the ratio of the grain diameter to the mean free separation distance between grains, and  $D$  is the grain diameter. Because the thickness of the fault gouge is nearly constant throughout the cylinder, and the change in gouge thickness during the wet tests is very small, Equation (6) can be modified as follows:

$$P \propto \rho(\lambda DV)^2. \quad (7)$$

This equation indicates that the difference in  $P$  between large and small grains increases towards the edge of the specimen, where  $V$  is at its highest. In the fault gouge under a granular-fluid shear flow (i.e. fluidized flow) at high slip rates, voids

tend to be formed around large grains because large grains can push small grains aside owing to the large difference in  $P$ . In this case, small grains have a higher probability of filling these voids than do the larger grains. Consequently, large grains are moved upwards as smaller grains fill the voids by downwards movement under gravity. This grain-size segregation process is comparable to the Brazil-nut effect (Williams 1976; Rosato *et al.* 1987; Breu *et al.* 2003). Namely, when grain mixtures are shaken or collided, the larger grains rise to the top. The Brazil-nut effect, accompanied by the downwards movement of small grains from gravity, is likely for the rotary shear, frictional testing apparatus of Kyoto University because the orientation of its revolution axis is vertical. In summary, the grain-size segregation in the fault gouge is due to the Brazil-nut effect caused by the large difference in  $P$  between large and small grains at high shear rates, and thus potentially an indicator of high-velocity fluidized flow.

### *Implications for seismic slip on natural faults*

Fluidized fault rocks have been reported in a variety of tectonic settings, including intra-continental strike-slip faults (Otsuki *et al.* 2003), a thrust fault in exhumed accretionary complex (Ujiie *et al.* 2007a), a low-angle normal fault (Smith *et al.* 2008) and a thrust fault in an arc–continent collision zone (Boullier *et al.* 2009). The main criteria for the recognition of fluidization are the presence of injection structures, the mixing and interpenetration of components, and the low values for the detection probability of fragmented counterparts (i.e. because clasts that were originally part of a larger clast are rapidly separated during fluidization, the likelihood of detecting fragmented counterparts is expected to be low in the fluidized material; see Monzawa & Otsuki 2003). Ujiie *et al.* (2008) found that the stretching of fluid inclusions in calcite (i.e. an increase in the volume of fluid inclusions by increased heating) occurred along the fluidized zone, a few centimetres thick, in subduction thrust exhumed from seismogenic depths (4–6 km), but was absent in the surrounding host rocks and hydrothermally altered rocks, most probably representing frictional heating along the localized slip zone. Thus, the fluidization would be caused by thermal pressurization. The resulting structures include the development of a random fabric and the mixing of materials from different origins without shear surfaces (Ujiie *et al.* 2007a), both of which were reproduced by our high-velocity friction experiments under dry conditions. However, CCA were not observed in the fluidized zone from the exhumed subduction thrust. Boullier *et al.* (2009) discovered CCA in the 2 cm-thick,

clay-rich fluidized zone at a depth of 1111 m in Taiwan Chelungpu Fault Drilling Project (TCDP) Hole A, which is believed to have slipped during the 1999 Chi-Chi earthquake ( $M_w$  7.6). In this case, the fluidization of the clay-rich fault gouge could have been caused by thermal pressurization associated with the liquid–vapour transition of water and resulting in the random distribution of clasts, including the CCA in the matrix.

The 3 mm-thick slip zone at a depth of 1136 m in TCDP Hole B is also believed to have slipped during the 1999 Chi-Chi earthquake, and is marked by a foliated gouge showing an alternation of clay-rich and clast-rich layers without CCA (Boullier *et al.* 2009). This structure may be comparable to the internal structure of the fault gouge after wet tests; the experimentally generated grain-size segregation is frequently observed in the foliated zone, resulting in the differentiation between clast-rich and clay-rich layers (Fig. 15). The grain-size segregation represents flow sorting in the high-velocity fluidized flow, which is consistent with the very weak dependence of  $\tau_{ss}$  on  $\sigma_n$  (Fig. 5c). Flow differentiation associated with granular collision in a fluidized flow tends to operate in a narrow zone (e.g. Bagnold 1954; Barrière 1976), which is consistent with the differentiation between clast-rich and clay-rich layers observed in the thin (thickness of 3 mm) slip zone in TCDP Hole B. Foliated gouge and foliated cataclasite are commonly observed in fault zones everywhere. However, if the thin foliated zone includes the grain-size segregation characterized by the concentration of large grains, this would be an indicator of fluidized flow at high slip rates. Another important implication for natural faults is that the grain-size segregation brought by the Brazil-nut effect is likely to occur in low- to moderate-dipping faults because the Brazil-nut effect requires a downwards movement of small grains by gravity.

Clay-rich fault gouges commonly exhibit velocity-strengthening behaviour at slow slip rates of less than  $100 \mu\text{m s}^{-1}$  (Morrow *et al.* 1992; Saffer & Marone 2003; Ikari *et al.* 2009). Thus, earthquake nucleation is unlikely to occur in clay-rich fault gouges. On the other hand, the propagation of an earthquake rupture may be controlled by the high-velocity frictional properties of clay-rich fault gouges. Our experimental data at seismic slip rates would be useful in understanding the frictional response associated with earthquake-rupture propagation from depth. The peak friction in the dry tests is higher than the frictional strength of the megasplay fault material at low slip rates ( $\leq 100 \mu\text{m s}^{-1}$ ) given by Ikari *et al.* (2009), which may be a barrier to rupture propagation toward the sea floor. However, once this frictional barrier is overcome, fault weakening can occur from the

thermal pressurization associated with the water-phase transition from liquid to vapour, resulting in the formation of CCA in the dark gouge. The experimental data obtained under wet conditions implies that earthquake ruptures propagate easily through clay-rich fault gouges by fluid pressurization and fluidization, with very small fracture energy. As  $\tau_{ss}$  is nearly independent of  $\sigma_n$ , a nearly complete stress drop and increased seismic efficiency can be expected at greater depths. In the shallow portion of the megasplay fault in the Nankai accretionary prism, slip is localized along the 10 mm-thick layer of dark gouge, which has a higher vitrinite reflectance probably because of frictional heating (Sakaguchi *et al.* 2011) (Fig. 1c). The clay-rich megasplay fault-zone materials exhibit a low permeability of less than  $5.5 \times 10^{-20} \text{ m}^2$  (Ikari *et al.* 2009). Therefore, high-velocity weakening by thermal pressurization may occur even in the shallow portions of megasplay faults; this weakening could enhance tsunamigenesis during a subduction earthquake.

## Conclusions

The high-velocity friction experiments on clay-rich fault gouges under dry and wet conditions revealed the frictional properties, physical processes and the resulting microstructures associated with thermal pressurization and fluidization. Slip weakening under dry conditions occurs by thermal pressurization. This is marked by dilation of the fault gouge in response to a water-phase transition from liquid to vapour, which is caused by the dehydration of clay minerals due to frictional heating. Slip weakening under wet conditions reflects the pore-fluid pressurization resulting from the shear-enhanced compaction of the water-saturated gouge and the generation of frictional heat. The wet tests exhibit smaller dynamic stress drop and shorter slip-weakening distance than the dry tests. A very weak dependence of  $\tau_{ss}$  on  $\sigma_n$  in the wet tests suggests fluid-like behaviour of the fault gouge and nearly complete stress drop at greater depths. The peak frictions in the dry and wet tests are, respectively, higher and comparable to the frictional strength of clay-rich fault gouges at low slip rates. Once this frictional resistance is overcome, high-velocity weakening can occur during earthquakes, which would enhance the propagation of an earthquake rupture.

The microstructures after the dry tests represent thermal pressurization-induced fluidization, which are shown by a random distribution of CCA in the matrix and the mixing of gouge components without shear surfaces. Similar structures have been reported for natural faults, in which a narrow fluidized zone is recognized with evidence for frictional

heating. The microstructures after the wet tests show that the foliated zone is accompanied by grain-size segregation in the gouge layer. The grain-size segregation represents the Brazil-nut effect caused by the difference in the dispersive pressure in a fluidized flow at high shear rates. The important implications for natural faults is that the grain-size segregation brought about by the Brazil-nut effect probably occurs in low- to moderate-dipping faults and that the occurrence of grain-size segregation in the thin foliated zone is an indicator of a fluidized flow at high shear rates, and thus would be useful for recognizing past seismic slip.

This research used samples and data provided by the Integrated Ocean Drilling Program (IODP). We are grateful to the Expedition 316 scientists, and the captain, drilling crew and technicians of the D/V *Chikyu* for their support and co-operation onboard the ship. We gratefully acknowledge the useful discussions with T. Hatano and Y. Fialko. This research was funded by Grant-in-Aid for Scientific Research (B) from JSPS (21340150) and by Grant-in-Aid for Scientific Research on Innovative Areas from MEXT (21107005).

## References

- AAGARD, B. T., HEATON, T. H. & HALL, J. F. 2001. Dynamic earthquake ruptures in the presence of lithostatic normal stresses: implications for friction models and heat production. *Bulletin of the Seismological Society of America*, **91**, 1765–1796.
- ANDREWS, D. J. 2002. A fault constitutive relation accounting for thermal pressurization of pore fluid. *Journal of Geophysical Research*, **107**, 2363, doi: 10.1029/2002JB001942.
- BAGNOLD, R. A. 1954. Experiments on a gravity-free dispersion of large solid spheres in a Newtonian fluid under shear. *Proceedings of the Royal Society of London, A*, **225**, 49–63.
- BARRIÉRE, M. 1976. Flowage differentiation: limitation of the ‘Bagnold effect’ to the narrow intrusions. *Contributions to Mineralogy and Petrology*, **55**, 139–145.
- BOULLIER, A.-M., YEH, E.-C., BOUTAREAUD, S., SONG, S.-R. & TSAI, C.-H. 2009. Microscale anatomy of the 1999 Chi-Chi earthquake fault zone. *Geochemistry Geophysics Geosystems*, **10**, Q03016, doi: 10.1029/2008GC002252.
- BOUTAREAUD, S., CALUGARU, D.-G., HAN, R., FABBRI, O., MIZOGUCHI, K., TSUTSUMI, A. & SHIMAMOTO, T. 2008. Clay-clast aggregates: a new textural evidence for seismic fault sliding? *Geophysical Research Letters*, **35**, L05302, doi: 10.1029/2007GL032554.
- BOUTAREAUD, S., BOULLIER, A.-M., ANDRÉANI, M., CALUGARU, D.-G., BECK, P., SONG, S.-R. & SHIMAMOTO, T. 2010. Clay-clast aggregates in gouges: new textural evidence for seismic faulting. *Journal of Geophysical Research*, **115**, B02408, doi: 10.1029/2008JB006254.
- BRANTUT, N., SCHUBNEL, A., ROUZAUD, J.-N., BRUNET, F. & SHIMAMOTO, T. 2008. High-velocity frictional properties of a clay-bearing fault gouge and

- implications for earthquake mechanics. *Journal of Geophysical Research*, **113**, B10401, doi: 10.1029/2007JB005551.
- BREU, A. P. J., ENSNER, H.-M., KRUETTLE, C. A. & REHBERG, I. 2003. Reversing the Brazil-Nut Effect: competition between percolation and condensation. *Physical Review Letters*, **90**, 014302, doi: 10.1103/PhysRevLett.90.014302.
- BUATIER, M. D., PEACOR, D. R. & O'NEIL, J. R. 1992. Smectite-illite transition in Barbados accretionary wedge sediments: TEM and AEM evidence for dissolution/crystallization at low temperature. *Clays and Clay Minerals*, **40**, 65–80.
- CLAUER, N., O'NEIL, J. R., BONNOT-COURTOIS, C. & HOLTZAPFEL, T. 1990. Morphological, chemical and isotopic evidence for an early diagenetic evolution of detrital smectite in marine sediments. *Clays and Clay Minerals*, **38**, 33–46.
- DEER, W. A., HOWIE, R. A. & ZUSSMAN, J. 1992. *An Introduction to the Rock-forming Minerals*. 2nd edn. Longmans, London.
- DI TORO, G., HIROSE, T., NIELSEN, A., PENNACCHIONI, G. & SHIMAMOTO, T. 2006. Natural and experimental evidence of melt lubrication of faults during earthquakes. *Science*, **311**, 647–649, doi: 10.1126/science.1121012.
- EXPEDITION 316 SCIENTISTS. 2009. Expedition 316 Site C0004. In: KINOSHITA, M., TOBIN, H. (eds) *Proceedings of the IODP, 314/315/316*. Integrated Ocean Drilling Program, Washington, DC, doi: 10.2204/iodp.proc.314315316.133.2009.
- FAULKNER, D. R., JACKSON, C. A. L., LUNN, R. J., SCHLISCHE, R. W., WIBBERLEY, C. A. J. & WITHJACK, M. O. 2010. A review of recent developments concerning the structure, mechanics and fluid flow properties of fault zones. *Journal of Structural Geology*, **32**, 1557–1575.
- FISHER, J. R. 1976. The volumetric properties of H<sub>2</sub>O – A graphical portrayal. *US Geological Survey Journal of Research*, **4**, 189–193.
- GRIM, R. E. & BRADLEY, W. F. 1940. Investigation of the effect of heat on the clay minerals illite and montmorillonite. *Journal of the American Ceramic Society*, **23**, 242–248.
- HAN, R., SHIMAMOTO, T., HIROSE, T., REE, J.-H. & ANDO, J. 2007. Ultralow friction of carbonate faults caused by thermal decomposition. *Science*, **316**, 878–881, doi: 10.1126/science.1139763.
- HANES, D. M. & INMAN, D. L. 1985. Observations of rapidly flowing granular-fluid materials. *Journal of Fluid Mechanics*, **150**, 357–380.
- HAYASHI, N. & TSUTSUMI, A. 2010. Deformation textures and mechanical behavior of a hydrated amorphous silica formed along an experimentally produced fault in chert. *Geophysical Research Letters*, **37**, L12305, doi: 10.1029/2010GL042943.
- IKARI, M. J., SAFFER, D. M. & MARONE, C. 2009. Frictional and hydrologic properties of a major splay fault system, Nankai subduction zone. *Geophysical Research Letters*, **36**, L20313, doi: 10.1029/2009GL040009.
- KAME, N., RICE, J. R. & DMOWSKA, R. 2003. Effects of pre-stress state and rupture velocity on dynamic fault branching. *Journal of Geophysical Research*, **108**, 2265, doi: 10.1029/2002JB002189.
- KANAMORI, H. & HEATON, T. H. 2000. Microscopic and macroscopic physics of earthquakes. In: RUNDLE, J., TURCOTTE, D. L. & KLEIN, W. (eds) *Geocomplexity and the Physics of Earthquakes*. American Geophysical Union, Geophysical Monograph, **120**, 147–163.
- KURODA, H. 2001. *Two-dimensional Heat Flow Analysis Program using Finite Element Method*. CQ Publishing, Tokyo (in Japanese).
- LACHENBRUCH, A. H. 1980. Frictional heating, fluid pressure, and the resistance to fault motion. *Journal of Geophysical Research*, **85**, 6097–6112.
- LEMMON, E. W., HUBER, M. L. & McLINDEN, M. O. 2002. Nist reference fluid thermodynamic and transport properties (REFPROP). Worldwide web address: <http://www.nist.gov/srd/nist23.htm>.
- MASE, C. W. & SMITH, L. 1987. Effects of frictional heating on the thermal, hydrological, and mechanical response of a fault. *Journal of Geophysical Research*, **92**, 6249–6272.
- MC CONVILLE, C. J. & LEE, W. E. 2005. Microstructural development on firing illite and smectite clays compared with that in kaolinite. *Journal of the American Ceramic Society*, **88**, 2267–2276, doi: 10.1111/j.1551-2916.2005.00390x.
- MIZOGUCHI, K., HIROSE, T., SHIMAMOTO, T. & FUKUYAMA, E. 2007. Reconstruction of seismic faulting by high-velocity friction experiments: an example of the 1995 Kobe earthquake. *Geophysical Research Letters*, **34**, L01308, doi: 10.1029/2006GL027931.
- MIZOGUCHI, K., HIROSE, T., SHIMAMOTO, T. & FUKUYAMA, E. 2009. High-velocity frictional behavior and microstructure evolution of fault gouge obtained from Nojima fault, southwest Japan. *Tectonophysics*, **471**, 285–296, doi: 10.1016/j.tecto.2009.02.033.
- MONZAWA, N. & OTSUKI, K. 2003. Commutation and fluidization of granular fault materials: implications for fault slip behavior. *Tectonophysics*, **367**, 127–143, doi: 10.1016/S0040-1951(03)00133-1.
- MOORE, G. F., BANGS, N., TAIRA, A., KURAMOTO, S., PANGBORN, E. & TOBIN, H. J. 2007. Three-dimensional splay fault geometry and implications for tsunami generation. *Science*, **318**, 1128–1131, doi: 10.1126/science.1147195.
- MORROW, C., RADNEY, B. & BYERLEE, J. 1992. Frictional strength and effective pressure law of montmorillonite and illite clays. In: EVANS, B. & WONG, T.-F. (eds) *Fault Mechanics and Transport Properties of Rocks*. International Geophysical Series, **51**. Academic Press, London, 69–88.
- OTSUKI, K., MONZAWA, N. & NAGASE, T. 2003. Fluidization and melting of fault gouge during seismic slip: identification in the Nojima fault zone and implications for focal earthquake mechanisms. *Journal of Geophysical Research*, **108**, 2192, doi: 10.1029/2001JB001711.
- PARK, J., TSURU, T., KODAIRA, S., CUMMINS, P. R. & KANEDA, Y. 2002. Splay fault branching along the Nankai subduction zone. *Science*, **297**, 1157–1160.
- RICE, J. R. 2006. Heating and weakening of faults during earthquake slip. *Journal of Geophysical Research*, **111**, B05311, doi: 10.1029/2005JB004006.

- ROSATO, A., STRANDBURG, K. J., PRINZ, F. & SWENDSEN, R. H. 1987. Why the Brazil nuts are on top: size segregation of particulate matter by shaking. *Physical Review Letters*, **58**, 1038–1040.
- SAFFER, D. M. & MARONE, C. 2003. Comparison of smectite- and illite-rich gouge frictional properties: application to the up-dip limit of the seismogenic zone along subduction megathrusts. *Earth and Planetary Science Letters*, **215**, 219–235.
- SAKAGUCHI, A., CHESTER, F. ET AL. 2011. Seismic slip propagation to the up-dip end of plate boundary subduction interface faults: vitrinite reflectance geothermometry on Integrated Ocean Drilling Program NanTroSEIZE cores. *Geology*, **39**, 395–398, doi: 10.1130/G31642.1.
- SHARP, Z. D., PAPIKE, J. J. & DURAKIEWICZ, T. 2003. The effect of thermal decarbonation on stable isotope compositions of carbonates. *American Mineralogist*, **88**, 87–92.
- SHIMAMOTO, T. & TSUTSUMI, A. 1994. A new rotary-shear high-velocity frictional testing machine: its basin design and scope of research. *Structural Geology*, **39**, 65–78 (in Japanese with English abstract).
- SIBSON, R. H. 1973. Interactions between temperature and pore-fluid pressure during earthquake faulting and a mechanism for partial or total stress relief. *Nature*, **243**, 66–68.
- SIBSON, R. H. 1975. Generation of pseudotachylite by ancient seismic faulting. *Geophysical Journal of the Royal Astronomical Society*, **43**, 775–794.
- SIBSON, R. H. & TOY, V. G. 2006. The habitat of fault-generated pseudotachylite: Presence v. absence of frictional melt. In: ABERCROMBIE, R., McGARR, A., DI TORO, G. & KANAMORI, H. (eds) *Earthquakes: Radiated Energy and the Physics of Faulting*. American Geophysical Union, Geophysical Monograph, **170**, 153–166.
- SMITH, S. A. F., COLLETTINI, C. & HOLDSWORTH, R. E. 2008. Recognizing the seismic cycle along ancient faults: CO<sub>2</sub>-induced fluidization breccias in the footwall of a sealing low-angle normal fault. *Journal of Structural Geology*, **30**, 1034–1046, doi: 10.1016/j.jsg.2008.04.010.
- TSUTSUMI, A. & SHIMAMOTO, T. 1997. High-velocity frictional properties of gabbro. *Geophysical Research Letters*, **24**, 699–702.
- UJIIE, K. & TSUTSUMI, A. 2010. High-velocity frictional properties of clay-rich fault gouge in a megasplay fault zone, Nankai subduction zone. *Geophysical Research Letters*, **37**, L24310, doi: 10.1029/2010GL046002.
- UJIIE, K., TSUTSUMI, A., FIALKO, Y. & YAMAGUCHI, H. 2009. Experimental investigation of frictional melting of argillite at high slip rates: implications for seismic slip in subduction-accretion complexes. *Journal of Geophysical Research*, **114**, B04308, doi: 10.1029/2008JB006165.
- UJIIE, K., YAMAGUCHI, A., KIMURA, G. & TOH, S. 2007a. Fluidization of granular material in a subduction thrust at seismogenic depths. *Earth and Planetary Science Letters*, **259**, 307–318, doi: 10.1016/j.epsl.2007.04.049.
- UJIIE, K., YAMAGUCHI, H., SAKAGUCHI, A. & TOH, S. 2007b. Pseudotachylites in an ancient accretionary complex and implications for melt lubrication during subduction zone earthquakes. *Journal of Structural Geology*, **29**, 599–613, doi: 10.1016/j.jsg.2006.10.012.
- UJIIE, K., YAMAGUCHI, A. & TAGUCHI, S. 2008. Stretching of fluid inclusions in calcite as an indicator of frictional heating on faults. *Geology*, **36**, 111–114, doi: 10.1130/G24263A.1.
- WILLIAMS, J. C. 1976. The segregation of particulate materials. A review. *Powder Technology*, **15**, 245–251.



# New faults v. fault reactivation: implications for fault cohesion, fluid flow and copper mineralization, Mount Gordon Fault Zone, Mount Isa District, Australia

G. S. NORTJE<sup>1</sup>\*, N. H. S. OLIVER<sup>1</sup>, T. G. BLENKINSOP<sup>1</sup>, D. L. KEYS<sup>1</sup>,  
J. G. MCLELLAN<sup>1</sup> & S. OXENBURGH<sup>2</sup>

<sup>1</sup>*Economic Geology Research Unit and Predictive Mineral Discovery Co-operative Research Centre (pmd\*CRC), School of Earth and Environmental Sciences, James Cook University, Townsville, QLD 4811, Australia*

<sup>2</sup>*Aditya Birla Minerals Ltd, PO Box 3074, Adelaide Terrace, Perth, WA 6832, Australia*

\*Corresponding author (e-mail: [forbinder@gmail.com](mailto:forbinder@gmail.com))

**Abstract:** Fluid flow leading to mineralization can occur both on newly formed faults and on faults that are reactivated subsequent to their initial formation. Conventional models of fault reactivation propose that, under high pore-fluid pressures, misorientated faults may reactivate due to low fault cohesion. Timing and orientation data for a mineralized Palaeo- to Mesoproterozoic terrain (Mount Gordon Fault Zone (MGFZ)) indicate that multiple successive new orientations of predominantly strike-slip faults developed (between 1590 and c. 1500 Ma), requiring that during the younger deformations some earlier formed faults were too cohesive and/or had insufficient pore-fluid pressures (or other potential fault-weakening effects) to induce reshear. Low pore-fluid pressures were probably not to blame for failed reactivation on all older faults because some young faults did form or reactivate due to high pore-fluid pressures, as evidenced by jigsaw-fit dilatant breccias, hypogene copper mineralization in veins and breccia infill, and subvertical tensile quartz veins aligned subparallel to  $\sigma_1$ . The assumption that old faults consistently have little or no cohesion appears to be incorrect in this terrain. Many older faults display prominent quartz veins along their length, which may explain this conclusion. Furthermore, faults with high cohesion may have acted as barriers and compartments, so that intersections between them and newly formed faults host mineralization, not because of reactivation, but because of interaction between new faults and cohesive materials defined either by fault precipitates or rock juxtaposition. Together, these results and observations provide new, simple tools to stimulate copper exploration within the region and in fault-hosted terrains.

The Proterozoic Mount Isa Block of northwestern Queensland, Australia is richly endowed with epigenetic, fault-related copper mineralization, including the world-class Mount Isa copper ore bodies. However, because of the immediate proximity of the Mount Isa copper deposits to equally large lead–zinc ores, controversy has surrounded their interpretation (Perkins 1984, 1989, 1990, 1997; Swager 1985; Swager *et al.* 1987; Bell *et al.* 1988; Heinrich & Cousens 1989; Bell 1991; Heinrich *et al.* 1995; Davis 2004; Wilde *et al.* 2006). To the north of the major deposits of the Mount Isa Valley (Fig. 1), the Mount Gordon Fault Zone (MGFZ) stretches more than 100 km northwards and contains excellent examples of fault-related copper mineralization, in most cases without attendant lead–zinc. In particular, the Mammoth (formerly ‘Gunpowder’) deposits lie on apparent ENE-trending splays of the MGFZ (Scott & Taylor 1982; Richardson & Moy 1998), and are

dominated by fault- and hydrothermal breccias in quartzite and siltstone units of the Myally Subgroup (Alsace Quartzite, Bortala Formation, Whitworth Quartzite).

The region north of Mount Isa has been important for reconstructions of the structural and tectonic evolution of the Mount Isa Block because of the excellent outcrop, the relatively low metamorphic grade (up to lower greenschist) and modest ductile strains imposed by the approximately 1600–1500 Ma Isan Orogeny. Reconstructions of the earliest basin-forming events have included recognition of several growth faults and a northward-trending rift (Derrick 1982; O’Dea *et al.* 1997; Betts 1999, 2000; Betts *et al.* 2003; Gibson 2005) including the oblique Mount Gordon Arch. The effects of the Isan Orogeny included north–south contraction, possibly with south-directed thrusting (Bell 1983) and east–west shortening, the latter reflected by folding and some foliation development

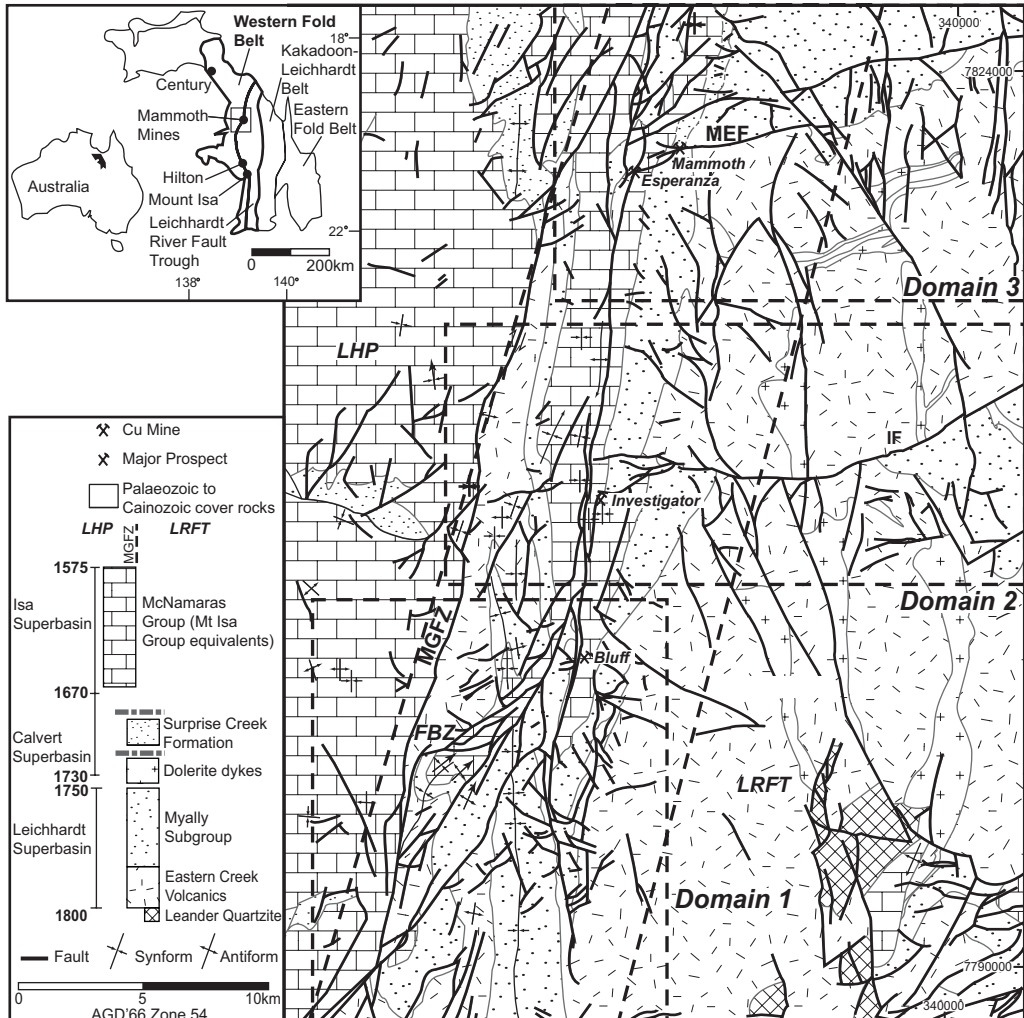


**Fig. 1.** The study area used for relative age analysis, with general geology, major fault zones (faults), major structures (folds), major mineral deposits and prospects. Domains 1–4 are indicated. Domain 1 is the southern half of the MGFZ; Domain 2 is the Investigator Fault Zone; Domain 3 is the Mammoth (Gunpowder) Mines region; and Domain 4 is the MGFZ. Abbreviations are as follows: LHP, Lawn Hill Platform; LRFT, Leichhardt River Fault Trough; MEF, Mammoth Extended Fault; IF, Investigator Fault Zone; MGFZ, Mount Gordon Fault Zone; FBZ, Fort Binder Fault Zone. Inset shows the location of the Mount Isa Inlier and regional tectonostratigraphical units (note WFB). Projection AGD 1966, zone 54 modified from Hutton *et al.* (1985).

(O'Dea & Lister 1995; O'Dea *et al.* 1997). Bell (1983) proposed, however, that no former rift architecture was required to explain the geometric details of the thrust array, which has been disputed by other researchers because of the ready recognition of criteria for growth faults and normal faults (Derrick 1982; O'Dea & Lister 1995; O'Dea *et al.* 1997). With a few local exceptions (see later), most workers also have not considered the detail of the 10 m- to km-scale fault orientations nor the

field-based evidence for their movement sense or potential reactivation, both of which we attempt to address here. Late in the Isan Orogeny, a large sinistral wrench system developed (Lister *et al.* 1986, 1987, 1999; O'Dea & Lister 1995; O'Dea *et al.* 1997), when most of the fault-related copper appears to have been introduced (Keys 2008).

At the core of the above-mentioned controversy in the overall interpretation of the architectural and kinematic elements is uncertainty regarding the

process of fault reactivation, along with parallel questions (particularly at Mount Isa) regarding the possibility of early base-metal mineralization and its potential 'remobilization' into favourable late-tectonic fault structures. Here, we assemble and compare the previous work on the geometric and kinematic evolution of the MGFZ, and add new field data on the history of fault activation and reactivation. Several key questions will be addressed.

- Which fault segments within either the early rifting (' $D_e$ ') or north-south convergence (' $D_1$ ') events developed and retained orientations that were favourable for further fault slip during the later wrenching (' $D_3$  or  $D_4$ ')?
- What were the combinations of far-field stresses and pore-fluid pressures that led to fault reactivation and new fault development during  $D_3$  or  $D_4$ ?
- How did all of the above combine to result in the presently observed distribution and styles of epigenetic copper mineralization formed during wrenching?

The aims of this analysis is to understand whether there is a firm basis for simply utilizing the known orientations of faults (of any timing) to predict the location of potentially undiscovered mineralization, a technique that is commonly used elsewhere, particularly in predictive numerical analysis of fault arrays (Holyland & Ojala 1997; Mair *et al.* 2000; Ojala & Nykänen 2007; McLellan & Oliver 2008). McLellan & Oliver (2008), for example, successfully predicted the location of the majority of epigenetic Cu ± Au deposits and prospects in the Eastern Fold Belt of the Mount Isa Block by assuming that the presently observed fault architecture could be used as a template for a numerical simulation, and applying small strains to this fault array. However, although details of the fault evolution were considered in part, this style of analysis places little emphasis on the locations of earlier structures and also of early mineralization unrelated to the late-Isan faulting, several examples of which are recognized in the Eastern Fold Belt (Oliver *et al.* 2008). Here we make some simple, conservative assumptions about fault-reactivation potential, then test the veracity of such assumptions by a spatial analysis and more detailed examination of anomalous results, particularly those situated at or near mineral deposits. The specific locations of mineral deposits in the MGFZ and elsewhere in the Mount Isa Block may relate to a protracted geometric evolution in a systematic way, rather than simply being on any fault of any previous age, reactivated or precipitated during the latest deformation event. Our analysis may thus assist with the distinction between earlier mineralization, whose present distribution reflects 100 m- to km-scale redistribution near the sites of former syngenetic or diagenetic

mineralization (related to rift faults), and late-tectonic deposits localized on faults and apparently independent of any earlier ore accumulations.

## Summary of regional geology relevant to mineralization

The Mount Isa Block (Fig. 1) has undergone a complex protracted deformation and metamorphic history related to cycles of extension and shortening from 1800 to 1500 Ma (Derrick 1982; Blake 1987; Etheridge *et al.* 1987; Blake & Stewart 1992). Here we focus on aspects of the faulting history pertinent to understanding the geometric and kinematic history that led to localization of copper deposits along and around faults within the Western Fold Belt (WFB) (Fig. 1). There are several main stages of interest.

### *Early stage*

Rifting, basin formation and sedimentation, in particular the Leichhardt (c. 1800–1740 Ma), the Calvert (c. 1730–1670 Ma) and the Isa (c. 1670–1575 Ma) superbasins, all of which are still variably preserved to some extent in the Leichhardt River Fault Trough (LRFT) of the Mount Isa Block including the MGFZ (Fig. 1) (Neumann *et al.* 2006; Gibson *et al.* 2008).

### *Mid stage*

Three main deformational events during the Isan Orogeny ( $D_1$ ,  $D_2$ ,  $D_3$ ) in the western Mount Isa Block. There is no universally accepted model for post-depositional deformation within the Mount Isa Block or the WFB (Fig. 1) (Derrick 1982; Bell 1983, 1991; Blake 1987; Blake & Stewart 1992; Nijman *et al.* 1992a, b; Stewart 1992; O'Dea & Lister 1995). The 1:250 000- and 1:100 000-scale maps can be interpreted to show that the original rift geometry is preserved and that the basement structures played an important part during the rifting process as well as in the post-depositional deformation of the region.  $D_1$ , the first deformational event, has been described as southwards-directed thrusting that produced east–west-orientated folds (Bell 1983). However, the presence of  $D_1$  has been widely debated (Derrick 1982; Bell 1983; O'Dea & Lister 1995). The main deformational event ( $D_2$ ) during the Isan Orogeny and the peak of metamorphism has been suggested to have taken place at around 1595–1580 Ma (Rubenach *et al.* 2008) and appears to have been an inlier wide east–west shortening event. Slightly later in the deformational history, an ENE-shortening ( $D_3$ ) event occurred, at approximately

1550 Ma (Bell 1983; Rubenach *et al.* 2008), and was interpreted to have been responsible for the reactivation of many major D<sub>2</sub> structures.

### Late stage

Miller (2007) at the Mount Isa Copper deposit has indicated that the orientation of the stress regime during brecciation and Cu mineralization was likely to have been with  $\sigma_1$  in the NW quadrant with a shallow plunge, as also suggested by Keys (2008). This D<sub>4</sub> deformation, the absolute timing of which is not well constrained in the WFB, resulted primarily in the strike-slip reactivation of major steeply dipping faults, the formation of new faults, including north–south-striking faults with sinistral strike-slip displacement, and brecciation and mineralization across the Mount Isa Block (Keys 2008). Although timing of D<sub>4</sub> is poorly constrained in the study area, a strong association of similar (orientation, shear sense and fault infill) faults, breccias and late tectonic granites in the Eastern Succession occurred at about 1527 Ma (Keys 2008; Rubenach *et al.* 2008). The Ernest Henry ore body, some regional sodic–calcic alteration and many small copper deposits were formed by fault-related fluid flow at this time in the Eastern Succession (Oliver *et al.* 2004, 2008; Rubenach 2005; McLellan & Oliver 2008). However, recent Re–Os work has suggested that an event around 1350 Ma may have been important, including dates on chalcopyrite from the Mount Isa copper deposit (Gregory *et al.* 2008) and on molybdenite from the Merlin deposit near Starra (Duncan *et al.* 2009). It is possible that D<sub>4</sub> relates to this age rather than to the end of the Isan Orogeny, although more work is required.

### Analysis of fault timing and orientation

Fluid flow leading to mineralization can occur both on newly formed faults and on faults that are reactivated subsequent to their initial formation (Sibson 1977, 1989, 1996, 2000, 2001; Cox *et al.* 2001; Kolb *et al.* 2004; Micklethwaite *et al.* 2010). In the Eastern Fold Belt, Oliver *et al.* (2008) demonstrated that copper mineralization occurred over a long period ( $\geq 100$  Ma). Therefore, the assumption that all mineralization occurred superimposed on the post-Isan fault geometry is incorrect, despite a reasonably high convergence of numerically predicted zones of low differential and mean stress, and the known sites of copper mineralization, both at Mount Isa and other locations with a protracted structural history (Ojala & Nykänen 2007; McLellan & Oliver 2008).

In order to try to assess the possible role of protracted fault evolution on the localization of

mineralization, we have attempted to reconstruct the sequence of faulting events, the change in geometries with time and the relative importance of new v. reactivated faults at different stages in the overall evolution of the LRFT. This is directed towards trying to understand whether the early elements of the rift architecture were crucial for the subsequent introduction of copper, or not.

The overall approach we have taken is as follows.

- Divide the MGFZ up into four subdomains to undertake a ‘relative age analysis’ (Fig. 1).
- Measure the orientation and length of all the faults and classify them according to their orientation using a length-weighted criterion on rose diagrams where the frequency is multiplied by the length of the fault segment (Fig. 2). In Figure 2, the longer petals of the rose diagram reflect longer fault segments: for example, NE-trending fault segments are longer in domain 1 (Fort Binder Fault Zone) (Fig. 2a). Faults were then classified into subsets based on the above criterion using letters A, B, C, D, E, F, G.
- Use a simplistic overprinting criterion to make a preliminary interpretation of the relative timing

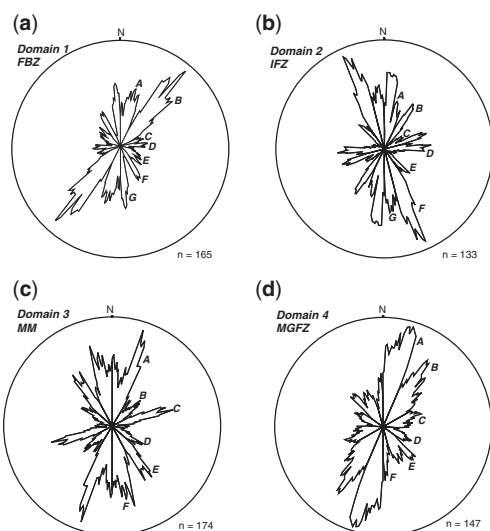


**Fig. 2.** Rose diagrams showing the length-weighted orientation of the four domains within the study area. (a) Domain 1, Fort Binder Fault Zone (FBZ) comprising seven fault sets. (b) Domain 2, Investigator Fault Zone (IFZ) comprising seven fault sets. (c) Domain 3, Mammoth Mines region comprising six fault sets. (d) Domain 4, Mount Gordon Fault Zone (MGFZ) comprising six fault sets. Letters A, B, C, D, E, F and G define different fault sets belonging to each domain (and not necessarily correlating between domains).

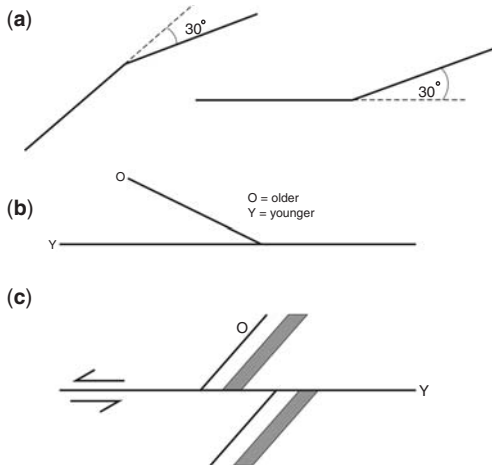


**Fig. 3.** Assumptions used to determine initial fault timing relationships. (a) A single fault bend. Null values were assigned to fault segments with angles of less than 30°. (b) 'Y' junction where the shorter segment is older than the longer segment. (c) Apparent offset of either faults or bedding.

- of intersecting faults based on their geometry (Fig. 3a–c). Faults, whose intersection angle was less than 30°, particularly where a possible displaced segment was not identified, were not included in the analysis, because these most probably represent fault-tip splays developed during one faulting event. Even if they are not synchronous splays, their omission does not greatly affect the conclusions.
- Apply the 'relative age table' approach of Angelier (1991, 1994) to define an apparent sequence of faulting events, and to establish clear v. vague overprinting relations.
  - Assess additional geological information (field relationships including the relationship of unconformities and folds to faults) to modify the preliminary sequence of faulting events.
  - Identify and distinguish fault rotations and reactivations on early faults that have led to their reorientation (or preservation of initial orientation) along directions potentially suitable for mineralization.

#### *Binary chronological matrix analysis (relative age analysis)*

Extracting incremental stress and strain, and deformation histories, from final geometries is very difficult. Standard geological analysis techniques where cross-cutting relationships are observed can yield vague and uncertain deformation histories, the interpretation of which can be controversial

(e.g. Bell 1983). Error can originate from unobserved rotations or displacements, the impossibility of determining unique strain histories from a single cumulative strain, and the variation of fault geometry and local kinematics at any one time, which may otherwise be interpreted as being the product of different events (Angelier 1991, 1994; Potts & Reddy 1999, 2000; Forster & Lister 2008).

Binary chronological matrix analysis, referred to as relative age analysis herein, is a form of combinatorial mathematics where successive permutations are carried over as large a data set as possible to obtain a relative chronology (Angelier 1991, 1994; Potts & Reddy 1999, 2000). The datum is the order or succession of two or more geological events. For  $n$  geological events there exist  $n(n - 1)$  relative chronologies (Angelier 1991, 1994; Potts & Reddy 1999, 2000). For example, for three geological events, here termed  $x$ ,  $y$ , and  $z$ , there are six possible relative chronologies that is  $xyz$ ,  $xzy$ ,  $yxz$ ,  $yzx$ ,  $zxy$  and  $zyx$  (Angelier 1991, 1994; Potts & Reddy 1999, 2000). In the present case, a robust analysis of this type may lead to a clear chronology of different faults with different orientations. However, if many or most of the faults developed at the same time, as a network of faults with several different orientations (e.g. the fault-fracture network of Sibson 1996, 2001), then the chronological analysis would confirm mutual cross-cutting relationships of differently orientated faults because there would not be a clear chronology of different faults with different orientations.

This overall approach is similar to the approach of Forster & Lister (2008) where tectonic sequence diagrams (TSDs) are used on an outcrop scale to determine the relative sequence of events without using a combinatorial mathematical framework. In their approach, a temporal sequence is inferred on an outcrop scale followed by selecting marker sequences and correlating between different TSDs (Forster & Lister 2008). They also confirm absolute ages of events based on geochronology of a particular event; for example, using Ar/Ar dating in the Otago schists, New Zealand.

The Angelier (1991, 1994), Potts & Reddy (1999, 2000) and Forster & Lister (2008) approaches are all advantageous because they remove  $D_1$ – $D_n$  nomenclature from conventional structural analysis and allow a more unambiguous approach to infer the structural evolution of a particular region. They also avoid the difficulty that arises from adding or subtracting a new  $D_n$  event to a  $D_n$  succession. One advantage of the combinatorial mathematics approach over the TSD method is that it forces the user to deal with contradictory observations, whereas the latter method does not explicitly address that particular problem.

	<i>x</i>	<i>y</i>	<i>z</i>
<i>x</i>		1	3
<i>y</i>	2		7
<i>z</i>		1	

**Fig. 4.** Initial arbitrary binary chronological matrix where the figures are ‘read’ from row (oldest) to column (youngest), for example, seven observations are made where *y* is older than *z*, and one apparent relationship where *z* is older than *y*. The grey shading indicates relationships between events of the same timing and are assigned a null value in the analysis.

#### Binary chronological matrix construction

For the example above, the six relative chronologies are built into a matrix so that one line and one column with the same rank correspond to the same event (Fig. 4). The order of ranking is arbitrary because the order of events is unknown to begin with (Fig. 4) (Angelier 1991, 1994; Potts & Reddy 1999, 2000).

	<i>y</i>	<i>x</i>	<i>z</i>
<i>y</i>		2	7
<i>x</i>	1		3
<i>z</i>	1		

**Fig. 5.** Revised binary chronology in which successive permutations are calculated based on the count of relative ages. This output provides the best possible mathematical solution (Angelier 1991, 1994). Therefore consistent chronologies (top-right half of the figure) are 85%, while inconsistent chronologies are 15%; these statistics are included in the output of CHRONO.exe (Angelier 1992).

Once all observations have been inserted into the matrix (Fig. 4) then the data can be arranged into a temporal sequence (Fig. 5). This solution provides the best possible *mathematical* solution based on the combinatorial (factorial) approach (i.e. successions for  $n$  events  $n!$  and  $n(n - 1)$ ) (Angelier 1991, 1992, 1994). However, relative age relationships that are ‘less reliable’ may emerge, in which the number of relationships where feature *x* is older than feature *y* is only slightly greater than relationships where *y* is older than *x*. This may mean that a particular feature may have repeated or reactivated, or two completely unrelated features produce similar characteristics other than timing relationships (e.g. a fracture network with several strands of different orientations but the same timing). Thus, once an optimal solution is obtained it is advisable that other geological information is inserted into the matrix to obtain a better solution and one that is more geologically realistic (equivalent, for example, to the use of Ar/Ar or other geo-chronological data in a structural history; Forster & Lister 2008). The reliability of the position in the relative age table can be treated as an additional factor for subsequent analysis. All relative age analysis plots (binary chronological matrices) were generated using CHRONO.exe (Angelier 1992). Because the data set was so extensive (362 880 relative chronologies were possible), a computational approach was necessary.

#### Initial orientation and relative age analysis

The MGFZ region lies within the Western Fold Belt, and Mount Isa Inlier presents an excellent opportunity to study and test the use of relative age tables. Existing government geological mapping (Mammoth Mines, Sheet 6758) and field observations were used to generate binary chronological matrices (Figs 1 & 6) for interpreting the relative and absolute chronology of faulting within the area. The analysis was carried out in two-dimensionally (2D) because most faults in their current configuration are steeply dipping, have apparent strike-slip offsets and locally show evidence of strike-slip displacements.

#### Domain subdivision

The study area was subdivided into four domains, based on the different styles and character of fault orientations, and lithological and stratigraphical patterns within the MGFZ. Domain 1 (Fort Binder Fault Zone, FBZ) comprises the southern half of the MGFZ (Fig. 1) and is host to seven fault sets based on orientation (Fig. 2a). The dominant rock

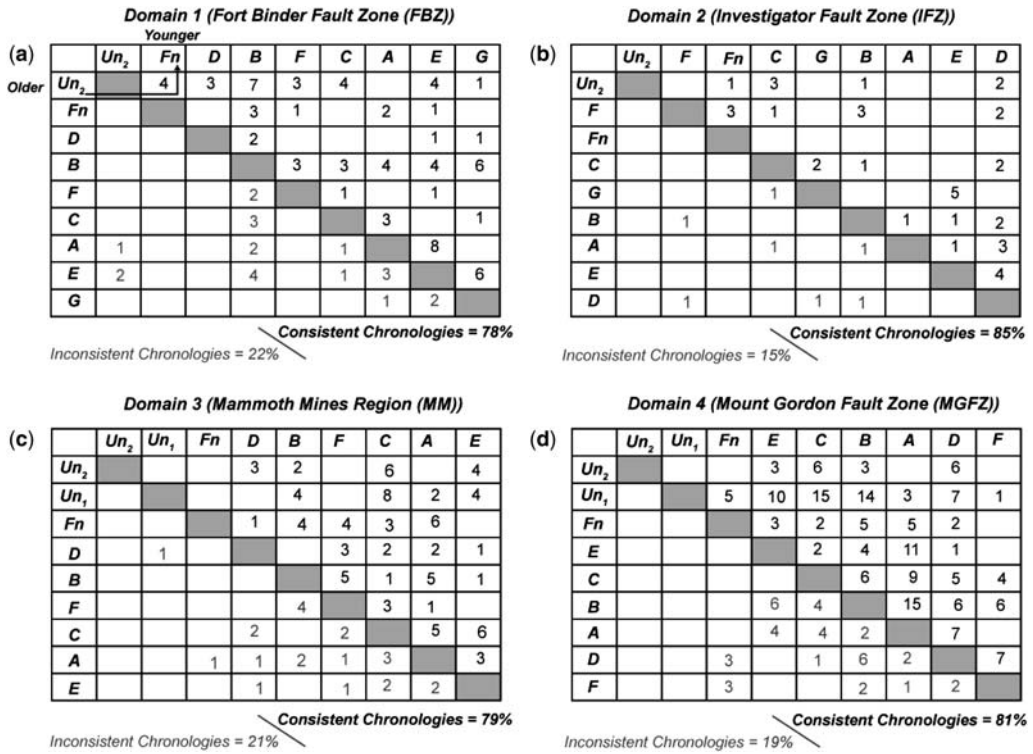


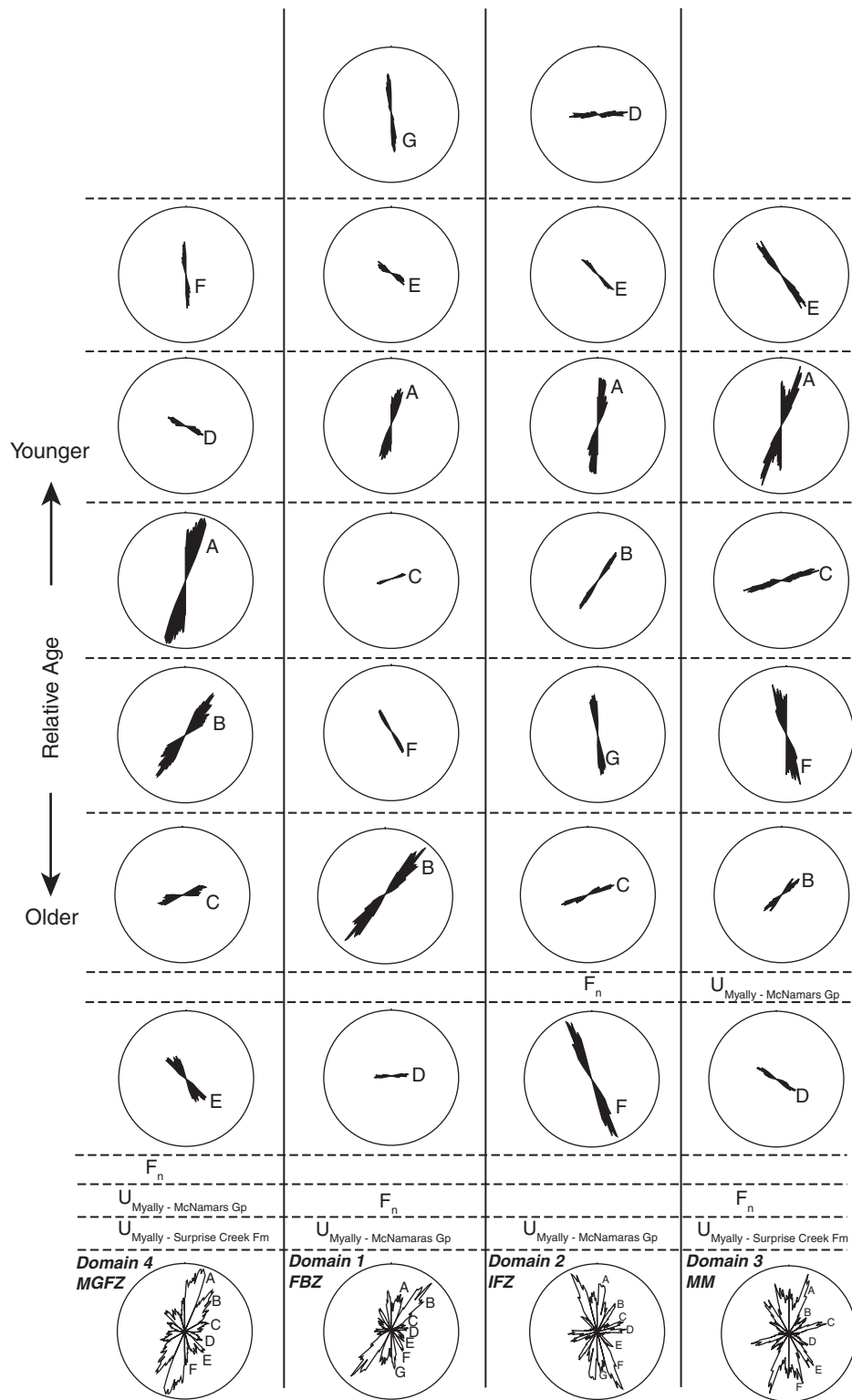
**Fig. 6.** Relative chronological matrix analysis values for: (a) Domain 1 (FBZ); (b) Domain 2 (IFZ); (c) Domain 3 (MM); and (d) Domain 4 (MGFZ). (a)–(d) also show the percentage of inconsistent and consistent chronologies at the bottom. These values are the output provided by CHRONO.exe (Angelier 1992). Un<sub>1</sub>, Myally–Surprise Creek unconformity; Un<sub>2</sub>, Myally–McNamara Group unconformity; F<sub>n</sub>, folding.

types in the area are basalts of the Eastern Creek Volcanics, quartzites of the Myally Subgroup and black shales of the McNamara Group. Here faults typically trend NNE, NE, east–west and ESE, and are mostly subvertical. Most faults have a dominant strike-slip separation (Fig. 1). The longer fault segments within this domain trend NE, while the shorter segments trend ENE–ESE (Fig. 2a).

Domain 2, the Investigator Fault Zone (IFZ), occurs immediately north of domain 1. The Investigator Fault zone comprises east–west fault segments of the Investigator Fault that intersect the NNE-trending MGFZ, and also comprises seven fault sets (Figs 1 & 2b). The dominant rock types in domain 2 are basalts from the Eastern Creek Volcanics, quartzites from the Myally Subgroup, black shales belonging to the McNamara Group and dolerite dykes. Fault orientation occupies the full spectrum of the rose diagram and faults are subvertical (Fig. 2b). The longest faults trend towards the SE and in places form dyke margins. The shortest fault segments trend towards the NE.

Domain 3, the Mammoth Mines region (MM), is north of domain 2 and comprises six fault sets (Figs 1 & 2c). This domain is host to the Gunpowder and Esperanza Cu ore bodies. This domain comprises east–west fault segments that belong to the Mammoth Extended Fault and Mammoth Fault, as well as NNE-trending segments of the MGFZ. The main rock types within the domain are the same as for domains 1 and 2 (Fig. 1). Here the longest faults trend NNE, while the shortest faults trend NE.

Domain 4 comprises the entire length of the Mount Gordon Fault Zone and has six fault sets (Figs 1 & 2d). Several different rock types host the fault zones, mostly Eastern Creek Volcanics and the Myally Subgroup in the west and south, while the McNamara Group is in the centre of the fault zone. The eastern half of the fault zone is bounded by basalts from the Eastern Creek Volcanics and quartzites from the Myally Subgroup. Even though this overlaps with the other domains, we have considered this as a separate domain because it contains the major structural break of the Mount Gordon Fault (Fig. 1).

**Fig. 7.**

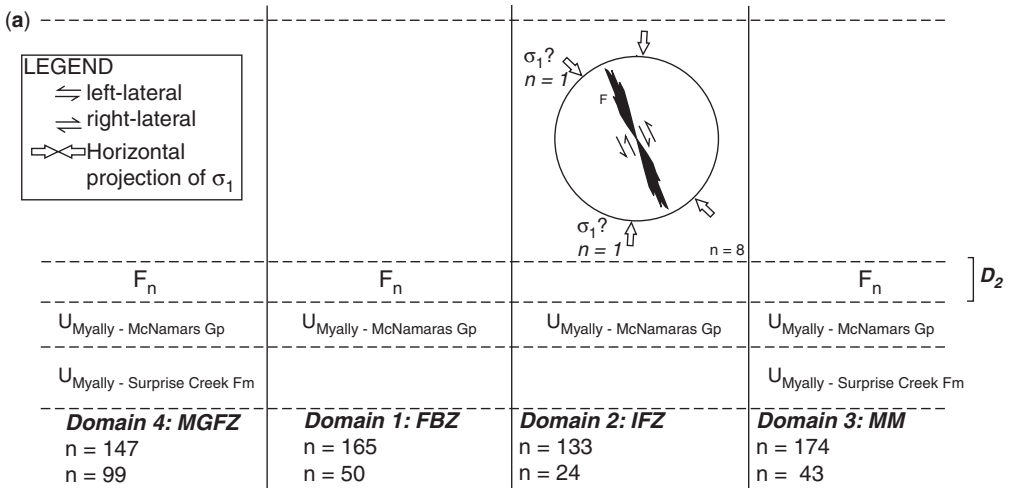


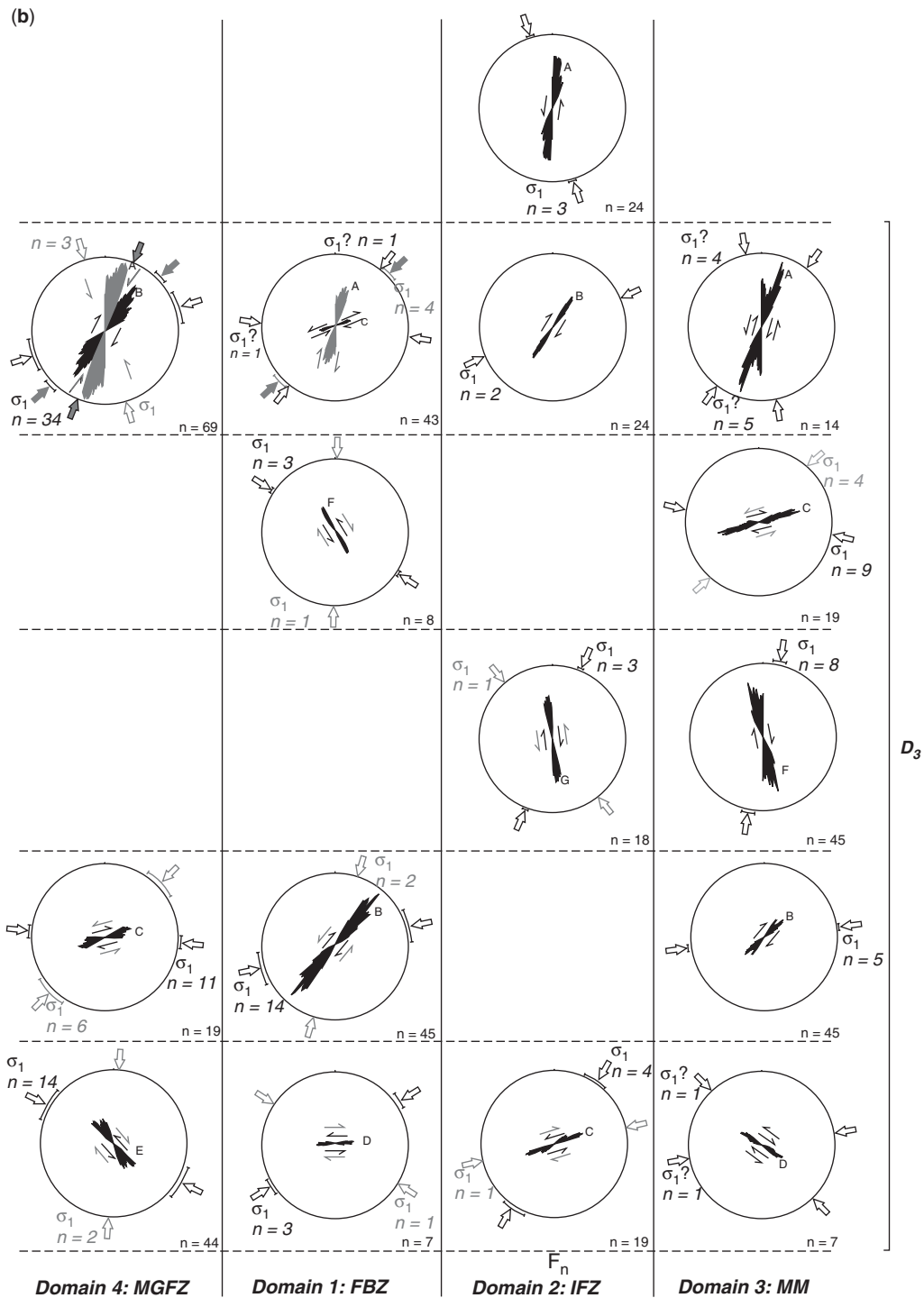
**Fig. 8.** (a)–(c) Rose diagrams of fault segments showing temporal evolution of the entire fault network within each domain. Columns with domains are plotted according to location with respect to each other; for example, Domain 4 (Mount Gordon Fault Zone) is plotted on the left side of the diagram (i.e. west, because it forms the western boundary of the study area). Refer to Figure 7 for the orientation of all fault segments within each domain and the data points ( $n$ ). The first ( $n$ ) is the total amount of faults within the domain and the second ( $n$ ) represents the faults with an apparent displacement. The horizontal dashed lines represent inferred temporal separation between successive faulting events. The Angelier method was used, along with the methods described in the text, to organize the faults into their age groupings based on overprinting criteria and some geometrical and geological considerations. Correlations between each domain are based on commonality of orientation and relative timing. On each rose diagram plot, a dominant shear sense is coloured black based on the dominant shear sense obtained from mapped relations. The arrows along each side of the rose diagram represent the horizontal trace of  $\sigma_1$  assuming that there is mostly strike-slip movement along most faults. Black arrows represent high-confidence interpretations. Grey arrows and  $\sigma_1$  represent a less dominant shear sense inferred from apparent mapped offsets. These grey arrows represent faults with opposing or uncertain shear senses (for which the timing may be wrong for that rose diagram). See also Figure 9.

### Geometrical assumptions

Some simplistic assumptions are required initially. The relationships shown in Figure 3 represent observed geometries of fault bends and intersections in the LRFT. The first assumption is that each orientation of fault or fault segment potentially represents a separate timing of fault activation/reactivation. The likelihood of this being true for all faults on the map is low, particularly for some of the geometries. The simplest geometry of a fault bend (Fig. 3a), for example, could readily form at one time in one faulting event – here, however, we initially assign them to two separate events based on orientation. However, because no overprinting of one segment over the other can be determined, this relationship is assigned a null value in the

relative age table (Table 3), so thus can be discriminated (at least by exclusion) from bona fide overprinting faults. The second geometry of the two faults (Fig. 3b) could also occur at one time by fault-tip branching, for example; but here we initially assume that the fault that terminates against another fault is older, even though the apparent displacement of the inferred older fault is not seen on the other side of the younger fault. This relationship is assigned a positive value (Fault X younger than Fault Y) in the relative age table but is flagged as a relationship that requires checking in the second phase of analysis. Finally, for relationships in which apparent fault offset is observed, along with the offset of another geological marker (Fig. 3c), the through-going fault most probably is the youngest feature. This relationship is assigned a positive

**Fig. 7.** Initial relative age analysis rose diagrams where domains 1–4 have been plotted according to geographical location, along with interpretation where the Myally–Surprise Creek and Myally–McNamaras Group unconformities (i.e.  $U_{\text{Myally - Surprise Creek Fm}}$ ) have been inserted into the analysis.  $F_n$  represents observed folding events (all folds are grouped together, i.e. fold generation is not taken into account,  $F_2$  v.  $F_4$ ). Early folded faults were identified geologically rather than via a relative age analysis approach – see Figure 11. North is up on all rose diagrams.

**Fig. 8.** *Continued.*

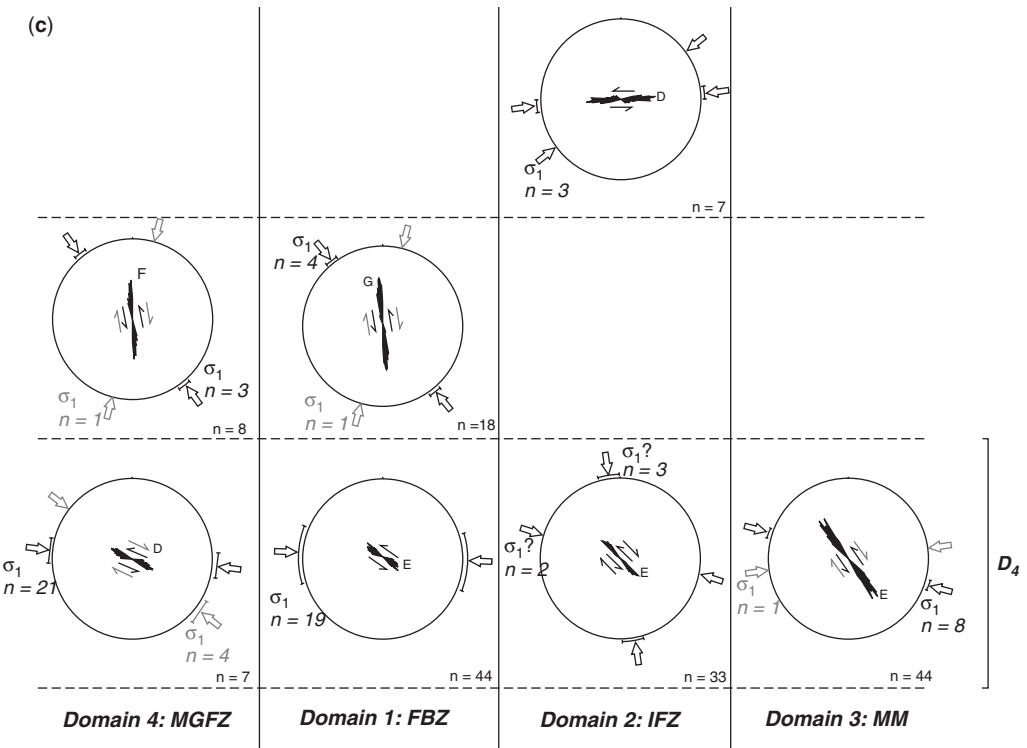


Fig. 8. Continued.

value (Fault X younger than Fault Y and the geological feature) with confidence in the relative age table. Because of these exclusions and validity assessments, analysis of these conservative assumptions has the potential to reveal false relationships (such as synchronous fault networks with several orientations).

The relative age table approach is then utilized to try to establish which fault orientations and segments are: (a) consistently; and (b) inconsistently timed relative to each other. For example, for two sets of faults (X and Y) with defined orientations, if the number of positive overprinting relationships (X younger than Y) greatly exceeds both opposite (negative) and null relationships, then it is likely that most faults with orientations of X formed later than those with orientations of Y. If two sets of faults with nearby orientations consistently show null relationships (e.g. simple fault bends), then it is likely that they formed at the same time. If two sets of faults show a high diversity of positive, negative and null relationships, then there are several possible interpretations but no clear temporal overprinting relationship. This could represent multiple fault events with similar orientations, complex overprinting and reactivation

associated with regional stress reorientation, complex conjugate or branching fault relationships for synchronous fault segments, or combinations thereof.

### Modification of first interpreted temporal–spatial patterning

There are several fault orientations that do appear to have consistent enough temporal relationships that a relative chronology can be constructed (Fig. 7). This figure also shows several orientations for which the temporal relationships are inconsistent. The next step involves insertion of known geological events into the constructed chart to try to break the fault groups into the absolute geological history. We inserted Myally–Surprise Creek Formation and Myally–McNamara Group unconformities, folded faults, as well as faults that offset folds and probably formed during the Isan Orogeny. This reveals four main clusters of fault orientation–time segments (Fig. 7). By consideration of the additional features noted above, we can then assign these fault clusters into pre-Myally, post-Myally and pre-D<sub>2</sub>, and post-D<sub>2</sub>, etc. (Fig. 8a–c).

Next, we assessed the extent to which the time–orientation relationships can be modified by identifying single curved faults in which fault segments of different orientation most probably formed contemporaneously. Representative examples include the Investigator Fault, the Mammoth Extended Fault and other unnamed faults throughout the region, particularly in the NE corner of the study area. The Investigator Fault is apparently folded by the D<sub>2</sub> event of the Isan Orogeny and truncates dolerite dykes that do not extend into the Mount Isa (McNamars) Group sediments; both of these features are consistent with this fault being initially developed prior to the Calvert Superbasin sequence sedimentation at 1730–1630 Ma (Gibson & Henson 2005; Gibson *et al.* 2008). By assigning the same timing relationships to differently orientated faults along the Investigator Fault (i.e. null), we modified the chart. The same procedure was applied to the other faults where they have clear relationships either with unconformities or folds of known absolute timing. For the Investigator Fault, it could be reasonably assumed that the fault was approximately linear prior to the Isan Orogeny. Thus, several strike orientations between 110° and 070° along this fault may represent fault segments that have rotated during folding, as can also be seen with bedding in the area, relative to their original position (Derrick 1982; O'Dea *et al.* 1997; Gibson & Henson 2005; Gibson *et al.* 2008). Furthermore, for this particular fault, the overall symmetry of the fault trace and the folded units and unconformities on the eastern side of the map suggests that it was initially east–west trending. This has also been suggested by other workers

(Derrick 1982; O'Dea *et al.* 1997; Gibson & Henson 2005; Gibson *et al.* 2008).

Following this step, field data (slickenlines, etc.) and the apparent offsets from the regional maps were used for each fault set in each domain to infer an apparent dominant displacement sense, and subordinate displacement sense if the data were inconsistent. From the average orientation(s) and strike-slip movement sense, an inferred  $\sigma_1$  direction was also calculated. This assumes standard Mohr–Coulomb rheology and fault-reactivation criterion; that is,  $\sigma_1$  lies approximately 27° from the fault plane, which infers a coefficient of friction of 0.72, and that the initiation of new faults occurs in homogeneous, anisotropic rock, or in the reactivation of optimally orientated faults (Sibson 1985). Figure 8a–c shows the inferred temporal evolution and stress field for each of the fault sets within the study area. Black rose diagram segments represent high-confidence interpretations with a consistent shear sense, and grey segments represent opposing or uncertain shear senses. In the latter case, the timing of those particular fault segments may be ‘wrong’ for that particular rose diagram or some of the faults (either the grey or the black) were reactivated at a later time with a reversed displacement sense. The arrows on the side refer to the corresponding orientation of  $\sigma_1$  assuming strike-slip movement on steep faults, and the grey shade represents the possible variation of this if the low-confidence faults are considered. By correlation with the literature, we assigned deformation stages on the right, as indicated. The D<sub>4</sub> event seems to be consistent and represents the preferred timing of much of the copper in this belt (Miller 2007; Keys 2008).

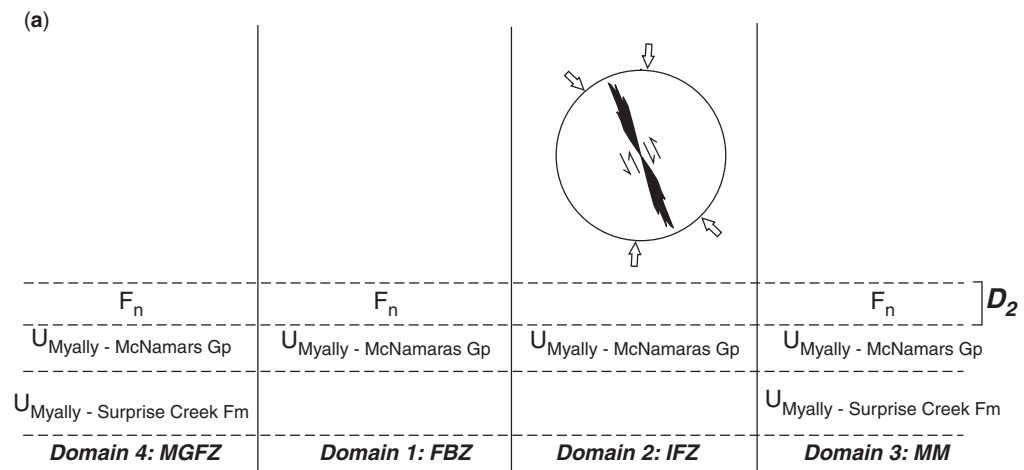


**Fig. 9.** (a)–(c) Coloured rose diagrams showing temporal evolution of the fault network with dominant trends of  $\sigma_1$  and shear sense displayed. To be viewed in conjunction with Figure 10. North is up on all rose diagrams.

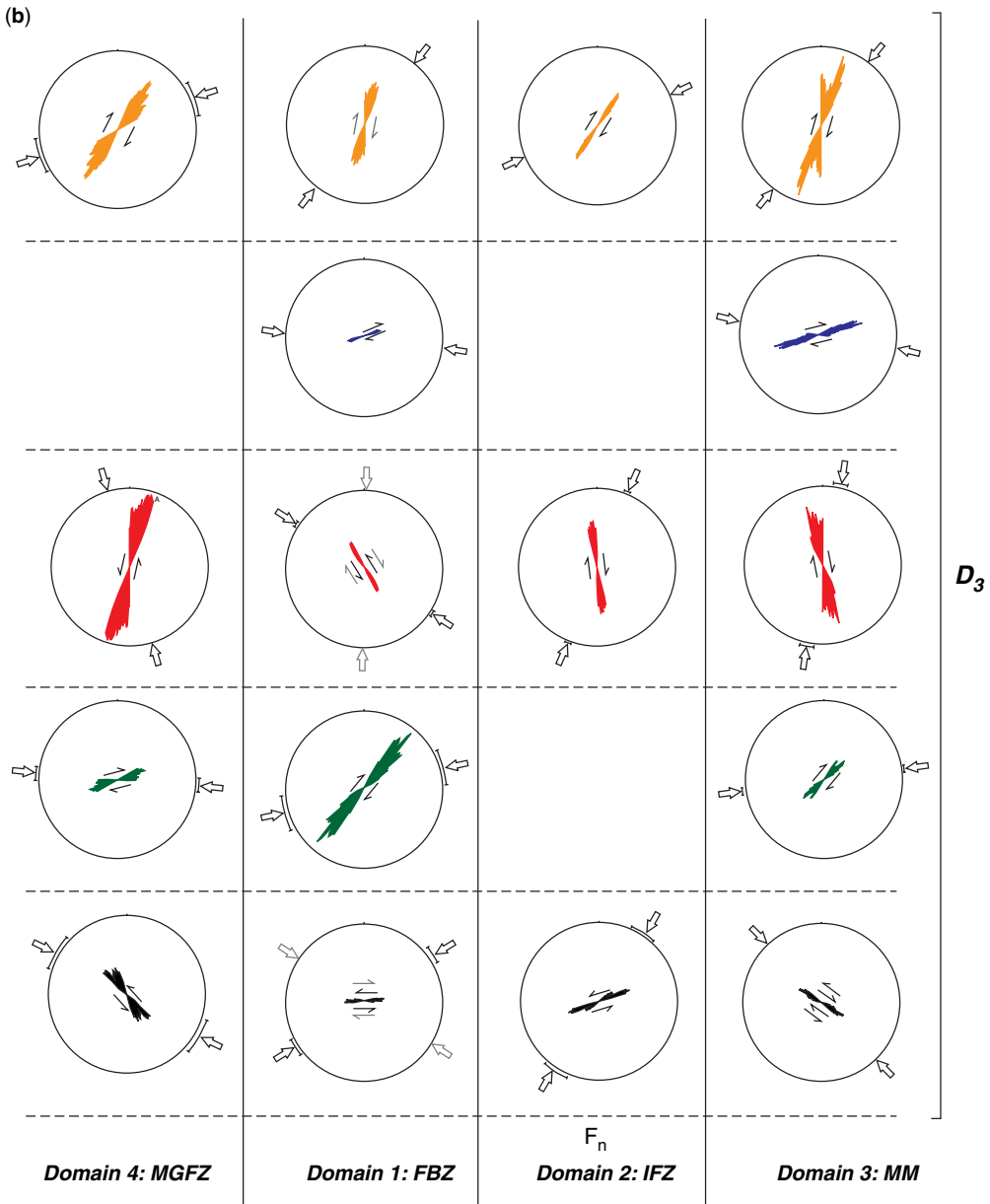
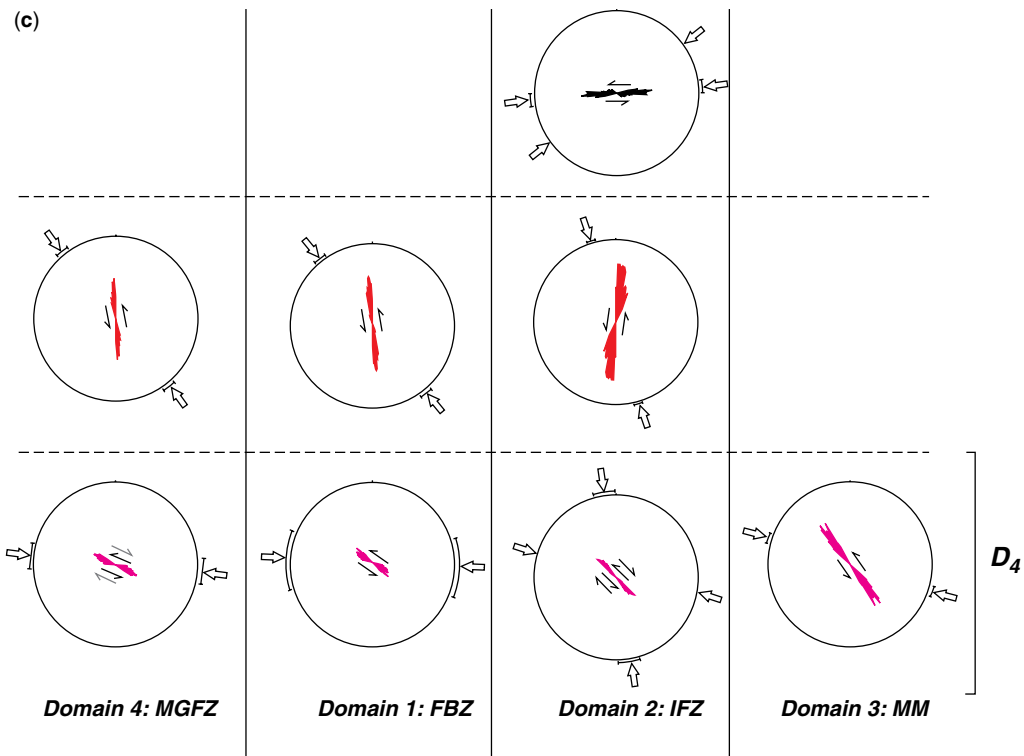


Fig. 9. *Continued.*

### Validity of initial geometrical assumptions

The geometrical relationships used to infer relative fault timing had variable degrees of reliability, as discussed previously. In particular, the assertion that a shorter fault segment along a 'Y' junction is older than a longer segment (Fig. 3) could lead to the erroneous allocation of temporal position if this type of relationship is common. However,

this relationship is uncommon on the Mammoth Mines map sheet (Sheet 6758), and there are far more numerous examples where more reliable displacements occur. For example, where faults offset stratigraphy and folds, as well as older faults, or apparent displacements on the map are confirmed with kinematic indicators in the field. Although the 'Y' junctions could represent fault branches with no distinct timing relationships, the



**Fig. 9.** *Continued.*

displacement on one side of the fault (without the branch) may have been accommodated parallel to bedding and consequently it has not been mapped. The only way to resolve this is to obtain more field data. However, the overall analysis is not seriously compromised by this assumption (Fig. 3) because of the infrequency of the occurrence of this type of 'Y' junction and because it is assigned a null value in the relative age analysis if the angle is less than 30°.

### Evolution of the MGFZ fault network

Here we attempt to describe the evolution of the region based on the binary chronological matrix analysis using Figures 9a–c and 10. Figures 9 and 10 display the evolution of the MGFZ fault network in rose diagram form (Fig. 9a–c) and map view showing a schematic evolution of the fault zone (Fig. 10). The evolutionary diagrams can be thought of as a 'fault reactivation' map (Figs 9 & 10). It is apparent from known cross-cutting relationships and field observations that the rock units have been deposited, affected by early faults, then folded and affected by later faults (Figs 1 & 8a–c). Folding

( $F_n$ ) is likely to be related to the peak metamorphic event that affected the whole Mount Isa inlier,  $D_2$  (Fig. 8a–c and domains 1–4).

Figures 9a and 10 show that the first fault set that was likely to reactivate was a NW-trending set in the Investigator Fault Zone (IFZ, Domain 2) (Figs 9a & 10). These faults are may be related to the intrusion of NNW-trending dyke sets that occur to the south and north of the IFZ, Domain 2 (Fig. 10b–d). Field evidence indicates that, at least locally, these dykes have been affected by the Isan Orogeny.

The second set of faults to reactivate was a set of NW (domains 4 and 3) and an east–west and ENE set of faults in domains 1 and 2 (Figs 8b, 9b & 10d). The first correlatable fault set to activate/reactivate(?) are SE-trending faults, with an apparent sinistral shear sense and  $\sigma_1$  orientated approximately 135°–315° in Domain 4 (MGFZ). A similar set of faults was also reactivated in Domain 3 (Mammoth Mines). In domains 1 and 2, more easterly trending faults were active at this time, with a left-lateral shear sense. Only Domain 3 has a moderately different orientation for  $\sigma_1$ , yet those faults also have a left-lateral shear sense. Faults in domains 4 and 3 have opposite shear

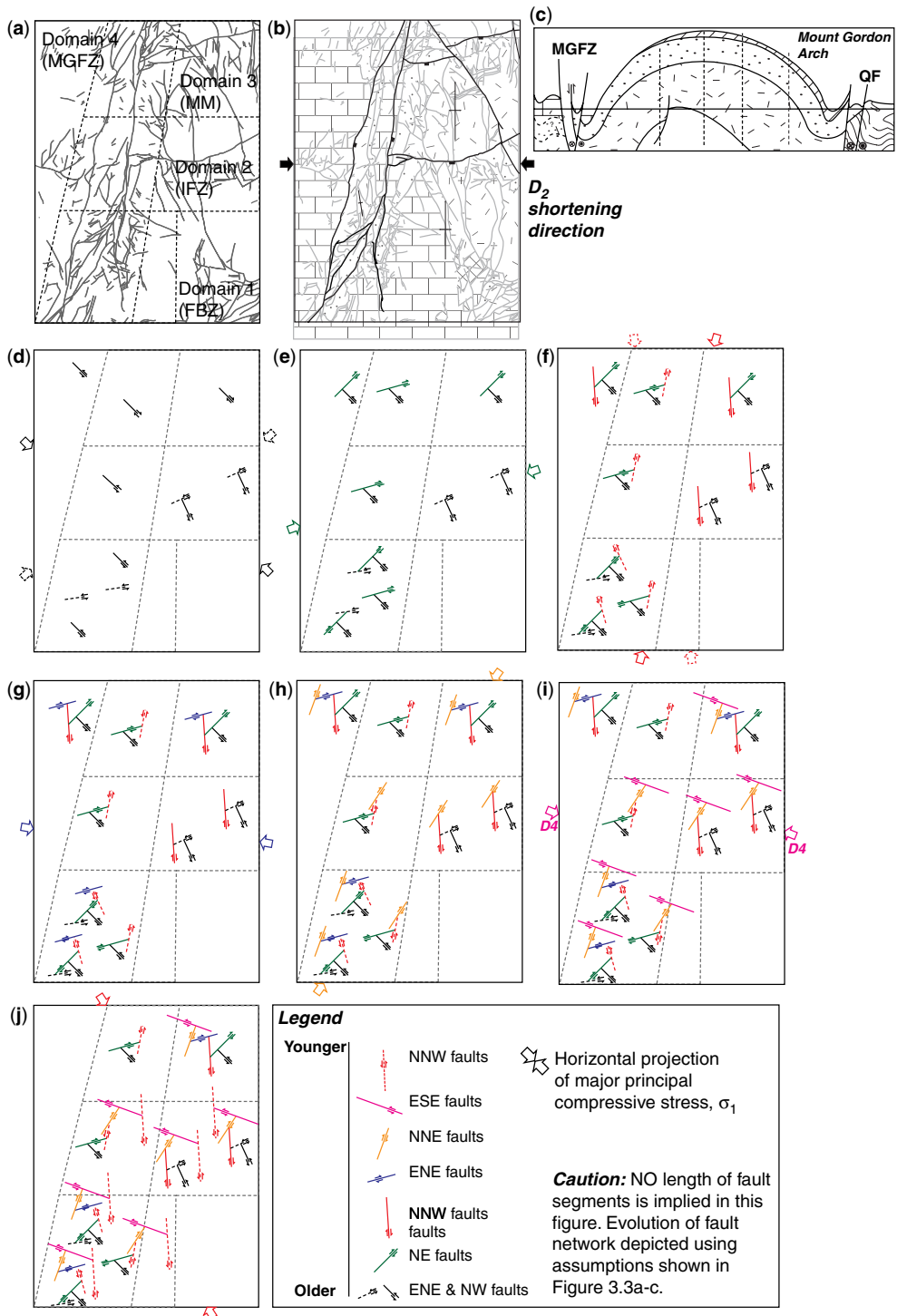


**Fig. 10.** Schematic block diagram showing the evolution of fault network within the study area. **(a)** Regional fault architecture (not to scale) and domain subdivision. **(b)** Geological map of the study area showing major normal faults and folding of the Mount Gordon Arch, a pre-Isan Orogeny feature (Derrick 1982; Gibson 2005). The major shortening

senses with a subparallel  $\sigma_1$ . In domains 1 and 2, the dominant shear sense is left-lateral with a NE–SW  $\sigma_1$  trend. This set of faults is problematic but, in the binary chronological matrix, the results indicate that they are an early fault set to reactivate or form. They are unresolvable in the sense that there are different orientations of  $\sigma_1$  and dominant shear senses, so probably reflect more than one stage of faulting.

The next set of faults to develop (reactivate) are a predominantly NE set of faults with a dominant right-lateral shear sense, and a WSW–ENE  $\sigma_1$  trend in domains 4, 1 and 3 (Figs 8, 9 & 10e).

Within domains 4, 1 and 3, ENE- to NE-trending faults were active with a dominant right-lateral shear sense with an ENE orientation for  $\sigma_1$  (Figs 8b, 9b & 10e). Domain 2 (IFZ) does not appear to have any faults active at this time and this may mean that the timing criterion is incorrect or that the domain was not affected by this faulting event and/or deformation may have been taken up by the Investigator Fault.

Faults of the next activation or reactivation event are north–south-trending faults from domains 2 (IFZ) and 3 (MM) (Figs 8, 9 & 10f), with a dominant right-lateral shear sense and NNE-orientated  $\sigma_1$ . The north–south faults from domains 4 (MGFZ) and 1 (FBZ) are only active at a much later stage in the faulting history. This implies that, at least locally, these north–south faults may have had sufficient cohesion not to reactivate because it is likely that some of these faults are ‘old’ basin bounding structures and possibly represent old basement faults. It is also apparent that the north–south faults from domains 4 (MGFZ) and 1 (FBZ) would be in an optimal orientation to reactivate (Sibson 2001), yet they have not (see the Discussion).

In domains 1 and 3 (FBZ and MM) ENE faults are active with a right-lateral shear sense and an ESE-trending  $\sigma_1$  (Figs 8, 9 & 10g). The final

faulting event within the proposed D<sub>3</sub> event are NNE-trending faults with a dominant right-lateral shear sense from all domains, with a NE-orientated  $\sigma_1$  (Figs 8–10).

The next faulting event is the inferred D<sub>4</sub> copper-mineralizing event (McLellan *et al.* 2006; Miller 2007; Keys 2008). In Figures 8, 9 and 10i the dominant sense of shear is sinistral, with  $\sigma_1$  orientated approximately 110°–120°, thus confirming the propositions of Miller (2007) and Keys (2008) derived by independent methods. Only domains 4 (MGFZ) and 3 (MM) have a minor component of right-lateral shear, with SE- and ENE-orientated  $\sigma_1$ , respectively (Figs 8–10).

The final faulting event affected domains 4 (MGFZ), 1 (FBZ) and 2 (IFZ). Here north–south-trending faults were reactivated with a dominant left-lateral shear sense and a SE-orientated  $\sigma_1$ . It is likely that these faults were reactivated rather than being newly formed because there are north–south faults that were active earlier on in the temporal evolution of faulting (Figs 8a–c, 9a–c & 10). The alternative is that these faults are newly formed but that implies large differential stresses ( $\sigma_1$ – $\sigma_3$ ) or extremely high pore-fluid pressures with low differential stresses in order to not touch the frictional reshear envelope (see later).

## Discussion

Sibson (1977, 1989, 2001) proposed that the presence of pre-existing faults in rocks could substantially modify the mechanics and kinematics of propagation of younger faults through the rock mass. ‘Old’ faults potentially represent zones of low cohesion, damage or soft fault infill that may be reactivated during subsequent deformation events if certain combinations of far-field stress orientations, fluid pressures and fault orientations are met. The generation of new faults in previously

**Fig. 10. (Continued)** direction during D<sub>2</sub> (east–west) in the Isan Orogeny is also shown as it is likely to have folded the Investigator Fault. (c) A generalized cross-section looking north showing the MGFZ in the west and the George–Creek–Quilalar fault system in the east, with the Mount Gordon Arch (Leichhardt anticline), a pre-Isan Orogeny feature modified from Derrick (1982) and Gibson (2005). See Figure 1 for the legend. Modified from Derrick (1982), O’Dea *et al.* (1997) and Gibson (2005). (d) Development of NW-trending faults, with mostly left-lateral separation and two orientations of  $\sigma_1$  with two major sets of faults forming. (e) Development of NE-trending faults with mostly right-lateral separation. (f) North–south-orientated faults develop; however, these could also represent reactivated basement structures. (g) Development of ENE-trending faults through the MGFZ (Domain 4) with a dominant right-lateral shear sense. (h) Development of a NE right-lateral fault system during the waning stages of D<sub>3</sub>, which would agree with the interpretation of the MGF being a D<sub>3</sub> structure (Gibson & Henson 2005). (i) D<sub>4</sub> event where copper mineralization occurred along ESE-trending faults with an approximately 110°  $\sigma_1$  (Keys 2008). (j) Likely reactivation of NNW-trending faults in a NNW- to NW-orientated stress field, as well as the possible development (reactivation?) of north–south faults within the Fort Binder Fault Zone (FBZ), Domain 1. Arrows outside the boxes represent inferred orientation of stress assuming mostly strike-slip movement along subvertical faults. The length of individual fault segments does not imply that those faults are longer but that they obey our initial assumption (Fig. 3a–c).

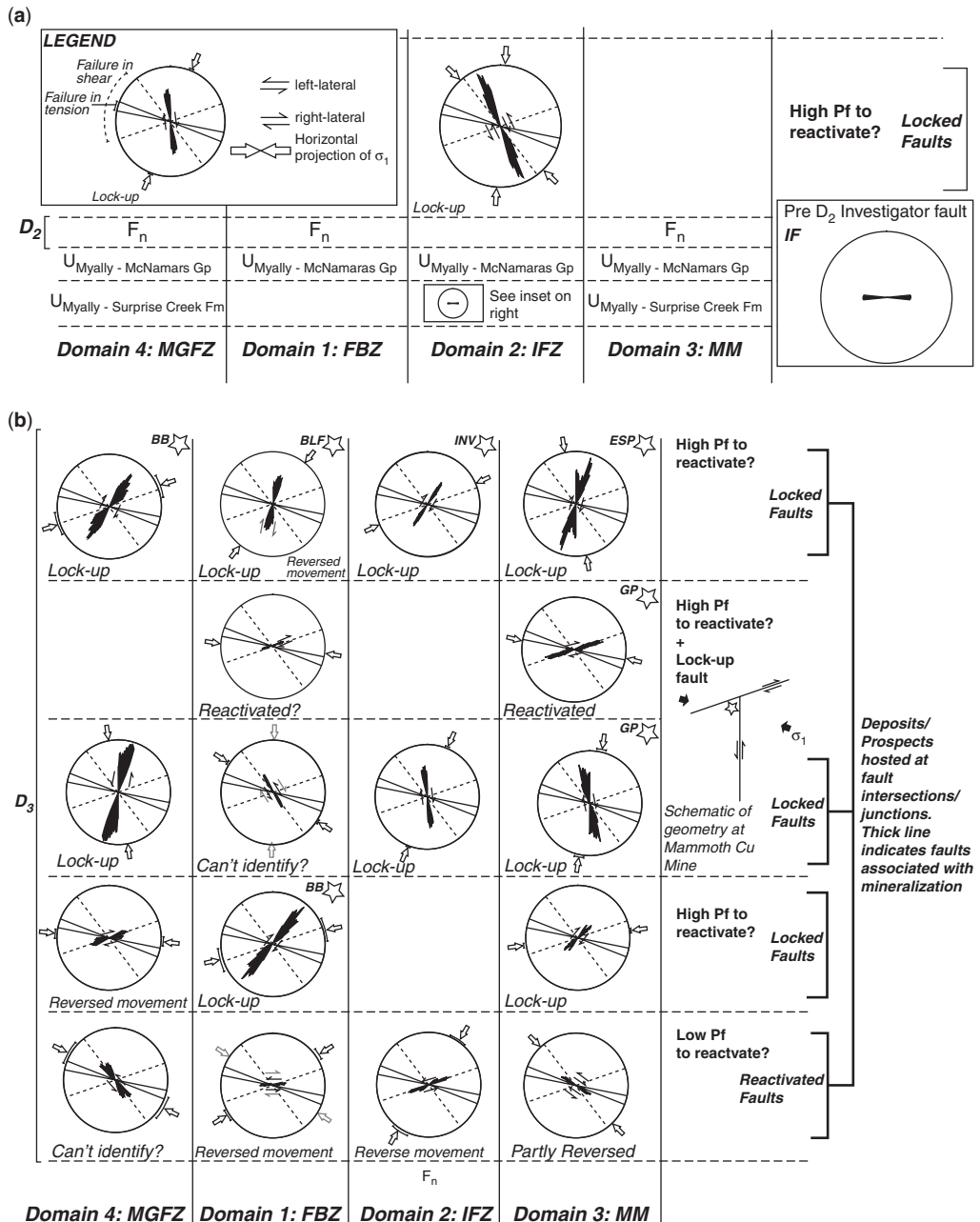


**Fig. 11.** (a)–(c). Rose diagram plot of the relative chronology of faulting events with an applied  $D_4$  stress field overlaid on older fault segments. The dominant shear sense and  $\sigma_1$  orientations are shown. Solid red lines on the overlayed stereonet indicate failure in tension, while blue dashed lines indicate failure in shear according to conventional fault-reactivation analysis techniques (Sibson 1985). The text in each box indicates whether or not the fault set will reactivate under the applied  $D_4$  stress field, that is, lock-up, reversed movement sense, reactivated with same shear sense. The far-right column indicates the inferred criterion for fault reactivation to occur and a simplified geometry from the Mammoth Mines region. Stars in the top-right corners of the boxes indicate deposits and prospects on particular faults. Abbreviations as follows: BB, BigBen; BLF, Bluff; INV, Investigator; ESP, Esperanza; GP, Gunpowder.

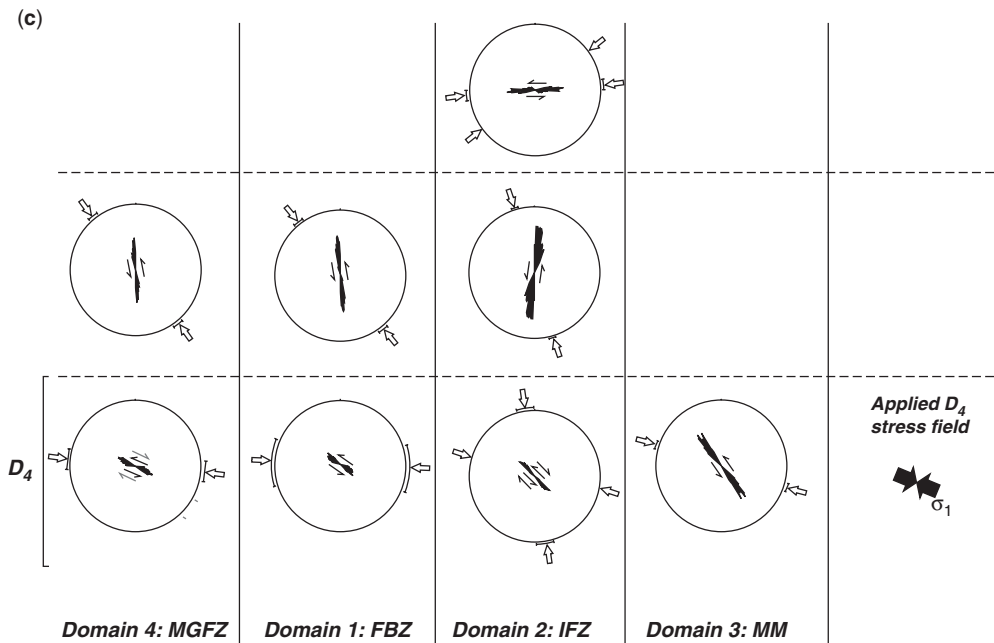


**Fig. 11.** *Continued.*

faulted rock masses implies that: (a) the older faults develop cohesion with time, sufficient such that the younger deformation does not ‘see’ the older faults (Cox *et al.* 2001); (b) that the far-field stresses associated with the younger deformation are sufficiently misorientated relative to the earlier faults that reactivation is not possible; or (c) that fluid pressures associated with the younger deformation are insufficient for reactivation along the older structures. The features observed in this field area along fault traces range from distinctive quartz ‘blows’ – veins up to 10 m wide and 1–200 m long (which would most likely have high cohesion during subsequent deformation events) – to recessive valleys with poor exposure of rare fault gouge or clay-filled breccia that may have had low cohesion during potential reactivation events.

#### Conventional fault-reactivation analysis

Fluid flow leading to mineralization can occur on both newly formed faults and on faults that are reactivated subsequent to their initial formation (Cox *et al.* 2001; Sibson 2001). Popular models of fault reactivation propose that, under high pore-fluid pressures, misorientated faults may move again due to low fault cohesion (Cox *et al.* 2001; Sibson 2001). Using the standard criterion for reactivation along faults, a reactivation analysis is shown.

For the main  $D_4$  copper-mineralizing event, the greatest principal compressive stress ( $\sigma_1$ ) was subhorizontally orientated at approximately  $110^\circ$ , with  $\sigma_2$  subvertical (McLellan *et al.* 2006; Miller 2007; Keys 2008). For this stress field, faults that strike subparallel to  $110^\circ$  should have reactivated as dilational fractures possibly with breccias, and faults whose orientation is between approximately  $27^\circ$  and  $54^\circ$  from  $\sigma_1$  should have been optimally orientated for shear failure (Sibson 1986, 1996, 2000, 2001). Figure 11 shows this imposed  $D_4$  stress field for faults that are older than the  $D_4$  faults.

The far right column in Figure 11 describes whether or not faults could reactivate in tension (faults lying between the red lines), shear (faults lying in the acute angle between the blue dashed lines) or may not have reactivated due to their high angle to  $\sigma_1$  (faults lying outside the blue dashed lines). Faults have been labelled either as ‘locked faults’ or ‘reactivated faults’, based on the theoretical orientation analysis of reactivation just described. For locked faults to reactivate they would require high pore-fluid pressure, while optimally orientated faults should reactivate either in shear or tension, potentially with lower pore-fluid pressures (Fig. 11).

It is apparent from Figure 11 that many of the older faults from all four domains should have

reactivated under a D<sub>4</sub> stress field in tension or in shear, but many did not. Figure 11 shows the youngest event D<sub>4</sub> (ESE–WNW), for which the inferred stress field is applied to all older faults to check their potential for reactivation in tension and shear (Figs 12–14). Figure 12 shows late D<sub>3</sub> faults (Fig. 11) with the applied D<sub>4</sub> stress field. Late D<sub>3</sub> faults host mineralization (Fig. 12) yet they are all severely misorientated for reactivation, which implies that they required sufficiently high pore-fluid pressures and low cohesion to reactivate under a D<sub>4</sub> stress field. The existence of the D<sub>4</sub> faults, however, seems to require that, at some point, the late D<sub>3</sub> faults did not reactivate, but that new faults formed instead, implying a change either in pore-fluid pressure conditions or in cohesion of the late D<sub>3</sub> faults after they formed (see below).

Figure 13 shows mid-D<sub>3</sub> faults under the applied D<sub>4</sub> stress regime. While these faults do not host economic grades of mineralization, other than the Mammoth Mines domain, these faults would also have required high pore-fluid pressure to reactivate, along with low cohesion.

Figure 14 depicts early D<sub>3</sub> faults under the applied D<sub>4</sub> stress regime. These faults should have reactivated in shear and/or tension, but apparently did not (no shear-sense reversal or tensile veins on the fault). This is likely due to these faults having either a high cohesion during reactivation and/or low pore-fluid pressure (Fig. 14).

For the formation of new faults under a D<sub>4</sub> stress field (Fig. 11), it is likely that high differential stresses would be needed. The simple observation that many different fault orientations exist, with an apparent consistency of relative timing relationships, requires that new faults commonly developed in rocks that already contained older faults. Thus, the majority of the older faults would have had to have sufficiently high cohesion so as not to ‘see’ the younger deformation (Cox *et al.* 2001), unless pore-fluid pressures were quite low during the younger events. However, the occurrence of dilatational hydrothermal mineralization on *some* young faults would appear to be evidence that high pore-fluid pressures were locally attained and faults were reactivated in tension.

### *Exploration implications*

Deposits and prospects commonly lie at the intersection between faults of differing ages and orientations; however, this analysis does not specifically include the fault intersections for consideration. For example, the Mammoth copper ore body is located at an intersection between ENE- and north–south-trending faults (mid-D<sub>3</sub> faults) (Figs 11 & 13). A possible model for the formation

of this deposit is that the north–south fault locked up owing to its severe misorientation under an applied D<sub>4</sub> ESE stress field. The ENE-trending fault may have reactivated in shear mode, as suggested by field relationships and by quartz textures in the fault fill (Nortje 2009). This reactivated fault may have acted as a fluid conduit during reactivation, providing a source of copper-bearing fluids, further facilitated by the fairly large size of this fault (with potential connections to diverse copper sources). The ‘locking’ of a fault during a regional reactivation event can lead to increases in pore-fluid pressure, prior to a potential large earthquake event when slip finally occurs (Sibson 1977, 1989, 2001; Cox *et al.* 2001). If such a locked fault is connected to a fault that is being successfully reactivated along at least some of its length, then the latter fault could act as a conduit for fluids to be directed towards the locked fault, depending on the overall geometrical configuration. Thus, at the point where the two faults meet, a zone of particularly high pore-fluid pressure may develop that would accentuate the potential for eventual catastrophic failure localization at the junction. This may also be assisted by local perturbations of the stress field at the junction. The location of mineralized breccia at the Mammoth deposit is considered to reflect this type of fault interaction; palaeostress modelling at that junction also suggests anomalously high pore-fluid pressures on one side of the junction coupled with an anomalous stress field (Fig. 15) (Keys *et al.* 2006).

A regionally testable hypothesis is that low-cohesion faults are recessive, with clays and damage zones dominating the fault fill; that is, predominantly north–south-trending faults. Faults that trend ESE–SE, or east–west, containing protruding fault fill of coarse quartz, brecciated quartz and fibrous quartz were likely to be highly cohesive faults. Faults with high cohesion may have acted as barriers and compartments, so that intersections between them and newly formed faults provided exploration targets, not because of reactivation but because of the interaction between new faults and the cohesive materials defined either by fault precipitates or by rock juxtaposition (Fig. 16).

### **Conclusions**

- The relative age analysis method (binary chronological matrix analysis) has been shown to be a valid tool to use in the study of the evolution of a Proterozoic mineralized and faulted terrain.
- Further evidence for D<sub>4</sub> being the main copper-mineralizing event, as proposed elsewhere at the Mount Isa, Mammoth and Mount Kelly Cu

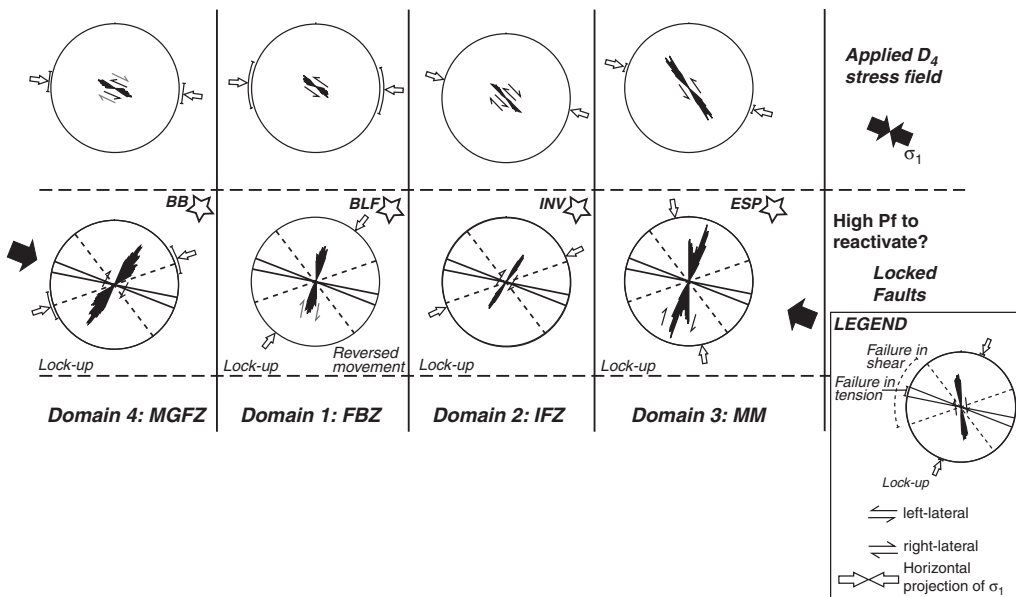


**Fig. 12.**  $D_4$  stress field applied to late  $D_3$  faults, and these faults are mineralized during  $D_4$  and are in 'lock up' orientation under a  $D_4$  stress field. These faults are likely to have had low cohesion and required high pore-fluid pressure to reactivate in tension. Solid red lines on the overlayed stereonet indicate potential reactivation by failure in tension, while blue dashed lines indicate reactivation in shear according to conventional fault-reactivation analysis techniques (Sibson 1985).

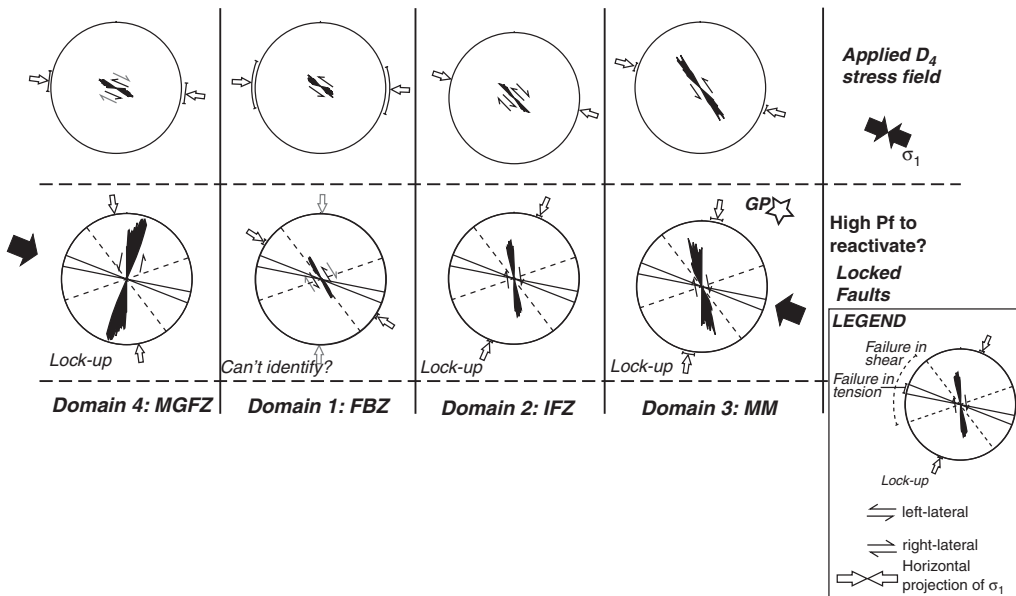


**Fig. 13.** Mid- $D_3$  faults under a  $D_4$  stress field. These faults are in 'lock up' orientation with little or no mineralization, with one exception (Gunpowder). These faults probably had insufficient pore-fluid pressure for reactivation on low-cohesion faults. Solid red lines on the overlayed stereonet indicate reactivation potential for failure in tension, while blue dashed lines indicate potential failure in shear according to conventional fault-reactivation analysis techniques (Sibson 1985).

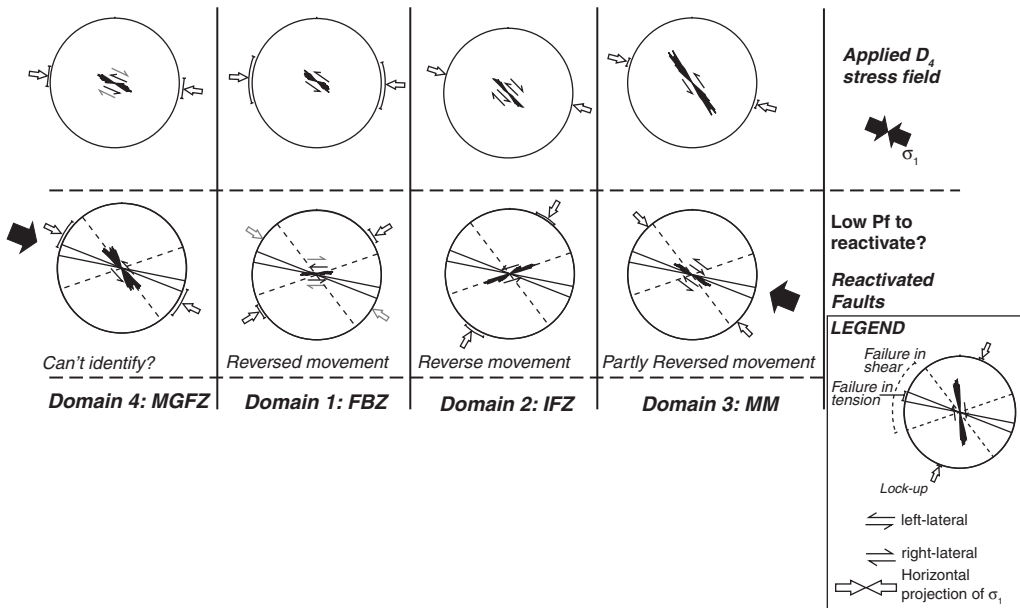


**Fig. 14.** Early-D<sub>3</sub> faults under a D<sub>4</sub> stress field. These faults are in a good orientation to reactivate but apparently did not reactivate, and several younger generations of faults cut these faults. It is likely that these faults had high cohesion during the attempted reactivation. Solid red lines on the overlayed stereonet indicate failure in tension, while blue dashed lines indicate failure in shear according to conventional fault-reactivation analysis techniques (Sibson 1985).

deposits, is independently verified here for the study area.

- The temporal evolution of faults within the region, with new faults forming in rocks that already contained faults, requires that many older faults developed sufficient cohesion that they did not subsequently reactivate, even in favourable orientations for reactivation. In contrast, at certain locations, fault reactivation in tension, at high pore-fluid pressures, produced breccias and mineralization.
- Faults with high cohesion may have acted as barriers and compartments, so that intersections between them and newly formed faults provided exploration targets, not because of reactivation but because of the interaction between new faults and the cohesive materials defined either by fault precipitates or rock juxtaposition.
- The general assumption that older faults generally have low cohesion is not borne out by this study. Rather, this study points towards the need to recognize the potential for high-cohesion old faults, as these may be places where pore-fluid pressure was forced upwards. The faults did not reactivate but, rather, the combination of high fluid pressures and fault ‘locking’ permitted brecciation and focused fluid flow, leading to mineralization.

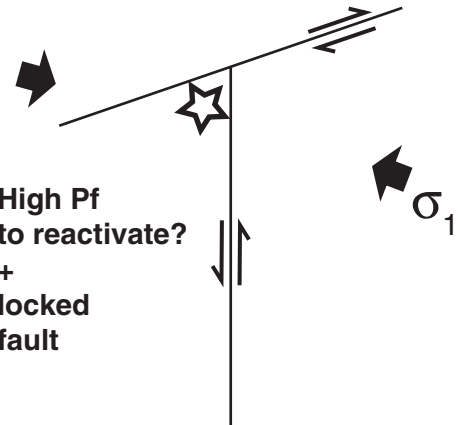


**Fig. 15.** Simplified model for the formation of the Mammoth Mines (Gunpowder) and deposits/prospects in the general in the study area. Under an applied D<sub>4</sub> ESE stress field, the old north–south fault locks, while the ENE-trending fault reacts in shear. The north–south fault facilitates the build up of high pore-fluid pressures, while the ENE-trending fault behaves like a fluid conduit where fluid focusing occurs at the intersection of the two faults, resulting in mineralization.

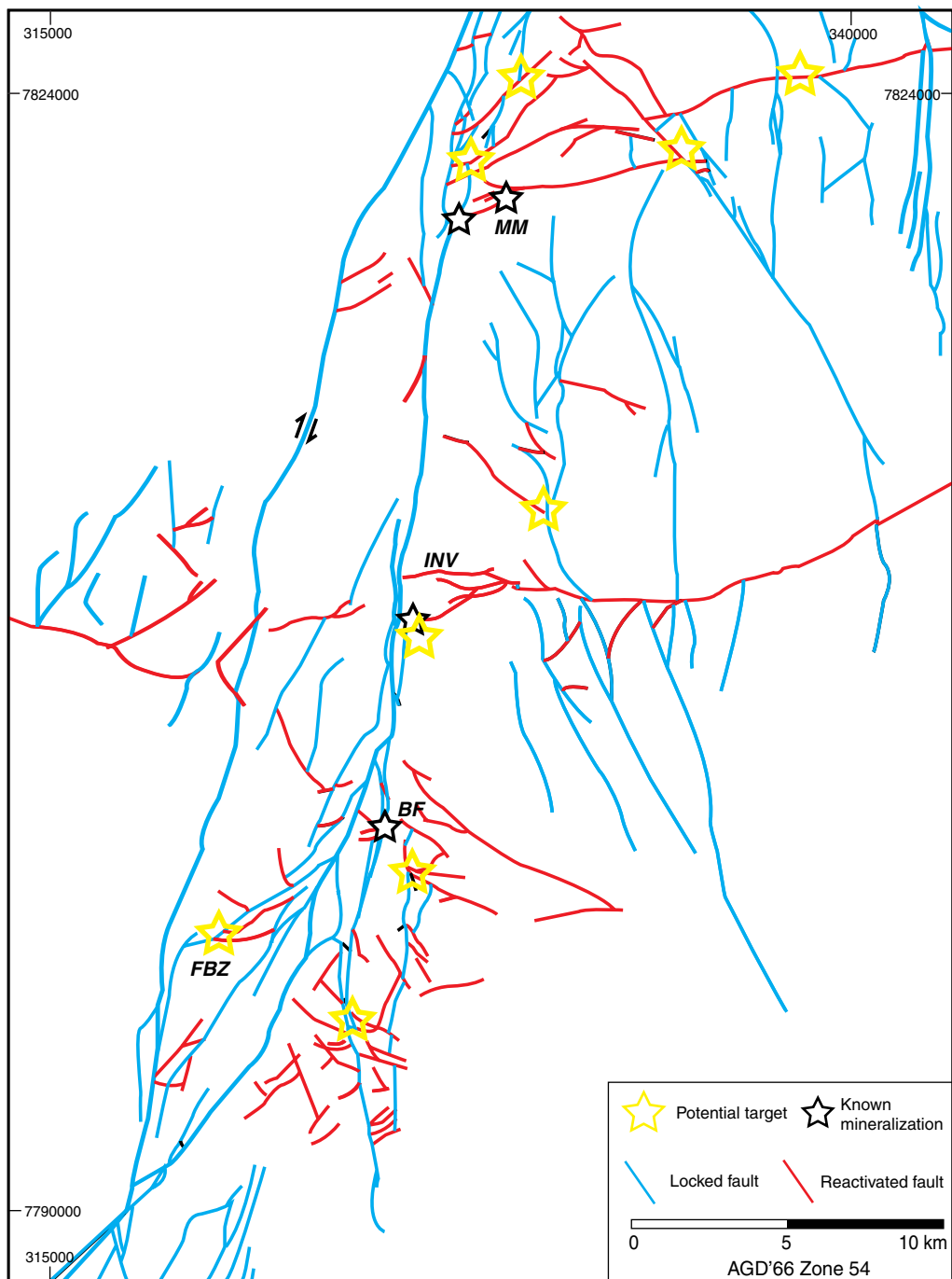


**Fig. 16.** Fault map of locked (recessive faults – blue) and reactivated (protruding faults – red) faults based on an applied  $D_4$  stress field (Figs 11–14). Locked faults (blue) are known to be recessive but some are predicted to be recessive using this method. The white stars show known mineralization and the yellow stars show potential targets. Map projection AGD 1966 zone 54.

This work was supported by the Predictive Mineral Discovery Cooperative Research Centre (pmd\*CRC). We thank AdityaBirla Ltd, CopperCo Ltd, and Xstrata Copper (Mount Isa) for providing invaluable assistance while G. S. Nortje and D. L. Keys undertook fieldwork. G. S. Nortje and D. L. Keys were awarded pmd\*CRC top-up scholarships. G. S. Nortje thanks G. Dryden and D. Brigden of SunWater Ltd for providing the necessary assistance to his complete postgraduate study. We thank D. Healy, J. Kolb and Å. Fagereng (editor) for insightful and constructive reviews that greatly improved the clarity of the manuscript.

## References

- ANGELIER, J. 1991. Analyse chronologique matricielle et succession régionale des événements tectoniques. *Comptes Rendu de l'Academie des Sciences Paris, 312*, 1633–1638.
- ANGELIER, J. 1992. CHRONO, **1.07**, Paris, France.
- ANGELIER, J. 1994. Fault Slip Analysis and Palaeostress Reconstruction. In: HANCOCK, P. L. (ed.) *Continental Deformation*. Pergamon Press, New York, 421.
- BELL, T. H. 1983. Thrusting and duplex formation at Mount Isa. *Nature*, **304**, 493–497.
- BELL, T. H. 1991. The role of thrusting in the structural development of the Mount Isa Mine and its relevance to exploration in the surrounding region. *Economic Geology*, **86**, 1602–1625.
- BELL, T. H., PERKINS, W. G. & SWAGER, C. P. 1988. Structural controls on development and localization of syntectonic copper mineralization at Mount Isa, Queensland. *Economic Geology and the Bulletin of the Society of Economic Geologists*, **83**, 69–85.
- BETTS, P. 2000. Asymmetric extension of the lithosphere and its influence on Palaeoproterozoic Pb–Zn deposits of the Western fold belt, Mount Isa Terrane. *Journal of the Virtual Explorer*, **1**, 28–42.
- BETTS, P. G. 1999. Palaeoproterozoic mid-basin inversion in the northern Mt Isa terrane, Queensland. *Australian Journal of Earth Sciences*, **46**, 735–748.
- BETTS, P. G., GILES, D. & LISTER, G. S. 2003. Tectonic environment of shale-hosted massive sulfide Pb–Zn–Ag deposits of Proterozoic northeastern Australia. *Economic Geology and the Bulletin of the Society of Economic Geologists*, **98**, 557–576.
- BLAKE, D. H. 1987. Geology of the Mount Isa Inlier and environs, Queensland and Northern Territory. *Canberra, Bureau of Mineral Resources Bulletin, 225*, 83.
- BLAKE, D. H. & STEWART, A. J. 1992. Stratigraphic and tectonic framework, Mount Isa Inlier. In: STEWART, A. J. & BLAKE, D. H. (eds) *Detailed Studies of the Mount Isa Inlier*. Australian Geological Survey Organisation Bulletin, Canberra, **243**, 1–11.
- COX, S. F., KNACKSTEDT, M. A. & BROWN, J. 2001. Principles of structural control on permeability and fluid flow in hydrothermal systems. In: RICHARDS, J. P. & TOSDAL, R. M. (eds) *Structural Controls on Ore Genesis. Reviews in Economic Geology 14*. Society of Economic Geologists, Littleton, CO, 1–22.
- DAVIS, T. P. 2004. Mine-scale structural controls on the Mount Isa Zn–Pb–Ag and Cu orebodies. *Economic Geology and the Bulletin of the Society of Economic Geologists*, **99**, 543–559.
- DERRICK, G. M. 1982. A Proterozoic rift zone at Mount Isa, Queensland, and implications for mineralization. *BMR Journal of Australian Geology and Geophysics*, **7**, 81–92.
- DUNCAN, R., HITZMANN, M., NELSON, E., STEIN, H., ZIMMERMAN, A. & KIRWIN, D. 2009. Re–Os Molybdenite Ages for the Southern Cloncurry IOCG District, Queensland, Australia: Protracted Mineralisation Over 210 myr. In: WILLIAMS, P. J. (ed.) *Smart Science for Exploration and Mining, Volume 2: Townsville, QLD, Australia*. Economic Geology Research Unit and Society for Geology Applied to Mineral Deposits, Townsville, 626–628.
- ETHERIDGE, M. A., RUTLAND, R. W. R. & WYBORN, L. 1987. Orogenesis and tectonic process in the early to Middle Proterozoic of northern Australia. In: KRÖNER, A. (ed.) *Precambrian Lithospheric Evolution*. American Geophysical Union, Geodynamic Series 17, 131–147.
- FORSTER, M. A. & LISTER, G. S. 2008. Tectonic sequence diagrams and the structural evolution of schists and gneisses in multiply deformed terranes. *Journal of the Geological Society*, **165**, 923–939.
- GIBSON, G. M. 2005. Chapter 3: Chronostratigraphy and geodynamic evolution of the Western Succession. In: GIBSON, G. M. & HITCHMAN, A. P. (eds) *Project I 1: 3D Basin Architecture & Mineral Systems in the Mt Isa Western Succession*. Predictive Mineral Discovery Cooperative Research Centre, Canberra, 31–82.
- GIBSON, G. M. & HENSON, P. A. 2005. Chapter 6: Post-depositional deformation in the Western Succession. In: GIBSON, G. M. & HITCHMAN, A. P. (eds) *Project I 1: 3D Basin Architecture & Mineral Systems in the Mt Isa Western Succession*. Predictive Mineral Discovery Cooperative Research Centre, Canberra, 147–176.
- GIBSON, G. M., RUBENACH, M. J., NEUMANN, N. L., SOUTHGATE, P. N. & HUTTON, L. J. 2008. Syn- and post-extensional tectonic activity in the Palaeoproterozoic sequences of Broken Hill and Mount Isa and its bearing on reconstructions of Rodinia. *Precambrian Research*, **166**, 350–369.
- GREGORY, M., SCHAFER, B., KEAYS, R. & WILDE, A. 2008. Rhodium–osmium systematic of the Mt Isa copper ore body and the Eastern Creek Volcanics, Queensland, Australia: implications for ore genesis. *Mineralium Deposita*, **43**, 553–573.
- HEINRICH, C. A. & COUSENS, D. R. 1989. Semiquantitative electron microprobe analysis of fluid inclusion salts from the Mount Isa copper deposit (Queensland, Australia). *Geochimica et Cosmochimica Acta*, **53**, 21–28.
- HEINRICH, C. A., BAIN, J. H. C., MEMAGH, T. P., WYBORN, L. A. I., ANDREW, A. S. & WARING, C. L. 1995. Fluid and mass transfer during metabasalt alteration and copper mineralization at Mount Isa, Australia. *Economic Geology*, **90**, 705–730.
- HOLYLAND, P. W. & OJALA, V. J. 1997. Computer-aided structural targeting in mineral exploration: two- and three-dimensional stress mapping. *Australian Journal of Earth Sciences*, **44**, 421–432.

- HUTTON, L. J., DERRICK, G. M. & GALLAGHER, J. 1985. *Geology of the Mammoth Mines Region 1:100 000, Geological Series Sheet 6758*. Australia, Bureau of Mineral Resources, Canberra.
- KEYS, D. L. 2008. *Mechanical localisation of copper deposits in the Mt Isa Inlier, North Queensland*. Unpublished PhD thesis, James Cook University, 338p.
- KEYS, D. L., OLIVER, N. H. S. & MCLELLAN, J. G. 2006. Resolving the structural setting of the Gunpowder copper deposits, using numerical modelling. North Queensland GSA 18th Australian Geological Convention, Melbourne, 2006.
- KOLB, J., ROGERS, A., MEYER, F. M. & VENNEMANN, T. W. 2004. Development of fluid conduits in the auriferous shear zones of the Huti Gold Mine, India: evidence for spatially and temporally heterogeneous fluid flow. *Tectonophysics*, **378**, 65–84.
- LISTER, G. S., O'DEA, M. G. & SOMAIA, I. 1999. A tale of two synclines: rifting, inversion and transpressional popouts at Lake Julius, northwestern Mt Isa Terrane, Queensland. *Australian Journal of Earth Sciences*, **46**, 233–250.
- LISTER, G. S., THOMAS, A. & DUNN, J. 1986. Tectonic processes in the Mount Isa Inlier; the significance of transpressional strike-slip faulting. In: BRANCH, C. D. (ed.) *Eighth Australian Geological Convention; Geological Society of Australia; Earth Resources in Time and Space*. Geological Society of Australia, Adelaide, **15**, 127–128.
- LISTER, G. S., THOMAS, A. D., DUNN, J. 1987. The significance of transpressional strike-slip faulting in the Lake Julius area, Mount Isa Inlier. In: ANONYMOUS (ed.) *International Conference on Deformation of Crustal Rocks*. Geological Society of Australia, Mt Buffalo, **19**, 39–40.
- MAIR, J. L., OJALA, V. J., SALIER, B. P., GROVES, D. I. & BROWN, S. M. 2000. Application of stress mapping in cross-section to understanding ore geometry, predicting ore zones and development of drilling strategies. *Australian Journal of Earth Sciences*, **47**, 895–912.
- MCLELLAN, J. G. & OLIVER, N. H. S. 2008. Discrete element modelling applied to mineral prospectivity analysis in the eastern Mount Isa Inlier. *Precambrian Research*, **163**, 174–188.
- MCLELLAN, J. G., OLIVER, N. H. S. & HOBBS, B. E. 2006. The relative effects of deformation and thermal advection on fluid pathways in basin-related mineralization. *Journal of Geochemical Exploration*, **89**, 217–275.
- MICKLETHWAITE, S., SHELDON, H. A. & BAKER, T. 2010. Active fault and shear processes and their implications for mineral deposit formation and discovery. *Journal of Structural Geology*, **32**, 151–165.
- MILLER, J. McL. 2007. Structural controls on the Mt Isa Copper deposit, QLD, Project I7, Predictive Mineral Discovery CoOperative Research Centre, 70.
- NEUMANN, N. L., SOUTHGATE, P. N., GIBSON, G. M. & MCINTYRE, A. 2006. New SHRIMP geochronology for the Western Fold Belt of the Mt Isa Inlier: developing a 1800–1650 Ma event framework. *Australian Journal of Earth Sciences*, **53**, 1023–1039.
- NIJMAN, W., MIJNLIEFF, H. F. & SCHALKWIJK, G. 1992a. The Hero Fan Delta (Lower Mount Isa Group) and its structural control: deformation in the Hero/Western Fault Zone and Paroo Range compared, Proterozoic, Mount Isa Inlier, Queensland, Australia. In: STEWART, A. J. & BLAKE, D. H. (eds) *Detailed Studies of the Mount Isa Inlier*. Australian Geological Survey Organisation, Canberra, **243**, 75–110.
- NIJMAN, W., VAN LOCHM, J. H., SPLIETHOFF, H. & FEIJTH, J. 1992b. Deformation model and sedimentation patterns of the Proterozoic of the Paroo Range, Mount Isa Inlier, Queensland, Australia. In: STEWART, A. J. & BLAKE, D. H. (eds) *Detailed Studies of the Mount Isa Inlier*. Australian Geological Survey Organisation Bulletin 243, Canberra.
- NORTJE, G. S. 2009. *Evolution and dynamics of fault controlled copper mineralization in the Mount Gordon Fault Zone, Mt Isa, Queensland, Australia*. Unpublished PhD thesis, James Cook University, 369pp.
- O'DEA, M. G. & LISTER, G. S. 1995. The role of ductility contrast and basement architecture in the structural evolution of the Crystal Creek Block, Mount Isa Inlier, NW Queensland, Australia. *Journal of Structural Geology*, **17**, 949–960.
- O'DEA, M. G., LISTER, G. S., BETTS, P. G. & POUND, K. S. 1997. A shortened intraplate rift system in the Proterozoic Mount Isa Terrane, NW Queensland, Australia. *Tectonics*, **16**, 425–441.
- OJALA, V. J. & NYKÄNEN, V. 2007. Palaeo-stress modeling of the Central Lapland Greenstone Belt: Implications for gold exploration. In: OJALA, V. J. (ed.) *Gold in the Central Lapland Greenstone Belt, Finland*. Geological Survey of Finland, Rovaniemi, Espoo, Special Paper, **44**, 225–250.
- OLIVER, N. H. S., BUTERA, K. M. ET AL. 2008. The protracted hydrothermal evolution of the Mount Isa Eastern Succession: a review and tectonic implications. *Precambrian Research*, **163**, 108–130.
- OLIVER, N. H. S., CLEVERLEY, J. S. M. G., POLLARD, P. J. F. B., MARSHALL, L. J. R. M. J. & WILLIAMS, P. J. B. T. 2004. Modeling the role of sodic alteration in the genesis of iron oxide–copper–gold deposits, eastern Mount Isa Block, Australia. *Economic Geology and the Bulletin of the Society of Economic Geologists*, **99**, 1145–1176.
- PERKINS, W. G. 1984. Mount Isa silica dolomite and copper orebodies: the result of a syntectonic hydrothermal alteration system. *Economic Geology*, **79**, 601–637.
- PERKINS, W. G. 1989. Mount Isa copper orebodies; evidence against a cogenetic relationship with lead–zinc. *Abstracts of Seminars on North Queensland Mineral Deposits, 1973–1988*, **5**, 15.
- PERKINS, W. G. 1990. Mount Isa copper orebodies. *Geology of the Mineral Deposits of Australia and Papua New Guinea*, **14**, 935–941.
- PERKINS, W. G. 1997. Mount Isa lead–zinc orebodies; replacement lodes in a zoned syndeformational copper–lead–zinc system? *Ore Geology Reviews*, **12**, 61–111.
- POTTS, G. J. & REDDY, S. M. 1999. Construction and systematic assessment of relative deformation histories. *Journal of Structural Geology*, **21**, 1245–1253.
- POTTS, G. J. & REDDY, S. M. 2000. Application of younging tables to the construction of relative deformation histories-1: fracture systems. *Journal of Structural Geology*, **22**, 1473–1490.

- RICHARDSON, S. M. & MOY, A. D. 1998. Gunpowder copper deposits. *Geology of Australian and Papua New Guinean mineral deposits*, **22**, 743–752.
- RUBENACH, M. J. 2005. Tectonothermal evolution of the Eastern Fold Belt, Mt Isa Inlier. In: BLENKINSOP, T. G. (ed.) *Total Systems Analysis of the Mount Isa Eastern Succession, I 2+3 Final Report*. Predictive Minerals Discovery Cooperative Research Centre.
- RUBENACH, M. J., FOSTER, D. R. W., EVINS, P. M., BLAKE, K. L. & FANNING, C. M. 2008. Age constraints on the tectonothermal evolution of the Selwyn Zone, Eastern Fold Belt, Mount Isa Inlier. *Precambrian Research*, **163**, 81–107.
- SCOTT, K. M. & TAYLOR, G. F. 1982. Eastern Creek Volcanics as the source of copper at the Mammoth Mine, northwest Queensland. *Journal of Australian Geology and Geophysics*, **7**, 93–98.
- SIBSON, R. H. 1977. Fault rocks and fault mechanisms. *Journal of the Geological Society, London*, **133**, 191–213.
- SIBSON, R. H. 1985. A note on fault reactivation. *Journal of Structural Geology*, **7**, 751–547.
- SIBSON, R. H. 1986. Brecciation processes in fault zones: inferences from earthquake rupturing. *Pure and Applied Geophysics*, **124**, 159–174.
- SIBSON, R. H. 1989. Earthquake faulting as a structural process. *Journal of Structural Geology*, **11**, 1–14.
- SIBSON, R. H. 1996. Structural permeability of fluid-driven fault-fracture meshes. *Journal of Structural Geology*, **18**, 1031–1042.
- SIBSON, R. H. 2000. Fluid involvement in normal faulting. *Journal of Geodynamics*, **29**, 469–499.
- SIBSON, R. H. 2001. Seismogenic framework for hydrothermal transport and ore deposition. In: RICHARDS, J. P. & TOSDAL, R. M. (eds) *Structural Controls on Ore Genesis. Reviews in Economic Geology*. Society of Economic Geologists, Littleton, CO, **14**, 25–47.
- STEWART, A. J. 1992. The role of thrusting in the structural development of the Mount Isa Mine and its relevance to exploration in the surrounding region; discussion. *Economic Geology and the Bulletin of the Society of Economic Geologists*, **87**, 1659–1664.
- SWAGER, C. P. 1985. Syndeformational carbonate-replacement model for the copper mineralization at Mount Isa, Northwest Queensland; a microstructural study. *Economic Geology and the Bulletin of the Society of Economic Geologists*, **80**, 107–125.
- SWAGER, C. P., PERKINS, W. G. & KNIGHTS, J. G. 1987. Stratabound phyllosilicate zones associated with syntectonic copper orebodies at Mt. Isa, Queensland. *Australian Journal of Earth Sciences*, **34**, 463–476.
- WILDE, A., JONES, P. A., GESSNER, K., AILLERES, L., GREGORY, M. J. & DUNCAN, R. 2006. A Geochemical Process Model for the Mount Isa Copper Orebodies. *Economic Geology*, **101**, 1547–1567.



# First-order splay faults: dip-slip examples

CHRISTOPHER H. SCHOLZ

Lamont-Doherty Earth Observatory, Columbia University, Palisades, NY 10964-1000,  
USA (e-mail: scholz@ldeo.columbia.edu)

**Abstract:** First-order splay faults are secondary faults that form at acute angles to the primary fault when the latter becomes critically misaligned with the direction of maximum principal stress. They are first order in the sense that their slip rate is of the same order as their primary fault. First-order splay faults have been previously described for strike-slip faults and examples are here shown of first-order dip-slip splay faults. For dip-slip faults in sedimentary sequences, friction is often anisotropic, being lower parallel to, rather than oblique to, bedding, and the position of the primary fault is often controlled by a décollement guided by a layer of particularly low friction or a structural feature. In this latter situation, the primary fault may become frictionally misaligned with the direction of maximum principal stress and first-order splay faults may then form. Examples shown are megasplays in subduction zones, ramp faults in fold and thrust belts, and synthetic and antithetic splays of low-angle normal faults.

Anderson (1951) proposed that faults form according to the Coulomb fracture criterion and, with the additional provision that the free surface is a principal plane, explained the optimum orientation of faults with respect to the principal stress directions and the Earth's surface. Implicit in his thesis, which employed a Mohr circle analysis, is that the orientations of the principal stresses are regionally uniform. This assumption has been validated by the World Stress Map Project, the main finding of which was: 'Stress orientations are remarkably uniform over broad regions (length scales up to thousands of kilometers), despite large changes in crustal geology, tectonic history, and crustal thickness' (Zoback & Zoback 2007, p. 254).

Sibson (1985, 1990) explored the conditions in which faults could remain active in orientations that are non-optimum with respect to the principal stress directions. Here we take the discussion further to ask the question: at what degree of misorientation of a fault will a new fault be expected to form, and what will be its orientation? This question is addressed in the Mohr diagram shown in Figure 1, in which there are two failure envelopes: a frictional one,  $\tau = \mu\sigma$ , that defines the criterion for slip on a pre-existing fault; and a Coulomb one,  $\tau = \tau_0 + \mu\sigma$ , that defines the conditions for forming a new fault in intact isotropic rock, where  $\tau_0$  is cohesion,  $\mu$  is friction and the friction angle  $\Psi = \tan^{-1}\mu$ . In this Figure 1,  $\tau$  is shear stress and  $\sigma$  is the effective normal stress; that is, the applied normal stress minus the pore pressure. By defining the axes this way, we incorporate any variations in pore pressures, such as those featured in the discussion of Sibson (1990).

As shown in the inset to Figure 1, as the old (primary) fault becomes misoriented in the stress

field, the stress difference ( $\sigma_1 - \sigma_3$ ) must increase so that the primary fault remains active. At a critical point, shown in the main part of Figure 1, a new fault forms at the optimum angle for faulting in the new stress field and at an angle,  $\alpha_0$ , to the primary fault. The new secondary fault formed in this way was called a 'first order splay fault' by Scholz *et al.* (2010) because, unlike splay faults that are formed in the stress concentration at the tip or other irregularities of the primary fault, these faults grow in the regional stress field and hence may be of the same order as the primary fault in terms of length and/or slip rate. Thus, these secondary faults are subsequent but not subordinate to the primary fault. Various ways in which the primary fault may become misaligned with the principal stress directions are described in Scholz *et al.* 2010.

Scholz *et al.* (2010) applied this analysis to strike-slip faults. Here we present several examples of first-order splay faults of the dip-slip type. Notice from Figure 1 that two types of primary fault misorientation can occur: H or L, which refer to high or low normal stress. The associated splays are referred to as H-splays and L-splays. In Figure 2 the four possibilities for dip-slip faults are shown: H- and L-splays for both thrust and normal faults, respectively, shown in the vertical section refer to the orientation of the maximum principal stress,  $\sigma_1$ .

In the case of strike-slip faults, Scholz *et al.* (2010) showed that the symmetry of L- and H-splays with respect to the San Andreas Fault requires that the friction angle,  $\Psi$ , be the same for sliding on the primary fault and for the formation of the splay faults, as in the case shown in Figure 1. They also showed that for a reasonable range of rock strength (cohesion) the angle,  $\alpha_0$ , between splay and primary should be in the range

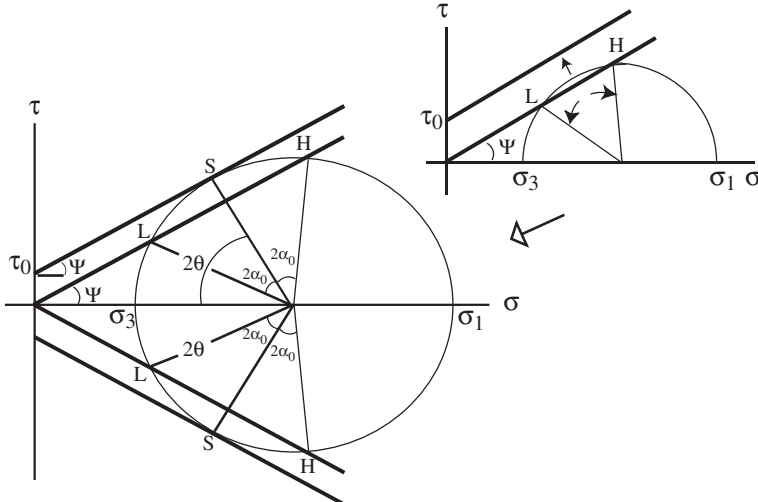
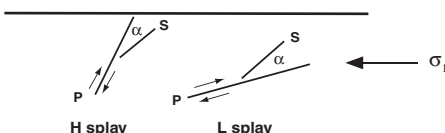


**Fig. 1.** A Mohr diagram with two failure criteria: a friction criterion for sliding on a pre-existing fault; and a Coulomb criterion for forming a new fault in an intact isotropic rock. The axes are  $\tau$ , shear stress, and  $\sigma$ , effective normal stress. The friction angle is  $\Psi = \tan^{-1} \mu$  and  $\tau_0$  is cohesion. The inset shows how the stress difference ( $\sigma_1 - \sigma_3$ ) for sliding increases as the primary fault rotates with respect to the stress axes. The main figure shows the condition for formation of a splay fault (S) at the optimum orientation,  $\theta$ . The splay fault is at an angle  $\alpha_0$  to the primary fault, which has an orientation denoted L or H, for low and high normal stress, respectively (from Scholz *et al.* 2010).

12°–22°. The situation for dip-slip faults in sedimentary sequences is more complex. In that case, the strength is likely to be anisotropic, with a lower strength on bedding planes than for cross-cutting planes. In particular, dip-slip faults are often found to be guided by beds of particularly low frictional strength: décollements. Décollements may also form at structural features such as subduction zone interfaces. This case is illustrated in Figure 3, where the primary fault is governed by a

lower frictional strength than that of a possible splay fault. The case illustrated is the one in which the primary fault, slipping at a lower friction angle,  $\Psi^*$ , is in the L position at which a splay forms on a fault with a higher friction angle,  $\Psi$ , at an angle,  $\alpha_0^*$ , to it. In this case, the angle,  $\alpha_0^*$ , will be greater than the value  $\alpha_0$  for the corresponding case of uniform friction, shown by the dashed line in Figure 3. In both cases, however, the angle  $\alpha_0$  or  $\alpha_0^*$  is less than the optimum angle,  $\theta$ , of the

#### (a) thrust fault case (vertical section)



#### (b) normal fault case (vertical section)

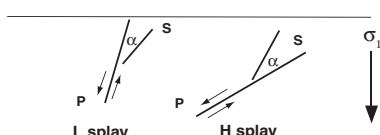


**Fig. 2.** Vertical section showing the configuration of the primary (P) and splay (S) faults. (a) Thrust faults. (b) Normal faults.

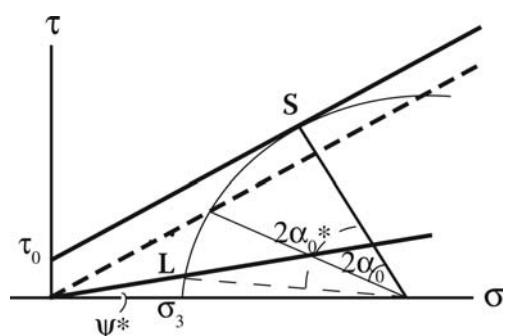


**Fig. 3.** Similar to Figure 1 except that the primary fault slips at a lower friction angle,  $\Psi^*$ , than the splay fault. The angle between the primary and splay,  $\alpha_0^*$ , is greater than  $\alpha_0$  for the case when the friction angle is the same (dashed line).

primary for all conditions in which  $\sigma_3 > 0$ . This ensures that the critical angle of the primary fault at splay formation will be less than the frictional lock-up angle,  $2\theta$  (Sibson 1985), so that both faults will be simultaneously active. This, in addition to the angular relationship of the faults, is an important criterion for recognizing first-order splay faults.

In the following sections, various examples of first-order splay faults of the dip-slip variety are presented as gleaned from the literature. There is no attempt to make an exhaustive list: these are simply a few cases that have been well studied and which show evidence for both primary and splay faults being simultaneously active.

## Thrust splay faults

### Subduction-zone mega-splays

These splays commonly occur above subduction-zone mega-thrusts. A seismic section across the Nankai Trough in SW Japan is shown in Figure 4 (modified slightly from Strasser *et al.* 2009). There a splay fault, termed a mega-splay, is developed above the subduction interface. This splay incurred major slip in the 1944  $M 8.1$  Tonankai earthquake (Baba *et al.* 2006) and is a long-lived feature, having been active for at least 1.5 Ma (Strasser *et al.* 2009).

This type of subduction-zone splay was first recognized by Plafker (1965) on Middleton Island following the 1964 Alaskan earthquake. They are common in subduction zones (Collot *et al.* 2008)

and, when active, are thought to be an important source of tsunamigenic earthquakes (Fukao 1979).

An analysis of accretionary prisms, such as that at Nankaido, using wedge-taper theory (Davis *et al.* 1983) shows that the friction coefficient of the basal décollement is about 0.1–0.2, whereas the friction for faults cutting the wedge is in the range 0.5–0.6 (Suppe 2007). This indicates that the configuration shown in Figure 3 is the appropriate one in this case.

For Nankaido, the average dip of the basal décollement where the splay is formed is  $7^\circ$ – $8^\circ$  and the dip of the splay fault is  $25^\circ$ – $30^\circ$  (both measured from the section in Fig. 4). Because in this case we can assume  $\sigma_1$  to be horizontal, the dip of the splay is approximately correct as the optimum angle of faulting for a friction coefficient of  $\mu = 0.6$ . However, assuming  $\mu = 0.1$ – $0.2$  for the basal shear, its optimal dip should be  $39^\circ$ – $42^\circ$ . The average dip of the mega-thrust rupture in the 1946  $M 8.3$  Nankaido earthquake was  $35^\circ$  (Fitch & Scholz 1971), which is in good agreement with that considering that the subduction interface is curved convex upwards and, hence, steepens down-dip. Because of this curvature, the interface dip decreases as the surface is approached, and at the point where the splay fault forms, it is misoriented by more than  $30^\circ$ , in the L direction, from its optimum orientation. This is an example in which the fault becomes misoriented in space, rather than in time, in contrast to the examples given in Scholz *et al.* (2010). Thus, at the point of formation of the splay, the stress state is like that shown in Figure 3, and the mega-splay is an L-splay.

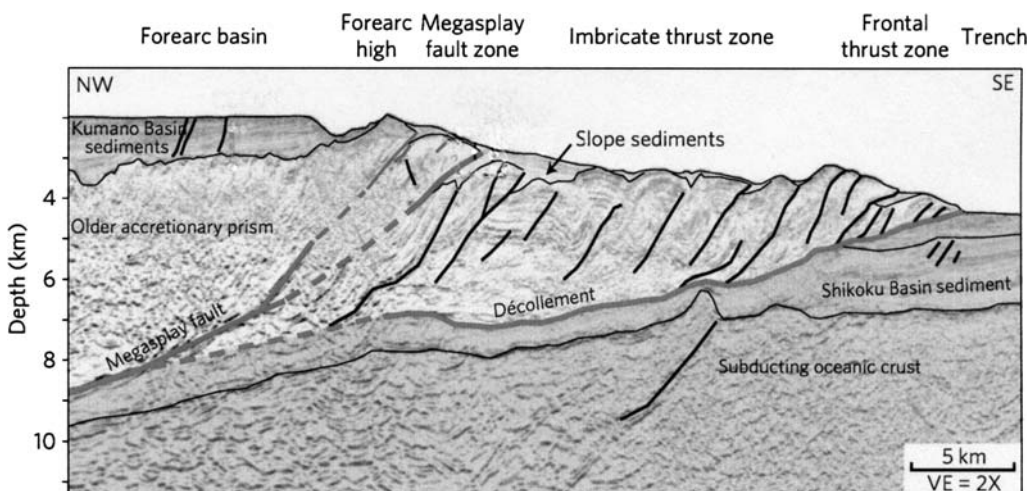


**Fig. 4.** Seismic cross-section of the Nankai Trough, showing the mega-splay fault and the décollement. Modified slightly from Strasser *et al.* (2009), reproduced with permission from Macmillan Publishers Ltd.

### Fold and thrust belts

The geometry of fold and thrust belts is similar to the upper part of subduction zones (Elliott 1976). They are characterized by a thrust-fault system that cuts up through the stratigraphic sequence in a series of ‘ramps’ – this is either in an imbricate series of ramps cutting up from a basal décollement or a staircase of ramps and bedding-plane controlled ‘flats’. In our terminology, the ramps are the splay faults and the décollements, or flats, the primary faults. These, like subduction zones, are often discussed in terms of critical-wedge theory in various forms (Hardy *et al.* 1998; Panian & Wiltzschko 2007). The low basal friction version (Fig. 3) is thus the more appropriate model in this case.

This case is very similar to the subduction case described earlier. The primary faults, whether they are basal décollements or flats, are highly misoriented with respect to  $\sigma_1$ , also horizontal in this case, and so the ‘ramps’ are L-splays.

Evidence for the simultaneous activity of a splay and primary fault of this type is given by the Chelengpu Fault in western Taiwan that ruptured in the  $M 7.6$  Chi-chi earthquake of 1999. The Chelengpu Fault, (Fig. 5) is a splay dipping  $20^\circ$  to the east. It soles into the Changhua Décollement, controlled by the Chinshui shales, which dips  $3^\circ E$  and slips aseismically (Simoes *et al.* 2007).

The splays in fold and thrust belts typically form imbricate series, in which the spacing between ramps is controlled by the thrust-sheet thickness, presumably so that each fault forms just outside the stress shadow of the previously formed fault (e.g. Hu & Evans 1989). The ramps form in sequence, which can be in either direction (Boyer & Elliott 1982). Strike-slip splays also, and for the same reason, form sequentially in evenly spaced systems (see Scholz *et al.* 2010 for a discussion of them).

### Normal-fault splays

#### Active low-angle normal faults

The Alto Tiberina Fault is a normal fault that dips  $15^\circ$ – $20^\circ$  to the NE beneath the Sansepolcro Basin

in central Italy (Barchi & Ciaccio 2009). Two synthetic splay faults, the Sovara and the Anghiari, both dip  $30^\circ$  to the NE and sole into it (SoF and AnF in Fig. 6). From geological and geomorphic evidence, all three of these faults are active. The Sovara and Anghiari faults both have seismicity associated with them (Chiaraluce *et al.* 2007) and GPS data indicate that the Alto Tiberina Fault is aseismically creeping (Hreinsdóttir & Bennett 2009). In this case, in which  $\sigma_1$  can be assumed to be vertical, the Alto Tiberina Fault is highly misoriented in the H direction, regardless of what friction is assumed for it. However, to be slipping at a dip of less than  $20^\circ$ , it must have a friction coefficient,  $\mu$ , of  $<0.35$  (as the fault angle must not exceed the lock-up angle  $2\theta$ , where  $\theta$  is the optimum angle: Sibson 1985). Another low-angle normal fault in the Northern Apenninic system has been shown to have a friction coefficient in the range 0.25–0.31 (Collettini *et al.* 2009), that results from its talc-rich phyllosilicate fault gouge. Thus, in this case too, Figure 3 is the appropriate one, and the splay faults are H-splays. Notice that for this stress state, we might also expect the formation of antithetic normal faults conjugate to the synthetic ones. This is represented by the Sansepolcro Fault (SnF), an antithetic normal fault that dips  $40^\circ$  to the SW. The shallow dips of these splay faults, however, are not consistent with the model unless they have been rotated subsequent to their formation. There is some evidence for this from tilted blocks within the basin (Barchi & Ciaccio 2009).

#### Crustal normal faults

In the  $M 7.5$  Hegben Lake, Montana, earthquake of 1959, two normal faults were activated within seconds of one another (Doser 1985). The first to rupture was the Red Canyon Fault, a normal fault that dips approximately  $45^\circ$  to the south, followed by rupture of the Hegben Lake Fault, a  $60^\circ$ – $70^\circ$  south-dipping normal fault in the hanging wall of the Red Canyon Fault and with a surface rupture 6 km to the south of the Red Canyon fault scarp. Doser (1985) offered two interpretations of the

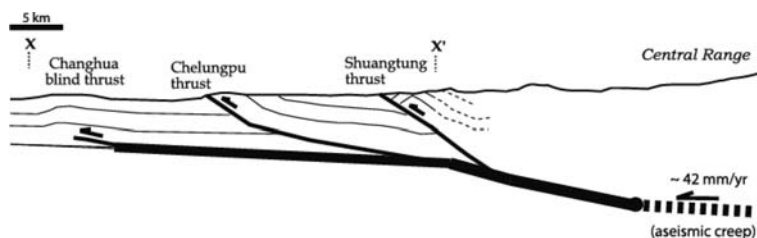


**Fig. 5.** Cross-section showing the Chelengpu Fault, Taiwan, which was ruptured in the  $M 7.6$  Chi-Chi earthquake of 1999, and the associated Changhua Décollement. Reproduced from Simoes *et al.* (2007), with permission.

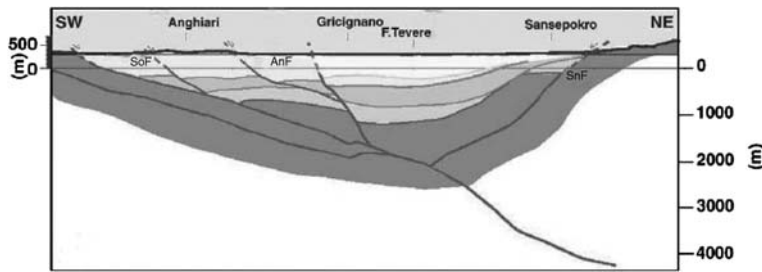


**Fig. 6.** Cross-section of the Sansepolcro Basin, central Italy, showing the basal low-angle normal fault, the Alto Tiberino Fault, its active synthetic splay faults, the Sovara (SnF) and Anghiari (AnF) faults, and the antithetic Sansepolcro Fault (SnF). Reproduced from Barchi & Ciacchio (2009), with permission.

data, shown in Figure 7 (after Bruhn & Schultz 1996). An interpretation of Figure 7a is that these are normal faults and the Hegben Lake Fault is an H-type splay of the Red Canyon Fault. There is ambiguity in this case, however. Both slip events may have occurred on reactivated Laramide thrusts (Doser 1985). In this case, one can interpret the model of Figure 7b as depicting thrust faults in which the Heggen Lake Fault is the primary fault and the Red Canyon Fault is an H-splay. In either case, both faults are simultaneously active, the slip sense is of normal faulting and the stress state must be that of the H-splay in Figure 2b.

## Discussion

The simple analysis presented shows not only why first-order splay faults develop at the orientations that they do but also why they and their associated primary faults are simultaneously active at

comparable slip rates in the same state of stress. In dip-slip cases, in which a weak layer or décollement often guides the primary fault, it can become misaligned with the  $\sigma_1$  direction for just that reason. In the case of thrust faulting, this leads to the common formation of mega-splays in subduction zones, and 'ramps' in fold and thrust belts, both of which are L-splays. In low-angle normal-fault settings, this leads to synthetic and antithetic splays, both being H-splays.

There are many ways in which faults may become unfavourably orientated. Various possibilities have been described by Scholz *et al.* (2010) for the case of strike-slip faults and by Sibson (1990) for dip-slip faults. These range from auto-rotation (dominoing) to external changes in the tectonic regime. Further discussion of these is beyond the purview of this paper. We make two points: (1) at a critical stage of misalignment of a fault, a first-order splay fault will be formed at an acute angle

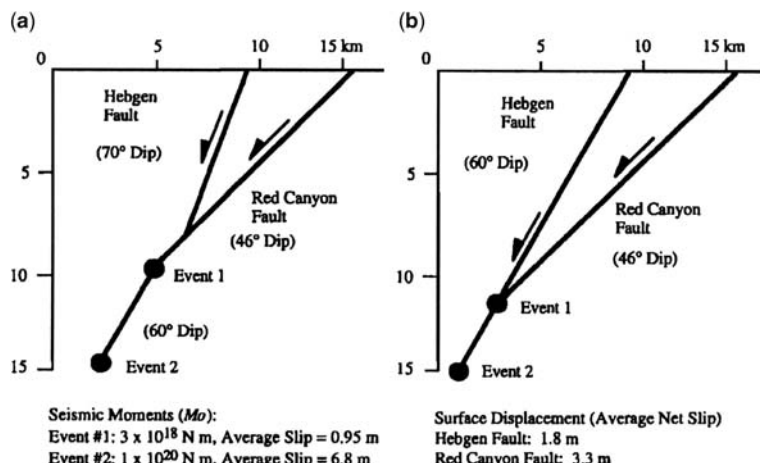


**Fig. 7.** Two interpretations by Doser (1985) of the two ruptures of the  $M = 7.5$  Hegben Lake, Montana, earthquake of 1959. Reproduced from Bruhn & Schultz (1996), with permission.

to the primary fault; and (2) this will, in all but a special case, occur prior to frictional lock-up of the primary fault, so that both faults are simultaneously active within the same stress state.

I thank R. Ando, B. Shaw and L. Seeber for useful discussions, and C. Collettini for a helpful review of the manuscript.

## References

- ANDERSON, E. M. 1951. *The Dynamics of Faulting*. Oliver & Boyd, Edinburgh.
- BABA, T., CUMMINS, P. R., HORI, T. & KANEDA, Y. 2006. High precision slip distribution of the 1944 Tonankai earthquake inferred from tsunami waveforms: possible slip on a splay fault. *Tectonophysics*, **426**, 119–134.
- BARCHI, M. R. & CIACCIO, M. G. 2009. Seismic images of an extensional basin, generated at the hanging-wall of a low-angle normal fault: the case of the Sansepolcro basin (Central Italy). *Tectonophysics*, **479**, 285–293.
- BOYER, S. E. & ELLIOTT, D. 1982. Thrust systems. *Bulletin of the American Association of Petroleum Geologists*, **66**, 1196–1230.
- BRUHN, R. L. & SCHULTZ, R. A. 1996. Geometry and slip distribution in normal fault systems: implications for mechanics and fault-related hazards. *Journal of Geophysical Research – Solid Earth*, **101**, 3401–3412.
- CHIARALUCE, L., CHIARABBA, C., COLLETTINI, C., PICCININI, D. & COCCO, M. 2007. Architecture and mechanics of an active low-angle normal fault: Alto Tiberina Fault, northern Apennines, Italy. *Journal of Geophysical Research – Solid Earth*, **112**, B12399, doi: 10.1029/2007JB005471.
- COLLETTINI, C., NIEMEIJER, A., VITI, C. & MARONE, C. 2009. Fault zone fabric and fault weakness. *Nature*, **462**, 907–910.
- COLLOT, J. Y., AGUDELO, W., RIBODETTI, A. & MARCAILLOU, B. 2008. Origin of a crustal splay fault and its relation to the seismogenic zone and underplating at the erosional north Ecuador–south Colombia oceanic margin. *Journal of Geophysical Research – Solid Earth*, **113**, B12102, doi: 10.1029/2008JB005691.
- DAVIS, D., DAHLEN, F. A. & SUPPE, J. 1983. Mechanics of fold-and-thrust belts and accretionary wedges. *Journal of Geophysics Research*, **88**, 1153–1172.
- DOSER, D. I. 1985. Source parameters and faulting processes of the 1959 Hebgen Lake, Montana, earthquake sequence. *Journal of Geophysical Research – Solid Earth and Planets*, **90**, 4537–4555.
- ELLIOTT, D. 1976. Motion of thrust sheets. *Journal of Geophysical Research*, **81**, 949–963.
- FITCH, T. J. & SCHOLZ, C. H. 1971. Mechanism of underthrusting in southwest Japan: a model of convergent plate interactions. *Journal Geophysics Research*, **76**, 7260–7292.
- FUKAO, Y. 1979. Tsunami earthquakes and subduction processes near deep-sea trenches. *Journal Geophysics Research*, **84**, 2303–2314.
- HARDY, S., DUNCAN, C., MASEK, J. & BROWN, D. 1998. Minimum work, fault activity and the growth of critical wedges in fold and thrust belts. *Basin Research*, **10**, 365–373.
- HREINSDOTTIR, S. & BENNETT, R. A. 2009. Active aseismic creep on the Alto Tiberina low-angle normal fault, Italy. *Geology*, **37**, 683–686.
- HU, M. S. & EVANS, A. G. 1989. The cracking and decohesion of thin-films on ductile substrates. *Acta Metallurgy*, **37**, 917–925.
- PANIAN, J. & WILTSCHKO, D. 2007. Ramp initiation and spacing in a homogeneous thrust wedge. *Journal of Geophysical Research – Solid Earth*, **112**, B05417, doi: 10.1029/2004JB003596.
- PLAFKER, G. 1965. Tectonic deformation associated with 1964 Alaska earthquake – earthquake of 27 March 1964 resulted in observable crustal deformation of unprecedented areal extent. *Science*, **148**, 1675–1689.
- SCHOLZ, C. H., ANDO, R. & SHAW, B. E. 2010. The mechanics of first order splay faulting: the strike-slip case. *Journal of Structural Geology*, **32**, 118–126.
- SIBSON, R. H. 1985. A note on fault reactivation. *Journal of Structural Geology*, **7**, 751–754.
- SIBSON, R. H. 1990. Rupture nucleation on unfavorably oriented faults. *Bulletin of the Seismological Society of America*, **80**, 1580–1604.
- SIMOES, M., AVOUAC, J. P. & CHEN, Y. G. 2007. Slip rates on the Chelungpu and Chushiang thrust faults inferred from a deformed strath terrace along the Dungpuna river, west central Taiwan. *Journal of Geophysical Research – Solid Earth*, **112**, B03S10, doi: 10.1029/2005JB004200.
- STRASSER, M., MOORE, G. F. ET AL. 2009. Origin and evolution of a splay fault in the Nankai accretionary wedge. *Nature Geoscience*, **2**, 648–652.
- SUPPE, J. 2007. Absolute fault and crustal strength from wedge tapers. *Geology*, **35**, 1127–1130.
- ZOBACK, M. L. & ZOBACK, M. D. 2007. Lithospheric stress and deformation. In: WATTS, A. B. & SCHUBERT, G. (eds) *Earthquake Seismology*. Treatise on Geophysics, **6**. Elsevier, Amsterdam, 253–274.

# The scope of earthquake geology

RICHARD H. SIBSON

*Department of Geology, University of Otago, PO Box 56, Dunedin 9054, New Zealand  
(e-mail: rick.sibson@otago.ac.nz)*

**Abstract:** Earthquakes give rise to three principal effects – fault rupture (with subsidiary fracturing), ground shaking from wave propagation, and stress ( $\pm$  fluid-pressure) changes – that influence a wide range of geological processes at varying distances from the source. Many intermittent events are recognizable in the geological record (e.g. an individual turbidite bed in a flysch sequence; renewal of fracture permeability followed by hydrothermal precipitation) and are potentially attributable to seismic events, but positive identification of an earthquake as the cause is often difficult. Earthquake Geology has grown enormously as a discipline since the advent of palaeoseismic techniques for dating prehistoric fault ruptures as an aid to hazard assessment, but has largely focused on surface processes. There is a need to expand our concept of Earthquake Geology to include subsurface as well as surface effects in the full gamut of tectonic settings. The likelihood is that many Earth processes that have hitherto been considered smooth and progressive are, in fact, intermittent and tied to the seismic stress cycle that is integral to deformation in the Earth's crust and lithosphere.

Earthquake Geology evolved as a discipline over the past 40 years largely through the development of palaeoseismology as a technique for hazard assessment (e.g. Sieh 1978, 1984). As a consequence, there is now a tendency to equate Earthquake Geology solely with palaeoseismological investigations (McCalpin 1996), but its scope is really much broader. Earthquake effects are increasingly recognized as being involved in a wide range of geological processes (Yeats *et al.* 1997; Burbank & Anderson 2001). This note outlines the potential for a broader appreciation of Earth processes coupled to earthquake activity.

Early field studies revealed a great deal about the macroseismic effects produced by shallow crustal earthquakes (e.g. Mallett 1862) but the development of instrumental seismology in the late 19th century and the powerful insights arising from its application meant that earthquakes increasingly were studied remotely by physicists, mathematicians and engineers. Seismicity maps dating from that period resemble shotgun patterns at the local scale with no clear links to individual geological structures, although the major Circum-Pacific and Alpine–Asiatic belts were defined. Lyell (1868) gave the first clear attribution of a large earthquake – the 1855  $M_c$  8 rupture on the West Wairarapa Fault in New Zealand – to incremental movement on an existing fault (Sibson 2006). Documentation of surface faulting accompanying major earthquakes also occurred for the 1891 Nobi earthquake in Japan (Koto 1893) and for the 1906 San Francisco, California, earthquake (Lawson 1908). From a geodetic analysis of strain relief associated with this major strike-slip rupture, Reid (1908)

identified ‘elastic rebound’ as the likely causative mechanism for earthquakes.

We now know from seismology, geodesy and field investigations that the vast majority of earthquakes result from increments of shearing displacement on faults, and that detailed maps of surface ruptures can yield useful information on rupture complexity and subsidiary fracturing (e.g. Ambreys & Tchalenko 1969). Occasional ‘non-double-couple’ events are recognized but are comparatively rare (Julian *et al.* 1998). Moreover, through empirical scaling relationships (Wells & Coppersmith 1994), rupture dimensions and the likely slip may be approximately related to earthquake magnitude (see Table 1 below). It is also apparent for some, but not all, seismic zones that earthquake rupturing accounts for a large proportion of tectonic displacement in the upper crust (Jackson & McKenzie 1988).

In a ‘standard’ earthquake, the duration of slip at a point on the fault,  $T_s$ , ranges up to 10 s or so. Over the past decade it has become apparent that these ‘standard’ earthquakes lie at the fast end of a broad spectrum of fault slip behaviour extending down to completely steady aseismic creep at measured rates of  $1\text{--}100 \text{ mm year}^{-1}$  where  $T_s \rightarrow \infty$  (Peng & Gomberg 2010). Aside from fault creep events ( $10^3 < T_s < 10^6$  s) and major earthquake afterslip ( $10^6 < T_s < 10^8$  s), a plethora of slow-slip modes have now been recognized – low frequency earthquakes (LFE), very low frequency earthquakes (VLF,  $10 < T_s < 100$  s), slow-slip events (SSE,  $10^5 < T_s < 10^7$  s), and episodic tremor and slip (ETS,  $10^6 < T_s < 10^7$  s) (Ide *et al.* 2007; Rubinstein *et al.* 2010). Our principal focus

**Table 1.** Approximate source parameters for different magnitude earthquakes, with average stress drop (3 MPa) over a circular rupture ( $L = W$ ), plus estimates of their relative frequency (where  $N$  is the number of events per year) within a seismically active region

Magnitude of $M_w$	Average slip	Length ( $L$ ) = width ( $W$ )	Area ( $A$ )	Relative frequency
9	c. 10 m	c. 300 km	c. $10^5 \text{ km}^2$	0.001 $N$
8	c. 3 m	c. 100 km	c. $10^4 \text{ km}^2$	0.01 $N$
7	c. 1 m	c. 30 km	c. $10^3 \text{ km}^2$	0.1 $N$
6	c. 30 cm	c. 10 km	c. $100 \text{ km}^2$	$N$
5	c. 10 cm	c. 3 km	c. $10 \text{ km}^2$	10 $N$
4	c. 3 cm	c. 1 km	c. $1 \text{ km}^2$	$10^2 N$
3	c. 1 cm	c. 300 m	c. $10^5 \text{ m}^2$	$10^3 N$
2	c. 3 mm	c. 100 m	c. $10^4 \text{ m}^2$	$10^4 N$
1	c. 1 mm	c. 30 m	c. $10^3 \text{ m}^2$	$10^5 N$
0	c. 0.3 mm	c. 10 m	c. $10^2 \text{ m}^2$	$10^6 N$
-1	c. 0.1 mm	c. 3 m	c. $10 \text{ m}^2$	$10^7 N$

This table may be extended downwards

here, however, is on the effects associated with ‘standard’ crustal earthquakes, although reference is made locally to some of these other fault slip modes.

### Seismogenic zones

Earthquake activity is concentrated at plate boundaries in both continental and oceanic lithosphere (Isacks *et al.* 1968) with intraplate events diffusely distributed over broad areas, especially in areas of continental collision. Notably, the plate boundaries are sites of active mountain building and sedimentation with slopes and sediment accumulations critically organized at the edge of failure, highly susceptible to disruption by fault rupture and earthquake shaking.

Modern seismograph networks have vastly improved the precision of earthquake locations, particularly the depth distribution of microseismicity, which can be employed to define seismogenic zones in different settings. Deformation textures and microstructures of fault rocks, coupled with laboratory rock deformation experiments, have been used to construct rheological models of crustal fault zones that do much to explain the depth distribution of earthquake activity in different tectonic regimes and the gross mechanical behaviour of fault zones (Sibson 1983; Handy *et al.* 2007; Bürgmann & Dresen 2008). Further refinement of these fault-zone models is a major endeavour for Earthquake Geology but is not considered further because the focus here is on the geological effects of a single earthquake.

In terms of depth distribution related to tectonic setting, four principal categories of earthquake activity can be recognized (Fig. 1).

### Continental seismogenic zone

Along active margins with moderate–high heat flow away from subduction interfaces – for example, Japan (Ito 1999; Shibazaki *et al.* 2008) and southern California (Nazareth & Haucksson 2004) – the depth of microseismic activity is largely restricted to the upper 10–20 km. Larger ruptures also appear to be confined within the same upper-crustal seismogenic zone (Fig. 2). Temperatures at the base of this zone are inferred to range from 350 to 450 °C, corresponding to the onset of low- to mid-greenschist-facies metamorphic conditions (Sibson 1984). Note, however, that low-frequency earthquakes and tremor have now been recognized in the vicinity of the Moho below the San Andreas Fault near Parkfield (Shelly 2010) and beneath the 2000  $M_w$  6.7 Western Tottori earthquake sequence in central Honshu (Ohmi *et al.* 2004), at about twice the depth of the crustal seismogenic zone. This activity appears to indicate local quasi-brittle failure in downward continuations of the strike-slip faults through what would generally be regarded as the ductile regime (Fig. 2).

In colder continental crust intraplate activity extends to greater depth and in ancient continental lithosphere earthquakes occasionally occurs in the very deep crust, with activity apparently bounded by the 600 °C isotherm (Maggi *et al.* 2000; McKenzie *et al.* 2005).

### Oceanic seismogenic zone

In the ocean basins seismic activity extends through the crust into the upper mantle, progressively deepening away from spreading ridges, and is also apparently bounded by the 600 °C isotherm (McKenzie *et al.* 2005; Géli & Sclater 2008). For

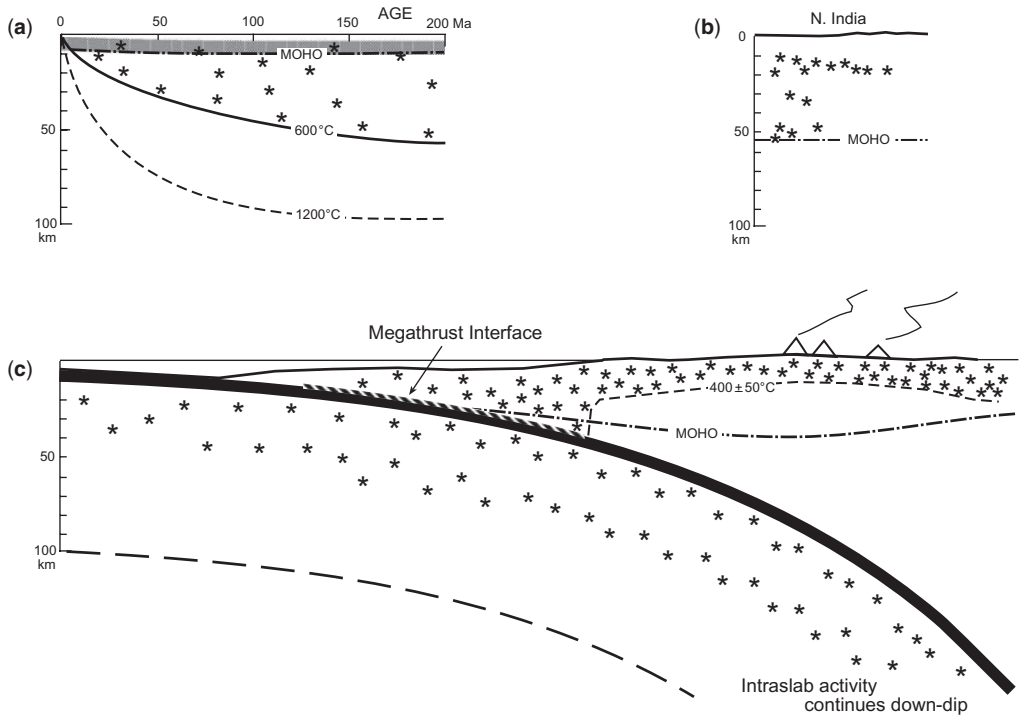


**Fig. 1.** Seismogenic zones (stars, earthquake foci) in different tectonic settings. (a) Cartoon illustrating the control of seismic activity by the 600 °C isotherm progressively deepening with age (or distance from a spreading ridge) to extend below the crust (shaded band) in oceanic lithosphere (after McKenzie *et al.* 2005). (b) Depth distribution (schematic) of earthquakes in the cratonic shield of north India below the Ganges Basin (after Maggi *et al.* 2000). (c) Cartoon illustration of earthquake depth distribution within the magmatic arc of NE Honshu (after Shibazaki *et al.* 2008) and in the subducting lithosphere below the island arc (after Zhao *et al.* 2009).

lithosphere less than approximately 30 Ma old, earthquakes are confined to depths of less than 15–20 km, but activity deepens to roughly 40 km for 100 Ma or older lithosphere.

#### Transcrustal megathrust interface

The largest earthquakes known occur along low-dipping transcrustal megathrust interfaces at continent–ocean convergent margins (e.g. the 1960  $M_w$  9.5 Chile, 1964  $M_w$  9.2 Alaskan and 2004  $M_w$  9.2 Sumatra earthquakes). These huge ruptures extend along strike for up to 1000 km or more, and down-dip for perhaps 100–200 km (Hyndman 2007). The same megathrust structures are responsible for most of the great earthquakes ( $M_w > 8$ ) that occur on Earth. Subsidiary seismicity adjacent to such megathrust interfaces also extends through the full depth of continental crust because of the refrigerating effect of subduction (Shibazaki *et al.* 2008). Concentrations of slow-slip events (VLFs, LFEs, tremor) occur along the base of the locked portion of the subduction interface that

gives rise to great megathrust earthquakes (Obara 2002; Peng & Gomberg 2010; Rubinstein *et al.* 2010).

#### Earthquakes within subducting lithosphere

Earthquakes in subducting lithosphere occur to maximum depths approaching 700 km. Although most have only a limited effect at the surface, occasional large events do occur with energy channelled upwards along the cold subducting slab that acts as a wave guide. Examples include the hugely damaging 1977  $M_w$  7.1 Vrancea earthquake at a depth of about 90 km below Romania (Fan *et al.* 1998), and the 1994  $M_w$  8.3 earthquake that occurred at a depth of roughly 640 km below Bolivia (Silver *et al.* 1995). Shear failure at such depths is unlikely to result from simple brittle–frictional instability and the responsible mechanisms remain contentious. Possibilities include dehydration embrittlement, plastic instabilities, shear-induced melting, polymorphic phase transformations and instabilities accompanying recrystallization (Frohlich 2006).

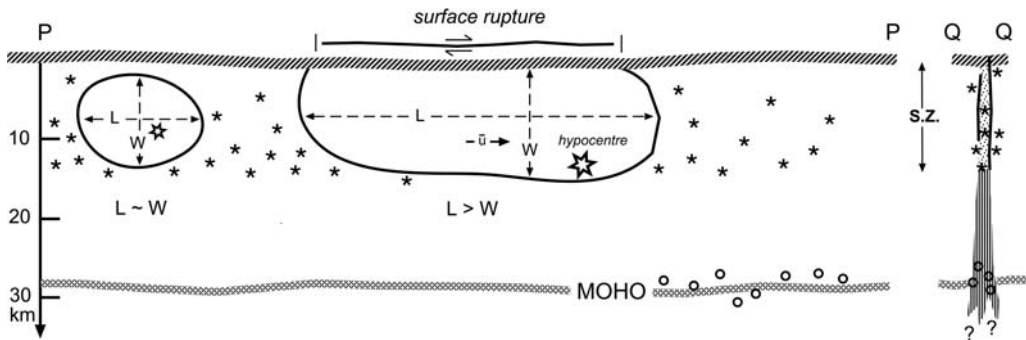


**Fig. 2.** Cartoon profiles of a strike-slip fault zone parallel to strike ( $P-P'$ ) and across strike ( $Q-Q'$ ) based loosely on the San Andreas Fault near Parkfield (after Shelly 2010), illustrating the difference between small ( $L \sim W$ ) and large ( $L > W$ ) earthquake ruptures with average slip,  $\bar{u}$ , occupying an upper-crustal seismogenic zone (S.Z.) defined by microearthquake activity (asterisks). Open circles denote LFEs and tremor events.

### Earthquake size and source parameters

Geometric source parameters for an earthquake include the rupture length along strike,  $L$ , the down-dip rupture width,  $W$ , the rupture area,  $A \approx LW$ , and the mean slip averaged over the rupture area,  $\bar{u}$  (Fig. 2). Seismic moment, defined as  $M_o = G\bar{u}A = G\bar{u}LW$ , where  $G$  is the elastic shear modulus, is now widely employed to define earthquake size and forms the basis of a moment-derived magnitude scale,  $M_w$  (Hanks & Kanamori 1979). This relationship holds because of the near constancy (to within about an order of magnitude) of the shear-stress drop accompanying rupturing, with most estimates for moderate–large earthquakes lying in the range  $1 < \Delta\tau < 10$  MPa (Kanamori & Anderson 1975) and outliers restricted to  $0.3 < \Delta\tau < 50$  MPa (Allman & Shearer 2009).

These relationships are used to estimate ‘typical’ source parameters associated with earthquakes of different magnitude, assuming a simple circular rupture and  $G = 3 \times 10^{10}$  N m $^{-2}$  (Table 1). Because of the variance in actual stress drops, the quoted values should only be regarded as very approximate guides. Maximum slip will be about twice the average value quoted. Depending on the dip of the fault, rupture width may be constrained by the depth of the seismogenic zone (Fig. 2), which leads to a change in the scaling relationships (see Scholz 2002 for an extended discussion). Suffice it to say here that when earthquake ruptures are confined within a thin upper-crustal seismogenic zone,  $M_w > 6$  ruptures on steeply dipping faults are likely to have along-strike rupture lengths significantly greater than for the circular model (Fig. 2). The relative frequency of different size events is also shown in Table 1. While the precise form of the frequency–magnitude relationship varies from one seismically active region to another, earthquake

frequency generally increases by about a factor of 10 for every unit decrease in magnitude ( $b$  value = 1). New Zealand, for example, typically experiences about one  $M_w 6$  earthquake per year and the frequency of different magnitude events scales accordingly.

### Earthquake recurrence

Palaeoseismic investigations (e.g. McCalpin 1998) show that recurrence intervals between successive large earthquakes along a fault segment agree broadly with expectations from Wallace’s (1970) recurrence equation:

$$\text{R.I.} = \bar{u}_c / (\nu_{\text{t.a.}} - \nu_{\text{aseis.}}) \quad (1)$$

where R.I. is the recurrence interval,  $\bar{u}_c$  is the ‘characteristic’ slip for the fault segment,  $\nu_{\text{t.a.}}$  is the time-averaged slip-rate and  $\nu_{\text{aseis.}}$  is any aseismic contribution to the slip-rate (commonly negligible). Along plate-boundary fault segments with time-averaged slip rates of 10–100 mm year $^{-1}$ , recurrence intervals between major earthquakes ( $M_w > 7$ ) with  $\bar{u} > 1$  m are typically tens to hundreds of years. For second-order fault structures with slip rates of 1–10 mm year $^{-1}$ , recurrence intervals between successive large earthquakes are typically hundreds to thousands of years. Recurrence intervals on recognized active faults in intraplate areas may approach 10 000 years or more.

### Physical conditions of failure within the seismogenic zone

Temperature exerts a primary control on the depth of the seismic activity, its lower boundary being defined by a temperature ( $T$ ) of around 600 °C in

oceanic lithosphere and 350–450 °C in quartz-feldspathic continental crust. Within this seismogenic zone, fault strength and stability appear to be largely governed by a criterion of Coulomb form whereby the shear strength of a planar discontinuity is:

$$\tau = c + \mu_s \sigma'_n = c + \mu_s (\sigma_n - P_f) \quad (2)$$

where  $c$  is the intrinsic cohesion of the discontinuity,  $\mu_s$  is the coefficient of static friction with typical values  $0.6 < \mu_s < 0.85$  (Byerlee 1978),  $P_f$  is the pore-fluid pressure and  $\sigma_n$  is the normal stress across the discontinuity (Scholz 2002). Note that shear failure may be induced by raising shear stress or lowering normal stress (stress-driven failure), but also by raising fluid pressure (fluid-driven failure).

There is an enduring debate over the level of shear stress driving fault failure within the seismogenic zone – whether  $\tau$  is approximately 100 MPa or so at the 10–15 km nucleation depth of large ruptures or  $\tau$  approximately 10 MPa or so, comparable with the larger shear-stress drops accompanying rupture (see the review by Brune & Thatcher 2002). The first range is compatible with the ‘hydrostatic-Byerlee’ stress state measured in deep boreholes within cratonic areas, consistent with stress levels being governed by the frictional strength of optimally oriented faults possessing ‘Byerlee’ friction under hydrostatic fluid pressure (Townend & Zoback 2000). The second low-stress inference comes from the lack of observable frictional heating on fast-moving plate-boundary faults, coupled with continued activity of major transform faults at high angles to regional trajectories of maximum compressive stress (Townend & Zoback 2004).

Critical to this debate is the fluid pressure state within the continental seismogenic zone and its effect on the fault strength profile (Fig. 3). If hydrostatic pore-fluid pressures and ‘Byerlee’ friction prevail throughout the seismogenic zone, shear-stress levels will approach 100 MPa or so at nucleation depths for large ruptures. On the other hand, if fluid pressure increases progressively (or through a succession of overpressured compartments) to near-lithostatic values under the greenschist metamorphic conditions prevailing around the base of the seismogenic zone, the average shear resistance is reduced and the peak in the shear resistance profile moves to shallower depths. Such a circumstance is especially likely in compressional settings capable of ‘holding in’ overpressure; one example being NE Honshu where intense upper-crustal seismic activity occurs right across the magmatic arc overlying subducting and dehydrating oceanic

lithosphere (Hasegawa *et al.* 2005; Sibson 2009; Zhao *et al.* 2009).

## Earthquake effects

Three principal earthquake effects can be recognized: (1) the nucleation and growth of a rupture, usually along an existing fault; (2) ground shaking from the elastic waves radiated by the propagating rupture; and (3) changes in the local stress state (and fluid pressure) resulting from the increment of fault slip. Provisional lists of subsidiary geological processes associated with these three principal effects are given in Table 2. Note that while some of the effects are essentially coseismic, taking place during rupture propagation (generally <1–10 min) and the spread of seismic waves across the Earth (<1 h), others (e.g. fluid redistribution (Pelzer *et al.* 1996) or viscous relaxation of the lower crust and mantle (Freed & Bürgmann 2004)) are post-seismic and probably coincident with the aftershock period (<days, months or years depending on mainshock size). As an example, consider the enormous 2004  $M_w$  9.2 Sumatra–Andaman megathrust earthquake with a rupture dimension of approximately 1500 km (Lay *et al.* 2005; Shearer & Bürgmann 2010), which produced measureable static displacements at up to 5000 km from the source, perturbed fault-zone properties (Taira *et al.*

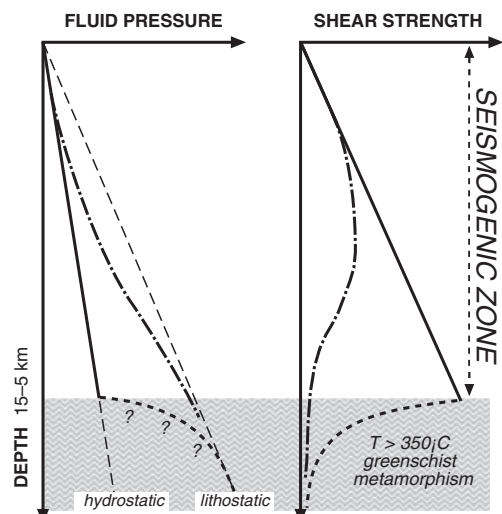


**Fig. 3.** Effect of fluid overpressuring on fault strength. The solid line represents hydrostatic fluid pressure and the associated frictional shear-strength profile throughout the seismogenic zone; dash-dot line represents the progressive transition to the near-lithostatic fluid pressure plus associated strength profile.

2009), and dynamically triggered tectonic and volcanic swarm activity (West *et al.* 2005; Velasco *et al.* 2008) on the opposite side of the globe, whilst emplacing tsunami deposits around the periphery of the Indian Ocean (Moore *et al.* 2006) – a demonstration of just how far-reaching the effects of a single giant earthquake can be.

### Fault rupture

Only rarely does fault rupture involve shear failure of intact crust or lithosphere; significant earthquakes generally involve the reshear of all or part of an existing fault surface as a consequence of frictional stick-slip instability (Scholz 2002). Following nucleation, the rupture expands over the fault surface from the hypocentre commonly at rates approaching the seismic shear wave velocity of around  $3 \text{ km s}^{-1}$ . Rupture propagation may be

unilateral, bilateral or omnidirectional. At any one place on the fault, the slip increment is usually accomplished in 1–10 s, a typical slip rate being of the order of approximately  $1 \text{ m s}^{-1}$ . Characteristic shear displacements for different magnitude earthquakes are listed in Table 1. Shear displacements range up to tens of metres for subduction megathrust earthquakes but only rarely exceed 10 m for the largest intracontinental earthquakes (Rodgers & Little 2006). Tectonic and geomorphic changes are manifested in the incremental growth of mountains and individual fold structures, in regional tilt increments and in the subsidence of sedimentary basins (Burbank & Anderson 2001). Slip increments are recorded within the causative fault zone by episodes of predominantly cataclastic fault-rock deformation (Sibson 1986; Isaacs *et al.* 2008) and by subsidiary fracturing extending into the wall rocks that continues through the aftershock period. Modern

**Table 2.** Earthquake effects

EARTHQUAKE		
Ground Shaking (wave propagation)	Fault Rupture	Stress Change ( $\Delta\tau$ , $\Delta\sigma_m$ , $\Delta P_f$ )
<b>Mass movement</b> <ul style="list-style-type: none"> <li>• landslides</li> <li>• rockfalls</li> <li>• avalanches</li> <li>• submarine slumping</li> </ul>	<b>Tectonic increments</b> <ul style="list-style-type: none"> <li>• mountain building</li> <li>• basin subsidence</li> <li>• regional tilting</li> <li>• tsunami generation</li> </ul>	<b>Shear-stress drop</b> <ul style="list-style-type: none"> <li>• coupled changes in other stress components</li> <li>• poroelastic effects</li> </ul>
<b>Sedimentation</b> <ul style="list-style-type: none"> <li>• debris flows</li> <li>• turbidites</li> <li>• seismites</li> <li>• tsunami deposits</li> </ul>	<b>Deformation</b> <ul style="list-style-type: none"> <li>• fault slip and growth</li> <li>• fault-rock deformation</li> <li>• subsidiary fracturing</li> <li>• fold growth</li> <li>• dynamic metamorphism</li> </ul>	<b>Redistribution of stress-strain heterogeneities</b> <b>Fluid redistribution</b> (diagenetic, hydrothermal, hydrocarbon, magmatic and metamorphic fluids) <ul style="list-style-type: none"> <li>• hydrothermal flow and mineral deposition</li> <li>• oil-gas migration</li> </ul>
<b>Consolidation</b> <ul style="list-style-type: none"> <li>• compaction</li> <li>• liquefaction</li> <li>• lateral spreading</li> <li>• changes in fracture permeability</li> </ul>	<b>Landscape evolution</b> <ul style="list-style-type: none"> <li>• scarp formation</li> <li>• river incision</li> <li>• coastal change</li> <li>• ponding</li> </ul>	<b>by</b> <ul style="list-style-type: none"> <li>• ‘fault-valve’ action from overpressured crust</li> <li>• ‘dilatancy pumping’ from mean-stress cycling</li> <li>• ‘suction-pump’ action at dilational stepovers</li> </ul>
<b>Far-field triggering</b> <ul style="list-style-type: none"> <li>• swarm activity</li> <li>• volcanic unrest</li> <li>• geyser perturbation</li> </ul>	<b>Tsunami generation</b> <ul style="list-style-type: none"> <li>• tsunami propagation</li> </ul>	<b>Near-field triggering</b> <ul style="list-style-type: none"> <li>• aftershocks</li> <li>• geysering</li> </ul>

remote-imaging techniques are revealing the extent of this coseismic subsidiary deformation and its time-dependent recovery (e.g. Fielding *et al.* 2009).

Relating deformation features in exhumed fault zones to different stages of the earthquake stress cycle, particularly distinguishing fast seismic from slow aseismic cataclastic deformation, remains a challenge, although progress has been made. At a typical seismic slip rate of  $1 \text{ m s}^{-1}$ , average kinetic shear resistances of, respectively, 10 and 100 MPa lead to power dissipation at 10 and 100 MW  $\text{m}^{-2}$  over the fault surface, implying dramatic increases in temperature if slip is well localized. Fault-hosted pseudotachylite friction-melt is an unequivocal diagnostic of localized coseismic slip, but its seeming scarcity in exhumed fault zones raises the issue of whether it is rare because of low preservation potential as a consequence of cataclastic overprinting and hydrothermal alteration or whether dynamic weakening processes (e.g. acoustic fluidization, thermal pressurization, hydrodynamic lubrication or interface separation) reduce shear resistance during slip and inhibit friction-melting (Sibson & Toy 2006). Are there other diagnostics of deformation resulting from a seismic slip episode? For example, Boutareaud *et al.* (2008) have suggested that rounded clay-clast aggregates developed during dynamic friction experiments may be diagnostic of seismic slip in natural clay-rich fault gouges. Are clastic dykes of gouge leading off fault surfaces diagnostic of transient thermal pressurization of pore fluids during seismic slip? Are incrementally cemented high-dilation wall-rock breccias at dilatational stepovers necessarily the product of hydraulic implosion arising from fluid pressure imbalances created by seismic slip (Sibson 1986)? Combining field studies of exhumed fault-rock assemblages with dynamic friction experiments (e.g. Di Toro *et al.* 2006) is a promising avenue for research into the macro- and microstructural characteristics of deformation products of various postulated slip processes. This whole area of discriminating fast deformation from slow and exploring dynamic slip processes linking geological observations to the physics of earthquake rupturing is a fruitful field for future research.

#### *Ground shaking and radiated waves*

Elastic waves are radiated during propagation of a mainshock rupture over a frequency spectrum dictated by rupture size. Wave amplitude diminishes variably with distance from the source with the high-frequency content attenuating most quickly. Ground shaking is most intense within the near-field (i.e. approximately within a distance comparable to rupture width) of the rupture, especially in the

vicinity of rupture irregularities. Strong near-field shaking may give rise to ground accelerations that approach or even exceed  $1 \text{ g}$ , especially in the hanging walls of propagating thrust ruptures (Somerville *et al.* 1996).

Obviously mass-movement effects of an earthquake (landscapes, rockfalls, avalanches onshore; submarine slumping offshore) tend to be concentrated within the near-field, roughly defined by the intensity VIII isoseismal, although other factors such as the degree of ground saturation at the time of shaking may also be important. It also has to be kept in mind that in seismically active areas, mountain landscapes and sediment accumulations, such as river mouth and submarine deltas, are critically organized with slopes at the edge of failure under static loading. Dynamic ground shaking then acts as the trigger for a large mass movement event. Sedimentation events resulting from such mass movements may be immediate and almost coseismic (e.g. a turbidity current slumping off a deltaic accumulation of sediment) or delayed substantially into the post-seismic period (e.g. a heavy rainfall event occurring some time after earthquake-triggered landsliding).

The geological record holds many examples of repeated intermittent events (e.g. successions of turbidite sandstone beds in flysch assemblages; incremental records of precipitation events within hydrothermal veins) but the critical issue in interpretation remains one of discrimination – whether, for example, a sedimentation event can unequivocally be attributed to an earthquake or may have been caused by some other trigger such as a major storm event. Goldfinger *et al.* (2003) have made a convincing correlation between the Holocene record of large turbidite emplacement off the Cascadia subduction margin with the onshore palaeoseismic record of major earthquakes. Likewise, Bull (1996) has inferred a rupture history for the Alpine Fault, New Zealand, over the past 1100 years from coincident lichenometric age determinations for rockfall events distributed over broad areas. However, extending such interpretations beyond the Holocene is fraught with difficulty because of varying tectonic settings, lack of precision in dating techniques and the possibility of climatic perturbations.

Consolidation and compaction can occur on an enormous scale. The New Madrid area of the Mississippi River valley experienced an extended intra-plate earthquake sequence over a period of 2 months in 1811–1812 involving at least four events with estimated  $7.0 < M_w < 7.5$  (Johnston & Schweig 1996; Hough 2009). Liquefaction with development of sand volcanoes occurred over more than  $10\,000 \text{ km}^2$  of the Mississippi flood-plain deposits. Sand volcanoes and other seismites are widely distributed through the sedimentary record and can

be used to infer past seismic activity on basin-flanking fault systems (Marco & Agnon 1995; Montenat *et al.* 2007).

### *Far-field triggering*

In recent years an exciting development has been the recognition of far-field ( $>1000$  km) dynamic triggering of small earthquakes by the surface waves arising from large earthquakes (Hill *et al.* 1993; Gomberg *et al.* 2004). The effects appear to be concentrated in the direction of rupture propagation (a directivity effect), and are most pronounced in areas of geothermal and/or volcanic activity within extensional or transtensional regimes but have been documented in most tectonic settings (Velasco *et al.* 2008). Dynamic stresses generated by 15–30 s period surface waves thousands of kilometres from the source rupture are estimated to have values of less than 1 MPa (Hill 2008), implying that the affected fault systems are in a critical state of incipient failure. In some cases the areas of triggered seismicity also exhibit anomalous hydrothermal activity (e.g. perturbed geyser systems) and signs of volcanic unrest in the form of enhanced heat flux (Donne *et al.* 2010). It is becoming apparent that volcanic activity may also sometimes be induced by large earthquakes either through near-field changes in the static elastic strain field (e.g. Walter & Amelung 2007) or through dynamic triggering in the far-field, or by some combination of the two effects (Hill *et al.* 2002; Walter *et al.* 2009). Considerable uncertainty remains, however, over the precise nature of the mechanism (Manga & Brodsky 2006).

### *Renewal of fracture permeability*

Increased hydrological discharge following large earthquakes, especially in mountainous terrain, has led to the inference of increased fracture permeability from intense near-field shaking (Rojstaczer *et al.* 1995; Wang *et al.* 2004). Distributed fracture permeability may also be enhanced from the passage of seismic waves from comparatively far-field earthquakes (Elkhouri *et al.* 2006). Rupture permeability of the fault rupture zone itself is likely to increase dramatically post-failure (Fig. 4) because of the fractal roughness of fault surfaces (Brown & Bruhn 1996). Geological evidence in support of this comes from incrementally deposited hydrothermal veins hosted on faults exhumed from the lower reaches of the seismogenic zone, interpreted as the products of ‘fault-valve’ behaviour with substantial post-seismic fluid discharge along enhanced fault permeability (Sibson 1990). Widespread occurrence of crack–seal textures in extension veins distributed

through low-grade metamorphic assemblages testifies to repeated episodes of re-opening, hydrothermal flow and cementation (Ramsay 1980).

It appears, therefore, that fault permeability transecting the seismogenic zone, together with fracture permeability distributed through the surrounding rock mass, may be enhanced by coseismic rupturing and shaking. This is inferred to have occurred on a massive scale in the hanging wall of a subduction megathrust rupture in Chile from observations of variations in the ratio of seismic P-wave to S-wave velocities ( $V_P/V_S$ ) over time (Husen & Kissling 2001). Such permeability enhancement is likely to be transient, however, especially in the active hydrothermal environment of the lower seismogenic zone ( $T > 150$  °C) where the self-sealing of fractures is probably rapid (Parry 1998), perhaps coinciding with the post-seismic aftershock period.

### *Stress cycling and fluid redistribution*

Faults rupture to reduce the tectonic shear stress acting on their surfaces, with the resulting static shear-stress drop commonly lying in the range  $1 < \Delta\tau < 10$  MPa (Kanamori & Anderson 1975). A critical issue is whether the shear-stress drop is comparable to the ambient level of shear stress driving faulting or is just a small fraction (<10%) of it, critically affecting the extent of changes in the stress field around the fault from before to after failure (Brune & Thatcher 2002). Fault rupture also leads inevitably to coupled changes in the normal stress,  $\sigma_n$ , on the fault (varying with faulting mode), and thus to the level of mean stress,  $\sigma_m$ . These fluctuations in mean stress may induce changes in pore-fluid pressure through poro-elastic effects (Fig. 4). Restoration of shear stress occurs through the interseismic period leading up to the next earthquake rupture. While the amplitude of these coseismic and interseismic stress changes diminishes with distance from the fault, they will extend through the volume of rock in the near-field of the mainshock rupture and also into the more ductile mid-crust below the seismogenic zone (Ellis & Stoeckert 2004; Nüchter & Ellis 2011). Stress cycling from episodic seismic rupturing thus extends throughout significant volumes of rock surrounding the active structure.

For a simple planar rupture, shear stress is lowered along most of the rupture plane but becomes enhanced at the rupture tips, while mean stress both increases and decreases in a quadrantal pattern around the rupture tips (Fig. 5). Areas where shear stress has increased and mean stress has lowered have enhanced the probability of subsequent failure according to Coulomb failure theory. This has given rise to Coulomb stress-transfer

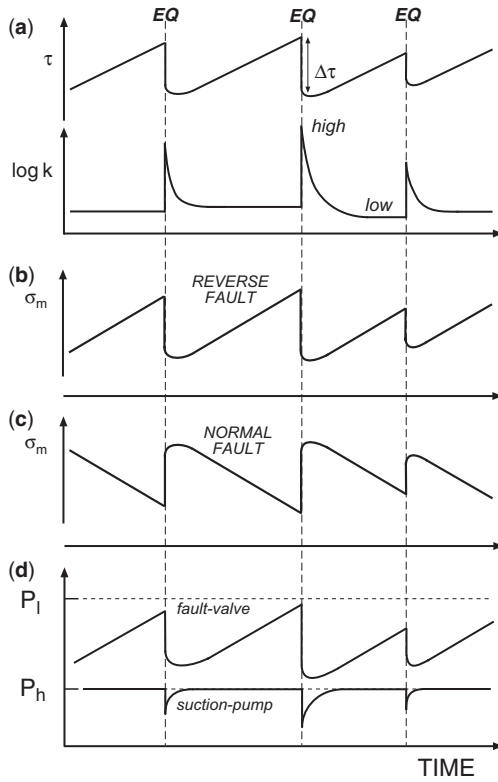


**Fig. 4.** Stress cycling in the seismogenic zone and associated effects (EQ, earthquake rupture;  $\tau$ , shear stress;  $k$ , permeability;  $\sigma_m$ , mean stress;  $P_h$  and  $P_f$ , hydrostatic and lithostatic levels of fluid pressure, respectively). (a) Shear-stress cycle and inferred variations in fault permeability. (b) & (c) Associated mean stress variations on reverse and normal faults, respectively. (d) Local fluid-pressure fluctuations associated with 'fault-valve' action in overpressured crust, and 'suction pump' action at dilatational sites.

modelling (King *et al.* 1994; Stein 1999), which has had considerable success in explaining the distribution of aftershocks around complex mainshock ruptures in terms of static stress changes within about one rupture length of the mainshock, plus the migration with time of large earthquakes along segmented faults (Stein *et al.* 1997). The technique has also been adapted for modelling stress interactions between earthquakes and volcanoes (Hill *et al.* 2002; Walter & Amelung 2007).

A range of fluid-redistribution mechanisms tied to the seismic stress cycle promote fluid redistribution in the near-field within the crustal seismogenic zone (Sibson 2001). Where parts of the seismogenic zone are fluid-overpressured above hydrostatic, coseismic increases in permeability along the primary rupture and subsidiary fractures are critical

factors contributing to 'fault-valve' behaviour, where overpressured fluid is discharged along the rupture zone post-failure. Post-failure changes in mean stress cause fluid to be redistributed from areas of elevated to areas of lowered mean stress, a form of 'dilatancy pumping'. Extreme reductions in mean stress, sometimes coupled with void creation, allow dilatational stepovers along ruptures to function as 'suction pumps' post-failure, drawing in fluid from the surroundings and creating favourable circumstances for intense, localized hydrothermal precipitation along linking extension fractures.

## Discussion

The crustal seismogenic zone is a significant source of hazard affecting humanity, particularly along subduction and transform boundaries. Rocks from its upper levels are also our principal source of energy, metals and other materials. Many of the hydrothermal mineral deposits and petroleum systems that we exploit reside in parts of the crust that are either currently, or were formerly, seismically active and subject to stress and permeability cycling and, in many cases, were also magmatically active.

At first sight it might be thought that larger crustal earthquakes ( $M_w > 7$ ) with repeat times of hundreds to thousands of years are the most important because the associated stress cycling and intense ground shaking occurs over large areas. Moreover, their capacity to generate surface waves allows 'action-at-a-distance', influencing hydrothermal–volcanic systems in the distant far-field. However, the high density of microseismic and small earthquakes with short repeat times in and around major active fault systems ensures that deforming crust is subject to multiple superposed stress/permeability cycles, albeit of short wavelength, occurring over different time periods. The interdependence of fault failure on both stress and fluid-pressure levels allows for the possibility that, in areas of strong fluid release (e.g. compacting sedimentary basins, zones of active metamorphic dewetting, areas of magmatic intrusion), seismic failure may be at least partly 'fluid-driven' rather than being purely 'stress-driven'.

Note that Table 2 is by no means an exhaustive list of geological processes related to earthquakes; its purpose is simply to serve as a stimulus to consider the diverse range of earthquake effects on geological processes in both the near-field and far-field. For pre-Holocene times, the precision of available dating techniques soon exceeds earthquake recurrence intervals. One of the challenges for the future is to develop sampling and statistical techniques that make it possible to identify positively

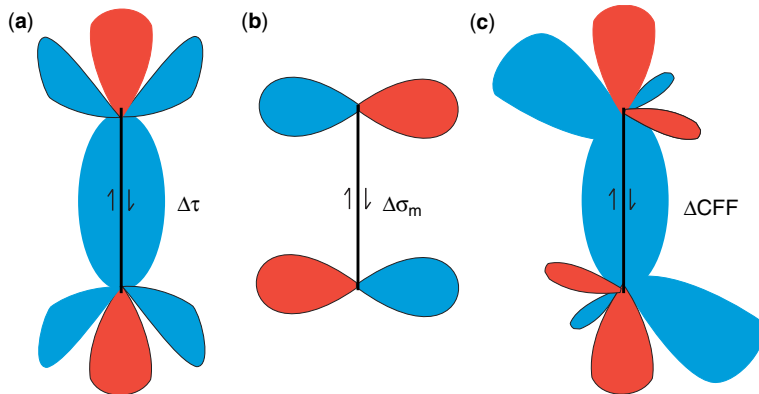


**Fig. 5.** Cartoon sketches of Coulomb stress changes associated with the rupture of a dextral strike-slip fault segment for failure on parallel strike-slip fault segments (red and blue indicate increases and decreases, respectively, in stress components). (a) Shear-stress change ( $\Delta\tau$ ). (b) Change in mean stress ( $\Delta\sigma_m$ ). (c) Regions of enhanced and lowered stress conditions for failure ( $\Delta CFF$ ) (modified from King *et al.* 1994).

the occurrence of major seismic events affecting the geological record.

This paper is dedicated to the memory of Bob Wallace (1916–2007) of the US Geological Survey, pioneer Earthquake Geologist, and to all his colleagues who instructed me in the rudiments of earthquake science. Special thanks to F. Ghisetti, D. Hill, R. Bürgmann and A. Fagereng for constructive criticism and many helpful suggestions.

## References

- ALLMAN, B. P. & SHEARER, P. 2009. Global variations of stress drop for moderate to large earthquakes. *Journal of Geophysical Research*, **114**, B01310, doi: 10.1029/2008JB005821.
- AMBRASEYS, N. N. & TCHALENKO, J. S. 1969. The Dasht-e-Bayaz (Iran) earthquake of August 31, 1968: a field report. *Bulletin of the Seismological Society of America*, **59**, 1751–1792.
- BOUTAREAUD, S., CALUGARU, D.-G., HAN, R., FABBRI, O., MIZOGUCHI, K., TSUTSUMI, A. & SHIMAMOTO, T. 2008. Clay–clast aggregates: a new textural evidence for seismic fault sliding? *Geophysical Research Letters*, **35**, L05032, doi: 10.1029/2007GL032554.
- BROWN, S. R. & BRUHN, R. L. 1996. Formation of voids and veins during faulting. *Journal of Structural Geology*, **18**, 657–671.
- BRUNE, J. N. & THATCHER, W. 2002. Strength and energetics of active fault zones. In: LEE, W. H. K., KANAMORI, H., JENNINGS, P. C. & KISSLINGER, C. (eds) *International Handbook of Earthquake and Engineering Seismology*, Volume 81A. Academic Press, London, 569–588.
- BULL, W. B. 1996. Prehistorical earthquakes on the Alpine Fault, New Zealand. *Journal of Geophysical Research*, **101**, 6037–6050.
- BURBANK, D. W. & ANDERSON, R. S. 2001. *Tectonic Geomorphology*. Blackwell, Oxford.
- BÜRGMANN, R. & DRESEN, G. 2008. Rheology of the lower crust and upper mantle: evidence from rock mechanics, geodesy, and field observations. *Annual Review of Earth and Planetary Sciences*, **36**, 531–567.
- BYERLEE, J. D. 1978. Friction of rocks. *Pure & Applied Geophysics*, **116**, 615–626.
- DI TORO, G., HIROSE, T., NIELSEN, S., PENNACCHIONI, G. & SHIMAMOTO, T. 2006. Natural and experimental evidence of melt lubrication of faults during earthquakes. *Science*, **311**, 647–649.
- DONNE, D. D., HARRIS, A. J. L., RIPEPE, M. & WRIGHT, R. 2010. Earthquake-induced thermal anomalies at active volcanoes. *Geology*, **38**, 771–774.
- ELKHOURY, J. E., BRODSKY, E. E. & AGNEW, D. C. 2006. Seismic waves increase permeability. *Nature*, **441**, 1135–1138.
- ELLIS, S. M. & STOECKHERT, B. 2004. Elevated stresses and creep rates beneath the brittle–ductile transition caused by seismic faulting in the upper crust. *Journal of Geophysical Research*, **109**, B05407, doi: 10.1029/2003JB002744.
- FAN, G., WALLACE, T. C. & ZHAO, D. 1998. Tomographic imaging of deep velocity structure beneath the Eastern and Southern Carpathians, Romania: implications for continental collision. *Journal of Geophysical Research*, **103**, 2705–2723.
- FREED, A. M. & BÜRGMANN, R. 2004. Evidence of power-law flow in the Mojave Desert mantle. *Nature*, **430**, 548–551.
- FIELDING, E. J., LUNDGREN, P. R., BÜRGMANN, R. & FUNNING, G. J. 2009. Shallow fault-zone dilatancy recovery after the 2003 Bam earthquake in Iran. *Nature*, **458**, 64–68.
- FROHLICH, C. 2006. *Deep Earthquakes*. Cambridge University Press, Cambridge.
- GÉLI, L. & SCLATER, J. 2008. On the depth of oceanic earthquakes: brief comments on ‘The thermal structure of oceanic and continental lithosphere’ by McKenzie, D., Jackson, J. & Priestley, K. *Earth Planet. Sci. Lett.* **233**, [2005], 337–349. *Earth and Planetary Science Letters*, **265**, 769–775.

- GOLDFINGER, C., NELSON, C. H., JOHNSON, J. E. & THE SHIPBOARD SCIENTIFIC PARTY. 2003. Deep-water turbidites as Holocene earthquake proxies: the Cascadia subduction zone and Northern San Andreas Fault systems. *Annals of Geophysics*, **46**, 1169–1194.
- GOMBERG, J., BODIN, P., LARSON, K. & DRAGERT, H. 2004. Earthquake nucleation by transient deformations caused by the  $M = 7.9$  Denali, Alaska, earthquake. *Nature*, **427**, 620–624.
- HANDY, M. R., HIRTH, G. & HOVIUS, N. (eds). 2007. *Tectonic Faults: Agents of Change on a Dynamic Earth. Report of the 95th Dahlem Workshop on the Dynamics of Fault Zones*, Berlin, January 16–21, 2005. MIT Press, Cambridge, MA.
- HANKS, T. C. & KANAMORI, H. 1979. A moment magnitude scale. *Journal of Geophysical Research*, **84**, 2348–2350.
- HASEGAWA, A., NAKAJIMA, N., UMINO, N. & MIURI, S. 2005. Deep structure of the northeastern Japan arc and its implications for crustal deformation and shallow seismic activity. *Tectonophysics*, **403**, 59–75.
- HILL, D. P. 2008. Dynamic stresses, Coulomb failure, and remote triggering. *Bulletin of the Seismological Society of America*, **98**, 66–92.
- HILL, D. P., REASENBERG, P. A. ET AL. 1993. Seismicity remotely triggered by the magnitude 7.3 Landers, California, earthquake. *Science*, **260**, 1617–1623.
- HILL, D. P., POLLITZ, F. & NEWHALL, C. 2002. Earthquake–volcano interactions. *Physics Today*, **55**, 41–47.
- HOUGH, S. E. 2009. Cataloging the 1811–1812 New Madrid, central U.S., earthquake sequence. *Seismological Research Letters*, **80**, 1045–1053, doi: 10.1785/gssrl.80.6.1045.
- HUSEN, S. & KISSLING, E. 2001. Postseismic fluid flow after the large subduction earthquake of Antogasta, Chile. *Geology*, **29**, 847–850.
- HYNDMAN, R. D. 2007. The seismogenic zone of subduction thrust faults: what we know and what we don't know. In: DIXON, T. H. C & MOORE, J. C. (eds) *The Seismogenic Zone of Subduction Thrust Faults*. Columbia University Press, New York, 15–40.
- IDE, S., BEROZA, G. C., SHELLY, D. R. & UCHIDE, T. 2007. A scaling law for slow earthquakes. *Nature*, **447**, 76–79.
- ISAACS, A. J., EVANS, J. P., KOLESAR, P. T. & NOHARA, T. 2008. Composition, microstructures, and petrophysics of the Mozumi fault, Japan: *in situ* analyses of fault zone properties and structures in sedimentary rocks from shallow crustal levels. *Journal of Geophysical Research*, **113**, B12408, doi: 10.1029/2007JB005314.
- ISACKS, B., OLIVER, J. & SYKES, L. R. 1968. Seismology and the new global tectonics. *Journal of Geophysical Research*, **73**, 5855–5899.
- ITO, K. 1999. Seismogenic layer, reflective lower crust, surface heat flow and large inland earthquakes. *Tectonophysics*, **306**, 423–433.
- JACKSON, J. & MCKENZIE, D. 1988. The relationship between plate motions and seismic moment tensors, and the rates of active deformation in the Mediterranean and Middle East. *Geophysical Journal International*, **93**, 45–73.
- JOHNSTON, A. C. & SCHWEIG, E. S. 1996. The enigma of the New Madrid earthquakes of 1811–1812. *Annual Review of Earth and Planetary Sciences*, **24**, 339–384.
- JULIAN, B. R., MILLER, A. D. & FOULGER, G. R. 1998. Non-double-couple earthquakes I. Theory. *Reviews of Geophysics*, **36**, 525–549.
- KANAMORI, H. & ANDERSON, D. 1975. Theoretical basis of some empirical relations in seismology. *Bulletin of the Seismological Society of America*, **65**, 1073–1095.
- KING, G. C. P., STEIN, R. S. & LIN, J. 1994. Static stress changes and the triggering of earthquakes. *Bulletin of the Seismological Society of America*, **84**, 935–953.
- KOTO, B. 1893. On the cause of the great earthquake in central Japan. *Journal of the College of Science, Imperial University of Japan*, **5**, 295–353.
- LAWSON, A. C. (CHAIRMAN) 1908. *The California Earthquake of April 18, 1906: Report of the State Earthquake Investigation Commission* (2 vols). Carnegie Institute of Washington Publication, **87**.
- LAY, T., KANAMORI, H. ET AL. 2005. The great Sumatra–Andaman earthquake of December 26, 2004. *Science*, **308**, 1127–1133.
- LYELL, C. 1868. *Principles of Geology*, 10th edn. John Murray, London.
- MAGGI, A., JACKSON, J. A., PRIESTLEY, K. & BAKER, C. 2000. A re-assessment of focal depth distributions in southern Iran, the Tien Shan and northern India: do earthquakes really occur in the continental mantle? *Geophysical Journal International*, **143**, 629–661.
- MALLET, R. 1862. *The Great Neapolitan Earthquake of 1857 – The First Principles of Observational Geology* (2 vols). Chapman & Hall, London.
- MANGA, M. & BRODSKY, E. 2006. Seismic triggering of eruptions in the far field. *Annual Review of Earth and Planetary Sciences*, **34**, 263–291.
- MARCO, S. & AGNON, A. 1995. Prehistoric earthquake deformations near Masada, Dead Sea graben. *Geology*, **23**, 695–698.
- MCCALPIN, J. (ed.) 1996. *Paleoseismology*. Academic Press, San Diego, CA.
- MCKENZIE, D., JACKSON, J. & PRIESTLEY, K. 2005. Thermal structure of oceanic and continental lithosphere. *Earth Planetary Science Letters*, **233**, 337–349.
- MONTENAT, C., BARRIER, P., d'ESTEVOU, P. O. & HIBSCH, C. 2007. Seismites: an attempt at critical analysis and classification. *Sedimentary Geology*, **196**, 5–30.
- MOORE, A., NISHIMURA, Y., GELFENBAUM, G., KAMATAKI, T. & TRIYONO, R. 2006. Sedimentary deposits of the 26 December 2004 tsunami on the northwest coast of Aceh, Indonesia. *Earth, Planets, Space*, **58**, 253–258.
- NAZARETH, J. & HAUKSSON, E. 2004. The seismogenic thickness of the southern California crust. *Bulletin of the Seismological Society of America*, **94**, 940–960.
- NÜCHTER, J.-A. & ELLIS, S. 2011. Mid-crustal controls on episodic stress-field rotation around major reverse, normal and strike-slip faults. In: FAGERENG, Å., TOY, V. G. & ROWLAND, J. V. (eds) *Geology of the Earthquake Source: A Volume in Honour of Rick Sibson*. Geological Society, London, Special Publications, **359**, 187–201.

- OBARA, K. 2002. Nonvolcanic deep tremor associated with subduction in southwest Japan. *Science*, **296**, 1679–1681.
- OHMI, S., HIROSE, I. & MORI, J. J. 2004. Deep low-frequency earthquakes near the downward extension of the seismogenic fault of the 2000 Western Tottori earthquake. *Earth, Planets, Space*, **56**, 1185–1189.
- PARRY, W. T. 1998. Fault-fluid compositions from fluid-inclusion observations and solubilities of fracture-sealing minerals. *Tectonophysics*, **290**, 1–26.
- PELZER, G., ROSEN, P., ROGEZ, F. & HUDNUT, K. 1996. Postseismic rebound in fault stepovers caused by pore fluid flow. *Science*, **273**, 1202–1204.
- PENG, Z. & GOMBERG, J. 2010. An integrated perspective of the continuum between earthquakes and slow slip phenomena. *Nature Geoscience*, **3**, 599–607.
- RAMSAY, J. G. 1980. The crack–seal mechanism of rock deformation. *Nature*, **284**, 135–139.
- REID, H. F. 1908. The mechanics of the earthquake. In: *The California Earthquake of April 18, 1906: Report of the State Earthquake Investigation Commission*, Volume 2. Carnegie Institute of Washington Publication, 87.
- RODGERS, D. W. & LITTLE, T. A. 2006. World's largest coseismic strike-slip offset: the 1855 rupture of the Wairarapa Fault, New Zealand, and implications for displacement/length scaling of continental earthquakes. *Journal of Geophysical Research*, **111**, B12408, doi: 10.1029/2005JB004065.
- ROJSTACZER, S., WOLF, S. & MICHEL, R. 1995. Permeability enhancement in the shallow crust as a cause of earthquake-induced hydrological changes. *Nature*, **373**, 237–239.
- RUBINSTEIN, J. L., SHELLY, D. R. & ELLSWORTH, W. L. 2010. Non-volcanic tremor: a window into the roots of fault zones. In: CLOETINGH, S. & NEGENDANK, J. (eds) *New Frontiers in Integrated Solid Earth Sciences*. International Year of Planet Earth Book Series (doi: 10.1007/978-90-481-2737-5\_8). Springer, Berlin, 287–314.
- SCHOLZ, C. H. 2002. *The Mechanics of Earthquakes and Faulting*, 2nd edn. Cambridge University Press, Cambridge.
- SHEARER, P. & BÜRGMANN, R. 2010. Lessons learned from the 2004 Sumatra-Andaman megathrust rupture. *Annual Review of Earth and Planetary Sciences*, **38**, 103–131.
- SHELLY, D. R. 2010. Migrating tremors illuminate complex deformation beneath the seismogenic San Andreas fault. *Nature*, **463**, 648–652.
- SHIBAZAKI, B., GARATANI, K., IWASAKI, T., TANAKA, A. & IIO, Y. 2008. Faulting processes controlled by the non-uniform structure thermal of the crust and uppermost mantle beneath the northeastern Japanese island arc. *Journal of Geophysical Research*, **113**, B08415, doi: 10.1029/2007JB005361.
- SIBSON, R. H. 1983. Continental fault structure and the shallow earthquake source. *Journal of the Geological Society, London*, **140**, 741–767.
- SIBSON, R. H. 1984. Roughness at the base of the seismogenic zone: contributing factors. *Journal of Geophysical Research*, **89**, 5791–5799.
- SIBSON, R. H. 1986. Earthquakes and rock deformation in crustal fault zones. *Annual Review of Earth and Planetary Sciences*, **14**, 149–175.
- SIBSON, R. H. 1990. Conditions for fault-valve behaviour. In: KNIFE, R. J. & RUTTER, E. H. (eds) *Deformation Mechanisms, Rheology, and Tectonics*. Geological Society, London, Special Publications, **54**, 15–28.
- SIBSON, R. H. 2001. Seismogenic framework for hydrothermal transport and ore deposition. *Reviews in Economic Geology*, **14**, 25–47.
- SIBSON, R. H. 2006. Charles Lyell and the 1855 Wairarapa Earthquake in New Zealand: recognition of fault rupture accompanying an earthquake. *Seismological Research Letters*, **77**, 358–363.
- SIBSON, R. H. 2009. Rupturing in overpressured crust during compressional inversion – the case from NE Honshu, Japan. *Tectonophysics*, **473**, 404–416.
- SIBSON, R. H. & TOY, V. 2006. The habitat of fault-generated pseudotachylite: presence vs. absence of friction-melt. In: ABERCROMBIE, R., McGARR, A., KANAMORI, H. & DI TORO, G. (eds) *Radiated Energy and the Physics of Faulting*. American Geophysical Union, Geophysical Monograph, **170**, 153–166.
- SIEH, K. 1978. Prehistoric large earthquakes recorded by produced by slip on the San Andreas fault at Pallet Creek, California. *Journal of Geophysical Research*, **83**, 3907–3939.
- SIEH, K. 1984. Lateral offsets and revised dates of large earthquakes at Pallet Creek, California. *Journal of Geophysical Research*, **89**, 7641–7670.
- SILVER, P. G., BECK, S. L., WALLACE, T. C., MEADE, C., MYERS, S. C., JAMES, D. E. & KUEHNEL, R. 1995. Rupture characteristics of the deep Bolivian earthquake of 9 June 1994 and the mechanism of deep-focus earthquakes. *Science*, **268**, 69–73.
- SOMERVILLE, P., SAIKIA, C., WALD, D. & GRAVES, R. 1996. Implications of the Northridge earthquake for strong ground motions from thrust faults. *Bulletin of the Seismological Society of America*, **86**, S115–S225.
- STEIN, R. S. 1999. The role of stress transfer in earthquake occurrence. *Nature*, **402**, 605–609.
- STEIN, R. S., BARKA, J. J. & DIETERICH, J. H. 1997. Progressive failure on the North Anatolian fault since 1939 by earthquake stress triggering. *Geophysical Journal International*, **128**, 594–604.
- TAIRA, T., SILVER, P. G., NIU, F. & NADEAU, R. M. 2009. Remote triggering of fault-strength changes on the San Andreas fault at Parkfield. *Nature*, **461**, 636–639.
- TOWNSEND, J. & ZOBACK, M. D. 2000. How faulting makes the crust strong. *Geology*, **28**, 399–402.
- TOWNSEND, J. & ZOBACK, M. D. 2004. Regional tectonic stress near the San Andreas fault in central and southern California. *Geophysical Research Letters*, **31**, L15S11, doi: 10.1029/2003GL018918.
- VELASCO, A. A., HERNANDEZ, S., PARSONS, T. & PANKOW, K. 2008. Global ubiquity of dynamic earthquake triggering. *Nature Geoscience*, **1**, 375–379.
- WALLACE, R. E. 1970. Earthquake recurrence intervals on the San Andreas fault. *Geological Society of America Bulletin*, **81**, 2875–2890.
- WALTER, T. R. & AMELUNG, F. 2007. Volcanic eruptions following  $M \geq 9$  megathrust earthquakes: implications for the Sumatra-Andaman volcanoes. *Geology*, **35**, 539–542.

- WALTER, T. R., WANG, R., ACOCELLA, V., NERI, M., GROSSER, H. & ZSCHAU, J. 2009. Simultaneous magma and gas eruptions at three volcanoes in southern Italy: an earthquake trigger? *Geology*, **37**, 251–254.
- WANG, C.-Y., WANG, C.-O. & MANGA, M. 2004. Coseismic release of water from mountains: evidence from the 1999 ( $M_w = 7.5$ ) Chi-Chi, Taiwan, earthquake. *Geology*, **30**, 769–772.
- WELLS, D. L. & COPPERSMITH, K. J. 1994. New empirical relationships among magnitude, rupture length, rupture width, rupture area, and surface displacement. *Bulletin of the Seismological Society of America*, **84**, 974–1002.
- WEST, M., SÁNCHEZ, J. J. & McNUTT, S. R. 2005. Periodically triggered seismicity at Mount Wrangell, Alaska, after the Sumatra earthquake. *Science*, **308**, 1144–1146.
- YEATS, R. S., SIEH, K. & ALLEN, C. 1997. *The Geology of Earthquakes*. Oxford University Press, Oxford.
- ZHAO, D., WANG, Z., UMINO, N. & HASEGAWA, A. 2009. Mapping the mantle wedge and interplate thrust zone of the northeast Japan arc. *Tectonophysics*, **467**, 89–106.



# Index

Page numbers in *italics* refer to Figures. Page numbers in **bold** refer to Tables.

- accretionary prism, deformation style 67  
adularia veins 120, 255  
afterslip, defined 90–91, 319  
Alaska earthquake (1964) 315  
albite veins 254  
Alpine Fault Zone (New Zealand) 6  
geological setting 116  
map 116  
pseudotachylites  
formation  
controls 125, 127–128  
depth 125, **130**  
temperature **130**  
habitat **121**  
type i 120, **121**  
type ii 120, **121**, 122  
type iii **121**, 122  
type iv **121**, 122–123  
host rock chemical relations 120  
host rock and morphology 116–120  
melt phase evidence 123–125, 128, **130**  
microtextrites 126  
relation to seismicity 128–129, 131, 132  
summary 132  
Alto Tiberina Fault 316, **317**  
Amontons' law 2  
amphibolite facies 4, 182  
amygdules 125, 127, 129  
Anghiari splay fault 316, **317**  
ankerite veins **24**, 25, 254–255  
Apennines, deformation events 99  
<sup>40</sup>Ar/<sup>39</sup>Ar dating Eidsfjord Shear Zone 173  
aseismic creep 69, 135, 183  
asperity deformation 4  
attenuation 39  
Australia *see* Mount Isa Block; Taemas  
Vein Swarm  
Baikal rift system 182  
Baraq Fault 230, 231  
vein geochemistry **233**, **234**, **239**, 240–241, 244, 245  
Barbados accretionary prism 17  
basement, fabric and failure 135  
bedding-parallel veins, Taemas Vein Swarm 208, 209, 211, 217  
binary chronological matrix analysis *see* relative age analysis  
biotite, Serre Massif pseudotachylite 156, **160**, 161, **162**, 165  
black fault rock, Pasagshak Point Thrust 79, 88–89  
boudinage 58, 60, 63, 65  
breccias, fault, Zuccale Fault 103, 107  
brittle failure 8, 65, 135, 229–230  
problems of dating 229  
broken formation 59  
 $\delta^{13}\text{C}$   
carbonate veins  
East Anatolian and Dead Sea Fault Zones  
methods of analysis 232  
results **233**, 235, 236–237, 238, 240, 241  
results discussed 242–244  
Taemas Vein Swarm  
methods 211–212  
results 213  
Calabria terrane *see* Serre Massif  
calcite veins **24**, 230  
Chelungpu Fault 30  
Dead Sea Fault Zone vein geochemistry  
methods of analysis 232  
results **233**, **234**, 235–241  
results discussed 242–244  
East Anatolian Fault Zone vein geochemistry  
methods of analysis 232  
results **233**, **234**, 235  
results discussed 241–242  
Taiwan 254, 255  
Taemas Vein Swarm  
classification 206  
bedding-parallel veins 208  
extension veins 208–209, **210**  
fault veins 206  
geochemical analysis  
methods 211–213  
results 213–215  
class effects 217–218  
outcrop effects 216–217  
stratigraphy effects 215–216  
results discussed  
fluid flow 219–224  
fluid sources 218–219  
stress levels 224–225  
calcite-ultramylonites 102–103,  
105–106, 108  
California, University of vii  
Carmel Fault **230**, 231  
vein geochemistry **233**, **234**, 237–240, 243–244  
Cascadia subduction zone 90  
cataclasites and cataclasites 5, 6, 7, 8, 63, 108  
Pasagshak Point Thrust  
analogue experiments 86–88  
relation to black fault rock 90  
textures 82, 83, 84–86  
types 80, **81**, 84  
Zuccale Fault 103, 106–107  
Changua décollement 316  
Chelungpu Fault (Taiwan) 316  
Drilling Project (TCDP) 11  
energy budgeting 28  
fluid budgeting 30–31  
principal slip zone 28–30  
setting 26–28  
summary 31–32  
map 27  
setting 26  
Chi-chi earthquake (1999) 26, 27, 316

- Chile subduction zone 90  
 China, Wenchuan earthquake Fault Scientific Drilling (WFSD) 17  
 chlorite veins **24**, 272, 274, 275  
     Taiwan 254, 255, 277  
 Chrystals Beach Complex (New Zealand)  
     assemblages 57–59  
 deformation fabrics  
     continuous 59–60  
     discontinuous 60  
 deformation mechanisms  
     continuous 65  
     discontinuous 65–67  
     sequence 61–64  
 modern analogues 70–72  
     setting 56–57  
 clay minerals **24**, 25  
 clay–clast aggregates 279, 280, 281, 282, 283, 325  
 cleavage development 59  
     shear failure 66  
 Colima–Jalisco earthquake (1995) 91  
 Colorado Mineral Belt Shear Zone 136  
 composition, role in deformation 4  
 copper mineralization, Mount Gordon Fault Zone 287,  
     289, 291–292  
 exploration potential by relative age analysis  
 domains 292–294  
 geometrical assumptions 295–297  
     validity 299–300  
 initial orientation 292  
 modifications 297–298  
 predicted evolution 300–302  
     results discussed 302–305  
     summary 305–308  
 Corinth Rift (Greece) Laboratory 17  
 Coulomb failure theory 65, 313–314, 326–327, 328  
     *see also* Mohr–Coulomb diagrams  
 crack–seal bands 60, 209, 211  
 creep  
     aseismic 69, 319  
     dislocation 4, 8  
     grain-size sensitive 3–4  
     thermal activation 189  
     viscous 7  
 crust, peak strength 9  
 crystal-plasticity 108, 135  
 damage zone 39  
     defined 20  
 Dead Sea Fault Zone  
     geological setting 231–232  
     map 230  
     vein geochemistry  
         methods of analysis 232  
         results **233**, **234**, 235–241  
         results discussed 242–244  
 décollements 314, 316  
 deformation  
     Chrystals Beach Complex  
         fabrics 59–60  
         mechanisms 61–67  
     experimental work 100  
     hydrothermal minerals 23, **24**, 25  
         mechanisms 3–4, 86, 108  
     processes 77  
     relation to geochemistry 20  
 Dieterich–Ruina law 2  
 diffusion-limited creep 4  
 diffusive mass transfer 8, 109  
 dilatancy hardening 5  
 dilatational hydro-shears 66  
 dip slips *see* normal faults; thrust faults  
 dislocation creep 3, 7, 8, 108  
     flow law 4  
 dislocation glide 4, 86  
 displacement measurements  
     Chelungpu Fault 26  
     Nojima Fault 18  
 dissolution–precipitation creep 3–4, 5, 7, 8, 25, 63,  
     65, 67, 108  
 dolomite reactions 109  
 Düziçi Fault 230, 231  
     vein geochemistry **233**, **234**, 235, **239**,  
     241–242, 244  
 dynamic friction, defined 2  
 earthquakes  
     characteristics 322  
     effects 323–324  
         fault rupture 324–325  
         ground shaking **324**, 325–326  
         stress changes **324**, 326–327  
         summary 327–328  
     frequency 10, **320**  
     magnitude 9, 319, **320**  
     size scaling 9–11  
     slip mechanisms 1–2  
     thermal impact 20  
 East Anatolian Fault Zone  
     geological setting 231–232  
     map 230  
     vein geochemistry  
         methods of analysis 232  
         results **233**, **234**, 235  
         results discussed 241–242  
 eclogite-facies 153  
 Eidsfjord Shear Zone  
     deformation timing 173  
     geological setting 169, 171  
     map 170  
     microstructures 176, 178, 179  
     mylonites 171–173  
     petrology 173–174  
     pseudotachylite 175  
         thermobarometry  
             methods 177, 178, 181  
             results **180**, 181–182  
             results discussed 182–183  
     elastic rebound, first recognized 319  
     elastohydrodynamic lubrication 129  
 Elba *see* Zuccale Fault  
 energy budget  
     Chi-chi earthquake 28  
     Kobe earthquake 23  
 experimental work  
     cataclasite formation 86–87  
         foliated 87  
         non-foliated 87–88

- deformation 100  
frictional melts 124  
high-velocity friction 267–268  
methods 268–269  
results  
dry tests 270–271  
microstructure 274–275  
temperature evolution 272, 273  
wet tests 271–272  
XRD 272–274, 275  
results discussed  
significance for seismic slip 282–283  
slip rates 278–282  
weakening mechanisms 276–278  
exploration for mineralization by relative  
age analysis  
domains 292–294  
geometrical assumptions 295–297  
validity 299–300  
initial orientation 292  
modifications 297–298  
predicted evolution 300–302  
results discussed 302–305  
summary 305–308  
extension  
fractures 60, 65, 66  
veins 60, 63, 66, 71  
Taemas Vein Swarm 208–209, 210, 211, 217–218  
zones and seismic frequency 169  
*see also* normal faults  
extensional-shear fractures 65  
fault breccia 5, 103, 107  
fault gouge 5, 20, 230  
high-velocity friction experiments  
267–268  
methods 268–269  
results  
dry tests 270–271  
microstructure 274–275  
temperature evolution 272, 273  
wet tests 271–272  
XRD 272–274, 275  
results discussed  
significance for seismic slip 282–283  
slip rates 278–282  
weakening mechanisms 276–278  
local studies  
Dead Sea Fault Zone 238  
San Andreas Fault 43  
Zuccale Fault 103, 107–108  
fault lock-up 187  
fault valve theory vii  
fault veins *see* veins  
fault-fracture mesh 60, 61, 66–67, 71, 72  
fault-zone drilling projects 17  
fault-zone guided waves 39, 40, 44, 45  
fault-zone model 7–9  
faults 65  
first-order splay  
defined 313  
dip-slip types 313, 314, 315, 316, 317–318  
frequency 169  
friction 2  
movement 2  
relation to stress field 313  
numerical modelling  
method 188–190  
results 190–192  
results discussed 192–198  
rock assemblage and internal structure 4–7  
shearing displacement 319  
slip distance-length ratio 9  
slip speed 1  
temperature 79–80  
zone deformation 3–4  
zone model 7–9  
*see also* Heier's Zone; Mount Gordon Fault Zone; Zuccale Fault  
feldspar  
deformation temperatures 4, 7  
Serre Massif pseudotachylite 156, 159, 160, 161, 162, 165  
ferrimagnetic resonance (FMR) 20  
first-order splay faults 313, 314, 315, 316, 317–318  
Fiskfjord Shear Zone 169  
geological setting 173  
map 170  
microstructures 179  
petrology 174, 176  
pseudotachylite  
thermobarometry 176  
methods 177, 178, 181  
results 180, 181–182  
results discussed 182–183  
fissure veins 255  
flats and ramps 316  
flow mechanisms 65  
fluid flow at faults  
budget  
Chelungpu Fault 30–31  
Nojima Fault 23–25  
effect on calcite vein development 218–224, 230  
effect on frictional melting 129  
Mount Gordon Fault Zone mineralizing fluids  
relative age analysis 291–292  
domains 292–294  
geometrical assumptions 295–297  
validity 299–300  
initial orientation 292  
modifications 297–298  
predicted evolution  
description 300–302  
discussion 302–305  
summary 305–308  
timing and orientation 290–291  
Taiwan hydrothermal systems 251, 258–260, 260–262  
fluid inclusions 23, 79–80  
fluidization, defined 267  
frictional faulting 7  
frictional heating 20, 153  
frictional melt 5, 77, 79, 115, 124, 129, 153  
frictional sliding 4, 5, 7, 8  
experiments on high-velocity friction 267–268  
methods 268–269

- frictional sliding (*continued*)  
 results  
   dry tests 270–271  
   microstructure 274–275  
   temperature evolution 272, 273  
   wet tests 271–272  
   XRD 272–274, 275  
 results discussed  
   significance for seismic slip 282–283  
   slip rates 278–282  
   weakening mechanisms 276–278
- frictional stability 3
- garnet  
 Heier's Zone pseudotachylite 176, 177, 178, 179, **180**, 181, 182–183  
 Serre Massif pseudotachylite 158, 160, 161, **162**, 163, 164, 165, 166
- geochemistry 20  
 Dead Sea Fault Zone  
   methods of analysis 232  
   results **233**, **234**, 235–241  
   results discussed 242–244  
 East Anatolian Fault Zone  
   methods of analysis 232  
   results **233**, **234**, 235  
   results discussed 241–242  
 Taemas Vein Swarm  
   methods 211–213  
   results 213–215  
     class effects 217–218  
     outcrop effects 216–217  
     stratigraphy effects 215–216  
   results discussed  
     fluid flow 219–224  
     fluid sources 218–219  
     stress levels 224–225  
 glass 123–124  
 goethite, Chelungpu Fault 30  
 Gölbaşı–Türkoğlu Fault 231, **233**, **234**  
 gold deposits, hydrothermal veins in Taiwan  
   254–255  
 gouge *see* fault gouge  
 grain behaviour, classification 86  
 grain-size distribution, fault-rock characterization  
   23, 28  
 grain-size sensitive creep 3–4  
 granular flow 3, 8, 77, 87, 92  
 granular fluidization 129  
 granulite facies 4, 154, 156  
 gravitational flow 67  
 Grebe Shear Zone (New Zealand) 6  
 greenschist facies 4, 7, 8, 125  
   Taiwan 254, 255  
 Griffith–Coulomb failure envelope 65, 66  
 Grizzly Creek Shear Zone (Colorado)  
   coexisting tectonite paradox 145  
     cyclicity 145  
     structure and anisotropy 145–147  
   geological setting 136–137  
   lithological units 137, 139  
   map 138  
   structural features 139  
   summary 148
- tectonites  
   mylonite 139, **142**  
   mylonitic pseudotachylite 143–144  
   pseudotachylite 139–143  
   ultramylonite 144  
 Gutenberg–Richter relationship 10
- H-splays 313, 314, 315, 316, 317–318  
 Har Zefiyya Fault **230**, 231  
   vein geochemistry **233**, **234**, 235–237, **239**, 242–243, 244  
 heat *see* frictional heating  
 heat flow budget, Taiwan 255–257  
 Hebrides, Outer vii  
 Hegben Lake earthquake (1959) 316–317  
 Heier's Zone 169, **170**, 171  
   Eidsfjord Shear Zone  
     deformation timing 173  
     microstructures 176, 178, 179  
     mylonites 171–173  
     petrology 173–174  
     pseudotachylite 175  
       thermobarometry  
         methods 177, 178, 181  
         results **180**, 181–182  
         results discussed 182–183  
   Fiskfjord Shear Zone 169  
     microstructures 179  
     petrology 174, 176  
     pseudotachylite  
       thermobarometry 176  
         methods 177, 178, 181  
         results **180**, 181–182  
         results discussed 182–183  
 Hikurangi subduction margin 68–69  
   compared with Chrystalls Beach Complex 70–72  
   seismic style 69–70  
 Hill fault/fracture meshes 30  
 Hinnøya *see* Fiskfjord Shear Zone  
 Homestake Shear Zone 136, 147  
 hot springs, fluid flow indicators 249, 255  
 hydro-shears 66  
 hydrothermal minerals, relation to deformation 23, **24**, 25  
 hydrothermal systems, Taiwan cf. New Zealand **251**, 260–262  
 hydrothermal veins 5  
   Taemas Vein Swarm 204, 205  
     classification 206, 208–209, **210**  
     geochemical analysis  
       methods 211–213  
       results 213–218  
       results discussed 219–225  
     stratigraphy **206**, 207  
     textures 209  
 Idaho Springs–Ralston Shear Zone 136  
 illite 25, 272, 274, 277  
 Imperial College, London University vii  
 Imperial Valley earthquake (1979) 91  
 implosion breccia 5  
 inclusion bands 209  
 interseismic coupling 9  
 isotope geochemistry *see*  $\delta^{13}\text{C}$ ;  $\delta^{18}\text{O}$ ; Sr isotope analysis; U/Th dating

- Israel *see* Dead Sea Fault Zone  
 Italy *see* Sansepolcro Basin; Serre Massif;  
 Zuccale Fault
- Japan *see* Kobe earthquake; Nankai Trough;  
 Nojima Fault  
 jelly-sandwich model 153  
 Kobe earthquake (1995) 17, 18, 20  
 Kodiak Island (Alaska) 78, 79  
 Pasagshak Point Thrust  
   black fault rock 88–89  
   cataclasites  
     formation 86  
       analogue experiments 86–88  
       textures 82, 83, 84–86  
       types 80, 81, 84  
   fault temperature estimates 79–80  
   seismic cycle and strain rates 90–92
- L-splays 313, 314, 315, 316, 317–318  
 Langøya *see* Eidsfjord Shear Zone  
 L’Aquila earthquake (2008) 91  
 laumontite 23, 24  
 Lishan Fault 250, 252, 254, 255  
 lock-up 187  
 London University vii  
 Longmen Shan active fault zone 17  
 Love-type waves 39  
 low-velocity channel 39
- magnetic susceptibility, Chelungpu Fault 30  
 magnetite, Chelungpu Fault 30  
 mass balance, deformation and geochemistry 20  
 mass transfer, fluid-assisted 108, 109  
 megathrusts, subduction-zone 55  
 mélange  
   Chrystalls Beach Complex 67–68  
   defined 59  
 melt phase 123  
   evidence for 124–125  
   *see also* frictional melt  
 mica, deformation temperatures 7  
 micro-transforms 60  
 microfracturing, role in creep 4  
 microlites 124, 159  
 mineralization, exploration by relative age analysis  
   Mount Gordon Fault Zone 287, 289, 291–292  
     domains 292–294  
     geometrical assumptions 295–297  
       validity 299–300  
     initial orientation 292  
     modifications 297–298  
     predicted evolution 300–302  
       results discussed 302–305  
       summary 305–308  
 modelling  
   stress field and faulting  
     method 188–190  
     results 190–192  
     results discussed 192–198  
 wave behaviour  
   SAFOD  
     application 45–49  
     discussion 49–51
- Mohr diagram 65, 66, 313, 314  
 Mohr–Coulomb criterion for slip 189  
 monazite, Serre Massif pseudotachylite 165  
 montmorillonite 5, 25  
 Mount Gordon Fault Zone *see under* Mount Isa Block  
 Mount Isa Block (Australia)  
   faulting history 289–290  
   geological setting 287–289  
   map 288  
 Mount Gordon Fault Zone  
   relative age analysis 291–292  
   domains 292–294  
   geometrical assumptions 295–297  
     validity 299–300  
   initial orientation 292  
   modifications 297–298  
   predicted evolution  
     description 300–302  
     discussion 302–305  
     summary 305–308  
   timing and orientation 290–291  
 Murrumbidgee Group 204, 206  
 mylonite 6, 7, 8, 135  
   Grizzly Creek Shear Zone 135–136, 139, 143–144  
   Heier’s Zone (Norway) 171–173, 182
- Nankai accretionary prism 268, 269  
 Nankai Trough 17  
   mega-splay 315  
   slip rate 90  
 Nankaido earthquake (1946) 315  
 NanTroSeize experiment 17  
 Naukluft Thrust (Namibia) 6  
 New Zealand  
   hydrothermal systems 251  
   Southern Alps, fluid flow regime 260–262  
   *see also* Alpine Fault Zone; Chrystalls Beach Complex;  
   Hikurangi margin  
 Nobi earthquake (1891) 319  
 Nojima Fault 18, 19  
   drilling project 11  
     energy budgeting 23  
     fault characterization 18–20  
     fluid budgeting 23–25  
     healing 25  
     logging during drilling 18  
     principal slip zone 20  
     pseudotachylites 20–23  
     summary 25–26  
 normal faults 169  
   Eidsfjord Shear Zone 169, 170, 171  
     deformation timing 173  
     microstructures 176, 178, 179  
     mylonites 171–173  
     petrology 173–174  
     pseudotachylite 175  
       thermobarometry  
         methods 177, 178, 181  
         results 180, 181–182  
         results discussed 182–183  
   Fiskfjord Shear Zone 169, 170, 171  
     microstructures 179  
     petrology 174, 176  
     pseudotachylite

- normal faults (*continued*)
  - thermobarometry 176
  - methods 177, 178, 181
  - results **180**, 181–182
  - results discussed 182–183
- H and L splays 313, 314, 316
- modelling kinematics and stress *191, 192, 193, 194, 195, 197*
- Zuccale Fault (Elba) 98, 99–100
  - field description *101, 102, 103, 104*
  - microstructures
    - amphibole schists 104
    - calcite-ultramylonites 105–106
    - fault breccias 107
    - fault gouges 107–108
    - foliated cataclasites 106–107
    - phyllonites 104–105
  - significance of rock sequence 108–110
  - zonation *100*
- North America *see* Kodiak Island
- Norway *see* Eidsfjord Shear Zone; Fiskfjord Shear Zone
- numerical modelling
  - stress field and faulting
    - method 188–190
    - results 190–192
    - results discussed 192–198
- $\delta^{18}\text{C}$ 
  - carbonate veins
    - East Anatolian and Dead Sea Fault Zones
      - methods of analysis 232
      - results **233, 235, 236–237, 238, 240, 241**
      - results discussed 242–244
    - methods of analysis 211–212
    - results *213, 214, 215, 216, 217*
    - results discussed 218–221, 224
- Taiwan Slate Belt veins 255, 257, 258, 260
- olistostromes 59
- olivine, deformation temperatures 4
- Otago Schist 67
- Otago University vii
- Outer Hebrides vii
- Pasagshak Point Thrust *see under* Kodiak Island
- permeability, relation to strain in Taiwan 257–258
- phacoids 60
- phyllonites, Zuccale Fault 102–103, 104–105
- pinch-and-swell 63, 65
- plate boundaries and seismogenic zones 320–321
- Porto Azzuro pluton 99
- pressure solution (solution creep) 3, 5, 77, 79, 86, 87, 88, 90, 92
  - cleavage 58
- principal slip zone
  - character 39
  - identification 20
- pseudotachylite vii 5, 6, 135
  - Alpine Fault System 116
    - formation
      - controls 125, 127–128
      - depth 125, **130**
      - temperature **130**
- habitats
  - type i 120, **121**
  - type ii 120, **121, 122**
  - type iii **121, 122**
  - type iv **121, 122–123**
- host rock and chemical relationships 120
- host rock and morphology 116–120
- melt phase proof 123–125, *128, 130*
- microtextures *126*
- relation to seismicity 128–129, 131–132
- summary 132
- black fault rock, Pasagshak Point Thrust *79, 88–89*
- co-occurrence with mylonite 135–136
  - Grizzly Creek Shear Zone 139–143
- formation 7, 8, 77, 115, 153
- Nojima Fault 20–23
- Heier's Zone *175*
  - thermobarometry study
    - methods 177, 178, 181
    - results **180, 181–182**
    - results discussed 182–183
- Serre Massif
  - methods of analysis 156
  - results
    - geochemistry 161, **162, 163**
    - petrography
      - matrix 159–160
      - rock fragments 159
      - veins 157–159
      - wall rocks 156–157
    - results discussed 163–166
- pyrrhotite, Chelungpu Fault 30
- quartz
  - deformation temperatures 4, 7
  - Serre Massif pseudotachylite 156, 159, *160, 165*
  - veins, Taiwan 254, 255
  - velocity-strengthening 9
- quartzofeldspathic rocks, deformation 7
- ramps and flats 316
- rare earth elements
  - calcite veins
    - East Anatolian and Dead Sea Fault Zones
      - methods of analysis 232
      - results **234, 235, 237, 240, 241**
      - results discussed 241–242, 243–244
    - Taemas Vein Swarm 204, 215, 217, 223–224
- Rayleigh-type waves 39
- Red Canyon Fault 316–317
- relative age analysis
  - Mount Gordon Fault Zone 291–292
    - domains 292–294
    - geometrical assumptions 295–297
      - validity 299–300
    - initial orientation 292
    - modifications 297–298
    - predicted evolution 300–302
      - results discussed 302–305
      - summary 305–308
- reverse faults, modelling kinematics and stress *191, 192, 193, 194, 195, 197*
- rheology and seismic style 7, 55

- rift settings, seismicity 169  
 rupture characteristics 10  
 Ryoke granodiorite 20, 21
- S-C fabric 59, 60, 84  
 Saint-Barthélemy Massif 147  
 San Andreas Fault, H and L splays 313  
 San Andreas Fault Observatory at Depth (SAFOD) 11, 17  
 borehole 41–43  
 deep rock damage modelling  
     method 45  
     results 45–49  
     results discussed 49–51  
 fault-zone guided waves 44–45  
 low-velocity zone 43–44, 49  
 setting 40–41
- San Andreas Fault System 7  
 San Francisco earthquake (1906) 319  
 Sansepolcru Basin 316, 317  
 Santa Barbara, University of California vii  
 seismic coupling 7  
 seismic moment 9–10  
 seismic slip 77, 90  
 seismic tremor 71, 72  
 seismic-aseismic transition zone 8, 9, 63  
 seismogenic deformation, Taiwan 257–258  
 seismogenic rupture 135  
 seismogenic zones 8, 9  
     conditions of failure 322–323  
     earthquake effects 323–324  
         fault rupture 324–325  
         ground shaking 324, 325–326  
         stress changes 324, 326–327  
         summary 327–328  
 plate positions  
     continental 320  
     oceanic 320–321  
     subducting lithosphere 321  
     transcrustal megathrust 321  
 thermal control 55
- Serre Massif  
 geological setting 154  
 map 155  
 pseudotachylite study  
     methods of analysis 156  
     results  
         geochemistry 161, **162**, 163  
         petrography  
             matrix 159–160  
             rock fragments 159  
             veins 157–159  
         wall rocks 156–157  
     results discussed 163–166
- shear  
 accommodation at convergence 55  
 displacement 319, **320**, 324  
 experiments  
 cataclasite formation 86–87  
     foliated 87  
     non-foliated 87–88  
 fractures and failure 65, 66  
 zones  
 Eidsfjord Shear Zone
- deformation timing 173  
 microstructures 176, 178, 179  
 mylonites 171–173  
 petrology 173–174  
 pseudotachylite 175  
     thermobarometry  
         methods 177, 178, 181  
         results **180**, 181–182  
         results discussed 182–183
- Fiskfjord Shear Zone 169  
 microstructures 179  
 petrology 174, 176  
 pseudotachylite  
     thermobarometry 176  
         methods 177, 178, 181  
         results **180**, 181–182  
         results discussed 182–183
- Grebe Shear Zone 6  
 Grizzly Creek Shear Zone 136–137, 138, 139, 148  
 coexisting tectonite paradox 145  
     cyclicity 145  
     structure and anisotropy 145–147  
 lithological units 137, 139  
 tectonites  
     mylonite 139, 142  
     mylonitic pseudotachylite 143–144  
     pseudotachylite 139–143  
     ultramylonite 144
- Sibson, R. H. vii, viii 1
- siderite **24**, 25
- sillimanite, Serre Massif pseudotachylite 156, 159, 165
- slickenfibres 58, 60, 61, 62, 71  
 Taemas Vein Swarm 208
- slickenlines  
 Dead Sea Fault Zone 235, 236, 237  
 Taemas Vein Swarm 208
- slip, accommodation styles 55  
 slip magnitude 319, **320**, 324  
 slip rate/velocity 18, 26, 324  
     relation to strain 90  
     types 77, 79  
 slip zones, character 39, 278–279  
 slip-hardening 4  
 slow-slip events 69, 71, 72, 77, 90, 319  
 smectite 25, 274, 275, 277  
 solution creep *see* pressure solution  
 South Alaska subduction zone 90  
 Southern Alps (NZ), fluid flow budget 260–262  
 Sovara splay fault 316, 317  
 splay faults 313, 314, 315, 316, 317–318  
 Sr isotope analysis  
     carbonate veins  
         methods 212  
         results 213, 214, 215, 216, 217, 218  
         results discussed 219–220, 224
- strain rates 90, 92, 135  
 Taiwan 257–258  
 stress, role in deformation 4  
 stress cycling 327  
 stress drop 10  
 stress and faulting 313  
 stress field variation and faulting 187–188  
     numerical modelling  
         method 188–190

- stress field variation and faulting (*continued*)
   
    results 190–192
   
    results discussed 192–198
- strike-slip faults
   
    H and L splays 313
   
    modelling kinematics and stress 191, 192, 193, 194, 196, 197
- stylolites 65
- subduction thrust on Kodiak Island 78, 79
- Pasagshak Point Thrust
   
    black fault rock 88–89
   
    cataclasites
   
        formation 86
   
        analogue experiments 86–88
   
        textures 82, 83, 84–86
   
        types 80, 81, 84
   
    fault temperature estimates 79–80
   
    seismic cycle and strain rates 90–92
- subduction zones 55, 90
   
    Hikurangi margin 68–72
   
    Nankai Trough 17, 315
- Sumatra–Andaman earthquake (2004) 91, 92, 323
- Taiwan *see* Chelungpu Fault; Chi-chi earthquake
- Taiwan Slate Belt
   
    fluid flow budget 258–260
   
        cf. Southern Alps 260–262
   
    heat flow budget 255–257
   
    hot springs 251, 255
   
    map 250
   
    strain energy and seismicity 257–258
   
    tectonic setting 252–254
   
    vein systems
   
        field setting 253, 254
   
        gold deposits 254–255
   
    talc formation 100, 109
- Taemas Vein Swarm (Australia)
   
    classification 206
   
        bedding-parallel veins 208
   
        extension veins 208–209, 210
   
        fault veins 206
   
    geochemical analysis
   
        methods 211–213
   
        results 213–215
   
            class effects 217–218
   
            outcrop effects 216–217
   
            stratigraphy effects 215–216
   
    results discussed
   
        fluid flow 219–224
   
        fluid sources 218–219
   
        stress levels 224–225
   
    geological setting 204
   
    map 205
   
    stratigraphy 206, 207
   
    textures 209
- temperature
   
    role in deformation 4, 8, 20
   
    role in high-velocity friction heating
   
        experiments 272
   
    role in ion substitution 204
- temperature estimates
   
    Pasagshak Point Thrust 79–80
   
    pseudotachylite formation 130
- textures
   
    deformation 1, 4–5, 7
   
    frictional 5–7
   
    viscous 7
   
    relation to slip rate 5
- thermal budget
   
    Chi-chi earthquake 28
   
    Kobe earthquake 23
- thermal impact 20
- thermal pressurization 129, 267, 268
- thermobarometry
   
    Heier's Zone (Norway)
   
        pseudotachylite 175
   
            methods 177, 178, 181
   
            results 180, 181–182
   
            results discussed 182–183
   
    Pasagshak Point Thrust 79–80
- thrust faults, H and L splays 313, 314, 315, 316
- Tonankai earthquake (1944) 91, 315
- trace element analysis
   
    carbonate veins
   
        methods 212–213
   
        results 214, 215, 217, 219–224
- tremor 71, 72
- Turkey *see* East Anatolian Fault Zone
- Tyrrhenian Basin 99
- U/Th dating
   
    East Anatolian and Dead Sea Fault Zones
   
        method 232
   
        results 239, 240, 241
   
        results discussed 242, 243, 244, 245
   
    ultracataclasites 5, 6, 123
   
        Chelungpu Fault 28–29, 30
   
        Nojima fault 20, 21, 23
   
    ultramylonites 123, 144
   
        calcite 102–103, 105–106, 108
   
        Eidsfjord Shear Zone 173
- USA *see* Grizzly Creek Shear Zone; Kodiak Island
- veins
   
    Dead Sea Fault Zone 230, 231–232
   
    vein geochemistry
   
        methods of analysis 232
   
        results 233, 234, 235–241
   
        results discussed 242–244
   
    East Anatolian Fault Zone 230, 231–232
   
        vein geochemistry
   
            methods of analysis 232
   
            results 233, 234, 235
   
            results discussed 241–242
   
    Taiwan Slate Belt
   
        field setting 253, 254
   
        fluid flow analyses 255, 258–260
   
        gold deposits 254–255
   
    Taemas Vein Swarm 204, 205, 206, 207
   
        classification 206
   
            bedding-parallel veins 208
   
            extension veins 208–209, 210
   
            fault veins 206
   
        geochemical analysis
   
            methods 211–213
   
            results 213–215

- class effects 217–218  
outcrop effects 216–217  
stratigraphy effects 215–216  
results discussed  
    fluid flow 219–224  
    fluid sources 218–219  
    stress levels 224–225  
textures 209  
velocity strengthening 3, 4, 5, 9  
velocity weakening 3, 4, 5, 9  
vesicles 125, 127  
viscous creep 7  
viscous flow, role in mineral deformation 4  
vitrinite reflectance studies 79–80, 268  
  
waveguide 39, 44, 45  
Wenchuan earthquake Fault Scientific Drilling  
    (WFSD) 17  
West Wairarapa Fault 319  
  
Woodroffe Thrust 147  
World Stress Map Project 313  
  
XRD analysis, fault gouge 101, 272–274, 275, 277  
  
zeolites **24**  
Zuccale Fault (Elba) 98, 99–100  
    fault rocks  
        field site description 101, 102, 103, 104  
        methods of analysis 101  
        microstructures  
            amphibole schists 104  
            calcite-ultramylonites 105–106  
            fault breccias 107  
            fault gouges 107–108  
            foliated cataclasites 106–107  
            phyllonites 104–105  
        significance of rock sequence 108–110  
        zonation 100

Professor Richard (Rick) Sibson revolutionized structural geology by illustrating that fault rocks contain an integrated record of earthquakes. Fault-rock textures develop in response to geological and physical variables such as composition, environmental conditions (e.g. temperature and pressure), fluid presence and strain rate. These parameters also determine the rate- and state-variable frictional stability of a fault, the dominant mineral deformation mechanism and shear strength, and ultimately control the partitioning between seismic and aseismic deformation. This volume contains a collection of papers that address the geological record of earthquake faulting from field-based or theoretical perspectives. The papers cover observations in active fault zones, the relationships between fault rocks and fault-slip styles, interpretation of fault-rock textures from the base of the seismogenic zone, consideration of the effects of fluids on faulting, discussion of fault reactivation v. initiation, and a review of future directions in geological earthquake research by Professor Sibson.